MULTISCALE LATTICES AND COMPOSITE MATERIALS: OPTIMAL DESIGN, MODELING AND CHARACTERIZATION

EDITED BY: Fernando Fraternali, Chiara Daraio and Julian J. Rimoli
PUBLISHED IN: Frontiers in Materials

frontiers Research Topics

ISSN 1664-8714
ISBN 978-2-88963-185-8
DOI 10.3389/978-2-88963-185-8

About Frontiers

Frontiers is more than just an open-access publisher of scholarly articles: it is a pioneering approach to the world of academia, radically improving the way scholarly research is managed. The grand vision of Frontiers is a world where all people have an equal opportunity to seek, share and generate knowledge. Frontiers provides immediate and permanent online open access to all its publications, but this alone is not enough to realize our grand goals.

Frontiers Journal Series

The Frontiers Journal Series is a multi-tier and interdisciplinary set of open-access, online journals, promising a paradigm shift from the current review, selection and dissemination processes in academic publishing. All Frontiers journals are driven by researchers for researchers; therefore, they constitute a service to the scholarly community. At the same time, the Frontiers Journal Series operates on a revolutionary invention, the tiered publishing system, initially addressing specific communities of scholars, and gradually climbing up to broader public understanding, thus serving the interests of the lay society, too.

Dedication to Quality

Each Frontiers article is a landmark of the highest quality, thanks to genuinely collaborative interactions between authors and review editors, who include some of the world's best academicians. Research must be certified by peers before entering a stream of knowledge that may eventually reach the public - and shape society; therefore, Frontiers only applies the most rigorous and unbiased reviews.
Frontiers revolutionizes research publishing by freely delivering the most outstanding research, evaluated with no bias from both the academic and social point of view. By applying the most advanced information technologies, Frontiers is catapulting scholarly publishing into a new generation.

What are Frontiers Research Topics?

Frontiers Research Topics are very popular trademarks of the Frontiers Journals Series: they are collections of at least ten articles, all centered on a particular subject. With their unique mix of varied contributions from Original Research to Review Articles, Frontiers Research Topics unify the most influential researchers, the latest key findings and historical advances in a hot research area! Find out more on how to host your own Frontiers Research Topic or contribute to one as an author by contacting the Frontiers Editorial Office: researchtopics@frontiersin.org

MULTISCALE LATTICES AND COMPOSITE MATERIALS: OPTIMAL DESIGN, MODELING AND CHARACTERIZATION

Topic Editors:
Fernando Fraternali, University of Salerno, Italy
Chiara Daraio, California Institute of Technology, United States
Julian J. Rimoli, Georgia Institute of Technology, United States

Citation: Fraternali, F., Daraio, C., Rimoli, J. J., eds. (2019). Multiscale Lattices and Composite Materials: Optimal Design, Modeling and Characterization. Lausanne: Frontiers Media. doi: 10.3389/978-2-88963-185-8

Table of Contents

frontiers in Materials

EDITORIAL
published: 20 August 2019
doi: 10.3389/fmats.2019.00199

Editorial: Multiscale Lattices and Composite Materials: Optimal Design, Modeling and Characterization

Fernando Fraternali[1]*, *Chiara Daraio*[2] *and Julian Rimoli*[3]

[1] *Department of Civil Engineering, University of Salerno, Fisciano, Italy,* [2] *Division of Engineering and Applied Science, California Institute of Technology, Pasadena, CA, United States,* [3] *School of Aerospace Engineering, Georgia Tech, Atalnta, GA, United States*

Keywords: lattice materials, mechanical metamaterials, innovative composites, multiscale mechanics, structural health monitoring, hyperspectral imaging

Editorial on the Research Topic

Multiscale Lattices and Composite Materials: Optimal Design, Modeling and Characterization

OPEN ACCESS

Edited by:
Nicola Maria Pugno,
University of Trento, Italy

Reviewed by:
Marco Miniaci,
Swiss Federal Laboratories for Materials Science and Technology, Switzerland

****Correspondence:***
Fernando Fraternali
f.fraternali@unisa.it

Specialty section:
This article was submitted to Mechanics of Materials, a section of the journal Frontiers in Materials

Received: *20 May 2019*
Accepted: *05 August 2019*
Published: *20 August 2019*

Citation:
Fraternali F, Daraio C and Rimoli J (2019) Editorial: Multiscale Lattices and Composite Materials: Optimal Design, Modeling and Characterization. Front. Mater. 6:199. doi: 10.3389/fmats.2019.00199

The Research Topic "Multiscale lattices and composite materials:" (MLCM) is focused on the optimal design, modeling, and characterization of novel lattices, composite materials, and structures at different scales, through the control of the internal architecture of the system.

A fundamental goal of this article collection is the study of mechanical metamaterials that are able to form next-generation-generation cellular solids; lattice materials, multiscale composites; and structural-scale systems. The collection took inspiration from the peculiar behaviors exhibited by structured materials at multiple scales (Bosia et al., 2018). The latter include, for example, high stiffness, strength, and toughness at extremely low densities (Meza et al., 2014), phononic band-gaps (Lu et al., 2009), sound control ability (Cummer et al., 2016); negative effective mass density (Liu et al., 2000); localized confined waves (Theocharis et al., 2013), to name but a few examples. The research reported devoted special attention to the creation of complex mechanical systems with properties derived mainly from their geometric design rather than their chemical composition (Cummer et al., 2016; Bertoldi et al., 2017). Also investigated was the use of multiscale lattices to optimally design reinforcing elements for novel composite materials (Fleck et al., 2010; Li et al., 2014). The chosen modeling and experimental approaches were able to predict and characterize the intrinsically complex mechanical behavior of the analyzed systems through multiscale techniques.

The papers forming the MLCM collection can be grouped into two basic categories. The first of these is centered around the design, modeling, and characterization of lattice structures at different scales, through the maximization of the frequency bandgap width at suitable center frequencies (Arretche and Matlack; Bacigalupo et al.); the optimal design and mechanical modeling of tensegrity metamaterials (De Tommasi et al.), superstable pre-stressed networks (Kelly et al.), graphene sheets (Genoese et al.); dome-shaped auxetic metamaterials (Easey et al.); and solar façades that employ dynamic sunscreens with tensegrity architecture (Babilio et al.). This first group of papers also includes contributions dealing with the development of non-destructive testing and structural health monitoring techniques that make use of guided elastic waves (Miniaci et al.), as well as the experimental characterization of the microstructure of the Nephila dragline silk (Stehling et al.).

A second category focuses on the modeling and characterization of novel composite materials, with emphasis on the mechanical properties, for example, of bamboo fiber-reinforced composites (Javadian et al.); the effects of defects, porosity, and damage on the mechanical properties of metallic materials to be employed in additive manufacturing processes (Goodall et al.); the macroscopic response of micropolar continua with anisotropic microstructure (Fantuzzi et al.); the addition of lattice-shaped inclusions to metaconcretes (Briccola et al.); and the propagation of pressure waves in three-dimensional arrangements of coated spheres (Dupont et al.).

Our hope is that the research presented in this collection will stimulate new and exciting research in the fields of mechanical metamaterials and multiscale composite materials and structures, through an integrated approach that includes the design and the mechanical modeling of real-scale, or reduced-scale prototypes; the optimal control of suitable design variables; and the experimental validation of the theoretical predictions.

AUTHOR CONTRIBUTIONS

All authors listed have made a substantial, direct and intellectual contribution to the work, and approved it for publication.

REFERENCES

Bertoldi, K., Vitelli, V., Christensen, J., and Van Hecke, M. (2017). Flexible mechanical metamaterials. *Nat. Rev. Mater.* 2:17066. doi: 10.1038/natrevmats.2017.66

Bosia, F., Krushynska, A. O., Miniaci, M., Morvan, B., and Pugno, N. M. (2018). Editorial: advances in mechanical metamaterials. *Front. Mater.* 5:56. doi: 10.3389/fmats.2018.00056

Cummer, S. A., Christensen, J., and Alu, A. (2016). Controlling sound with acoustic metamaterials. *Nat. Rev. Mater.* 1:16001. doi: 10.1038/natrevmats.2016.1

Fleck, N. A., Deshpande, V. S., and Ashby, M. F. (2010). Micro-architectured materials: past, present and future. *Proc. R. Soc. A* 466, 2495–2516. doi: 10.1098/rspa.2010.0215

Li, J., Wu, Z., Huang, C., and Li, L. (2014). Multiscale carbon nanotube-woven glass fiber reinforced cyanate ester/epoxy composites for enhanced mechanical and thermal properties. *Compos. Sci. Technol.* 104, 81–88. doi: 10.1016/j.compscitech.2014.09.007

Liu, Z., Zhang, X., Mao, Y., Zhu, Y. Y., Yang, Z., Chan, C. T., et al. (2000). Locally resonant sonic materials. *Science* 289, 1734–1736. doi: 10.1016/S0921-4526(03)00487-3

Lu, M. H., Feng, L., and Chen, Y. F. (2009). Phononic crystals and acoustic metamaterials. *Mater. Today* 12, 34–42. doi: 10.1016/S1369-7021(09)70315-3

Meza, L. R., Das, S., and Greer, J., R. (2014). Strong, lightweight, and recoverable three-dimensional ceramic nanolattices. *Science* 345, 1322–1326. doi: 10.1126/science.1255908

Theocharis, G., Boechler, N., and Daraio, C. (2013). "Nonlinear phononic structures and metamaterials," in *Acoustic Matematerials and Phononic Crystals,* ed P. A. Deymier (Berlin; Heidelberg: Springer-Verlag), 173.

Conflict of Interest Statement: The authors declare that the research was conducted in the absence of any commercial or financial relationships that could be construed as a potential conflict of interest.

The handling editor declared a past collaboration with the authors FF, CD.

frontiers in Materials

ORIGINAL RESEARCH
published: 20 November 2018
doi: 10.3389/fmats.2018.00068

On the Interrelationship Between Static and Vibration Mitigation Properties of Architected Metastructures

*Ignacio Arretche and Kathryn H. Matlack**

Department Mechanical Science and Engineering, University of Illinois Urbana-Champaign, Urbana, IL, United States

Continuous demand for improvement of material performance in structural applications pushes the need for materials that are able to fulfill multiple functions. Extensive work on effective static properties of different architected materials have shown their ability to push the modulus-density design space, in terms of high effective moduli at low relative density. On the other hand, variations in geometry allow for these materials to manipulate mechanical wave propagation, producing band gaps at certain frequency ranges. The enhanced static and vibration properties of architected metamaterials make them ideal candidates for multi-functional purposes. In this paper, we take inspiration from the mass-efficient static behavior of different lattice geometries to fully explore the capabilities of a periodic and locally resonant metastructure design platform. We numerically study the influence of four different lattice topologies on the dynamic and static behavior of metastructures that combine a periodic lattice geometry with locally resonant inclusions. We analyze the influence of lattice geometry on band gap frequencies in terms of the lattice effective static properties. We show that vibration mitigation over a wide range of frequencies is achieved by tailoring the lattice geometry for constant unit cell mass and size. Specifically, by selectively placing material inside the unit cell, we achieve up to a 6-fold change of lower edge band gap frequency and up to an 8-fold change of normalized band gap width, for metastructures with low-density lattices. We introduce multi-functional performance parameters to evaluate the metastructures in terms of their effective static stiffness and band gap properties. These parameters can inform the design of tailored materials that have desired mechanical and dynamic properties for applications in e.g., aerospace and automotive components, and energy infrastructure.

Keywords: metamaterials, multifunctionality, vibration mitigation, architected materials, band gaps

OPEN ACCESS

Edited by:
Fernando Fraternali,
University of Salerno, Italy

Reviewed by:
Enrico Babilio,
Università degli Studi di Napoli
Federico II, Italy
Juan Manuel Munoz-Guijosa,
Universidad Politécnica de Madrid
(UPM), Spain

****Correspondence:***
Kathryn H. Matlack
kmatlack@illinois.edu

Specialty section:
This article was submitted to
Mechanics of Materials,
a section of the journal
Frontiers in Materials

Received: *24 August 2018*
Accepted: *29 October 2018*
Published: *20 November 2018*

Citation:
Arretche I and Matlack KH (2018) On the Interrelationship Between Static and Vibration Mitigation Properties of Architected Metastructures.
Front. Mater. 5:68.
doi: 10.3389/fmats.2018.00068

INTRODUCTION

Modern engineering continuously pushes the need for higher levels of mass efficiency. Light, load bearing materials on aerospace, aircraft, and automotive components are fundamental for the pursuit of higher performing systems. In addition, vibration propagation control is not only crucial for customer satisfaction, especially in aircraft, and automotive systems, but also for the safety of the components such us protecting satellites or electronic equipment from their dynamic environment during satellite launch. In many cases, suppressing vibrations typically require additional damping material or active control mechanisms. A stiff, mass efficient material that additionally includes vibration control capabilities can avoid the need to add alternative vibration attenuation mechanisms.

Architected materials have shown enhanced static properties as well as the ability to control elastic wave propagation, making them ideal for multifunctional applications. On one hand, they have opened up new areas of the material property space. This, in addition to evolving 3D printing techniques that enable their manufacturing, have motivated researchers to explore a variety of architectures (Schaedler and Carter, 2016) ranging from lattice topologies (Gibson and Ashby, 1997; Deshpande et al., 2001b; Luxner et al., 2004; Moongkhamklang et al., 2010; Vigliotti and Pasini, 2012; Zheng et al., 2014), foam-like metamaterials (Berger et al., 2017) triply periodic minimal surface geometries (Wang et al., 2011; Dalaq et al., 2016), hierarchical structures (Doty et al., 2012; Meza et al., 2015), honeycomb structures (Gibson and Ashby, 1997; Wadley, 2006; Fleck et al., 2010), and woven topologies (Erdeniz et al., 2015; Ryan et al., 2015; Zhang et al., 2015).

On the other hand, through Bragg scattering and local resonance phenomena, architected materials have shown to support band gap formation (Deymier, 2013; Hussein et al., 2014 and references therein; Bayat and Gaitanaros, 2018). Particularly, recent efforts have been made targeting low and broadband band gaps. Wang et al. (2015) demonstrated that locally resonant band gaps can be achieved in 2D periodic lattices by tuning their connectivity; D'Alessandro et al. (2016) and D'Alessandro et al. (2018) developed a 3D single-phase phononic crystal that shows ultra-wide complete band gaps. Taniker and Yilmaz (2015) use inertial amplification mechanisms to obtain wide and low frequency band gaps in an octahedron lattice.

These enhanced dynamic and static properties make architected materials promising for multifunctional applications. For example, previous investigations have explored architected materials with static, thermo-mechanical and energy absorption properties (Evans et al., 1998, 2001; Wadley, 2006; Valdevit et al., 2011; Wang et al., 2011, 2017; Dou et al., 2018), tunable Poisson's ratio and vibration mitigation (Chen et al., 2017), and honeycomb sandwich panel structures that are stiff and can attenuate noise (Han et al., 2017; Tang et al., 2017). The relationship between static and band gap properties of architected materials has also been studied in the literature (Phani et al., 2006; Nemat-Nasser et al., 2011).

Here we build on this prior work, and we present a systematic comparison of static elastic properties to band gap properties in metastructures, and a way to interpret the band gap frequencies in terms of local static effective properties of their constituents. To do this, we expand the design space of metastructures that combine geometric lattices with embedded resonators, originally introduced in Matlack et al. (2016). We study this metastructure design because it has numerically and experimentally shown to support tailorable band gaps through small manipulations of its lattice geometry. Band gaps in these metastructures are bounded between acoustic modes and optical modes, which makes them particularly suitable for achieving low frequency band gaps. Further, it is a 3D structure so it could conceivably be incorporated into structural components, and a straightforward manufacturing procedure was previously introduced to fabricate these metastructures (Matlack et al., 2016). The main objectives of this paper are to show how this metastructure design platform can achieve band gaps across different frequency ranges, to understand why different metastructures have different band gaps, and to understand the trade-offs between their band gap frequencies and widths and their static stiffness.

In this article, we analyze four different lattice-resonator metastructures with different lattice topologies: cubic, Kelvin, octet and idealized foam. We use finite element methods (FEM) to numerically analyze their static and dynamic behaviors. We analyze the effective static properties of both the individual lattices and the metastructures, for lattice relative densities ranging from 1% to 28%. We analyze wave propagation through metastructures with 1D periodicity, to understand the influences of lattice geometry and relative density on their band gaps. Modal analysis is used to qualitatively explain the differences in the dispersion curves in terms of the interaction between the lattice and resonators, as well as lattice effective properties. We calculate vibration transmission through finite metastructures to study the efficiency of wave mitigation. Finally, we compare the metastructure's dynamic performance in terms of their broadband and low-frequency band gap characteristics and introduce multifunctional performance parameters that evaluate the metastructures in terms of their vibration mitigation behavior and static stiffness.

METASTRUCTURE GEOMETRIES

The metastructures studied combine a periodic lattice geometry with embedded local resonators, introduced previously (Matlack et al., 2016). These metastructure unit cells (**Figure 1B**) are composed of an array of lattice unit cells modeled as polycarbonate (**Figure 1A**) with an embedded solid steel cube resonator. Four different lattice unit cells are studied: idealized foam (Gibson and Ashby, 1982), Kelvin or tetrakaidekahedron, cubic, and octet (**Figure 1A**). The metastructure unit cells studied contain a *5L x 5L x 6L* array of the lattice (**Figure 1B**). Note the *6L* dimension along the length is to accommodate the idealized foam geometry configuration.

The idealized foam lattice is based on the geometry originally proposed by Gibson and Ashby (Gibson and Ashby, 1982). It is designed to contain 3 struts at each node in order to introduce bending deformations in a cubic unit cell, which results in a modified cubic unit cell of *2L* to maintain a cube side length of *L*. All other lattices geometries contain a unit cell length of *L*. Finite metastructures explored in the multifunctional analysis are configured as 6 metastructure unit cells in length (**Figure 1C**) since it has been shown that this is enough to approximate band gaps of an infinitely periodic medium (Matlack et al., 2016).

The static properties of the lattice geometries and the static and dynamic properties of the metastructures are evaluated in terms of the relative density of their *lattice* unit cells (ρ_{rel}). We hold the lattice unit cell length (L) constant and vary the thickness (t) to achieve lattice relative densities from 1% to 28% without

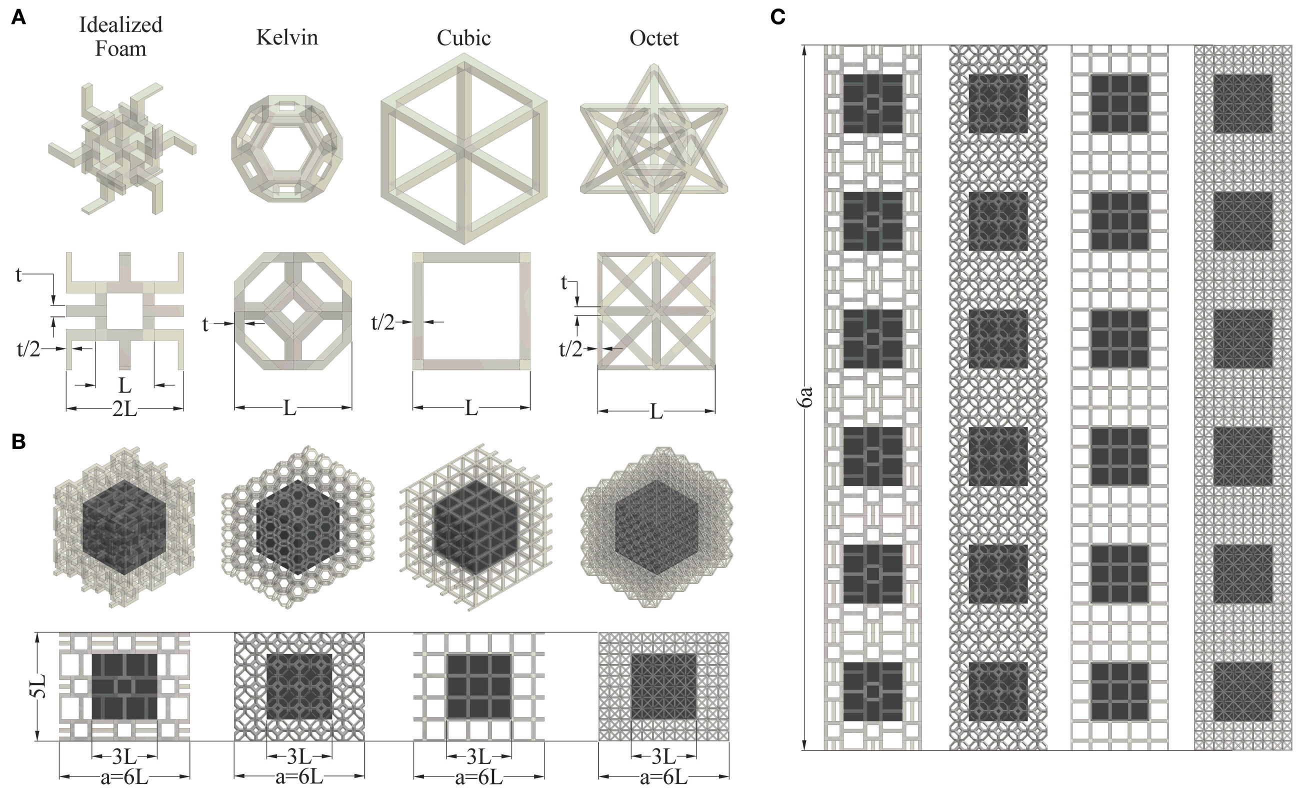

FIGURE 1 | Metastructure geometries. **(A)** Lattice unit cells. **(B)** Metastructure unit cells. **(C)** Finite metastructures.

TABLE 1 | Dimensions of the metastructures studied.

t (mm)	ρ_{rel} (%)	L (mm)	a (mm)
swept	1→ 28	4	24

changing the metastructure periodicity constant (*a*). Geometry dimensions of the lattices are given in **Table 1**.

We must explicitly point out that ρ_{rel} does not include the resonator, whose mass and size remains constant across all metastructures presented here. Including the resonator, the *metastructure* relative densities studied here range from 61% to 72%, where 100% relative density represents the steel resonator embedded in bulk polycarbonate. We present results in terms of lattice relative density to highlight the differences in band gaps that can be achieve due only to differences in geometry, while keeping the total mass constant. This treatment also allows us to confirm the lattice unit cell static results to those in the literature (e.g., Gibson and Ashby, 1982; Deshpande et al., 2001b; Luxner et al., 2004; Zheng et al., 2014), and to interpret band gaps of the metastructures in terms of the lattice unit cell properties. However, a fair comparison with other vibration mitigation materials should be done in terms of the metastructure relative density, and not the lattice relative density. To address this, we include metastructure relative density as a reference in figures related to metastructure properties.

STATIC PROPERTY RESULTS

Lattice Static Properties

Prior work has shown the ability to open new areas of the stiffness-relative density space through lattice materials, e.g., (Gibson and Ashby, 1982; Deshpande et al., 2001b; Luxner et al., 2004; Zheng et al., 2014). Furthermore, at low relative densities where the strut cross section is small compared to its length and the effects of vertex stiffness do not play a major role, the scaling laws of static effective properties of the lattice material can be described by the following power-law approximations (Gibson and Ashby, 1997):

$$\frac{E_{lattice}}{E_s} = C{\rho_{rel}}^{n} \tag{1}$$

$$\frac{G_{lattice}}{E_s} = D{\rho_{rel}}^{r} \tag{2}$$

where ρ_{rel} is the lattice relative density, C, D, n, and r are proportionality constants and scaling exponents that depend on the lattice geometry, E_s is the Young's modulus of the bulk material and $E_{lattice}$ and $G_{lattice}$ are the lattice effective Young's and shear moduli, respectively. Lattice materials can be further classified into bend- and stretch-dominated structures, depending on the predominant deformation of their struts when exposed to external loading (Deshpande et al., 2001a). Effective

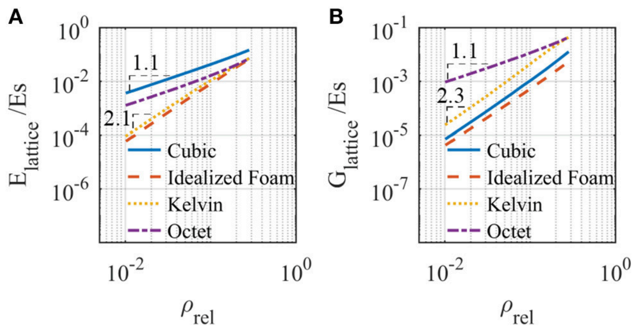

FIGURE 2 | Lattice effective mechanical properties in terms of lattice relative density. Effective **(A)** Young's modulus and **(B)** shear modulus.

TABLE 2 | Scaling exponents and proportionality constants for power-law approximations of $E_{lattice}$ and $G_{lattice}$ for the four lattice geometries.

Geometry	*n*	*r*	C	D
Idealized foam	2.1	2.1	1.1	0.1
Kelvin	2.1	2.3	1.2	0.9
Cubic	1.1	2.2	0.5	0.2
Octet	1.1	1.1	0.2	0.1

moduli of bend-dominated lattices have a quadratic dependence on relative density ($n = 2, r = 2$) while effective moduli of stretch-dominated lattices have a linear dependence ($n = 1$, $r = 1$).

Here, we characterize the effective moduli of the four lattice geometries (without an embedded resonator) presented in **Figure 1A**. We will use these lattice properties to understand the static and dynamic behavior of the metastructures. Results are plotted in double logarithmic scale in **Figure 2** and calculated scaling exponents n and r and proportionality constants C and D are presented in **Table 2**.

We observe a stretch-dominated behavior of the octet lattice and bend-dominated behaviors of Kelvin and idealized foam lattices, consistent with many prior works (Gibson and Ashby, 1982; Deshpande et al., 2001b; Luxner et al., 2004; Zheng et al., 2014). The cubic lattice exhibits a mixed behavior. Under tension or compression, its behavior is stretch-dominated since the struts parallel to the applied force compress while the perpendicular ones have a negligible deformation. However, under shear deformation, struts perpendicular to the load direction bend, and struts parallel to the load direction have negligible deformation, thus its behavior is bend-dominated.

This behavior applies to the low relative density range (up to about 15%). At larger lattice relative densities, the rigidity of the vertex has a larger influence, i.e., bending deformation in stretch-dominated structures and axial deformation in bend-dominated structures cease to be negligible. The moduli at higher relative densities gradually deviate from the presented approximations.

Metastructure Static Properties

We calculate the static stiffness, K_{static}, of finite metastructures shown in **Figure 1C**. The finite metastructures have a beam like geometry, thus we can numerically calculate effective axial (K_{axial}), bending (K_{bend}) and torsional (K_{tors}) stiffnesses using the force-displacement relations that define static stiffness of a conventional cantilever beam (see section Finite Metastructure Static Stiffness). We characterize K_{static} for metastructures to (1) understand the influence of $E_{lattice}$ and $G_{lattice}$ (lattice static properties) on K_{static} (metastructure static properties), and (2) to characterize the multifunctional properties of finite metastructures in terms of their static and dynamic (band gap) properties. We focus on stiffness properties of metastructures (as opposed to modulus values) because due to their beam-like geometry, we can characterize the metastructure static behavior in terms of well-known concepts of beam axial, bending and torsional stiffness.

TABLE 3 | Scaling exponents for power-law approximations of axial, bending, and torsional stiffness of finite metastructures.

Geometry	K_{axial}	K_{bend}	K_{tors}
Idealized foam	2.1	2.2	2.2
Kelvin	2.1	2.1	2.3
Cubic	1.1	1.6→ 1.3	2.2
Octet	1.1	1.1	1.1

The calculated K_{static} of the metastructures as a function of *lattice* relative density (**Figure 3**) follow the power-law approximation in Equation 1 for lattice effective properties. We observe that the scaling exponents of K_{axial} (**Table 3**) agree with those of $E_{lattice}$ (**Table 2**). Thus, we infer that $K_{axial} \propto E_{lattice}$. In the same way, agreement of scaling exponents of K_{tors} (**Table 3**) with those of $G_{lattice}$ (**Table 2**) suggest that $K_{tors} \propto G_{lattice}$. For K_{bend}, both $E_{lattice}$ and $G_{lattice}$ seem to be involved. The transition in slope in the double logarithmic scale of the cubic metastructure (**Figure 3B**) from 1.6 to 1.3 suggests a stronger dependence on $E_{lattice}$ with increasing lattice relative density. This is consistent with shear deformations observed at lower lattice relative density (**Figure 3D**) that decrease in magnitude at higher lattice relative density values (**Figure 3E**). Note the transition is not present in other lattices due to the similar scaling exponents of their $E_{lattice}$ and $G_{lattice}$.

While we keep the resonator size constant throughout all static analyses of finite metastructures in this work, it should be noted that the size of the resonator changes K_{static}. The resonator stiffens the lattice within the metastructure at the lattice-resonator interface, resulting in an overall increase in K_{static}. An increase in resonator surface area increases K_{static}, and an increase in resonator volume also increases K_{static} since the resonator material is significantly stiffer than that of the lattice. As we decrease resonator size, K_{static} asymptotically approaches values of K_{static} for a metastructure made purely of lattice material without a resonator.

WAVE PROPAGATION IN METASTRUCTURES

Band Gaps

The dispersion relations and modal displacements of the four different metastructures for a lattice relative density of 8.3% are

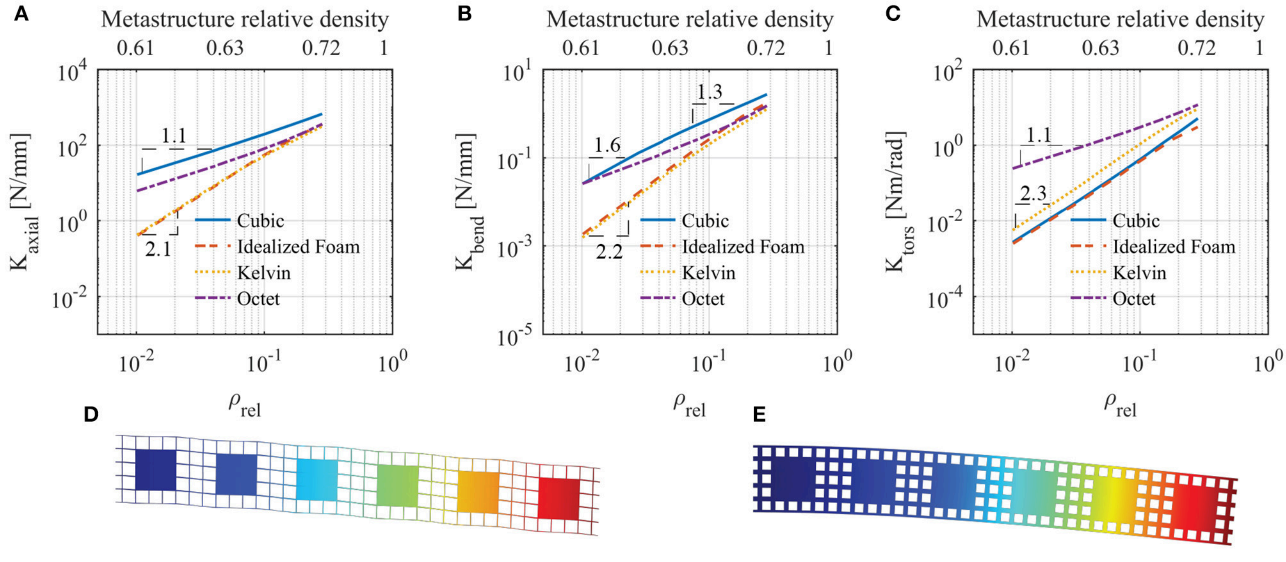

FIGURE 3 | Finite metastructures mechanical properties. **(A)** K_{axial} **(B)** K_{bend} **(C)** K_{tors} **(D)** Deformation of cubic finite metastructure with 1% relative density under bending. **(E)** Deformation of cubic finite metastructure with 28% relative density under bending. Metastructure relative densities are shown for comparison.

presented in **Figure 4**. In order to achieve the same lattice relative density and constant unit cell size across all geometries, we use different lattice thicknesses for the different metastructures. Dispersion curves show that the selective placement of the material inside the lattice unit cell space results in considerable differences in band gaps of the metastructures. The lower edge of the band gap ranges from 1,099 Hz in the idealized foam metastructure to 2579Hz in the octet metastructure. This is about a 2-fold difference without any change in total mass. In the same manner, normalized band gap widths range from 101% in the octet metastructure to 37% in the cubic metastructure (about a 3-fold change in normalized band gap width). These metastructures show a large range of their band gap properties while keeping the total mass constant, solely due to the difference in lattice geometry.

Analyzing Band Gaps in Terms of Lattice Static Properties

Analysis of the modal displacements presented in **Figure 4** shows that the band gaps are generated between lower frequency resonator modes, where most of the modal mass is concentrated in the resonator, and higher frequency lattice modes, where modal mass is concentrated in the lattice. We observe four low-frequency resonator modes: two bending modes, one torsional mode, and one axial mode. As an example, we analyze these modes and their dependence on lattice static properties through the example of the octet metastructure (**Figure 5**). However, this analysis can be extended to other metastructure geometries since, as we observe in **Figure 4**, they show analogous modal displacements to that of the octet.

Resonator Modes

The first bending resonator mode (**Figures 4**a1,b1,c1,d1) is characterized by a translation of the resonator perpendicular to the axis of wave propagation. In this dispersion branch, there are actually two degenerate bending modes due to symmetry and material isotropy. The modal displacements reveal that the transverse motion of the resonator produces shearing of the lattice units to the left and right of the resonator (**Figure 5**d1). From this observation, we infer that the modal stiffness of this mode will be proportional to $G_{lattice}$. This is consistent with the fact that the frequency at the band edge increases with increasing $G_{lattice}$ (in ascending order: idealized foam, cubic, Kelvin, octet).

The second resonator bending mode (**Figures 4** a4,b4,c3,d4) is characterized by a rotation of the resonator about an axis perpendicular to the axis of wave propagation. Like the first bending mode, there are two of these modes (rotation about the *y* and *z*-axis), which are degenerate. Because of its higher order nature, this mode does not start from the origin of the dispersion diagram, thus it is interesting to inspect its evolution along the wavenumber spectrum. At $ka/\pi = 0$ (long wavelength regime) the Floquet boundary conditions (see section Dispersion Relations) impose equal displacement fields on the two faces of periodicity. As a result, the rotation of the resonator generates shearing of the lattice units that surround it (**Figure 5**d4 (***ka/π*=*0***)). The deformation of the unit cells suggest that the modal stiffness of this mode is dominated by $G_{lattice}$. At $ka/\pi = 1$, the Floquet boundary condition impose displacement fields of the periodic faces to be equal in magnitude and opposite in sign. Here, we observe relative displacement in the *y*-direction (or *z* for the analogous mode) between lattice units in front of and behind the resonator as it rotates. These units now stretch or compress (depending on their location) and the shear deformation of top and bottom lattice units seems to be reduced (**Figure 5**d4). From analyzing the mode shapes, we predict that modal stiffness will transition from being proportional to $G_{lattice}$ to being proportional to $E_{lattice}$, as wavenumber increases. We observe that as $G_{lattice}$ increases so do the frequencies

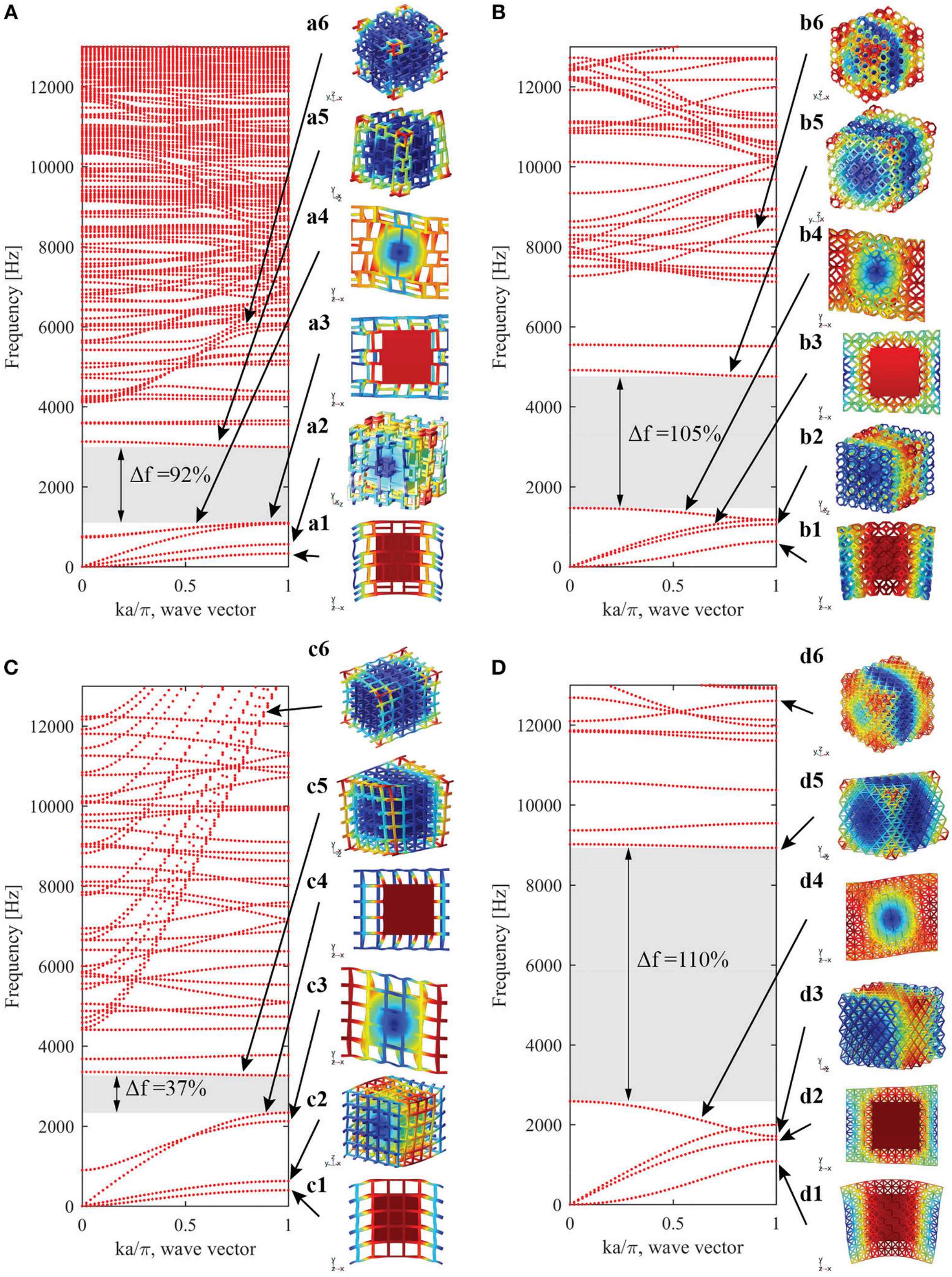

FIGURE 4 | Dispersion relations and modal displacement for the different metastructures with lattice relative density equal to 8.3%. **(A)** Idealized foam. **(B)** Kelvin. **(C)** Cubic **(D)** Octet. (Modal displacements are taken at ka/π=1).

of this mode at the long wavelength edge (idealized foam, cubic, Kelvin, octet in ascending order). Frequencies at the low wavelength edge increase with $E_{lattice}$ (idealized foam, Kelvin, octet, cubic in ascending order). Cubic and idealized foam metastructures exhibit a positive slope of this mode whereas octet and Kelvin metastructures have a negative slope. The relationship between $E_{lattice}$ and $G_{lattice}$ of individual lattices does not solely explain why the sign of the slope of this mode varies among metastructures, so there must be additional influences related to how strongly the lattice properties contribute to modal stiffness and differences in modal mass at $ka/\pi=0$ compared to $ka/\pi=1$.

The torsional resonator mode (**Figures 4**a2,b2,c2,d3) consists of the rotation of the resonator about the axis of wave propagation. This mode involves shear deformation of the lattice unit cells (**Figure 5**d3). The modal displacement increases with *x*-distance from the resonator, and the lattice units

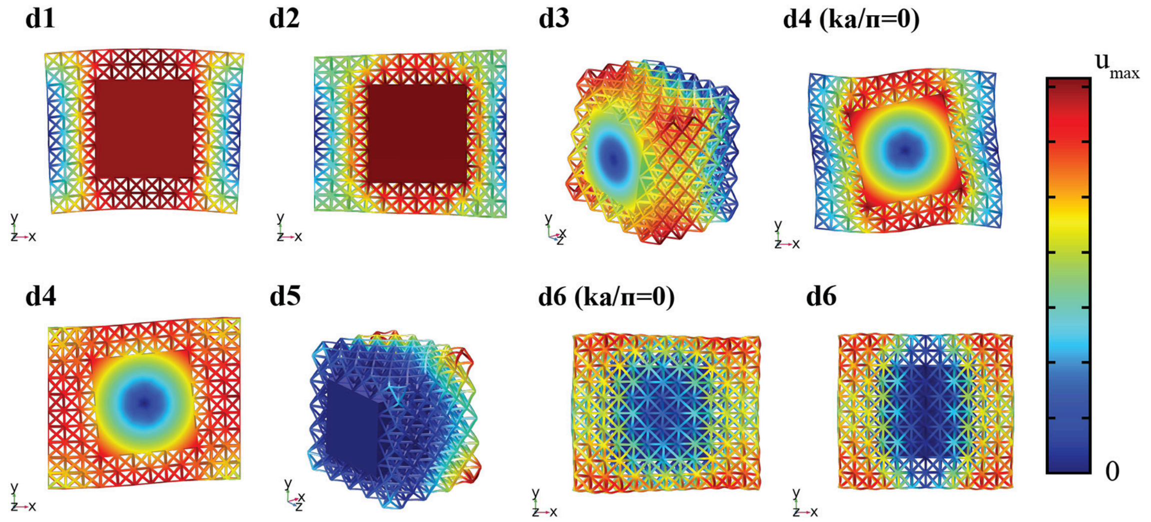

FIGURE 5 | Detailed view of octet modal displacements, according to **Figure 4**. Geometries are cross-sectioned for a better description of motion. Modal displacements are taken at ka/π=1 unless specified.

immediately surrounding the resonator simply rotate without any deformation. We look once more at the dispersion diagram and confirm that the frequency of this mode increases with $G_{lattice}$ (in ascending order: idealized foam, cubic, Kelvin, octet).

In the axial resonator mode (**Figures 4**a3,b3,c4,d2) the resonator translates in the direction of wave propagation. The lattice deforms under both shear and compression/tension depending on their location (**Figure 5**d2). While lattice unit cells to the left and right of the resonator compress and stretch, unit cells located at the top and bottom of the resonator shear. The modal stiffness of this mode is thus dictated by both $E_{lattice}$ and $G_{lattice}$. We inspect the dispersion relations and observe that frequencies of this mode increase with $E_{lattice} + G_{lattice}$ (in ascending order: idealized foam, Kelvin, octet, and cubic). Note this mode was used in prior work to change the number of beams undergoing stretch, to preferentially lower the band gap (Matlack et al., 2016).

We gather further supporting evidence of the effects of lattice effective properties on the metastructure band gaps by observing how modal stiffness of each mode evolves with lattice relative density. Following the form of lattice and metastructure static properties, we predict that the modal stiffness will follow a power-law behavior with respect to the lattice relative density. We calculate the scaling exponents of the best-fit curve of modal stiffness vs. lattice relative density and present them in **Table 4**. We observe that scaling exponents of the 1st bending mode agree quite well with those of $G_{lattice}$ (**Table 2**) for all metastructures. Thus, the modal stiffness 1st bending mode is proportional to $G_{lattice}$. Similarly, we find agreement between scaling exponents of 2nd bending ($ka/\pi = 0$) modal stiffness and $E_{lattice}$, 2nd bending ($ka/\pi = 1$) modal stiffness and $G_{lattice}$, 1st torsional modal stiffness and $G_{lattice}$. The 1st axial modal stiffness depends on both $E_{lattice}$ and $G_{lattice}$ and so it requires special attention. For all lattices except the cubic, their scaling exponents are the same for both $E_{lattice}$ and $G_{lattice}$ and they agree with that of 1st axial modal stiffness. In the cubic case, we observe agreement between cubic $E_{lattice}$ and 1st axial modal stiffness scaling exponent. This is because the cubic $E_{lattice}$ is large compared to its $G_{lattice}$ and the effects of $G_{lattice}$ become negligible.

By analyzing the mode shapes, we conclude that the modal stiffness of the resonator modes depends strongly on the effective properties of the lattice. The first bending modes are dominated by the $G_{lattice}$, the second bending modes transition from being dominated by $G_{lattice}$ to being dominated by $E_{lattice}$, the axial mode is dominated by a combination of $E_{lattice}$ and $G_{lattice}$ and the torsional mode is dominated by the $G_{lattice}$. Since the lower edge of the band gap in these metastructures are generally dominated by the resonator modes, this gives us a way to estimate the lower edge frequency range or inform the design of the metastructure to tune the lower edge of the band gap to the desired frequency range.

Lattice Modes

In the metastructure's high frequency range, the resonator's displacement is negligible, and the modal displacement is isolated in the lattice units (**Figures 4**a5-6,b5-6,c5-6,d5-6). Since the modal mass is much smaller than that of the resonator modes, these modes are generated at higher frequencies. As observed in **Figure 4** there are numerous upper lattice modes. Since we are interested in low frequency band gaps, we will only analyze those that define the upper edge of the first full and polarized band gaps (see section Performance Parameters for polarized band gap definition).

Torsional and full band gaps upper edge is defined by the second torsional mode (**Figures 4**a5,b5,c5,d5). Taking a closer look at the modal displacements it can be observed that since the resonator has small movement so do the faces of the lattice units attached to it (**Figure 5**d5). The displacement of the rest of the unit cell is parallel to the resonator's face and increases further away from it. The displacement visually approximates shearing

TABLE 4 | Scaling exponents for power-law approximations of modal stiffness vs. relative density.

Geometry	1st bending	2nd bending ($ka/\pi=0$)	2nd bending	1st torsional	1st axial	2nd torsional	2nd axial ($ka/\pi=0$)
Idealized foam	2.1	2.1	2.1	2.2	2.4	2.2	2.2
Kelvin	2.3	2.3	2.1	2.3	2.2	2.2	2.3
Cubic	2.2	2.2	1.2	2.2	1.2	2.1	2.2
Octet	1.1	1.1	1.1	1.1	1.2	1.2	1.3

Modal stiffnesses are calculated at $ka/\pi=1$ unless otherwise specified.

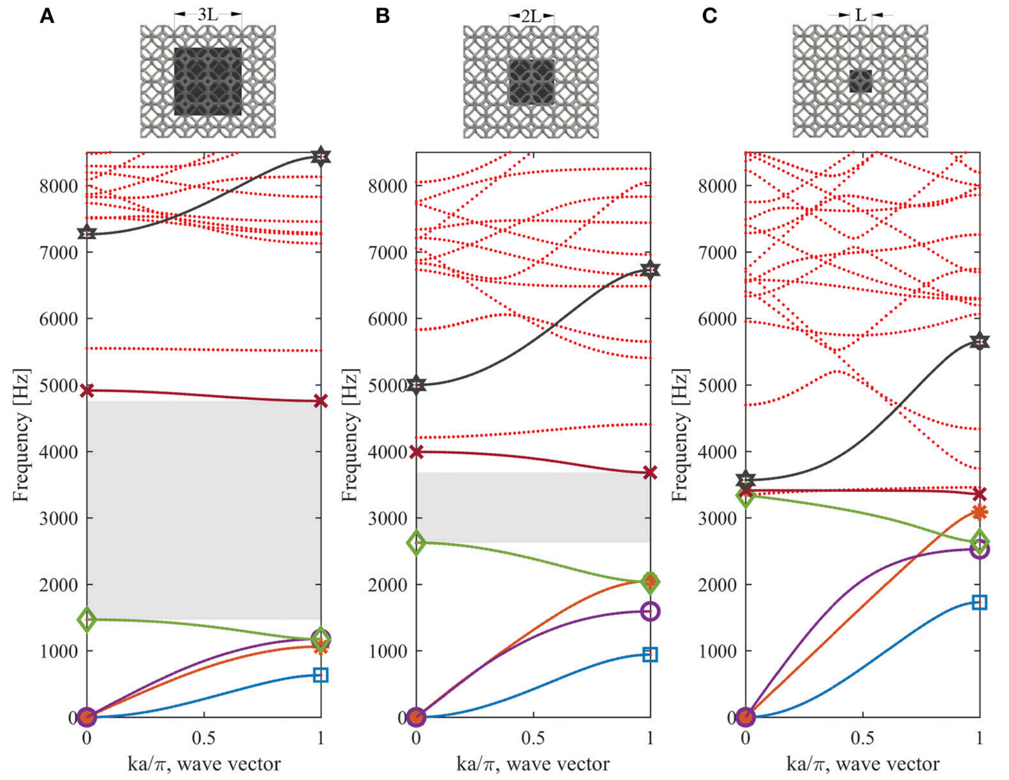

FIGURE 6 | Dispersion relations for the Kelvin metastructure with lattice relative density of 8.3% and resonator side length equal to **(A)** *3L*, **(B)** *2L*, and **(C)** *L*. The lowest band gaps are indicated by gray boxes. Markers indicate the edge frequencies of modes of interest: 1st bending resonator mode (blue-square), torsional resonator mode (orange-asterisk), axial resonator mode (purple-circle), 2nd bending resonator mode (green-diamond), torsional lattice mode (red-cross), and axial lattice mode (gray-star).

of the lattice unit cells, so we hypothesize that this upper mode modal stiffness should primarily depend on $G_{lattice}$. We inspect the dispersion diagrams and find that the upper mode frequencies increase with $G_{lattice}$ (idealized, cubic, Kelvin, octet in ascending order). This is further supported by the good agreement, for all topologies, between scaling exponents of the modal stiffness of the 2nd torsional mode (**Table 4**) and $G_{lattice}$ (**Table 2**).

Upper edge of the axial band gaps is defined by the second axial mode in the long wavelength region (**Figures 4**a6, b6, c6,d6**)**. As in the second torsional mode, we observe shearing of the units that surround the resonator (**Figure** 5d6 (***ka/π=0***)). Thus, we predict that the modal stiffness of this mode at small wavenumber will depend on $G_{lattice}$. We inspect the dispersion curves and observe that the frequencies increase with $G_{lattice}$ (in ascending order: idealized, cubic, Kelvin, octet). We gain further evidence from the good agreement in scaling exponents of 2nd axial mode ($ka/\pi=0$) modal stiffness (**Table 4**) and $G_{lattice}$ (**Table 2**) for cubic, idealized foam, and Kelvin metastructures. In the octet metastructure, a slight difference between scaling exponents is observed (about 16%). This may be due to the higher frequency nature of this mode. Dynamic effects seem to introduce bending deformation of the lattice struts, raising the scaling exponent. Like the 2nd bending mode, we observe a transition on lattice property dependence of the 2nd axial mode as wavenumber increases. In the long wavelength region, the modal stiffness seems to depend on a combination of $E_{lattice}$ and $G_{lattice}$. However, since this side of the *k*-space does not define any of the band gaps of interest, we will not go into further detail.

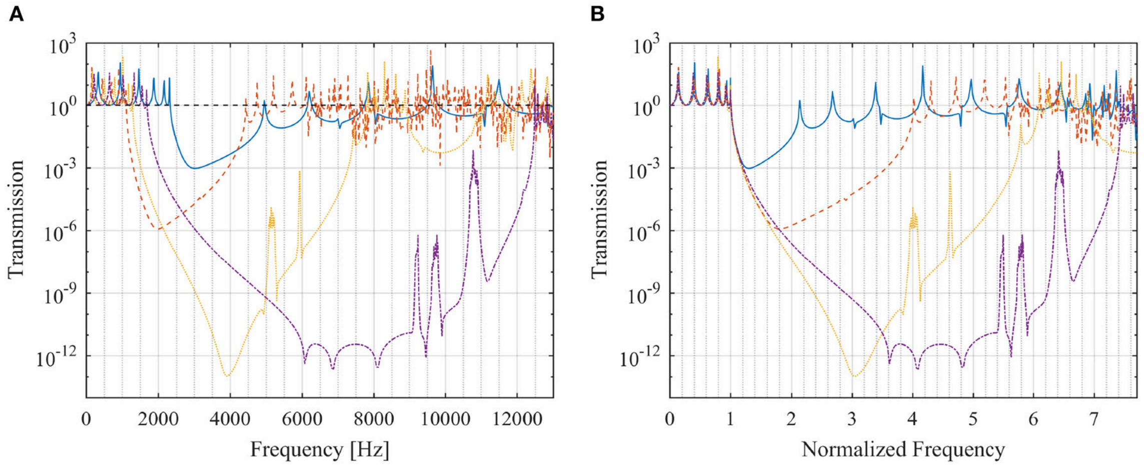

FIGURE 7 | Frequency-dependent transmission for the cubic (blue solid), idealized foam (red dashed), Kelvin (yellow dotted) and octet (purple dashed-dotted) metastructures with lattice relative density equal to 8.3%. **(A)** Transmission vs. frequency. **(B)** Transmission vs. normalized frequency.

It is important to mention that at densities lower than about 3%, the octet metastructure upper modes deviate from the power-law approximation. At these lower densities, bending stiffness of the lattice struts of this metastructure is low compared to the $G_{lattice}$ (due to increasing slenderness ratio of the struts with decrease in relative density). Thus, waves propagate through the outermost struts and no shear like deformation is observed on the unit cells surrounding the resonator.

It is not straightforward to realize a quantitative model that predicts the modal frequencies based on lattice effective properties presented in section Lattice Static Properties, however we present a general form to represent these frequencies in section Dynamic Performance Parameters. This is because in the effective properties calculations, the lattice unit is assumed to be periodic in all three dimensions, but the local boundary conditions of each lattice unit inside the metastructure depends on its location, i.e., some lattice unit cells have one face attached to the resonator, some lattice unit cells have one face that is traction free, while other lattice unit cells are connected to the surrounding lattice. The difference in boundary conditions changes the behavior of the lattice units inside the metastructure. Furthermore, because of the difference in geometry of the lattices, the effects of boundary conditions may be different for the different geometries. Predicting modal frequencies from static properties becomes even more challenging for lattice modes due to their higher frequency. It has been shown that a frequency-dependent elasticity is necessary to fully capture the dynamic behavior at the high frequency range (Nemat-Nasser et al., 2011; Srivastava, 2015). Instead, here we present a qualitative understanding of the physical differences among dispersion curves of different metastructures. These results motivate exploring more deeply the lattice-resonator metastructure framework due to its rich variety of wave propagation behaviors.

Influence of Resonator Size

To understand the influence of resonator size on band gaps, we calculate dispersion relations for the Kelvin metastructure for three different resonator sizes, at 8.3% lattice relative density (**Figure 6**). We observe differences in the dispersion relations for both resonator and lattice modes. A decrease in the resonator's side length, L_{reso}, causes two competing effects on the lower resonator modes. One is that the stiffness of the lattice and thus the modal stiffness decreases with decreasing L_{reso}, due to an increase in distance between the resonator and the metastructure outer surface. Note that we refer here to the *stiffness* of the lattice (dependent on length), as opposed to the *modulus* of the lattice (independent of length) discussed in earlier sections. The second effect is that the modal mass decreases, causing an increase in frequency of lower resonator modes: this effect dominates, since overall the resonator mode frequencies increase with a decrease in resonator size (**Figure 6**).

The quantitative effect of resonator size on resonator mode frequency depends on the mode shape. In the limit where the lattice has a negligible contribution to modal mass, the modal mass of resonator modes that involve *translation* of the resonator, M_t (1st bending resonator mode and axial resonator mode) is proportional to the resonator's mass, m_{reso}, and thus volume of the cube resonator, such that $M_t \propto L_{reso}^3$. The modal mass of resonator modes that involve *rotation* of the resonator, M_r (2nd bending resonator mode and torsional resonator mode) is proportional to the resonator's moment of inertia about its center of mass, $I_{reso} = \frac{1}{6} m_{reso} L_{reso}^2$, such that $M_r \propto L_{reso}^5$. This explains why the 2nd bending resonator mode and torsional resonator mode frequencies increase at a faster rate with a decrease in resonator size, compared to the 1st bending resonator mode and axial resonator mode frequencies. This is evident in the comparison of mode edge frequencies indicated with markers in **Figures 6A,B**. Note that when the resonator size decreases so much so that the lattice contribution to modal mass is non-negligible, e.g., **Figure 6C**, these relationships must include an additional term that accounts for the lattice modal mass.

Upper lattice mode frequencies decrease with a decrease in the resonator side length: lattice length between the resonator and exterior surface of the metastructure increases, decreasing the modal stiffness. In addition, the total lattice mass increases, increasing the modal mass of the lattice modes. Both of these effects result in an overall decrease in upper lattice mode frequencies.

Overall, a decrease in resonator size increases the frequencies of resonator modes and decreases the frequencies of lattice modes. This decreases the band gap width, and eventually the band gap closes (**Figure 6C**).

Finite Metastructure Transmission Analysis

To understand the attenuation efficiency of the proposed metastructures, we simulated the frequency-dependent transmission for a harmonic axial excitation through 6-unit cell finite metastructures at the same relative density as the presented dispersion curves in **Figure 4**. Results (**Figure 7A**) show that the efficiency strongly depends on the metastructure's geometry. In general, wider band gaps result in stronger attenuation. Interesting comparisons arise when the transmission is normalized on the frequency axis by the frequency of the lower edge of the band gap (**Figure 7B**). The structural peaks (lattice-resonator "acoustic" modes) at low frequency almost align, and the initial slope of the transmission into the band gap is the same for all metastructures. This highlights that in the low frequency range of the resonator modes, all metastructures behave similarly, and are simply scaled with their lattice effective properties. Beyond the band gap lower edge frequency, all metastructures have very different frequency-dependent behaviors, indicating that the dynamics of the lattice geometries dominate. The Kelvin metastructure has a sharp, deep attenuation dip, though it does not have the widest band gap. The octet metastructure has the widest band gap with a large range of deep attenuation. Localized modes appear in the band gap of the octet and Kelvin metastructures. In all cases, the attenuation regions in the transmission curves correspond well to the axially-polarized band gap frequencies (see section Performance Parameters). We expect similar behavior in the other polarizations, as seen in prior work (Matlack et al., 2016).

PERFORMANCE PARAMETERS

It is our final objective to evaluate the metastructures in terms of their static and dynamic properties. Here, we analyze standard band gap properties and introduce multifunctional (dynamic and static) performance parameters to compare the different metastructures over the range of lattice relative densities. We use the concept of *polarized band gaps* (Matlack et al., 2016) meaning band gaps bounded by modes of a specific polarization, i.e., axial, bending, and torsional modes. The metastructure's modal displacements reveal the mode's polarization, which we use to determine the *axial, bending, and torsional polarized band gaps*. We use polarized band gaps because it clarifies to which static stiffness we should compare the band gaps. Further, in most structural applications, it is typical to treat stiffness requirements in terms of the deflection direction, such that requirements are imposed on well-studied concepts of axial, bending and torsional stiffness. The mode of vibration that propagates through the component is typically the same as the static stiffness requirement. This approach allows us to systematically compare the band gaps to the static behavior of the metastructures, by comparing the polarized band gaps to the corresponding K_{axial}, $K_{bend,}$ and K_{tors} (section Metastructure Static Properties). It can also aid in the selection of architected materials for structural components that must comply with a minimum static stiffness while providing vibration mitigation in the corresponding polarization.

For complex load conditions and cases where mode conversion occurs, the corresponding band gaps occur in the overlapping region of the polarized band gaps involved, and the relevant static properties would depend on the specific application. The full band gap of these metastructures (**Figure 4**) is simply the overlap of all the polarized band gaps.

It is important to highlight that since the major interest lies in achieving low band gap frequencies, we analyze only the first band gap of each metastructure for each polarization. Our objective with the performance parameters is to evaluate for low frequency and wide bands gaps, and high static stiffness, all of which are highly relevant for most structural applications. Further, it should be noted that the load carrying capabilities of metastructures at low relative densities has not been considered here, which is beyond the scope of the paper but crucial in applications. However, stress analysis of metastructure unit cells at the lowest lattice relative density shows a maximum von Mises stress of about 5 MPa due to weight of the resonator, which is well-below the ultimate strength of 3D printable stiff polycarbonate materials.

Dynamic Performance Parameters

We evaluate the metastructures in terms of two standard dynamic performance parameters: lower edge band gap frequency (f_{low}) and normalized band gap width (Δf), defined as:

$$\Delta f = \frac{2(f_{high} - f_{low})}{f_{high} + f_{low}} \tag{3}$$

where f_{high} is the upper edge band gap frequency. Since we want to achieve low frequency and broadband mitigation, metastructures with lower f_{low} and higher Δf are considered more efficient.

We present these parameters in terms of lattice relative density for full, axial, bending, and torsional polarizations in **Figure 8.** The results show a large variation in band gap parameters that strongly depends on geometry and lattice relative density. At lower relative densities, we achieve a 6-fold change in full f_{low} and up to an 8-fold change in full Δf, only by changing the lattice geometry and keeping mass constant. As density increases, the difference in dynamic behavior of the metastructures decreases.

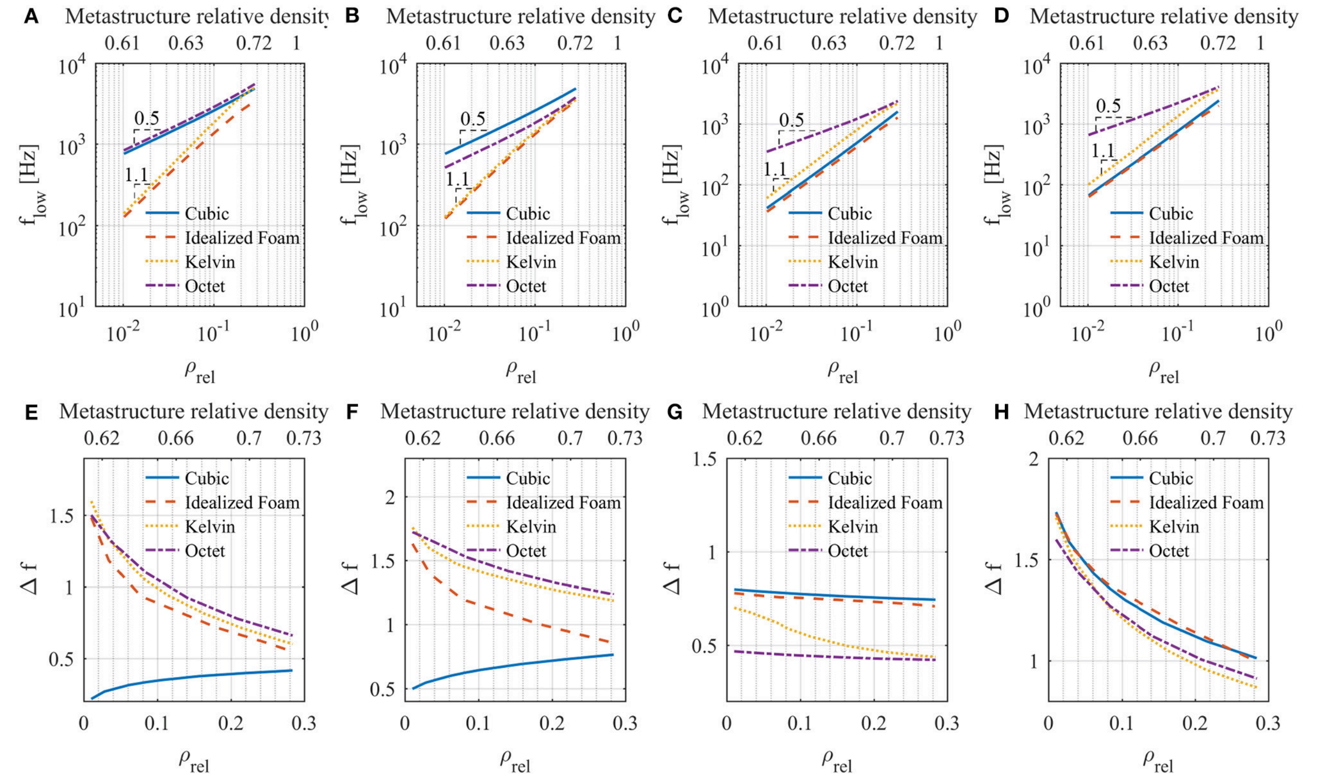

FIGURE 8 | Dynamic performance parameters for all polarizations. **(A)** Full f_{low}. **(B)** Axial f_{low}. **(C)** Bending f_{low}. **(D)** Torsional f_{low}. **(E)** Full Δf. **(F)** Axial Δf. **(G)** Bending Δf. **(H)** Torsional Δf. Metastructure relative densities are shown for comparison.

This is expected since as we increase the relative density, we approach the bulk material.

We observe that Kelvin and idealized foam metastructures are the "best performing" in terms of full dynamic parameters since they support the lowest and close to the widest band gaps. For axial polarization, the idealized foam and Kelvin metastructures have the lowest band gaps and the octet and the Kelvin metastructures have the widest band gaps, and for bending and torsional polarizations, the cubic and idealized foam metastructures have the lowest and widest band gaps.

Full band gaps are defined between mode numbers **4** and **5** (see **Figure 4**) for most relative densities studied. This only changes for the idealized foam geometry at relative densities above 25% where mode **a3** becomes stiffer than mode **a4** redefining the lower band gap edge. The lower edge modes of the full band gaps are resonator modes (see d1–d4 in **Figure 5**). Thus, the change in lattice relative density has a negligible effect on modal mass. We can thus approximate f_{low} as proportional to the square root of the static effective properties of the lattices:

$$f_{low} \propto \sqrt{aE_{lattice} + bG_{lattice}} \tag{4}$$

where a and b are participation factors that account for the dependence of the modal stiffness of the mode that defines f_{low} on lattice static properties (section Analyzing Band Gaps in Terms of Lattice Static Properties).

The polarization of the full band gap lower edge mode is different for each metastructure. For Kelvin and octet metastructures, the lower edge is defined by the second bending mode in the long wavelength region. The stiffness of this mode is proportional to $G_{lattice}$ and Equation 4 is reduced to:

$$f_{low} \propto \sqrt{bG_{lattice}} \approx \sqrt{(bE_sD)}\rho_{rel}{}^{r/2} \tag{5}$$

For the idealized foam metastructure, the mode defining the lower edge is the second bending mode at high wave number, where modal stiffness is proportional to $E_{lattice}$. We can then express f_{low} as:

$$f_{low} \propto \sqrt{aE_{lattice}} \approx \sqrt{(aE_sC)}\rho_{rel}{}^{n/2} \tag{6}$$

The cubic metastructure lower edge mode is an axial mode that depends on both $G_{lattice}$ and $E_{lattice}$. However, as mentioned before, the cubic lattice has a large $E_{lattice}$ compared to $G_{lattice}$, so we neglect the $G_{lattice}$ dependence and assume its behavior can be represented by Equation 6. Lower edge frequencies for full band gaps are plotted in double logarithmic scale in **Figure 8A**. There is good agreement between these results and Equations 4–6, especially in the low relative density range. As lattice relative

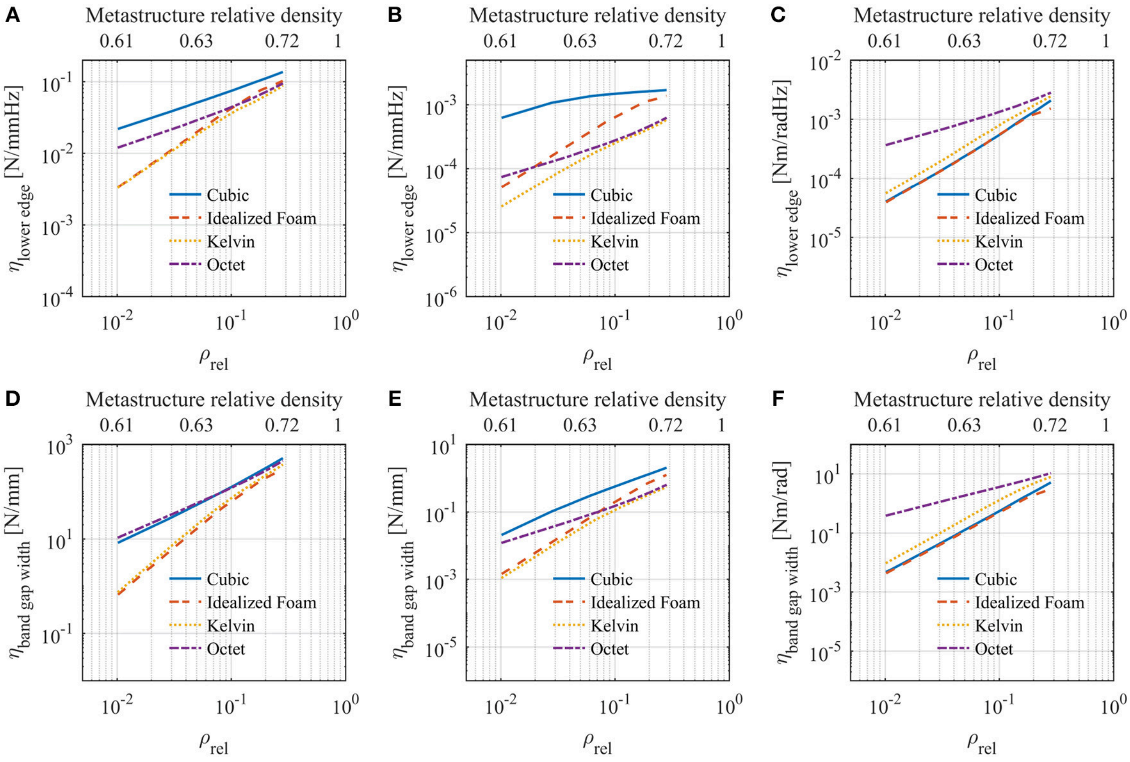

FIGURE 9 | Multifunctional performance parameters for all polarizations. **(A)** Axial $\eta_{lower\ edge}$. **(B)** Bending $\eta_{lower\ edge}$. **(C)** Torsional $\eta_{lower\ edge}$. **(D)** Axial $\eta_{band\ gap\ width}$. **(E)** Bending $\eta_{band\ gap\ width}$. **(F)** Torsional $\eta_{band\ gap\ width}$. Metastructure relative densities are shown for comparison.

density increases, we observe a slight decrease in slope because of increasing significance of lattice mass on total modal mass of the metastructure.

The upper edge mode of the full band gaps is defined by the 2nd torsional mode (**Figure 5**d5). Coming up with a simple power expression that describes the behavior of the frequencies of this mode is far more challenging than for the lower modes and escapes the scope of this article. However, the modal mass of this mode increases with increase in lattice relative density (since displacement is mostly concentrated in the lattice) while modal mass of lower modes remains approximately constant (since most modal mass is in the resonator). An increase in modal mass causes a decrease in modal frequency; thus, f_{high} grows at a slower rate than f_{low}. This is why, for most metastructures we observe a decrease in Δf (**Figure 8E**) with increasing lattice relative density. The cubic metastructure is an exception to this trend. The reason behind this is the mixed nature (in terms of stretch and bend dominated behavior) of this lattice geometry. As mentioned in section Wave Propagation in Metastructures, the modal stiffness of the 2nd torsional mode is proportional to $G_{lattice}$, where $G_{lattice} \propto \rho_{rel}^2$ for the cubic lattice, while the cubic metastructure lower edge mode is dominated by $E_{lattice}$ (Equation 6), where $E_{lattice} \propto \rho_{rel}$ for the cubic lattice. The larger scaling exponent of $G_{lattice}$ seems to prevail over the increase in modal mass. The result is that f_{high} grows at a faster rate than f_{low}, causing an increase in Δf with increasing lattice relative density.

In contrast to the other polarizations, the bending band gaps are generated between two resonator modes (**Figures 4**a1,a4,b1,b4,c1,c3,d1,d4). Thus, we expect the general form presented in Equation 4 to hold for both upper and lower edge modes. The lower edge modal stiffness was shown to be proportional to $G_{lattice}$, so Equation 5 can be applied. However, the upper edge mode is more complex, since the location in wavenumber spectrum that bounds the band gap varies with geometry. For cubic and idealized foam metastructures, f_{high} is bounded at $ka/\pi=0$, where modal stiffness is proportional to $G_{lattice}$ (Equation 5). However, for octet and Kelvin metastructures, f_{high} is bounded at $ka/\pi=1$, where modal stiffness is proportional to $E_{lattice}$ (Equation 6). The scaling exponents of the lattice properties that dominate the lower edge modes are equal to the ones that dominate the upper edge modes for the cubic, octet, and idealized foam metastructures. Thus, we predict a relatively small change in Δf across the relative density range. This is confirmed by results presented in **Figure 8G**. The Kelvin lattice has a slightly higher $G_{lattice}$ scaling exponent compared to its $E_{lattice}$, which supports the fact that Δf decreases with relative density.

A similar analysis can be done for both axial and torsional dynamic parameters (**Figures 8B,D,F,H**). In both cases, the lower edge is defined by a resonator mode and the upper edge by a lattice mode. Similar to the full band gaps, the axial parameters show the mixed behavior of the cubic lattice produces an increase in Δf with relative density. This does not occur in the torsional polarization since both lower and upper edge modes are dominated by $G_{lattice}$.

Multifunctional Performance Parameters

Here, we evaluate the metastructures in terms of their multifunctional properties of static deformation and band gap properties. We analyze three different static stiffnesses: K_{axial}, K_{bend}, and K_{tors}, which we can compare to the axial, bending, and torsional polarized band gaps. We define two multifunctional parameters that relate these properties:

$$\eta_{lower\ edge} = \frac{K_{static}}{f_{low}} \tag{7}$$

$$\eta_{band\ gap\ width} = K_{static}\Delta f \tag{8}$$

where values of K_{static} are presented in section Metastructure Static Properties and values of f_{low} and Δf are presented in the section Dynamic Performance Parameters. For simplicity, we choose to weight stiffness and frequency parameters equal in our evaluation. We evaluate the metastructures in terms of these performance metrics compared to lattice and metastructure relative densities in **Figure 9**.

Incorporating static properties into performance metrics changes the way the metastructures are evaluated. For example, for axial deformations, the cubic metastructure has the lowest performance in terms of f_{low}. This changes completely in the multifunctional analysis. The cubic metastructure axial $\eta_{lower\ edge}$ is the highest for all relative densities. Similarly, the octet metastructure has a poor torsional f_{low} but the highest torsional $\eta_{lower\ edge}$. In bending, the cubic metastructure is the "best performing" for both dynamic and multifunctional parameters.

"Best performing" metastructures in terms of $\eta_{band\ gap\ width}$ are also different than those of Δf for axial and torsional polarization. For axial $\eta_{band\ gap\ width}$, the highest values of performance are achieved by the octet metastructure at low lattice densities and the cubic metastructure at higher ones. The octet metastructure has the highest torsional $\eta_{band\ gap\ width}$. In bending, the cubic metastructure shows the highest values similar to the dynamic analysis.

The differences in the outcome of the dynamic and multifunctional performance metrics show the importance of a multifunctional analysis. The stiffness or frequency parameters could be weighted differently if the specific application requires better performance of one parameter compared to another. One could redefine these parameters to include other mechanical properties such as energy absorption, heat transfer, or yield strength to fit certain criteria. Defining multifunctional metrics, can aid the design process, and achieve higher levels of performance of multifunctional architected materials.

Static Stiffness vs. Lower Band Gap Edge Frequency

As another metric of performance, we directly compare K_{static} of the metastructures with their f_{low} for axial, bending and torsional polarizations (**Figure 10**). The idealized foam metastructure shows slightly higher values of K_{axial} relative to f_{low} for axial polarizations (**Figure 10A**), and the idealized foam and cubic metastructures show slightly higher K_{tors} relative to f_{low} for torsional polarization (**Figure 10C**). However, overall there is not much difference in the metastructure's axial and torsional behavior, mainly because in these polarizations, the metastructure's K_{static} and the modal stiffness associated with f_{low} are proportional to the same lattice effective property.

More significant differences between metastructure geometries are observed for K_{bend} vs. f_{low} for bending (**Figure 10B**). This is because K_{bend} is proportional to both $E_{lattice}$ and $G_{lattice}$, while the modal stiffness associated with f_{low} (1st bending mode) is proportional to only $G_{lattice}$. Higher ratios of $E_{lattice}$ to $G_{lattice}$ for the cubic and idealized foam lattices compared to that of the octet and Kelvin lattices (**Figure 2**) explain the significantly higher values of K_{bend} that can be achieved at a given f_{low} with the cubic and idealized foam metastructures. Furthermore, the mixed behavior of the cubic lattice allows us to break the typical quadratic relationship between K_{static} and f_{low} for the bending polarization. While all other stiffness-frequency curves follow the well-established quadratic relationship between stiffness and frequency, this relationship is instead approximately linear for the cubic metastructure under bending. This is due to the mixed behavior of the cubic lattice (section Lattice Static Properties), i.e., it has different scaling exponents of $E_{lattice}$ and $G_{lattice}$ (**Table 2**). In general, K_{bend} is proportional to both $E_{lattice}$ and $G_{lattice}$ such that for the cubic metastructure $K_{bend} \propto \rho_{rel}^{1.45}$ (on average, see **Table 3**), and $f_{low} \propto \sqrt{G_{lattice}} \propto {\rho_{rel}}^{1.1}$ (**Figure 8C**), which results in an approximately linear relationship between K_{bend} and f_{low} for bending.

CONCLUSION

In this article, we studied static properties and vibration mitigation behavior of metastructures that consist of different lattice geometries with embedded resonators. Through calculations of the static stiffness of finite metastructures, we show that metastructure stiffness is closely related to the effective static moduli of the lattice materials that compose them. The band gaps of these metastructures with iso-density lattices show that we can achieve large differences in band gaps by selectively placing the mass inside the lattice unit cell. By inspecting the modal displacements and the dispersion curves, we developed a qualitative understanding of the differences in band gap parameters in terms of the effective static properties of the lattices. We compared the exponential dependence on relative density of the modal stiffnesses of each metastructure mode, in the vicinity of the lowest band gap, to the static effective properties of the lattices to further support this point. We analyzed the transmission of the metastructures and found that the attenuation efficiency strongly depends on lattice topology. Our results show that the lattice effective properties drive the band gap frequencies, which is interesting since the lattice is extremely finite with various boundary conditions: there are only a few lattice unit cells in between each resonator, and only a few lattice unit cells in the other dimensions.

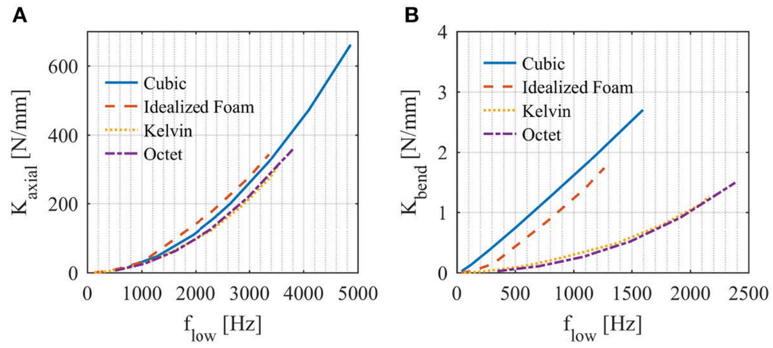

FIGURE 10 | K_{static} vs. f_{low}. **(A)** Axial polarization. **(B)** Bending polarization **(C)** Torsional polarization.

TABLE 5 | Material properties used for finite element simulations.

Material	Density (kg/m^3)	Young's modulus (GPa)	Poisson's ratio
Polycarbonate	1,097	1	0.35
Steel	7,850	215	0.31

We evaluated the metastructures over a range of lattice relative densities from 1% to 28% (corresponding to metastructure relative densities from 61% to 72%). Dynamic parameters of lower edge band gap frequency and band gap width show the ability to tailor the band gap to a wide range of frequencies, especially at lower relative density values. We introduce multifunctional performance metrics to evaluate the metastructures in terms of their band gap properties and static stiffness, for general structural application considerations. In both cases, performance of the metastructure strongly depends on the polarization considered, and on whether only dynamic or both static and dynamic properties are considered. This type of evaluation can be used to formulate performance metrics that more accurately describe certain applications and could be modified to preferentially weight certain parameters more than others. Finally, we directly compare metastructure static stiffness to polarized lower band gap edge frequency. A particularly interesting behavior is observed in the bending polarization for the cubic metastructure, where the relationship between static stiffness and lower edge frequency approaches a linear behavior. This is primarily due to the mixed behavior of the cubic lattice unit cell under shear and compression.

While these metastructures may have application-specific drawbacks of additional resonator mass, we show that this metastructure design can be used to obtain a wide range of static and band gap properties by simply changing the lattice geometry. Further, our presented approach of understanding the dynamic properties of metastructures in terms of the effective properties of the lattice could be used to evaluate and interpret other designs, where optimal performance may be obtained.

MATERIALS AND METHODS

Dispersion Relations

We obtain the dispersion relations by 3D Finite Element simulations in COMSOL Multiphysics V5.3 software. We model a single metastructure unit (**Figure 1B**) and use 10-node tetrahedral elements. Mesh size was chosen to ensure convergence of results. We impose Floquet boundary conditions in the external faces perpendicular to the x-direction to account for x-axis periodicity. The wave number, k, is swept in the first irreducible Brillouin zone and the eigenfrequency problem is solved to obtain the dispersion relations. The relative density of the lattice unit cells is varied by keeping unit length constant and sweeping the thickness of the struts that compose it. We calculate modal stiffness as:

$$K^{(i)} = {u^{(i)}}^T [K] \, u^{(i)} \tag{9}$$

where $K^{(i)}$ is the modal stiffness of mode i, $u^{(i)}$ is the vector containing the modal displacements of mode i and $[K]$ is the stiffness matrix.

Finite Metastructure Transmission Analysis

We obtain the transmission curves by 3D Finite Element simulations in COMSOL Multiphysics V5.3 software. We model a six-unit one-dimensional finite metastructure (**Figure 1C**) and use 10-node tetrahedral elements. Mesh size was chosen to ensure convergence of results. We fix one end of the metastructure and we apply a harmonic displacement (δ_x) parallel to the direction of periodicity to the opposite end. We perform a frequency sweep analysis over a range of frequencies from 0 to 13,000 Hz. We define transmission as the ratio of output to input force amplitudes.

Lattice Effective Properties

We calculate lattice effective properties ($E_{lattice}$ and $G_{lattice}$) using 3D Finite Element simulations in COMSOL Multiphysics V5.3 software. We model a single lattice unit cell (**Figure 1A**) and use 10-node tetrahedral elements. Mesh size was chosen to ensure convergence of results. We perform a series of static linear analysis where appropriate displacement boundary conditions and periodic boundary conditions (Wallach and Gibson, 2001;

Dalaq et al., 2016) are imposed to calculate the effective stiffness matrix considering the cubic symmetry of the lattice unit cells. We then calculate effective Young's modulus and effective shear modulus from the effective stiffness matrix. We vary the relative density of the lattice cells by keeping unit length constant and sweeping the thickness of the struts that compose it.

Finite Metastructure Static Stiffness

We obtain finite metastructure static stiffness (K_{static}) properties from 3D Finite Element simulations in COMSOL Multiphysics V5.3. We model a six-unit one-dimensional finite metastructure (**Figure 1C**) and use 10-node tetrahedral elements. Mesh size was chosen to ensure convergence of results. We numerically calculate the force and displacement profiles of the finite metastructure under static loading, and then use force-displacement relations of a conventional cantilever beam to calculate the axial, bending, and torsional stiffnesses of the metastructures. For axial stiffness (K_{axial}), we fix one end of the metastructure and we apply a displacement (δ_x) parallel to the direction of periodicity to the opposite end. We calculate K_{axial} as:

$$K_{axial} = \frac{F_x}{\delta_x} \tag{10}$$

where F_x is the total reaction force at the fixed end parallel to the direction of periodicity. For bending stiffness (K_{bend}), we fix one end of the metastructure and we apply a displacement (δ_y) perpendicular to the direction of periodicity to the opposite end. We calculate K_{bend} as:

$$K_{bend} = \frac{F_y}{\delta_y} \tag{11}$$

where $F_y$is the total reaction force at the fixed end perpendicular to the direction of periodicity. For torsional stiffness (K_{tors}), we fix one end of the metastructure and we apply a rigid connector to the opposite end. We apply an angular displacement (θ_x) about the direction of periodicity to this face. We calculate K_{tors} as:

$$K_{tors} = \frac{M_x}{\theta_x} \tag{12}$$

where $M_x$is the total reaction moment at the fixed end about to the direction of periodicity. The relative density of the lattice cells is varied by keeping unit length constant and sweeping the thickness of the struts that compose it.

Material Properties

For all simulations, materials are based on prior 3D printed metastructures (Matlack et al., 2016) but chosen to be isotropic. Even though 3D printing methods do not achieve isotropy due to the material properties dependence on printing direction, it is the main objective of the paper to identify effects due to geometry changes and not due to material anisotropy. We use a linear elastic material model with no damping. Material properties used in all models are given in **Table 5**.

AUTHOR CONTRIBUTIONS

IA performed the research, analyzed the data, developed the performance parameters, and wrote the paper. KM designed the research, analyzed the data, developed the performance parameters, and wrote the paper.

ACKNOWLEDGMENTS

This work was partially supported by a University Research Program from Ford Motor Company.

REFERENCES

Bayat, A., and Gaitanaros, S. (2018). Wave directionality in three-dimensional periodic lattices. *J. Appl. Mech.* 85:011004. doi: 10.1115/1.4038287

Berger, J. B., Wadley, H. N. G., and McMeeking, R. M. (2017). Mechanical metamaterials at the theoretical limit of isotropic elastic stiffness. *Nature* 543, 533–537. doi: 10.1038/nature21075

Chen, Y., Li, T., Scarpa, F., and Wang, L. (2017). Lattice metamaterials with mechanically tunable poisson's ratio for vibration control. *Phys. Rev. Appl.* 7:024012. doi: 10.1103/PhysRevApplied.7.024012

Dalaq, A. S., Abueidda, D. W., Abu Al-Rub, R. K., and Jasiuk, I. M. (2016). Finite element prediction of effective elastic properties of interpenetrating phase composites with architectured 3D sheet reinforcements. *Int. J. Solids Struct.* 83, 169–182. doi: 10.1016/j.ijsolstr.2016.01.011

D'Alessandro, L., Belloni, E., Ardito, R., Corigliano, A., and Braghin, F. (2016). Modeling and experimental verification of an ultra-wide bandgap in 3D phononic crystal. *Appl. Phys. Lett.* 109:221907. doi: 10.1063/1.4971290

D'Alessandro, L., Zega, V., Ardito, R., and Corigliano, A. (2018). 3D auxetic single material periodic structure with ultra-wide tunable bandgap. *Sci. Rep.* 8:2262. doi: 10.1038/s41598-018-19963-1

Deshpande, V. S., Ashby, M. F., and Fleck, N. A. (2001a). Foam topology: bending versus stretching dominated architectures. *Acta Mater.* 49, 1035–1040. doi: 10.1016/S1359-6454(00)00379-7

Deshpande, V. S., Fleck, N. A., and Ashby, M. F. (2001b). Effective properties of the octet-truss lattice material. *J. Mech. Phys. Solids* 49, 1747–1769. doi: 10.1016/S0022-5096(01)00010-2

Deymier, P. A. (ed.). (2013). *Acoustic Metamaterials and Phononic Crystals*. Berlin; Heidelberg: Springe

Doty, R. E., Kolodziejska, J. A., and Jacobsen, A. J. (2012). Hierarchical polymer microlattice structures. *Adv. Eng. Mater.* 14, 503–507. doi: 10.1002/adem.201200007

Dou, N. G., Jagt, R. A., Portela, C. M., Greer, J. R., and Minnich, A. J. (2018). Ultralow thermal conductivity and mechanical resilience of architected nanolattices. *Nano Lett.* 18, 4755–4761. doi: 10.1021/acs.nanolett.8b01191

Erdeniz, D., Levinson, A. J., Sharp, K. W., Rowenhorst, D. J., Fonda, R. W., and Dunand, D. C. (2015). Pack aluminization synthesis of superalloy 3D woven and 3D braided structures. *Metall. Mater. Trans. A* 46, 426–438. doi: 10.1007/s11661-014-2602-9

Evans, A. G., Hutchinson, J. W., and Ashby, M. F. (1998). Multifunctionality of cellular metal systems. *Prog. Mater. Sci.* 43, 171–221. doi: 10.1016/S0079-6425(98)00004-8

Evans, A. G., Hutchinson, J. W., Fleck, N. A., Ashby, M. F., and Wadley, H. N. G. (2001). The topological design of multifunctional cellular metals. *Prog. Mater. Sci.* 46, 309–327. doi: 10.1016/S0079-6425(00)00016-5

Fleck, N. A., Deshpande, V. S., and Ashby, M. F. (2010). Micro-architectured materials: past, present and future. *Proc. R. Soc. A Math. Phys. Eng. Sci.* 466, 2495–2516. doi: 10.1098/rspa.2010.0215

Gibson, L. J., and Ashby, M. F. (1982). The mechanics of three-dimensional cellular materials. *Proc. R. Soc. Lond. A. Math. Phys. Sci.* 382, 43–59. doi: 10.1098/rspa.1982.0088

Gibson, L. J., and Ashby, M. F. (1997). *Cellular Solids: Structure and Properties*, *2nd Edn*. Cambridge, UK: Cambridge University Press.

Han, B., Zhang, Z.-J., Zhang, Q.-C., Zhang, Q., Lu, T. J., and Lu, B.-H. (2017). Recent advances in hybrid lattice-cored sandwiches for enhanced multifunctional performance. *Extrem. Mech. Lett.* 10, 58–69. doi: 10.1016/j.eml.2016.11.009

Hussein, M. I., Leamy, M. J., and Ruzzene, M. (2014). Dynamics of phononic materials and structures: historical origins, recent progress, and future outlook. *Appl. Mech. Rev.* 66:040802. doi: 10.1115/1.4026911

Luxner, M. H., Stampfl, J., and Pettermann, H. E. (2004). "Linear and nonlinear numerical investigations of regular open cell structures" in *Proceedings of ASME 2004 International Mechanical Engineering Congress and Exposition* (Anaheim, CA: ASME), 469–475. doi: 10.1115/IMECE2004-62545

Matlack, K. H., Bauhofer, A., Krödel, S., Palermo, A., and Daraio, C. (2016). Composite 3D-printed metastructures for low-frequency and broadband vibration absorption. *Proc. Natl. Acad. Sci.U.S.A.* 113, 8386–8390. doi: 10.1073/pnas.1600171113

Meza, L. R., Zelhofer, A. J., Clarke, N., Mateos, A. J., Kochmann, D. M., and Greer, J. R. (2015). Resilient 3D hierarchical architected metamaterials. *Proc. Natl. Acad. Sci. U.S.A.* 112, 11502–11507. doi: 10.1073/pnas.1509120112

Moongkhamklang, P., Deshpande, V. S., and Wadley, H. N. G. (2010). The compressive and shear response of titanium matrix composite lattice structures. *Acta Mater.* 58, 2822–2835. doi: 10.1016/j.actamat.2010.01.004

Nemat-Nasser, S., Willis, J. R., Srivastava, A., and Amirkhizi, A.V. (2011). Homogenization of periodic elastic composites and locally resonant sonic materials. *Phys. Rev. B* 83:104103. doi: 10.1103/PhysRevB.83.104103

Phani, A. S., Woodhouse, J., and Fleck, N. A. (2006). Wave propagation in two-dimensional periodic lattices. *J. Acoust. Soc. Am.* 119, 1995–2005. doi: 10.1121/1.2179748

Ryan, S. M., Szyniszewski, S., Ha, S., Xiao, R., Nguyen, T. D., Sharp, K. W., et al. (2015). Damping behavior of 3D woven metallic lattice materials. *Scr. Mater.* 106, 1–4. doi: 10.1016/j.scriptamat.2015.03.010

Schaedler, T. A., and Carter, W. B. (2016). Architected cellular materials. *Annu. Rev. Mater. Res.* 46, 187–210. doi: 10.1146/annurev-matsci-070115-031624

Srivastava, A. (2015). Elastic metamaterials and dynamic homogenization: a review. *Int. J. Smart Nano Mater.* 6, 41–60. doi: 10.1080/19475411.2015.1017779

Tang, Y., Ren, S., Meng, H., Xin, F., Huang, L., Chen, T., et al. (2017). Hybrid acoustic metamaterial as super absorber for broadband low-frequency sound. *Sci. Rep.* 7:43340. doi: 10.1038/srep43340

Taniker, S., and Yilmaz, C. (2015). Design, analysis and experimental investigation of three-dimensional structures with inertial amplification induced vibration stop bands. *Int. J. Solids Struct.* 72, 88–97. doi: 10.1016/j.ijsolstr.2015.07.013

Valdevit, L., Jacobsen, A. J., Greer, J. R., and Carter, W. B. (2011). Protocols for the optimal design of multi-functional cellular structures: from hypersonics to micro-architected materials. *J. Am. Ceram. Soc.* 94, s15–s34. doi: 10.1111/j.1551-2916.2011.04599.x

Vigliotti, A., and Pasini, D. (2012). Stiffness and strength of tridimensional periodic lattices. *Comput. Methods Appl. Mech. Eng.* 229–232, 27–43. doi: 10.1016/j.cma.2012.03.018

Wadley, H. N. G. (2006). Multifunctional periodic cellular metals. *Philos. Trans. R. Soc. A Math. Phys. Eng. Sci.* 364, 31–68. doi: 10.1098/rsta.2005.1697

Wallach, J. C., and Gibson, L. J. (2001). Mechanical behavior of a three-dimensional truss material. *Int. J. Solids Struct.* 38, 7181–7196. doi: 10.1016/S0020-7683(00)00400-5

Wang, L., Lau, J., Thomas, E. L., and Boyce, M. C. (2011). Co-continuous composite materials for stiffness, strength, and energy dissipation. *Adv. Mater.* 23, 1524–1529. doi: 10.1002/adma.201003956

Wang, P., Casadei, F., Kang, S. H., and Bertoldi, K. (2015). Locally resonant band gaps in periodic beam lattices by tuning connectivity. *Phys. Rev. B* 91:020103. doi: 10.1103/PhysRevB.91.020103

Wang, Y., Gao, J., Luo, Z., Brown, T., and Zhang, N. (2017). Level-set topology optimization for multimaterial and multifunctional mechanical metamaterials. *Eng. Optim.* 49, 22–42. doi: 10.1080/0305215X.2016.1164853

Zhang, Y., Ha, S., Sharp, K., Guest, J. K., Weihs, T. P., and Hemker, K. J. (2015). Fabrication and mechanical characterization of 3D woven Cu lattice materials. *Mater.* 85, 743–751. doi: 10.1016/j.matdes.2015.06.131

Zheng, X., Lee, H., Weisgraber, T. H., Shusteff, M., DeOtte, J., Duoss, E. B., et al. (2014). Ultralight, ultrastiff mechanical metamaterials. *Science* 344, 1373–1377. doi: 10.1126/science.1252291

Conflict of Interest Statement: The authors declare that the research was conducted in the absence of any commercial or financial relationships that could be construed as a potential conflict of interest.

frontiers in Materials

ORIGINAL RESEARCH
published: 25 January 2019
doi: 10.3389/fmats.2018.00084

Revealing Spider Silk's 3D Nanostructure Through Low Temperature Plasma Etching and Advanced Low-Voltage SEM

*Nicola Stehling, Kerry J. Abrams, Chris Holland and Cornelia Rodenburg**

Department of Materials Science and Engineering, University of Sheffield, Sheffield, United Kingdom

The excellent mechanical properties of spider dragline silk are closely linked to its multiscale hierarchical structuring which develops as it is spun. If this is to be understood and mimicked, multiscale models must emerge which effectively bridge the length scales. This study aims to contribute to this goal by exposing structures within *Nephila* dragline silk using low-temperature plasma etching and advanced Low Voltage Scanning Electron Microscopy (LV-SEM). It is shown that Secondary Electron Hyperspectral Imaging (SEHI) is sensitive to compositional differences on both the micro and nano scale. On larger scales it can distinguish the lipids outermost layer from the protein core, while at smaller scales SEHI is effective in better resolving nanostructures present in the matrix. Key results suggest that the silks spun at lower reeling speeds tend to have a greater proportion of smaller nanostructures in closer proximity to one-another in the fiber, which we associate with the fiber's higher toughness but lower stiffness. The bimodal size distribution of ordered domains, their radial distribution, nanoscale spacings, and crucially their interactions may be key in bridging the length scale gaps which remain in current spider silk structure-property models. Ultimately this will allow successful biomimetic implementation of new models.

Keywords: spider silk, biopolymer, protein, hierarchical structure, multiscale material, natural materials, low voltage scanning electron microscopy

Edited by:
Fernando Fraternali,
University of Salerno, Italy

Reviewed by:
Francesco Colangelo,
Università degli Studi di Napoli
Parthenope, Italy
Rupinder Singh,
Department of Production
Engineering, Guru Nanak Dev
Engineering College, India

***Correspondence:**
Cornelia Rodenburg
c.rodenburg@sheffield.ac.uk

Specialty section:
This article was submitted to
Mechanics of Materials,
a section of the journal
Frontiers in Materials

Received: *30 November 2018*
Accepted: *31 December 2018*
Published: *25 January 2019*

Citation:
Stehling N, Abrams KJ, Holland C and
Rodenburg C (2019) Revealing Spider
Silk's 3D Nanostructure Through Low
Temperature Plasma Etching and
Advanced Low-Voltage SEM.
Front. Mater. 5:84.
doi: 10.3389/fmats.2018.00084

INTRODUCTION

Spider silk is of great interest to a range of scientific communities due to its high-performance and unique mechanical properties (Vollrath and Porter, 2009; Walker et al., 2015; Koeppel and Holland, 2017; Holland et al., 2018b). These properties are attributed to a hierarchical arrangement of ordered and disordered protein structures within a single fiber (Vollrath and Porter, 2009; Vollrath et al., 2011; Porter et al., 2013). This nanostructure has been extensively explored by bulk and space-averaging techniques such as calorimetry (Cebe et al., 2013; Vollrath et al., 2014; Holland et al., 2018a), spectroscopy (Dicko et al., 2007; Boulet-Audet et al., 2015) small angle scattering X-ray and neutron diffraction (Termonia, 1994; Riekel et al., 2000; Greving et al., 2010; Wagner et al., 2017) and solid state nuclear magnetic resonance (NMR) (Willis et al., 1972; Hijirida et al., 1996; Kümmerlen et al., 1996; Yang et al., 2000; Holland et al., 2008; McGill et al., 2018), which together have provided the fuel for a range of modeling approaches (Giesa et al., 2011; Cranford, 2013; Ebrahimi et al., 2015; Rim et al., 2017). In comparison, spatially resolved techniques are yet to be fully explored, but have already hinted at a diverse set of rich nano- and microscale features such as micelles (Lin et al., 2017; Oktaviani et al., 2018; Parent et al., 2018), nanofibrils (Wang and Schniepp, 2018), elongated cavities (Frische et al., 2002), and an overall radial variation of composition and structure (Li et al., 1994; Knight et al., 2000; Frische et al., 2002; Sponner et al., 2007; Brown et al., 2011). Therefore, in order to uncover the secret of spider silk's mechanical response, the precise spatial distribution of structural elements inside the fiber needs to be better understood.

Investigations of the radial distribution of structures within spider dragline silk show that the composition of the shell, comprising of the lipid, and glycoprotein coating and protein skin, is substantially different compared to that of the core. In a typical dragline fiber of 5 µm diameter, the coating is approximately 100 nm in thickness and can be further differentiated into a waxy lipids and a glycoprotein layer, which together are attributed with the control of moisture content, antimicrobial properties, and pheromonal communication (Augsten et al., 2000; Sponner et al., 2005, 2007). Although it is chemically diverse, the contribution of the coating to the fiber's overall tensile behavior has been proposed to be very small (Yazawa et al., 2018). The underlying skin is of similar thickness to the coating and has been found to compose mostly of minor ampullate spidroin protein (MiSp) which is the main component of minor ampullate fibers (Sponner et al., 2007).

Remarkably, there is a further differentiation of structure within the radial profile of the spider silk's core: below the thin (∼100 nm) proteinous skin lies the β-sheet rich outer-core and finally the proline-rich and more structurally disordered inner core (Li et al., 1994; Knight et al., 2000; Vollrath and Knight, 2001; Sponner et al., 2007). The greatest contribution to the mechanical properties of the fiber arise from these core layers as they make up the bulk of the fiber's volume. The core contains the ordered β-sheet structures but also the disordered amorphous phases. The β-sheet structures have been of intense interest to structural analysis (McGill et al., 2018) and mechanical modeling (Keten et al., 2010; Giesa et al., 2011) whereas the disordered amorphous components have attracted less scientific attention, in part due to the difficulty of structurally characterizing them.

Currently, mechanical models do not consider this radial structure present in the most extensively studied *Nephila* dragline silk, which is at odds with the widespread agreement that multi-scale organization is integral to the fiber's characteristic tensile response (Nova et al., 2010; Giesa et al., 2011; Skelton and Nagase, 2012; López Barreiro et al., 2018; Yarger et al., 2018). A better dataset concerning the 3D mechanical properties and spatial distribution of different structural units within the silk will allow for better multi-scale mechanical models and will be important in successfully designing spider-silk mimicking fibers and polymers with tailored properties (Koeppel and Holland, 2017).

In this study a controlled variation of reeling speed is utilized to produce silk of varying mechanical and structural properties. To elucidate the differences in structure, the fibers are analyzed unstained and uncoated in the secondary electron microscope (SEM) by Secondary Electron Hyperspectral Imaging (Wan et al., 2017) and structures are revealed by low temperature plasma etching. The ultimate goal is to spatially characterize the 3D distribution of nanostructure radially and longitudinally and presenting results which will aid in the parameterization of multi-scale mechanical models.

MATERIALS AND METHODS

Collection of Single Fiber Dragline Silk

All spider silk samples used in the Secondary Electron Hyperspectral Imaging (SEHI) and the mechanical testing stem from one continuous thread of a single mature *Nephila inaurata* female. The spider was kept in a lab environment and was fed crickets and waxworms *ad libidum*. To obtain single fiber major ampullate dragline silk, the spider was anesthetized using carbon dioxide and subsequently immobilized on a polystyrene block with its underside facing upward. The spider was left to regain consciousness for 30 min to eliminate any effect of the carbon dioxide on the spinning process (Riekel et al., 2004). Under an optical stereo microscope (Leica MZ6), a single major ampullate dragline thread was separated from other silks and taken up onto the reeling device. The reeling device was designed in-house to allow simultaneous control over rotational and lateral translational speeds of the reel, allowing the collection of single fibers with approximately 1 cm lateral spacing at well-defined speeds of 5, 20, and 40 mm s^{-1} and facilitating further sample preparation.

Mechanical Testing

While ensuring that the tension of the fibers was maintained, the *N. inaurata* fibers were applied to stiff paper frames as is common protocol for tensile testing spider silk (Kitagawa and Kitayama, 1997) and were glued above and below the tensile testing window to ensure good adhesion and a gauge length of 5 mm. 18 tensile samples were prepared for each reeling speed. After the glue was left to set for at least 24 h the paper frames were loaded into a Zwick tensile tester equipped with a 5 N loading cell using crocodile clamps, and the frame was cut using nail clippers to obtain the free-standing fiber. Tensile tests of all samples were performed in a controlled lab environment and within 6 h to minimize variability arising from differences in temperature and humidity. The tests were strain controlled at 10 mm min^{-1} and were simultaneously videoed. A sample video the tensile test is available to watch in the **Supplementary Information**. Mechanical properties were extracted from the tensile curves applying cross-sectional areas derived from diameter measurements of each reeling speed obtained by LV-SEM imaging.

SEM and Image Data Processing

All SEM imaging and measurements were performed on a FEI Helios NanoLab SEM.

Imaging

Images were collected at a working distance of 4.1 mm, and a current of 13 pA. The scan preset was chosen to obtain minimum spatiotemporal electron exposure: the dwell time was set to the minimum 50 ns, a scan interlace of 8 was used and 32 scans were integrated using drift correction to obtain the image. Accelerating voltages of 500 eV or 1 keV were used and are further specified in the figure caption.

Spectral Acquisition

The FEI Helios NanoLab SEM is equipped with a through-lens detector with a voltage controlled mirror electrode, which deflects the SE signal into the detector. By scanning the voltage on the mirror electrode over a range and generating an image each, the energy range of collected SEs is controlled and spectra and hyperspectral images are obtained through post-processing of the spectral image series. The energy calibration of this process is performed through stage bias experiments, as described elsewhere (Kazemian et al., 2007). For a detailed discussion of the method please refer to (Stehling et al., 2018). When considering the SE signal originating from a cylindrical object such as spider silk, the effect of the SE emission angle must be considered. In all spectra and hyperspectral images presented this effect has been corrected for by taking two spectra, the second of which was taken with a stage rotation of 180° relative to the initial spectrum. For each energy the spectral images were averaged to cancel out angular effects and detector shadowing in post-processing to yield geometrically corrected results. The success of this correction was confirmed by the comparison of the non-corrected to the corrected hyperspectral images of a Si calibration standard sample of known geometry.

Image Processing

Image processing was performed using Fiji software (Schindelin et al., 2012). All images presented have been optimized for their brightness and contrast using histogram normalization.

The Voronoi tessellation was performed by assigning the 8-bit greyscale values 255–141 to the nanostructure in the hyperspectral images of the given energy range. The resulting binary image was subsequently skeletonized to represent the bright nanostructure as a one-pixel line using Zang and Suen's algorithm (Zhang and Suen, 1984) and this was used as input for the Voronoi tessellation. A color look-up-table was applied to better illustrate the distances between particles along the tessellation lines and is displayed adjacent to the tessellation maps.

Low Temperature Plasma Treatment

Plasma treatment was performed in a Diener Electronic Zepto plasma cleaner at 40 kHz, 100 W, and 0.3 mbar air for the specified total times. Samples were exposed to the plasma for no longer than 3 min at a time to exclude the effects of sample heating which have been shown to lead to surface modification of a different kind (Yip et al., 2002). For treatment times of more than 3 min, the sample was treated for 3 min, then left to cool for 5 min before a subsequent treatment was performed to make up the total treatment time.

RESULTS

To gain a complete understanding of the structural mechanical make-up of spider dragline silk, the radial as well as the longitudinal structures present within silk need to be considered. Generally, analysis techniques used for the characterization of structures on different scales are either space-averaging, such as nuclear magnetic resonance spectroscopy (NMR) and X-ray diffraction (XRD), or surface sensitive, such as atomic force microscopy (AFM) and electron microscopy (EM). This poses a practical challenge if 3D information with high spatial resolution in all dimensions is sought. If differences in nanostructure alignment and distribution, such as those proposed in literature are to be spatially resolved, the internal structure's 3D distribution must be revealed.

Plasmas are reactive environments in the gas phase and thus modify surfaces in response to the underlying structural composition (Yip et al., 2006). The use of a low temperature plasma for defined periods of time has previously been shown to lead to selective etching of fiber surfaces, with the treated surface morphology being a result of the fiber's crystallinity and its strain history (Wakida and Tokino, 1996; Yip et al., 2002,?, 2006; Stehling et al., 2018). In our experiments, plasma treatment was used to firstly etch away layers of the fiber radially to obtain images showing structure in the fiber axis at a given depth, and secondly to expose any nanostructure which may be influenced by the reeling speed and multi-scale organization of the fiber. Diameter measurements performed in the SEM after plasma treatment confirm that this process etches more material with increased treatment time at a rate of approximately 100 nm min^{-1} (**Figure 1**). Thus, this process opens a pathway to exposing selected radial layers through etching, giving insights into the core of the fiber and the nanostructure within.

After 10 min of plasma treatment, a fiber with an original diameter of 5.02 μm was etched by 0.98 μm (0.49 μm either side) to its outer-core, where β-sheet crystals are thought to characterize the nanostructure and the mechanical response (Knight et al., 2000; Sponner et al., 2007). The nanostructures evident in **Figure 1** inset are most likely a result of the presence of β-sheet rich and ordered nano-domains which etch at a slower rate compared to the disordered amorphous phases. Their appearance is consistent with structures observed in dragline silk by SEM after the shell has been washed away by phosphate buffered saline (Augsten et al., 2000) and are similar to those observed in silkworm silk (Wan et al., 2017).

In order to confirm the effects of the etching process and describe the features revealed, a range of reeling speeds was used to generate different order/disorder ratios (Liu et al., 2005). For each reeling speed, the fibers were treated for 4 and 10 min and the comparison of the resulting nanostructures with reeling speed and plasma treatment are presented in **Figure 2**.

To the naked eye, there is no evident trend in the change in nanostructure with reeling speed. However, there are clear differences across all samples in response to plasma treatment time. Based on predictions from **Figure 1**, the images shown in **Figure 2** for both plasma etching times result in the lipid and glycoprotein coating being etched away to expose the outer core of the fiber—at 4 min the outer core just beneath the skin is exposed, while the 10 min etch predictably exposes the outer core close to the inner core.

The observed differences in nanostructure size may be explained by irregularities in the boundary between the skin

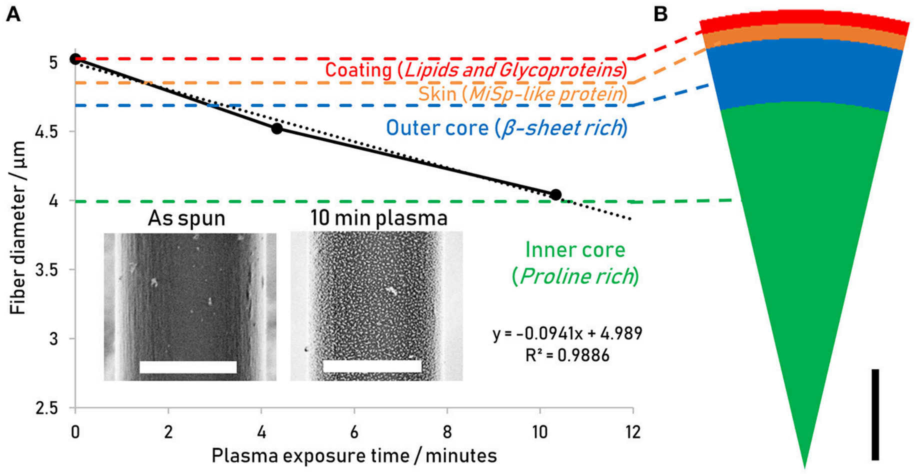

FIGURE 1 | (A) Reduction of diameter with increasing plasma treatment time. Different layers relative to the overall diameter are indicated according to Sponner et al. (2007). Insets: Regular secondary electron images of *Nephila inaurata* dragline silk before and after 10 min plasma treatment, imaged at 500 eV. Scalebars measure 3 μm **(B)** Schematic of radial structure of spider silk, scalebar shows 500 nm. Adapted (labels omitted, rotated, and color coded) from Sponner et al. (2007) under a CC BY 2.0 license (https://creativecommons.org/licenses/by/2.0/uk/), ©2007 Sponner et al.

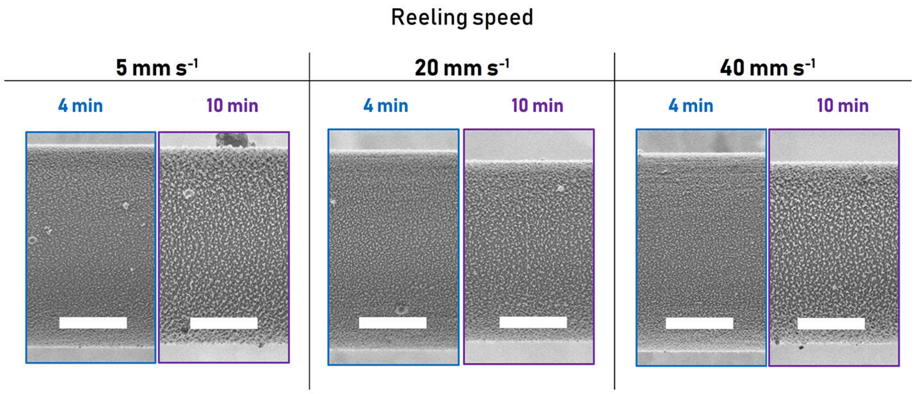

FIGURE 2 | Nanostructures revealed by plasma etching for 4 min (blue) and 10 min (purple) for the different reeling speeds obtained by regular SE imaging at 1 keV. Scalebars measure 2 μm.

and the outer-core which have previously been observed in AFM and immunostaining studies (Li et al., 1994; Sponner et al., 2005), leading to the 4 min treated surface being more skin-like in composition, whereas the 10 min treated surface is characteristic of the proline devoid and β-sheet crystal rich outer core. The reduced etching rate of the β-sheet crystals may also play a role in the increased size of nanostructure features after 10 min treatment, if after etching through the outer-core more β-sheet-rich ordered domains remain and protrude topographically in the image to appear brighter due to the SEM's edge effect prevalent in regular SE imaging.

The predominance of topographical contrast in regular SE images, specifically the edge effect, can pose a problem to image analysis as it exaggerates the size of the nanostructures and could obscure any contrast arising from material differences between the ordered nanostructures and the surrounding disordered matrix. Thus, the influence of topography is a significant impairment in any attempt to quantifiably characterize differences between the visible structures when using standard Low Voltage SEM.

To better separate the compositional information from the topographical information present in the untreated and plasma treated fiber surfaces we used Secondary Electron Spectroscopy in conjunction with Secondary Electron Hyperspectral Imaging (SEHI) in the SEM under the same conditions. SEHI makes use of the fact that the secondary electron signal from which SEM images are commonly generated incorporates energy information as well as spatial information. It has previously been shown that depending on the SE energy window selected, topography can be excluded and energy ranges can be assigned to different compositions or phases with sensitivity to elemental composition, hybridization state, degree of order and crystallinity

(Masters et al., 2015; Kumar et al., 2017; Wan et al., 2017; Dapor et al., 2018; Stehling et al., 2018).

SEHI was performed on the silk surface to compare the secondary electron energy signatures of the skin of the as-spun fiber with those of plasma etched fiber. The resulting secondary electron signal arises from the surface of the sample, which in the case of the as-spun fiber is the lipid layer, and in the case of the 10 min plasma treated fiber is the outer-core. Indeed, the difference between the spectrum of the as-spun (**Figure 3A**, blue line) and the etched fiber (**Figure 3D**) is the increased spectral emission intensity of the as-spun surface at lower secondary electron energies of 0–3 eV, so that this energy window may be assigned to the very outer lipid and glycoprotein layer, in the following referred to as the coating. Thus, the 0–3 eV energy window may be characterized as "coating-like."

This hypothesis is further validated by the fact that the "coating-like" energy-window 0–3 eV, indicated by the dashed orange line, has increased intensity toward the edges of the as-spun fiber, where a higher fraction of the escaping secondary electrons have escaped from the electron-thin coating rather than the layers closer to the core (**Figure 3A** red line). Conversely, the higher energy range of 3–5 eV which exhibits higher intensity in the treated fiber can be characterized as the "core-like" window, as marked by the green dashed lines.

While SE information is generally considered to be from the very top surface, information depths of secondary electrons can range up to 100 nm in insulators (Seiler, 1983; Hessel and Gross, 1992). According to Sponner et al. the very outer coating containing lipid and glycoprotein layers around *Nephila* dragline silk only measure approximately 10–20 and 60 nm, respectively (Sponner et al., 2007), resulting in a contribution of the lower proteinous skin layer to the SE signal and spectrum in the untreated fiber—that is, the SE signal arising from the underlying protein layer shines through the coating and is collected by the detector. Note that the fibers investigated in this work are neither sputter coated nor stained, as is common practice for other electron imaging techniques (Yarger et al., 2018). Thus, the difference between the "coating-like" and "core-like" energy windows can be observed and is likely to arise from the different compositional make-ups of the layers, with the "coating-like" spectrum reflecting its lipid composition and the "core-like" region responding to proteinous layers.

This correlation between layer composition and emission energy can be exploited using SEHI to obtain spatially resolved compositional information in the form of hyperspectral images, which map the emission intensity of a certain energy range with increased brightness of a pixel translating to increased emission

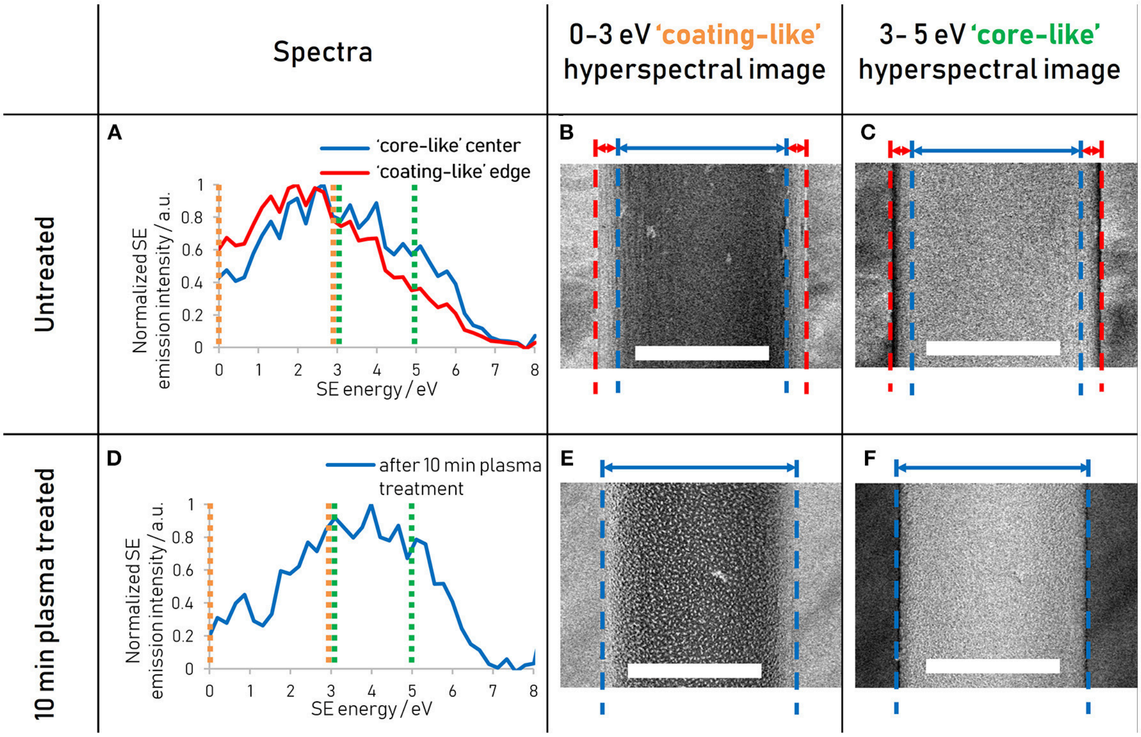

FIGURE 3 | (A) Spectra of untreated *Nephila inaurata* dragline silk highlighting differences between the coating-like spectrum arising from the edge (red lines) and the core-like spectrum arising form the middle (blue lines). **(B)** Hyperspectral image of the untreated fiber representing the energy range of 0–3 eV highlighting the coating-like emissions and **(C)** 3–5 eV energy range hyperspectral image highlighting the core-like emissions. **(D)** Spectrum of *Nephila inaurata* dragline silk after the removal of the coating and skin via a 10 min plasma etch. **(E)** and **(F)** as **(B)** and **(C)** for the 10 min treated sample. The hyperspectral energy ranges of 0–3 and 3–5 eV are represented by orange and green dashed lines in the spectra of **(A,D)**, respectively. All spectral images acquired with 500 eV primary beam energy. Scalebars measure 3 μm.

TABLE 1 | Summary of energy ranges used to isolate compositions on different scales.

Energy range/eV	Dominant SE signal response
0–3	Coating
1.5–4	Ordered nanostructure in core
3–5	Core with contribution from nanostructure
4–6	Disordered matrix in core

intensity (Wan et al., 2017). Note that these hyperspectral images are geometrically corrected to eliminate any potential image artifacts arising from angular dependencies of SE emission (for details please refer to the materials and methods section). As expected, the edges of the untreated fiber appear bright in the "coating-like" hyperspectral image (**Figure 3B**) and dark in the "core-like" hyperspectral image (**Figure 3C**), illustrating how the fraction of SEs emerging from the electron-thin coating gradually increases toward the fiber edge due to the cylindrical profile of the fiber. For the treated fiber, where the skin has been etched away, the "coating-like" hyperspectral image does exhibit bright edges, although this is readily explained by the fact that this energy range also responds to the nanostructures revealed by the plasma etching both at the edges and in the middle of the fiber, as seen clearly in the hyperspectral image (**Figure 3E**). The "core-like" hyperspectral image shows a uniform distribution of the gray levels across the fiber and especially at the edges in the treated fiber, illustrating how all SEs originate from the core layer (**Figure 3F**), whereas the "core-like" energy window in the untreated fiber shows a gradual reduction in gray levels as the number of SEs originating from the proteinous skin and core diminishes toward the edges (**Figure 3C**). Note how this energy window is not only insensitive to the difference in composition between the nanostructure and the matrix (**Figure 3F**), but also represses the topography arising from the different etching rates of the β-sheet crystals and amorphous regions.

Analogously to the way the coating and the core energy signatures have been compared in **Figure 3**, the energy signature of the nanostructures present in the plasma treated fiber can be compared to that of the matrix by spatially separating the two phases using thresholding of the greyscale values (**Figure 4**). It is clear from the spectra that the nanostructure and the matrix are best distinguished in the energy ranges from 1.5 to 4 eV, where the nanostructure dominates, and from 4 to 6 eV, where the matrix dominates.

The energy ranges isolated for the different components are summarized in **Table 1**. These energy range assignments overlap and are not absolute, so that a quantification in this way using spectral intensities would be problematic. However, the assignment of energy ranges in this fashion allows the determination of optimal energy windows in which the contrast between two components will be amplified compared to a regular SE image.

Thus, the energy windows selected using the spectra in **Figure 4** were used to generate hyperspectral images to isolate the nanostructure, by adding the 1.5–4 eV hyperspectral image to the inverse of the 4–6 eV hyperspectral image, as shown in **Figure 5**. The detailed images d-f illustrate how an isolation based on energy can yield a hyperspectral image with pinpointed information: The nanostructure appears less diffuse in the hyperspectral image compared to the regular SE images and resolves multiple smaller features which appear as one larger feature in the regular SE image (**Figure 5e** blue arrow). Importantly, besides increasing the apparent resolution of the energy-selected nanostructures, the selected energy range also reveals smaller scale structures present within the matrix, such as structures linking the larger particles highlighted in the yellow circle (**Figure 5d**) and sub 10 nm structures present in between

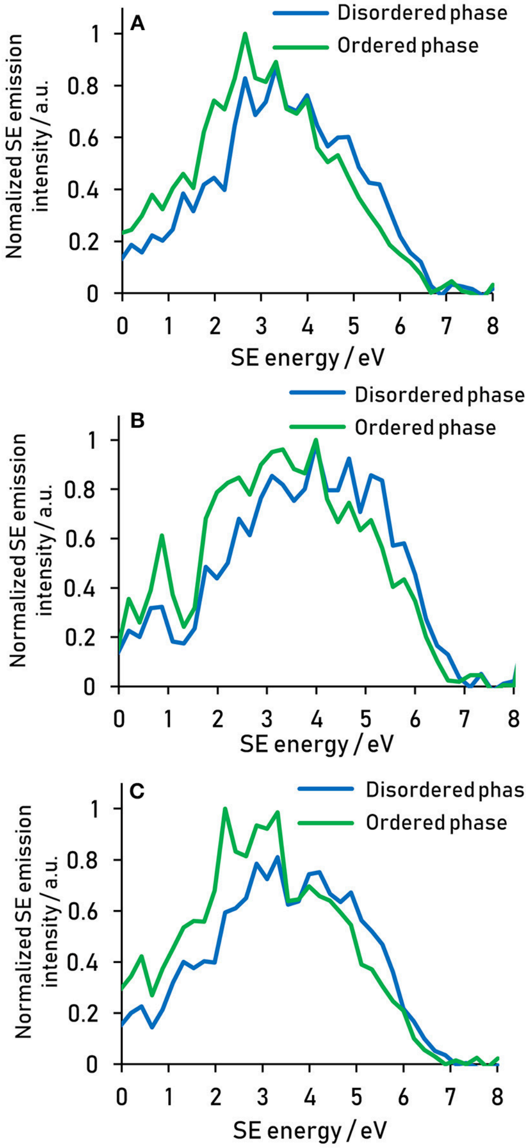

FIGURE 4 | Secondary electron spectral differences between the ordered nanostructure and the disordered matrix present after 10 min plasma treatment for reeling speeds of **(A)** 5 **(B)** 20, and **(C)** 40 mm s^{-1}. Spectra acquired at 500 eV primary beam energy.

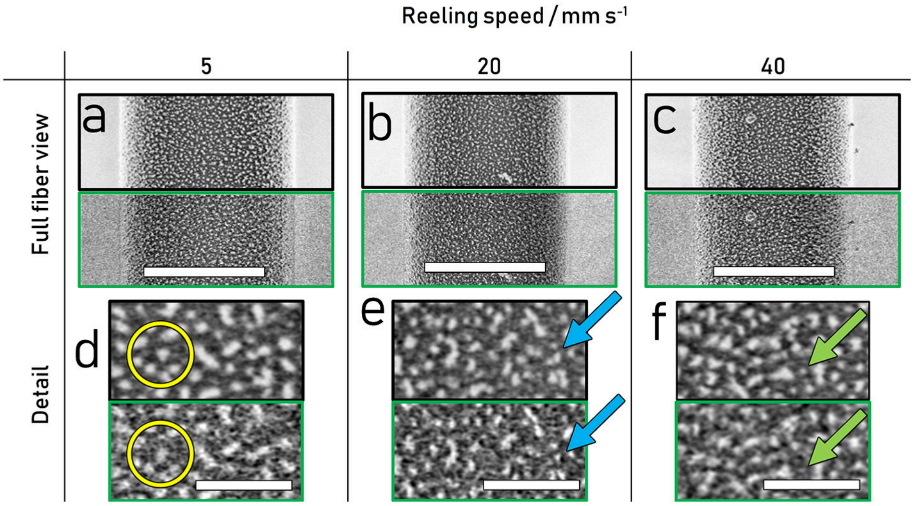

FIGURE 5 | Comparison of regular SE (top with black border) and contrast-optimized hyperspectral images (bottom with green border) of 10 min plasma etched spider dragline silk reeled at 5, 20 and 40 mm s^{-1}. **(a–c)** View across fiber, scalebars measure 3 µm **(d–f)** Detailed representation showing higher resolution and increased detail in the hyperspectral images, scalebars measure 500 nm. All images acquired at 500 eV primary beam energy.

the larger nanostructures highlighted by the green arrow in **Figure 5f**.

Currently these structures are barely resolved in the presented images and difficult to separate from noise. However, their presence in the nanostructure optimized image and absence in the corresponding regular SE image suggests their composition may lie in between the more ordered and disordered components. Higher resolution hyperspectral images of targeted energies may give a clearer picture of the nature of these structures.

The differences in nanostructure with varying reeling speed are not readily seen with the naked eye in the hyperspectral images in **Figure 5**. To characterize and quantify the nanostructure, different image analysis tools were applied to the hyperspectral images in **Figure 5**, with the results presented in **Figure 6**. Firstly, the bright nanostructures were isolated from the darker matrix using thresholding. The resulting binary images presented in **Figure 6A** were analyzed for the area fraction of the nanostructure and for its size distribution. The area fraction of the particles in the total sampled area decreased from 35 to 31 to 29% for the reeling speeds of 5, 20, and 40 mm s^{-1}, respectively. Interestingly, plotting the area distributions of the nanostructure as a histogram shows indications of a bi-modal distribution of nanostructure sizes consistent with literature (Trancik et al., 2006) (see **Figure S1**). However, there are limits to the area data recorded; Firstly, objects smaller than 6.5 nm cannot be resolved with the given image resolution, and secondly the total area is subject to error introduced by differences in brightness and contrast between images.

To eliminate the sensitivity to differences in brightness and contrast of the source images, a Voronoi tessellation was chosen as a processing tool because it considers only the center of the particle (in this case the nanostructure) and not its entire area (Voronoi, 1908). Furthermore, it not only considers the properties of the structures, but also characterizes their location relative to one another. In a Voronoi tessellation as shown in **Figure 6B**, the tessellation lines run along where one particle center is equidistant to its nearest neighbor. The color value simultaneously encodes the magnitude of the distance of the Voronoi tessellation boundary to the center of either particle. The increased occurrence of higher distance values with increased reeling speed is evident from the Voronoi diagrams (**Figure 6B**) and the frequency histogram of the Voronoi tessellation was (**Figure S1**). This result is consistent with the indication of a bimodal size distribution of the area distribution, that is, the smaller reeling speeds have an increased number of particles smaller than 20 nm, which in turn results in the higher number of smaller particle distances seen in the Voronoi diagrams. Conversely, at higher reeling speeds the nanostructures are further apart from one another.

It seems then that it is not only the size and size distribution of nanostructures that matters, but also their distances from one-another within the matrix. This would imply that the interaction between the nanostructures and the matrix play an important role in the tensile properties of the outer core. To get a better understanding of the absolute numbers associated with particle distances (i.e., considering the size of the particles as well), the distance map of the binary images presented in **Figure 6A** were generated and analyzed (**Figure 6C**). The population of distances shows the same trend as the Voronoi tessellation distributions: at higher reeling speeds the smaller distances become less frequent while the larger distances become more frequent. This confirms that the trend is not only influenced by the size of a nanostructure, but also by the distribution of the matrix in between the particles. The result is a larger fraction of the matrix further away from any nanostructures at higher reeling speeds,

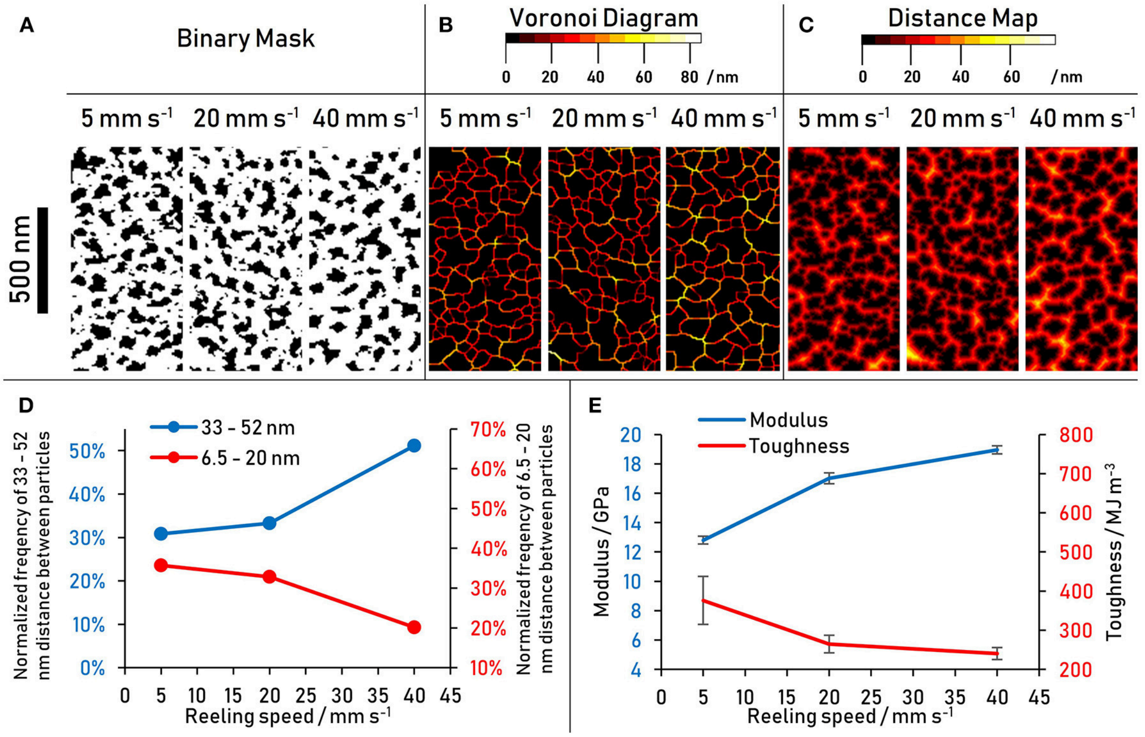

FIGURE 6 | (A–C) Particle analysis of nanostructure in 10 min plasma treated spider dragline silk performed on hyperspectral images shown in **Figure 5**. The images show a sample of a total sample area of 4 μm^2. **(D)** Frequency of larger (33–52 nm) and smaller (6.5–20 nm) nanostructure Voronoi distances with reeling speed **(E)** Modulus and toughness with reeling speed of the same spider silk thread.

resulting in less scope for matrix-nanostructure interactions and more prominent matrix-matrix interactions. The critical distance between nanostructures where the trend reverses is 20 nm, which may indicate that a bi-modal size distribution and thus a multi-scale organization is present not only within the crystalline nanostructure but also in the disordered domains.

Voronoi tessellation distances of 6.5–20 and 33–52 nm have been grouped to plot this trend in **Figure 6D**. The tensile results of the same silk thread (**Figure 6E**) are shown next to the results of the nanostructure analysis in an attempt to link nanoscale structure to macroscale properties. Assuming that the distribution of the ordered nanostructure within the fiber directly affects mechanical properties of the material, the data suggest that shorter distances between the ordered β-sheet crystals beget toughness, while larger distances contribute to a higher modulus. Potential explanations for this relationship are proposed in the Discussion section.

DISCUSSION

The size and orientation of the ordered domains and especially the β-sheet crystals within spider silk have been subject to intense experimental interest with regards to their contribution to the desirable tensile properties of spider silk (Yang et al., 1997; Riekel and Vollrath, 2001; Sampath et al., 2012; McGill et al., 2018). Thus, modeling studies have focused on their tensile behavior in isolation from the matrix on length scales of atomistic to nanoscale models (Thiel et al., 1997; Keten et al., 2010; Giesa et al., 2011). The idea that the crystallinity alone is responsible for the dragline fiber's renowned mechanical response is in direct conflict with the fact that both minor ampullate spider silk of the same species and *Bombyx mori* silk have a substantially larger crystalline fraction and less desirable tensile properties (Riekel and Vollrath, 2001; Sampath et al., 2012). The results in this study suggest that the matrix and specifically the matrix-nanostructure interactions are key in the tensile response of the fibers. Although there are promising developments in elucidating the secondary structure and general organization of the amorphous phase (McGill et al., 2018), its inherent lack of order has posed a challenge to the structural analysis community as it cannot be readily described using most methods applied to the crystalline fractions of the fiber. This gives us a possible explanation why there is an underappreciation for its role in spider silk's mechanical response. Although this hypothesis requires further validation, our results suggest that the modulus is governed though the matrix-matrix interactions, whereas matrix-nanocrystal interactions supply a toughening mechanism especially at lower reeling speeds. Through their X-ray and NMR work, Grubb and Jelinski have come to a similar conclusion; that is that spider silk is best described on the macroscale as a filled elastomer, with the β-sheets acting as fillers to enhance the mechanical properties of the rubber-like amorphous and ordered amorphous matrix (Simmons et al., 1996; Grubb and Jelinski, 1997).

To link the parameters given by atomistic models to a larger scale, spider silk fiber has been modeled as a bundle of nanofibrils with diameters of 20–150 nm (Giesa et al., 2011). Initially thought to be cylindrical and spatially confined like those observed in *Bombyx mori* silk, more recent AFM and TEM studies have shown more diffuse structures which are oriented in the fiber direction, with some models considering spider silk thread as a bundle of fibrils (Giesa et al., 2011; Xu et al., 2014) or globules (Cranford, 2013). A directional anisotropy of structures on such length scales were not evident in this work, with the orientation of the exposed nanostructure in the outer-core being broadly isotropic. The size of the revealed structures is however consistent with accounts of a bi-modal size distribution of the higher-order fractions (Trancik et al., 2006). In our current work we see indications of the smaller size population, especially using hyperspectral imaging, although it is still below the resolution limit. Our dominant observed nanostructure is consistent with the larger population of ordered structures of 20–150 nm extension transverse to the fiber direction. The use of SEHI in combination with low temperature plasma etching provides access to a larger number of particles compared to data published in previous AFM (Miller et al., 1999; Du et al., 2006; Schäfer et al., 2008; Brown et al., 2011; Wang and Schniepp, 2018) and TEM (Thiel et al., 1997; Trancik et al., 2006) studies. This is essential to build a quantitative picture of nano- and microstructure distribution, especially considering that spider silk modeling approaches have yet to incorporate our knowledge of these multi-scale structures (Yarger et al., 2018). The various approaches taken to date in the mechanistic modeling of spider silk have been summed up in a recent review (López Barreiro et al., 2018). Various modeling approaches have had some success in reproducing spider silk's mechanical behavior but the incorporation of multiscale structures and their interactions into mechanistic models is yet to be realized in part due to the practical difficulty of liking atomistic approaches to micron scale models.

A complete 3D model of spider silk with its multi-scale organization is additionally hampered by the difficulties of revealing its internal make-up. The largest single fiber silk from a large spider only measures around 5 μm in diameter to start with, and provenly exhibits structures down to 2 nm in size (Trancik et al., 2006). Furthermore, the structures under investigation are sensitive to strain, thermal and chemical treatment and can undergo undesired and unknown structural modification through sample preparation. Thus, it cannot simply be cut or sectioned without potentially manipulating the structures of interest. Previously reported sample preparation procedures employ epoxy embedding, which cures exothermically and may result in thermal modification of fibers, and wax embedding involving solvent dehydration, embedding in molten wax, and rehydration steps. While the results contributed from these studies supply important pieces to the puzzle, such as the observation of a differential in mechanical properties between the inner and the outer core (Brown et al., 2011), it must be kept in mind that the fiber may have been substantially chemically transformed.

In this work we have used low-temperature plasma etching as a non-thermal, surface-acting technique. Previous work considering the surface modifications of polyamide(6,6) fibers in low temperature plasma establish that the surface morphology after plasma treatment is a result of the sample's crystallinity content and strain history (Yip et al., 2006), which makes this approach especially suitable for the analysis of spider silk force reeled at different speeds. While the methodology requires further optimization, we were able to identify differences in the resulting morphology with reeling speed exposed in the outer-core of the fiber. We show that comparably, plasma treatment may be a mild preparation method to uncover certain layers within the radial structure of spider silk.

Compared to conventional spatially resolved techniques such as conventional SEM, TEM and AFM our secondary electron hyperspectral imaging (SEHI) has key advantages when imaging spider silk and associated nanostructures. The Low-Voltage SEM imaging requires no sample preparation besides the plasma treatment, and thus eliminates potentially damaging or obscuring processes such as coating or staining. Our comparison of SE spectra and hyperspectral images illustrates how powerful this method is in distinguishing natural organic materials and compositions, such as lipids and proteins, while simultaneously enabling the suppression of topographical information of SEs. Secondly, through the systematic selection of energy ranges, we have increased the compositional contrast between the nanostructures and the matrix, revealing structures which are not visible in a conventional SE image. In future studies this approach will be further developed to resolve the sub 10 nm features prevalent in the matrix in between the larger nanostructures, especially in the lower reeling speeds.

We present low temperature plasma etching as a novel tool to uncover layers along the radial profile of *Nephila* spider silk. The use of Secondary Electron Hyperspectral Imaging (SEHI) has allowed high resolution mapping of the different compositions of the components contributing to the multi-scale design of dragline silk, with distinct energy signatures arising from the skin and core on the microscale, and the nanostructures and matrix on the nanoscale. The use of these energy ranges in hyperspectral images has revealed smaller scale structures than those evident in regular SE images. While there were no significant differences in nanostructure area fraction and orientation with reeling speed, the spatial situation of the >20 nm nanostructures is shown to change, with larger distances between nanostructures prevalent at higher reeling speeds.

The combination of plasma etching, LV-SEM, and SEHI provides a top-down approach for the structural analysis of spider silk which bridges multiple length scales and supplies compositional and spatial information simultaneously. Further work will involve varying etching times and thus exposing fiber layers systematically to obtain an extensive dataset illustrating the radial evolution of nanostructures within the fiber. Specifically, such a dataset will serve to bridge the length scale gaps between the current molecular and larger scale models and will help to map out the yet poorly defined disordered domains and the situation of the ordered domains within. A multiscale mechanical model capable of incorporating this information and reproducing silk's complex tensile behavior will be a large step forward in engineering structure-property relationships for bio-inspired man-made materials.

AUTHOR CONTRIBUTIONS

NS performed the majority of the experimental work and data analysis and wrote the manuscript. KA performed instrument calibration and validation work central to the spectral data in the manuscript. CH and CR contributed to the experimental design, project supervision, and the writing of the manuscript.

FUNDING

Any expenses pertaining to experimental work were covered by the EPSRC grants EP/K005693/1 and EN/N008065. As this is an invited contribution, the publication fees are waived (see cover letter).

ACKNOWLEDGMENTS

CR and CH would like to thank the EPSRC for funding (EP/N008065/1 and EP/K005693/1).

SUPPLEMENTARY MATERIAL

The Supplementary Material for this article can be found online at: https://www.frontiersin.org/articles/10.3389/fmats.2018.00084/full#supplementary-material

REFERENCES

Augsten, K., Muehlig, P., and Herrmann, C. (2000). Glycoproteins and skin-core structure in Nephila clavipes spider silk observed by light and electron microscopy. *Scanning* 22, 12–15. doi: 10.1002/sca.4950220103

Boulet-Audet, M., Vollrath, F., and Holland, C. (2015). Identification and classification of silks using infrared spectroscopy. *J. Exp. Biol*. 218, 3138–3149. doi: 10.1242/jeb.128306

Brown, C. P., MacLeod, J., Amenitsch, H., Cacho-Nerin, F., Gill, H. S., Price, A. J., et al. (2011). The critical role of water in spider silk and its consequence for protein mechanics. *Nanoscale* 3, 3805–3811. doi: 10.1039/c1nr10502g

Cebe, P., Hu, X., Kaplan, D. L., Zhuravlev, E., Wurm, A., Arbeiter, D., et al. (2013). Beating the heat-fast scanning melts silk beta sheet crystals. *Sci. Rep*. 3:1130. doi: 10.1038/srep01130

Cranford, S. W. (2013). Increasing silk fibre strength through heterogeneity of bundled fibrils. *J. R. Soc. Interface* 10:20130148. doi: 10.1098/rsif.2013.0148

Dapor, M., Masters, R. C., Ross, I., Lidzey, D. G., Pearson, A., Abril, I., et al. (2018). Secondary electron spectra of semi-crystalline polymers – A novel polymer characterisation tool? *J. Electron Spectros. Relat. Phenomena* 222, 95–105. doi: 10.1016/j.elspec.2017.08.001

Dicko, C., Porter, D., Bond, J. E., Kenney, J. M., and Vollrath, F. (2007). Structural disorder in silk proteins reveals the emergence of elastomericity. *Biomacromolecules* 9, 216–21. doi: 10.1021/bm701069y

Du, N., Liu, X. Y., Narayanan, J., Li, L., Lim, M. and Li, D. (2006). Design of superior spider silk: from nanostructure to mechanical properties. *Biophys. J*. 91, 4528–4535. doi: 10.1529/biophysj.106.089144

Ebrahimi, D., Tokareva, O., Rim, N. G., Wong, J. Y., Kaplan, D. L., and Buehler, M. J. (2015). Silk–its mysteries, how it is made, and how it is used. *ACS Biomater. Sci. Eng*. 1, 864–876. doi: 10.1021/acsbiomaterials.5b00152

Frische, S., Maunsbach, A. B., and Vollrath, E. (2002). Elongate cavities and skin–core structure in Nephila spider silk observed by electron microscopy. *J. Microsc*. 189, 64–70. doi: 10.1046/j.1365-2818.1998.00285.x

Giesa, T., Arslan, M., Pugno, N. M., and Buehler, M. J. (2011). Nanoconfinement of spider silk fibrils begets superior strength, extensibility, and toughness. *Nano Lett*. 11, 5038–5046. doi: 10.1021/nl203108t

Greving, I., Dicko, C., Terry, A., Callow, P., and Vollrath, F. (2010). Small angle neutron scattering of native and reconstituted silk fibroin. *Soft. Matter*. 6, 4389–4395. doi: 10.1039/c0sm00108b

Grubb, D. T., and Jelinski, L. W. (1997). Fiber morphology of spider silk: the effects of tensile deformation. *Macromolecules* 30, 2860–2867. doi: 10.1021/ma961293c

Hessel, R., and Gross, B. (1992). Escape depth of secondary electrons from electron-irradiated polymers. *IEEE Trans. Electr. Insul*. 27, 831–834. doi: 10.1109/14.155806

Hijirida, D. H., Do, K. G., Michal, C., Wong, S., Zax, D., and Jelinski, L. W. (1996). 13C NMR of Nephila clavipes major ampullate silk gland. *Biophys. J*. 71, 3442–3447. doi: 10.1016/S0006-3495(96)79539-5

Holland, C., Hawkins, N., Frydrych, M., Laity, P., Porter, D., and Vollrath, F. (2018a). Differential scanning calorimetry of native silk feedstock. *Macromol. Biosci*. 9:1800228. doi: 10.1002/mabi.201800228

Holland, C., Numata, K., J., Rnjak-Kovacina, and Seib, F. P. (2018b). The biomedical use of silk: past, present, future. *Adv. Healthc. Mater*. 8:1800465. doi: 10.1002/adhm.201800465

Holland, G. P., Creager, M. S., Jenkins, J. E., Lewis, R. V., and Yarger, J. L. (2008). Determining secondary structure in spider dragline silk by carbon– carbon correlation solid-state NMR spectroscopy. *J. Am. Chem. Soc*. 130, 9871–9877. doi: 10.1021/ja8021208

Kazemian, P., S.,Mentink, A. M., Rodenburg, C., and Humphreys, C. J. (2007). Quantitative secondary electron energy filtering in a scanning electron microscope and its applications. *Ultramicroscopy* 107, 140–150. doi: 10.1016/j.ultramic.2006.06.003

Keten, S., Xu, Z., Ihle, B., and Buehler, M. J. (2010). Nanoconfinement controls stiffness, strength and mechanical toughness of [beta]-sheet crystals in silk. *Nat. Mater*. 9, 359–367. doi: 10.1038/nmat2704

Kitagawa, M., and Kitayama, T. (1997). Mechanical properties of dragline and capture thread for the spider Nephila clavata. *J. Mater. Sci*. 32, 2005–2012. doi: 10.1023/A:1018550116930

Knight, D. P., Knight, M. M., and Vollrath, F. (2000). Beta transition and stress-induced phase separation in the spinning of spider dragline silk. *Int. J. Biol. Macromol*. 27, 205–210. doi: 10.1016/S0141-8130(00)00124-0

Koeppel, A., and Holland, C. (2017). Progress and trends in artificial silk spinning: a systematic review. *ACS Biomater. Sci. Eng*. 3, 226–237. doi: 10.1021/acsbiomaterials.6b00669

Kumar, V., Schmidt, W. L., Schileo, G., Masters, R. C., Wong-Stringer, M., Sinclair, D. C., et al. (2017). Nanoscale mapping of bromide segregation on the cross sections of complex hybrid perovskite photovoltaic films using secondary electron hyperspectral imaging in a scanning electron microscope. *ACS Omega* 2, 2126–2133. doi: 10.1021/acsomega.7b00265

Kümmerlen, J., Van Beek, J. D., Vollrath, F., and Meier, B. H. (1996). Local structure in spider dragline silk investigated by two-dimensional spin-diffusion nuclear magnetic resonance. *Macromolecules* 29, 2920–2928. doi: 10.1021/ma951098i

Li, S. F., McGhie, A. J., and Tang, S. L. (1994). New internal structure of spider dragline silk revealed by atomic force microscopy. *Biophys. J*. 66, 1209–1212. doi: 10.1016/S0006-3495(94)80903-8

Lin, T. Y., Masunaga, H., Sato, R., Malay, A. D., Toyooka, K., Hikima, T., et al. (2017). Liquid crystalline granules align in a hierarchical structure to produce spider dragline microfibrils. *Biomacromolecules* 18, 1350–1355. doi: 10.1021/acs.biomac.7b00086

Liu, Y., Shao, Z., and Vollrath, F. (2005). Relationships between supercontraction and mechanical properties of spider silk. *Nat. Mater*. 4, 901–905. doi: 10.1038/nmat1534

López Barreiro, D., Yeo, J., Tarakanova, A., F. J., Martin-Martinez, and Buehler, M. J. (2018). Multiscale modeling of silk and silk-based biomaterials—a review. *Macromol. Biosci*. e1800253. doi: 10.1002/mabi.201800253. [Epub ahead of print].

Masters, R. C., Pearson, A. J., Glen, T. S., F.-,Sasam, C., Li, L., Dapor, M., et al. (2015). Sub-nanometre resolution imaging of polymer-fullerene photovoltaic blends using energy-filtered scanning electron microscopy. *Nat. Commun*. 6:6928. doi: 10.1038/ncomms7928

McGill, M., Holland, G. P., and Kaplan, D. L. (2018). Experimental methods for characterizing the secondary structure and thermal properties of silk proteins. *Macromol. Rapid Commun*. 40:e1800390. doi: 10.1002/marc.201800390

Miller, L. D., Putthanarat, S., Eby, R. K., and Adams, W. W. (1999). Investigation of the nanofibrillar morphology in silk fibers by small angle X-ray scattering and atomic force microscopy. *Int. J. Biol. Macromol*. 24, 159–165. doi: 10.1016/S0141-8130(99)00024-0

Nova, A., Keten, S., Pugno, N. M., Redaelli, A., and Buehler, M. J. (2010). Molecular and nanostructural mechanisms of deformation, strength and toughness of spider silk fibrils. *Nano Lett*. 10, 2626–2634. doi: 10.1021/nl101341w

Oktaviani, N. A., Matsugami, A., Malay, A. D., Hayashi, F., Kaplan, D. L., and Numata, K. (2018). Conformation and dynamics of soluble repetitive domain elucidates the initial β-sheet formation of spider silk. *Nat. Commun*. 9:2121. doi: 10.1038/s41467-018-04570-5

Parent, L. R., Onofrei, D., Xu, D., Stengel, D., Roehling, J. D., Addison, J. B., et al. (2018). Hierarchical spidroin micellar nanoparticles as the fundamental precursors of spider silks. *Proc. Natl. Acad. Sci. U.S.A*. 115, 11507–11512. doi: 10.1073/pnas.1810203115

Porter, D., Guan, J., and Vollrath, F. (2013). Spider silk: super material or thin fibre? *Adv. Mater*. 25, 1275–1279. doi: 10.1002/adma.201204158

Riekel, C., Madsen, B., Knight, D., and Vollrath, F. (2000). X-ray diffraction on spider silk during controlled extrusion under a synchrotron radiation X-ray beam. *Biomacromolecules* 1, 622–626. doi: 10.1021/bm000047c

Riekel, C., Rössle, M., Sapede, D., and Vollrath, F. (2004). Influence of CO2 on the micro-structural properties of spider dragline silk: X-ray microdiffraction results. *Naturwissenschaften* 91, 30–33. doi: 10.1007/s00114-003-0482-8

Riekel, C., and Vollrath, F. (2001). Spider silk fibre extrusion: combined wide- and small-angle X-ray microdiffraction experiments. *Int. J. Biol. Macromol*. 29, 203–210. doi: 10.1016/S0141-8130(01)00166-0

Rim, N. G., Roberts, E. G., Ebrahimi, D., Dinjaski, N., Jacobsen, M. M., Martín-Moldes, Z., et al. (2017). Predicting silk fiber mechanical properties through multiscale simulation and protein design. *ACS Biomater. Sci. Eng*. 3, 1542–1556. doi: 10.1021/acsbiomaterials.7b00292

Sampath, S., Isdebski, T., Jenkins, J. E., V., Ayon, J., Henning, R. W., et al. (2012). X-ray diffraction study of nanocrystalline and amorphous structure within major and minor ampullate dragline spider silks. *Soft. Matter*. 8, 6713–6722. doi: 10.1039/c2sm25373a

Schäfer, A., Vehoff, T., Glišovi,ć, A., and Salditt, T. (2008). Spider silk softening by water uptake: an AFM study. *Eur. Biophys. J*. 37, 197–204. doi: 10.1007/s00249-007-0216-5

Schindelin, J., Arganda-Carreras, I., Frise, E., Kaynig, V., Longair, M., Pietzsch, T., et al. (2012). Fiji: an open-source platform for biological-image analysis. *Nat. Methods* 9:676. doi: 10.1038/nmeth.2019

Seiler, H. (1983). Secondary electron emission in the scanning electron microscope. *J. Appl. Phys*. 54, R1–R18. doi: 10.1063/1.332840

Simmons, A. H., Michal, C. A., and Jelinski, L. W. (1996). Molecular orientation and two-component nature of the crystalline fraction of spider dragline silk. *Science* 271, 84–87. doi: 10.1126/science.271.5245.84

Skelton, R. E., and Nagase, K. (2012). Tensile tensegrity structures. *Int. J. Sp. Struct*. 27, 131–137. doi: 10.1260/0266-3511.27.2-3.131

Sponner, A., Unger, E., Grosse, F., and Weisshart, K. (2005). Differential polymerization of the two main protein components of dragline silk during fibre spinning. *Nat. Mater*. 4, 772–775. doi: 10.1038/nmat1493

Sponner, A., Vater, W., Monajembashi, S., Unger, E., Grosse, F., and Weisshart, K. (2007). Composition and hierarchical organisation of a spider silk. *PLoS ONE* 2:e998. doi: 10.1371/journal.pone.0000998

Stehling, N., Masters, R., Zhou, Y., O'Connell, R., Holland, C., Zhang, H., et al. (2018). New perspectives on nano-engineering by secondary electron spectroscopy in the helium ion and scanning electron microscope. *MRS Commun*. 8, 226–240. doi: 10.1557/mrc.2018.75

Termonia, Y. (1994). Molecular modeling of spider silk elasticity. *Macromolecules* 27, 7378–7381. doi: 10.1021/ma00103a018

Thiel, B. L., Guess, K. B., and Viney, C. (1997). Non-periodic lattice crystals in the hierarchical microstructure of spider (major ampullate) silk. *Biopolym. Orig. Res. Biomol.* 41, 703–719. doi: 10.1002/(SICI)1097-0282(199706)41:7&<;703::AID-BIP1&>;3.0.CO;2-T

Trancik, J. E., Czernuszka, J. T., Bell, F. I., and Viney, C. (2006). Nanostructural features of a spider dragline silk as revealed by electron and X-ray diffraction studies. *Polymer* 47, 5633–5642. doi: 10.1016/j.polymer.2005.01.110

Vollrath, F., Hawkins, N., Porter, D., Holland, C., and M., Boulet-Audet (2014). Differential scanning fluorimetry provides high throughput data on silk protein transitions. *Sci. Rep*. 4:5625. doi: 10.1038/srep05625

Vollrath, F., and Knight, D. P. (2001). Liquid crystalline spinning of spider silk. *Nature* 410, 541–548. doi: 10.1038/35069000

Vollrath, F., and Porter, D. (2009). Silks as ancient models for modern polymers. *Polymer* 50, 5623–5632. doi: 10.1016/j.polymer.2009.09.068

Vollrath, F., Porter, D., and Holland, C. (2011). There are many more lessons still to be learned from spider silks. *Soft Matter* 7, 9595–9600. doi: 10.1039/c1sm05812f

Voronoi, G. (1908). Nouvelles applications des paramètres continus à la théorie des formes quadratiques. Deuxième mémoire. Recherches sur les parallélloèdres primitifs. *J. Für Die Reine Und Angew. Math*. 134, 198–287.

Wagner, J. A., Patil, S. P., Greving, I., Lämmel, M., Gkagkas, K., Seydel, T., et al. (2017). Stress-induced long-range ordering in spider silk. *Sci. Rep*. 7:15273. doi: 10.1038/s41598-017-15384-8

Wakida, T., and Tokino, S. (1996). Surface modification of fibre and polymeric materials by discharge treatment and its application to textile processing. *Indian J. Fibre Textile Res*. 21, 69–78.

Walker, A. A., Holland, C., and Sutherland, T. D. (2015). More than one way to spin a crystallite: multiple trajectories through liquid crystallinity to solid silk. *Proc. R. Soc. B* 282:20150259. doi: 10.1098/rspb.2015.0259

Wan, Q., K. J., Abrams, K. J., R. C., Masters, R. C., Talari, A. C. S., Rehman I. U., Claeyssens, F., et al. (2017). Mapping nanostructural variations in silk by secondary electron hyperspectral imaging. *Adv. Mater*. 29:1703510. doi: 10.1002/adma.201703510

Wang, Q., and Schniepp, H. C. (2018). Strength of recluse Spider's silk originates from nanofibrils. *ACS Macro Lett.* 7, 1364–1370. doi: 10.1021/acsmacrolett.8b00678

Willis, R. F., Fitton, B., and Skinner, D. K. (1972). Study of carbon-fiber surfaces using Auger and secondary electron emission spectroscopy. *J. Appl. Phys*. 43, 4412–4419. doi: 10.1063/1.1660936

Xu, G., Gong, L., Yang, Z., and Liu, X. Y. (2014). What makes spider silk fibers so strong? From molecular-crystallite network to hierarchical network structures. *Soft Matter* 10, 2116–2123. doi: 10.1039/C3SM52845F

Yang, Z., Grubb, D. T., and Jelinski, L. W. (1997). Small-angle X-ray scattering of spider dragline silk. *Macromolecules* 30, 8254–8261. doi: 10.1021/ma970548z

Yang, Z., Liivak, O., Seidel, A., LaVerde, G., Zax, D. B., and Jelinski, L. W. (2000). Supercontraction and backbone dynamics in spider silk: 13C and 2H NMR studies. *J. Am. Chem. Soc*. 122, 9019–9025. doi: 10.1021/ja0017099

Yarger, J. L., Cherry, B. R., and A., Van Der Vaart (2018). Uncovering the structure–function relationship in spider silk. *Nat. Rev. Mater*. 3:18008. doi: 10.1038/natrevmats.2018.8

Yazawa, K., Malay, A. D., Masunaga, H., and Numata, K. (2018). Role of skin layers on mechanical properties and supercontraction of spider dragline silk fiber. *Macromol. Biosci*. 1800220. doi: 10.1002/mabi.201800220. [Epub ahead of print].

Yip, J., Chan, K., Sin, K. M., and Lau, K. S. (2002). Low temperature plasma-treated nylon fabrics. *J. Mater. Process. Technol*. 123, 5–12. doi: 10.1016/S0924-0136(02)00024-9

Yip, J., Chan, K., Sin, K. M., and Lau, K. S. (2002). Study of plasma-etched and laser-irradiated polyamide materials. *Mater. Res. Innov*. 6, 44–50. doi: 10.1007/s10019-002-0169-3

Yip, J., Chan, K., Sin, K. M., and Lau, K. S. (2006). Formation of periodic structures by surface treatments of polyamide fiber: part II. Low temperature plasma treatment. *Appl. Surf. Sci*. 253, 2493–2497. doi: 10.1016/j.apsusc.2006.05.004

Zhang, T. Y., and Suen, C. Y. (1984). A fast parallel algorithm for thinning digital patterns. *Commun. ACM* 27, 236–239. doi: 10.1145/357994.358023

Conflict of Interest Statement: The authors declare that the research was conducted in the absence of any commercial or financial relationships that could be construed as a potential conflict of interest.

frontiers in Materials

ORIGINAL RESEARCH
published: 31 January 2019
doi: 10.3389/fmats.2019.00002

Optimal Design of the Band Structure for Beam Lattice Metamaterials

Andrea Bacigalupo[1]*, Marco Lepidi*[2]*, Giorgio Gnecco*[1]*, Francesca Vadalà*[2] *and Luigi Gambarotta*[2]*

[1] *IMT School for Advanced Studies Lucca, Lucca, Italy,* [2] *DICCA, University of Genoa, Genoa, Italy*

Sonic or acoustic metamaterials may offer a mechanically robust and highly customizable solution to open large band gaps in the low-frequency dispersion spectrum of beam lattice materials. Achieving the largest possible stop bandwidth at the lowest possible center frequency may be a challenging multi-objective optimization issue. The paper presents a first effort of analysis, systematization and synthesis of some recent multi-disciplinary studies focused on the optimal spectral design of beam lattice materials and metamaterials. The design parameter vector is a finite set including all the microstructural properties characterizing the periodic material and the local resonators. Numerical algorithms are employed as leading methodology for solving various instances of the optimization problem. Methodological alternatives, based on perturbation methods and computational modeling, are also illustrated. Some optimal results concerning the dispersion spectrum of hexachiral, tetrachiral and anti-tetrachiral materials and metamaterials are summarized. The concluding remarks are accompanied by preliminary ideas to overcome some operational issues in solving the optimization problem.

Keywords: architectured materials, wave propagation, dispersion properties, band gaps, local resonators, acoustic metamaterials

Edited by:
Fernando Fraternali,
University of Salerno, Italy

Reviewed by:
Georgios Theocharis,
UMR6613 Laboratoire d'Acoustique de l'Universite du Maine (LAUM), France
Anastasiia O. Krushynska,
Department of Civil, Environmental and Mechanical Engineering, University of Trento, Italy
Giuseppe Zurlo,
National University of Ireland Galway, Ireland

Correspondence:
Luigi Gambarotta
luigi.gambarotta@unige.it

Specialty section:
This article was submitted to Mechanics of Materials, a section of the journal Frontiers in Materials

Received: *23 October 2018*
Accepted: *07 January 2019*
Published: *31 January 2019*

Citation:
Bacigalupo A, Lepidi M, Gnecco G, Vadalà F and Gambarotta L (2019) Optimal Design of the Band Structure for Beam Lattice Metamaterials. Front. Mater. 6:2. doi: 10.3389/fmats.2019.00002

1. INTRODUCTION

An increasing research attention is being currently paid to the characterization of the acoustic properties of periodic materials with beam lattice microstructure. In particular, several studies have been developed to parametrically assess the dispersion relations governing the free propagation of elastic waves (Phani et al., 2006; Spadoni et al., 2009; Paggi, 2010; Tee et al., 2010; Colquitt et al., 2011; Tie et al., 2013; Reda et al., 2016; Amendola et al., 2018; Bordiga et al., in press), as well as the associated transfer of mechanical energy (Langley, 1994, 1995, 1996; Bacigalupo and Lepidi, 2018). An objective of major theoretical interest for engineering applications, including for instance wave trapping, vibration shielding, noise silencing and invisibility cloaking, is the realization of phononic filters by designing and optimizing the stop bands of the frequency spectrum. Specifically, since the intrinsic dissipation of conventional materials is inherently weak in the low-frequency range, the achievement of a spectral band gap with the highest amplitude at the lowest center frequency motivates several scientific studies focused on beam lattice materials (Martinsson and Movchan, 2003; Ruzzene et al., 2003; Spadoni et al., 2009; Celli and Gonella, 2014; Wang et al., 2015; Ronellenfitsch et al., 2018).

Sonic or acoustic metamaterials offer a mechanically robust and highly customizable solution to open band gaps in the dispersion spectrum of beam lattice materials, without compromising the load bearing capacity given by the microstructural stiffness. The working principle of an acoustic metamaterial (also known as elastic or inertial metamaterial) is the dynamic interaction between the periodic material and auxiliary oscillators (*local resonators*) elastically connected to the cellular microstructure (Liu et al., 2000, 2005; Huang et al., 2009; Mei et al., 2012; Zhu et al., 2012; Krushynska et al., 2014, 2017). The band gap is opened by a localized mode and is approximately centered around the natural frequency of the local resonator. Although tuning the oscillator frequency with the desired center frequency may appear a straightforward operation, targeting the lowest possible center frequency and achieving the largest possible bandwidth is a challenging multi-objective optimization issue. The optimal solution must be sought for in a properly-bounded multi-dimensional space of the mechanical parameters describing the periodic microstructure and the resonators. In this respect, extra difficulties can be actually represented by the boundaries imposed to the admissible ranges of the mechanical parameters by geometrical and physical constraints. The parametric optimization is usually tackled by numerically maximizing a multi-variable multi-objective function defined to the purpose (Wang et al., 2015, 2016; Bacigalupo et al., 2016b, 2017). Alternative approaches can be based on the analytical—although asymptotically approximate—solution of an inverse spectral problem (Lepidi and Bacigalupo, 2018b).

The present paper represents a first effort of multi-disciplinary analysis, systematization and synthesis of several analytical formulations and numerical results achieved by the authors in recent studies on the optimal spectral design of beam lattice materials and metamaterials. The mechanical formulations are primarily based on lagrangian models, while the methodologies range from the asymptotic techniques and computational approaches commonly used in structural and solid dynamics to the numerical algorithms typically employed in operational research, non-linear programming and passive control theory. First, a dynamic linear model suited to parametrically describe the free propagation of elastic waves in non-dissipative beam lattice materials and acoustic metamaterials is presented (section 2). Second, an optimization problem for the search of full and partial band gaps with the largest amplitude and lower center frequency is stated. A solution strategy based on an iterative algorithm and a quasi-random initialization is outlined (section 3). Therefore, some optimal results concerning the dispersion spectrum of hexachiral, tetrachiral and anti-tetrachiral materials and metamaterials are summarized (section 4). Some complementary findings achievable by means of perturbation methods and computational modeling are also illustrated, as design alternatives to numerical optimization for specific targets (section 5). Concluding remarks and some possible future developments are finally pointed out.

2. BEAM LATTICE MODEL

Focusing on the microscopic scale, cellular metamaterials characterized by a periodic cell, fully tiling a two-dimensional infinite domain, are considered. A beam lattice model is formulated to describe the linear elasto-dynamic response of the periodic cell, which can be featured by either chiral or antichiral topologies (**Figure 1**). The internal structure, or *microstructure*, of the elementary cell is typically composed by circular rings connected by tangent ligaments (upper part of **Figure 2**). The *rolling-up* mechanism, responsible for the auxetic behavior, consists in the same-sign (chiral) or opposite-sign (antichiral) rotations developed by any pair of adjacent disks, if the cell is stretched along certain directions.

A rigid body model is adopted for all the massive and highly-stiff rings, possessing mean diameter D. The small ring width S is considered a free parameter, allowing the independent assignment of the rigid body mass M and moment of rotational inertia J. A linear, extensible, unshearable model of massless beam is employed for all the light, flexible, and slender ligaments, in the small-deformation range. The beam-ring connections are ideally supposed to realize perfectly-rigid joints. By virtue of the geometric periodicity, the cell boundary usually crosses the midspan—and halves the natural length—of all the inter-cellular ligaments. Assuming the same linear elastic material (with Young's modulus E) and cross-section shape (with area A and second area moment I) for each ligament, all the beams have identical extensional rigidity EA and flexural rigidity EI. The effects of a homogeneous soft matrix, which may likely embed the microstructure, are neglected as first approximation.

Moving from this general microstructural layout, acoustic metamaterials can be realized by supplying each ring with a light soft annular filler, hosting a central heavy circular inclusion, serving as inertial resonator with adjustable mechanical properties. All the inclusions are modeled as rigid disks, co-centered with the respective housing rings, with body mass M_r and moment of rotational inertia J_r. As long as the internal (local) coupling provided by the filler can be assumed linearly elastic, the ring-resonator differential displacements are affected by equivalent translational and rotational stiffnesses (Bacigalupo and Gambarotta, 2016). Therefore, the local (translational and rotational) motion of each resonator is essentially characterized by its natural frequencies Ω_r and Ω_θ.

Introducing certain quantities as known dimensional references for the space (i.e., the characteristic length L of the periodic cell), a suited minimal-dimension vector $\boldsymbol{\mu}_s$ of independent non-dimensional parameters, sufficient to describe the inertial, elastic and geometric properties of the periodic cell, can be introduced. Together with these microstructural parameters, the acoustic metamaterials are further characterized by a vector $\boldsymbol{\mu}_r$ of additional non-dimensional parameters, describing the dynamic properties of the local resonators. Therefore, the vector $\boldsymbol{\mu} = (\boldsymbol{\mu}_s, \boldsymbol{\mu}_r)$ can be defined to collect all the mechanical parameters. In the absence of resonators, it is understood that $\boldsymbol{\mu} = \boldsymbol{\mu}_s$.

2.1. Equations of Motion

According to the mechanical assumptions, the linear dynamics of the elementary cell is governed by a multi-degrees-of-freedom lagrangian model, referred to a set of N configurational nodes, pointed by the position vectors $\mathbf{x}_i$ (with $i = 1, ..., N$) in the natural configuration (see the lower part of **Figure 2**). The actual configuration of the i-th node is described by three time-dependent non-dimensional components of motion, corresponding to the horizontal displacement u_i, the vertical

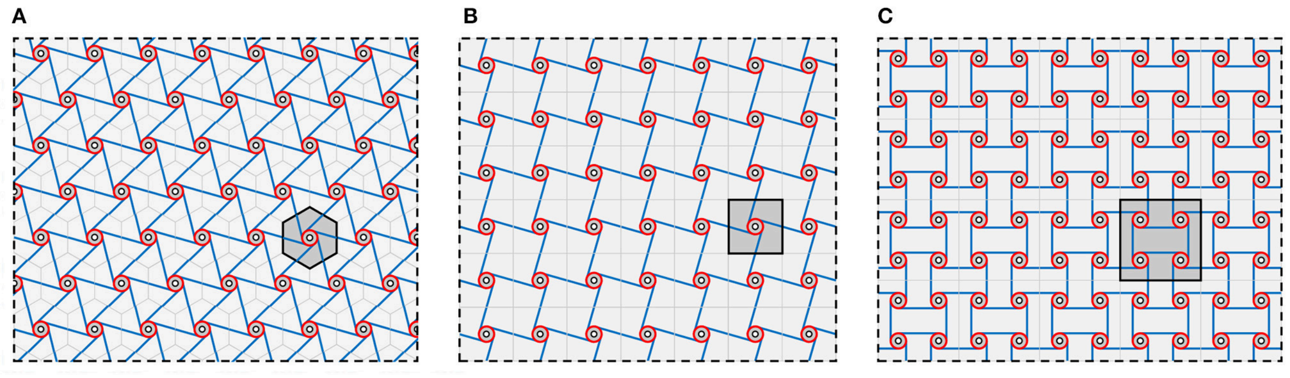

FIGURE 1 | Acoustic metamaterials characterized by periodic microstructure and different cell topologies: **(A)** hexachiral, **(B)** tetrachiral, **(C)** anti-tetrachiral.

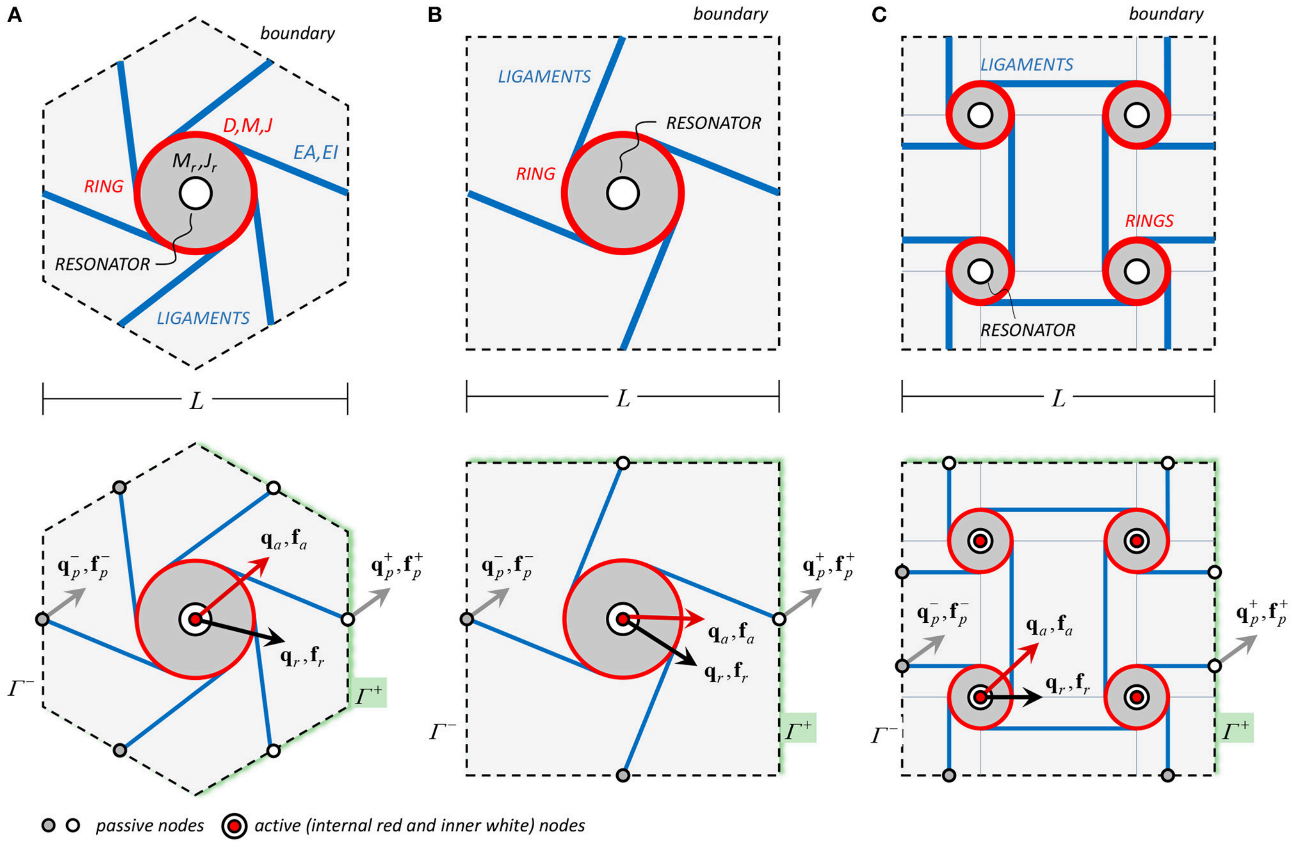

FIGURE 2 | Periodic microstructures and beam lattice models for different cell topologies: **(A)** hexachiral, **(B)** tetrachiral, **(C)** anti-tetrachiral.

displacement v_i and the in-plane rotation ϕ_i. All the non-dimensional configuration variables can be collected in the $3N$-by-one displacement column-vector $\mathbf{q} = (\mathbf{q}_1, ..., \mathbf{q}_i, ..., \mathbf{q}_N)$, where the i-th nodal subvector is $\mathbf{q}_i = (u_i, v_i, \phi_i)$.

Depending on the centroid position for the massive rings and the midspan position for the inter-cellular beams, the configurational nodes can conveniently be distinguished into three subsets:

i. N_a *internal* nodes located at the massive ring centroids (internally to the elementary cell), whose $3N_a$ *active* displacements can be collected in the subvector $\mathbf{q}_a$;
ii. N_p *external* nodes located at the inter-cellular ligament midspans (lying exactly on the cell boundary), whose $3N_p$ *passive* displacements can be collected in the subvector $\mathbf{q}_p$;
iii. N_r *inner* nodes located at the disk centroids, whose $3N_r$ *active resonant* displacements can be collected in the subvector $\mathbf{q}_r$.

The distinction remarks that the *internal* and *inner* nodes develop both elastic ($\boldsymbol{\sigma}_a, \boldsymbol{\sigma}_r$) *and* inertial forces ($\mathbf{f}_a, \mathbf{f}_r$), which actively participate in the dynamic cell equilibrium. On the contrary, the *external* nodes can develop only elastic forces $\boldsymbol{\sigma}_p$, which quasi-statically balance the reactive forces $\mathbf{f}_p$ transferred by the adjacent cells. Due to the geometric assumptions, the positions of the *internal* and *inner* node sets coincide in the undeformed configuration.

According to the partition of the displacement vector $\mathbf{q} = (\mathbf{q}_r, \mathbf{q}_a, \mathbf{q}_p)$ and partitioning the force vectors consistently, the non-dimensional equilibrium equation governing the undamped free oscillations of the discrete model has the matrix form

$$\begin{pmatrix} \mathbf{f}_r \\ \mathbf{f}_a \\ \mathbf{0} \end{pmatrix} + \begin{pmatrix} \boldsymbol{\sigma}_r \\ \boldsymbol{\sigma}_a \\ \boldsymbol{\sigma}_p \end{pmatrix} = \begin{pmatrix} \mathbf{0} \\ \mathbf{0} \\ \mathbf{f}_p \end{pmatrix} \tag{1}$$

or, making explicit the force dependence on the nodal acceleration or displacements

$$\begin{bmatrix} \mathbf{M}_r & \mathbf{O} & \mathbf{O} \\ \mathbf{O} & \mathbf{M}_a & \mathbf{O} \\ \mathbf{O} & \mathbf{O} & \mathbf{O} \end{bmatrix} \begin{pmatrix} \ddot{\mathbf{q}}_r \\ \ddot{\mathbf{q}}_a \\ \ddot{\mathbf{q}}_p \end{pmatrix} + \begin{bmatrix} \mathbf{K}_r & -\mathbf{K}_r & \mathbf{O} \\ -\mathbf{K}_r & \mathbf{K}_{aa} + \mathbf{K}_r & \mathbf{K}_{ap} \\ \mathbf{O} & \mathbf{K}_{pa} & \mathbf{K}_{pp} \end{bmatrix} \begin{pmatrix} \mathbf{q}_r \\ \mathbf{q}_a \\ \mathbf{q}_p \end{pmatrix} = \begin{pmatrix} \mathbf{0} \\ \mathbf{0} \\ \mathbf{f}_p \end{pmatrix} \tag{2}$$

where the dot indicates differentiation with respect to the non-dimensional time and $\mathbf{O}$ are matrices with all-zero entries.

Focusing on the micro-structural matrices, the *global* mass submatrix $\mathbf{M}_a$ is diagonal, as far as a lumped mass description is assumed. The symmetric submatrices $\mathbf{K}_{aa}$ and $\mathbf{K}_{pp}$ account for the *global* stiffness of the internal and external nodes, respectively. The rectangular submatrix $\mathbf{K}_{ap} = \mathbf{K}_{pa}^{\top}$ expresses the elastic *global* coupling among the internal and external nodes. Focusing on the resonators, both the *local* mass and stiffness submatrices $\mathbf{M}_r$ and $\mathbf{K}_r$ are diagonal. The submatrix $\mathbf{K}_r$ accounts also for the *global-local* coupling between the inner and internal nodes.

2.2. Free Wave Propagation

The free wave propagation along the bi-dimensional cellular domain can be studied according to the Floquet-Bloch theory (Brillouin, 2003). In this respect, the active, resonant and passive displacement/force vectors can be mathematically related to their transformed counterparts $\tilde{\mathbf{q}}_a, \tilde{\mathbf{f}}_a, \tilde{\mathbf{q}}_r, \tilde{\mathbf{f}}_r, \tilde{\mathbf{q}}_p, \tilde{\mathbf{f}}_p$ according to the Floquet-Bloch decomposition

$$\begin{aligned} \mathbf{q}_a &= \mathbf{F}_a \tilde{\mathbf{q}}_a, \quad \mathbf{f}_a = \mathbf{F}_a \tilde{\mathbf{f}}_a, \quad \mathbf{q}_r = \mathbf{F}_r \tilde{\mathbf{q}}_r, \\ \mathbf{f}_r &= \mathbf{F}_r \tilde{\mathbf{f}}_r, \quad \mathbf{q}_p = \mathbf{F}_p \tilde{\mathbf{q}}_p, \quad \mathbf{f}_p = \mathbf{F}_p \tilde{\mathbf{f}}_p \end{aligned} \tag{3}$$

where the block diagonal matrices $\mathbf{F}_a$, $\mathbf{F}_r$, $\mathbf{F}_p$ have j-th block $\mathbf{I}\, e^{\mathrm{i}\,\mathbf{k}\cdot\mathbf{x}_j}$ (with $\mathbf{I}$ standing for the three-by-three unit matrix and $j = 1, ..., N_a, j = 1, ..., N_r, j = 1, ..., N_p$ respectively). In each block, i denotes the imaginary unit and $\mathbf{k} = (k_1, k_2)$ is the (dimensional) wavevector.

The cell boundary Γ can be separated into the complementary negative and positive sub-boundaries Γ^- and Γ^+, where the external nodes are linked by the periodicity vectors $\mathbf{d}$. Accordingly, the passive displacement and force vectors can be ordered and partitioned as $\mathbf{q}_p = (\mathbf{q}_p^-, \mathbf{q}_p^+)$, $\mathbf{f}_p = (\mathbf{f}_p^-, \mathbf{f}_p^+)$ to separate the variable pairs $(\mathbf{q}_p^-, \mathbf{f}_p^-)$ belonging to the negative sub-boundary Γ^- from the corresponding variable pairs $(\mathbf{q}_p^+, \mathbf{f}_p^+)$ belonging to the positive sub-boundary Γ^+. Extending the same partition to the respective transformed variables, the Equation (3) can be written as

$$\begin{aligned} \mathbf{q}_p^- &= \mathbf{F}_p^- \tilde{\mathbf{q}}_p^-, \qquad \mathbf{q}_p^+ = \mathbf{F}_p^+ \tilde{\mathbf{q}}_p^+, \\ \mathbf{f}_p^- &= \mathbf{F}_p^- \tilde{\mathbf{f}}_p^-, \qquad \mathbf{f}_p^+ = \mathbf{F}_p^+ \tilde{\mathbf{f}}_p^+ \end{aligned} \tag{4}$$

where, based on the decomposition, the block diagonal matrices $\mathbf{F}_p^-$ and $\mathbf{F}_p^+$ include the blocks related to the external nodes lying on the sub-boundaries Γ^- and Γ^+, respectively.

Imposing the periodicity conditions on the transformed variables ($\tilde{\mathbf{q}}_p^+ = \tilde{\mathbf{q}}_p^-$ and $\tilde{\mathbf{f}}_p^+ = -\tilde{\mathbf{f}}_p^-$), the free wave propagation throughout the cell domain between the two complementary boundaries is governed by the quasi-periodicity conditions on the anti-transformed variables

$$\mathbf{q}_p^+ = \mathbf{L}\mathbf{q}_p^-, \qquad \mathbf{f}_p^+ = -\mathbf{L}\mathbf{f}_p^- \tag{5}$$

where, following from the Equations (4), the block diagonal transfer matrix $\mathbf{L}$ has generic block $\mathbf{I}\, e^{\mathrm{i}\,\mathbf{k}\cdot\mathbf{d}_{ij}}$ where $\mathbf{d}_{ij} = \mathbf{x}_j - \mathbf{x}_i$ represents the vector connecting the i-th external node (belonging to the sub-boundary Γ^-) and the j-th external node (belonging to the sub-boundary Γ^+).

Consistently with the passive displacement and force decomposition, and imposing the quasi-periodicity conditions (5), the lower (quasi-static) part of Equation (2) reads

$$\begin{bmatrix} \mathbf{K}_{pa}^- \\ \mathbf{K}_{pa}^+ \end{bmatrix} \mathbf{q}_a + \begin{bmatrix} \mathbf{K}_{pp}^= & \mathbf{K}_{pp}^\mp \\ \mathbf{K}_{pp}^\pm & \mathbf{K}_{pp}^\# \end{bmatrix} \begin{bmatrix} \mathbf{I} \\ \mathbf{L} \end{bmatrix} \mathbf{q}_p^- = \begin{bmatrix} \mathbf{I} \\ -\mathbf{L} \end{bmatrix} \mathbf{f}_p^- \tag{6}$$

where $\mathbf{I}$ is a unit matrix of proper dimensions. This equation can be solved to express the passive variables as slave functions of the master active displacements, yielding

$$\begin{aligned} \mathbf{q}_p^- &= \mathbf{R}\big(\mathbf{K}_{pa}^+ + \mathbf{L}\mathbf{K}_{pa}^-\big)\mathbf{q}_a, \\ \mathbf{f}_p^- &= \big(\mathbf{K}_{pa}^- + \big(\mathbf{K}_{pp}^= + \mathbf{K}_{pp}^\mp \mathbf{L}\big)\mathbf{R}\big(\mathbf{K}_{pa}^+ + \mathbf{L}\mathbf{K}_{pa}^-\big)\big)\mathbf{q}_a \end{aligned} \tag{7}$$

where the $\mathbf{k}$-dependent auxiliary matrix $\mathbf{R} = -\big(\mathbf{L}\mathbf{K}_{pp}^\mp \mathbf{L} + \mathbf{L}\mathbf{K}_{pp}^= + \mathbf{K}_{pp}^\# \mathbf{L} + \mathbf{K}_{pp}^\pm\big)^{-1}$.

Similarly, the enforcement of the quasi-periodicity conditions to the upper (dynamic) part of the Equation (2) leads to a coupled equation that, after *condensation* of the passive variables by virtue of the enslaving relations (7), depends on the active variables only:

$$\begin{bmatrix} \mathbf{M}_r & \mathbf{O} \\ \mathbf{O} & \mathbf{M}_a \end{bmatrix} \begin{pmatrix} \ddot{\mathbf{q}}_r \\ \ddot{\mathbf{q}}_a \end{pmatrix} + \begin{bmatrix} \mathbf{K}_r & -\mathbf{K}_r \\ -\mathbf{K}_r & \mathbf{K}_r + \mathbf{K}_a \end{bmatrix} \begin{pmatrix} \mathbf{q}_r \\ \mathbf{q}_a \end{pmatrix} = \begin{pmatrix} \mathbf{0} \\ \mathbf{0} \end{pmatrix} \tag{8}$$

where the condensed stiffness matrix $\mathbf{K}_a = \mathbf{K}_{aa} + (\mathbf{K}_{ap}^- + \mathbf{K}_{ap}^+ \mathbf{L})\mathbf{R}(\mathbf{K}_{pa}^+ + \mathbf{L}\mathbf{K}_{pa}^-)$ is known to be Hermitian by virtue of the symmetries $\mathbf{K}_{ap}^- = (\mathbf{K}_{pa}^-)^{\top}$ and $\mathbf{K}_{ap}^+ = (\mathbf{K}_{pa}^+)^{\top}$.

As brief discussion, the upper part of Equation (8) governs the local dynamics of the resonator, whereas the lower part governs the global dynamics of the cell microstructure. It is worth noting that the passive variable condensation, including the enforcement of the quasi-periodicity, is not mathematically affected by the resonator presence. Indeed, the condensed *global* stiffness matrix $\mathbf{K}_g = (\mathbf{K}_r + \mathbf{K}_a)$ of the metamaterial is not formally different from the matrix $\mathbf{K}_a$ governing the wave propagation in the resonator-free material, apart for the mere addition of the *local* stiffness term $\mathbf{K}_r$. Conversely, the uncoupled global dynamics of the resonator-free material can be restored by simply zeroing the local matrices $\mathbf{M}_r$ and $\mathbf{K}_r$. Physically, this remark can immediately be justified by the absence of any internal coupling between the resonant active variables $\mathbf{q}_r$ and the condensed passive variables $\mathbf{q}_p$.

Introducing the unknown non-dimensional frequency ω, the harmonic solutions $\mathbf{q}_a = \mathbf{F}_a\boldsymbol{\psi}_a\,\mathrm{e}^{\mathrm{i}\,\omega\tau}$ and $\mathbf{q}_r = \mathbf{F}_r\boldsymbol{\psi}_r\,\mathrm{e}^{\mathrm{i}\,\omega\tau}$ can be imposed in the Equation (8). Eliminating the dependence on time, an eigenproblem in the unknown eigenvalues $\lambda = \omega^2$ and eigenvectors $\boldsymbol{\psi} = (\boldsymbol{\psi}_r, \boldsymbol{\psi}_a)$ can be stated in the non-standard form $(\mathbf{K} - \lambda\mathbf{M})\,\mathbf{F}\boldsymbol{\psi} = \mathbf{0}$, or more explicitly

$$\left(\begin{bmatrix}\mathbf{K}_r & -\mathbf{K}_r\\ -\mathbf{K}_r & \mathbf{K}_a\end{bmatrix} - \lambda\begin{bmatrix}\mathbf{M}_r & \mathbf{O}\\ \mathbf{O} & \mathbf{M}_a\end{bmatrix}\right)\begin{pmatrix}\mathbf{F}_r\boldsymbol{\psi}_r\\ \mathbf{F}_a\boldsymbol{\psi}_a\end{pmatrix} = \begin{pmatrix}\mathbf{0}\\ \mathbf{0}\end{pmatrix} \tag{9}$$

where the diagonal block matrices $\mathbf{F}_r = \mathbf{F}_a$ have generic block $\mathbf{I}\,\mathrm{e}^{\mathrm{i}\,\mathbf{k}\cdot\mathbf{x}_j}$, where $\mathbf{x}_j$ is the position vector pointing the active internal and inner nodes.

The eigenproblem solution gives $N_a + N_r$ real-valued eigenvalues λ_i (or frequencies ω_i). It is worth remarking that, owing to the Hermitian property, the $\mathbf{K}$-matrix is certainly non-defective, that is, possesses a complete eigenspace spanned by $N_a + N_r$ proper eigenvectors. Therefore, each eigenvalue λ_i has coincident algebraic and geometric multiplicity m_i and corresponds to a complex-valued eigenvector $\boldsymbol{\psi}_i$, collecting the sub-eigenvectors $\boldsymbol{\psi}_{ri}$ and $\boldsymbol{\psi}_{ai}$. The passive sub-eigenvectors depend on the active sub-eigenvectors through the quasi-static relations $\boldsymbol{\psi}_{pi}^- = \mathbf{R}(\mathbf{K}_{pa}^+ + \mathbf{L}\mathbf{K}_{pa}^-)\boldsymbol{\psi}_{ai}$ and $\boldsymbol{\psi}_{pi}^+ = \mathbf{L}\boldsymbol{\psi}_{pi}^-$.

Fixed an admissible vector $\boldsymbol{\mu}$ of mechanical parameter values for the beam-lattice and the resonators, the eigenvalues (or frequencies) and the corresponding eigenvectors can be determined under variation of the non-dimensional wavevector $\mathbf{b} = (\beta_1, \beta_2)$, composed of the wavenumbers $\beta_1 = k_1 L$ and $\beta_2 = k_2 L$ ranging in the non-dimensional first Brillouin domain $\mathcal{B}$ (**Figure 3**). The frequency loci vs. the varying wavevector constitute the Floquet-Bloch spectrum, composed of $N_a + N_r$ dispersion surfaces for the metamaterial or N_a dispersion curves for the resonator-free material. In the spectrum, the two loci attaining zero value at the $\mathcal{B}$-origin ($\beta_1 = \beta_2 = 0$) are referred to as *acoustic surfaces*. The other loci are referred to as *optical surfaces*.

3. BAND-GAP OPTIMIZATION PROBLEM

Parametric analyses can be performed by considering the dispersion functions $\omega(\mathbf{b}, \boldsymbol{\mu})$, where $\boldsymbol{\mu}$ plays the role of multi-dimensional variable. These parametric analyses of the dispersion spectrum typically reveal that resonator-free materials possess a highly-dense spectrum, with persistent absence of full band-gaps in the low-frequency range (where only partial band gaps are usually obtainable). Introducing inter-ring resonators is an efficient technique to enforce the opening of stop bands in the closeness of the resonator frequency. Nonetheless, the resonator frequency cannot be reduced without recurring to high mass-to-stiffness ratio. Therefore, even in the presence of resonators, searching admissible parameter combinations that open low-frequency band-gaps—and hopefully maximize their bandwidth—is a challenging task, which can seldom be successfully approached manually. More efficient approaches can be represented by analytically inverting the eigenvalue problem, under acceptable asymptotic approximations (Lepidi and Bacigalupo, 2018b), or by numerically stating and solving optimization problems, under suited mechanical constraints (Bacigalupo et al., 2016a,b, 2017).

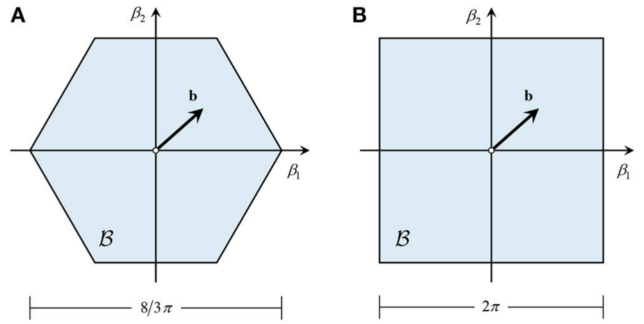

FIGURE 3 | Non-dimensional first Brillouin domain $\mathcal{B}$ associated to: **(A)** hexachiral periodic cell, **(B)** tetrachiral and anti-tetrachiral periodic cell.

Within this context, the detection, quantification and—as a final target—design of metamaterials showing desiderable properties of mechanical filtering by virtue of low-frequency band-gap remains a research issue of major interest (D'Alessandro et al., 2016, 2018).

3.1. Problem Formulation

The bandwidth maximization of low-frequency band-gaps can be based on the definition of a suited $\boldsymbol{\mu}$-dependent objective function, which simultaneously accounts for the gap amplitude and the band center-frequency, hence qualifying in this respect as a multi-objective function. To this purpose, the following non-dimensional ratio can be defined:

$$\Delta\omega_{kh}(\boldsymbol{\mu}) = \frac{\min\limits_{\mathbf{b}\in\mathcal{B}}\left(\omega_k\left(\mathbf{b},\boldsymbol{\mu}\right)\right) - \max\limits_{\mathbf{b}\in\mathcal{B}}\left(\omega_h\left(\mathbf{b},\boldsymbol{\mu}\right)\right)}{\frac{1}{2}\left[\min\limits_{\mathbf{b}\in\mathcal{B}}\left(\omega_k\left(\mathbf{b},\boldsymbol{\mu}\right)\right) + \max\limits_{\mathbf{b}\in\mathcal{B}}\left(\omega_h\left(\mathbf{b},\boldsymbol{\mu}\right)\right)\right]} \tag{10}$$

where, supposing that the frequencies are sorted in ascending order, the numerator stands for the typically positive (even if possibly zero) gap amplitude between the k-th and h-th consecutive dispersion surfaces (where $k = h + 1$), while the denominator stands for the band center-frequency. When the numerator is negative, no band gap is present between the two surfaces.

Therefore, the optimization problem essentially consists in searching for the parameter vector $\boldsymbol{\mu}$ that maximizes the objective function in the admissible parameter region. Consequently, the optimization issue can be mathematically formulated as a constrained maximization problem:

$$\begin{aligned} &\underset{\boldsymbol{\mu}}{\text{maximize}}\ \Delta\omega_{kh}(\boldsymbol{\mu}) \\ &\text{s.t.}\quad \boldsymbol{\mu}_{\min} \leq \boldsymbol{\mu} \leq \boldsymbol{\mu}_{\max} \\ &\qquad\ \ \boldsymbol{g}(\boldsymbol{\mu}) \leq \mathbf{0} \end{aligned} \tag{11}$$

where $\boldsymbol{\mu}_{\min}$ and $\boldsymbol{\mu}_{\max}$ fix the boundaries of admissibility for the parameter vector, and $\boldsymbol{g}(\boldsymbol{\mu})$ denotes a vector function defining additional relations, introduced—if necessary—to constrain a certain slave parameter as a known function of the other master parameters (Bacigalupo et al., 2016a, 2017). Altogether, the constraints define a properly-bounded space for the parameter vector.

Due to its mathematical formulation, the optimization problem turns out to be a challenging task in non-linear programming. Moreover, since the multi-variable objective function is not concave in the general case, the function maximization cannot be treated as a concave maximization problem. Multiple solutions associated to local maxima can co-exist. Therefore, the global maximum is necessarily approximated by the highest among several local maxima obtained numerically. If no full band gaps are found, then the optimization problem is re-formulated to search for partial band-gaps, by considering only certain directions of wave propagation.

Following a well-established methodology adopted for similar issues in material design (Sigmund and Jensen, 2003; Diaz et al., 2005), the optimization problem (11) can be solved by employing the *Globally Convergent Method of Moving Asymptotes*, or GCMMA (Svanberg, 1987, 2002). Loosely speaking, this solution method consists in tackling a sequence of concave-maximization subproblems, locally approximating the original non-linear optimization problem (a different approximation at each sequence iteration). In each subproblem, both the objective function and the constraints of the original optimization problem are approximated by separable functions, i.e., sums of functions depending each on a single different variable. This property simplifies solving the associated dual optimization subproblem. The moving asymptotes, which characterize the method, are asymptotes of the functions used in the approximations, and typically change from one subproblem to the successive one. Finally, the GCMMA method is globally convergent in the sense that, for every initial choice of the vector of optimization variables, it is proved to converge to a stationary point of the original optimization problem.

In Bacigalupo et al. (2016a,b, 2017), a quasi-Monte Carlo multi-start technique is also used in conjunction with the GCMMA, to increase the probability of finding a good approximation of the global maximum by virtue of a set of quasi-random initializations of the sequence. Indeed, the quasi-Monte Carlo initialization has the advantage—in comparison with the Monte Carlo initialization—of generating more uniform sequences of initial points (**Figure 4**). Furthermore, the quasi-Monte Carlo initialization, obtained at first generating a quasi-random Sobol' sequence (then keeping only elements of the sequence that satisfy the constraints of the original optimization problem), has the complementary advantage of being exactly replicable (Sobol, 1998).

For the sake of clarity, it is worth remarking that the present issue differs from other band gap maximization problems, which specifically deal with the topological optimization of phononic materials. Indeed, although pursuing the same objective (the largest gap amplitude), the *topological optimization* seeks for the optimal distribution of two or more material phases in a sufficiently-fine pixelation of the periodic cell (Cox and Dobson, 2000; Shen et al., 2003; Sigmund and Jensen, 2003; Kaminakis and Stavroulakis, 2012; Bruggi et al., 2017). On the contrary, here, for both the beam lattice material and metamaterial, the topology of the periodic cell is fixed a priori, whereas the *parametric optimization* is limited to the cellular micro-structural parameters, whose values allow to distinguish among different materials belonging to the same topological class. To some extent, the present analyses are aligned with the search for the maximum stop bandwidth achievable by varying the connection number and the joint rigidity in periodic lattices made of beam frameworks, in the absence of resonators (Wang et al., 2015).

4. RESULTS AND DISCUSSION

The general mathematical form (11) of the optimization problem has been specialized for different chiral and anti-chiral topologies of materials and metamaterials. In particular, the maximal gap amplitude at the lowest center frequency has been searched for the hexachiral case (section 4.1), the tetrachiral case (section 4.2) and the anti-tetrachiral case (section 4.3).

4.1. Hexachiral Material and Metamaterial

The hexachiral material is characterized by a periodic cell with hexagonal shape and non-orthogonal periodicity vectors. Each cell contains one central ring connected to six tangent inter-cellular ligaments (**Figure 2A**). The beam lattice model is featured by three active degrees-of-freedom ($N_a = 3$). The dispersion spectrum is composed by three frequency surfaces, defined over a hexagonal first Brillouin zone. The hexachiral metamaterial is realized by introducing a single local resonator in the central ring. Consequently, the beam lattice model is enriched by three active resonant degrees-of-freedom ($N_r = 3$). The corresponding dispersion spectrum is composed by three frequency surfaces in addition to those of the resonator-free material. The mass and stiffness matrices governing the eigenproblem (9) can be found in Bacigalupo and Gambarotta (2016) and Bacigalupo et al. (2016b).

The optimization problem for the hexachiral material can be formulated as the constrained maximization of a three-variables objective function defined according to Equation (10). Thus, the search for the optimal solution is performed in a properly-bounded three-dimensional space of the non-dimensional mechanical parameters expressing the ligament slenderness, the ring-to-cell aspect ratio and

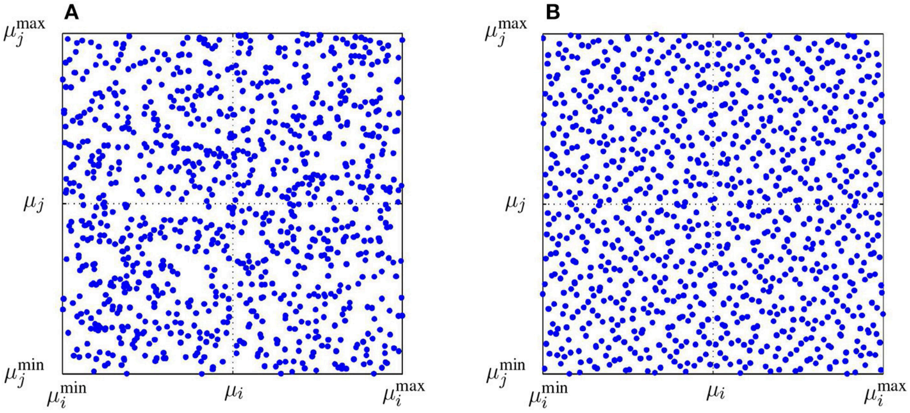

FIGURE 4 | Initialization of a 2-dimensional admissible region of the parameter domain: **(A)** Montecarlo sampling and **(B)** quasi-Montecarlo sampling.

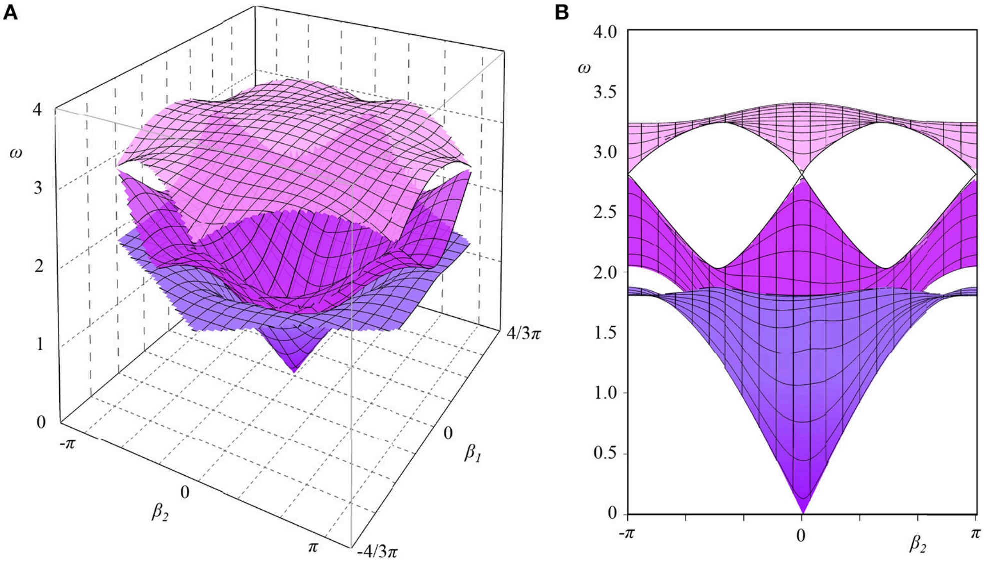

FIGURE 5 | Dispersion spectrum for the optimized beam lattice model of the hexachiral material: **(A)** 3D view and **(B)** 2D view.

the chirality angle. The optimization problem is found not to admit solutions corresponding to full band gaps in the admissible parameter space. If the problem is reformulated to search for partial band-gaps, the largest stop bandwidth at the lowest center frequency is found between the second acoustic surface and the optical surface along the three propagation directions connecting two opposite-side vertices of the hexagonal cell (Bacigalupo et al., 2016b). The dispersion spectrum of the optimized hexachiral material is shown in **Figure 5**.

The optimization problem for the hexachiral metamaterial can again be formulated as the constrained maximization of an enriched objective function, defined in an enlarged space of the non-dimensional mechanical parameters describing the hexachiral cell and the auxiliary resonator. The four extra non-dimensional parameters account for the resonator-to-cell aspect ratio, the resonator-to-ring mass ratio, and the two coefficients (Young modulus and Poisson ratio) of the elastic ring-to-resonator coupling. The optimization problem is found to admit a solution corresponding to a full band gap between the second acoustic surface and the optical surface (Bacigalupo et al., 2016b). The dispersion spectrum of the optimized hexachiral metamaterial is illustrated in **Figure 6**, where a second full band gap can be recognized to occur in the high-frequency range, between the fifth and sixth optical surfaces.

From a qualitative viewpoint, it can be remarked that the largest amplitude of the full band gap can reach nearly half the maximum value of the lowest frequency in the spectrum of the hexachiral metamaterial. From a design perspective, it is worth pointing out that the optimized full band gaps can be obtained for small-radius rings and highly-slender, inclined but non-tangent ligaments. Correspondingly, the optimized resonators are found to possess nearly half the radius of the rings and be embedded in a highly-soft matrix.

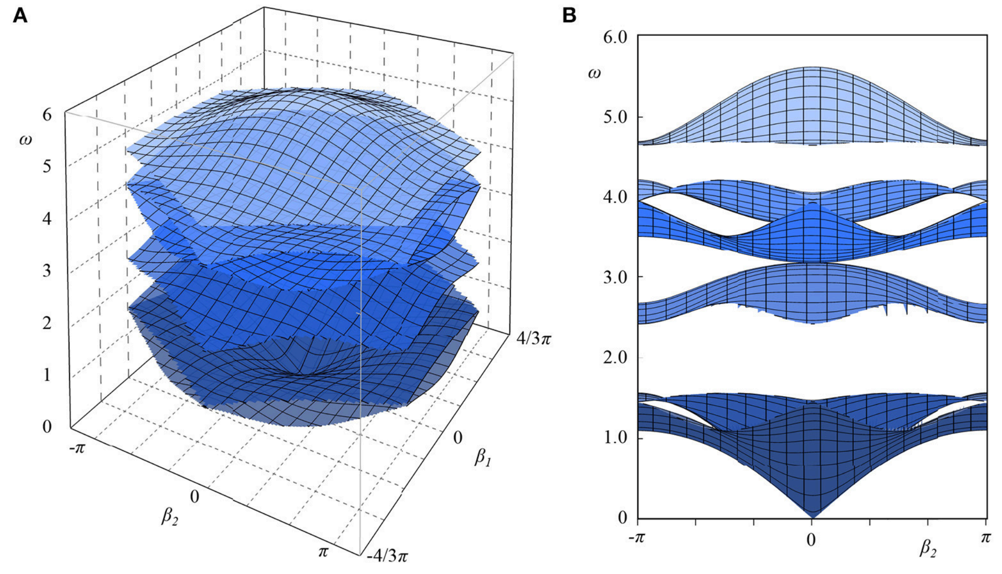

FIGURE 6 | Dispersion spectrum for the optimized beam lattice model of the hexachiral metamaterial: **(A)** 3D view and **(B)** 2D view.

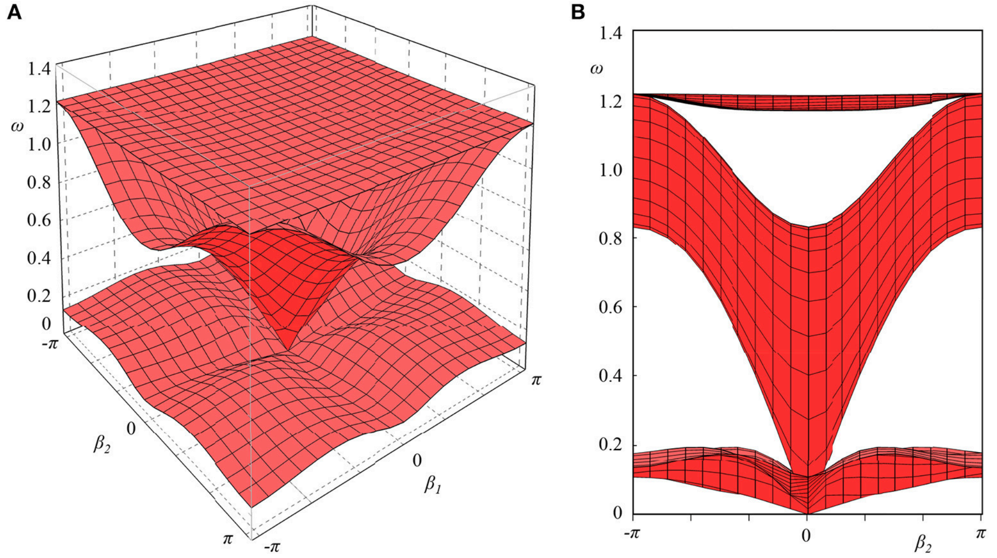

FIGURE 7 | Dispersion spectrum for the optimized beam lattice model of the tetrachiral material: **(A)** 3D view and **(B)** 2D view.

4.2. Tetrachiral Material and Metamaterial

The tetrachiral material is characterized by a periodic cell with square shape and orthogonal periodicity vectors. Each cell contains one central ring connected to four tangent inter-cellular ligaments (**Figure 2B**). The beam lattice model is featured by three active degrees-of-freedom ($N_a = 3$). The dispersion spectrum is composed by three frequency surfaces, defined over a square first Brillouin zone. The tetrachiral metamaterial is realized by introducing a single local resonator in the central ring. Consequently, the beam lattice model is enriched by three active resonant degrees-of-freedom ($N_r = 3$). The corresponding dispersion spectrum is composed by three frequency surfaces in addition to those of the resonator-free material. The mass and stiffness matrices governing the eigenproblem (9) can be found in Bacigalupo et al. (2016a) and Vadalà et al. (2018).

The optimization problem for the tetrachiral material can be formulated as the constrained maximization of a four-variables objective function defined according to Equation (10). Therefore, the search for the optimal solution is performed in a properly-bounded four-dimensional space of the non-dimensional mechanical parameters expressing the ligament slenderness, the ring-to-cell aspect ratio, the chirality angle and the ring-to-ligament width ratio. Similarly to the hexachiral case, the optimization problem for the tetrachiral material is found not to admit solutions corresponding to full band gaps in the admissible parameter space. If the problem is reformulated to search for partial band-gaps, the highest amplitude stop band at the lowest center frequency is found between the second acoustic surface and the optical surface along the two orthogonal propagation directions connecting the centroids of adjacent rings (Bacigalupo et al., 2016b). The dispersion spectrum of the optimized tetrachiral material is illustrated in **Figure 7**.

The optimization problem for the tetrachiral metamaterial can again be formulated as the constrained maximization of an enriched objective function, defined in the enlarged space of the non-dimensional mechanical parameters describing the tetrachiral cell and the auxiliary resonator. Similarly to the hexachiral case, the four extra non-dimensional parameters account for the resonator-to-cell aspect ratio, the resonator-to-ring mass ratio, and the two coefficients (Young modulus and Poisson ratio) of the elastic ring-to-resonator coupling. The constrained optimization problem is found not to have an admissible solution corresponding to a full band gap between the acoustic and optical surfaces. Instead, an admissible solution can be found for a full band gap separating the first and second optical surfaces. This solution preserves the ring-resonator interaction, by virtue of a weighting multiplier (proportional to the fourth pass bandwidth), properly applied to the stop bandwidth in the definition of the objective function (Bacigalupo et al., 2016a). The dispersion spectrum of the optimized tetrachiral metamaterial is illustrated in **Figure 8**.

From a qualitative viewpoint, it can be remarked that the largest amplitude of the full band gap can be twice the maximum value of the lowest frequency in the spectrum of the tetrachiral metamaterial. From a design perspective, it is worth pointing out that the optimized full band gaps can be obtained for large-radius rings and highly-slender, non-tangent ligaments with quasi-negligible inclination (corresponding to a nearly-vanishing chirality angle). Similarly to the hexachiral case, the optimized resonators are found to possess nearly half the radius of the rings and be embedded in a highly-soft matrix.

4.3. Anti-tetrachiral Material and Metamaterial

The anti-tetrachiral material is characterized by a periodic cell with square shape and orthogonal periodicity vectors. Each cell contains four rings, each connected to four tangent (two inter-cellular and two intra-cellular) ligaments (**Figure 2C**). The beam lattice model is featured by 12 active degrees-of-freedom ($N_a = 12$). The dispersion spectrum is composed by twelve frequency surfaces, defined over a square first Brillouin zone. The anti-tetrachiral metamaterial is realized by introducing a single local resonator in each ring. Consequently, the beam lattice model is enriched by twelve active resonant degrees-of-freedom ($N_r = 12$). The corresponding dispersion spectrum is composed by twelve frequency surfaces in addition to those of the resonator-free material. The mass and stiffness matrices governing the eigenproblem (9) can be found in Bacigalupo et al. (2017).

The optimization problem for the anti-tetrachiral material can be formulated as the constrained maximization of a three-variables objective function defined according to Equation (10). Since the chirality angle is not defined in the anti-chiral microstructural topology, the search for the optimal solution is performed in a properly-bounded three-dimensional space of the non-dimensional mechanical parameters expressing the ligament slenderness, the ring-to-cell aspect ratio and the ring-to-ligament width ratio. Similarly to the previous cases, the optimization problem for the anti-tetrachiral material is found not to admit solutions corresponding to full band gaps in the admissible parameter space. If the problem is reformulated to search for partial band-gaps, then the highest amplitude stop band at the lowest center frequency is found between the second and third optical surfaces along the two orthogonal propagation directions connecting diagonally two vertices of the square cell (Bacigalupo et al., 2017). The dispersion spectrum of the optimized anti-tetrachiral material is illustrated in **Figure 9**.

The optimization problem for the anti-tetrachiral metamaterial can again be formulated as the constrained maximization of an enriched objective function, defined in the enlarged space of the non-dimensional mechanical parameters describing the tetrachiral cell and the auxiliary resonator. Similarly to the previous cases, the four extra non-dimensional parameters account for the resonator-to-cell aspect ratio, the resonator-to-ring mass ratio, and the two coefficients (Young modulus and Poisson ratio) of the elastic ring-to-resonator coupling. Furthermore, since the anti-tetrachiral material is characterized by a multi-ring cell, the number (ranging from one to four) and placement of the resonators can be considered additional unknowns to be optimized. The constrained optimization problem is found not to have an admissible solution corresponding to a full band gap between the acoustic and optical surfaces. Instead, an admissible solution can be found for a full band gap separating the fourth and fifth optical surfaces. This solution corresponds to two resonators placed into the ring pair located along one of the two diagonals of the square cell (Bacigalupo et al., 2017). It is worth noting that other solutions, maximizing the same objective function for a different number and placement of the resonators, correspond to full band gaps at higher center frequencies and lower stop bandwidth. The dispersion spectrum of the optimized anti-tetrachiral metamaterial is illustrated in **Figure 10** (the lowest twelve dispersion surfaces are reported), where a second full band gap can be recognized to occur in the high-frequency range.

From the qualitative viewpoint, the anti-tetrachiral metamaterial has been systematically found to offer the largest band gap amplitudes when the resonators are placed along one of the cell diagonals. From a design perspective, it is worth pointing out that the optimized full band gaps can be obtained by a strong ring-to-ligament compositeness of the cell microstructure (maximum admissible ring radius). Differently from the previous cases, the optimized resonators are found to be large and heavy (maximum admissible resonator inertia), but also weakly coupled with their hosting rings (minimum elastic resonator stiffness).

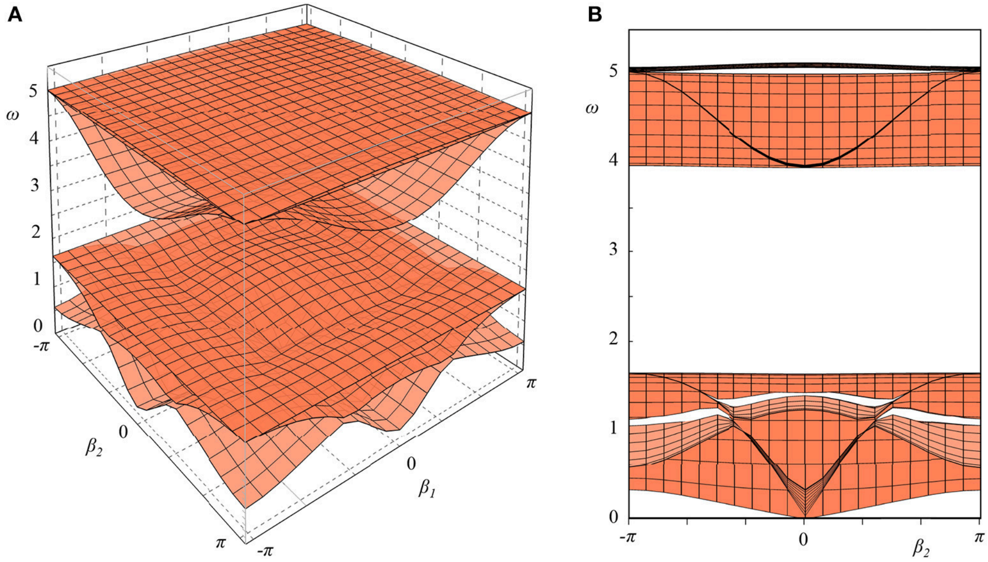

FIGURE 8 | Dispersion spectrum for the optimized beam lattice model of the tetrachiral metamaterial: **(A)** 3D view and **(B)** 2D view.

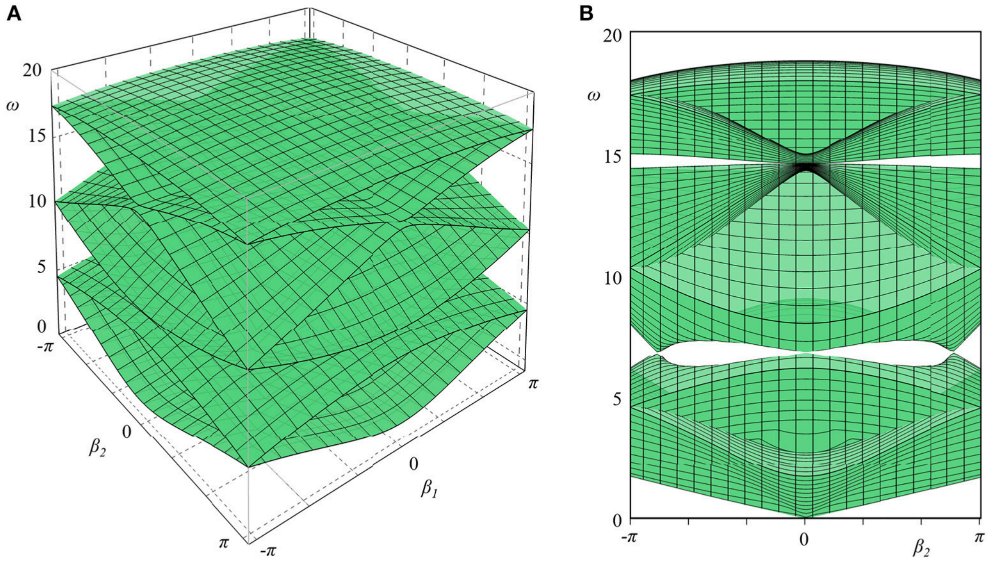

FIGURE 9 | Dispersion spectrum for the optimized beam lattice model of the anti-tetrachiral material: **(A)** 3D view and **(B)** 2D view.

5. BAND DESIGN AT TARGET FREQUENCY

The numerical approaches to the spectral optimization can present two major applicative drawbacks. First, the admissible parameter space cannot overcome a certain dimension without compromising the computational feasibility (in terms of times and costs) of the optimal solution search. In this respect, different alternatives can turn out to be more convenient, if some simplifying hypotheses of the beam lattice model are relaxed (for instance, the lumped mass assumption). The consequent enlargement of the free parameter space offers more design possibilities, that can be explored by formulating continuous solid models. Their governing equations can be solved through numerical approaches (section 5.1). Second, the simplest numerical approaches to the optimization problem do not return an analytical form of the optimal solution (design parameters) as an explicit function of suitable objective variables. This shortcoming could be by-passed by analytically inverting and solving the spectral problem, provided that the designer accepts reasonable approximations. In this respect, perturbation-based techniques may offer a flexible mathematical tool to

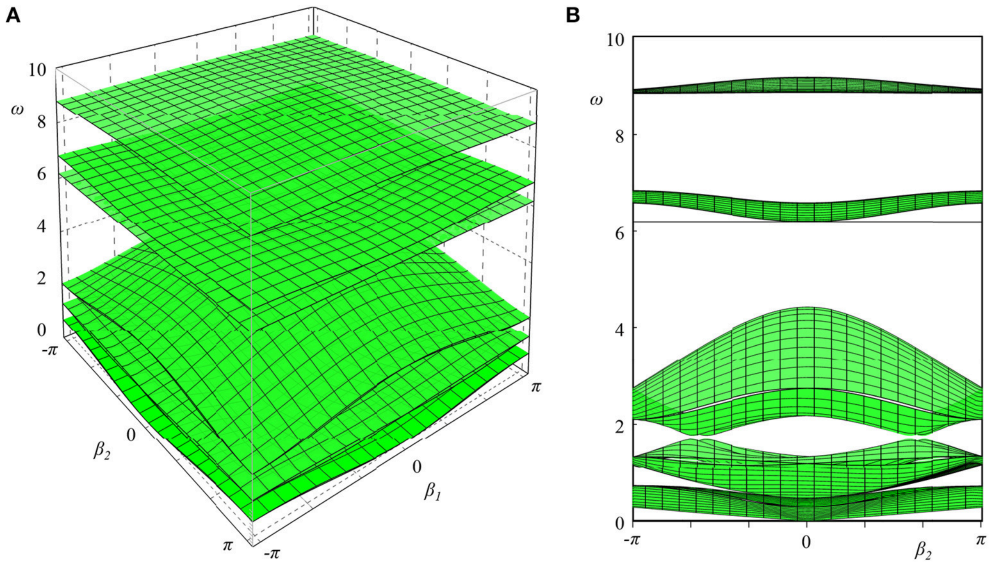

FIGURE 10 | Dispersion spectrum for the optimized beam lattice model of the anti-tetrachiral metamaterial: **(A)** 3D view and **(B)** 2D view.

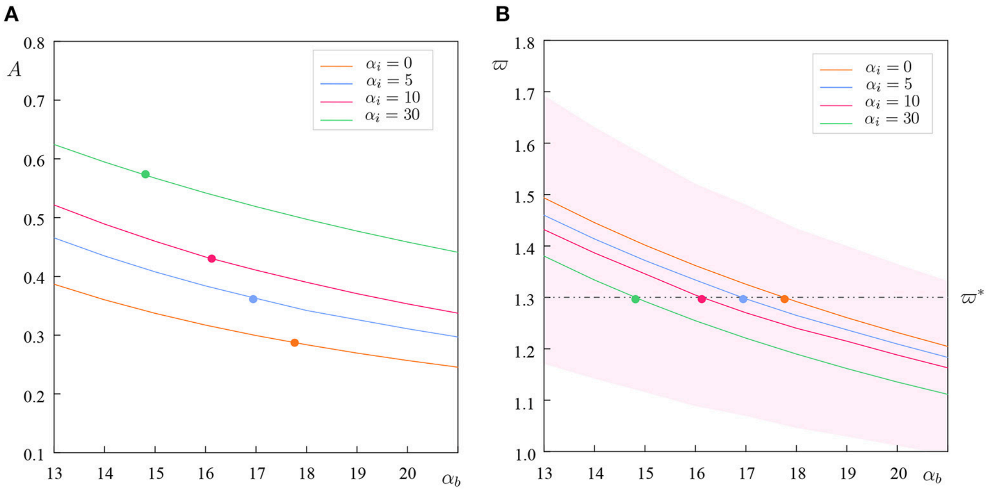

FIGURE 11 | Dispersion spectrum of the tetrachiral material: **(A)** full band gap amplitude A and **(B)** center frequency ϖ vs. the ligament-to-ring mass ratio α_b for different filler-to-ring mass ratios α_i.

asymptotically approximate the inverse problem solutions (section 5.2).

5.1. Tetrachiral Material

Focusing on the reference lagrangian model for the tetrachiral material, a mechanical enrichment can be introduced by removing the strong hypothesis of massless ligaments. Furthermore, a heavy elastic material can be considered to fill the central rings of the periodic cell. According to these enrichments, the parameter space is enlarged by the ligament-to-ring mass ratio α_b and the filler-to-ring mass ratio α_i.

The admissible range of the enlarged parameter space—spanned by the additional mass ratios—has been investigated to check if some (α_b, α_i)-combinations realize a full band gap in the low-frequency pass band of the reference lagrangian model. The investigation results confirm that a low-frequency band gap with amplitude A and center frequency ϖ can be achieved. The achievable amplitude A vs. the mass ratio α_b is shown in **Figure 11A** for different mass ratios α_i. It is worth noting that the band gap amplitude A decreases monotonically for increasing values of the ligament-to-ring mass ratio α_b. Larger amplitudes A can be obtained for higher filler-to-ring mass ratios α_i. The center frequency ϖ shows a similar dependence on the mass ratio parameters, as illustrated is **Figure 11B**, where the pink zone embraces the frequency ranges included in the stop band for $\alpha_i = 10$. The figure could be used for design purposes by—for instance—fixing a target center frequency ϖ^* (dashed line) to extract the corresponding design points (dots) in the α_i and α_b ranges. Further details can be found in Vadalà et al. (2018).

5.2. Anti-tetrachiral Material

Focusing on the lagrangian models of beam lattice materials, a local sensitivity analysis of the dispersion spectrum can be performed by virtue of multi-parameter perturbation methods. This mathematical approach has been systematically formulated to achieve analytical—although asymptotically approximate up to the desired order—expressions for the dispersion relations, as explicit functions of the mechanical parameters and the wavenumbers. Within the limits of the local approximation, these analytical expressions have been found to closely fit the exact dispersion functions of the direct spectral problem for the anti-tetrachiral material, among the others.

The approximate analytical solutions of the direct spectral problem can properly be inverted to state convenient formulas to determine the design parameters as explicit functions of the inverse problem data. These target data may include—for instance—a desired frequency ϖ^* at a certain wavenumber β^* in the anti-tetrachiral material spectrum. **Figure 12** shows how the fourth dispersion curve $\omega_4(\beta)$ can be designed to include the desired frequencies ϖ^*_- (slightly lower that unity - *softer material*) or ϖ^*_+ (slightly higher that unity - *stiffer material*) at different assigned wavenumbers β^*. The design target pairs (ϖ^*, β^*) can be obtained for different anti-tetrachiral materials featured by low-density or high-density, to be selected according to extra design requirements. Further details can be found in Lepidi and Bacigalupo (2018b). Other achievable design targets are the stop bandwidth and the center frequency in the dispersion spectrum of anti-tetrachiral metamaterials (Lepidi and Bacigalupo, 2018a).

6. CONCLUSIONS AND FUTURE DEVELOPMENTS

The dynamic response of composite materials with periodic microstructure can be analytically described by lagrangian beam lattice models. The free propagation of elastic waves in these low-dimensional models can be studied according to the Floquet-Bloch theory. The dispersion spectrum is composed of pass and stop bands that can be customized to let the material functionally behave as mechanical waveguide, filter or directional filter. Among the other functional features, low-frequency, high-amplitude band gaps are desirable spectral properties for many technological applications. To this purpose, the microstructural properties of the periodic cell can be employed as design parameters to optimize the band structure.

The optimization problem has been systematically formulated as a non-linear maximization problem by defining a non-concave multi-objective function, targeted at achieving the largest stop bandwidth at the lowest center frequency. The numerical search for the optimal solution has been opportunely constrained to focus on the admissible range of the design parameters. The optimization procedure can be applied to material and acoustic metamaterials governed by lagrangian models depending on a few mechanical parameters, including the number, placement and properties of local resonators.

Different cellular topologies have been optimized. Low-frequency high-amplitude full band gaps have been designed as outcome of the optimization process applied to hexachiral,

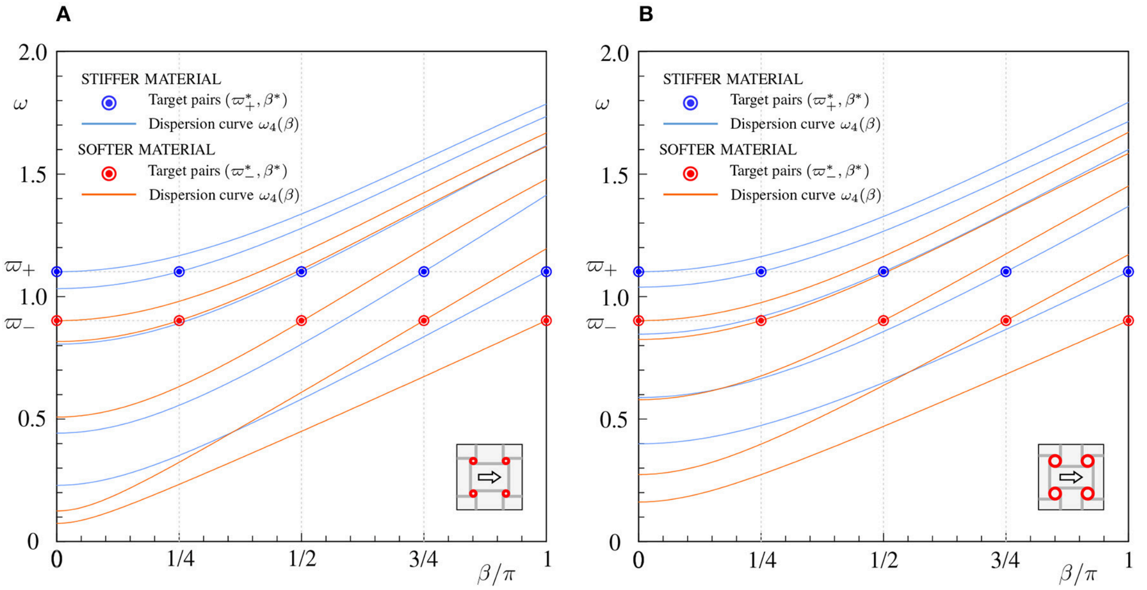

FIGURE 12 | Dispersion spectrum of the anti-tetrachiral material: dispersion curves $\omega_4(\beta)$ designed to include the target frequencies $\varpi^*_\pm$ (for different wavenumbers $\beta^* = 0, 1/4\pi, 1/2\pi, 3/4\pi, \pi$): **(A)** low-density material, **(B)** high-density material.

tetrachiral and anti-tetrachiral metamaterials. According to the peculiar properties of microstructural symmetry assumed for the periodic cell, only partial band gaps for different propagation directions have been obtained in the absence of resonators. For each topology, design recommendations have been synthesized about the optimal inertial, elastic and geometric ratios among the microstructural parameters and the resonator properties.

As final achievements, alternative approaches to the spectral design have been summarized. First, the augmented design possibilities offered by an enlargement of the parameter space, resulting from the removal of some simplifying mechanical assumptions, have been explored. Second, the actual potential of perturbation methods to provide analytical, although asymptotically approximate, solutions of the inverse spectral problem has been successfully verified.

As outlook for future developments, the optimization strategy could be applied to the Rayleigh-Lamb wave propagation in heterogeneous macrostructures like multilayered beams or plates (Nayfeh et al., 1999; Chen et al., 2007; Pelassa and Massabò, 2015; Massabò, 2017). Furthermore, some shortcomings in the classical iterative algorithms for solving the optimization problem could be addressed. Specifically, a major improvement would be to reduce the time-consumption required to complete each iteration, depending on the model dimension, the wavevector discretization and the precision requirements. In this respect, a feasible countermeasure could be to replace the objective function with a more-easily computable approximation, exploiting techniques from surrogate optimization (Koziel and Leifsson, 2013). In this respect, the approximation can be based on a mesh-free method for interpolation, employing a finite number of strictly positive-definite Gaussian Radial Basis Functions (Fasshauer, 2007). According to this alternative, a two-phase procedure can be established, in which a suboptimal solution is, first, found via a ultra-fast global search based on the approximate objective (first phase) and, second, locally re-optimized using the original objective (second phase). Preliminary results have been obtained for the maximization of a specific partial band gap in the tetrachiral metamaterial (Bacigalupo and Gnecco, 2018). The findings are promising since, in each repetition, the values of the surrogate and original objective functions evolve in a similar way during the various iterations of the Sequential Linear Programming algorithm applied therein. Besides the reduction of the computational costs, a further advancement could be to merge parametric and topological optimization issues. Indeed, the techniques developed in this work could be applied also to topology optimization. A promising idea is the employment of level set methods (Sethian, 1999; Gibou et al., 2018) to represent the topology, since these methods allow for merging and splitting of contours during the optimization. The reduction of such a problem to a finite number of optimization parameters could be carried out by approximating the level set function by a neural network, perhaps composed by a single hidden layer and sigmoidal computational units (Haykin, 1994).

AUTHOR CONTRIBUTIONS

All authors listed have made a substantial, direct and intellectual contribution to the work, and approved it for publication.

ACKNOWLEDGMENTS

We acknowledge financial support of the (MURST) Italian Department for University and Scientific and Technological Research in the framework of the research MIUR Prin15 project 2015LYYXA8, Multi-scale mechanical models for the design and optimization of micro-structured smart materials and metamaterials, coordinated by Prof. A. Corigliano. We also thankfully acknowledge financial support by National Group of Mathematical Physics (GNFMINdAM).

REFERENCES

Amendola, A., Krushynska, A., Daraio, C., Pugno, N. M., and Fraternali, F. (2018). Tuning frequency band gaps of tensegrity mass-spring chains with local and global prestress. *Int. J. Solids Struct.* 155, 47–56. doi: 10.1016/j.ijsolstr.2018.07.002

Bacigalupo, A., and Gambarotta, L. (2016). Simplified modelling of chiral lattice materials with local resonators. *Int. J. Solids Struct.* 83, 126–141. doi: 10.1016/j.ijsolstr.2016.01.005

Bacigalupo, A., and Gnecco, G. (2018). Metamaterial filter design via surrogate optimization. *J. Phys. Conf. Ser.* 1092:012043. doi: 10.1088/1742-6596/1092/1/012043

Bacigalupo, A., Gnecco, G., Lepidi, M., and Gambarotta, L. (2016a). "Design of acoustic metamaterials through nonlinear programming," in *Springer Lecture Notes in Computer Science - The Second International Workshop on Machine Learning, Optimization and Big Data - MOD 2016*, eds G. Giuffrida, G. Nicosia, and P. Pardalos (Volterra: Springer), 170–181. doi: 10.1007/978-3-319-51469-7_14

Bacigalupo, A., Gnecco, G., Lepidi, M., and Gambarotta, L. (2017). Optimal design of low-frequency band gaps in anti-tetrachiral lattice meta-materials. *Compos. B* 115, 341–359. doi: 10.1016/j.compositesb.2016.09.062

Bacigalupo, A., and Lepidi, M. (2018). Acoustic wave polarization and energy flow in periodic beam lattice materials. *Int. J. Solids Struct.* 147, 183–203. doi: 10.1016/j.ijsolstr.2018.05.025

Bacigalupo, A., Lepidi, M., Gnecco, G., and Gambarotta, L. (2016b). Optimal design of auxetic hexachiral metamaterials with local resonators. *Smart Mater. Struct.* 25:054009. doi: 10.1088/0964-1726/25/5/054009

Bordiga, G., Cabras, L., Bigoni, D., and Piccolroaz, A. (in press). Free and forced wave propagation in a rayleigh-beam grid: flat bands, dirac cones, and vibration localization vs isotropization. *Int. J. Solids Struct.* doi: 10.1016/j.ijsolstr.2018.11.007

Brillouin, L. (2003). *Wave Propagation in Periodic Structures: Electric Filters and Crystal Lattices.* Mineola, NY: Courier Corporation.

Bruggi, M., Zega, V., and Corigliano, A. (2017). Synthesis of auxetic structures using optimization of compliant mechanisms and a micropolar material model. *Struct. Multidiscipl. Opt* 55, 1–12. doi: 10.1007/s00158-016-1589-9

Celli, P., and Gonella, S. (2014). Low-frequency spatial wave manipulation via phononic crystals with relaxed cell symmetry. *J. Appl. Phys.* 115:103502. doi: 10.1063/1.4867918

Chen, J., Pan, E., and Chen, H. (2007). Wave propagation in magneto-electro-elastic multilayered plates. *Int. J. Solids Struct.* 44, 1073–1085. doi: 10.1016/j.ijsolstr.2006.06.003

Colquitt, D., Jones, I., Movchan, N., and Movchan, A. (2011). Dispersion and localization of elastic waves in materials with microstructure. *Proc. R. Soc. Lond. A* 467, 2874–2895. doi: 10.1098/rspa.2011.0126

Cox, S. J., and Dobson, D. C. (2000). Band structure optimization of two-dimensional photonic crystals in h-polarization. *J. Comput. Phys.* 158, 214–224. doi: 10.1006/jcph.1999.6415

D'Alessandro, L., Belloni, E., Ardito, R., Corigliano, A., and Braghin, F. (2016). Modeling and experimental verification of an ultra-wide bandgap in 3d phononic crystal. *Appl. Phys. Lett.* 109:221907. doi: 10.1063/1.4971290

D'Alessandro, L., Zega, V., Ardito, R., and Corigliano, A. (2018). 3d auxetic single material periodic structure with ultra-wide tunable bandgap. *Sci. Rep.* 8:2262. doi: 10.1038/s41598-018-19963-1

Diaz, A., Haddow, A., and Ma, L. (2005). Design of band-gap grid structures. *Struct. Multidiscipl. Opt.* 29, 418–431. doi: 10.1007/s00158-004-0497-6

Fasshauer, G. E. (2007). *Meshfree Approximation Methods with MATLAB*, Vol. 6. London, UK: World Scientific. doi: 10.1142/6437

Gibou, F., Fedkiw, R., and Osher, S. (2018). A review of level-set methods and some recent applications. *J. Comput. Phys.* 353, 82–109. doi: 10.1016/j.jcp.2017.10.006

Haykin, S. (1994). *Neural Networks: A Comprehensive Foundation*. Prentice Hall PTR.

Huang, H., Sun, C., and Huang, G. (2009). On the negative effective mass density in acoustic metamaterials. *Int. J. Eng. Sci.* 47, 610–617. doi: 10.1016/j.ijengsci.2008.12.007

Kaminakis, N. T. and Stavroulakis, G. E. (2012). Topology optimization for compliant mechanisms, using evolutionary-hybrid algorithms and application to the design of auxetic materials. *Comp. B Eng.* 43, 2655–2668. doi: 10.1016/j.compositesb.2012.03.018

Koziel, S., and Leifsson, L. (2013). *Surrogate-Based Modeling and Optimization: Applications in Engineering*. New York, NY: Springer Science & Business Media.

Krushynska, A., Kouznetsova, V., and Geers, M. (2014). Towards optimal design of locally resonant acoustic metamaterials. *J. Mech. Phys. Solids* 71, 179–196. doi: 10.1016/j.jmps.2014.07.004

Krushynska, A., Miniaci, M., Bosia, F., and Pugno, N. (2017). Coupling local resonance with bragg band gaps in single-phase mechanical metamaterials. *Extreme Mech. Lett.* 12, 30–36. doi: 10.1016/j.eml.2016.10.004

Langley, R. (1994). On the modal density and energy flow characteristics of periodic structures. *J. Sound Vibr.* 172, 491–511. doi: 10.1006/jsvi.1994.1191

Langley, R. (1995). Wave transmission through one-dimensional near periodic structures: optimum and to random disorder. *J. Sound Vibr.* 188, 717–743. doi: 10.1006/jsvi.1995.0620

Langley, R. (1996). A transfer matrix analysis of the energetics of structural wave motion and harmonic vibration. *Proc. R. Soc. Lond. A* 452, 1631–1648. doi: 10.1098/rspa.1996.0087

Lepidi, M., and Bacigalupo, A. (2018a). Multi-parametric sensitivity analysis of the band structure for tetrachiral acoustic metamaterials. *Int. J. Solids Struct.* 136-137, 186–202. doi: 10.1016/j.ijsolstr.2017.12.014

Lepidi, M., and Bacigalupo, A. (2018b). Parametric design of the band structure for lattice materials. *Meccanica* 53, 613–628. doi: 10.1007/s11012-017-0644-y

Liu, Z., Chan, C. T., and Sheng, P. (2005). Analytic model of phononic crystals with local resonances. *Phys. Rev. B* 71:014103. doi: 10.1103/PhysRevB.71.014103

Liu, Z., Zhang, X., Mao, Y., Zhu, Y. Y., Yang, Z., Chan, C. T., and Sheng, P. (2000). Locally resonant sonic materials. *Science* 289, 1734–1736. doi: 10.1126/science.289.5485.1734

Martinsson, P., and Movchan, A. (2003). Vibrations of lattice structures and phononic band gaps. *Q. J. Mech. Appl. Math.* 56, 45–64. doi: 10.1093/qjmam/56.1.45

Massabò, R. (2017). Propagation of rayleigh-lamb waves in multilayered plates through a multiscale structural model. *Int. J. Solids Struct.* 124, 108–124. doi: 10.1016/j.ijsolstr.2017.06.020

Mei, J., Ma, G., Yang, M., Yang, Z., Wen, W., and Sheng, P. (2012). Dark acoustic metamaterials as super absorbers for low-frequency sound. *Nat. Commun.* 3:756. doi: 10.1038/ncomms1758

Nayfeh, A. H., Faidi, W., and Abdelrahman, W. (1999). An approximate model for wave propagation in piezoelectric materials. I. laminated composites. *J. Appl. Phys.* 85, 2337–2346. doi: 10.1063/1.369547

Paggi, M. (2010). Singular, hypersingular and singular free electromagnetic fields at wedge tips in metamaterials. *Int. J. Solids Struct.* 47, 2062–2069. doi: 10.1016/j.ijsolstr.2010.04.003

Pelassa, M., and Massabò, R. (2015). Explicit solutions for multi-layered wide plates and beams with perfect and imperfect bonding and delaminations under thermo-mechanical loading. *Meccanica* 50, 2497–2524. doi: 10.1007/s11012-015-0147-7

Phani, A. S., Woodhouse, J., and Fleck, N. (2006). Wave propagation in two-dimensional periodic lattices. *J. Acous. Soc. Am.* 119, 1995–2005. doi: 10.1121/1.2179748

Reda, H., Rahali, Y., Ganghoffer, J.-F., and Lakiss, H. (2016). Analysis of dispersive waves in repetitive lattices based on homogenized second-gradient continuum models. *Comp. Struct.* 152, 712–728. doi: 10.1016/j.compstruct.2016.05.080

Ronellenfitsch, H., Stoop, N., Forrow, A., and Dunkel, J. (2018). Designing spectral bandgaps in phononic networks. *arXiv:1802.07214*.

Ruzzene, M., Scarpa, F., and Soranna, F. (2003). Wave beaming effects in two-dimensional cellular structures. *Smart Mater. Struct.* 12, 363–372. doi: 10.1088/0964-1726/12/3/307

Sethian, J. A. (1999). *Level Set Methods and Fast Marching Methods: Evolving Interfaces in Computational Geometry, Fluid Mechanics, Computer Vision, and Materials Science*, Vol. 3. Cape Town: Cambridge University Press.

Shen, L., Ye, Z., and He, S. (2003). Design of two-dimensional photonic crystals with large absolute band gaps using a genetic algorithm. *Phys. Rev. B* 68:035109. doi: 10.1103/PhysRevB.68.035109

Sigmund, O. and Jensen, J. S. (2003). Systematic design of phononic band–gap materials and structures by topology optimization. *Philos. Trans. R. Soc. Lond. A* 361, 1001–1019. doi: 10.1098/rsta.2003.1177

Sobol, I. M. (1998). On quasi-monte carlo integrations. *Math. Comput. Simul.* 47, 103–112. doi: 10.1016/S0378-4754(98)00096-2

Spadoni, A., Ruzzene, M., Gonella, S., and Scarpa, F. (2009). Phononic properties of hexagonal chiral lattices. *Wave Motion* 46, 435–450. doi: 10.1016/j.wavemoti.2009.04.002

Svanberg, K. (1987). The method of moving asymptotes - a new method for structural optimization. *Int. J. Num. Methods Eng.* 24, 359–373. doi: 10.1002/nme.1620240207

Svanberg, K. (2002). A class of globally convergent optimization methods based on conservative convex separable approximations. *SIAM J. Opt.* 12, 555–573. doi: 10.1137/S1052623499362822

Tee, K., Spadoni, A., Scarpa, F., and Ruzzene, M. (2010). Wave propagation in auxetic tetrachiral honeycombs. *J. Vibr. Acoust.* 132, 031007. doi: 10.1115/1.4000785

Tie, B., Tian, B., and Aubry, D. (2013). Theoretical and numerical investigation of hf elastic wave propagation in two-dimensional periodic beam lattices. *Acta Mech. Sin.* 29, 783–798. doi: 10.1007/s10409-013-0087-1

Vadalà, F., Bacigalupo, A., Lepidi, M., and Gambarotta, L. (2018). Bloch wave filtering in tetrachiral materials via mechanical tuning. *Comp. Struct.* 201, 340–351. doi: 10.1016/j.compstruct.2018.05.117

Wang, P., Casadei, F., Kang, S. H., and Bertoldi, K. (2015). Locally resonant band gaps in periodic beam lattices by tuning connectivity. *Phys. Rev. B* 91:020103. doi: 10.1103/PhysRevB.91.020103

Wang, Y. F., Wang, Y. S., and Zhang, C. (2016). Two-dimensional locally resonant elastic metamaterials with chiral comb-like interlayers: Bandgap and simultaneously double negative properties. *J. Acoust. Soc. Am.* 139, 3311–3319. doi: 10.1121/1.4950766

Zhu, R., Huang, G., and Hu, G. (2012). Effective dynamic properties and multi-resonant design of acoustic metamaterials. *J. Vibr. Acoust.* 134:031006. doi: 10.1115/1.4005825

Conflict of Interest Statement: The authors declare that the research was conducted in the absence of any commercial or financial relationships that could be construed as a potential conflict of interest.

frontiers in Materials

ORIGINAL RESEARCH
published: 06 February 2019
doi: 10.3389/fmats.2019.00007

On the Kinematics and Actuation of Dynamic Sunscreens With Tensegrity Architecture

Enrico Babilio[1]*, *Raffaele Miranda*[2] *and Fernando Fraternali*[2]

[1] Department of Structures for Engineering and Architecture, University of Naples "Federico II", Naples, Italy, [2] Department of Civil Engineering, University of Salerno, Fisciano, Italy

This paper presents a mechanical study on the use of tensegrity lattices for the design of energy efficient sun screens, inspired by the dynamic solar façades of the Al Bahar Towers in Abu Dhabi. The analyzed screens tassellate origami modules formed by 12-bar and 3-string tensegrity systems. The actuation of each module is controlled through the stretching of the perimeter strings, which form macro-triangles moving parallel to the building, while all the bars and the fabric mesh infills form micro-triangles that are allowed to move rigidly in space. We developed an analytic formulation of the deformation mapping associated with such an actuation motion, giving rise to a morphing-type behavior. We also estimated the energy required to activate the analyzed shading system, and established a comparison between its weight and that of the original screens of the Al Bahar Towers. The proposed tensegrity design concept leads to the realization of shading screens that are markedly lightweight, operate on very low energy consumption and can be usefully employed to harvest solar and wind energies.

Keywords: tensegrity structures, dynamic solar façades, energy efficient buildings, foldable structures, morphing lattices

OPEN ACCESS

Edited by:
Alberto Corigliano,
Politecnico di Milano, Italy

Reviewed by:
Stefano Vidoli,
Sapienza University of Rome, Italy
Zbigniew Wojciech Bieniek,
Rzeszów University of Technology, Poland
Seung Hee Jeong,
Harvard University, United States

***Correspondence:**
Enrico Babilio
enrico.babilio@unina.it

Specialty section:
This article was submitted to Mechanics of Materials, a section of the journal Frontiers in Materials

Received: *25 November 2018*
Accepted: *14 January 2019*
Published: *06 February 2019*

Citation:
Babilio E, Miranda R and Fraternali F (2019) On the Kinematics and Actuation of Dynamic Sunscreens With Tensegrity Architecture. Front. Mater. 6:7. doi: 10.3389/fmats.2019.00007

1. INTRODUCTION

Sustainable engineering and architecture aim at designing buildings with limited environmental impact and improved energy efficiency, comfort and indoor air quality, through appropriate construction techniques (refer, e.g., to Schittich, 2003; Quesada et al., 2012a,b and references therein). A sustainable design approach looks at the optimal design and control of natural ventilation systems, building orientation and shading, through passive and/or active techniques. The latter calls for the incorporation of home automation systems and renewable energy supplies within the building, typically in correspondence with the buildings "skin" (Kuhn et al., 2010; Balduzzi et al., 2012; Bai et al., 2018).

The European Union (EU) requires Member States to develop long-term national plans to encourage efficient re-development of buildings and reduction of CO_2 emissions by between 80% and 85% compared to 1990 Directive UE (2018/844). The EU policy for the energy efficiency of buildings is aimed at formulating long-term strategies that facilitate the transformation of residential and non-residential buildings, into efficient and decarbonised structures by 2050, with the aim of achieving almost zero net energy consumption (Lombard et al., 2010). The demand for energy savings and the reduction of CO_2 emissions has called for the use of new interactive building envelopes. Such active façades must respond to the variations of the external climatic conditions through automatic control devices, with the aim of significantly optimizing the energetic performance of the building.

Recent research has proposed the use of tensegrity structures for the construction of renewable energy supplies forming dynamic envelopes of energy efficient buildings, due to the special ability of such structures to act as deployable systems, which can also convert the strain energy stored in cables, into electric power (Skelton and de Oliveira, 2010; Fraternali et al., 2015; Cimmino et al., 2017). Tensegrity systems are truss structures whose compressive members (or bars) can be described as rigid of partially deformable bodies, while the tensile members (cables or strings) exhibit high compliance. The strings are usually pre-stretched, and are inserted into the structure in order to stabilize the compressed members (Skelton and de Oliveira, 2010).

This paper continues and significantly expands the study initiated in Fraternali et al. (2015), on the use of tensegrity systems for the actuation of dynamic sun screens. We design tensegrity screens that mitigate air conditioning consumption resulting from direct exposure to solar rays of an energy efficient building, and derive the exact kinematics of such structures under operating conditions. We also study the stress response of the examined tensegrity systems to wind loading, and quantify their lightweight nature and the energy cost required for their activation. The geometry of the solar façade analyzed in this work is inspired by that of the sun screens protecting the Al Bahar Towers in Abu Dhabi, United Arab Emirates, designed by Aedas Architects-UK (now AHR) in 2007, in collaboration with the Arup Group (Karanouh and Kerber, 2015; Attia, 2017). These towers are 29-story skyscrapers that host the headquarters of the Abu Dhabi Investment Council's and the Al Hilal Bank. The screens of the Al Bahar Towers mimic the shading lattice-work "ashrabiya" through "origami" panels that are dynamically opened at night, and are progressively closed during daylight hours (Karanouh and Kerber, 2015). We refer to the shading façade designed by Aedas architects as the "Al Bahar Screen" (ABS) throughout this paper.

The tensegrity solution that we propose for the re-design of the ABS controls the tension in selected cables forming the shading structure. It is aimed at demonstrating that the use of tensegrity concepts for the design of active solar façades leads to lightweight morphing systems that require minimal storage of internal energy and reduced operation costs. Such a design can easily be generalized to dynamic skins of energy efficient buildings featuring different topologies, upon retaining the use of morphing architectures (Fleck et al., 2010), and deployment mechanisms controlled through cable stretching and relaxation (Fraternali et al., 2015). We label the sun screen designed in the present work as the "Tensegrity Al Bahar Screen" (TABS).

The structure of the paper is as follows. We begin by reviewing the AHR design of the ABS in section 2. Next, we move on to design a basic TABS module, by developing an analytic formulation of the kinematics of such a structure. We prove that the employed actuation mechanism requires the deformation of a limited number of members, and exhibits a morphing-type response (section 3). The stress analysis of the TABS module is conducted in section 4, while an estimate of the energy costs associated with its actuation is presented in section 5. We highlight the main advantages of the TABS technology in section 6, where we also draw potential future extensions of the present research.

2. A REVIEW OF THE ABS DESIGN

The biggest challenge that contemporary architecture has to address, in order to make progress in sustainability, is to optimize natural resources and minimize energy consumption. To provide the best answer to this need it is necessary to design flexible and reconfigurable building envelopes able to dynamically react on the base of the evolution of weather and environmental conditions (**Figure 1**). The adaptive architecture of the Al Bahar tower façade by AHR develops a new design approach based on structural systems that can change their shape by reacting to the surrounding environment. The heart of the Al Bahar tower project consists of a modern-day re-interpretation of the traditional "mashrabiya" shading system. The latter is a passive shading technology typical of the Arab world, which consist of perforated wooden screens forming wonderful geometric patterns, which reduce solar gain and mitigate air conditioning consumption resulting from direct exposure to solar rays (Armstrong et al., 2013).

The peculiarity of the adaptive ABS consists in no longer interpreting the mashrabiya as a static and two-dimensional system, but rather as a façade design approach generating three-dimensional origami shapes (**Figure 1B**), whose motion in space can be controlled by sensors and actuators during daylight hours (typically, from 9 a.m. through 5 p.m.) (Al-Kodmany, 2016). The evaluation of the insulation property of a façade, the so-called U-value (defined as the amount of heat passing per unit of surface of the screen, under one Kelvin temperature gradient between indoor and outdoor), is a topic of paramount interest for the architects and engineers operating in the field. Energy studies conducted on the ABS lead to conclude that the overall U-value of this building envelope is equal to 2.0 W/m^2K, which corresponds to that of a solid brick wall (Designing Buildings Wiki)[1]. The origami panels are covered by a polytetrafluoroethylene (PTFE) coated fiber mesh, which reduces the G-value of the façade more than 50% (i.e., the ratio between the total solar heat gain and the incident solar radiation), as compared to a glazed envelope (Karanouh and Kerber, 2015). The activation of the ABS is driven by a centrally positioned electric screw-jack linear actuator (piston-actuated computer-controlled technology) that operates on low energy consumption. The linear actuator stroke reaches up to 1,000 mm, which folds the panels and provides up to 85% clear opening area (Armstrong et al., 2013) (**Figure 1C**). The structural elements of the ABS are made of duplex (austenitic-ferritic) stainless steel supporting frames and Aluminum dynamic frames, with each triangle of the screen covered by a glass fiber panel (**Figure 1B**) (Karanouh and Kerber, 2015; Attia, 2017). The umbrella-like module of the ABS has a height of 4,200 mm, and a width ranging between 3,600 and 5,400 mm. In total, each tower has 1,049 shading

---

[1] Available online at: https://www.designingbuildings.co.uk/wiki/U-values.

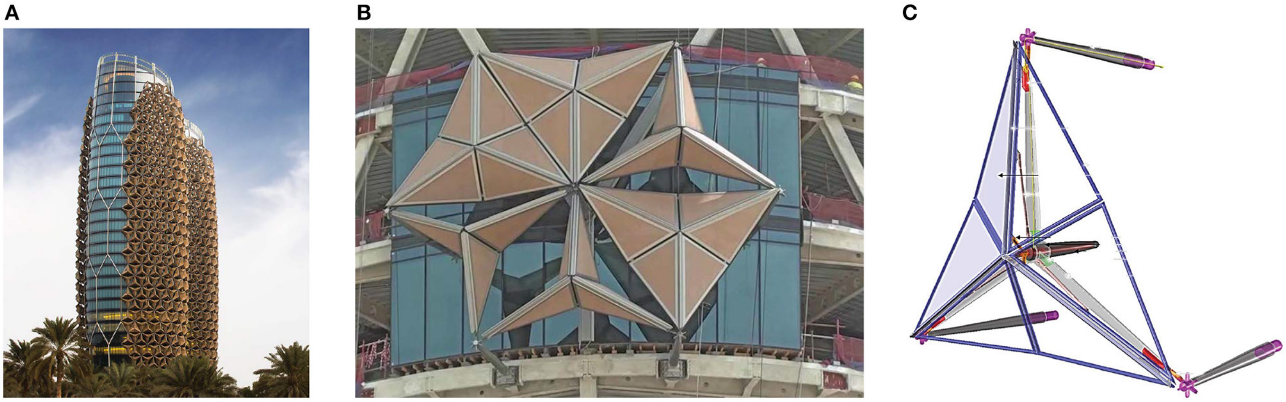

FIGURE 1 | (A) Illustration of the Al Bahar towers in Abu Dhabi. **(B)** detail of a module of the ABS (picture taken during the mounting of the screens). **(C)** ABS actuation mechanism (reproduced with permission from Karanouh and Kerber, 2015).

modules, each weighing a 1.5 tons (Armstrong et al., 2013; Attia, 2017).

3. KINEMATICS OF A TABS MODULE

The TABS concept is illustrated in **Figure 2**, with reference to a basic module of the structure. The analyzed module is composed of six "micro-triangles," and is such that its boundary forms a "macro-triangle" when projected onto a plane parallel of the building façade (umbrella-like module). The activation mechanism of the TABS module is driven by a linear actuator, which stretches the perimeter strings, by pushing against a vertex of the macro-triangle along its bisector, in parallel to the building façade. The mechanism is guided by two linear springs controlling the in-plane displacements of the other two vertices of the macro-triangle, and a telescopic collar guiding the out-of-plane displacement of the center of mass of the module (**Figure 2**). It is worth remarking that such a "tangentially" activated mechanism substantially differs from that driving the ABS module, since the latter pushes orthogonally to the building façade, against the center of mass of the module (Armstrong et al., 2013; Karanouh and Kerber, 2015; Attia, 2017) .We study in section 3.1 the existence of a deformation mapping of the TABS module, which corresponds to the described actuation mechanisms and ensures that all the micro-triangles move rigidly in space. Such a morphing-type behavior (Hutchinson and Fleck, 2006; Fleck et al., 2010) induces minimal storage of internal energy during the actuation phase, and ensures high stiffness and stability when the actuation mechanism is not triggered (cf. Sections 4, 5).

The model of the TABS adopted in following analytical and numerical developments is reported in **Figure 3**, to which we refer for notation. The module is described as a tensegrity system formed by 3 strings parallel to the building façade and aligned with the edges of the macro-triangle (red-colored members), and 12 bars forming the edges of the micro-triangles (black-colored members). **Figure 3** depicts the completely folded configuration (**Figure 3A**) of the tensegrity model, which we assume as reference, and the unfolded, perfectly flat configuration (**Figure 3B**). The TABS model is formed by seven nodes (numbered from 0 to 6 in **Figure 3**), for a total of 21 degrees of freedom ($n_{\text{dof}} = 21$). The adopted Cartesian frame is reported in **Figure 3**.

In agreement with the activation mechanism described above, the boundary conditions (BCs) of the TABS module are as follows

$$\begin{aligned}
&\text{on node 0:} && u_{0(x)} = 0\,,\ u_{0(y)} = 0\,,\\
&\text{on node 2:} && u_{2(x)} = 0\,,\ u_{2(z)} = 0\,,\\
&\text{on node 4:} && u_{4(y)} = \frac{u_{4(x)}}{\sqrt{3}}\,,\ u_{4(z)} = 0\,,\\
&\text{on node 6:} && u_{6(y)} = -\frac{u_{6(x)}}{\sqrt{3}}\,,\ u_{6(z)} = 0\,,
\end{aligned} \tag{1}$$

where $u_{i(x)}$, $u_{i(y)}$ and $u_{i(z)}$ are the Cartesian components of the nodal displacement vector $\mathbf{u}_i$ exhibited by the generic node i. The BCs (1) must be complemented by three additional equations, respectively associated with the linear actuator acting on node 2, and the two springs acting on nodes 4 and 6 (actuation constraints, cf. Section 3.1).

3.1. Rigid Body Transformation

Let us investigate on the existence of a rigid body transformation of the TABS deprived of external constraints, which cause stretching (positive) strains only in the perimeter strings connecting nodes 2, 4, and 6 (cf. **Figure 3**), measured from the fully-folded configuration (rest configuration), while keeping all the bars undeformed.

The rigid-body deformation mapping under investigation is constrained by the 11 BCs defined above, plus 12 rigidity constraints associated with the bars forming the module. In agreement with BCs (1), the displacement vector of node 2 attached to the linear actuator of the TABS module is given by

$$\mathbf{u}_2 = U\,\mathbf{e}_y\,, \qquad U \geq 0\,, \tag{2}$$

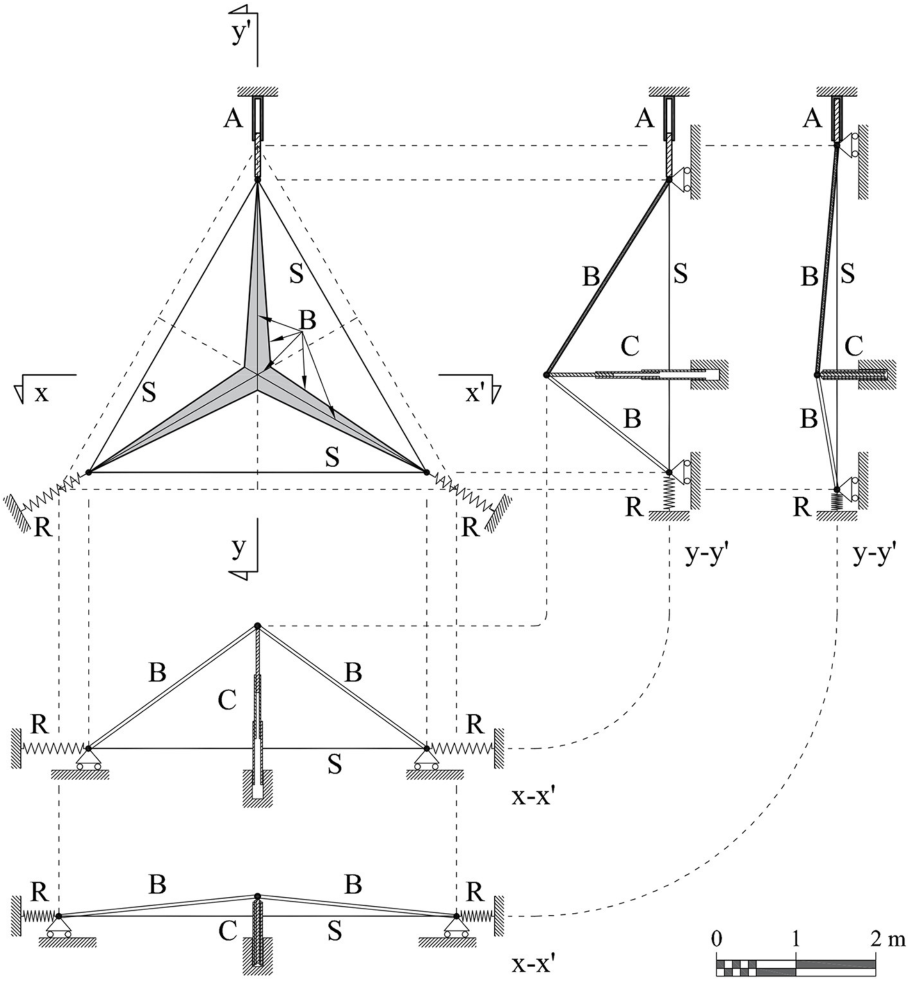

FIGURE 2 | Schematic views of the TABS concept: top view and mid-plane sections (in two different configurations): A, linear actuator; B, bars; C, telescopic collar; R, elastic restraints; S, perimeter strings. Restraints are idealized and not reported in scale.

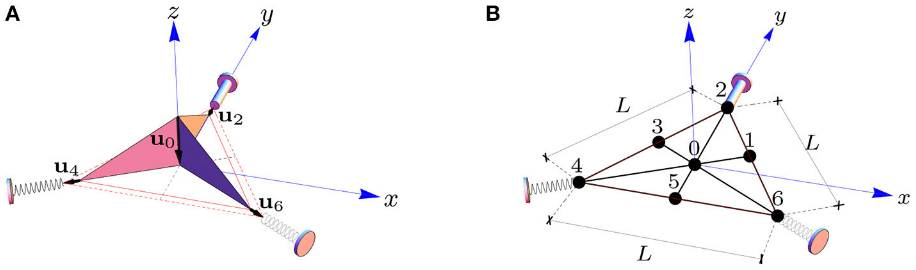

FIGURE 3 | Reference **(A)** and deformed **(B)** configurations of a tensegrity model of the TABS module. **(A)** shows the folded configuration of the structure corresponding to the fully opened screen. **(B)** depicts the flat configuration (fully closed screen), where the module reduces to an equilateral triangle with side L. Nodes 2, 4, and 6 are mutually connected through deformable strings (red-colored members), which are at rest in the reference configuration, and fully stretched in the flat configuration. The strings are superimposed to the perimeter bars in the flat configuration **(B)**.

U denoting the time-dependent norm of such a displacement, which is measured from the fully folded configuration. Due to constructive needs, we require that the researched rigid body transformation is such that the displacements of nodes 4 and 6 exhibit the same norm U of $\mathbf{u}_2$ (due to symmetry), and nodes 5, 3, and 1, respectively move along the y-axis (i.e., the projected 5–2 edge onto x, y-plane, see **Figure 3**), the projected 3–6 edge (aligned with the y-axis rotated of $\pi/3$), and the projected 1–4 edge (aligned with the y-axis rotated of $-\pi/3$). Our next developments will show that such assumptions are equivalent to the enforcement of the actuation constraints at the vertices of the TABS module. Overall, the deformation mapping associated with the researched rigid body transformation of the TABS is described by Equation (2), and the following additional displacement laws

$$\mathbf{u}_0 = -\alpha \mathbf{e}_z \,, \tag{3}$$

$$\mathbf{u}_1 = \frac{\sqrt{3}\beta}{2}\mathbf{e}_x - \frac{\beta}{2}\mathbf{e}_y + \gamma \mathbf{e}_z \,, \tag{4}$$

where α, β, and γ are unknown functions of U, to be determined on enforcing rigidity constraints on all the bars. In the completely folded and flat configurations it trivially results

$$\alpha = 0\,, \quad \beta = 0\,, \quad \text{and} \quad \gamma = 0 \quad \text{for} \quad U = 0\,, \tag{5}$$

and

$$\alpha \;=\; \frac{L\sqrt{3}}{6}\,, \quad \beta = 1\,, \quad \text{and} \quad \gamma = 0\,, \quad \text{for} \quad U \;=\; \bar{U} \;=\; \frac{2\sqrt{3}-3}{6}L\,. \tag{6}$$

Let us label the position vectors of the generic point i in reference and deformed configurations as $\mathbf{X}_i$ and $\mathbf{x}_i$, respectively. The rest and deformed lengths of the e^{th} element attached to nodes i and j are given by

$$L_e = \sqrt{(\mathbf{X}_i - \mathbf{X}_j)\cdot(\mathbf{X}_i - \mathbf{X}_j)}\,, \tag{7}$$

$$\ell_e = \sqrt{(\mathbf{x}_i - \mathbf{x}_j)\cdot(\mathbf{x}_i - \mathbf{x}_j)}\,, \tag{8}$$

where dot symbol $(\cdot)$ denotes the scalar product between vectors. The rigidity constraints to be considered require that it results

$$L_e^2 = \ell_e^2\,, \tag{9}$$

in correspondence to all the bars (here, squared lengths are used for algebraic convenience). It is easily shown that the enforcement of such constraints leads us to the following system of three independent (nonlinear) equations

$$\begin{aligned} 3\alpha^2 - \sqrt{3}L\alpha + 3LU + 3U^2 &= 0\,, \\ 3(\alpha+\gamma)^2 - \sqrt{3}L(\alpha+\gamma) + 3\beta^2 &= 0\,, \\ 2\beta^2 + 2\gamma^2 - L\beta - 2U\beta + 2LU + 2U^2 &= 0\,, \end{aligned} \tag{10}$$

which admit four distinct sets of solutions for α, β and γ, as it can be verified through the use of the `Solve` function of *Mathematica®* . Three of such solutions violate Equations (5) and (6), while the unique admissible solution has the following expression

$$\begin{aligned} \alpha &= \frac{L - \sqrt{L^2 - 12LU - 12U^2}}{2\sqrt{3}}\,, \\ \beta &= \frac{2LU}{L - 6U}\,, \\ \gamma &= -\frac{\sqrt{3}U\sqrt{L^2 - 12LU - 12U^2}}{L - 6U}\,. \end{aligned} \tag{11}$$

We are therefore led to the following expression of the 7×3 matrix $\hat{\mathbf{x}}(U)$ that collects the deformed coordinates of nodes from 0 to 6 of the TABS module,

$$\hat{\mathbf{x}} = \begin{pmatrix} 0 & 0 & \frac{\sqrt{L^2-12LU-12U^2}}{2\sqrt{3}} \\ \frac{\sqrt{3}LU}{L-6U} & \frac{LU}{L-6U} & -\frac{\sqrt{3}U\sqrt{L^2-12LU-12U^2}}{L-6U} \\ 0 & U+\frac{L}{2} & 0 \\ -\frac{\sqrt{3}LU}{L-6U} & \frac{LU}{L-6U} & -\frac{\sqrt{3}U\sqrt{L^2-12LU-12U^2}}{L-6U} \\ -\frac{\sqrt{3}}{4}(L+2U) & -\frac{1}{4}(L+2U) & 0 \\ 0 & -\frac{2LU}{L-6U} & -\frac{\sqrt{3}U\sqrt{L^2-12LU-12U^2}}{L-6U} \\ \frac{\sqrt{3}}{4}(L+2U) & -\frac{1}{4}(L+2U) & 0 \end{pmatrix}. \tag{12}$$

Equation (12) gives the analytic description of the researched actuation motion of the TABS module. Graphic illustrations of such a transformation are provided in **Figures 4–6**, on assuming $L = 4.55$ m, as in the ABS (Karanouh and Kerber, 2015), and the displacement U of the actuated node as order parameter. It is worth noting that the elongation (i.e., the change in length) exhibited by the perimeter strings is equal to $\sqrt{3}\,U$, which corresponds to the engineering strain $\varepsilon = 2U/L$. For $U = \bar{U}$ (perfectly flat configuration) the engineering strain exhibited by the perimeter strings is considerably high, and approximately equal to 15%. In correspondence to the examined value of L, it is immediate to verify that it results that $\bar{U} = 0.352$ m, and that the norm u_0 of the out-of-plane displacement of node 0 is equal to 1.313 m (unfolding displacement of the umbrella module).

Figure 4 shows that the mid nodes 1, 3, and 5 of the edges of the macro triangle exhibit negative z-displacements, which implies that such nodes move toward the building façade during the actuation of the TABS (cf. also **Figure 6**). It is useful to compute the minimum value of the z displacement of such nodes during the TABS actuation, with aim of sizing the gap to be allowed between such a structure and the building façade. Making use of Equation (12) and the `Solve` function of *Mathematica®* , it is not difficult to verify that it results $\mathrm{d}u_{1(z)}/\mathrm{d}U = 0$ for $U = U^\circ = 0.059\,L$, and $u_{1(z)\min} = -0.079\,L$. In particular, for $L = 4.55$ m, one gets $U^\circ = 0.268$ m, and $u_{1(z)\min} = -0.359$ m. We therefore conclude that the TABS module must be placed at least at $\sim$ 36 cm from the building façade. It is worth noting that the Aedas design of the Al Bahar Towers places the ABS at 2.8 m from the façade of the towers, for window cleaning and shading system maintenance (Armstrong et al., 2013; Attia, 2017).

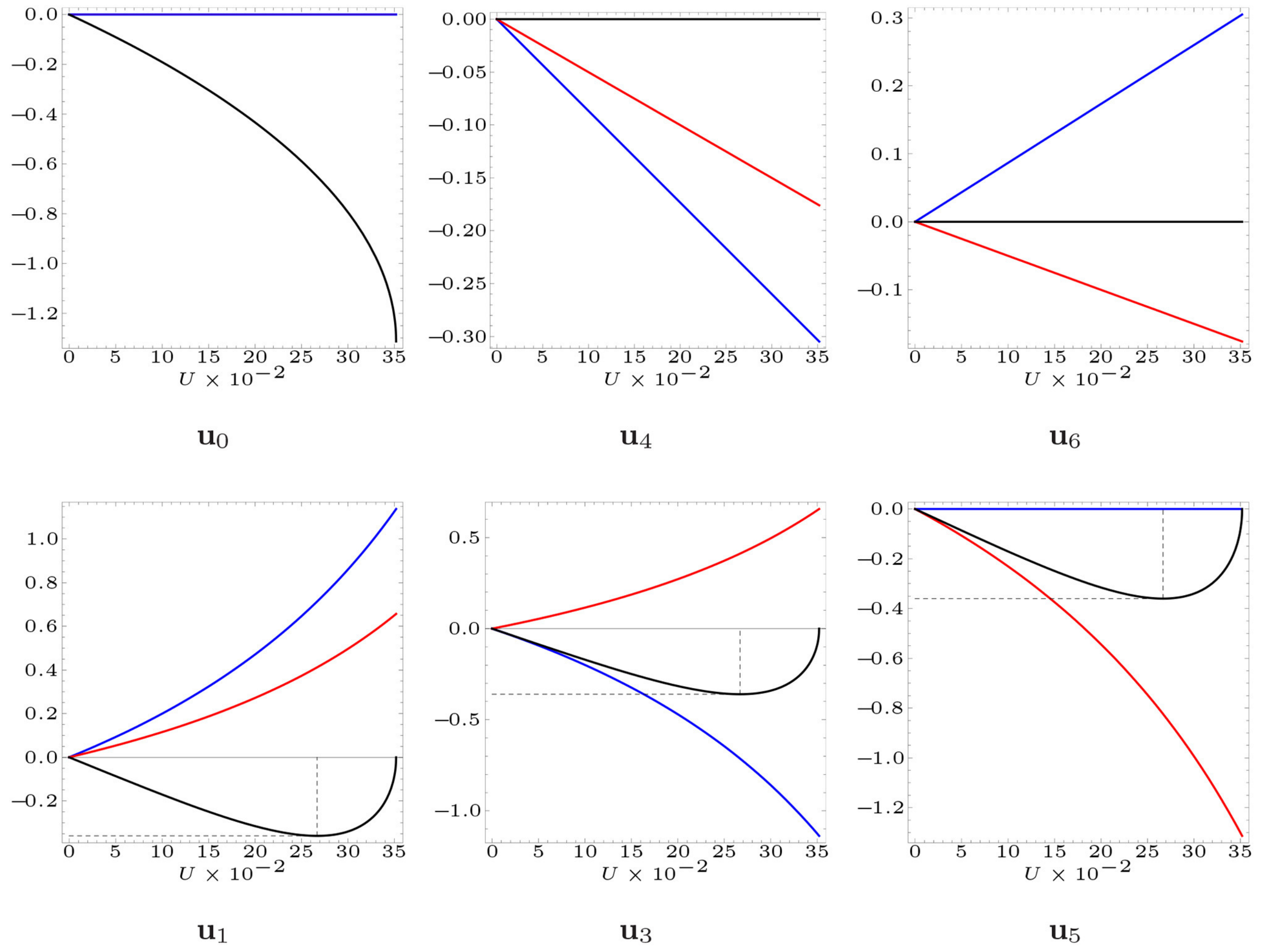

FIGURE 4 | Nodal displacements from the fully folded configuration exhibited by the non-actuated nodes of the TABS module, assuming $L = 4.55$ m. The Cartesian components of the nodal displacements along the x-axis are marked in blue, while the components along the y-axis are marked in red, and those along the z-axis are marked in black.

4. STRESS ANALYSIS OF TABS

The present Section is devoted to the computation of the axial forces carried by the members of the TABS model under the actuation motion (section 4.1), and wind-induced forces (section 4.2). For the sake of simplicity, and considering the common operation times of the analyzed sun screens (Armstrong et al., 2013; Karanouh and Kerber, 2015; Attia, 2017), we assume that the TABS structure reacts to such loading conditions through a quasi-static deformation process, by neglecting inertial and damping (i.e., dynamical) effects.

Upon extending the mechanical theory presented in Modano et al. (2018) and Mascolo et al. (2018) to the TABS model under consideration, we describe the generic member of such a structure as a linear spring that carries an axial force t_e obeying the following constitutive law

$$t_e = k_e (\ell_e - L_e) , \tag{13}$$

where it results

$$k_e = \frac{E_e A_e}{L_e} , \tag{14}$$

E_e denoting the Young's modulus of the material, and A_e denoting the cross section area.

Our physical model of the TABS assumes $L = 4,550$ mm (cf. Section 3.1), and makes use of Aluminum alloy hollow tubes for the bars and nylon-fiber ropes for the strings, whose properties are given in **Tables 1**, **2**, respectively. Aluminum bars were chosen because of their lightweight nature and high corrosion resistance (Mazzolani, 1994), while nylon-fiber ropes were selected due to the fact that such elements combine a considerably low Young's modulus, elastic elongation to failure (or yield strain) slightly greater than the deformation needed for actuation purposes ($\approx$ 15%, cf. Section 3.1), and considerably high tensile strength (see **Table 2**, where the given mechanical properties have been

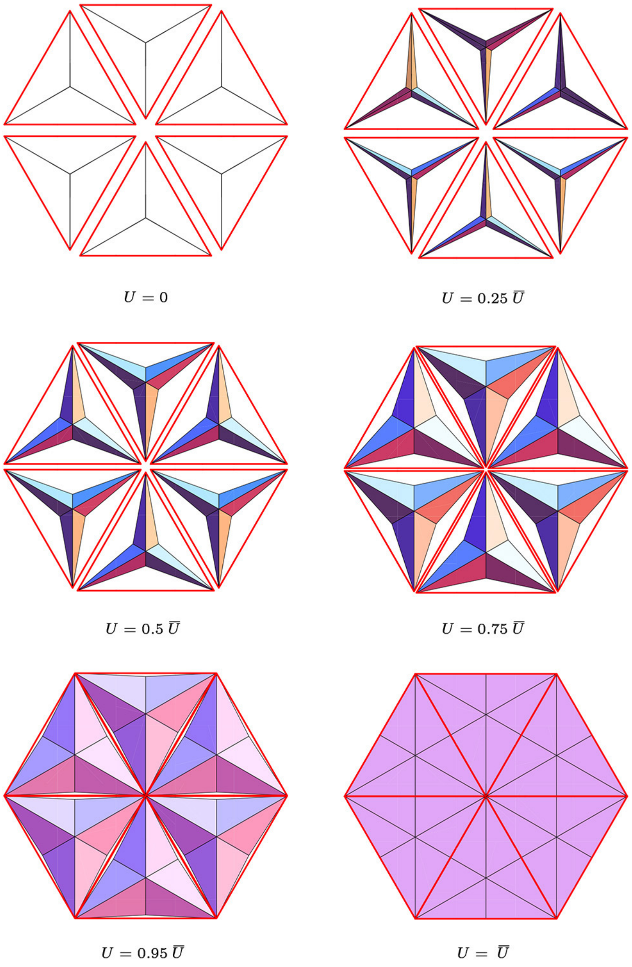
$U = 0$ $U = 0.25\,\bar{U}$

$U = 0.5\,\bar{U}$ $U = 0.75\,\bar{U}$

$U = 0.95\,\bar{U}$ $U = \bar{U}$

FIGURE 5 | Top views of different frames of the TABS actuation motion. (see the **Supplementary Video** for an animation of the TABS actuation).

imported from a web source, 2018[2]; refer, e.g., to Nylonrope, 2018 for fabrication information). Other possible choices for the strings of the TABS may employ suitable natural or artificial fibers (see Naveen et al., 2018 and references therein), or rubber materials (Soru, 2014). The adopted physical model adequately approximates the rigid-elastic response analyzed in section 3.1 (rigid bars and flexible strings), since it includes bars exhibiting axial stiffness much greater than the axial stiffness of the strings ($E_b A_b = 493.625\, E_s A_s$, subscripts b and s denoting bars and strings, respectively, see **Tables 1**, **2**).

The total potential energy of the TABS model under consideration is given by

$$\Pi = \frac{1}{2} \sum_{e=1}^{n} t_e (\ell_e - L_e) + \frac{K}{2} \left(u_{4(x)}^2 + u_{6(x)}^2 \right), \qquad (15)$$

where K denotes the stiffness of the actuation springs applied to nodes 4 and 6 (cf. **Figure 2**) that we assume equal to 67 kN m^{-1} ($K = E_s A_s / L$). The equilibrium equations of the TABS model under arbitrarily large nodal displacements $\hat{u}_j$ ($j = 1, ..., n_{\mathrm{dof}}$) are obtained by imposing stationarity of the total potential energy (Equation 15) with respect to such quantities, which leads us the following system of equations

$$r_j = \frac{\partial \Pi}{\partial \hat{u}_j} = \sum_{e=1}^{m} t_e \frac{\partial \ell_e}{\partial \hat{u}_j} - \hat{\lambda} w_j = 0, \qquad j = 1, ..., n_{\mathrm{dof}}. \qquad (16)$$

Here, the index e runs from one to the total number of members m, which include bars, perimeter strings and actuation springs, while the quantity $\hat{\lambda}$ denotes a scalar multiplier of the nodal forces w_j ($j = 1, ..., n_{\mathrm{dof}}$).

We computed the solution of the nonlinear system (Equation 16) through the path-following algorithm described in Mascolo et al. (2018), with reference to two distinct deformation processes. The first process is aimed at estimating the mechanical response of the examined physical model under the actuation motion studied in section 3.1 (cf. Section 4.1). In the second process, the structure is deployed from the fully-folded configuration to the almost closed configuration corresponding to $U = 0.95\,\bar{U}$, and next is subject to wind-forces acting on such a configuration (cf. Section 4.2). The reason for applying wind forces on the configuration with $U = 0.95\,\bar{U}$ (instead of the fully flat configuration corresponding to $U = \bar{U}$) is two-fold, technological and aesthetic. From a technological point of view, we note that the fully flat configuration of the TABS module is not completely deployable, due to the finite size of the bars forming such a system, which unavoidably get in touch before the configuration with $U = \bar{U}$ is reached (see **Figures 1**, **5**). Regarding aesthetic issues, we observed that having a "technologically closed" configuration of the TABS module, which is not perfectly flat, ensures that such a structure has an origami shape in correspondence to all the steps of the actuation motion (cf. **Figures 5**, **6**), as in the original ABS design (Karanouh and Kerber, 2015; Attia, 2017).

4.1. Forces and Stresses Induced by the Actuation Process

Let us focus our attention on the forces carried by the perimeter strings in correspondence with the fully-flat configuration with $U = \bar{U}$, and the almost closed configuration with $U = 0.95\,\bar{U}$, alongside the actuation motion of the TABS. It is an easy task to compute such quantities using the path-following algorithm described in Mascolo et al. (2018), or, alternatively, by simply observing that the elongation of the perimeter strings is equal to $\sqrt{3}\,U$ in the generic, deformed configuration of the TABS (cf. Section 3.1). The forces, strains and stresses carried by the perimeter strings in the above configurations of the TABS are shown in **Table 3**. It is immediate to verify that the stresses carried by the strings in correspondence to the analyzed configurations, are slightly lower than the tensile strength of 616 MPa of the adopted nylon-fiber ropes (cf. **Table 2**).

The use of the path-following procedure outlined in section 4 leads us to obtain the nodal forces acting on the TABS module for $U = \bar{U}$ and $U = 0.95\,\bar{U}$, which are shown in **Table 4**.

---

[2] http://publica.fraunhofer.de/documents/N-161087.html.

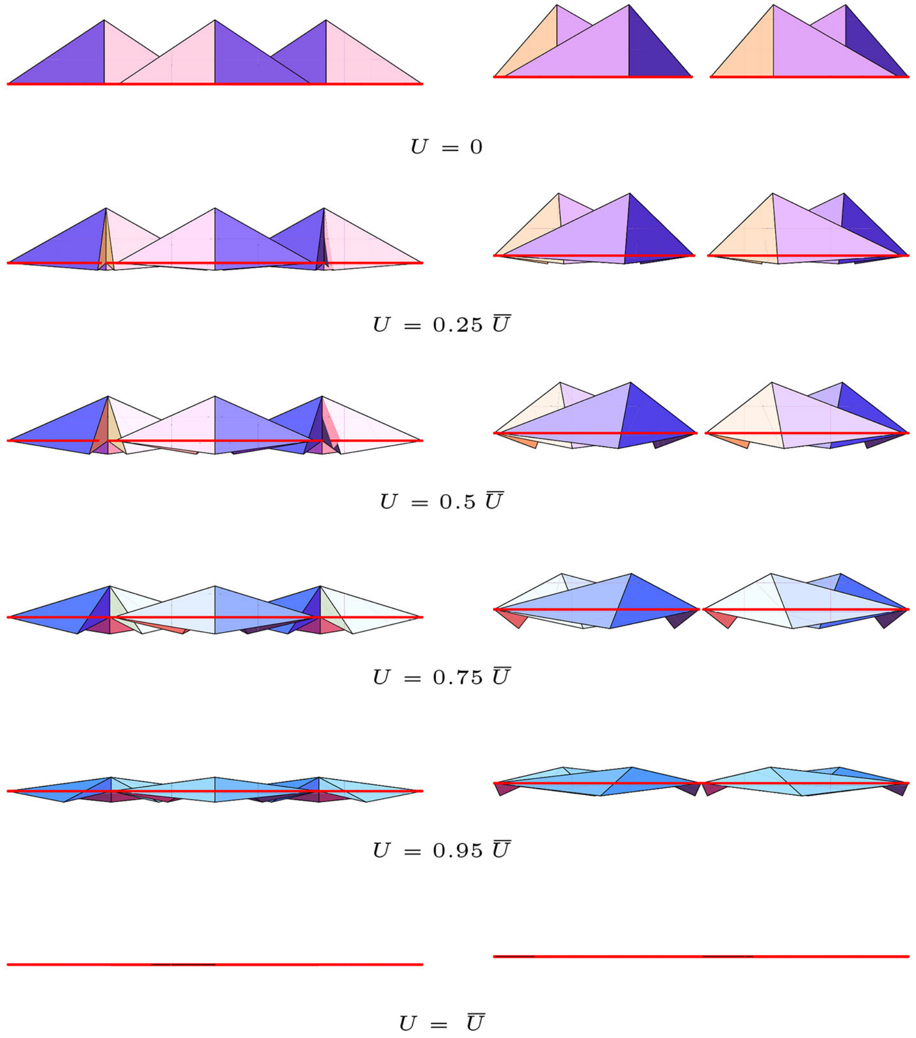

FIGURE 6 | Side views of different frames of the TABS actuation motion (see the **Supplementary Video** for an animation of the TABS actuation).

TABLE 1 | Geometric and mechanical data of 6082-T5 Aluminum bars.

Width w (mm)	Height h (mm)	Thickness t (mm)	Material	Young's modulus E (GPa)	Density ρ (kg m^{-3})	Yield stress σ (MPa)	Yield strain ϵ_b (%)
150	70	5	6082-T5	72	2.70×10^3	260	0.2

The force acting on the node 2 will be employed in section 5 to select the linear actuator to be applied to the TABS module under consideration.

4.2. Effects of Wind Loading

Relevant external loads for the stress analysis of the TABS are those induced by the action of positive and negative (i.e., suction) wind pressures on the closed configuration of the structure (Karanouh and Kerber, 2015). It is known that wind induces dynamic, intrinsically random, and time-dependent loads on wind-exposed structures, whose direction is variable in time and influenced by a number of different factors (refer, e.g., to the European standard for wind actions EN 1991-1-4, 2005).

By addressing a dynamical treatment of wind forces on the TABS to future work, in the present study we focused our attention on the equivalent static wind load analysis, which is contemplated by technical standards (EN 1991-1-4, 2005; Blaise and Denoël, 2013). We considered a fixed direction of wind forces parallel to the z-axis of the adopted Cartesian frame (**Figure 3**). Making use of the results of wind tunnel tests on full-scale

TABLE 2 | Geometric and mechanical (effective) data of (nylon-fiber ropes).

Diameter d (mm)	Material	Young's modulus E_s (GPa)	Density ρ_s (kg m^{-3})	Tensile strength σ_s (MPa)	Yield strain ϵ_s (%)
10	Nylon filaments	3.9	1.14×10^3	616	15.8

TABLE 3 | Strain, stress and axial force carried by the generic perimeter string in the almost fully-flat ($U = 0.95\,\bar{U}$) and fully-flat ($U = \bar{U}$) configurations.

$U = 0.95\,\bar{U}$			$U = \bar{U}$		
Strain ε (%)	Stress σ_s (MPa)	Axial force N (kN)	Strain ε (%)	Stress σ_s (MPa)	Axial force N (kN)
14.6	568.657	44.662	15.4	598.255	46.987

TABLE 4 | Nodal forces acting in the almost fully-flat ($U = 0.95\,\bar{U}$) and fully-flat ($U = \bar{U}$) configurations.

	$U = 0.95\,\bar{U}$			$U = \bar{U}$		
Node	R_x (kN)	R_y (kN)	R_z (kN)	R_x (kN)	R_y (kN)	R_z (kN)
0	0	−297.975	0	0	−313.723	0
2	0	276.167	−25.318	0	290.759	−11.024
4	19.286	10.904	12.659	20.304	11.482	5.512
6	−19.286	10.904	12.659	−20.304	11.482	5.512

TABLE 5 | Strains, stresses and axial forces produced by the application of positive wind pressure forces on the TABS configuration corresponding to $U = 0.95\,\bar{U}$.

Element	Strain ε (%)	Stress σ_s (MPa)	Axial force N (kN)	Buckling load N_b (kN)
1 − 0	0.000	0.105	0.221	−728.031
2 − 0	0.080	57.462	120.669	−182.008
2 − 1	0.025	17.758	37.292	−242.677
3 − 0	0.000	0.105	0.221	−728.031
2 − 3	0.025	17.758	37.292	−242.677
4 − 0	−0.110	−78.954	−165.803	−182.008
4 − 3	0.025	17.757	37.290	−242.677
5 − 0	0.000	0.091	0.192	−728.031
4 − 5	0.023	16.786	35.250	−242.677
6 − 0	−0.110	−78.954	−165.803	−182.008
6 − 5	0.023	16.786	35.250	−242.677
6 − 1	0.025	17.757	37.290	−242.677
2 − 6	14.586	568.868	44.680	0
6 − 4	14.476	564.569	44.341	0
4 − 2	14.586	568.868	44.680	0

TABLE 6 | Strains, stresses and axial forces produced by the application of negative wind pressure forces on the TABS configuration corresponding to $U = 0.95\,\bar{U}$.

Element	Strain ε (%)	Stress σ_s (MPa)	Axial force N (kN)	Buckling load N_b (kN)
1 − 0	0.000	−0.247	−0.519	−728.031
2 − 0	0.177	127.276	267.279	−182.008
2 − 1	−0.025	−18.285	−38.399	−242.677
3 − 0	0.000	−0.247	−0.519	−728.031
2 − 3	−0.025	−18.285	−38.399	−242.677
4 − 0	−0.021	−15.435	−32.414	−182.008
4 − 3	−0.025	−18.284	−38.394	−242.677
5 − 0	0.000	−0.226	−0.475	−728.031
4 − 5	−0.024	−17.143	−36.000	−242.677
6 − 0	−0.021	−15.435	−32.414	−182.008
6 − 5	−0.024	−17.143	−36.000	−242.677
6 − 1	−0.025	−18.284	−38.396	−242.677
2 − 6	14.581	568.665	44.663	0
6 − 4	14.466	564.163	44.309	0
4 − 2	14.581	568.665	44.663	0

prototypes of the ABS presented in Attia (2017) and Karanouh and Kerber (2015), we assumed the wind pressure $\hat{\lambda} = 3.5$ kPa over the projection of the screen onto the x, y-plane. Said $|| \cdot ||$ the Euclidean vector norm, $\times$ the vector product symbol, and introduced two vectors $\mathbf{a}_p$ and $\mathbf{b}_p$ lying along the edges of the generic micro-triangle (or panel) forming the TABS, the surface area A_p of such an element was computed as follows

$$A_p = \frac{1}{2} ||\mathbf{a}_p \times \mathbf{b}_p|| \,, \tag{17}$$

while its unit normal is given by

$$\mathbf{n}_p = \frac{\mathbf{a}_p \times \mathbf{b}_p}{||\mathbf{a}_p \times \mathbf{b}_p||} \,. \tag{18}$$

The wind force acting over the generic panel p, along its normal vector, was computed through (EN 1991-1-4, 2005; Blaise and Denoël, 2013)

$$\boldsymbol{\omega}_p = \hat{\lambda} \, A_p (\mathbf{n}_p \otimes \mathbf{n}_p) \mathbf{e}_z \,, \tag{19}$$

$\mathbf{e}_z$ denoting the unit vector along the z-axis, and $\otimes$ denoting the tensor product symbol. The wind force acting on the generic node of the TABS was finally obtained as follows

$$\mathbf{w}_i = \frac{1}{3} \sum_{p=1}^{n_i} \boldsymbol{\omega}_p \,, \tag{20}$$

n_i denoting the number of panels attached to node i.

As already anticipated, we applied both positive and negative wind pressure forces on the almost flat configuration of the

TABLE 7 | Main parameters of Rolaram® linear actuators.

Config.	Product code	Dynamic load (kN)	Linear speed (mm/min)	Power (kW)	Energy consumption (Wh)	Weight (kN)
P	R2501190	294.0	1190	7.5	35	4.23
RA	R2250340	300.0	340	2.2	36	3.01
P	R2500790	327.0	790	5.5	39	4.09
RA	R2501140	329.0	1140	7.5	37	4.74
RA	R2500670	386.0	670	5.5	46	4.74
P	R2500470	402.0	470	4.0	47	3.97

The drive is a brake motor, mounted either at right angles (configuration RA) or parallel (configuration P) to the actuator ram.

TABS corresponding to $U = 0.95\,\bar{U}$. An application of the path-following algorithm described in Mascolo et al. (2018) lead us to the results reported in **Tables 5**, **6**, which show the axial strains, stresses and forces carried by all the members of the TABS module under such loading conditions, assuming tensile strains, stresses and forces as positive. The results shown in **Tables 5**, **6** highlight that the stresses carried by the strings and bars are lower than the corresponding yield strengths, and that the axial forces carried by the bars, when negative, are lower than the local Eulerian buckling loads. In particular, the axial stresses carried by the bars are significantly lower than the yield stress of 260 MPa. We accept that the bars can be loaded either in compression (negative bar forces) or in tension (positive bar forces), while we requite that the strings must always work in tension. **Tables 3**, **5**, and **6** show that the strings of the TABS module (members 2–6, 6–4, and 4–2) always carry positive forces. This is due to the actuation mechanism of the module, which leads the strings to be fully stressed under a tensile strain of the order of 15% in the (theoretically) fully closed configuration of the screen. It is worth remarking that the marked stretching of the strings in the closed configuration of the system, confers significant geometric stiffness (Fraternali et al., 2015) to such elements, preventing them from going slack, e.g, under the action of suction wind forces.

5. ENERGY COST AND WEIGHT

The present Section is primarily devoted to estimate the energy cost associated with the operation of the linear actuator applied to node 2 (see **Figure 3**) of the system illustrated in **Figure 2**. We begin by sizing such an actuator, using a commercially available, electro-mechanical actuator of the *Rolaram®* series by Power Jacks (2018). The activation force (or dynamic load) prescribed to the actuator is assumed coincident with the nodal force computed at node 2 of the configuration with $U = 0.95\,\bar{U}$, which is equal to $F_a = 290.759$ kN (cf. **Table 4**). **Table 7** shows different *Rolaram®* actuators ensuring dynamic load capacity of the same order of magnitude of F_a. The activation time of such actuators have been computed through the product of the inverse of the actuation speed by the stroke $U = 0.95\,\bar{U} \approx 334$ mm, while the corresponding energy consumptions have been computed by multiplying the activation time by the power requested by the actuator.

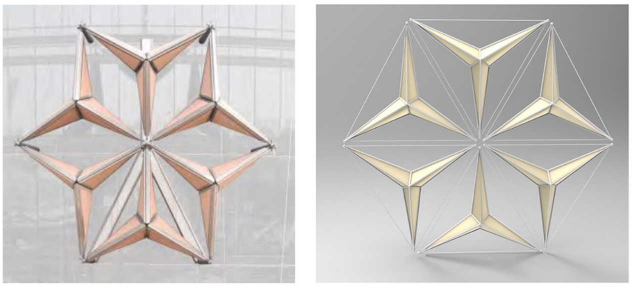

FIGURE 7 | Graphical comparison between ABS **(left)** and TABS **(right)** modules.

The device that is most suited for our scopes in **Table 7** is the actuator *Rolaram®* R2501190, which shows 294 kN dynamic loading capacity and maximum stroke of 3,500 mm (Power Jacks, 2018). The activation time of such an actuator, which is required to take the TABS module from the fully folded to the almost flat configuration ($U = 0.95\,\bar{U}$), can be rather short, and approximately equal to 17 s. The corresponding energy consumption is markedly low, equal to that needed to keep a light bulb of 35 W lit for 1 h. Obviously, such an activation time can be suitably relaxed for operational purposes, as a function of the programmed opening and closure times of the screen. We wish to remark that the "parallel" actuation mechanism of the TABS module analyzed in the present work contemplates a stroke that is equal to 33 % of that needed to actuate the analogous module of the ABS via a central piston (1,000 mm, cf. Karanouh and Kerber, 2015; Attia, 2017).

We close the present section by presenting a comparison between the weight of the examined physical module of the TABS and that of the ABS module designed by Aedas architects (Alotaibi, 2015). **Figure 7** shows a graphical comparison of ABS and TABS umbrella modules, highlighting the different sizes of the structural members that form such systems. It is useful to observe that the ABS solution presents different families of bars: primary bars placed behind the screens supporting the actuation mechanism; Aluminum frames supporting the panels; stabilizers connecting the first two sets of bars; and cantilever struts separating the screens from the façade of the towers (see **Figure 1C**, and Figure 17 of Karanouh and Kerber, 2015). The total weight of the ABS module is reported as approximately equal to 1.5 tons (14.71 kN) in Attia (2017) and Armstrong et al. (2013).

The TABS module is instead formed by 12 bars placed along the perimeters of the six micro-triangles forming the system (**Figures 2**, **3**). The weight of the structural part of the TABS module equipped with Aluminum bars and nylon-fiber ropes (see data in **Tables 1**, **2**) is easily computed, and amounts to 1.43 kN. We safely doubled such a weight, in order to grossly account for the additional weights of joints, rails, springs and secondary elements. The weight of the infill panels amounts to about 0.13 kN, on using PTFE panels, as in the original ABS design (Armstrong et al., 2013; Karanouh and Kerber, 2015; Attia, 2017), which have self weight per unit area of 0.015 kN m^{-2} and cover an area of about 9 m^2 per module (see e.g., Structurflex, 2018 for fabrication information). The total weight of the actuator is 4.41 kN, by summing the weight of the selected device (4.23 kN, see **Table 7**) to the weight of 0.18 kN of the roller screw (Power Jacks, 2018). By summing the above weights, we finally estimate the total weight of the TABS module approximately equal to 7.40 kN. It is worth observing that such weight is 50% lower than the ABS weight per module reported in Armstrong et al. (2013). The greater lightness of the TABS module vs. the corresponding ABS module can be visibly appreciated in **Figure 7**. We don't have numerical data on the energy consumption required by the deployment of the ABS module, which nevertheless is reported to work "on very low energy consumption," too (Karanouh and Kerber, 2015). It is worth noting that the significant reductions of the stroke of the linear actuator and the weight of the TABS module, over the ABS design, are expected to further reduce operation costs and the environmental impact of the system.

6. CONCLUDING REMARKS

Today's technological development of active solar façades is strictly tied to the production of new technologies that permit the realization of lightweight building envelopes featuring sufficiently high stiffness and stability. The lightness is a fundamental prerequisite to guarantee easy deployability of the active modules of a solar façade, in order to reduce overall costs, and to favor easy installation and transportation of the structure.

We have shown in the present study that tensegrity concepts can be profitably employed to design dynamic sun screens that exhibit a morphing-type response, with limited use of materials and very low energy consumption. A tensegrity design of dynamic sun screens that replicate the well-known, origami screens of the Al Bahar towers in Abu Dhabi has been presented, by deriving the exact kinematics of the modules forming such screens, conducting the stress-analysis of the investigated structures under the actuation motion and wind loading, and estimating their weight and activation energy. We have shown that the tensegrity design formulated in the present work leads us to approximately obtain a 50% weight reduction over the ABS design reported in Armstrong et al. (2013). Such a result leads to marked improvements of the system performance in terms of the environmental impact of the construction process, due to a significant reduction of construction materials (cf. Section 5), which is known to greatly influence the building's carbon emissions over its lifetime (Construction, 2018), while keeping the U-value (the insulation characteristics) and the G-value (the shading coefficient) of the façade unchanged with respect to the ABS design (as a consequence of the use of identical geometry and materials of the infill panels).

The structures presented in this work allows us to create "tensegrity skins" of energy efficient buildings, which can serve as lightweight shading envelopes and are, at the same time, able to harvest solar and wind energies. Since the units of such skins are controlled by stretching or relaxing selected cables, suitably designed tensegrity systems can indeed be used not only as shading barriers, but also as actuators orienting solar panels toward the sun, and/or as novel micro-eolic power generators converting the wind-excited strain energy of the cables into electrical power (Skelton and de Oliveira, 2010). We address such generalizations and extensions of the tensegrity systems analyzed in the present study to future work, with the aim of designing solar façades featuring various geometries and deployment schemes, and understanding the versatility of the tensegrity architectures across different scales of the unit cells. Such studies will make use of fractal geometry (Skelton et al., 2014), parametric design concepts (Pottman et al., 2007) and advanced computational models (Infuso and Paggi, 2015). Additional future research lines will be oriented to investigate the application of 3D- and 4D-printing technologies for the fabrication of reduced-scale mockups of active tensegrity façades (Amendola et al., 2015). We plan to tackle the technological challenge related to the application of the internal prestress by recourse to multimaterial 3D printing technologies that use materials with different thermo-hygroscopic properties (see e.g., the polyjet technology described in Stratasys, 2018).

AUTHOR CONTRIBUTIONS

EB led the mechanical modeling and the stress analysis, and supervised the preliminary design of the analyzed structures. RM led the technological part of the study. FF proposed the topic and supervised all the phases of the project.

ACKNOWLEDGMENTS

RM and FF gratefully acknowledge financial support from the Italian Ministry of Education, University and Research (MIUR) under the Departments of Excellence grant L.232/2016.

SUPPLEMENTARY MATERIAL

The Supplementary Material for this article can be found online at: https://www.frontiersin.org/articles/10.3389/fmats.2019.00007/full#supplementary-material

REFERENCES

Al-Kodmany, K. (2016). Sustainable tall buildings: cases from the global south. *Arch. Int. J. Archit. Res.* 10, 52–66. doi: 10.26687/archnet-ijar.v10i2.1054

Alotaibi, F. (2015). The role of kinetic envelopes to improve energy performance in buildings. *J. Archit. Eng. Tech.* 4:149. doi: 10.4172/2168-9717.1000149

Amendola, A., Nava, E. H., Goodall, R., Todd, I., Skelton, R. E., and Fraternali, F. (2015). On the additive manufacturing, post-tensioning and testing of bi-material tensegrity structures. *Compos. Struct.* 131, 66–71. doi: 10.1016/j.compstruct.2015.04.038

Armstrong, A., Buffoni, G., Eames, D., James, R., Lang, L., Lyle, J., et al. (2013). The Al bahar towers: multidisciplinary design for Middle East high-rise, Abu Dhabi, United Arab Emirates. *Arup J.* 2, 60-73. Available online at: https://www.arup.com/perspectives/publications/the-arup-journal

Attia, S. (2017). Evaluation of adaptive facades: the case study of Al Bahr Towers in the UAE. Sci. Connect Shap. Qatar's Sustain. Built Environ. 2 2017:6. doi: 10.5339/connect.2017.qgbc.6

Bai, Y., Jantunen, H., and Juuti, J. (2018). Hybrid, multi-source, and integrated energy harvesters. *Front. Mater.* 5:65. doi: 10.3389/fmats.2018.00065

Balduzzi, F., Bianchini, A., and Ferrari, L. (2012). Microeolic turbines in the built environment: influence of the installation site on the potential energy yield. *Renew. Energ.* 45, 163–174. doi: 10.1016/j.renene.2012.02.022

Blaise, N., and Denoël, V. (2013). Principal static wind loads. *J. Wind Eng. Ind. Aerodyn.* 113, 29–39. doi: 10.1016/j.jweia.2012.12.009

Cimmino, M. C., Miranda, R., Sicignano, E., Ferreira, A. J. M., Skelton, R. E., and Fraternali, F. (2017). Composite solar façades and wind generators with tensegrity architecture. *Compos. B Eng.* 115, 275–281. doi: 10.1016/j.compositesb.2016.09.077

Construction (2018). *Construction, Real Estate, and Carbon Emissions*. Available online at: https://climatesmartbusiness.com/wp-content/uploads/2013/10/CS-Construction-Industry-Brief.pdf

Directive (UE) 2018/844. *European Parliament and of the Council of 30 May 2018 on Energy Efficiency, Amending Directives 2012/27/UE and 2010/31/EU.*

EN 1991-1-4 (2005). *(English): Eurocode 1: Actions on Structures - Part 1-4: General actions - Wind Actions*. (Authority: The European Union Per Regulation 305/2011, Directive 98/34/EC, Directive 2004/18/EC).

Fleck, N. A., Deshpande, V. S., and Ashby, M. F. (2010). Micro-architectured materials: past, present and future. *Proc. R. Soc. A* 466, 2495–516. doi: 10.1098/rspa.2010.0215

Fraternali, F., De Chiara, E., and Skelton, R. E. (2015). On the use of tensegrity structures for kinetic solar façades of smart buildings. *Smart. Mater. Struct.* 24:105032. doi: 10.1088/0964-1726/24/10/105032

Hutchinson, R. G., and Fleck, N. A. (2006). The structural performance of the periodic truss. *J. Mech. Phys. Solids* 54, 756–782. doi: 10.1016/j.jmps.2005.10.008

Infuso, A., and Paggi, M. (2015). Computational modeling of discrete mechanical systems and complex networks: where we are and where we are going. *Front. Mater.* 2:18. doi: 10.3389/fmats.2015.00018

Karanouh, A., and Kerber, E. (2015). Innovations in dynamic architecture. *J. Façade Design Eng.* 3, 185–221. doi: 10.3233/FDE-150040

Kuhn, T. E., Herkel, S., and Henning, H.-M. (2010). "Active solar façades (PV and solar thermal)," in *PALENC 2010*. Available online at: http://publica.fraunhofer.de/documents/N-161087.html

Lombard, L. P., Ortiz, J., and Pout, C. (2010). A review on buildings energy consumption information. *Energ. Build.* 40, 394–398. doi: 10.1016/j.enbuild.2007.03.007

Mascolo, I., Amendola, A., Zuccaro, G., Feo, L., and Fraternali, F. (2018). On the geometrically nonlinear elastic response of class $\theta = 1$ tensegrity prisms. *Front. Mater.* 5:16. doi: 10.3389/fmats.2018.00016

Mazzolani, F. (1994). *Aluminum Alloy Structures*. London: CRC Press.

Modano, M., Mascolo, I., Fraternali, F., and Bieniek, Z. (2018). Numerical and analytical approaches to the self-equilibrium problem of class $\theta = 1$ tensegrity metamaterials. *Front. Mater.* 5:5. doi: 10.3389/fmats.2018.00005

Naveen, J., Jawaid, M., Zainudin, E. S., Sultan, M. T. H., and Yahaya, R. B. (2018). Selection of natural fiber for hybrid kevlar/natural fiber reinforced polymer composites for personal body armor by using analytical hierarchy process. *Front. Mater.* 5:52. doi: 10.3389/fmats.2018.00052

Nylonrope (2018). *Quality Nylon Rope, Nylon Ropes and Cords*. Available online at: https://www.qualitynylonrope.com/all-products/nylon/

Pottman, H., Asperl, A., and Kilian, A. (2007). *Architectural Geometry*. Exton, PA: Bentley Institute Press.

Power Jacks. (2018). Rolaram, Electric Linear Actuators. Available online at: https://www.powerjacks.com/perch/resources/brochure/pjlab-rolaram-en-01-1b.pdf

Quesada, G., Rousse, D., Dutil, Y., Badache, M., and Hallé, S. (2012a). A comprehensive review of solar façades. Opaque solar façades Renew. *Sust. Energ. Rev*. 16, 2820–2832. doi: 10.1093/ijlct/ctv020

Quesada, G., Rousse, D., Dutil, Y., Badache, M., and Hallé, S. (2012b). A comprehensive review of solar façades. Transparent and translucent solar façades Renew. *Sust. Energ. Rev*. 16, 2643–2651. doi: 10.1016/j.rser.2012.01.078

Schittich, C., (ed.). (2003). "Solar architecture. Strategies, visions, concepts," in *Detail Series*. München: Birkhäuser Architecture.

Skelton, R. E., and de Oliveira, M. C. (2010). *Tensegrity Systems*. Berlin: Springer.

Skelton, R. E., Fraternali, F., Carpentieri, G., and Micheletti, A. (2014). Minimum mass design of tensegrity bridges with parametric architecture and multiscale complexity. *Mech. Res. Commun.* 58, 124–132. doi: 10.1016/j.mechrescom.2013.10.017

Soru, M. (2014). *A Spatial Kinetic Structure Applied to an Active Acoustic Ceiling for a Multipurpose Theatre*. MSc. thesis report, Delft University of Technology, Faculty of Civil Engineering and Geosciences, Track Structural Engineering.

Stratasys (2018). *PolyJet Technology*. Available online at: https://www.stratasys.com/it/polyjet-technology

Structurflex (2018). *PTFE Fiberglass*. Available online at: https://www.structurflex.com/materials/ptfe-fiberglass/

Conflict of Interest Statement: The authors declare that the research was conducted in the absence of any commercial or financial relationships that could be construed as a potential conflict of interest.

frontiers in Materials

ORIGINAL RESEARCH
published: 13 February 2019
doi: 10.3389/fmats.2019.00015

Mechanical Properties of Bamboo Through Measurement of Culm Physical Properties for Composite Fabrication of Structural Concrete Reinforcement

***Alireza Javadian*[1]*, Ian F. C. Smith*[2]*, Nazanin Saeidi*[1] *and Dirk E. Hebel*[3]**

[1] Future Cities Laboratory, Singapore ETH-Centre, Singapore, Singapore, [2] Applied Computing and Mechanics Laboratory (IMAC), School of Architecture, Civil and Environmental Engineering (ENAC), Civil Engineering Institute, Swiss Federal Institute of Technology, Lausanne, Switzerland, [3] Department of Architecture, Karlsruhe Institute of Technology, Karlsruhe, Germany

Bamboo fibers with high mechanical properties can be a sustainable alternative to synthetic fibers for application in fiber reinforced polymer composites. The first aim of this study is to evaluate the dependence of mechanical properties of *Dendrocalamus asper,* known as bamboo Petung from Indonesia, on physical properties of the culm, including culm diameter, wall thickness, height, moisture content and specific density. Correlations between mechanical properties including tensile strength, modulus of rupture and modulus of elasticity in flexure and tension and culm physical properties have been studied. The results demonstrate that specific density is directly correlated with all these mechanical properties of bamboo while the moisture content values are correlated only with value of modules of rupture. Although wall thicknesses value of the culm are correlated with all of the mechanical properties studied, the culm diameter was only correlated with modulus of rupture and modulus of elasticity in flexure. Therefore, measurements of the culm geometry and specific density of raw bamboo have the potential for rapid, non-destructive evaluations of the quality of the bamboo, particularly in nurseries and forests where there is limited access to testing facilities. The second aim of this study is to evaluate whether such tests allow for an evaluation of the mechanical potential of the bamboo for production of high performance bamboo fiber reinforced polymer composites. Use of these formulas is illustrated through a case study of bamboo composite reinforcement for structural concrete. Pull-out tests and beam testing using this composite successfully validate the usefulness of this strategy for sustainable construction.

Keywords: bamboo, natural fiber reinforced polymer, mechanical properties, culm geometry, correlation study, statistical analysis

Edited by:
Fernando Fraternali,
University of Salerno, Italy

Reviewed by:
Enrico Radi,
University of Modena, Italy
Anastasiia O. Krushynska,
University of Trento, Italy

****Correspondence:***
Alireza Javadian
javadian@arch.ethz.ch

Specialty section:
This article was submitted to
Mechanics of Materials,
a section of the journal
Frontiers in Materials

Received: *22 October 2018*
Accepted: *25 January 2019*
Published: *13 February 2019*

Citation:
Javadian A, Smith IFC, Saeidi N and Hebel DE (2019) Mechanical Properties of Bamboo Through Measurement of Culm Physical Properties for Composite Fabrication of Structural Concrete Reinforcement.
Front. Mater. 6:15.
doi: 10.3389/fmats.2019.00015

INTRODUCTION

The demand for construction materials is increasing worldwide as populations and their aspirations are growing. Developing countries in Africa and Asia are struggling to meet this demand due to missing infrastructures and industries. To satisfy the demands for housing and infrastructure for the increasing population in new cities, countries, such as Indonesia, Thailand, Vietnam, and

Myanmar have to rely on mostly imported building materials, for example sand, cement, steel and also timber for construction. However, in the long-term, this could be problematic since these construction materials are either finite for local supply (sand or timber) or they are only available through import (copper, iron ore, steel, or other metals). Without alternatives, many nations may no longer be able to satisfy the rising demands for construction materials. Fortunately, proposals are emerging to replace timber and steel with renewable, low-cost and sustainable forms of construction materials that are found locally in developing regions.

Fiber reinforced composite materials have enabled much industrial innovation. Currently composites reinforced by glass fibers and carbon fibers are being used extensively for many structural applications. However, there are economic and environmental challenges. Most of the synthetic fibers are difficult to recycle and are produced from chemicals made from refined petroleum. Furthermore, their fabrication procedures are energy-intensive. Composite materials based on synthetic inorganic fibers are thus expensive and environmentally unsuitable. A promising alternative is to employ natural fibers instead of the synthetic inorganic fibers. Advantages, in comparison with synthetic fibers, are their abundance, renewability, biodegradability and lower cost. Among various natural fibers, bamboo has shown to be a sustainable yet affordable alternative.

Bamboo is one of the locally available natural materials that has gained attention in recent years for fabrication of new category of sustainable bamboo-fiber-reinforced composite materials. Bamboo is a fast growing, inexpensive and available natural resource in most developing countries and it has outstanding material qualities. The cultivation and industrial processing of bamboo offers a huge potential for a new generation of building materials fabricated through embedding natural bamboo fibers into a resin matrix for applications in architecture and construction (Faruk et al., 2014; Hebel et al., 2014; Yu et al., 2014; Javadian et al., 2016; Javadian, 2017; Rahman et al., 2017; Archila et al., 2018).

Bamboo is a natural hierarchical cellular material which has good mechanical properties, including tensile and flexural strength, along its fiber direction. Since bamboo is a functionally graded natural composite the interfaces between its different ingredients including the fibers, parenchyma cells, and lignin matrix can have significant impact on its mechanical properties (Wegst and Ashby, 2004). The hierarchical microstructure of bamboo arises from the vascular bundles in the parenchyma matrix being surrounded by supporting cellulose fibers. These fibers provide the main mechanical properties of bamboo. Furthermore, the cellulose fibers act as reinforcement to strengthen the lignin matrix, similarly to fiber reinforced polymer matrix composites. This structure creates the crystalline and amorphous regions within the microstructure of bamboo where linear chains of glucose with hydrogen bonds form the crystalline regions while irregular hydrogen bonds create amorphous regions (Gibson, 2012; Youssefian and Rahbar, 2015).

Bamboo has higher mechanical properties along its fiber direction than across it. The unique microstructural properties of natural bamboo with respect to its mechanical properties make it a suitable renewable material for composites in high performance applications.

Usually, the density of bamboo is higher on the outer surface and decreases toward the inner layers of the wall cross section (Lakkad and Patel, 1981; Murphy and Alvin, 1992; Ray et al., 2004; Zou et al., 2009; Wahab et al., 2010; Kaur et al., 2016). Therefore, the outer layers of bamboo culms are supposed to have better mechanical properties (Liese, 1985; Lo et al., 2008; Yu et al., 2008). However, to date, no comprehensive and systematic studies of properties of bamboo in terms of density and culm geometry—including wall thickness, culm diameter and culm height—have been found. The identification of sections with higher fiber densities and therefore possible superior quality in terms of physical and mechanical properties has the potential to have a significant impact on the performance of fabricated composite materials.

Previous studies of bamboo *Guadua angustifolia* from Columbia have shown that the top portion of the culm has the highest strength and modulus of elasticity compared with lower portions, since top portion of the culm has higher density (Correal et al., 2010). However, this study did not include top culm sections and thus, correlations of the culm position with mechanical and physical properties have not been studied.

Similar studies were carried out in Bangladesh on mechanical properties, moisture content and density of four indigenous bamboo species in relationship to the respective culm height (Kamruzzaman et al., 2008). In this study *Bambusa balcooa*, *Bambusa tulda*, *Bambusa salarkhanii* and *Melocanna baccifera* were tested to determine the modulus of elasticity and the modulus of rupture. However, no correlation between the culm height and the mechanical properties has been found.

Bamboo *Gigantochloa levis* (buluh beting) of Malaysia was studied for the variation of density, modulus of rupture and modulus of elasticity with height and age of the culm (Nordahlia et al., 2012). The study showed that although the modulus of rupture did not change significantly with the culm height, the modulus of elasticity increased with increases in culm height. However, no information has been provided on values for tensile strength and modulus of elasticity in bending along with their effects on wall thickness or culm height.

Wakchaure and Kute have studied moisture content, specific gravity, water absorption, dimensional changes, tensile and compressive strength of bamboo *Dendrocalamus strictus* from India at several heights (Wakchaure and Kute, 2012). They found no significant difference between bottom and middle portions for tensile, compressive strength and modulus of elasticity. Moisture content decreased from bottom to top sections while specific density increased. Unfortunately, the effect of culm wall thickness and culm diameter on the physical and mechanical properties has not been studied.

Moisture content (MC) is an important property of raw bamboo, especially in building and construction applications and for composite fabrication. MC may adversely affect the bonding strength of bamboo fibers in composite products and bamboo laminates as has been shown in studies carried out by Okubo et al. (2004), Chen et al. (2009), Kushwaha and Kumar (2009).

Therefore, the MC is expected to have a major impact on the performance and service life of new bamboo composite materials.

In addition to MC influence on mechanical properties of raw bamboo, such as tensile strength and flexural strength, it also affects geometrical properties of raw bamboo, such as dimensional stability. Although several studies have included the effect of water absorption on dimensional stability of raw bamboo and bamboo composite specimens, they did not examine the correlation between water absorption of green bamboo and its mechanical properties (Rowel and Norimoto, 1988; Nugroho and Ando, 2000, 2001). Rapid moisture changes can result in severe shrinkage or expansion of bamboo layers, which may, especially in laminates or composites, result in layer-bond failure (Lee et al., 1996; Zaidon et al., 2004; Malanit et al., 2011). Therefore, it is important to determine the MC of various sections of raw bamboo and classify the MC according to the location within the culm length before processing the raw bamboo fibers into composites or laminates.

The specific density (SD) is the oven-dry weight of a given volume of raw bamboo divided by the weight of an equal volume of water. SD values are closely related to MC values. A standard method for measuring SD and MC is needed to ensure that results are comparable with other studies. The SD of raw bamboo is a potential indicator of properties of bamboo-based products, such as laminates and bamboo composite materials and therefore, it is important to measure both SD and MC values and relate them to the mechanical properties of raw bamboo.

As the fiber density changes over the wall thickness, SD values will differ from the outer to inner section of the wall cross section. Therefore, for any application of raw bamboo, it is important to know which part of the wall cross section is processed and what are the corresponding MC and SD of that part. Measuring MC and SD values to correlate them with values for wall thickness and mechanical properties provides an affordable and valuable method for selecting the best bamboo sections for the production of bamboo-based products having pre-defined qualities.

Research into the mechanical properties of hierarchical structures of raw bamboo should lead to better control of fabrication and quality of the novel bamboo-based composites. Since bamboo is a grass, which reaches its full height of 20–30 m within an extremely short period of only a few months, the mechanical properties along culm lengths may vary substantially (Liese, 1998).

Similar variation of properties may be encountered in all three principle directions e.g., longitudinal, radial and tangential (Liese, 1987). Studies have been carried out on various species of bamboo to investigate differences in mechanical properties (Limaye, 1952; Liese and Jackson, 1985; Rao et al., 1988; Hidalgo-Lopez, 2003; Janssen, 2012). However, neither the effects of wall thickness nor culm geometry on the mechanical properties was investigated or correlated to bamboo's natural hierarchical structure.

Some studies investigated the mechanical properties of laminates and composites made from *Dendrocalamus asper* (Malanit et al., 2009, 2011; Febrianto et al., 2012). The results show that composites and boards made from *Dendrocalamus asper* have high mechanical properties compared with commercial products made from wood. However, these studies also did not take into account variations of mechanical properties of various sections of *Dendrocalamus asper* and various culm diameters.

In this paper, a comprehensive and systematic study of Moisture Content (MC), Specific Density (SD), Tensile Strength (TS) along the fiber direction, modulus of Elasticity in tension (E_t), flexural strength or Modulus of Rupture (MOR), and modulus of Elasticity in flexure (E_f) is presented. These properties are then correlated with the respective culm geometry of bamboo to have a better understanding of its hierarchical structure which then can be considered for synthesis of novel bamboo-fiber-reinforced composite materials fabricated from bamboo *Dendrocalamus asper*. Finally, the use of these relationships is examined through a case study involving the development of a bamboo composite for use in reinforced concrete. Mechanical test results are then used to validate this new approach.

MATERIALS AND METHODS

Bamboo Species

Dendrocalamus asper or Petung Putih bamboo was selected from a bamboo forest on the Java island of Indonesia. This bamboo is widely available in Java and mostly being used for construction of small housing in local villages. The *Dendrocalamus asper* from Java had an average culm length of 15 m. The outer diameter of the selected culms were between 80 and 150 mm. The selected culms had wall thicknesses between 6 and 20 mm. The initial MC of the culms ranged between 12 and 15%. The culms were cut into three sections and labeled as top, middle and bottom. Each section was 5 m in length. Samples for this study were obtained only from the middle and bottom sections as the top portion of the culms were not available for this study.

Sample Preparation

Fifteen culms of 15 m length were chosen for this study. The bottom and middle sections were eventually divided into five subsections with a length of 1 m. The 1 m section was then split lengthwise and samples of varying thicknesses were cut randomly for the physical and mechanical tests. The subsections have been classified into seven groups according to culm diameter and wall thickness as shown in **Table 1**.

Sections with bigger diameters typically have larger wall thicknesses as compared with sections of smaller diameter. For class 6 and 7, the samples with larger wall thicknesses of up to 20 mm were used for testing to evaluate the effect of thicker than 15 mm wall section on culm properties.

Moisture Content

The MC was measured for samples taken from the 1 m subsections. From each subsection, 10 samples were prepared. The ASTM D4442-07 standard test method for direct moisture content determination of wood and wood-based materials was followed (ASTM International, 2015). The sample size was (10) mm × (10) mm × (thickness of the section). Once the samples were cut from the culms, they were weighed using a Shimadzu BL320H balance with an accuracy of 0.001 g. The samples were

TABLE 1 | Classification of the samples used in this study according to culm diameter and wall thickness.

Culm diameter (mm)	Wall thickness (mm)
80–90 *Class 1*	6–7
	7–8
	8–9
90–100 *Class 2*	6–7
	7–8
	8–9
	9–10
	10–11
100–110 *Class 3*	6–7
	7–8
	8–9
	9–10
	10–11
110–120 *Class 4*	6–7
	7–8
	9–10
120–130 *Class 5*	8–9
	9–10
	10–11
	11–12
130–140 *Class 6*	10–11
	11–12
	12–13
	14–15
140–150 *Class 7*	11–12
	12–13
	16–17
	19–20

then dried using a convection oven that could maintain 103°C for 24 h. MC was calculated from Equation (1):

$$MC, \% = \frac{A - B}{B} \times 100 \tag{1}$$

where, A is the original weight in gram and B is the dried weight in grams.

Specific Density

Samples for SD measurement were prepared according to ASTM D2395-14 standard test method for density and specific gravity of wood and wood-based materials (ASTM International, 2014a). From each subsection, 10 samples were prepared randomly. For each sample, the width, the length and the thickness were determined for the volume (V) calculation. The initial mass (m) of each sample was measured with the Shimadzu BL320H balance with an accuracy of 0.001 g. The density (ρ) and SD were calculated using the following formulae:

$$\rho = \frac{m}{V} \tag{2}$$

$$SD = K.\rho \tag{3}$$

where $K = 1{,}000\ \text{mm}^3/\text{g}$, ($m$) is in grams and ($V$) is in mm^3.

Tensile Strength Along the Fiber

The tensile strength of the samples was measured with reference to the ASTM D143-09 standard test method for small clear specimens of timber using a Shimadzu AG-IC 100 kN tensile-testing machine (ASTM International, 2014b). Samples were cut from the 1 m sections of bamboo culms and were chosen from various radial locations along the sections and then prepared into dog-bone shapes. The average width and length of the sample grips was 25 and 50 mm, respectively. The average gauge length was 130 mm.

The samples prepared from thick culms were first split into sections with the same thickness along the length. Subsequently each section was papered according to ASTM D143-09 into dog-bone shapes and tested.

Average values from the tensile tests of the two sections were then used for analysis and evaluation. Five samples were taken from the internodes of 1 m subsections. The loading rate was set to 1 mm/min. All tests were carried out at room temperature and 65% relative humidity. The tensile strength (σ_t) was calculated by measuring the ultimate load at failure of the test (F_{ult}) and then dividing it by the cross section of the sample across the gauge length (A). The following formula was used to determine the tensile strength.

$$\sigma_t = \frac{F_{ult}}{A} \tag{4}$$

Modulus of Elasticity in Tension (E_t)

The modulus of elasticity in tension was measured using a Shimadzu AG-IC 100 kN machine according to the ASTM D143-09 standard test method for small clear specimens of timber (ASTM International, 2014b). Dog-bone shape tensile strength samples were used for this test. The gauge length was adjusted for modulus of elasticity test to 80 mm and the grip width and length remain unchanged. An Epsilon axial extensometer with a gauge length of 80 mm was used to measure the sample deformation during the test. The loading rate was set to 1 mm/min. Load-deformation curves were obtained from each test to measure the modulus of elasticity in tension. The modulus of elasticity has been calculated from the slope of the initial linear portion of the stress-strain curve derived from the load-deformation curves.

Modulus of Rupture (MOR)

MOR or flexural strength was measured according to ASTM D3043-00(2011) standard test method for structural panels in flexure (ASTM International, 2011). A two-point flexural test was carried out in this study. The advantage of a two-point flexure test over a center-point flexure test is that a larger area of the sample is subjected to peak stress—unlike the center-point flexure test, where the peak stress is applied to an isolated location. Therefore, the probability that any crack or flaw exists between two loading supports will be higher and the results will be more reliable in a two-point flexure test. Five Samples without nodes were prepared from 1 m subsections of each culm. The loading rate was calculated according to ASTM D3043 with respect to sample thickness and width.

Modulus of Elasticity in Flexure (E_f)

The modulus of elasticity in flexure was measured by obtaining the load-deformation curve in the flexural strength test. An Epsilon extensometer with a travel gauge of 25 mm was used to measure the mid-span deflection of the samples during the flexural strength test. The measurement and calculation of the modulus of elasticity were carried out according to ASTM D3043-00(2011) at room temperature and 65% relative humidity. Multiple comparisons between several wall thicknesses and culm diameters were conducted in this study.

Statistical Analysis

Statistical analysis was performed on the data obtained in this study by using SPSS version 22 (SPSS Inc., Chicago, IL). Pearson's correlation coefficients (r) were calculated to find the relationship between the culm geometry, SD, MC and the mechanical properties of bamboo. Three levels of correlation were defined (i.e., strong, $r > 0.5$; moderately strong, $0.3 < r < 0.5$; and weak, $r < 0.3$). To further examine the relationships between the culm geometry and mechanical properties of hierarchical structure of natural bamboo, stepwise multiple linear regressions were performed. The model performance was assessed with an adjusted r^2 value, which represents the percentage of the variations that are described by independent variables. The r^2 in general is a statistical parameter to demonstrate that the results of the study are close to the model obtained through multiple regression analysis. The values of r^2 are normally between 0 and 1; however, if the values of r^2 are closer to 1, it indicates that the model obtained can represent more of the data points.

RESULTS AND DISCUSSION

Moisture Content (MC)

The moisture content has been measured at two relative humidity conditions: one at 20°C with 65% relative humidity and one at 45°C with 80% relative humidity. The results for the samples from various categories of bamboo *Dendrocalamus asper* are shown in **Table 2**.

TABLE 2 | Moisture content of bamboo Petung at two relative humidity conditions for different classes.

Culm diameter (mm)	Wall thickness (mm)	MC(%) at 20°C with 65% relative humidity	MC(%) at 45°C with 80% relative humidity
80–90 *Class 1*	6–7	9.8	13.2
	7–8	9.0	11.7
	8–9	8.7	11.5
90–100 *Class 2*	6–7	10.7	13.6
	7–8	10.6	13.7
	8–9	10.7	13.4
	9–10	8.4	11.5
	10–11	10.9	14.2
100–110 *Class 3*	6–7	10.0	13.5
	7–8	10.7	14.2
	8–9	10.7	14.1
	9–10	11.2	15.0
	10–11	9.2	12.2
110–120 *Class 4*	6–7	9.8	12.9
	7–8	9.6	13.0
	9–10	10.4	13.7
120–130 *Class 5*	8–9	9.5	12.7
	9–10	9.8	12.7
	10–11	9.7	13.0
	11–12	10.8	14.6
130–140 *Class 6*	10–11	9.4	12.8
	11–12	10.3	14.0
	12–13	10.0	13.6
	14–15	9.9	13.3
140–150 *Class 7*	11–12	9.6	13.1
	12–13	10.1	13.6
	16–17	10.1	13.8
	19–20	10.5	13.8

At a relative humidity of 80%, the MC increases for all classes equally. This condition has been achieved after 6 days for wall thicknesses of more than 13 mm and after only 3 days for wall thickness of <13 mm. The increase in MC for all classes are in the range of 25–35%. The change in MC for class 4–7 is not significant at 80% relative humidity condition. **Figure 1** shows the comparison of average MC values together with the error bars for each class.

Although, the average MC under both relative humidity conditions for class 4–7 does not vary considerably, for class 1–3 the MC increases with increasing culm diameter. Culms with 100 mm or less in diameter and with thinner wall sections have lower percentage of lignin matrix and higher presence of cellulose fibers compared with culms larger than 100 mm in diameter, as shown in other studies (Alvin and Murphy, 1988; Murphy and Alvin, 1992; Mohmod et al., 1993).

Since bamboo has a hierarchical structure, its lignin matrix establishes hydrogen bonds with water, thus large culms are more stable when exposed to relative humidity variations compared with small culms with thinner wall sections. The thinner wall section in culms with smaller diameter has a higher fiber density and therefore, a lower percentage of lignin matrix when compared with large culms (Zou et al., 2009). As a result, the relative humidity variation will have a greater impact on MC of small culms with thin wall sections compared with large culms with thick wall sections. Despite the trend observed in MC variation with culm diameter and culm wall thickness, the differences in MC values of various classes of bamboo Petung for each relative humidity condition are not substantial.

For processing the raw bamboo culms into sections suitable for bamboo-based composite fabrication, it was essential to carefully analyze the hierarchical structure of natural bamboo with respect to the change in MC with various culm diameters and wall thicknesses. The average MC of the raw bamboo culms selected for processing should fall below 10% to reduce the effect of excessive delamination or long-term environmental impacts through the degradation of the final composite product. By measuring the moisture content of chosen bamboo culms for composite production, a preliminary estimation of the required

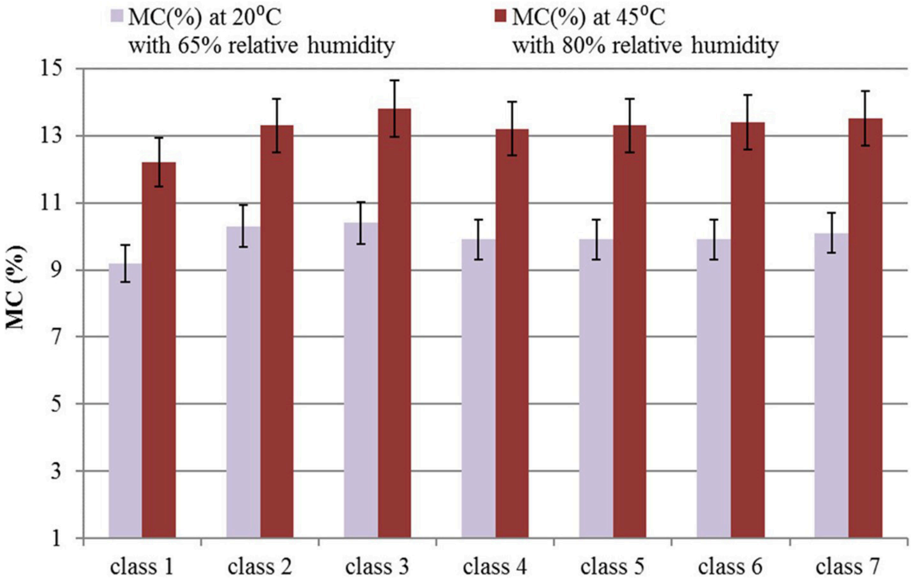

FIGURE 1 | Average MC comparison for all classes of bamboo petung under two relative humidity conditions with error bars at two standard deviations.

time to achieve a certain MC percentage suitable for processing of the raw bamboo and fabrication of composite became possible.

Specific Density (SD)

The results of SD measurement are presented in **Table 3** for various classes of bamboo culms.

One-way ANOVA (Analysis of Variance) test shows that there is no significant difference between SD values of wall thicknesses within class 1–3. SD for class 5–7 decreases with increasing culm diameter. The common wall thickness category between class 5, 6, and 7 is 11–12 mm. The SD for this category of wall thickness and for class 5, 6, and 7 was 0.741, 0.738, and 0.735, respectively. With increasing culm diameter for culms with diameter of 120–150 mm, the SD decreases.

The reduction in SD of larger culms is attributed to fiber density characteristics. Larger culm diameters with thicker walls are usually found at the bottom of the culm where the fiber density is lower. Generally, bamboo culms have higher fiber density at top parts where the fibers are closely packed as has been shown by other studies on microstructure of bamboo culm of different species (Alvin and Murphy, 1988; Ray et al., 2004). As a result, the SD will be lower in the bottom parts where the culm diameter and wall thickness are much greater as compared to the middle and top parts.

Tensile Strength Along the Fiber

The results of the tensile strength tests of the bamboo Petung samples along the fiber direction are provided in **Table 4**. The maximum tensile strength of class 1 samples is 295 MPa for a wall thickness of 7–8 mm. In the same class, wall thickness categories of 6–7 mm and 8–9 mm have similar tensile strength. In class 2, the samples with a wall thickness of 7–8 mm have the highest tensile strength of 298 MPa. Other categories of wall thickness have similar tensile properties and there is no significant difference between the values.

As **Figure 2** displays, there is no significant difference between average tensile strength of class 1–3 samples. However, the average tensile strength for class 4–7 decreases with increasing culm diameter. A relationship between the culm diameter, specific density and tensile strength is revealed when comparing the results from SD and tensile strength measurement. For class 1–3, there is no significant change in SD and tensile strength while increasing the culm diameter. For class 4–7, by increasing the culm diameter, both tensile strength and SD decreases.

For culm diameters above 110 mm the tensile strength is influenced by the fiber density of bamboo. Larger culms are likely to have lower cellulose fibers and higher lignin content. Therefore, the tensile strength of the raw bamboo, which mainly comes from the tensile capacity of the cellulose fibers, is largely reduced. This is in line with the trend observed for the SD of bamboo Petung. As mentioned earlier, SD is principally influenced by the fiber density, therefore declining the fiber density, results in lower SD as shown also in previous study (Ray et al., 2004). The correlation between SD, tensile strength and fiber density is important when selecting the bamboo culms for composite processing. Being able to distinguish culms with diverse tensile strengths by measuring only their SD is a valuable method for choosing the most appropriate culms for bamboo composite materials.

Modulus of Elasticity in Tension (E_t)

The modulus of elasticity in tension of bamboo Petung was measured for different classes of bamboo Petung with varying culm diameters and wall thicknesses according to ASTM D143-14. The results are summarized in **Table 5**.

TABLE 3 | Oven-dry SD for various culm diameters and wall thicknesses of bamboo Petung.

Culm diameter (mm)	Wall thickness (mm)	Specific density
80–90 *Class 1*	6–7	0.878
	7–8	0.842
	8–9	0.896
90–100 *Class 2*	6–7	0.837
	7–8	0.782
	8–9	0.794
	9–10	0.882
	10–11	0.837
100–110 *Class 3*	6–7	0.889
	7–8	0.848
	8–9	0.858
	9–10	0.869
	10–11	0.856
110–120 *Class 4*	6–7	0.940
	7–8	0.860
	9–10	0.920
120–130 *Class 5*	8–9	0.789
	9–10	0.772
	10–11	0.754
	11–12	0.741
130–140 *Class 6*	10–11	0.749
	11–12	0.738
	12–13	0.724
	14–15	0.720
140–150 *Class 7*	11–12	0.735
	12–13	0.720
	16–17	0.717
	19–20	0.711

TABLE 4 | Tensile strength of bamboo Petung for various culm diameters and wall thicknesses.

Culm diameter (mm)	Wall thickness (mm)	Tensile strength (MPa)
80–90 *Class 1*	6–7	281
	7–8	295
	8–9	285
90–100 *Class 2*	6–7	260
	7–8	298
	8–9	292
	9–10	280
	10–11	294
100–110 *Class 3*	6–7	288
	7–8	290
	8–9	285
	9–10	287
	10–11	301
110–120 *Class 4*	6–7	324
	7–8	320
	9–10	326
120–130 *Class 5*	8–9	340
	9–10	318
	10–11	303
	11–12	268
130–140 *Class 6*	10–11	310
	11–12	282
	12–13	263
	14–15	247
140–150 *Class 7*	11–12	244
	12–13	224
	16–17	203
	19–20	193

The modulus of elasticity of bamboo is a measure of the stiffness of the bamboo matrix and its resistance to elastic deformation. The highest modulus of elasticity is observed for class 4 samples with 9 mm to 10 mm wall thickness with 28,230 MPa while the lowest modulus of elasticity is found for class 7 samples with wall thicknesses of 19 mm to 20 mm at 18,140 MPa.

The one-way ANOVA test showed no significant difference between modulus of elasticity of various wall thicknesses within class 1 samples. The modulus of elasticity of the samples in class 4 has shown an increase compared with the samples from class 1, 2 and 3. In class 4, the modulus of elasticity increases with increasing wall thickness.

Within the seven classes of bamboo Petung, class 4 exhibits the highest average modulus of elasticity. In classes 5 to 7, the modulus of elasticity reduces with increasing wall thickness. Similar trends are observed for class 6 and 7 samples. This is in line with the trend observed for tensile strength of the samples from class 5 to class 7 where an increasing wall thickness lowered the tensile strength. Comparing **Table 5** to **Table 4** reveals that for class 5, 6, and 7, both tensile strength and modulus of elasticity decrease with increasing wall thickness.

As mentioned earlier, the high tensile capacity of bamboo is largely influenced by the tensile capacity of the cellulose fibers within the natural hierarchical structure of bamboo. This is also true for the modulus of elasticity of the bamboo. The modulus of elasticity may be estimated through taking the sum of the modulus of the cellulose fibers and the modulus of the lignin matrix weighted by their volumetric fractions. Culms with diameters of <110 mm, have nearly similar volumetric ratios of cellulose fibers and lignin, therefore they have shown similar modulus of elasticity in all categories of wall thicknesses.

By increasing the culm diameter, the wall thickness also increases. With increasing wall thickness in larger culms, the volumetric ratio of cellulose fibers to lignin is also reduced as has been observed in other studies (Alvin and Murphy, 1988; Murphy and Alvin, 1992). As a result, a higher percentage of lignin as compared with the cellulose fibers is expected in thicker wall sections. This leads to lower modulus of elasticity of larger bamboo culms compared to smaller culms in which the volumetric ratio of cellulose fibers to lignin is higher.

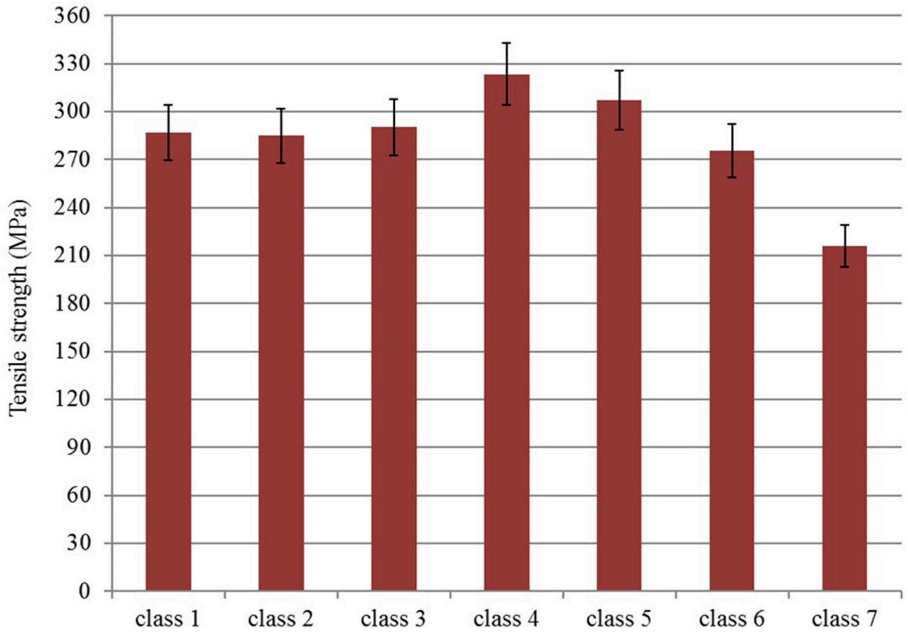

FIGURE 2 | Average tensile strength of bamboo Petung with error bars at two standard deviations.

Modulus of Rupture (MOR)

Table 6 summarizes the results of the MOR tests for varying wall thicknesses and culm diameters of bamboo Petung. Class 1 samples have the highest MOR with 209 MPa while class 7 samples have the lowest MOR with 121 MPa. For class 1 samples, increasing the wall thickness from 6 to 9 mm results in the reduction of the MOR from 209 to 198 MPa. For class 2 and 3 samples, no significant relationship is found between the wall thickness and the MOR. In class 4 samples, increasing the wall thickness from 6 to 10 mm, reduces the MOR from 166 to 155 MPa, which corresponds to a reduction of 6.7%. For class 5, the MOR for wall thickness of 10–11 mm is the lowest with 149 MPa. The MOR in class 5 is in the same range as for wall thickness of 9–12 mm with a standard deviation of 5%. For class 6 samples, similar trend is observed as compared with the classes 1, 4, and 5 of bamboo Petung.

The standard deviation of these samples in class 6 was <4%. The MOR for class 7 samples is reduced with an increase in wall thickness. Wall thicknesses between 19 and 20 mm had the lowest MOR of 121 MPa. **Figure 3** shows the average MOR for seven classes of bamboo Petung.

Culms with larger diameters have thicker walls particularly at bottom sections. The thicker wall thickness leads to a higher percentage of lignin and lower proportion of cellulose fibers. As observed earlier regarding the tensile capacity and its relationship with the fiber density, similar conclusions can be made concerning MOR. The cellulose fibers are densely packed at the top sections of the hierarchical structure of bamboo culms where a smaller diameter prevails. The MOR increases with decreasing culm diameter. Except for class 2 samples, the MOR decreases with increasing wall thickness within a class. This underlines the importance of the fiber density on the mechanical properties of raw bamboo. Cellulose fibers contribute to high mechanical properties of natural bamboo. The cellulose fiber density is higher at the outer layer of the wall sections and at the top portions of the culms. Therefore, the MOR increases with increasing fiber content and decreasing lignin content at the surroundings of the fibers.

Modulus of Elasticity in Flexure (E_f)

The modulus of elasticity in flexure is taken from the load deflection curve that has been obtained with the help of an extensometer. The effect of wall thickness and culm diameter on the modulus of elasticity in flexure is studied for all seven classes of bamboo Petung.

Table 7 presents the result of this test for the range of wall thicknesses and culm diameters that were tested according to ASTM D3043-00(2011).

The highest modulus of elasticity of 14,279 MPa was observed for class 2 samples with a wall thickness in the range of 9–10 mm. The lowest modulus of elasticity of 9,375 MPa was observed in samples of class 7 with wall thicknesses between 19 and 20 mm. This finding is comparable to the results of MOR tests where class 7 samples show the lowest MOR of all samples. When the results of various wall thicknesses were compared, random variations in modulus of elasticity with increasing the wall thickness were observed. However, as displayed in **Table 7**, bamboo Petung shows a decrease in the average modulus of elasticity in flexure with increasing culm diameter from 80 to 150 mm. Samples with culm diameters of <120 mm show less significant changes in the modulus of elasticity with varying the culm diameters. Nevertheless, for samples with culm diameters

TABLE 5 | Modulus of elasticity in tension of bamboo petung for different culm diamters and wall thicknesses.

Culm diameter (mm)	Wall thickness (mm)	Modulus of elasticity (MPa)
80–90 *Class 1*	6–7	21,570
	7–8	22,780
	8–9	21,240
90–100 *Class 2*	6–7	19,360
	7–8	20,180
	8–9	20,340
	9–10	21,670
	10–11	20,560
100–110 *Class 3*	6–7	23,970
	7–8	23,380
	8–9	22,370
	9–10	22,280
	10–11	21,750
110–120 *Class 4*	6–7	24,460
	7–8	25,660
	9–10	28,230
120–130 *Class 5*	8–9	23,890
	9–10	22,820
	10–11	21,510
	11–12	20,300
130–140 *Class 6*	10–11	22,150
	11–12	21,540
	12–13	21,920
	14–15	19,470
140–150 *Class 7*	11–12	20,710
	12–13	20,330
	16–17	19,450
	19–20	18,140

TABLE 6 | MOR of bamboo petung for seven classes.

Culm diameter (mm)	Wall thickness (mm)	MOR (MPa)
80–90 *Class 1*	6–7	209
	7–8	207
	8–9	198
90–100 *Class 2*	6–7	172
	7–8	180
	8–9	162
	9–10	190
	10–11	161
100–110 *Class 3*	6–7	172
	7–8	168
	8–9	158
	9–10	160
	10–11	168
110–120 *Class 4*	6–7	166
	7–8	159
	9–10	155
120–130 *Class 5*	8–9	159
	9–10	153
	10–11	149
	11–12	150
130–140 *Class 6*	10–11	165
	11–12	162
	12–13	160
	14–15	151
140–150 *Class 7*	11–12	138
	12–13	127
	16–17	125
	19–20	121

of 120 mm and larger, the modulus of elasticity drops with increasing the culm diameter.

The effect of the culm diameter on the modulus of elasticity in flexure is similar to MOR. With increasing culm diameter, the average modulus of elasticity decreases. This observation can be attributed to the culm hierarchical microstructure. With increasing culm diameter, mainly at the bottom and middle sections of bamboo, the fiber density decreases due to the higher lignin content as compared with the fiber content.

As described earlier, the top sections of a culm exhibit higher fiber densities as compared with the bottom sections. Such high fiber density is responsible for the strong mechanical features of the bamboo culm—especially the modulus of elasticity, MOR and the tensile strength.

Within one class of bamboo, the change in modulus of elasticity with varying wall thicknesses is not linear for all the samples. This is due to the spatially varying microstructure of the bamboo culm walls. Samples tested in this study have been randomly collected at different cross sections and varying height locations. Therefore, the variation in modulus of elasticity with wall thickness was expected from culm to culm.

Comparing the mechanical properties of bamboo Petung with available local timber species that are commonly used in structural applications in Indonesia, demonstrates the superior properties that bamboo Petung offers as compared with timber. **Table 8** presents the range of specific density, tensile strength along the fiber, modulus of elasticity in tension and MOR of timber species used commonly in structural applications as well as composite products (Green et al., 1999). Timber species commonly used in Indonesia are Balau, Sumatran Pine and Indonesian Rosewood.

The mean tensile strength of bamboo Petung is higher than Balau, Sumatran Pine, and Indonesian Rosewood. In terms of modulus of elasticity, bamboo Petung is stiffer than all timber species specified in **Table 8** except for the top range of Balau, which is close to the modulus of elasticity of the bamboo Petung. The Indonesian Rosewood has a low modulus of elasticity compared with bamboo Petung and other common timber species in Indonesia. Balau has the highest range of MOR among the common timber species. However, bamboo Petung has higher values of MOR compared with all timber species. Sections of bamboo Petung with the lowest mechanical

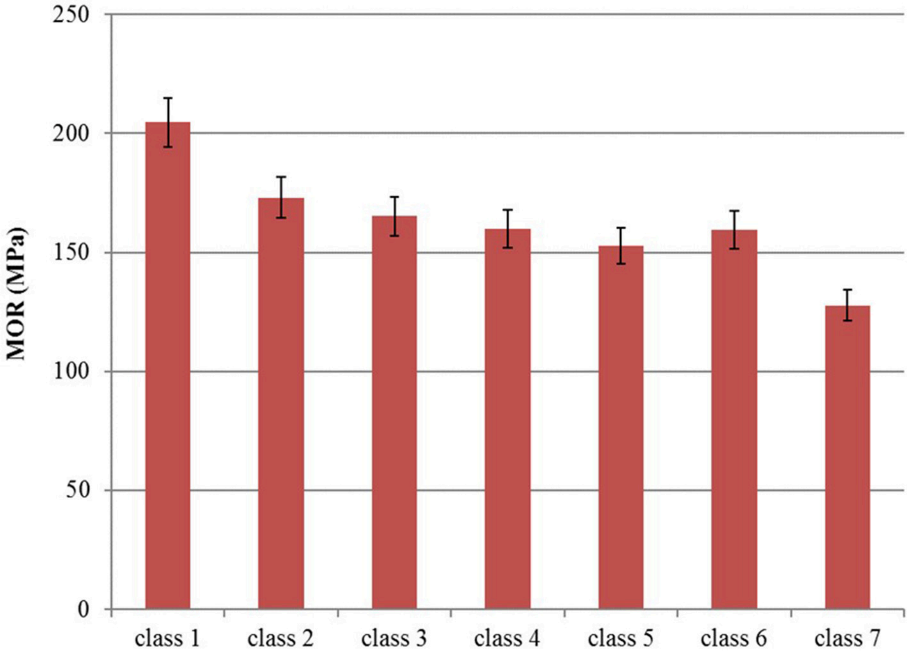

FIGURE 3 | Average MOR of bamboo Petung.

properties are still superior to some of the most common structural grade timber species found in Indonesia as shown in **Table 8**.

Correlation Studies and Statistical Modeling of Physical and Mechanical Properties

To measure the strength of any possible relationship between mechanical properties, culm diameter, wall thickness, specific density and moisture content, Pearson's correlation coefficients (r) are calculated. **Table 9** summarizes the correlation coefficients for only statistically significant correlations with a p-value of <0.05 by a two-tailed t-test between mechanical and physical properties measured in this study. As it is shown in **Table 9**, wall thickness of the culms and specific density (SD) have moderate to strong negative and positive correlations with all the mechanical properties, respectively. Culm diameter shows strong negative correlation with all the mechanical properties except modulus of elasticity in tension (E_t). This finding is in accordance with the results of the modulus of elasticity tests presented in **Table 5**. Moisture Content (MC) has only moderately negative correlation with Modulus of Rupture (MOR) in this study. Therefore, it is not viable to estimate mechanical properties including tensile strength and modulus of elasticity by only measuring the MC of the bamboo culm sections. The highest Pearson correlation coefficient is observed between tensile strength and wall thickness ($r = -0.742$) of the bamboo *Dendrocalamus asper*. Therefore, larger culm diameters would show lower tensile strength.

Among all the mechanical properties measured in this study, only Modulus of Rupture (MOR) showed strong correlation with the physical properties under study [culm geometry, Moisture Content (MC) and Specific Density (SD)]. The Pearson correlation coefficients show that by increasing either of the culm diameter, wall thickness and MC, MOR reduces and increasing the Specific Density (SD) will have a positive impact on MOR. As it is expected, Specific Density (SD) has positive correlation with all the mechanical properties. This is in agreement with previous studies carried out on other bamboo species regarding the effect of density on mechanical properties (Lakkad and Patel, 1981; Lo et al., 2004). SD represents the fiber density of the culm cross sections. Therefore, the higher the fiber density of bamboo cross sections, the larger is the SD and as a result, those sections show better mechanical properties. Furthermore, mathematical models and equations were suggested for estimating the mechanical properties of bamboo Petung by only measuring the culm diameter and wall thickness. **Table 10** displays linear-model parameter values created with the data obtained in this study. In **Table 14**, all mechanical properties have units of MPa while D and t are in mm and MC is in percentage. The empirical relations between MOR, Ef, Et, CS, TS, and culm physical properties are developed and summarized here. These equations should be considered to provide only preliminary estimation of the mechanical properties for bamboo Dendrocalamus asper. For other species of bamboo and bamboo from other regions around the world, the model coefficients and constants could differ.

$$MOR = -0.78D + 250 \tag{5}$$

$$E_f = -33D + 14300 \tag{6}$$

$$E_t = -362t + 25300 \tag{7a}$$

TABLE 7 | Modulus of elasticity in flexure for bamboo Petung.

Culm diameter (mm)	Wall thickness (mm)	Modulus of elasticity (MPa)
80–90 *Class 1*	6–7	11,517
	7–8	12,892
	8–9	13,091
90–100 *Class 2*	6–7	12,247
	7–8	12,463
	8–9	12,756
	9–10	14,279
	10–11	12,509
100–110 *Class 3*	6–7	11,951
	7–8	12,588
	8–9	13,267
	9–10	12,776
	10–11	11,878
110–120 *Class 4*	6–7	12,217
	7–8	12,903
	9–10	12,787
120–130 *Class 5*	8–9	11,695
	9–10	11,574
	10–11	12,752
	11–12	12,922
130–140 *Class 6*	10–11	12,517
	11–12	11,520
	12–13	11,842
	14–15	10,993
140–150 *Class 7*	11–12	10,427
	12–13	10,255
	16–17	10,103
	19–20	9,375

$$E_t = 18550SD + 6874 \quad (7b)$$
$$E_t = 33600SD + 70.4D + 13075 \quad (7c)$$
$$E_t = 27200SD + 95.1D - 364.6t - 7180 \quad (7d)$$
$$TS = -8.5t + 363 \quad (8)$$

Furthermore, SD of the bamboo culms can also be estimated through measuring only the culm diameter and wall thickness by using Equation 9.

$$SD = -0.002D - 0.009t + 1.075 \quad (9)$$

APPLICATION OF BAMBOO FOR COMPOSITE FABRICATION FOR REINFORCED CONCRETE

Concrete is currently being used widely around the world for major projects in building and construction industry. However, concrete has a major drawback; it has low tensile strength. Therefore, when it is used in applications where it has to sustain tensile forces, large cracks and premature failure are unavoidable.

To overcome this limitation, reinforcement bars with high tensile strength are used in structural concrete. Currently steel reinforcement is being used in a wide range of structural concrete buildings and infrastructure. However, a challenge associated with using steel reinforcement in concrete is the corrosion and the corrosion-related degradation of the reinforced concrete member. Corrosion of the steel reinforcement in concrete is initiated by either concrete carbonation or exposure of the concrete element to chloride ions as discussed in various works (Slater, 1983; Macias and Andrade, 1987). Therefore, in the presence of oxygen and moisture, the corrosion of rebar results in dissolution of iron in the form of ferrous hydroxide [$\mathrm{Fe(OH_2)}$] which subsequently forms a layer of rust surrounding the reinforcement bar. As a result of rust occupying a volume larger than the reinforcement bar, large tensile forces are generated in the concrete in the form of tensile stress. The tensile forces initiate the cracking of the concrete layers around the steel bars in the form of concrete delamination, or the debonding of the reinforcement bars from the concrete (Bertolini et al., 2013).

Alternative reinforcement materials including Fiber Reinforced Polymers (FRP) that do not corrode since the polymer matrix protects the fibers. They have comparable mechanical properties to steel reinforcement. There has been much interest in the application of natural fibers in the production of FRP composites to replace synthetic fibers, such as glass and carbon fibers. Natural fibers are widely available in nature and therefore require relatively low energy for production. When natural fibers are used in FRP composite production, they can result in high-performance composites which could potentially replace all, if not many, of the synthetic composite materials at lower prices for applications in the building and construction sector, where weight savings have significant impact on lowering energy consumption and overall cost of the building or infrastructure.

The application of natural fiber reinforced polymer composites in the building and construction industry has been successful in recent years, but mainly as non-structural elements applied as an insulation element for structural members, for floor and wall covers, in door and window frames, for fitting elements, such as door and window handles and for fencing. Among the various high-strength natural materials, bamboo is considered one of the oldest natural construction materials used in buildings particularly in South America, Africa and, in particular, in Southeast Asia.

The variation in the properties of bamboo FRP composites fabricated by various groups around the world is mainly associated with the species of bamboo, the length of bamboo fiber used in fabrication, fiber orientation, the type of epoxy/resin used and the type of treatment carried out on raw bamboo fibers (Ichhaporia, 2008). So far, no investigation has been carried out on utilizing bamboo for the fabrication of FRP composites for structural and load-bearing elements in the construction and building sector. Much of the work on bamboo FRP composites is dedicated to non-load-bearing elements, e.g., fencing or flooring in buildings where the structural properties and mechanical capacities are far lower than for any structural member, such as beams and columns (Jindal, 1986; Nugroho

TABLE 8 | Comparison of properties between common timber species in Indonesia and bamboo Petung (Green et al., 1999).

	Bamboo/timber	Mean specific density	Mean tensile strength along the fiber (MPa)	Mean modulus of elasticity (MPa)	Mean modulus of rupture (MPa)
Timber species	Bamboo Petung	0.72–0.91	216–323	19,600–26,110	130–205
	Balau	0.85–1.15	75–180	18,000–22,000	115–125
	Sumatran Pine	0.57–0.71	57–94	12,800–16,000	85–100
	Indonesian Rosewood	0.63–0.77	65–85	8,000–13,000	63–116

TABLE 9 | Pearson correlation between mechanical and physical properties.

Parameters	Correlations (*r*)			
	Culm diameter (mm)	Wall thickness (mm)	MC	SD
Modulus of elasticity in flexure (MPa)	−0.689	−0.668		0.614
MOR (MPa)	−0.721	−0.615	−0.427	0.43
Modulus of elasticity in tension (MPa)		−0.530		0.62
Tensile strength (MPa)	−0.451	−0.742		0.573

Only the correlation coefficients that are statistically significant with a P-value of <0.05 by two-tailed t-test are shown.

and Ando, 2000; Okubo et al., 2004). This research aims to fill this gap by providing a novel approach to enhance the properties of bamboo FRP composites through new processing and fabricating techniques for bamboo FRP composites and subsequently, through using the new material as reinforcing for structural-concrete elements.

Bamboo Composite Fabrication Using Material Correlation Relationships

In this study bamboo *Dendrocalamus asper* or Petung bamboo was used for fabrication of the high performance bamboo-fiber-reinforced polymer composite. In a detailed study carried out recently by the research team, patented processing tools were developed to process bamboo culms into bamboo fiber bundles of varying thicknesses, width and length (Hebel et al., 2014; Hebel and Heisel, 2016; Javadian et al., 2016; Javadian, 2017).

The processed bamboo fibers were first dried, in an air-circulated oven at 80°C until the moisture content was <10%. The moisture content was measured according to the ASTM D4442-07 standard test method. Subsequently processed bamboo fibers were sorted according to their thickness. The raw bamboo fiber bundles used in the study represented an average fiber collection from upper, middle and lower sections of the bamboo culm in nearly equal ratios.

Before processing the bamboo culms into fiber bundles, tensile and flexural properties of the raw materials were assessed only based on the correlation relationships established in section Correlation Studies and Statistical Modeling of Physical and Mechanical Properties assuming no testing devices available. The average culm diameter and wall thickness of bamboo used in this study were 90 and 8 mm, respectively. By using the material property relationships, the respective mechanical properties of bamboo culms can be found as below;

$$\begin{aligned} MOR &= -0.78D + 250 = -0.78\,(90) + 250 = 179.8\ MPa \\ E_f &= -33D + 14300 = -33\,(90) + 14300 = 11330\ MPa \\ E_t &= -362t + 25300 = -362\,(8) + 25300 = 22404\ MPa \\ TS &= -8.5t + 363 = -8.5\,(8) + 363 = 295\ MPa \end{aligned}$$

These values were used as the basis for the fabrication of bamboo-fiber-reinforced polymer composite in this study. Further evaluation of these numbers were carried out by measuring the mechanical properties of the final bamboo composite samples and comparing the results with the raw bamboo properties found based on the material relationships.

A two-component epoxy system with a resin and a hardener was employed as matrix. Once the resin and hardener of the epoxy system were mixed, each bamboo fiber bundle was impregnated with the epoxy matrix and aligned along the fiber direction. The impregnated fiber bundles were stacked on one another to form a layered structure. Subsequently, the impregnated bamboo fiber bundles were subjected to different pressures (between 15 and 25 MPa) and temperatures (between 80 and 140°C) at various press/hold times to achieve densely compressed composites. The boards were finally post-cured for another 48 h at a temperature of 55°C and then prepared into the suitable shapes to measure their mechanical properties. The post-curing curing time was to ensure that the optimal cross-link networks were fully developed at the recommended temperature by providing the essential energy to give the epoxy molecules the flexibility needed to move, and to fully form the networks within the microstructural cross sections of the epoxy matrix. The average specific density of the bamboo composite reinforcements was 1.33. This procedure provides sufficient environmental protection for the fibers, thus ensuring that their properties do not degrade over time (Javadian, 2017).

Figure 4 shows a bamboo composite reinforcing bar after it was removed from the hot-press machine.

Tensile properties of the bamboo composite sample, including tensile strength and modulus of elasticity in tension, were measured according to ASTM D3039-08, "Standard Test Method for Tensile Properties of Polymer Matrix Composite Materials" while flexural properties, including Modulus of Rupture (MOR) and modulus of elasticity in flexure, were measured according to ASTM D7264, "Standard Test Method for Flexural Properties

TABLE 10 | Multiple linear regression models for mechanical properties of bamboo *Dendrocalamus asper* (bamboo Petung).

Model	r^2	Model significance	Parameter	Coefficient	Significance	Constant
MOR						
1	0.50	<0.001	D	−0.78	<0.001	250.40
2	0.63	<0.001	D	−0.75	<0.001	363.56
			MC	−11.70	0.004	
Ef						
1	0.46	<0.001	D	−33.15	<0.001	14,375.91
Et						
1	0.36	<0.001	SD	18,550.28	<0.001	6,874.06
2	0.25	0.004	t	−362.70	0.004	25,303.91
3	0.54	<0.001	SD	33593.88	<0.001	−13,074.99
			D	70.44	0.002	
4	0.65	<0.001	SD	27,236.26	<0.001	−7,178.92
			D	95.10	<0.001	
			t	−364.57	0.008	
TS						
1	0.53	<0.001	t	−8.46	<0.001	362.56

FIGURE 4 | Bamboo composite sample.

TABLE 11 | Mechanical properties of bamboo composite samples.

Sample	MOR (MPa)	Modulus of elasticity in flexure (E_f) (MPa)	Tensile strength (TS) (MPa)	Modulus of elasticity in tension (E_t) (MPa)
1	290	24,880	333	32,176
2	282	22,777	308	32,597
3	277	20,271	309	31,308
4	297	21,746	319	32,925
5	301	25,757	310	31,224
Average	289	23,086	316	32,046

of Polymer Matrix Composite Materials through a four-point bending test." All the tests were carried out by using a Shimadzu AG-IC 100 kN machine. At least five specimens have been tested for each mechanical property and results exceeding a 10% standard deviation range, which was statistically set as confidence interval, were discarded. **Table 11** displays the mechanical properties of bamboo composite samples fabricated in this study.

As shown in **Table 11** the average mechanical properties of bamboo composite samples are higher than the average mechanical properties of raw bamboo fiber bundles. The results show that the novel techniques for processing the bamboo into fiber bundles together with new production methods used in this study improved the mechanical properties of the final bamboo composite. This has also been observed by Hebel et al. (2014), Javadian (2017), and Rahman et al. (2017). When the modulus of elasticity in flexure of the bamboo composite board is compared to the raw bamboo properties, an improvement of up to two times the raw bamboo modulus of elasticity in flexure is observed. Similarly, MOR, tensile strength and modulus of elasticity in tension of the bamboo composite boards are enhanced compared with the raw material by 30, 2, and 39%, respectively.

The correlation relationships helped to save the time needed for preliminary testing of the raw material before composite fabrication. Furthermore, through this study it is demonstrated that by employing novel techniques based on only mechanical processes, naturally available raw materials (such as bamboo) can be turned into high performance composite materials with applications in building industry for reinforcing structural concrete.

Reinforced Concrete Design Using Bamboo Composite Reinforcement

There are two types of reinforcement used in reinforcing the concrete beams: longitudinal and transverse (shear) reinforcement. The longitudinal reinforcements are placed parallel to the long axis of the beam to provide the required tensile capacity, while shear reinforcement is used to provide sufficient shear strength perpendicular to the long axis of the concrete beam.

All the bamboo composite reinforcement produced in this study have square cross sections of 10 × 10 mm. The square cross section is the result of the production process of the bamboo composite materials as explained earlier. The most common reinforcement currently being used for structural concrete have round cross sections with and without ribs on the surface, including steel and Glass Fiber Reinforced Polymer reinforcement (GFRP) systems. However, in this study, for simplicity only square cross sections are studied (Javadian, 2017). According to American Concrete Institute (ACI) 318 "Building Code Requirements for Structural Concrete and Commentary" (American Concrete Institute, 2008), to provide sufficient confinement to the longitudinal reinforcement of the beam, the shear reinforcement has a closed-loop shape in which it stays intact before failure is initiated from the longitudinal tension reinforcement. Furthermore, by having closed loop shape the failure of the concrete beam does not begin by the failure of the shear reinforcement. Instead, failure of the longitudinal reinforcement is observed. **Figure 5** displays the bamboo composite reinforcement system developed in this study for reinforcing concrete beam samples.

The bent portion of the shear reinforcement has lower mechanical properties compared with the straight parts of the shear reinforcements. Earlier study on the different types of Fiber Reinforced Polymer (FRP) shear reinforcements, including Glass Fiber Reinforced Polymer (GFRP) reinforcements, had shown a tensile strength reduction of up to 45% of the strength parallel to the fibers' direction for the bent sections, due to the localized stress concentration as a result of the curvature which introduced radial stresses within the bent portions (Javadian, 2017).

In an earlier study carried out by the research team, bonding mechanism of bamboo composite reinforcement system to the surrounding concrete matrix was investigated in detail (Javadian et al., 2016). A sufficient bond mechanism between concrete and bamboo composite reinforcements has contributed to a higher ultimate load-bearing capacity of the reinforced concrete member. It was shown that by providing an interfacial microstructure (coating system) which ensured smooth tensile stress transfer between concrete and reinforcement system the maximum mechanical capacities of the bamboo composite reinforcement could be activated thus resulting in a higher ultimate load-bearing capacity compare to non-coated reinforcement.

A series of pull-out tests were designed to find a suitable technique which enhanced the bonding between the two materials. To enhance the bond mechanism between the bamboo composite reinforcement and concrete matrix, four types of coatings and two bonding lengths of 200 mm (20 × thickness) and 100 mm (10 × thickness) were considered in the earlier study. A waterproof vapor barrier membrane system, a bio-based epoxy resin system, a two-part epoxy resin general coating and a two-part epoxy resin based surfacing system with and without sand particles were among the coatings used to investigate the bond mechanism. The average bond strength of bamboo composite reinforcement coated with waterproof vapor barrier membrane system and sand particles with an embedment length of 200 mm was similar to the bond strength of the plain Glass Fiber Reinforced Polymer (GFRP) reinforcement in normal

FIGURE 5 | Bamboo composite reinforcement system used for reinforcing concrete beam.

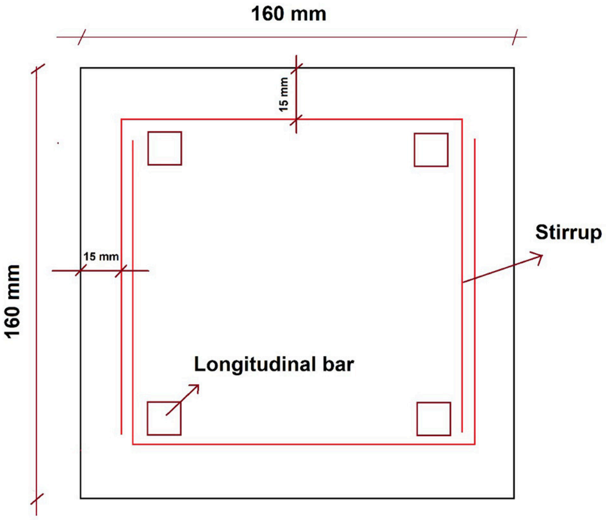

FIGURE 6 | Cross section of bamboo composite reinforced concrete beam.

TABLE 12 | Details of the bamboo composite reinforced concrete beams.

Beam label	Number of bottom reinforcement bars	Number and spacing of the shear reinforcement at each side of beam (mm)	Distance between load introduction points (mm)
A	2	6@70	350
B	2	4@115	350
C	4	8@50	350

strength concrete. Therefore, to evaluate the bamboo composite reinforcement within concrete beam samples, firstly they were coated with a coating and secondly an embedment length of 20 times the thickness of bamboo composite refinement was included as part of the beam design (Javadian et al., 2016).

The coating applied to the surface of the bamboo-composite reinforcement provides long-term resistance to alkaline environments and water ingress from the concrete matrix. Therefore, in concrete having an alkaline environment, the addition of coating on the surface of reinforcement bars provides supplementary protection for the reinforcement (in addition to the epoxy matrix) against long-term degradation and ensures the required bonding with the concrete matrix.

The American Concrete Institute's (ACI) guide for the design and construction of structural concrete reinforced with Fiber Reinforced Polymer (FRP) bars (ACI 440.1R-15) was used as the primary guideline during the design and evaluation of the bamboo composite reinforced concrete beams in this study (American Concrete Institute, 2015). ACI 440.1R-15 has provided the necessary design guides for the application of FRP materials as reinforcement in concrete to justify the lower ductility of the FRP (e.g., GFRP) reinforced concrete elements as compared with steel reinforced concrete members. The size of the bamboo composite reinforcement and the concrete beam in this study were designed in a way such that the loading capacity of the testing machine was not exceeded. All the longitudinal reinforcement in this study had similar cross-sectional dimensions of 10 × 10 mm, while the thickness of the shear reinforcement was 6 mm. **Figure 6** displays the schematic view of the concrete-beam cross-section reinforced with bamboo composite reinforcement.

In this study, all bamboo composite reinforced concrete beams had cross sections of 160 × 160 mm and total length of 1,300 mm while their loading span (L) was kept at 1,050 mm according to four-point (or so-called third-point loading) flexural test set-up. The four-point loading set-up allowed for a zero shear zone along the middle section of the bamboo composite reinforced concrete beam. The zero shear zone permits the elimination of the shear reinforcement in this study, thus the longitudinal reinforcement is loaded completely in tension and flexure and the calculation of the ultimate load-bearing capacity of the concrete beams became simplified. The longitudinal reinforcement had cross sections of 10 × 10 mm. A total of 15 concrete beams with a compressive strength of 20 MPa were prepared and tested in this study. The arrangement of the reinforcement and the loading distance are summarized in **Table 12**.

A total of three design scenarios were considered in this study by either changing the number of bottom reinforcement

FIGURE 7 | Bamboo composite reinforced concrete beam after failure.

TABLE 13 | Summary of results obtained in four-point flexural test of concrete beam samples.

Beam label	Specimen	Reinforcement ratio (%)	Initial cracking load (P/2) (kN)	Ultimate failure load (P/2) (kN)	Initial cracking MOR (MPa)	Ultimate MOR (MPa)
A	1	0.93	9.8	28.8	2.5	7.4
	2		11.1	29.8	2.8	7.6
	3		11.6	33.8	3.0	8.7
	4		10.8	33.6	2.8	8.6
	5		12.1	32.5	3.1	8.3
B	1	0.93	9	30.1	2.3	7.7
	2		10	21.2	2.6	5.4
	3		10.2	29.9	2.6	7.7
	4		9.8	18.8	2.5	4.8
	5		9.9	20.9	2.5	5.4
C	1	1.86	14.8	42.5	3.8	10.9
	2		15.6	41.2	4.0	10.6
	3		14.9	40.9	3.8	10.5
	4		14.3	43.5	3.7	11.2
	5		15.7	42.9	4.0	11.0

TABLE 14 | Comparison between ACI 440.1R-15 design values and experimental results obtained in this study.

	ACI 440.1R	Experiment	ACI 440.1R		Experiment
Beam design	**Design cracking load (P/2) (kN)**	**Initial cracking load (P/2) (kN)**	**Nominal ultimate failure load (P/2) (kN)**	**Design ultimate failure load (P/2) (kN)**	**Ultimate failure load (P/2) (kN)**
A	5.4	11.08	17.1	9.4	31.7
B	5.4	9.78	17.1	9.4	24.18
C	5.4	15.06	30.3	9.7	42.2

or number and spacing of the shear reinforcement as displayed in **Table 12**. For each design scenario, five samples were prepared and tested. Two reinforcement bars were used as top compression reinforcement for all the beams tested in this study. The concrete beams were tested until failure and for each test, ultimate failure load, ultimate flexural capacity (MOR), load corresponding to first crack, and flexural capacity at the time of first crack were obtained. **Table 13** contains the results of the flexural tests.

Figure 7 displays one of the beams tested in this study after ultimate failure. To evaluate the results obtained in this section on the ultimate failure load with respect to the recommendations and calculations specified in ACI 440.1R-15, a series of computations based on ACI 440.1R-15 were carried out to estimate the failure load.

Table 14 shows the comparison of the cracking loads, nominal and design ultimate failure loads between the values measured during the tests and design values obtained according to ACI 440.1R-15 standard recommendations. The values presented for the experimental results were the average values obtained for each beam series shown in **Table 13**.

The bamboo composite reinforcement showed better initial cracking load and much higher ultimate load-bearing capacity compared to the design values obtained through calculations according to ACI 440.1R-15. The estimated design cracking loads based on ACI 440.1R-15 were lower than the values obtained by testing the bamboo composite reinforced concrete beams. The cracking loads measured during the four-point flexural test of the beams on average was 2–5 times larger than the design values of the ACI 440.1R-15 standard, confirming the superior performance of the bamboo composite reinforcement in comparison to the estimates according to the ACI standard. Beam samples with only two bamboo composite reinforcement bars at the tension side of the concrete beam cross section failed mainly due to the rupture of the reinforcement, while beam samples with 4 bamboo composite tensile reinforcement bars had a tendency to fail due to concrete crushing at the compression side of the beam. In both cases, the bamboo-composite reinforcement performed well, showing that it is a suitable alternative to steel and GFRP reinforcement for concrete structures in terms of mechanical capacity and technical feasibility.

CONCLUSION

Bamboo *Dendrocalamus asper* locally known as bamboo Petung from Indonesia was selected to correlate its mechanical properties with physical properties of the culm including culm geometry, specific density and moisture content for composite fabrication for use in structural concrete. Based on the results obtained from the first part of this study, the following conclusions are relevant:

- Physical properties of the bamboo culm can be used to estimate the mechanical potential of bamboo for use in production of novel bamboo-based composite material applications in the building and construction sector.
- Mechanical properties of bamboo sections often decrease with increasing the wall thickness of the culm. This is associated with the reduced volumetric ratio of cellulose fibers to lignin as culm diameter increases.
- This study provides a simple method that allows estimation of the mechanical properties of bamboo through non-destructive measurement of only wall thickness and diameter. This capability is particularly useful in contexts of nurseries and in forests where there is limited access to testing facilities.

These findings are then used for the selection process of the raw bamboo for structural composite production when specific mechanical properties are required. A case study and independent mechanical testing of the novel bamboo-based composite reinforcement in concrete successfully validates the relationships proposed in this paper. Further work involves investigation of compressive and shear strength of bamboo, such as *Dendrocalamus asper* and evaluating the dependence on culm geometry including culm diameter, wall thickness and height. Further studies on microstructural analysis of bamboo-based composite reinforcement and the correlation with mechanical properties of bamboo will also be carried out.

AUTHOR CONTRIBUTIONS

AJ designed and performed the experiments. AJ and NS derived the models and analyzed the data. AJ and NS wrote the manuscript in consultation with IS and DH. IS was involved in planning and supervised the work.

DH contributed to the implementation of the research. All authors discussed the results and commented on the manuscript.

FUNDING

The research was conducted at the Future Cities Laboratory at the Singapore-ETH Centre, which was established collaboratively between ETH Zurich and Singapore's National Research Foundation (FI 370074016) under its Campus for Research Excellence and Technological Enterprise programme.

ACKNOWLEDGMENTS

The authors would like to gratefully acknowledge the support of Sawiris Foundation for Social Development and Singapore-MIT Alliance for Research and Technology Innovation Center in Singapore.

REFERENCES

Alvin, K., and Murphy, R. (1988). Variation in fibre and parenchyma wall thickness in culms of the bamboo Sinobambusa tootsik. *IAWA J.* 9, 353–361. doi: 10.1163/22941932-90001095

American Concrete Institute (2008). *Building Code Requirements for Structural Concrete (ACI 318–08) and Commentary*. Farmington Hills, MI: American Concrete Institute.

American Concrete Institute (2015). *ACI 440.1R-15 Guide for the Design and Construction of Structural Concrete Reinforced with Fiber-Reinforced Polymer Bars*. Farmington Hills, MI: ACI Committee 440.

Archila, H., Kaminski, S., Trujillo, D., Zea Escamilla, E., and Harries, K. A. (2018). Bamboo reinforced concrete: a critical review. *Mat. Struc.* 51:102. doi: 10.1617/s11527-018-1228-6

ASTM International (2011). *Standard Test Methods for Structural Panels in Flexure. ASTM D3043–00(2011)*. West Conshohocken, PA: ASTM International.

ASTM International (2014a). *Standard Test Methods for Density and Specific Gravity (Relative Density) of Wood and Wood-Based Materials. ASTM D2395-14e1*. West Conshohocken, PA: ASTM International.

ASTM International (2014b). *Standard Test Methods for Small Clear Specimens of Timber. ASTM D143-14*. West Conshohocken, PA: ASTM International.

ASTM International (2015). *Standard Test Methods for Direct Moisture Content Measurements of Wood and Wood-Base Materials. ASTM D4442-15*. West Conshohocken, PA: ASTM International.

Bertolini, L., Elsener, B., Pedeferri, P., Redaelli, E., and Polder, R. B. (2013). *Corrosion of Steel in Concrete: Prevention, Diagnosis, Repair*. Weinheim: John Wiley & Sons.

Chen, H., Miao, M., and Ding, X. (2009). Influence of moisture absorption on the interfacial strength of bamboo/vinyl ester composites. *Compos. Part A. Appl. S.* 40, 2013–2019. doi: 10.1016/j.compositesa.2009.09.003

Correal, D., Francisco, J., and Arbeláez, C. (2010). Influence of age and height position on Colombian Guadua angustifolia bamboo mechanical properties. *Maderas. Ciencia Tecnol.* 12, 105–113. doi: 10.4067/S0718-221X2010000200005

Faruk, O., Bledzki, A. K., Fink, H. P., and Sain, M. (2014). Progress report on natural fiber reinforced composites. *Macromol. Mater. Eng.* 299, 9–26. doi: 10.1002/mame.201300008

Febrianto, F., Hidayat, W., Bakar, E. S., Kwon, G.-J., Kwon, J.-H., Hong, S.-I., et al. (2012). Properties of oriented strand board made from Betung bamboo (Dendrocalamus asper (Schultes. f) Backer ex Heyne). *Wood Sci. Technol.* 46, 53–62. doi: 10.1007/s00226-010-0385-8

Gibson, L. J. (2012). The hierarchical structure and mechanics of plant materials. *J. R. Soc Interface* 9, 2749–2766. doi: 10.1098/rsif.2012.0341

Green, D. W., Winandy, J. E., and Kretschmann, D. E. (1999). "Wood handbook: mechanical properties of wood," in *General Technical Report FPL-GTR-113*, ed F. S. Department of Agriculture, Forest Product Laboratory (Madison, WI: United States Department of Agriculture), 4-1–4-44.

Hebel, D., and Heisel, F. (2016). *Bamboo Composite Material for Structural Applications and Method of Fabricating the Same*.

Hebel, D. E., Javadian, A., Heisel, F., Schlesier, K., Griebel, D., and Wielopolski, M. (2014). Process-controlled optimization of the tensile strength of bamboo fiber composites for structural applications. *Compos. Part B Eng.* 67, 125–131. doi: 10.1016/j.compositesb.2014.06.032

Hidalgo-Lopez, O. (2003). *Bamboo The Gift of The GODS*. Bogotá: D'VINNI LTDA.

Ichhaporia, P. K. (2008). *Composites from Natural Fibers*. Raleigh, NC: ProQuest.

Janssen, J. J. (2012). *Mechanical Properties of Bamboo*. Berlin: Springer Science & Business Media.

Javadian, A. (2017). *Composite Bamboo and its Application as Reinforcement in Structural Concrete*. Zurich: ETH Zurich.

Javadian, A., Wielopolski, M., Smith, I. F., and Hebel, D. E. (2016). Bond-behavior study of newly developed bamboo-composite reinforcement in concrete. *Constr. Build Mater.* 122, 110–117. doi: 10.1016/j.conbuildmat.2016.06.084

Jindal, U. (1986). Development and testing of bamboo-fibres reinforced plastic composites. *J. Compos. Mater.* 20, 19–29. doi: 10.1177/002199838602000102

Kamruzzaman, M., Saha, S., Bose, A., and Islam, M. (2008). Effects of age and height on physical and mechanical properties of bamboo. *J. Trop. For Sci.* 211–217.

Kaur, P. J., Kardam, V., Pant, K., Naik, S., and Satya, S. (2016). Characterization of commercially important Asian bamboo species. *Eur. J. Wood Wood Prod.* 74, 137–139. doi: 10.1007/s00107-015-0977-y

Kushwaha, P. K., and Kumar, R. (2009). Studies on water absorption of bamboo-polyester composites: effect of silane treatment of mercerized bamboo. *Polym. Plast. Technol. Eng.* 49, 45–52. doi: 10.1080/03602550903283026

Lakkad, S., and Patel, J. (1981). Mechanical properties of bamboo, a natural composite. *Fibre Sci. Technol.* 14, 319–322. doi: 10.1016/0015-0568(81)90023-3

Lee, A. W., Bai, X., and Peralta, P. N. (1996). Physical and mechanical properties of strandboard made from moso bamboo. *Forest Prod. J.* 46:84.

Liese, W. (1985). "Anatomy and properties of bamboo," in *International Bamboo Workshop* (Hangzhou), 196–208.

Liese, W. (1987). Research on bamboo. *Wood Sci. Technol.* 21, 189–209.

Liese, W. (1998). *The Anatomy of Bamboo Culms*. Boston, MA: BRILL.

Liese, W., and Jackson, A. (1985). *Bamboos Biology, Silvics, Properties, Utilization*. Eschborn: Deutsche Gesellschaft für Technische Zusammenarbeit (GTZ).

Limaye, V. (1952). *Strength of Bamboo (Dendrocalamus strictus)*. Dehradun: Manager of Publications.

Lo, T. Y., Cui, H., and Leung, H. (2004). The effect of fiber density on strength capacity of bamboo. *Mater. Lett.* 58, 2595–2598. doi: 10.1016/j.matlet.2004.03.029

Lo, T. Y., Cui, H., Tang, P., and Leung, H. (2008). Strength analysis of bamboo by microscopic investigation of bamboo fibre. *Constr. Build Mater.* 22, 1532–1535. doi: 10.1016/j.conbuildmat.2007.03.031

Macias, A., and Andrade, C. (1987). Corrosion of galvanized steel reinforcements in alkaline solutions: Part 1: electrochemical results. *Br. Corr. J.* 22, 113–118. doi: 10.1179/000705987798271631

Malanit, P., Barbu, M., and Frühwald, A. (2009). The gluability and bonding quality of an asian bamboo ("dendrocalamus asper") for the production of composite lumber. *J. Trop. For. Sci.* 21, 361–368.

Malanit, P., Barbu, M. C., and Frühwald, A. (2011). Physical and mechanical properties of oriented strand lumber made from an Asian bamboo (Dendrocalamus asper Backer). *Eur. J. Wood Wood Prod.* 69, 27–36. doi: 10.1007/s00107-009-0394-1

Mohmod, A. L., Amin, A. H., Kasim, J., and Jusuh, M. Z. (1993). Effects of anatomical characteristics on the physical and mechanical properties of Bambusa blumeana. *J. Trop. For. Sci.* 6, 159–170.

Murphy, R., and Alvin, K. (1992). Variation in fibre wall structure in bamboo. *IAWA J.* 13, 403–410. doi: 10.1163/22941932-90001296

Nordahlia, A., Anwar, U., Hamdan, H., Zaidon, A., Paridah, M., and Razak, O. A. (2012). Effects of age and height on selected properties of Malaysian bamboo (Gigantochloa levis). *J. Trop. For Sci.* 102–109.

Nugroho, N., and Ando, N. (2000). Development of structural composite products made from bamboo I: fundamental properties of bamboo zephyr board. *J. Wood Sci.* 46, 68–74. doi: 10.1007/BF00779556

Nugroho, N., and Ando, N. (2001). Development of structural composite products made from bamboo II: fundamental properties of laminated bamboo lumber. *J. Wood Sci.* 47, 237–242. doi: 10.1007/BF01171228

Okubo, K., Fujii, T., and Yamamoto, Y. (2004). Development of bamboo-based polymer composites and their mechanical properties. *Compos. Part A. Appl. S.* 35, 377–383. doi: 10.1016/j.compositesa.2003.09.017

Rahman, N., Shing, L. W., Simon, L., Philipp, M., Alireza, J., Ling, C. S., et al. (2017). Enhanced bamboo composite with protective coating for structural concrete application. *Energy Procedia* 143, 167–172. doi: 10.1016/j.egypro.2017.12.666

Rao, I. R., Gnanaharan, R., and Sastry, C. B. (1988). "Bamboos. current research. proceedings of the international bamboo workshop, Cochin, India, 14–18 Nov. 1988," in: *Bamboos. Current Research* (Cochin: Kerala Forest Research Institute), 217–290.

Ray, A. K., Das, S. K., Mondal, S., and Ramachandrarao, P. (2004). Microstructural characterization of bamboo. *J. Mater. Sci.* 39, 1055–1060. doi: 10.1023/B:JMSC.0000012943.27090.8f

Rowel, R., and Norimoto, M. (1988). Dimensional stability of bamboo particleboards made from acetylated particles. *Mokuzai Gakkaishi* 34, 627–629.

Slater, J. E. (1983). *Corrosion of Metals in Association with Concrete: A Manual Sponsored by ASTM Subcommittee G01. 14 on Corrosion of Reinforcing Steel, and Metal Properties Council*. Philadelphia, PA: ASTM International.

Wahab, R., Mustapa, M., Sulaiman, O., Mohamed, A., Hassan, A., and Khalid, I. (2010). Anatomical and physical properties of cultivated two-and four-year-old Bambusa vulgaris. *Sains Malays.* 39, 571–579. Available online at: http://www.ukm.my/jsm/

Wakchaure, M., and Kute, S. (2012). Effect of moisture content on physical and mechanical properties of bamboo. *Asian J. Civ. Eng. (Build Hous).* 13, 753–763.

Wegst, U., and Ashby, M. (2004). The mechanical efficiency of natural materials. *Philos. Magazine* 84, 2167–2186. doi: 10.1080/14786430410001680935

Youssefian, S., and Rahbar, N. (2015). Molecular origin of strength and stiffness in bamboo fibrils. *Sci. Rep.* 5:11116. doi: 10.1038/srep11116

Yu, H., Jiang, Z., Hse, C., and Shupe, T. (2008). Selected physical and mechanical properties of moso bamboo (Phyllostachys pubescens). *J. Trop. For. Sci.* 258–263.

Yu, Y., Wang, H., Lu, F., Tian, G., and Lin, J. (2014). Bamboo fibers for composite applications: a mechanical and morphological investigation. *J. Mater. Sci.* 49, 2559–2566. doi: 10.1007/s10853-013-7951-z

Zaidon, A., Paridah, M., Sari, C., Razak, W., and Yuziah, M. (2004). Bonding characteristics of Gigantochloa scortechinii. *J. Bamboo Rattan* 3, 57–65. doi: 10.1163/156915904772875644

Zou, L., Jin, H., Lu, W.-Y., and Li, X. (2009). Nanoscale structural and mechanical characterization of the cell wall of bamboo fibers. *Mater. Sci. Eng. C Mater. Biol. Appl.* 29, 1375–1379. doi: 10.1016/j.msec.2008.11.007

Conflict of Interest Statement: The authors declare that the research was conducted in the absence of any commercial or financial relationships that could be construed as a potential conflict of interest.

frontiers in Materials

ORIGINAL RESEARCH
published: 27 February 2019
doi: 10.3389/fmats.2019.00024

Elastic Response of an Optimal Tensegrity-Type Metamaterial

*Domenico De Tommasi, Giuseppe Puglisi and Francesco Trentadue**

Dipartimento Scienze Ingegneria Civile e Architettura, Politecnico di Bari, Bari, Italy

We study the elastic response of a class of optimal planar metamaterials designed as periodic patterns of tensegrity cells. Specifically, we consider an infinite slab constituted by prismatic cells whose sections on the middle plane are regular hexagons, squares or equilateral triangles subjected to a uniform normal stress. An attracting property of the proposed metamaterial is a very small tangential stiffness compared with the normal one. This property suggests the design of innovative isolation devices with extreme properties.

Keywords: metamaterials, global stability, tensegrities, optimization, isolation devices

Edited by:
Fernando Fraternali,
University of Salerno, Italy

Reviewed by:
Vagelis Plevris,
OsloMet-Oslo Metropolitan University, Norway
Zbigniew Wojciech Bieniek,
Rzeszów University of Technology, Poland

***Correspondence:**
Francesco Trentadue
francesco.trentadue@poliba.it

Specialty section:
This article was submitted to Mechanics of Materials, a section of the journal Frontiers in Materials

Received: *13 November 2018*
Accepted: *07 February 2019*
Published: *27 February 2019*

Citation:
De Tommasi D, Puglisi G and Trentadue F (2019) Elastic Response of an Optimal Tensegrity-Type Metamaterial. Front. Mater. 6:24. doi: 10.3389/fmats.2019.00024

1. INTRODUCTION

Metamaterials represent an innovative approach to the problem of obtaining unusual or extreme physical responses for advanced applications. Since their extreme macroscopic responses depend primarily on the internal low scale pattern, the understanding of how the microstructure topology influences the macroscopic properties is the key-point in the design of new advanced metamaterials.

The growing scientific and technological interest on these new designed materials is due to the possibility of getting electromagnetic and optical properties (Chen et al., 2010) or mechanical responses unreached by standard materials. Metamaterials can exhibit extreme static or dynamical behaviors, such as negative effective dynamic modulus (Fang et al., 2006), vanishing macroscopic shear modulus (Schittny et al., 2013) or selective buckling under external stresses (Paulose et al., 2015). Recently, the possibility of harnessing the postbuckling response of cellular materials for auxetic and dissipative properties has been analyzed by Bertoldi (2017). Based on these specific mechanical properties also the design of tensegrity-based metamaterials has been oriented to produce extreme or controllable behaviors. In particular, extreme behaviors in the propagation of mechanical waves have been considered by Amendola et al. (2018) and Fraternali et al. (2012, 2014), whereas elastic responses controllable by adjusting the level of self-equilibrated forces have been studied by Sabouni-Zawadzka and Gilewski (2019). Further, it has been recognized that the transmission and the control of forces in biological systems is diffusely achieved by means of systems based on tensegrity schemes (see e.g., Volokh et al., 2000; Ingber et al., 2014; Fraldi et al., 2019).

Metamaterials are usually classified into three-dimensional and surface (planar) materials and are frequently based on elementary geometric patterns (see e.g., Koohestani, 2017; Salahshoor et al., 2018; Zhang et al., 2018). Many studies approaching these periodic materials by means of lattice theory have been carried out. Within this research line, Hutchinson and Fleck (2006) studied the structural performance of periodic planar trusses. Buckling of a planar periodic frame was considered by Triantafyllidis and Schnaidt (1993). More recently, Thomsen et al. (2018) performed a topological optimization of 2D periodic materials undergoing buckling type instabilities. Moreover, the non-linear response of planar periodic materials has been analyzed by Vigliotti et al. (2014).

This paper is focused on the elastic response of a planar metamaterial made up of a pattern of equal tensegrity units, where each unit cell is a three dimensional T-bar (Skelton et al., 2017). In particular, we consider an infinite slab undergoing a uniform compressive macro stress. Based on a well-known result on planar tessellation, we consider systems with three different periodic patterns of identical prismatic cells filling the space, whose sections on the middle plane of the slab are equilateral triangles, squares, and regular hexagons (see **Figures 1**, **2**). The mass optimization of this metamaterial was discussed in a previous paper (DeTommasi et al., 2017b). Here we determine the overall (macro) elastic properties of these optimal slabs as functions of both design and actual applied loads. Interestingly, the proposed metamaterial exhibits a low shear stiffness coupled with a high extensional stiffness. This property suggests the possibility of obtaining isolation devices with extreme properties.

2. MORPHOLOGICAL OPTIMIZATION

As already stated, in our optimization problem we consider only slabs made up of periodic sequences of tensegrity cells having equilateral triangular, square, or regular hexagonal shapes, which are the unique shapes allowing us to tessellate the plane into identical regular polygons. On the external plane surfaces of the slab a normal compression macro stress Σ is applied, so that

$$P = A_{cell}\Sigma. \tag{1}$$

is the load applied to the single tensegrity cell (see **Figure 1**). Here, the cross section area A_{cell} for a cross section having p sides ($p = 3, 4, 6$) is given by

$$A_{cell} = \frac{p\,H^2}{8}\sin\left(\frac{2\pi}{p}\right)\tan^2\alpha, \qquad p = 3, 4, 6, \tag{2}$$

where H is the height of a cell and α is the angle formed by the principal struts and the principal cables (see **Figure 1**). Once the cell shape is defined, α represents the optimization geometrical parameter of the described metamaterial. The following assumptions are introduced:

(i) A prestress must be assigned such that both in the loaded and unloaded states only traction forces are exerted on cables;
(ii) Both in the loaded and unloaded states, cables respect material failure condition and struts both material failure and local Euler buckling conditions;
(iii) Equilibrium is *globally stable*.

For a fixed Σ, we aim to minimize the metamaterial volume density

$$\rho := \frac{\text{tensegrity volume}}{A_{cell}H}, \tag{3}$$

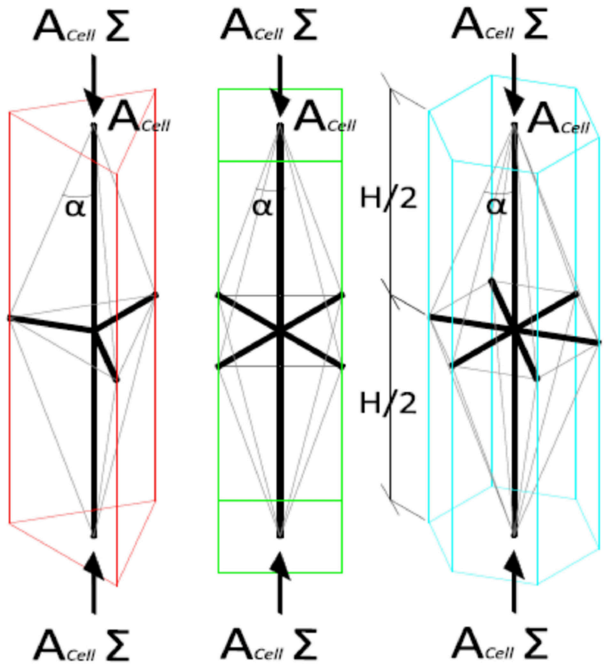

FIGURE 1 | The three tensegrity-type unit cells (equilateral triangles, squares, regular hexagons).

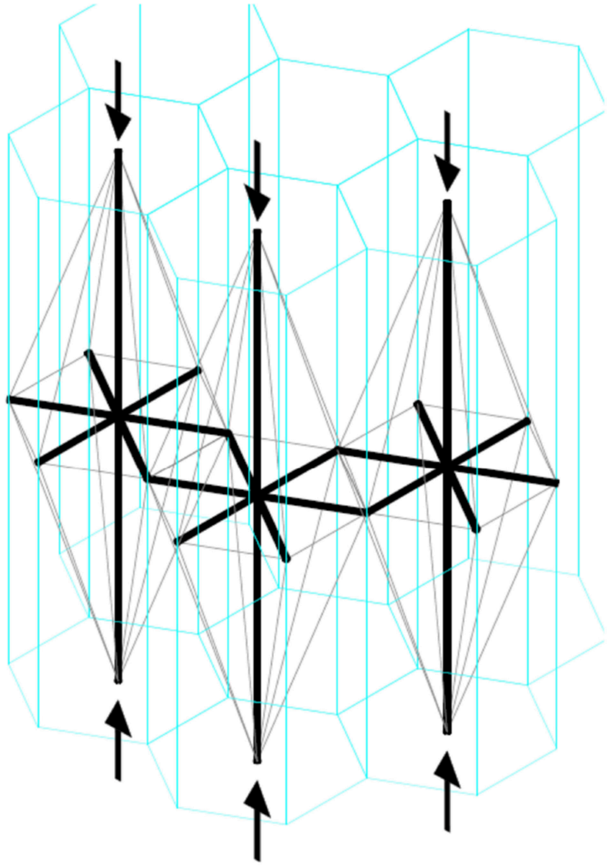

FIGURE 2 | Scheme of the slab composed of hexagonal cells.

where *tensegrity volume* is the global volume of all members of a tensegrity cell and A_{cell} is given by (2). We remark that, since we assume that all tensegrity units are made of the same material, the minimum value of ρ corresponds to the slab of minimal mass. Furthermore we observe that neighboring tensegrity units (see **Figure 2**) share the same transversal cables. Thus the areas of these cables considered for a singular unit are the half of the total ones. The above statements lead to the constrained minimum problem already discussed in DeTommasi et al. (2017b).

2.1. Elastic Equilibrium of Tensegrity Cells

Due to periodicity and symmetry properties of the metamaterial introduced above, any cell is two-degrees statically indeterminate. In the *loaded state* ($P = \Sigma A_{cell}$) two parameters β and τ are introduced to describe the internal forces

$$\begin{cases} \beta = \dfrac{N}{P} > 1 \\ \tau = \dfrac{T_t}{P} > 0 \end{cases}. \tag{4}$$

Here N is the compression force in the struts orthogonal to the middle plane and T_t is the traction force in the cables laying in the middle plane. Then the internal axial forces in the loaded state can be written as

$$\begin{cases} N &= \beta P \\ N_t &= \dfrac{2}{p}(\beta - 1)P\tan\alpha + 2\tau P \sin\dfrac{\pi}{p} \\ T &= \dfrac{(\beta-1)P}{p\sin\alpha} \\ T_t &= \tau P \end{cases}, \tag{5}$$

where T denotes the traction force in the cables out of the middle plane and N_t the compression force in the transversal struts laying on the middle plane.

Similarly, in the unloaded state ($P = 0$) we can describe the distribution of the internal forces by the parameters $\bar{\beta}$ and $\bar{\tau}$, defined as β and τ and given by

$$\begin{cases} \beta = \bar{\beta} + N_{[1]} \\ \tau = \bar{\tau} + T_{t[1]} \end{cases}. \tag{6}$$

Here $N_{[1]}$ is the compression force induced in the principal struts by a unitary compression force ($P = 1$) and $T_{t[1]}$ is the traction force induced in the tranversal cables by the same external force. In the unloaded state we have

$$\begin{cases} \bar{N} &= \bar{\beta}P \\ \bar{N}_t &= \dfrac{2}{p}\bar{\beta}P\tan\alpha + 2\bar{\tau}P\sin\dfrac{\pi}{p} \\ \bar{T} &= \dfrac{\bar{\beta}P}{p\cos\alpha} \\ \bar{T}_t &= \bar{\tau}P \end{cases}. \tag{7}$$

Though, as already discussed in DeTommasi et al. (2017b), a complete stability analysis should be carried out in the context of lattice theory (Triantafyllidis and Schnaidt, 1993), here, for sake of simplicity we assume that *all cells undergo identical critical displacements*. We deem that this assumption is satisfactory within the present analysis. Moreover, precritical displacements are assumed to be small with the deformed lengths of the members identified with the natural ones. Under these hypotheses the total potential energy (set equal to zero in the unloaded state) of the system can be written as

$$V(\boldsymbol{u}, P) = \sum_{j=1}^{2+3p} \left[\frac{EA^{(j)}}{2}\left(\frac{\Delta l^{(j)}}{l^{(j)}}\right)^2 l^{(j)} + N^{(j)}\Delta l^{(j)} \right] - 2Pu_1, \tag{8}$$

where

$$\Delta l^{(j)} = ||\Delta\boldsymbol{x}^{(j)} + \boldsymbol{T}^{(j)}\boldsymbol{u}|| - l^{(j)}.$$

Here $\boldsymbol{u}$ is the vector of generalized incremental displacements (see **Figure 3**); $2u_1$ is the contraction orthogonal to the middle plane; $l^{(j)}$, $\Delta l^{(j)}$, and $A^{(j)}$ are the length, the elongation and the area of the (j)-th member, respectively; $\Delta\boldsymbol{x}^{(j)}$ is the length vector and $\boldsymbol{T}^{(j)}\boldsymbol{u}$ is the relative incremental displacement vector between the end joints of the (j)-th member. Furthermore, the Young modulus E has a unique value for all the bars and cables, made up of the same material. In particular, we have

$$A^{(j)} = \begin{cases} A, & j = 1, 2 \\ A_t, & j = 3, 4, ..., p+2 \\ A_c, & j = p+3, p+4, ..., 2p+2 \\ A_{ct}, & j = 2p+3, 2p+4, ..., 3p+2 \end{cases}, \tag{9}$$

where A and A_t are the areas of the cross sections of the principal and transversal struts, respectively, and A_c and A_{ct} the cross section areas of the principal and traversal cables, respectively.

The lengths $l^{(j)}$ of the members are given by

$$l^{(j)} = \begin{cases} \dfrac{H}{2}, & j = 1, 2 \\ \dfrac{H\tan\alpha}{2}, & j = 3, 4, .., p+2 \\ \dfrac{H}{2\cos\alpha}, & j = p+3, p+4, ..., 2p+2 \\ H\sin\dfrac{\pi}{p}\tan\alpha, & j = 2p+3, 2p+4, ..., 3p+2 \end{cases}. \tag{10}$$

The axial forces $N^{(j)}$ (numbered with the same index of the lengths and the areas of the corresponding members) are given by (5). The tangent stiffness matrix $\boldsymbol{K}$ is the 10×10 Hessian matrix of the total potential energy in the loaded configuration:

$$\boldsymbol{K} = \frac{\partial^2 V}{\partial\boldsymbol{u}\partial\boldsymbol{u}}\bigg|_{\boldsymbol{u}=\boldsymbol{0}}, \tag{11}$$

that, for stable or critical equilibrium states, must be semidefinite positive

$$\boldsymbol{K} \succeq \boldsymbol{0}. \tag{12}$$

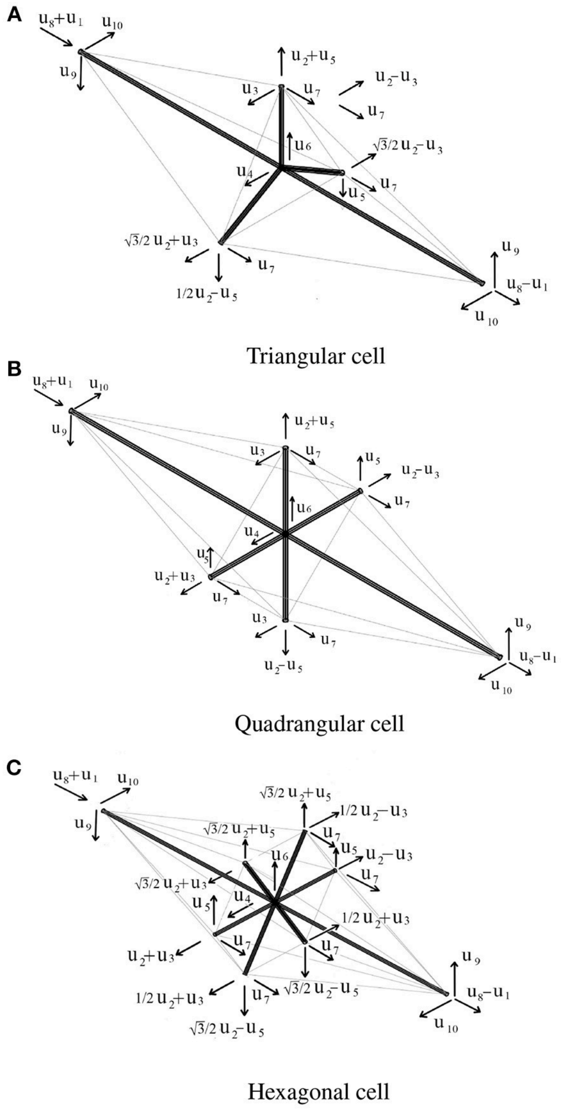

FIGURE 3 | Generalized displacements considered in the stability analysis for the three tensegrity cells. **(A)** Triangular cell. **(B)** Quadrangular cell. **(C)** Hexagonal cell.

Based on the symmetry properties of the tensegrity cell, in our numerical analysis we choose the generalized displacements shown in **Figure 3**. Thanks to this approach, the Hessian matrix $\boldsymbol{K}$ is a block diagonal matrix, with maximum dimension of the submatrices equal to 2 × 2. This choice significantly simplifies the numerical analysis of positiveness in the following described optimization procedure. In particular, the above positivity condition is imposed by requiring that its leading principal minors are all non-negative.

3. MACRO ELASTIC CONSTANTS

In this section the elastic constants of the slabs are evaluated. The tangent Young modulus E_m in the direction orthogonal to the middle plane is determined as

$$E_m = \frac{\dot{\Sigma}}{\dot{\epsilon}_1} = H\frac{\dot{\Sigma}}{2\dot{u}_1} \tag{13}$$

where $\dot{\epsilon}_1 = 2\dot{u}_1/H$ is the normal strain of the slab and $2\dot{u}_1$ is the incremental contraction of the thickness H of the slab (see **Figure 3**). In order to determine E_m, we determine the incremental contraction induced by a unitary incremental value of the compressive macrostress $2\dot{u}_1 = 2A_{cell}\{\boldsymbol{K}^{-1}\mathbf{1}_{\mathrm{E}}\}_1$, where the column vector $\mathbf{1}_{\mathrm{E}}$ has all components equal to zero, except the first one, set equal to 1. Then (13) becomes

$$E_m = \frac{H}{2A_{cell}\left\{\boldsymbol{K}^{-1}\mathbf{1}_E\right\}_1}\,. \tag{14}$$

Analogously, the effective shear modulus of the slab is determined as

$$G_m = \frac{\dot{T}}{\dot{\gamma}} = H\frac{\dot{T}}{2\dot{u}_9} \tag{15}$$

where $\dot{\gamma} = 2\dot{u}_9/H$ is the incremental shear strain, $2\dot{u}_9$ is the incremental tangential relative displacement between the two end faces of the slab (see **Figure 3**) and $\dot{T}$ is the incremental effective shear stress applied to the two end faces. As in the previous case, G_m is evaluated by determining the incremental displacement vector induced by a unitary incremental shear stress $A_{cell}\boldsymbol{K}^{-1}\mathbf{1}_{\mathrm{G}}$, where the column vector $\mathbf{1}_{\mathrm{G}}$ has all components are equal to zero, except the ninth one, set equal to 1. Then (15) becomes

$$G = \frac{H}{2A_{cell}\left\{\boldsymbol{K}^{-1}\mathbf{1}_G\right\}_9}\,. \tag{16}$$

It must be noted that for the three cells here considered the two last diagonal blocks of $\boldsymbol{K}$ are equal scalars. In other words, the only non-zero elements of the two last rows and columns are always the diagonal elements $K_{9,9}$ and $K_{10,10}$, which are identical. Then (16) can be also written as

$$G = H\frac{K_{9,9}}{2A_{cell}} = H\frac{K_{10,10}}{2A_{cell}}\,. \tag{17}$$

The two last expressions (17) show that the elastic modulus G is independent from the direction of incremental shear macro stress $\dot{T}$, so that the slabs exhibits a *transversely isotropic* type behavior.

4. NUMERICAL RESULTS

To discuss previous results, consider a slab with thickness $H = 100$ mm and struts with thin annular sections, whose ratio between the average radius and the thickness is equal to 10. The Young modulus is fixed to $E = 200$ GPa and the yield stress to $\sigma_y = 200$ MPa. The minimum volume density (3) has been determined for values of the design monoaxial macrostress Σ_d in the range $[10^{-5}, 10^{-1}]$ MPa.

In **Figure 4**, the optimal density is shown vs. Σ_d for the three tensegrity shapes considered here. As the figure shows, the hexagonal shape is the most convenient. Interestingly we find an almost *linear* log-log dependence. This "scale invariant" behavior has been previously observed for similar tensegrities in DeTommasi et al. (2015) and had been used in DeTommasi et al. (2017a) to obtain optimal fractal like tensegrity structures.

This is coherently reflected in the observation that the optimal value of the geometrical parameter α, which describes the cell geometry, varies only very slightly in the considered range of the design macro stress Σ_d. In particular, for all the three different shapes we have $\tan\alpha \in [0.10, 0.11]$. Interestingly also the optimal prestress parameters β and τ change only very slightly in the considered range of the design macro stress: $\beta \in [1.18, 1.20]$, $\tau \in [0.04, 0.05]$. We then deduce that our solution identifies an optimal shape which is almost independent from the design macro stress in the considered range. Of course, on the contrary the optimal cross section areas strongly depend on the design macro stress.

Figure 5 shows the dependence of the macro elastic moduli E_m and G_m of the optimal slabs from the design macro stress Σ_d. Also here we notice that the log-log graph is almost linear. Due to the small values of the shear modulus, we argue that the small deviations from the power law regime of graph can be ascribed to numerical reasons. A very important property of the considered metamaterial is that it is characterized by a difference of several orders of magnitude (from 2 to 5) between the Young's modulus E_m and the tangential elastic modulus G_m, especially for low values of the design macro stress. This feature can be explained by observing that, in the considered

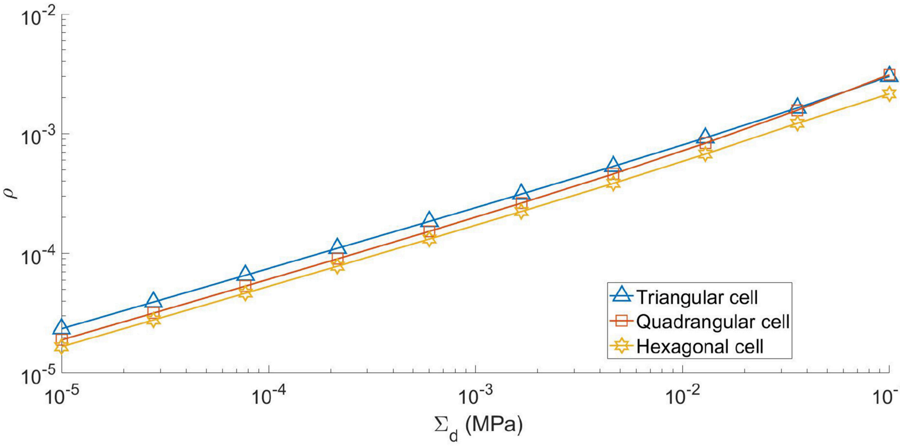

FIGURE 4 | Optimal volume density.

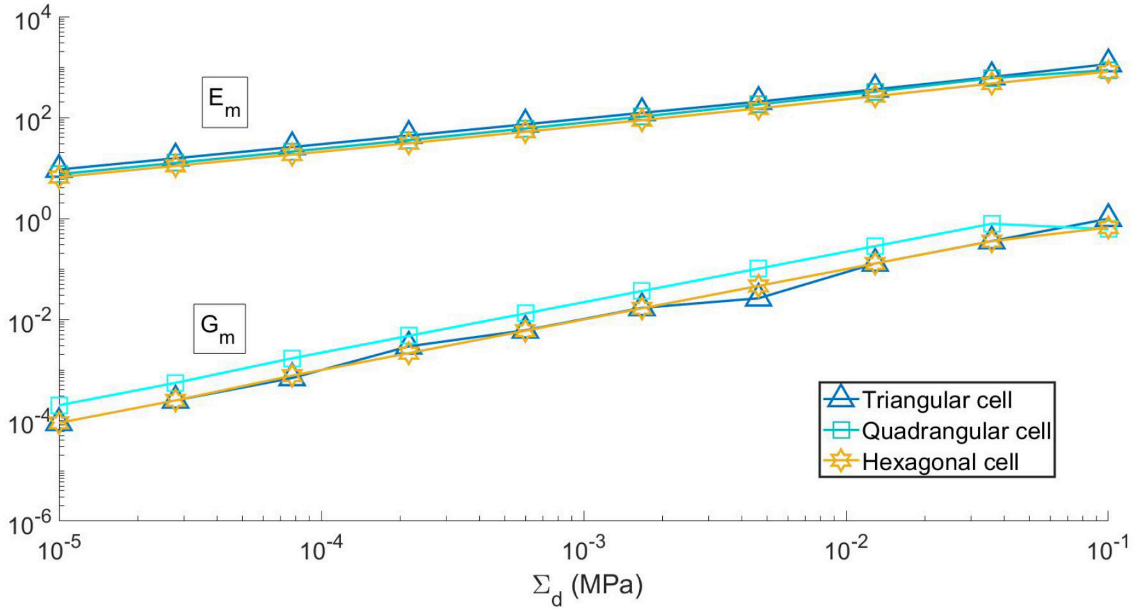

FIGURE 5 | E_m and G_m (MPa) vs. design macro stress.

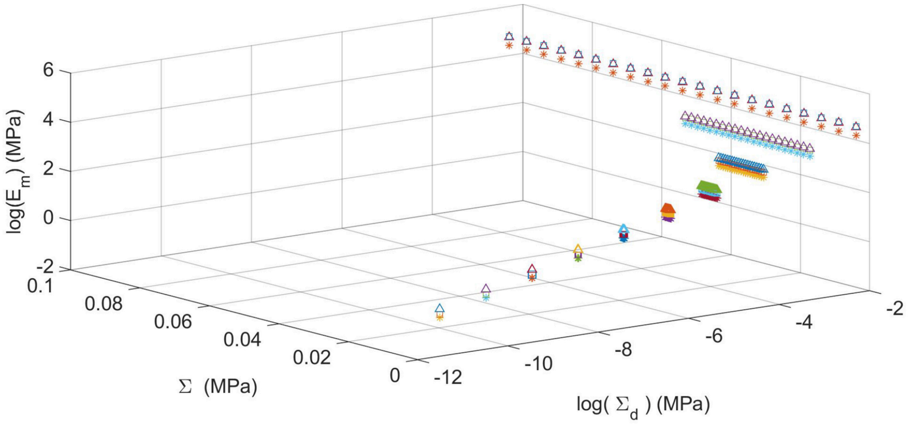

FIGURE 6 | Young modulus vs. the actual macrostress Σ at different values of the design macrostress Σ_d. The symbols △, □, *, refer to triangular, quadrangular, and hexagonal cells, respectively.

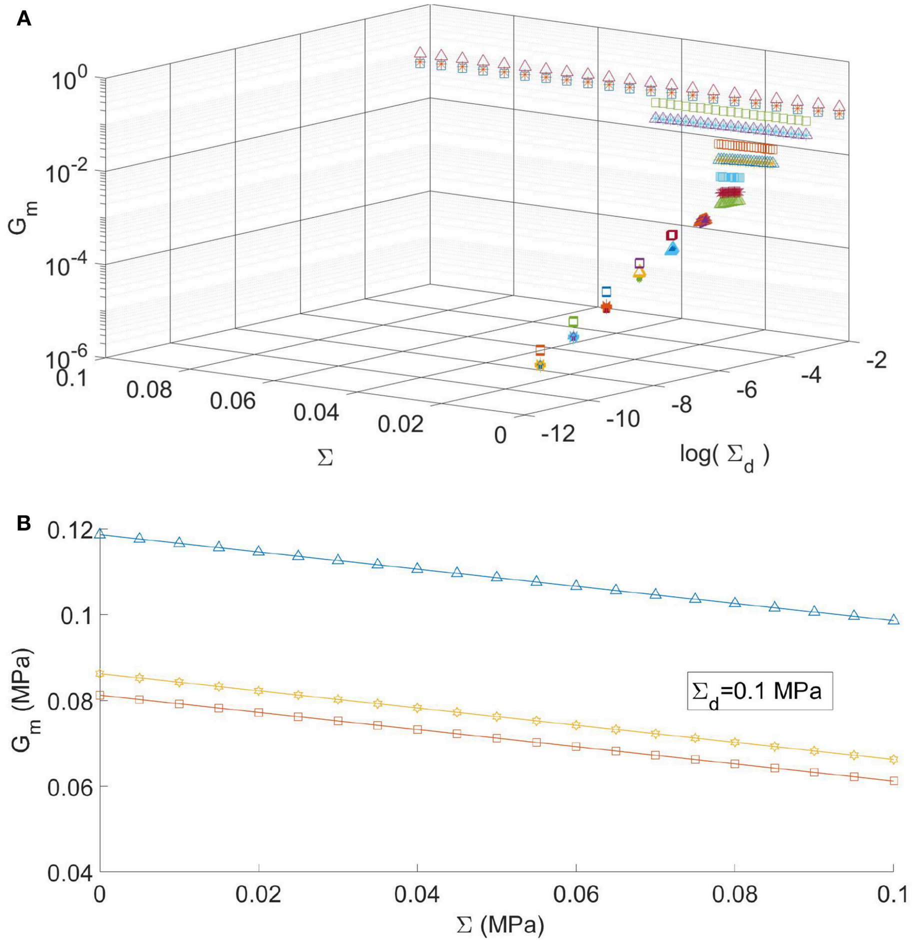

FIGURE 7 | (A) Tangent shear modulus G_m vs. the actual macrostress Σ for different values of the design macrostress Σ_d. The symbols △, □, * refer to triangular, quadrangular and hexagonal cells, respectively. **(B)** Tangent shear modulus vs. the actual macrostress Σ at ($\Sigma_d = 0.1$MPa) .

range of the design data, the cross sections of the struts are always determined by the local buckling constraints and are much greater than those of the cables, especially for low values of the design macrostress. Furthermore, as we already stated, the optimal value of the angle between the principal cables and the struts is always small ($\tan\alpha \simeq 0.10$).

In **Figure 6**, we represent the variation of the tangent Young modulus E_m with respect to both the actual applied macrostress Σ and the design macrostresses Σ_d. In particular, for each value of Σ_d it is shown that the tangent macro elastic modulus E_m is almost independent from Σ, which is varying from the unloaded state ($\Sigma = 0$) to the loaded state ($\Sigma = \Sigma_d$). Therefore we argue that the proposed metamaterial has a linear behavior with respect to the axial load Σ.

Similarly, in **Figure 7A**, we represent the tangent shear modulus G_m (MPa) of the optimal slabs. As in the previous figure, for different fixed design macrostresses Σ_d we analyze its dependence on the actual applied macrostress Σ, with Σ ranging from the unloaded state ($\Sigma = 0\,\text{MPa}$) to the loaded state ($\Sigma = \Sigma_d$). We point out that, differently from the previous case, for each value of Σ_d the tangent shear modulus G_m varies with the applied macro stress, even if its decrease (softening) with respect increasing values of the actual macro stress is quite limited. This is shown in detail in **Figure 7B** for a single fixed value of the design macro stress ($\Sigma_d = 0.1\text{MPa}$). Observe that the tangent shear modulus G_m decreases linearly as the applied macrostress grows, showing the same slope for the three geometries. A similar softening behavior has been also observed in the non-linear elastic analysis for laminated rubber bearings (see D'Ambrosio et al., 1995). Several augmentations of the obtained interesting behavior of these tensegrity slabs should be obtained by extending the optimization to multiscale tensegrity structures (see e.g., DeTommasi et al., 2015, 2017a) and by considering multilayer slabs.

CONCLUSIONS

In this paper he have optimized a planar metamaterial made up of periodically patterned tensegrity-type unit cells. With reference to different values of the design macro stress we have compared the mechanical responses of three different geometries of unit cells. Further, for each value of the design macro stress the optimal densities are compared, showing that the minimal density metamaterial is made up by hexagonal cells (see **Figure 2**). As already found previously, the optimal density of these slabs exhibits a log-log dependence on the applied macrostress. Here this result has been extended to the elastic macroscopic response, showing again a power law dependence of the macroscopic elastic moduli on the design macro stress. Interestingly, for each adopted geometry we have found shapes of the optimal tensegrity cells almost independent by the design macro stress. These results suggest a scale-invariant behavior of the proposed metamaterial. Finally, we remark that the optimal proposed metamaterial is characterized by a shear elastic modulus which is up to five orders of magnitude smaller than the Young modulus. This indicates that the proposed scheme of metamaterial is suitable for the design of new isolation devices.

AUTHOR CONTRIBUTIONS

All authors listed have made a substantial, direct and intellectual contribution to the work, and approved it for publication. In particular, all authors equally contributed to the theoretical modelling, while FT also developed numerical analysis.

FUNDING

DD and GP have been supported by the Italian Ministry MIUR-PRIN project COAN 5.50.16.01 code 2015JW9NJT.

REFERENCES

Amendola, A., Krushynska, A., Daraio, C., Pugno, N. M., and Fraternali, F. (2018). Tuning frequency band gaps of tensegrity mass-spring chains with local and global prestress. *Int. J. Solids Struct.* 155, 47–56. doi: 10.1016/j.ijsolstr.2018.07.002

Bertoldi, K. (2017). Harnessing instabilities to design tunable architected cellular materials. *Annu. Rev. Mater. Res.* 47, 51–61. doi: 10.1146/annurev-matsci-070616-123908

Chen, H., Chan, C. T., and Sheng, P. (2010). Transformation optics and metamaterials. *Nat. Mater.* 9, 387–396. doi: 10.1038/nmat2743

D'Ambrosio, P., DeTommasi, D., and Marzano, S. (1995). Nonlinear elastic deformations and stability of laminated rubber bearings. *J. Eng. Mech.* 121, 1041–1048. doi: 10.1061/(ASCE)0733-9399(1995)121:10(1041)

DeTommasi, D., Maddalena, F., Puglisi, G., and Trentadue, F. (2017a). Fractality in selfsimilar minimal mass structures. *J. Mech. Phys. Solids* 107, 433–450. doi: 10.1016/j.jmps.2017.07.002

DeTommasi, D., Marano, G., Puglisi, G., and Trentadue, F. (2015). Optimal complexity and fractal limits of self-similar tensegrities. *Proc. R. Soc. A* 471:20150250. doi: 10.1098/rspa.2015.0250

DeTommasi, D., Marano, G., Puglisi, G., and Trentadue, F. (2017b). Morphological optimization of tensegrity-type metamaterials. *Composites B Eng.* 115, 182–187. doi: 10.1016/j.compositesb.2016.10.017

Fang, N., Xi, D., Xu, J., Ambati, M., Srituravanich, W., Sun, C., et al. (2006). Ultrasonic metamaterials with negative modulus. *Nat. Mater.* 5, 452–456. doi: 10.1038/nmat1644

Fraldi, M., Palumbo, S., Carotenuto, A., Cutolo, A., Deseri, L., and Pugno, N. (2019). Buckling soft tensegrities: fickle elasticity and configurational switching in living cells. *J. Mech. Phys. Solids* 124, 299–324. doi: 10.1016/j.jmps.2018.10.017

Fraternali, F., Carpentieri, G., Amendola, A., Skelton, R., and Nesterenko, V. (2014). Multiscale tunability of solitary wave dynamics in tensegrity metamaterials. *Appl. Phys. Lett.* 105:201903. doi: 10.1063/1.4902071

Fraternali, F., Senatore, L., and Daraio, C. (2012). Solitary waves on tensegrity lattices. *J. Mech. Phys. Solids* 60, 1137–1144. doi: 10.1016/j.jmps.2012.02.007

Hutchinson, R., and Fleck, N. (2006). The structural performance of the periodic truss. *J. Mech. Phys. Solids* 54, 756–782. doi: 10.1016/j.jmps.2005.10.008

Ingber, D. E., Wang, N., and Stamenovic, D. (2014). Tensegrity, cellular biophysics, and the mechanics of living systems. *Rep. Progr. Phys.* 77:046603. doi: 10.1088/0034-4885/77/4/046603

Koohestani, K. (2017). On the analytical form-finding of tensegrities. *Composite Struct.* 166, 114–119. doi: 10.1016/j.compstruct.2017.01.059

Paulose, J., Meeussen, A. S., and Vitelli, V. (2015). Selective buckling via states of self-stress in topological metamaterials. *Proc. Natl. Acad. Sci. U.S.A.* 112, 7639–7644. doi: 10.1073/pnas.1502939112

Sabouni-Zawadzka, A., and Gilewski, W. (2019). Soft and stiff simplex tensegrity lattices as extreme smart metamaterials. *Materials* 12:187. doi: 10.3390/ma12010187

Salahshoor, H., Pal, R., and Rimoli, J. (2018). Material symmetry phase transitions in three-dimensional tensegrity metamaterials. *J. Mech. Phys. Solids* 119, 382–399. doi: 10.1016/j.jmps.2018.07.011

Schittny, R., Buckmann, T., Kadic, M., and Wegener, M. (2013). Elastic measurements on macroscopic three-dimensional pentamode metamaterials. *Appl. Phys. Lett.* 30:11905. doi: 10.1063/1.4838663

Skelton, R., Helton, J., Adhikari, R., Pinaud, J., and Chan, W. (2017). "An introduction to the mechanics of tensegrity structures," in *The Mechanical Systems Design Handbook: Modeling, Measurement, and Control*, ed Y. Hurmuzlu (Boca Raton, FL: CRC Press), 872.

Thomsen, C., Wang, F., and Sigmund, O. (2018). Buckling strength topology optimization of 2d periodic materials based on linearized bifurcation analysis. *Comput. Methods Appl. Mech. Eng.* 339, 115–136. doi: 10.1016/j.cma.2018.04.031

Triantafyllidis, N., and Schnaidt, W. (1993). Comparison of microscopic and macroscopic instabilities in a class of two-dimensional periodic composites. *J. Mech. Phys. Solids* 41, 1533–1565. doi: 10.1016/0022-5096(93)90039-I

Vigliotti, A., Deshpande, V., and Pasini, D. (2014). Non linear constitutive models for lattice materials. *J. Mech. Phys. Solids* 64, 44–60. doi: 10.1016/j.jmps.2013.10.015

Volokh, K., Vilnay, O., and Belsky, M. (2000). Tensegrity architecture explains linear stiffening and predicts softening of living cells. *J. Rep. Prog. Phys* 33, 1543–1549. doi: 10.1016/S0021-9290(00)00157-3

Zhang, L., Li, S., Zhu, S., Zhang, B., and Xu, G. (2018). Automatically assembled large-scale tensegrities by truncated regular polyhedral and prismatic elementary cells. *Composite Struct.* 184, 30–40. doi: 10.1016/j.compstruct.2017.09.074

Conflict of Interest Statement: The authors declare that the research was conducted in the absence of any commercial or financial relationships that could be construed as a potential conflict of interest.

frontiers in Materials

ORIGINAL RESEARCH
published: 27 February 2019
doi: 10.3389/fmats.2019.00026

Buckling Analysis of Single-Layer Graphene Sheets Using Molecular Mechanics

Alessandra Genoese, Andrea Genoese*, Nicola L. Rizzi and Ginevra Salerno

Applied Mathematics and Structural Mechanics Lab (LiMES), Department of Architecture, RomaTre University, Rome, Italy

The paper presents a nonlinear buckling analysis of single-layer graphene sheets using a molecular mechanics model which accounts for binary, ternary, and quaternary interactions between the atoms. They are described using a geometrically exact setting and by the introduction of Morse and cosine potential functions, equipped with an appropriate set of parameters. We examine the critical and post-critical behaviors of graphene, under compression in the zigzag and in the armchair directions, and shear. Our findings show the suitability of standard thin-plates theory for the prediction of simple critical behaviors under various edge constraint conditions.

Keywords: graphene, molecular mechanics, out-of-plane buckling, DREIDING potential, arc-length strategy

Edited by:
Fernando Fraternali,
University of Salerno, Italy

Reviewed by:
Nicholas Fantuzzi,
University of Bologna, Italy
Giuseppe Zurlo,
National University of Ireland Galway,
Ireland

****Correspondence:***
Andrea Genoese
andreagenoese_83@hotmail.it

Specialty section:
This article was submitted to
Mechanics of Materials,
a section of the journal
Frontiers in Materials

Received: *30 November 2018*
Accepted: *08 February 2019*
Published: *27 February 2019*

Citation:
Genoese A, Genoese A, Rizzi NL and Salerno G (2019) Buckling Analysis of Single-Layer Graphene Sheets Using Molecular Mechanics.
Front. Mater. 6:26.
doi: 10.3389/fmats.2019.00026

1. INTRODUCTION

Graphene is a two-dimensional hexagonal lattice of carbon atoms with unique physical and mechanical properties (Young et al., 2012), such as high room-temperature carrier mobility, high thermal conductivity, high tensile strength and stiffness and weak optical absorptivity. Owing to these remarkable properties, graphene has attracted considerable attention for applications in many fields (Choi et al., 2010; Li et al., 2014; Aïssa et al., 2015; Sun et al., 2015; Nguyen and Nguyen, 2016; Kumar et al., 2018; Mohan et al., 2018), including energy generation and storage (e.g., photovoltaic cells, hydrogen storage, supercapacitors), sensoring and actuating systems (e.g., gas sensors), electronics (e.g., conductive inks and flexible films), biotechnologies (e.g., membranes for water filtration, gas separation, DNA sequencing), composites.

The understanding and the control of the mechanical behaviors of graphene are crucial issues (Young et al., 2012; Akinwande et al., 2017) for many applications such as composites, membranes for water filtration, hydrogen storage and electronic devices. In this regard, it is worth emphasizing also that chemical-physical properties of any material at the nanoscale depend on the relative atomic positions. Tuning these properties in specific devices through deformation control is therefore possible, in principle.

The importance for these applications has motivated continuously increasing research efforts to understand the details of the mechanical response of graphene.

However, the technical difficulties and the costs of nanoscale experiments combine to make theoretical modeling approaches preferable. Among them, *ab-initio* simulations (Kudin et al., 2001; Baumeier et al., 2007; Liu et al., 2007) are the most accurate tools available to investigate the behavior of nanomaterials, including their mechanics, but they demand a lot of computer power and so they are not always feasible for systems with very many atoms. For this reason, increasing attention has been given to molecular dynamics/statics formulations (Liew et al., 2004; Lu et al., 2009; Xiao et al., 2009; Zhao et al., 2009; Georgantzinos et al., 2012; Silvestre et al., 2012; Berinskii and Borodich, 2013; Davini, 2014; Theodosiou and Saravanos, 2014; Gamboa et al., 2015; Korobeynikov et al., 2015, 2018; Budarapu et al., 2017; Davini et al., 2017; Genoese et al., 2017, 2018a,b, 2019; Hossain et al., 2018; Sgouros et al., 2018; Singh and Patel, 2018b) or their structural-mechanical approximations (e.g., nanoscale equivalent beam and truss models; Sakhaee-Pour, 2009a,b; Georgantzinos et al., 2010; Alzebdeh, 2012; Giannopoulos, 2012; Tserpes, 2012; Firouz-Abadi et al., 2016; Rafiee and Eskandariyun, 2017; Savvas and Stefanou, 2018) and to continuum models (Chang, 2010; Aminpour and Rizzi, 2016; Ghaffari et al., 2018; Singh and Patel, 2018a; Zhang et al., 2018).

Most of the research on graphene has focused on its rigidities, the frequencies of free vibration, and tensile failure properties and this has produced also a refinement of the parameters of simple bonding potentials (Genoese et al., 2017; Hossain et al., 2018; Korobeynikov et al., 2018), such as the DREIDING, the Stillinger-Weber or the modified Morse potentials. Currently, molecular statics formulations based on these potentials are considered to be the best compromise at the atomistic scale in non-linear contexts, where the simplicity of the models is a major requirement. Nevertheless, studies on out-of-plane buckling behaviors of graphene are not numerous (Sakhaee-Pour, 2009a; Duan et al., 2011; Giannopoulos, 2012; Korobeynikov et al., 2015; Firouz-Abadi et al., 2016; Sgouros et al., 2018). Duan (Duan et al., 2011) has investigated the development of wrinkles in rectangular graphene sheets under increasing in-plane shear displacements using the COMPASS potential. Modes jump phenomena have been reported, with sudden changes of the number of wrinkles as the displacements increase. Similar trends have been observed by Huang and Han (2017) through molecular dynamics simulations performed using the AIREBO potential. Sakhaee-Pour (2009a), Giannopoulos (2012), and Firouz-Abadi et al. (2016) have studied the linearised buckling of compressed graphene sheets and ribbons described as assemblages of Bernoulli-like beams and truss elements. Korobeynikov et al. (2015) have studied the buckling and the initial post-buckling of compressed graphene using the DREIDING potential. Very recently, Sgouros et al. (2018) have investigated compressed ribbons under various temperatures via molecular dynamics simulations incorporating the LCBOP potential.

In the present study, we propose a buckling analysis of single-layer graphene sheets through a molecular mechanics model which extends those used in our previous works (Genoese et al., 2017, 2018a,b, 2019) in order to account for binary, ternary and quaternary interactions between the atoms. They are described using a geometrically exact setting and introducing Morse and cosine potential functions, equipped with a proper set of parameters. To this regard, following the reasoning already proposed in Genoese et al. (2017, 2018a, 2019), a constitutive problem is solved only for purposes of giving a new parametrization of the dihedral potential. Then, by solving the equilibrium equations of the atomistic system through the arc-length strategy, we obtain the critical and post-critical behaviors of graphene under compression in the zigzag and in the armchair directions and shear. Case by case, the equilibrium paths are shown and the critical behaviors are discussed in comparison with available solutions for thin-plates (Timoshenko and Gere, 1963).

2. MATERIALS, MODEL, AND METHODS

2.1. The Molecular Mechanics Model

We assume that the reference configuration of the sheet is planar and stress free and that the atoms are point-particles in Euclidean space. Their interactions are usually separated into bonding interactions and long-range ones. Long-range interactions are considered to be negligible with respect to the bonding ones. In turn, bonding interactions are usually distinguished between binary, ternary and quaternary interactions, measured in terms of the bond length r_{ij}, valence angle θ_{ijk} and dihedral angle φ_{ijkl} (see **Figure 1**). The bonding interactions are derived from a potential U, here expressed in the additive form

$$U = \sum_b U_b^r + \sum_a U_a^\theta + \sum_d U_d^\varphi, \tag{1}$$

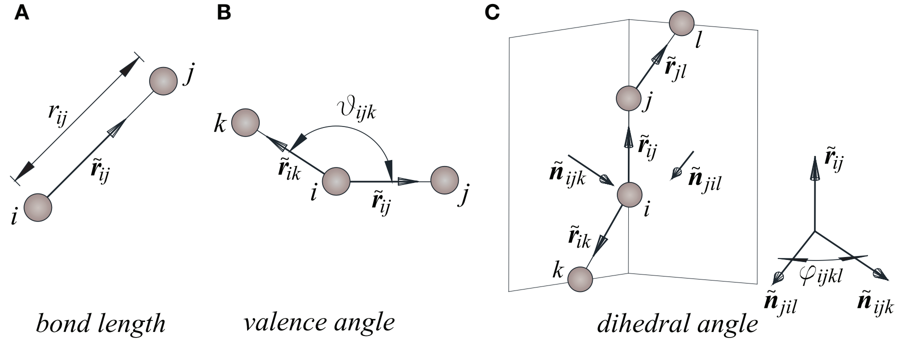

FIGURE 1 | The interatomic kinematics: **(A)** bond length, **(B,C)** valence, and dihedral angles.

where U_b^r, U_a^θ, and U_d^φ are the energy contributions related to the b^{th} bond length, to the a^{th} valence angle and to the d^{th} dihedral angle, respectively. In this paper, we use Morse and cosine energy functions (Mayo et al., 1990), which are defined to be

$$U_b^r = \bar{U}\left\{\left[1 - e^{-\beta(r_{ij}-\bar{r})}\right]^2 - 1\right\}, \tag{2a}$$

$$U_a^\theta = \frac{C}{2}\left(\cos\theta_{ijk} - \cos\bar{\theta}\right)^2, \tag{2b}$$

$$U_d^\varphi = \frac{V}{2}\left\{1 - \cos\left[p\left(\varphi_{ijkl} - \bar{\varphi}_{ijkl}\right)\right]\right\}. \tag{2c}$$

In Equations (2), $\bar{r} \approx 0.142$ nm, $\bar{\theta} = \frac{2\pi}{3}$ and $\bar{\varphi}_{ijkl} \in \{0, \pi\}$, are the length and angles in the resting configuration, $\bar{U}$ is the bond breaking energy, β, C and V are parameters which we define below and $p = 2$.

We denote by $\boldsymbol{x}_n$ and $\boldsymbol{u}_n$ the initial position vector of the n^{th} atom and its displacement vector. Then, its current position vector is given by $\boldsymbol{r}_n = \boldsymbol{x}_n + \boldsymbol{u}_n$. Similarly, $\boldsymbol{x}_{ij} = \boldsymbol{x}_j - \boldsymbol{x}_i$, $\boldsymbol{r}_{ij} = \boldsymbol{r}_j - \boldsymbol{r}_i$, and $\boldsymbol{u}_{ij} = \boldsymbol{u}_j - \boldsymbol{u}_i$ are the relative position vectors and the relative displacement vector of the atom j with respect to the atom i. Vector $\boldsymbol{r}_{ij}$ can be expressed as $\boldsymbol{r}_{ij} = \boldsymbol{x}_{ij} + \boldsymbol{u}_{ij}$.

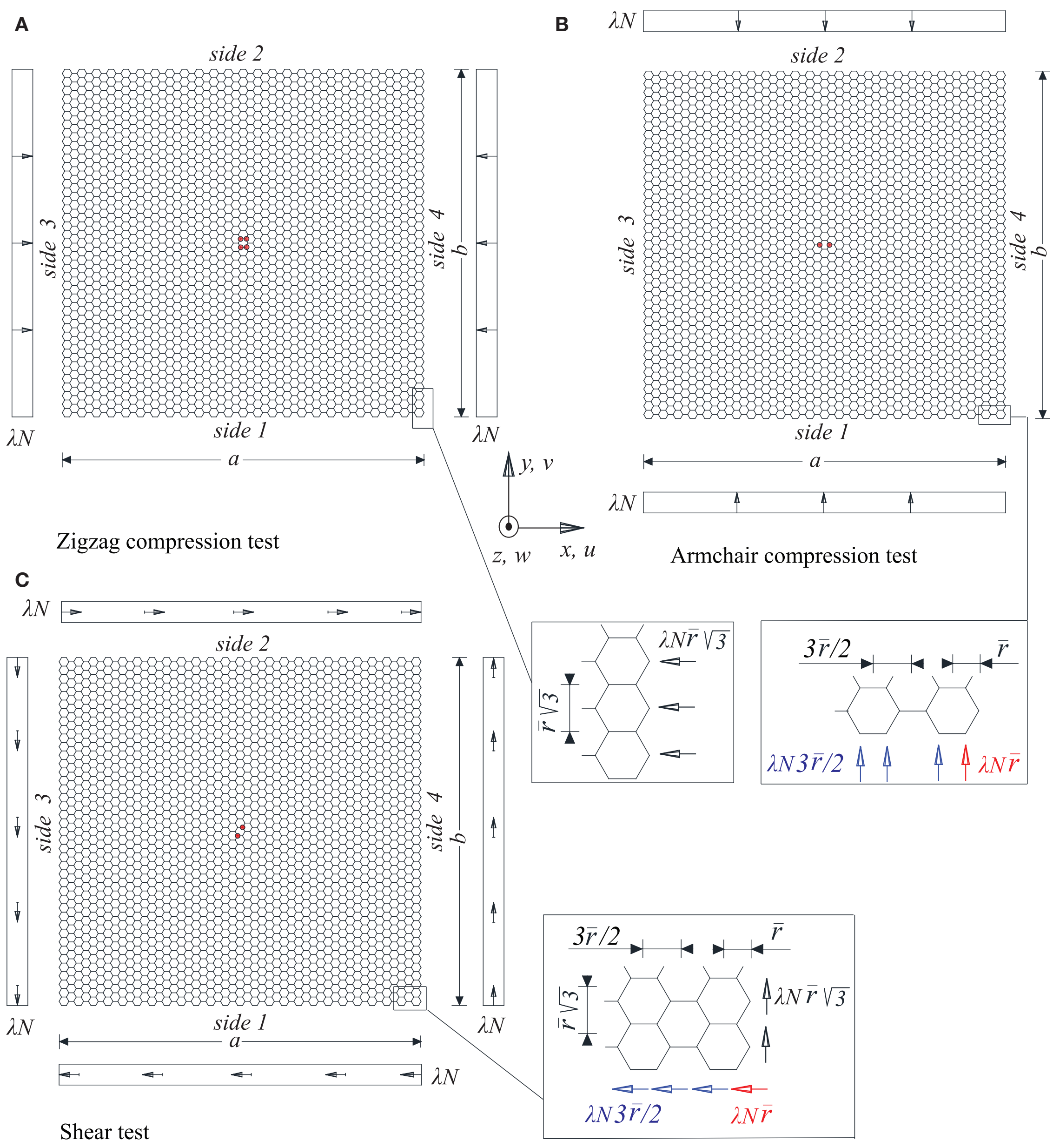

FIGURE 2 | Schemes of the compression and shear tests of the nearly square graphene sheet: **(A,B)** geometry and details of the applied loads for the compression tests in the zigzag and in the armchair directions, **(C)** geometry, and details of the applied loads for the shear test.

The bond length is given by

$$r_{ij} = ||\boldsymbol{r}_{ij}|| = \sqrt{\boldsymbol{r}_{ij} \cdot \boldsymbol{r}_{ij}}. \tag{3}$$

For what follows, $\tilde{\boldsymbol{r}}_{ij} = \boldsymbol{r}_{ij}/r_{ij}$ is the direction vector defined by a pair of atoms *i*-*j*. In addition, $\tilde{\boldsymbol{n}}_{ijk}$ and $\tilde{\boldsymbol{n}}_{jil}$ are, respectively, the unit vectors perpendicular to the plane determined by the current positions of the atoms *i*, *j* and *k* and to the plane determined by the current positions of the atoms *j*, *l* and *i*, given by:

$$\tilde{\boldsymbol{n}}_{ijk} = \frac{\boldsymbol{n}_{ijk}}{n_{ijk}}, \quad \boldsymbol{n}_{ijk} = \tilde{\boldsymbol{r}}_{ij} \times \tilde{\boldsymbol{r}}_{ik}, \quad n_{ijk} = ||\boldsymbol{n}_{ijk}||,$$
$$\tilde{\boldsymbol{n}}_{jil} = \frac{\boldsymbol{n}_{jil}}{n_{jil}}, \quad \boldsymbol{n}_{jil} = \tilde{\boldsymbol{r}}_{jl} \times \tilde{\boldsymbol{r}}_{ij}, \quad n_{jil} = ||\boldsymbol{n}_{jil}||.$$

The valence angle and the dihedral angle are defined as follows:

$$\cos\theta_{ijk} = \tilde{\boldsymbol{r}}_{ij} \cdot \tilde{\boldsymbol{r}}_{ik}, \tag{4}$$

$$\cos\varphi_{ijkl} = \tilde{\boldsymbol{n}}_{ijk} \cdot \tilde{\boldsymbol{n}}_{jil}, \qquad \sin\varphi_{ijkl}\tilde{\boldsymbol{r}}_{ij} = (\tilde{\boldsymbol{n}}_{jil} \times \tilde{\boldsymbol{n}}_{ijk}). \tag{5}$$

This said, the variations of r_{ij}, $\cos\theta_{ijk}$ and φ_{ijkl} are given by

$$\delta r_{ij} = \tilde{\boldsymbol{r}}_{ij} \cdot \delta\boldsymbol{u}_{ij}, \tag{6a}$$
$$\delta\cos\theta_{ijk} = \boldsymbol{n}^{\theta}_{ij} \cdot \delta\boldsymbol{u}_{ij} + \boldsymbol{n}^{\theta}_{ik} \cdot \delta\boldsymbol{u}_{ik}, \tag{6b}$$
$$\delta\varphi_{ijkl} = \boldsymbol{n}^{\varphi}_{ij} \cdot \delta\boldsymbol{u}_{ij} + \boldsymbol{n}^{\varphi}_{ik} \cdot \delta\boldsymbol{u}_{ik} + \boldsymbol{n}^{\varphi}_{jl} \cdot \delta\boldsymbol{u}_{jl}, \tag{6c}$$

where

$$\boldsymbol{n}^{\theta}_{ij} = \frac{1}{r_{ij}}(\tilde{\boldsymbol{r}}_{ik} - \cos\theta_{ijk}\tilde{\boldsymbol{r}}_{ij}), \quad \boldsymbol{n}^{\theta}_{ik} = \frac{1}{r_{ik}}(\tilde{\boldsymbol{r}}_{ij} - \cos\theta_{ijk}\tilde{\boldsymbol{r}}_{ik}),$$
$$\boldsymbol{n}^{\varphi}_{ij} = \frac{1}{r_{ij}}\left[\frac{\cos\theta_{jil}}{n_{jil}}\tilde{\boldsymbol{n}}_{jil} - \frac{\cos\theta_{ijk}}{n_{ijk}}\tilde{\boldsymbol{n}}_{ijk}\right],$$
$$\boldsymbol{n}^{\varphi}_{ik} = \frac{1}{r_{ik}n_{ijk}}\,\tilde{\boldsymbol{n}}_{ijk}, \quad \boldsymbol{n}^{\varphi}_{jl} = \frac{1}{r_{jl}n_{jil}}\,\tilde{\boldsymbol{n}}_{jil}.$$

We refer to Blondel and Karplus (1996), Korobeynikov et al. (2015), and Genoese et al. (2019) for more details. The equilibrium configurations of the system are sought through the stationarity condition of its total potential energy

$$\Pi = U - \sum_{n} \boldsymbol{p}_n \cdot \boldsymbol{u}_n, \tag{7}$$

where U, defined in Equations (1, 2), is a function of the displacements of the atoms by means of Equations (3–5), and $\boldsymbol{p}_n$ is the force applied to the n^{th} atom. Recalling Equation (6), the variation of the potential U is

$$\delta U = \sum_{b} \delta\boldsymbol{u}_{ij} \cdot \boldsymbol{s}^{r}_{ij} + \sum_{a}\left(\delta\boldsymbol{u}_{ij} \cdot \boldsymbol{s}^{\theta}_{ij} + \delta\boldsymbol{u}_{ik} \cdot \boldsymbol{s}^{\theta}_{ik}\right) + \sum_{d}\left(\delta\boldsymbol{u}_{ij} \cdot \boldsymbol{s}^{\varphi}_{ij} + \delta\boldsymbol{u}_{ik} \cdot \boldsymbol{s}^{\varphi}_{ik} + \delta\boldsymbol{u}_{jl} \cdot \boldsymbol{s}^{\varphi}_{jl}\right), \tag{8a}$$

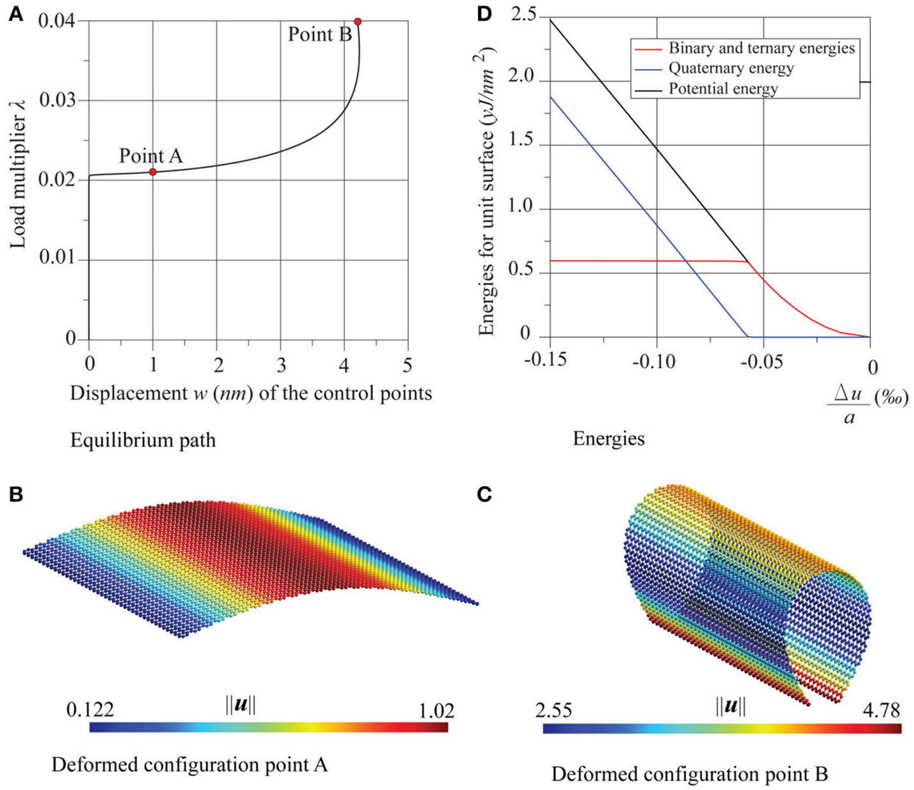

FIGURE 3 | Graphene sheet with two supported edges under compression in the zigzag direction: **(A)** equilibrium path, **(B,C)** deformed configurations at the points *A* and *B*, and **(D)** energies trends.

where

$$
\begin{aligned}
\boldsymbol{s}^{r}_{ij} &= \frac{d\, U^{r}_{b}}{d\, r_{ij}} \tilde{\boldsymbol{r}}_{ij}, \\
\boldsymbol{s}^{\theta}_{\alpha} &= \frac{d\, U^{\theta}_{a}}{d\, \cos\theta_{ijk}} \boldsymbol{n}^{\theta}_{\alpha}, \quad \alpha \in \left\{ij,\, ik\right\}, \\
\boldsymbol{s}^{\varphi}_{\beta} &= \frac{d\, U^{\varphi}_{d}}{d\, \varphi_{ijkl}} \boldsymbol{n}^{\varphi}_{\beta}, \quad \beta \in \left\{ij,\, ik,\, jl\right\}
\end{aligned}
\tag{8b}
$$

are the binary, ternary and quaternary interatomic force vectors. Finally, the equilibrium equations assume the following form

$$
\begin{aligned}
&\sum_{b} \boldsymbol{s}^{r}_{ij} \cdot (\delta \boldsymbol{u}_j - \delta \boldsymbol{u}_i) + \sum_{a} \left[\boldsymbol{s}^{\theta}_{ij} \cdot (\delta \boldsymbol{u}_j - \delta \boldsymbol{u}_i) + \boldsymbol{s}^{\theta}_{ik} \cdot (\delta \boldsymbol{u}_k - \delta \boldsymbol{u}_i) \right] \\
&+ \sum_{d} \left[\boldsymbol{s}^{\varphi}_{ij} \cdot (\delta \boldsymbol{u}_j - \delta \boldsymbol{u}_i) + \boldsymbol{s}^{\varphi}_{ik} \cdot (\delta \boldsymbol{u}_k - \delta \boldsymbol{u}_i) + \boldsymbol{s}^{\varphi}_{jl} \cdot (\delta \boldsymbol{u}_l - \delta \boldsymbol{u}_j) \right] \\
&= \sum_{n} \boldsymbol{p}_n \cdot \delta \boldsymbol{u}_n
\end{aligned}
\tag{9}
$$

for any $\delta \boldsymbol{u}_n$.

2.2. Nanoscale Material Parameters

The potential functions given in Equation (2) are characterized by four parameters, $\bar{U}$,β, C and V. In this work, we use $\beta = 21.671$ 1/nm, $\bar{U} = 0.79$ aJ, and $C = 1.893$ aJ, which provide the force constants $k_r = 742$ nN/nm and $k_\theta = 1.42$ aJ, since these values have shown to well describe the in-plane strength and rigidity of graphene (Genoese et al., 2017). In order to properly define V, we associate the potential related to the dihedral angle to that of a plate with thickness tending to zero in linearized elasticity. By doing this, it can be shown that the following equality holds[1]:

$$
D = \frac{14\sqrt{3}}{3} V,
$$

where D is the bending stiffness of the plate. Then, V is calculated from the *ab-initio* result $D = 0.234$ aJ in Kudin et al. (2001), and it results to be $V = 0.029$ aJ. Last but not least, we obtain the value of the corresponding force constant k_φ, given by

$$
k_\varphi = \left. \frac{d^2\, U^{\varphi}_{d}}{d\, \varphi^2_{ijkl}} \right|_{\varphi_{ijkl} = \bar{\varphi}_{ijkl}} = 2V = 0.058\, aJ. \tag{10}
$$

2.3. Numerical Methods

The model has been implemented in the MATLAB” language. By using FEM standard assembly procedures the equilibrium

---

[1] Analytical developments will be given in a forthcoming paper.

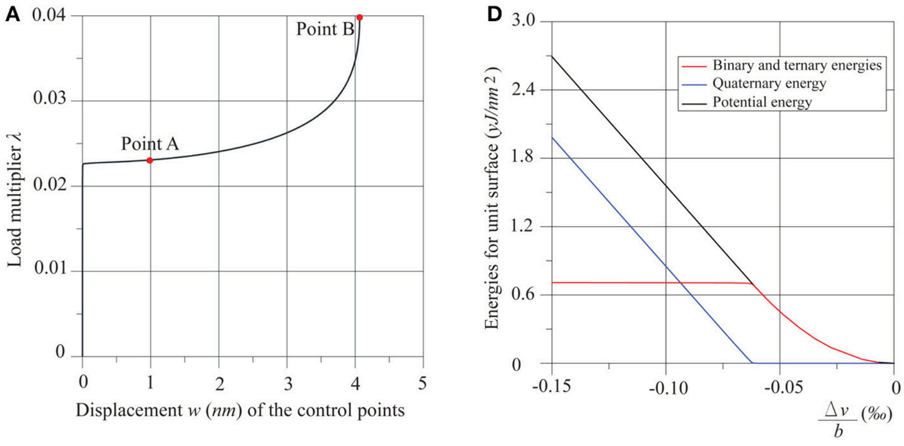

Equilibrium path

Energies

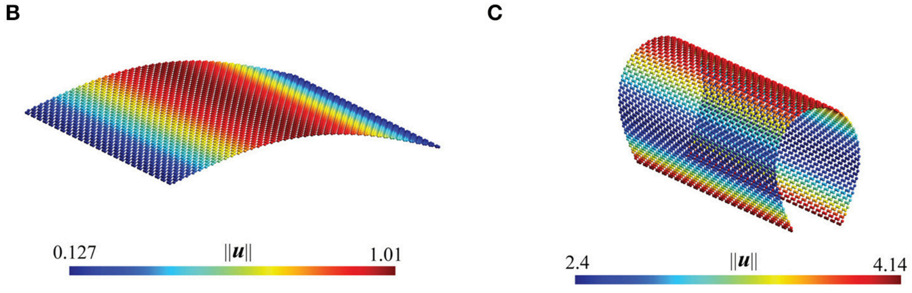

Deformed configuration point A

Deformed configuration point B

FIGURE 4 | Graphene sheet with two supported edges under compression in the armchair direction: **(A)** equilibrium path, **(B,C)** deformed configurations at the points *A* and *B*, and **(D)** energies trends.

equations are recast in the global form

$$\boldsymbol{s}[\boldsymbol{u}] - \boldsymbol{p} = \boldsymbol{0}, \tag{11}$$

where $\boldsymbol{u}$ collects all the kinematic variables, $\boldsymbol{s}$ is the inner force vector and $\boldsymbol{p}$ collects all the external loads which we express in the form $\boldsymbol{p} = \lambda\hat{\boldsymbol{p}}$, λ being a scalar load multiplier and $\hat{\boldsymbol{p}}$ the nominal loads vector. The pairs $(\boldsymbol{u}, \lambda)$ that satisfy Equation (11) define the equilibrium path of the graphene sheet. In this work it is obtained through the Riks arc-length method (Riks, 1979, 1984).

As opposed to the traditional step-by-step procedures based on a parametrization of the equilibrium path in terms of the load multiplier λ or of any displacement variable, the arc-length method describes the equilibrium path in terms of the variable ξ related to the arc-length. This implies adding a new constraint equation $\xi = g[\boldsymbol{u}, \lambda]$. The equilibrium points of the path are then obtained by solving a non-linear extended system, using the Modified Newton-Raphson method and condensing the constraint equation in order to assemble and decompose only the stiffness matrix $\boldsymbol{K} = \dfrac{\partial \boldsymbol{s}}{\partial \boldsymbol{u}}$. The modified set of equations become singular only at a bifurcation point that, however, can be transformed into a simple fold by introducing small imperfection loads spending work on the critical direction.

TABLE 1 | Comparison between critical multipliers.

	Zigzag		Armchair	
	λ_E	λ_{cr}	λ_E	λ_{cr}
First Mode	0.0209	0.02003	0.0227	0.0224

The numerical analysis becomes more complex when multiple simultaneous or nearly simultaneous modes are found on the fundamental equilibrium path. Using a step-by-step numerical algorithm based on Riks arc-length strategy, the presence of simultaneous or nearly simultaneous modes manifests itself in the form of abrupt changes of the equilibrium configurations, named as *mode jumping* in the literature (Duan et al., 2011). In these cases, the prior knowledge of such critical modes is necessary in order to understand which of these directions (or linear combination thereof) are actually

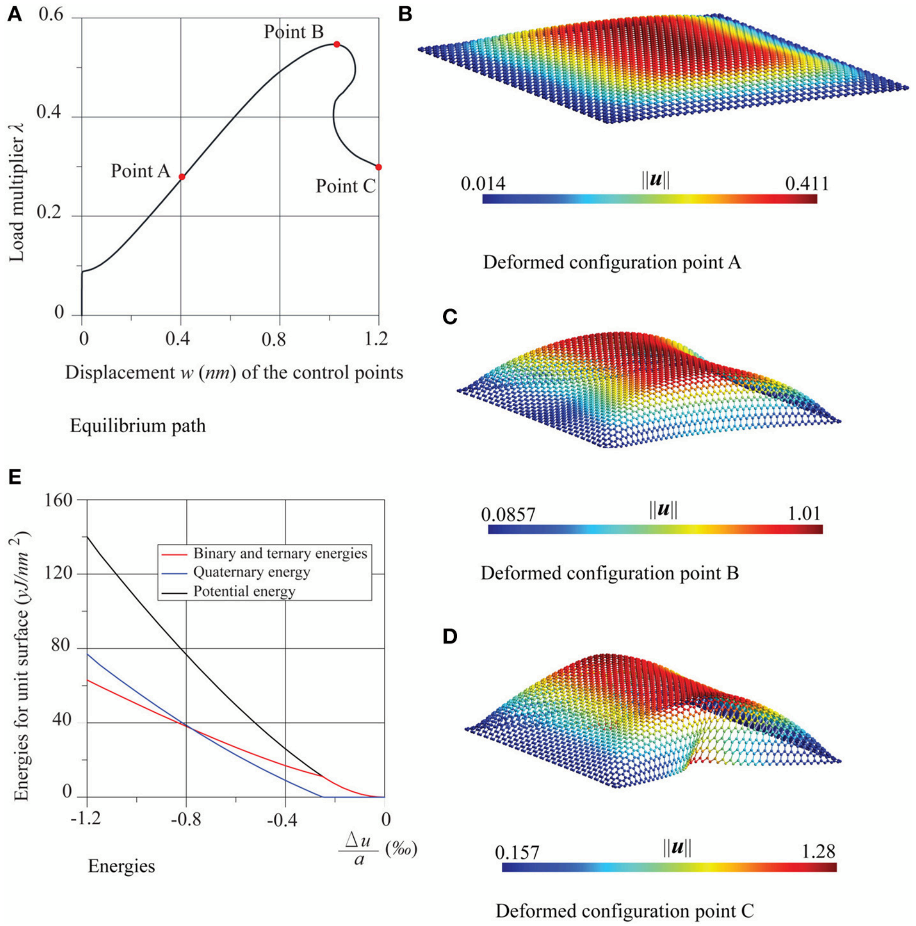

FIGURE 5 | Graphene sheet with four supported edges under compression in the zigzag direction: **(A)** equilibrium path, **(B–D)** deformed configurations at the points *A*, *B* and *C*, and **(E)** energies trends.

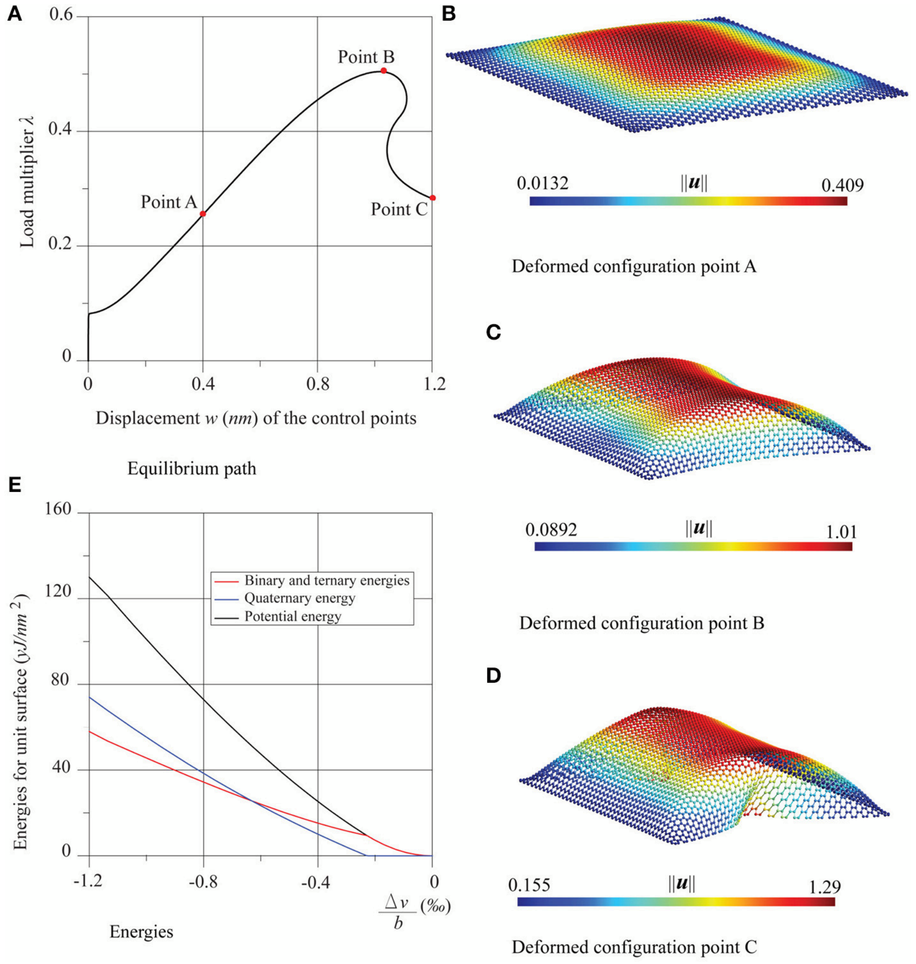

FIGURE 6 | Graphene sheet with four supported edges under compression in the armchair direction: **(A)** equilibrium path, **(B–D)** deformed configurations at the points *A*, *B* and *C*, and **(E)** energies trends.

TABLE 2 | Comparison between critical multipliers.

	Zigzag		Armchair	
	λ_E	λ_{cr}	λ_E	λ_{cr}
First Mode	0.0908	0.088	0.0837	0.082

reachable in post-critical analysis and which, instead, are geometrical *loci* of secondary bifurcations. For this purpose, any step of the analysis has been accompanied by the updating of the tangent stiffness matrix and determination of its kernel, by eigenvalue analysis, at very close values of the load parameter λ.

3. RESULTS

Numerical benchmark examples regarding graphene sheets under compression and shear are solved.

3.1. Square Graphene Under Compression and Shear

Figure 2 shows the geometrical configuration of a nearly square graphene sheet ($a = 10.508$ nm and $b = 10.084$ nm) and, in some detail, the loading conditions for the compression tests, in both zigzag and armchair directions, and for the pure shear test. The compression tests are carried out considering constraint conditions of simple support for the only loaded sides and for all the sides. The shear test is carried out considering conditions of simple support for all the sides. In all cases, $N = 1$ nN/nm is assumed. In addition, small imperfection forces, perpendicular to the plane of the sheet, are applied in correspondence to the atoms evidenced in red that are assumed to be control points to give the equilibrium paths.

In **Figures 3**, **4** the results of the compression tests in the case of two supported edges are shown. The equilibrium paths, very far beyond the first critical point, and the deformed configurations, at the points *A* and *B*, respectively, are depicted, revealing a typical stable behavior from Euler compressed rods. The comparison between critical multiplier values λ_{cr} and those obtained analytically by the Eulerian formula $\lambda_E N = \pi^2 D/a^2$ for the zigzag case, and $\lambda_E N = \pi^2 D/b^2$ for the armchair case is shown in **Table 1** which, on one hand, shows a good agreement between numerical and analytical results and, on the other hand, highlights the very low influence of chirality in the out-of plane nonlinear behavior of these nanostructures as already noticed in Sgouros et al. (2018). The small numerical differences found in the values calculated for zigzag and armchair cases are mostly related to the different values of a and b.

In the same **Figures 3**, **4** the trends of the potential energy of the sheet are shown, in the range of the equilibrium path between the initial undeformed configuration and that immediately successive to the critical one. Also, the energy contributions are shown as decoupled, separating the contribution due to membrane deformation, that is, the sum of binary and ternary energies, from the quaternary contribution, which is inherently flexural. All the energies are measured with respect to the resting state of the sheet and divided by its reference surface $a \times b$, while the deformation of the sheet is given in terms of the non-dimensional relative displacements $\Delta u/a = (\bar{u}_4 - \bar{u}_3)/a$ and $\Delta v/b = (\bar{v}_2 - \bar{v}_1)/b$, $\bar{u}_k$ and $\bar{v}_k$ being the mean values of the displacements along x and y on the side k.

Diagrams show that in these two cases pre-critical behavior employs purely membranal energy, while post-critical behavior uses bending energy. Moreover, it is worth noting that energy is quadratic in the pre-critical behavior, which coincides with what was reported in the literature (Liew et al., 2004; Silvestre et al., 2012) for compressed carbon nanotubes.

In **Figures 5**, **6** the results of the compression tests in the case of four supported edges are shown. The equilibrium paths and the deformed configurations, in the points A, B, and C are reported. The sheet presents a similar behavior, both with regard to the equilibrium path and the deformed configurations regardless of the direction of the compression. After an initial stable post-critical behavior (point A), the equilibrium paths present a limit load configuration (point B), followed by an unstable branch. The deformed configurations are similar, corresponding to the three points A, B, and C, which turn out first bubble-shaped and then increasingly wrapped.

Once again, the comparison is positive between the numerical critical multiplier values λ_{cr}, and those obtained analytically by the formulas of buckling of Timoshenko (Timoshenko and Gere, 1963) for fully supported thin plates, namely $\lambda_E N = k\pi^2 D/b^2$ for the zigzag case and $\lambda_E N = k\pi^2 D/a^2$ for the armchair case, with $k = 4$. The comparison is given in **Table 2**, which highlights the very low influence of chirality in the nonlinear behavior of these nanostructures. In the same **Figures 5**, **6**, the energy diagrams reveal that the pre-critical behavior of the sheets is likewise purely membranal and characterized by a linear behavior. However, unlike in the previous examples, in the post-critical behavior, membranal and flexural energies coexist. The same considerations can be made for the shear test, whose results are shown in **Figure 7**, where $\Delta u = \bar{u}_2 - \bar{u}_1$ and $\Delta v = \bar{v}_4 - \bar{v}_3$.

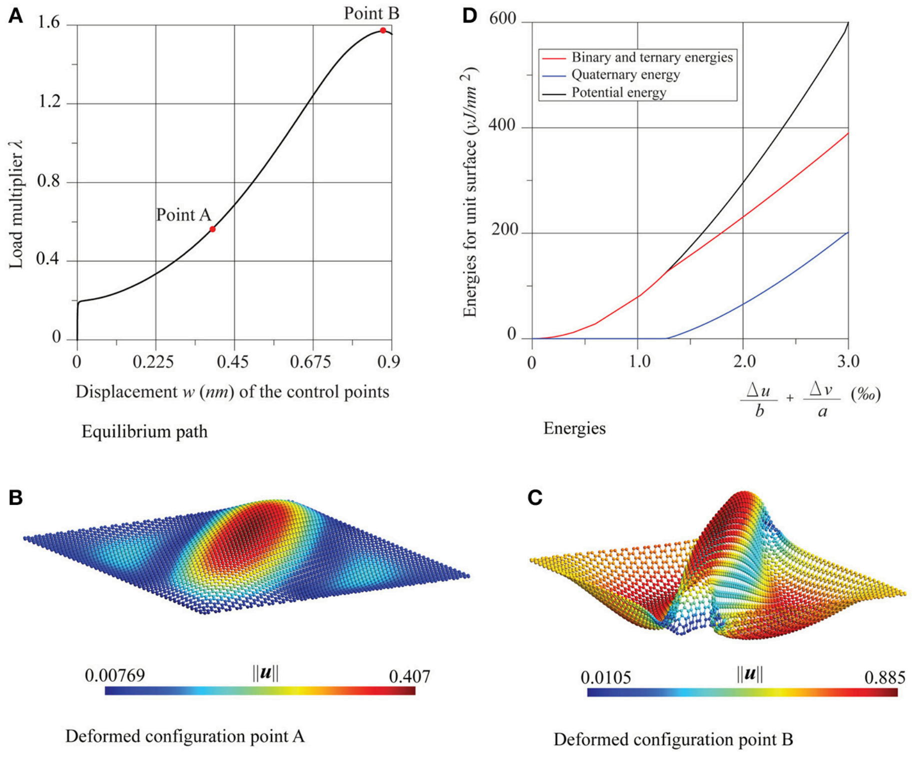

FIGURE 7 | Graphene sheet under shear: **(A)** equilibrium path, **(B,C)** deformed configurations at the points *A* and *B*, and **(D)** energies trends.

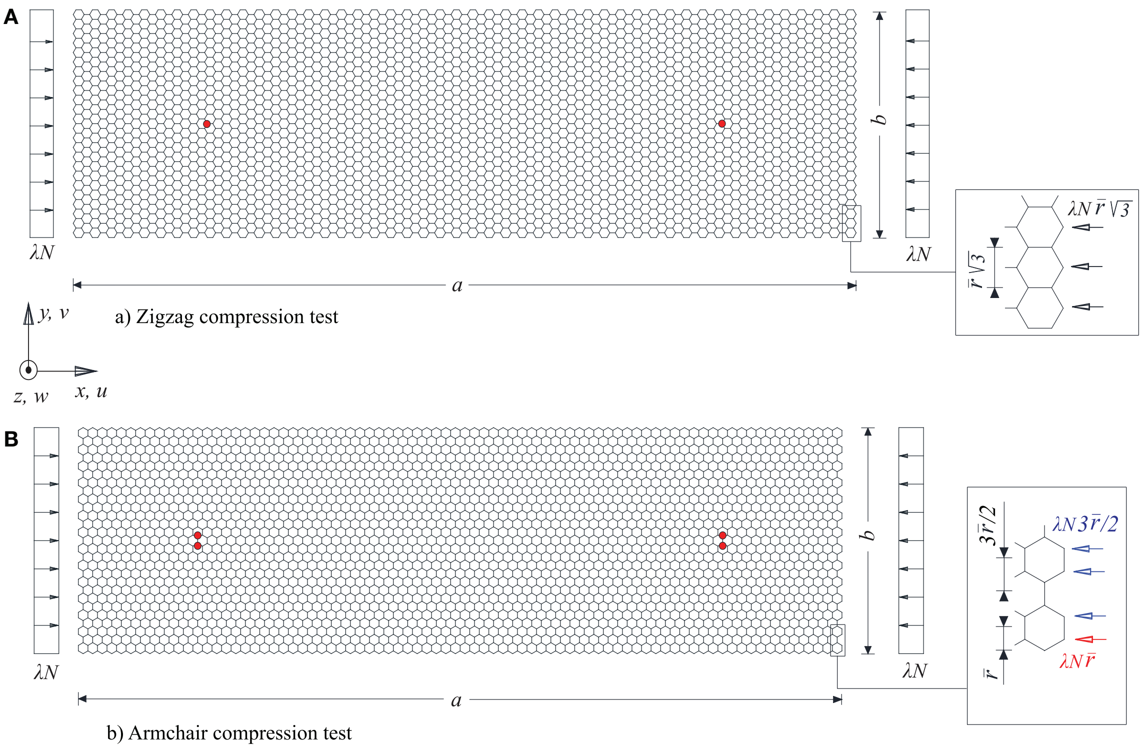

FIGURE 8 | Schemes of the compression tests of the graphene strips: **(A)** geometry and details of the applied loads for the compression test in the zigzag direction, **(B)** geometry, and details of the applied loads for the compression test in the armchair direction.

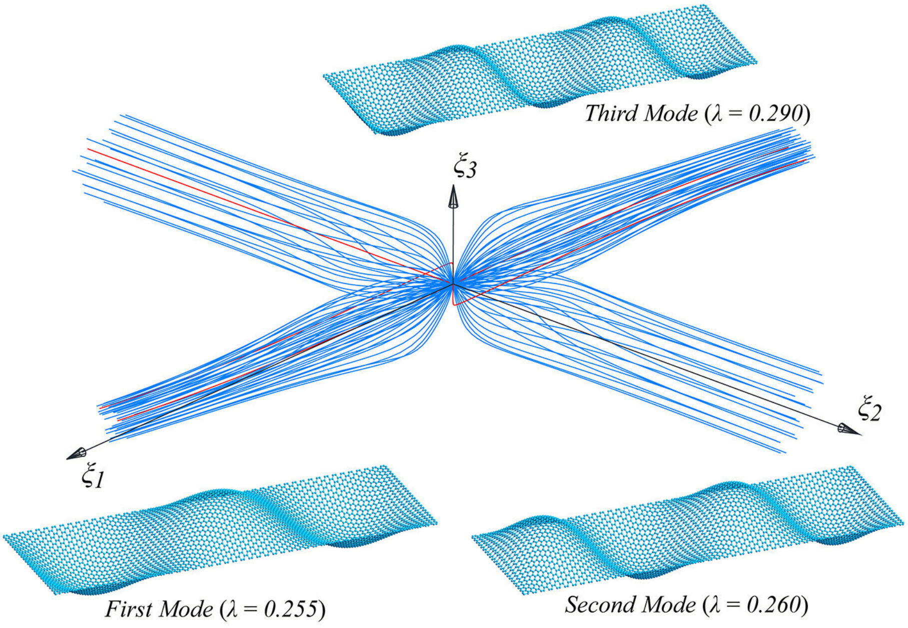

FIGURE 9 | Supported graphene strips under compression in the zigzag direction: first three buckling modes and their interaction.

The equilibrium path, after an initial stable post-critical behavior (point A), presents a limit load (point B). The critical multiplier estimated numerically λ_{cr} agrees well with the analytical value predicted by the theory of Timoshenko (Timoshenko and Gere, 1963) for thin plates subjected to shear, that is $\lambda_E N = k\pi^2 D/b^2$ where $k = 5.35 + 4(b/a)^2 = 9.0337$. The comparison is as follows:

$$\lambda_E = 0.205 \qquad \lambda_{cr} = 0.194.$$

The initial post-critical configuration (point *A*) has the shape of a bubble elongated toward the direction of the principal traction, already highlighted in the literature (Huang and Han, 2017). At the limit load configuration (point *B*) the deformation is accentuated and, in addition to the diagonal crest, two lateral troughs arise.

3.2. Graphene Strips Under Compression

Figure 8 shows the geometry and the nodal loads of the strips under compression in the zigzag ($a = 20.306$ nm and $b = 5.91$ nm) and in the armchair ($a = 19.676$ nm and $b = 5.822$ nm) directions. In both cases only conditions of simple support for the entire boundary are imposed and $N = 1$ nN/nm is assumed. The analyses have turned out to be more complex than in the case of the nearly square sheet, due to the presence of nearly simultaneous modes.

TABLE 3 | Comparison between critical multipliers.

	Zigzag		Armchair	
	λ_E	λ_{cr}	λ_E	λ_{cr}
First Mode	0.2701	0.255	0.2764	0.270
Second Mode	0.2712	0.260	0.2803	0.271
Third Mode	0.3039	0.290	0.3165	0.310

In that regard, **Figures 9**, **11** show that in both cases, the fundamental equilibrium path presents three nearly simultaneous modes, two of them almost coincident and the third one at a small distance from the first two. The critical multipliers determined by numerical analyses λ_{cr} show a good agreement with the analytical solution provided by Timoshenko for the first three critical modes for the same problem, whose expressions are $\lambda_E N = k\pi^2 D/b^2$, where $k = (mb/a + a/(bm))^2$, m is the number of the half-waves of the critical mode. The comparison between numerical and analytical results is shown in **Table 3**.

As can be seen in **Figures 9**, **11** many post-critical equilibrium paths are obtained when small imperfection loads are added, which are chosen to be a linear combination of the critical modes, and are projected onto the modal subspace (ξ_1, ξ_2, ξ_3) (Salerno and Casciaro, 1997). The number of overall analysis is 114, and each of them is characterized by a different shape (or direction) of the imperfection. In agreement with the literature (Salerno and Casciaro, 1997), the 114 equilibrium paths cluster around only two directions, the first two modes, whichever is the initial imperfection to which the path is initially pushed, creating the typical zone

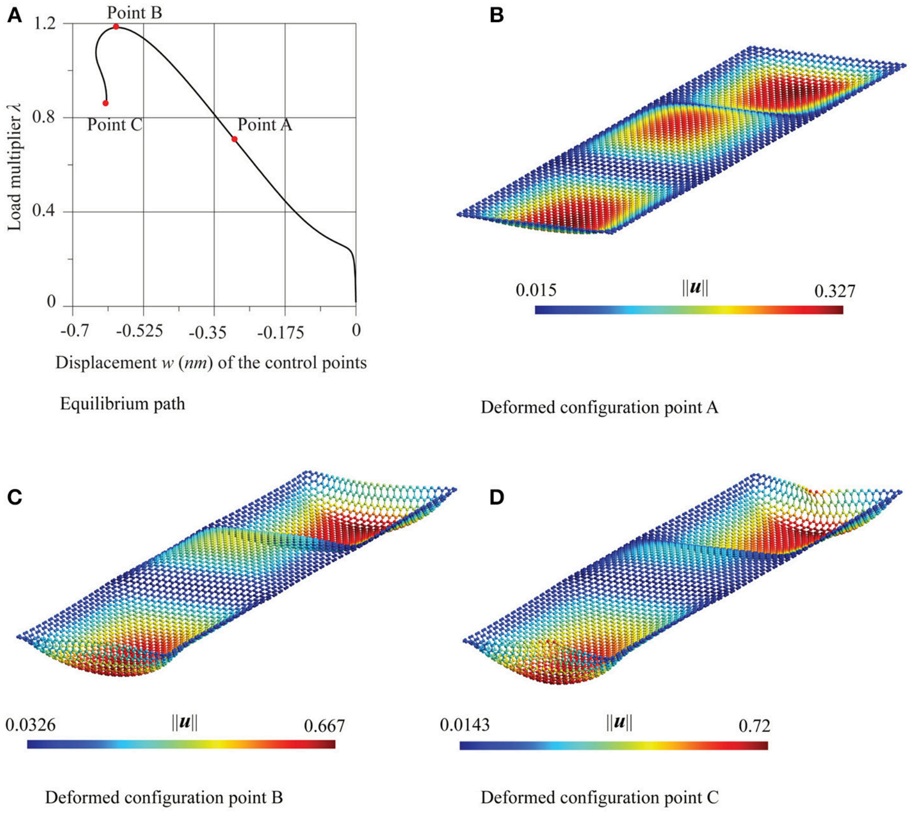

Equilibrium path

Deformed configuration point A

Deformed configuration point B

Deformed configuration point C

FIGURE 10 | Supported graphene strips under compression in the zigzag direction: **(A)** equilibrium path and **(B–D)** deformed configurations at the points *A*, *B*, and *C*.

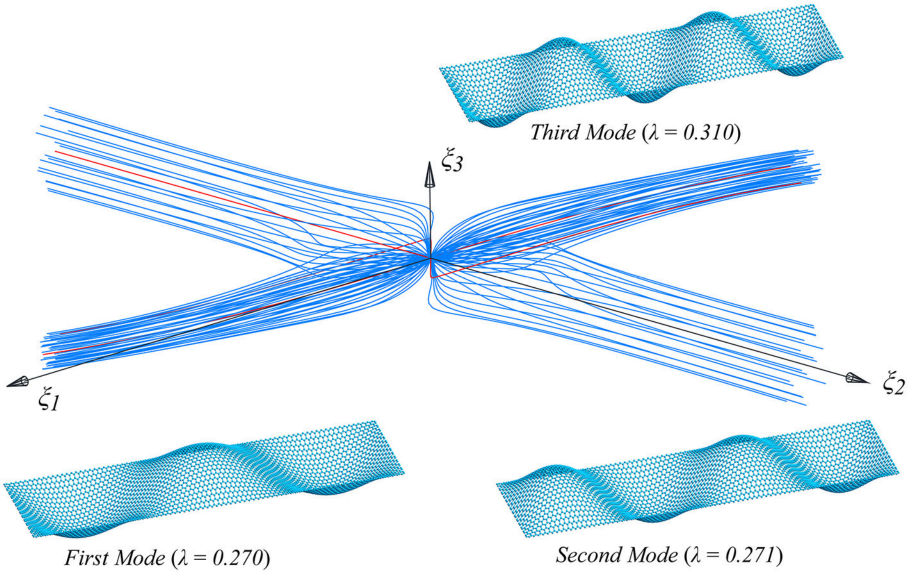

FIGURE 11 | Supported graphene strips under compression in the armchair direction: first three buckling modes and their interaction.

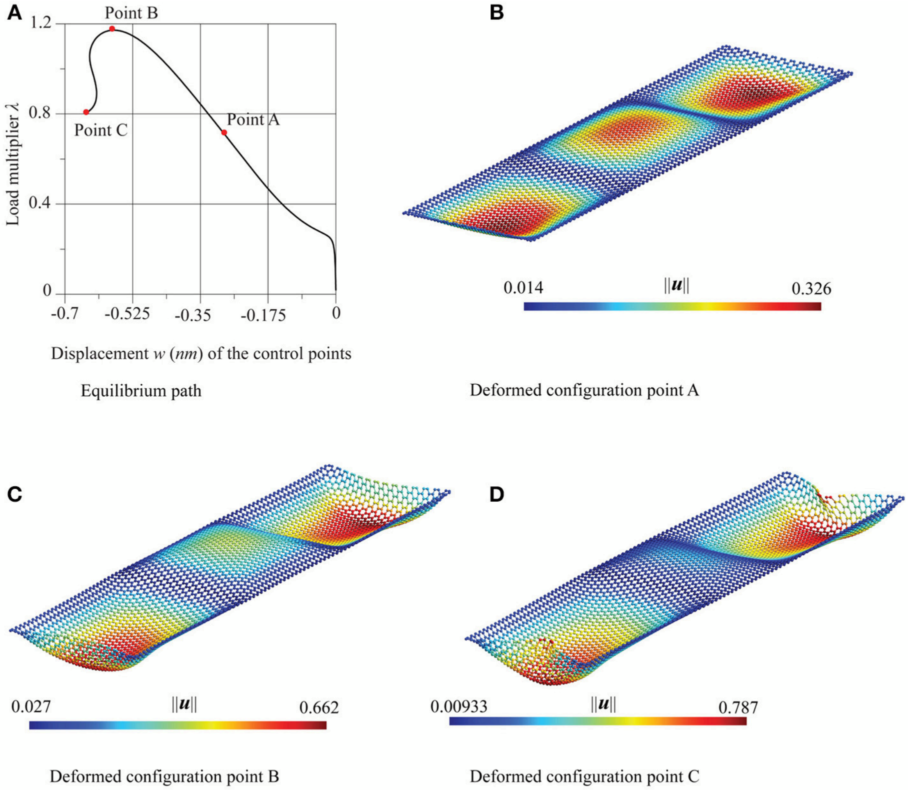

FIGURE 12 | Supported graphene strips under compression in the armchair direction: **(A)** equilibrium path and **(B–D)** deformed configurations at the points *A*, *B*, and *C*.

of post-critical attractiveness, with sudden post-critical bifurcations, shown in **Figures 9**, **11**, when moving in the direction of the third mode, which are usually called *mode jumping*.

That said, if we focus our attention just on the imperfection in the direction of the first mode, we get only one equilibrium path, characterized by the smallest limit load value, by the parity of the norm of the additional imperfection.

Figures 10, **12** show the paths relative to this imperfection with reference to the zigzag and the armchair case, respectively. In both cases, the displacement in abscissa is the transversal one of the control points evidenced in red in **Figure 8**. The paths share the same features: after an initial stable bifurcation, a limit load point is reached, followed by an unstable behavior. For both cases three successive configurations, in the points *A*, *B*, and *C* of the equilibrium path, are depicted. After an initial configuration characterized by three half-waves (point *A*), similarly to the selected critical mode, the successive configurations (points *B* and *C*) take a more wrapped form, also characterized by an approach of the edges of the strip left free to move horizontally. Both in terms of equilibrium path and of deformed configurations, the chirality has very little influence.

4. CONCLUSIONS

In the present paper, the critical and post-critical behaviors of graphene, under compression in the zigzag and in the armchair directions, and shear have been investigated. A molecular mechanics model that takes into account binary, ternary and quaternary interactions has been implemented extending our previous works (Genoese et al., 2017, 2018a,b, 2019) in which only the in-plane behavior of graphene has been addressed. A geometrically exact setting and Morse and cosine potential functions, equipped with a proper set of parameters have been used to model the interatomic interactions and, at the same time, a new parametrization of the dihedral potential has been given. For each case study, the equilibrium path has been reconstructed in the advanced post-critical behavior through the arc-length strategy and some deformed configurations, deemed to be the most significant, have been displayed. This adds significantly to the existing literature, as this type of behavior has so far been little investigated. Our findings show the suitability of standard thin-plates theories to predict simple critical behaviors both for nearby square sheets, under various edge constraint conditions, and strips. Moreover, they highlight the very low influence of chirality in the nonlinear behavior of these nanostructures. The research work carried out in this paper could be the first step toward investigating the nonlinear behavior of 2D nanomaterials other than graphene or of more complex 3-dimensional nanostructures, such as tubes.

AUTHOR CONTRIBUTIONS

ALG and ANG developed the formulation and the implementation of the molecular mechanics model under the supervision of GS and NR. All the authors collaborated on the writing of the manuscript.

ACKNOWLEDGMENTS

We are very grateful to the University Roma Tre for cofunding the research contracts of Ph.D. ALG and ANG.

REFERENCES

Aïssa, B., Memon, N. K., Ali, A., and Khraisheh, M. K. (2015). Recent progress in the growth and applications of graphene as a smart material: a review. *Front. Mater.* 2:58. doi: 10.3389/fmats.2015.00058

Akinwande, D., Brennan, C. J., Bunch, J. S., Egberts, P., Felts, J. R., and Gao, H. (2017). A review on mechanics and mechanical properties of 2D materials-graphene and beyond. *Extreme Mech. Lett.* 13, 42–72. doi: 10.1016/j.eml.2017.01.008

Alzebdeh, K. (2012). Evaluation of the in-plane effective elastic moduli of single-layered graphene sheet. *Int. J. Mech. Mater. Des.* 8, 269–278. doi: 10.1007/s10999-012-9193-7

Aminpour, H., and Rizzi, N. (2016). A one-dimensional continuum with microstructure for single-wall carbon nanotubes bifurcation analysis. *Math. Mech. Solids* 21, 168–181. doi: 10.1177/1081286515577037

Baumeier, B., Krüger, P., and Pollmann, J. (2007). Structural, elastic, and electronic properties of SiC, BN, and BeO nanotubes. *Phys. Rev. B* 76:085407. doi: 10.1103/PhysRevB.76.085407

Berinskii, I. E., and Borodich, F. M. (2013). Elastic in-plane properties of 2D linearized models of graphene. *Mech. Mater.* 62, 60–68. doi: 10.1016/j.mechmat.2013.03.004

Blondel, A., and Karplus, M. (1996). New formulation for derivatives of torsion angles and improper torsion angles in molecular mechanics: Elimination of singularities. *J. Comput. Chem.* 17, 1132–1141.

Budarapu, P. R., Javvaji, B., Sutrakar, V. K., Mahapatra, D. R., Paggi, M., Zi, G., et al. (2017). Lattice orientation and crack size effect on the mechanical properties of Graphene. *Int. J. Fract.* 203, 81–98. doi: 10.1007/s10704-016-0115-9

Chang, T. (2010). A molecular based anisotropic shell model for single-walled carbon nanotubes. *J. Mech. Phys. Solids* 58, 1422–1433. doi: 10.1016/j.jmps.2010.05.004

Choi, W., Lahiri, I., Seelaboyina, R., and Kang, Y. S. (2010). Synthesis of graphene and its applications: a review. *Crit. Rev. Solid State Mater. Sci.* 35, 52–71. doi: 10.1080/10408430903505036

Davini, C. (2014). Homogenization of a graphene sheet. *Continuum Mech. Thermodyn.* 26, 95–113. doi: 10.1007/s00161-013-0292-y

Davini, C., Favata, A., and Paroni, R. (2017). The Gaussian stiffness of graphene deduced from a continuum model based on Molecular Dynamics potentials. *J. Mech. Phys. Solids* 104, 96–114. doi: 10.1016/j.jmps.2017.04.003

Duan, W. H., Gong, K., and Wang, Q. (2011). Controlling the formation of wrinkles in a single-layer graphene sheet subjected to in-plane shear. *Carbon* 49, 3107–3112. doi: 10.1016/j.carbon.2011.03.033

Firouz-Abadi, R. D., Moshrefzadeh-Sany, H., Mohammadkhani, H., and Sarmadi, M. (2016). A modified molecular structural mechanics model for the buckling analysis of single layer graphene sheet. *Solid State Commun.* 225, 12–16. doi: 10.1016/j.ssc.2015.10.009

Gamboa, A., Vignoles, G. L., and Leyssale, J.-M. (2015). On the prediction of graphene's elastic properties with reactive empirical bond order potential. *Carbon* 89, 176–187. doi: 10.1016/j.carbon.2015.03.035

Genoese, A., Genoese, A., Rizzi, N. L., and G., S. (2017). On the derivation of the elastic properties of lattice nanostructures: the case of graphene sheets. *Compos B Eng.* 115, 316–329. doi: 10.1016/j.compositesb.2016.09.064

Genoese, A., Genoese, A., Rizzi, N. L., and Salerno, G. (2018a). Force constants of BN, SiC, AlN and GaN sheets through discrete homogenization. *Meccanica* 53, 593–611. doi: 10.1007/s11012-017-0686-1

Genoese, A., Genoese, A., and Salerno, G. (2018b). Elastic constants of achiral single-wall CNTs: analytical expressions and a focus on size and small scale effects. *Compos B Eng.* 147, 207–226. doi: 10.1016/j.compositesb.2018.04.016

Genoese, A., Genoese, A., and Salerno, G. (2019). On the nanoscale behaviour of single-wall C, BN and SiC nanotubes. *Acta Mech*. doi: 10.1007/s00707-018-2336-7. [Epubh ahead of print].

Georgantzinos, S. K., Giannopoulos, G. I., and Anifantis, N. K. (2010). Numerical investigation of elastic mechanical properties of graphene structures. *Mater. Des.* 31, 4646–4654. doi: 10.1016/j.matdes.2010.05.036

Georgantzinos, S. K., Katsareas, D. E., and Anifantis, N. K. (2012). Limit load analysis of graphene with pinhole defects: a nonlinear structural mechanics approach. *Int. J. Mech. Sci.* 55, 85–94. doi: 10.1016/j.ijmecsci.2011.12.006

Ghaffari, R., Duong, T. X., and Sauer, R. A. (2018). A new shell formulation for graphene structures based on existing ab-initio data. *Int. J. Solids Struct.* 135, 37–60. doi: 10.1016/j.ijsolstr.2017.11.008

Giannopoulos, G. I. (2012). Elastic buckling and flexural rigidity of graphene nanoribbons by using a unique translational spring element per interatomic interaction. *Comput. Mater. Sci.* 53, 338–395. doi: 10.1016/j.commatsci.2011.08.027

Hossain, M. Z., Hao, T., and Silverman, B. (2018). Stillinger-Weber potential for elastic and fracture properties in graphene and carbon nanotubes. *J. Phys. Condens Matter* 30:055901. doi: 10.1088/1361-648X/aaa3cc

Huang, J., and Han, Q. (2017). A molecular dynamic study on wrinkles in graphene with simply supported boundary under in-plane shear. *J. Nanomater.* 2017:1326790. doi: 10.1155/2017/1326790

Korobeynikov, S. N., Alyokhin, V. V., Annin, B. D., and Babichev, A. V. (2015). Quasi-static buckling simulation of single-layer graphene sheets by the molecular mechanics method. *Math. Mech. Solids* 20, 836–870. doi: 10.1177/1081286514554353

Korobeynikov, S. N., Alyokhin, V. V., and Babichev, A. V. (2018). Simulation of mechanical parameters of graphene using the DREIDING force field. *Acta Mech.* 229, 2343–2378. doi: 10.1007/s00707-018-2115-5

Kudin, K. N., Scuseria, G. E., and Yakobson, B. I. (2001). C_2F, BN, and C nanoshell elasticity from ab initio computations. *Phys. Rev. B* 64:235406. doi: 10.1103/PhysRevB.64.235406

Kumar, R., Singh, R., Hui, D., Feo, L., and Fraternali, F. (2018). Graphene as biomedical sensing element: state of art review and potential engineering applications. *Compos B Eng.* 134, 193–206. doi: 10.1016/j.compositesb.2017.09.049

Li, P., Chen, C., Zhang, J., Li, S., Sun, B., and Bao, Q. (2014). Graphene-based transparent electrodes for hybrid solar cells. *Front. Mater.* 1:26. doi: 10.3389/fmats.2014.00026

Liew, K. M., Wong, C. H., He, X. Q., Tan, M. J., and Meguid, S. A. (2004). Nanomechanics of single and multiwalled carbon nanotubes. *Phys. Rev. B* 69:115429. doi: 10.1103/PhysRevB.69.115429

Liu, F., Ming, P., and Li, J. (2007). Ab initio calculation of ideal strength and phonon instability of graphene under tension. *Phys. Rev. B* 76:064120. doi: 10.1103/PhysRevB.76.064120

Lu, Q., Arroyo, M., and Huang, R. (2009). Elastic bending modulus of monolayer graphene. *J. Phys. D Appl. Phys.* 42:102002. doi: 10.1088/0022-3727/42/10/102002

Mayo, S. L., Olafson, B. D., and Goddard III, W. A. (1990). DREIDING: A generic force field for molecular simulations. *J. Phys. Chem.* 94, 8897–8909. doi: 10.1021/j100389a010

Mohan, V. B., Lau, K.-T., Hui, D., and Bhattacharyy, D. (2018). Graphene-based materials and their composites: a review on production, applications and product limitations. *Compos B Eng.* 142, 200–220. doi: 10.1016/j.compositesb.2018.01.013

Nguyen, B. H., and Nguyen, V. H. (2016). Promising applications of graphene and graphene-based nanostructures. *Adv. Nat. Sci.* 7:023002. doi: 10.1088/2043-6262/7/2/023002

Rafiee, R. and Eskandariyun, A. (2017). Comparative study on predicting Young's modulus of graphene sheets using nano- scale continuum mechanics approach. *Physica E* 90, 42–48. doi: 10.1016/j.physe.2017.03.006

Riks, E. (1979). An incremental approach to the solution of snapping and buckling problems. *Int. J. Solids Struct.* 15, 529–551. doi: 10.1016/0020-7683(79)90081-7

Riks, E. (1984). Some computational aspects of the stability analysis of nonlinear structures. *Comput. Methods Appl. Mech. Engrgy* 47, 219–259. doi: 10.1016/0045-7825(84)90078-1

Sakhaee-Pour, A. (2009a). Elastic buckling of single-layered graphene sheet. *Comput. Mater. Sci.* 45, 266–270. doi: 10.1016/j.commatsci.2008.09.024

Sakhaee-Pour, A. (2009b). Elastic properties of single-layered graphene sheet. *Solid State Commun.* 149, 91–95. doi: 10.1016/j.ssc.2008.09.050

Salerno, G., and Casciaro, R. (1997). Mode jumping and attrative paths in multimode elastic buckling. *Int. J. Numer. Methods Eng.* 40, 833–861.

Savvas, D., and Stefanou, G. (2018). Determination of random material properties of graphene sheets with different types of defects. *Compos B Eng.* 143, 47–54. doi: 10.1016/j.compositesb.2018.01.008

Sgouros, A. P., Kalosakas, G., Papagelis, K., and Galiotis, C. (2018). Compressive response and buckling of graphene nanoribbons. *Sci. Rep.* 8:9593. doi: 10.1038/s41598-018-27808-0

Silvestre, N., Faria, B., and Canongia Lopes, J. (2012). A molecular dynamics study on the thickness and post-critical strength of carbon nanotubes. *Compos Struct.* 94, 1352–1358. doi: 10.1016/j.compstruct.2011.10.029

Singh, S., and Patel, B. P. (2018a). A computationally efficient multiscale finite element formulation for dynamic and postbuckling analyses of carbon nanotubes. *Comput. Struct.* 195, 126–144. doi: 10.1016/j.compstruc.2017.10.003

Singh, S., and Patel, B. P. (2018b). Nonlinear elastic properties of graphene sheet using MM3 potential under finite deformation. *Compos B Eng.* 136, 81–91. doi: 10.1016/j.compositesb.2017.10.024

Sun, C., Wen, B., and Bai, B. (2015). Recent advances in nanoporous graphene membrane for gas separation and water purification. *Sci. Bull.* 60, 1807–1823. doi: 10.1007/s11434-015-0914-9

Theodosiou, T. C., and Saravanos, D. A. (2014). Numerical simulation of graphene fracture using molecular mechanics based nonlinear finite elements. *Comput. Mater. Sci.* 82, 56–65. doi: 10.1016/j.commatsci.2013.09.032

Timoshenko, S. P., and Gere, J. M. (1963). *Theory of Elastic Stability*. New York, NY: McGraw–Hill.

Tserpes, K. I. (2012). Strength of graphenes containing randomly dispersed vacancies. *Acta Mech.* 223, 669–678. doi: 10.1007/s00707-011-0594-8

Xiao, J. R., Staniszewski, J., and Gillespie Jr., J. (2009). Fracture and progressive failure of defective graphene sheets and carbon nanotubes. *Compos Struct.* 88, 602–609. doi: 10.1016/j.compstruct.2008.06.008

Young, R. J., Kinloch, I. A., Gong, L., and Novoselov, K. S. (2012). The mechanics of graphene nanocomposites: a review. *Compos Sci. Technol.* 72, 1459–1476. doi: 10.1016/j.compscitech.2012.05.005

Zhang, Y., Liew, K. M., and Hui, D. (2018). Characterizing nonlinear vibration behavior of bilayer graphene thin films. *Compos B Eng.* 145, 197–205. doi: 10.1016/j.compositesb.2018.03.004

Zhao, H., Min, K., and Aluru, N. (2009). Size and chirality dependent elastic properties of graphene nanoribbons under uniaxial tension. *Nano Lett.* 9, 3012–3015. doi: 10.1021/nl901448z

Conflict of Interest Statement: The authors declare that the research was conducted in the absence of any commercial or financial relationships that could be construed as a potential conflict of interest.

frontiers in Materials

ORIGINAL RESEARCH
published: 08 March 2019
doi: 10.3389/fmats.2019.00035

The Influence of a Lattice-Like Pattern of Inclusions on the Attenuation Properties of Metaconcrete

Deborah Briccola, Marianna Tomasin, Teresa Netti and Anna Pandolfi*

Department of Civil and Environmental Engineering, Politecnico di Milano, Milan, Italy

The attenuation performance of metaconcrete specimens characterized by a lattice-like pattern of bi-material resonant inclusions was verified through nondestructive transmission tests spanning the sonic range of frequencies. Seven cubic specimens of metaconcrete with regularly disposed resonant inclusions have been cast from a standard concrete matrix. Inclusions were regularly spaced and symmetrically arranged in a three-dimensional setting. Specimens differ in terms of inclusion spacing, controlled by varying the number of inclusions (0, 8, 27, and 64) and the cement cover. Three-month cured specimens have been tested along the three symmetry axes, under a sinusoidal excitation with four linearly variable frequency sweeping ranges centered at the eigenfrequencies of the inclusions, to assess the relevance of inclusion packing and arrangement on the dynamic behavior of metaconcrete. With respect to the plain concrete specimen, all engineered specimens showed a marked attenuation of the transmitted signal at a frequency close or very close to the theoretical eigenfrequency of the resonant inclusion. The attenuation was weakly dependent on the density of the inclusions and apparently not affected by interspacing, cement cover, and direction of the excitation along the axes of the specimen. Experimental results confirmed the behavior of metaconcrete as predicted by theoretical investigations, and further proved that the attenuation properties of metaconcrete are due to the resonant behavior of the inclusions.

Keywords: metaconcrete, engineered resonant inclusions, lattice-like pattern, linear swept-frequency sinusoidal excitation, signal attenuation, sonic range

Edited by:
Chiara Daraio,
California Institute of Technology,
United States

Reviewed by:
Francesco Dal Corso,
University of Trento, Italy
Antonio DeSimone,
Sant'Anna School of Advanced Studies, Italy

***Correspondence:**
Anna Pandolfi
anna.pandolfi@polimi.it

Specialty section:
This article was submitted to Mechanics of Materials, a section of the journal Frontiers in Materials

Received: *17 December 2018*
Accepted: *18 February 2019*
Published: *08 March 2019*

Citation:
Briccola D, Tomasin M, Netti T and Pandolfi A (2019) The Influence of a Lattice-Like Pattern of Inclusions on the Attenuation Properties of Metaconcrete. Front. Mater. 6:35. doi: 10.3389/fmats.2019.00035

1. INTRODUCTION

Metaconcrete is a new type of concrete where engineered inclusions, made of heavy spherical (e. g., steel) cores coated by a compliant (e. g., polymeric) layer, replace part of the traditional stone and gravel aggregates embedded into a standard Portland cement matrix. Because of the unconventional mechanical behavior exhibited under dynamic excitation, metaconcrete is regarded as a metamaterial. Specifically, it has been demonstrated theoretically in Mitchell et al. (2014) and numerically in Mitchell et al. (2015) that, when the frequency range of a dynamic load approaches one of the resonance frequencies of the metaconcrete inclusions, aggregates sequester part of the mechanical energy of the system to activate their resonant behavior, thus reducing the mechanical engagement of the concrete matrix. An explanation of the observed energy sequestration resides in the opposition of phase of the motion of the heavy core with respect to the motion of the matrix.

The dominant resonant oscillation frequency f_I^T of the inclusions is estimated with a simple analytical expression derived from a mass-spring one-dimensional model. A targeted frequency can be tuned by a suitable choice of core and coating materials, core diameter, and coating thickness, cf. Mitchell et al. (2014). The elastic modulus of the coating is the design parameter most influent on the value of f_I^T, thus the coating material is the key design parameter, although the choice might be restricted by all important considerations concerning fabrication and durability issues.

Numerical modal analysis conducted on a metaconcrete unit cell revealed the presence of lower and higher eigenfrequencies associated to deformative modes, Mitchell et al. (2014). The brittle behavior of metaconcrete under dynamic load has been investigated numerically modeling fracture within an eigenerosion approach proposed in Pandolfi and Ortiz (2012), revealing a slower propagation of the fracture front and an overall behavior comparable to the one of the standard plain concrete, see Mitchell et al. (2016). The attenuation properties of metaconcrete in the supersonic range (frequencies $f > 20$ kHz) have been verified in an experimental program conducted on cylindrical samples with randomly disposed inclusions, fabricated according to the ASTM C192/C 12M-06 (Standard Practice for Making and Curing Concrete Test Specimens in the Laboratory), see Briccola et al. (2017).

The concept of metaconcrete is becoming familiar in the literature on metamaterials. An experimental investigation on an epoxy-matrix metaconcrete has been recently described in Kettenbeil and Ravichandran (2018), documenting a reduction of the dynamic strain in the matrix up to 70% with respect to the homogeneous material. The scarce relevance of the stiffness of the matrix where the resonant inclusion is embedded had been pointed out in El Sherbiny and Placidi (2018).

In the broader field of acoustic metamaterials, several recent works investigated the possibility to reduce the amplitude of mechanical waves by playing with the combination of materials and geometries. Khan et al. (2018) demonstrated that a one-dimensional array of resonating cells impacted by a pendulum demonstrated that the arrangement of different local resonators has negligible influence on wave attenuation, while a good design of the system can enhance the performance of elastic metamaterials. By varying the contact interaction between three-component resonant particles disposed in one-dimensional arrays, Bonanomi et al. (2015) proved theoretically and experimentally that is possible to tune the acoustic transmission.

Numerical studies conducted within a two-dimensional setting documented in An et al. (2018) indicated that the vibration attenuation properties of acoustic metamaterials consisting of discrete masses and springs is enhanced by increasing the number of the unit-cells. Numerical investigations discussed in Hu and Oskay (2018) considered transient shear wave propagation in two-dimensional domains characterized by periodic elastic and viscoelastic microstructures using spatial-temporal homogenization procedures. Multiscale nonlocal homogenization that accounts for dispersion and attenuation due to Bragg scattering was presented in Hu and Oskay (2019), and more complex techniques that account for the micro-inertia effects of the inclusions are reported in Sridhar et al. (2016). Multi-layered metamaterials have been also proposed theoretically and numerically (Wang et al., 2017). More in general, investigations on locally resonant acoustic metamaterials are becoming more and more appealing, in the view of producing materials with specific attenuation properties, see Krushynska et al. (2014), or of showing negative properties, see Li et al. (2018), within well defined frequency bands.

Theoretical and numerical studies in the field of civil engineering, where metaconcrete is likely employable, have been reported in Cheng et al. (2018): the dynamic performance of a multi-story frame building structure has been investigated by playing with material and geometrical parameters. Innovative tensegrity structures share the concept of combining materials and geometry to enhance the dynamic performance of the system, cf. Fabbrocino and Carpentieri (2017). Currently, a large part of the civil engineering research in metamaterials focuses in the definition of combinations of materials and geometry that can provide protection against seismic actions, see Krödel et al. (2015). As an additional example, the performance of a I-Girder metamaterial under dynamic excitation has been analyzed numerically in Zhong et al. (2018). Applications of metamaterials in soils have been also investigated in Maleki and Khodakarami (2017) and Dertimanis et al. (2016).

Yet, an accurate experimental investigation of metaconcrete to verify the presence of deformation eigen-modes in the sonic range (frequencies $f < 20$ kHz) is missing. Furthermore, all numerical tests described in previous works have been conducted using an ideal metaconcrete with a regular disposition of inclusions Mitchell et al. (2014, 2015) and no verification has been done to check whether numerical results are affected by the Bragg scattering. Finally, no investigations have been conducted considering multiple spatial directions of the transmitted signal.

With the objective to verify the observations of previous numerical studies, and to quantify the differences between the theoretical prediction and the actual performance of regularly manufactured specimens, a new experimental program has been planned. The main goals of the present study are to address specifically the presence of eigenfrequencies within the sonic range, to assess the relevance of the regular disposition of the inclusions on the attenuation performance along different directions, and to identify the anisotropy of the resonant behavior due to possible stratification of the components during the casting of the material. The results of this investigation are reported in the present work.

The paper is organized as follows. Section 2 describes the structure of the specimens, the experimental setup, and the experimental program. Section 3 illustrates the outcomes of the experiments. Section 4 collects considerations about the results and draws some conclusions and perspectives.

2. MATERIALS AND METHODS

Nondestructive tests on metaconcrete specimens loaded with waves spanning the sonic range (400 Hz–12.2 kHz) have been set up at the Laboratory of Materials Testing (LPM) at the Politecnico di Milano, Italy. The test layout was inspired by the specifications in ASTM C215-14 (Standard test method for fundamental transverse, longitudinal, and torsional resonant frequency of concrete specimens).

In the view of the goals of the investigation, specimens were cast in a cubic shape allowing the application of an electro-mechanical mass vibration exciter (transmitting unit) along the three symmetry axes in turn. Two receiving units (piezoelectric transducers), measuring the output signals on the two faces normal to the excited axis, allowed the recording of the frequency-response function of the samples. Details of the specimen casting and of the experimental setup are provided in the following.

2.1. Metaconcrete Specimens

To facilitate the comparison of the attenuation properties of metaconcrete along three mutually orthogonal directions (the

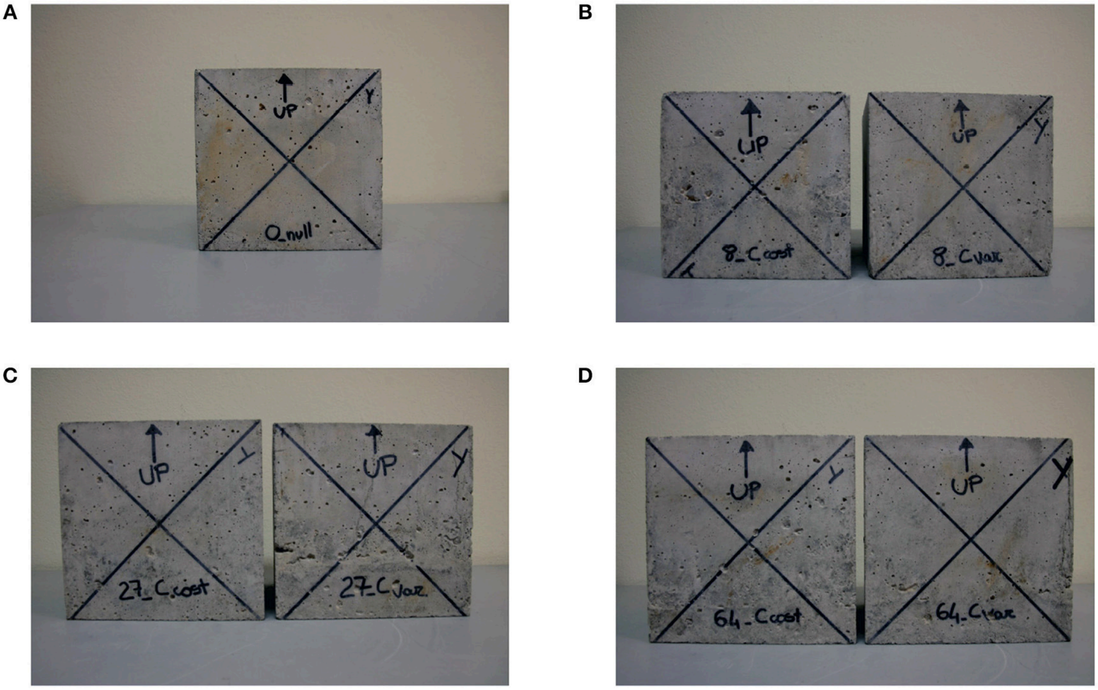

FIGURE 1 | Specimens used in the experiments. **(A)** S0: specimen without inclusions. **(B)** S8C-S8V: specimens with 8 inclusions (constant and variable cement cover and interspacing, respectively). **(C)** S27C-S27V: specimens with 27 inclusions (constant and variable cement cover and interspacing respectively). **(D)** S64C-S64V: specimens with 64 inclusions (constant and variable cement cover and interspacing respectively).

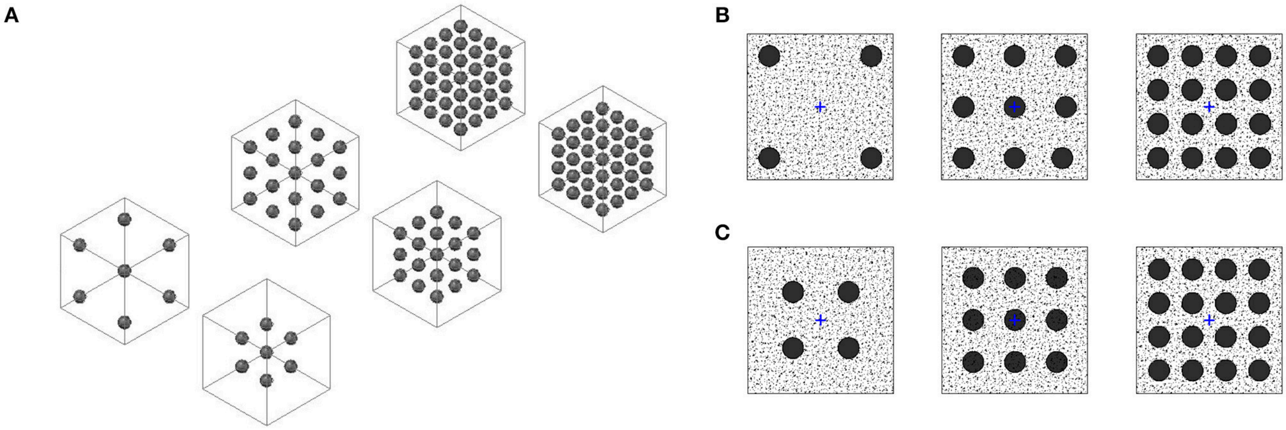

FIGURE 2 | Lattice-like patterns of the two batches of specimens with 8/27/64 inclusions and constant or variable cement cover. **(A)** Axonometric view of the two batches. **(B)** Top view of the specimens of batch 1 (S8C/S27C/S64C) with constant cement cover. **(C)** Top view of the specimens of batch 2 (S8V/S27V/S64V) with variable cement cover.

casting and other two perpendicular to it), a cubic shape was chosen instead of the prismatic shape recommended by ASTM C215-14. The choice allowed the arrangement of the inclusion in a regular lattice with the same geometrical structure along the three symmetry axes.

Cubic prototypes of metaconcrete (edge $d = 15$ cm) with regularly disposed inclusions have been cast according to UNI EN 206:2016 (Concrete-Specification, performance, production and conformity) and UNI EN 12390-1:2002 (Testing hardened concrete-Shape, dimensions, and other requirements for specimens and molds).

Specimens were cast using cubic disposable plastic molds using a mortar paste made of a mix of Portland cement, sand, and water. As done in previous experiments documented in Briccola et al. (2017), old-fashion mouse balls have been utilized as resonant inclusions. Commercially available mouse balls made of 10 mm radius steel spheres covered with a 1 mm thickness polydimetilsyloxhane (PDMS) coating matched the fundamental requirement of showing a primary resonance within the sonic range.

A neutral specimen with no inclusions was cast first to be taken as a reference for the estimate the attenuation properties of metaconcrete, see **Figure 1A**. Metaconcrete specimens were obtained from two batches of cubic specimens with different lattice length and cement cover. Each batch consisted of three specimens with a three-dimensional grid of $2 \times 2 \times 2$, $3 \times 3 \times 3$, and $4 \times 4 \times 4$ inclusions respectively, see **Figures 1B–D**. The inclusion patterns are shown in **Figure 2**.

The particular arrangement of inclusions in the mortar matrix imposed to adopt a specific casting procedure by layers, that required the use of plastic jigs with equi-spaced holes. Once the cement, sand, and water mix was prepared, the first concrete layer (with the thickness of the cover) was poured in the plastic molds. The subsequent layer containing the inclusions was arranged using the plastic jig. A new layer with the thickness of the interspacing was poured. The top surface of the interspacing layer was flattened as much as possible with the aid of a flat plastic jig with no holes. After the setting, each layer was compacted by means of a small tamping rod with rounded ends. To avoid the presence of cavities the external surface of the mold was tapped with a mallet. A lapse of a proper time after the casting of each layer was necessary to avoid the segregation of the inclusions.

Mechanical features of the specimens could be affected by the casting, therefore the casting direction was marked. Next, specimens were moved into the curing room and stored for 24 h. After one day, specimens were removed from molds, polished, and kept in a water storage tank for curing for 28 days. The weight of each specimen is shown in **Table 1**.

According to the theoretical derivation in Mitchell et al. (2014), by considering each inclusion as an ideal mass-spring system the first natural frequency f_I^T of the inclusion can be estimated as

$$f_I^T = \frac{1}{2\pi}\sqrt{\frac{3}{2}\frac{E_s}{R_c t_s \rho_c}} \tag{1}$$

where $R_c = 10$ mm is the core radius, $\rho_c = 7,850$ kg/m^3 is the core density, $t_s = 1$ mm is the coating thickness, and $E_s = 750$ kPa is the coating elastic modulus, leading to $f_I^T = 600$ Hz.

The values of the first four eigenfrequencies and eigen-modes of a unit cell of metaconcrete, geometrically similar to the one used here, were numerically computed by a finite element modal analysis in Mitchell et al. (2014), considering 10 mm radius lead spheres coated with 1 mm or 3 mm thickness rubber or nylon layer. The expected eigenfrequencies of the actual mouse balls,

TABLE 1 | Characteristics of the specimens.

Specimen	NN	W [kg]	V_m (%)	V_{core}(%)	$V_{coating}$(%)	F_a(%)
S0	0	7.35	100.00	0.00	0.00	0.00
S8C	8	7.50	98.68	0.99	0.33	3.73
S8V	8	7.53	98.68	0.99	0.33	3.73
S27C	27	7.86	95.54	3.35	1.11	12.59
S27V	27	7.71	95.54	3.35	1.11	12.59
S64C	64	8.47	89.43	7.94	2.63	29.85
S64V	64	8.50	89.43	7.94	2.63	29.85

Identification acronym (SNNX, NN, number of inclusions; X, constant (C) / variable (V) cover), W, weight; Vm, volume fraction of mortar; Vcoating, volume fraction of the soft coating; Vcore, volume fraction of the heavy core and Fa, inclusion mass fraction.

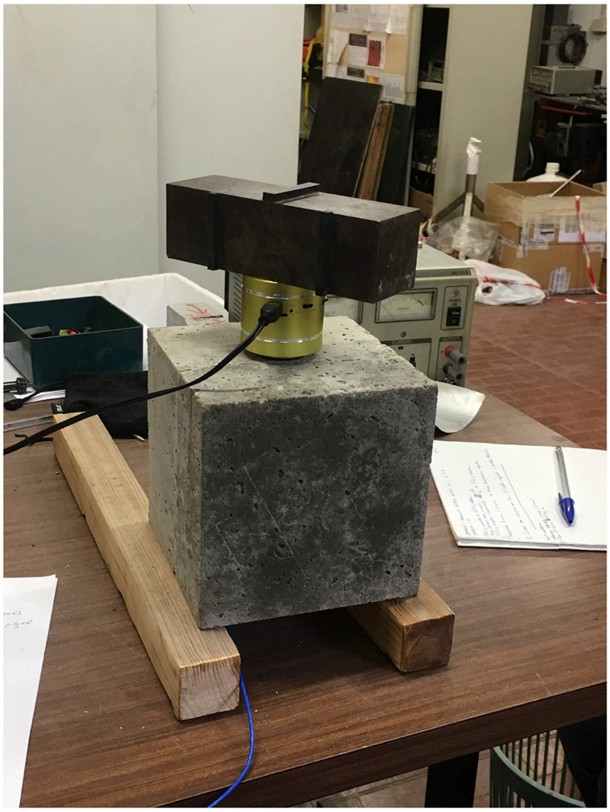

FIGURE 3 | Experimental setup, showing a metaconcrete specimen, the two transducers, and the vibration speaker pressurized with a weight to increase adherence.

where lead is replaced with steel and rubber or nylon are replaced with PDMS, have been estimated from the values reported in Mitchell et al. (2014) through linear regression, obtaining $f_I = 735 \pm 83$ Hz, $f_{II} = 1,960 \pm 117$ Hz, $f_{III} = 5,715 \pm 315$ Hz and $f_{IV} = 9,120 \pm 467$ Hz.

2.2. Experimental Setup

The experimental setup is shown in **Figure 3**. The driving circuit included a variable frequency audio oscillator, an amplifier, and a driving unit. The electric signal was triggered by a stand-alone audio oscillator driven by an engineering workbench (LabVIEW) and transformed into a mechanical wave by the driving unit. The driving unit consisted into an electro-mechanical mass vibration exciter (a commercially available VibeTribe Troll 2.0 characterized by 0.38 kg mass, 54 mm diameter, and 54 mm length), featuring a high signal-to-noise ratio. In each test, the vibration speaker was applied to one of the specimen surfaces normal to the excitation direction.

Two accelerometers (contact piezoelectric shear type transducers-PCB 353B15 SN) were mounted at the center of two opposite faces of the cubic specimens, see **Figure 2**, and made adherent by a thin layer of wax. The two transducers were used as pickup units for the acceleration at the opposite faces of the specimens. A data acquisition system (4 Channel, 24-Bit Analog Input Modules - NI USB-9239) transformed the accelerations into electric signals. The time-domain electric waveforms labeled Channel 1 represented the signals received at the face opposite to the vibration speaker. The waveforms labeled Channel 2 represented the signals received at the face where the vibration speaker was applied to.

From the geometrical point of view, specimens were characterized by a regular arrangement of inclusions and were expected to show an orthotropic behavior along the symmetry axes. The regularity of the distribution of the in-plane inclusion obtained by means of equi-spaced hole jigs guaranteed that the in-plane behavior along the x and y directions was very similar. Contrariwise, the behavior in the casting direction (the one marked) was expected to differ from the in-plane behavior in the view of possible segregation of the components due to the layered casting procedure. Therefore, specimens were tested dynamically in two directions, x and z.

Linear swept-frequency sinusoidal excitations with constant amplitude $A = 2$ Vpp were applied to each specimen along both x and z axes. Specimens were regularly rotated as so as the direction of propagation of the signal was always vertical, from top side to bottom side. Measurements were taken for signals transmitted in two opposite directions of each axis by flipping the specimen upside-down, and repeated three times for each specimen.

The range of experimental frequencies spanned by the swept-sine excitation were defined by taking into account both the inclusion eigenfrequencies, estimated theoretically and numerically, and the operative bandwidth of the transducers (±% 10 0.7–18,000 Hz). The width of the interval centered at the eigenfrequency f_r was set equal to $0.8 f_r$, obtaining the interval $\Delta f_r = f_r^{\text{end}} - f_r^{\text{begin}}$ where

$$f_r^{\text{begin}} = (1 - 0.4) f_r \qquad f_r^{\text{end}} = (1 + 0.4) f_r \,. \tag{2}$$

According to Gloth and Sinapius (2004), the attainment of a quasi-steady state response of the specimen within the frequency range Δf_r imposes an upperbound (in Hz/min) to the sweep rate

$$\dot{f}_{\max} = 54 \, \frac{f_r^2}{Q^2} \,, \qquad Q = \frac{1}{2\zeta} \tag{3}$$

where f_r is the targeted eigenfrequency, Q the dynamic amplification at the resonant frequency, and ζ a characteristic damping value, that for standard concrete can be assumed $\zeta = 5.0\%$. The maximum sweep rate defines, in turn, a minimum experimental time for each frequency range Δf_r as

$$\Delta T_{r\,\min} = 2\pi \, \frac{\Delta f_r}{\dot{f}_{\max}} \tag{4}$$

The actual experimental time was incremented by 40% above the minimum, by setting $\Delta T_r = 1.4 \, \Delta T_{r\,\min}$. The operative parameters of the linear swept-frequency sinusoidal excitations used in the experiments are listed in **Table 2**.

TABLE 2 | Parameters adopted for each frequency range during a linear sweep.

	f_r [Hz]	f_r^{begin} [Hz]	f_r^{end} [Hz]	ΔT_r [s]
f_I^T	600	400	1,200	40
f_I	735±83	400	1,200	40
f_{II}	1,960±117	1,000	3,000	5
f_{III}	5,715±315	3,300	8,000	5
f_{IV}	9,120±467	5,000	12,200	5

f_r, theoretically or numerically estimated resonant frequency of the inclusion; f_r^{begin}; r, lowest frequency; f_r^{end}, highest frequency; Δ T_r,time duration of the signal.

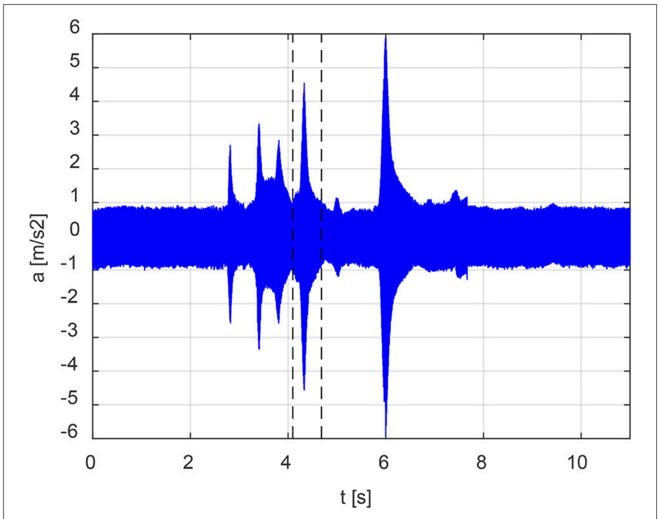

FIGURE 4 | Example of time history recorded by the transducer located at the opposite face with respect to the vibration speaker for tests performed on the specimen without inclusions. A linear swept-sine excitation with a start frequency of 1,000 Hz and an end frequency of 3,000 Hz has been applied in 10s.

At the beginning of each linear swept-sine excitation, a sine wave with frequency equal to the initial frequency of the sweep was applied for 2 s.

3. RESULTS

Acquired data were stored in sequential files and post-processed with a data-signal processing software. The electric signals were transformed in acceleration time histories through the sensitivity $s = 10/9.81$ mV s^2/m of the piezoelectric transducers. **Figure 4** shows an example of the acceleration signal recorded by the transducer located at the face opposite to the vibration speaker. The accelerations signals were characterized by an average value not large enough to become dominant with respect to all the other frequencies considered.

All acceleration records were analyzed by means of the Fast Fourier Transform (FFT) algorithm using a tracking low-pass filter in order to reduce noise at high frequencies. A feature of tracking filters, applied only to the frequency domain, is the preservation of the phase of the signal, thus the behavior of metaconcrete at resonance is expected to be captured.

The FFT has been evaluated on specific time domain windows covering the time intervals of interest. The time windows were set on the basis of the lowest and highest estimated eigenfrequencies that were expected to occur within the frequency band of the input signal reported in **Table 2**.

The operative procedure for the calculation of the time interval is explained with reference to the acceleration signal reported in **Figure 4** referring to the zero inclusion specimen. After the initial 2 s sine-wave signal, a linear swept-sine excitation in the range 1,000–3,000 Hz has been applied in a 5 s time interval. The second eigenfrequency was estimated as $f_{II} = 1,960$ Hz, thus the frequency bounds for the definition of the time interval were 1,843 and 2,077 Hz respectively, cf. **Table 2**. Therefore, the activation of the resonance of the inclusions was expected to occur within a time window comprised between 4.10 and 4.68 s, visualized with two broken vertical lines in **Figure 4**. Interestingly, although the specimen was normal concrete, the plot pointed out a resonance of the standard concrete.

Due to a linear swept-sine excitation, the FFT power-spectra are characterized by continuous plots between the frequency bounds of each eigenfrequency of the material. An example of FFT is visualized in **Figure 5**, with reference to **Figure 4**. The left graph represents the acceleration signal windowed in the bounded time interval (note that the time scale has been reset with respect to **Figure 4**). The right plot visualizes the corresponding amplitude of the FFT, which appears as a continuous line within the frequency limits 1,843 and 2,077 Hz.

The value of the power-spectrum within the frequency bands of interest for the first four expected eigenfrequencies has been considered as indicative of the dynamic behavior of the material. Thus, the comparison between the behavior of plain concrete specimen and metaconcrete specimens has been conducted in terms of power-spectrum amplitude. The comparison includes all the tests conducted on all the metaconcrete samples, differing by number of inclusions and by cement cover.

For each specimen and each direction of excitation (x or z), the amplitude $|A|_{\mathrm{N}}$ of the power-spectrum corresponding to each frequency band was evaluated as the average of the power-spectra values falling within the band in the three corresponding time-history accelerations. The response of the seven specimens measured in linear swept-sine excitations along the x-axis, backward and forward, is reported in **Table 3**. The columns labeled η_{N} contain the efficiency ratio, defined as

$$\eta_{\mathrm{N}} = \frac{|A|_{\mathrm{N}} - |A|_0}{|A|_0} \tag{5}$$

where $|A|_0$ is the amplitude referred to the zero inclusion specimen. **Figure 6A** visualizes the average amplitudes $|A|_{\mathrm{N}}$ for all the specimens considering the two direction of excitation.

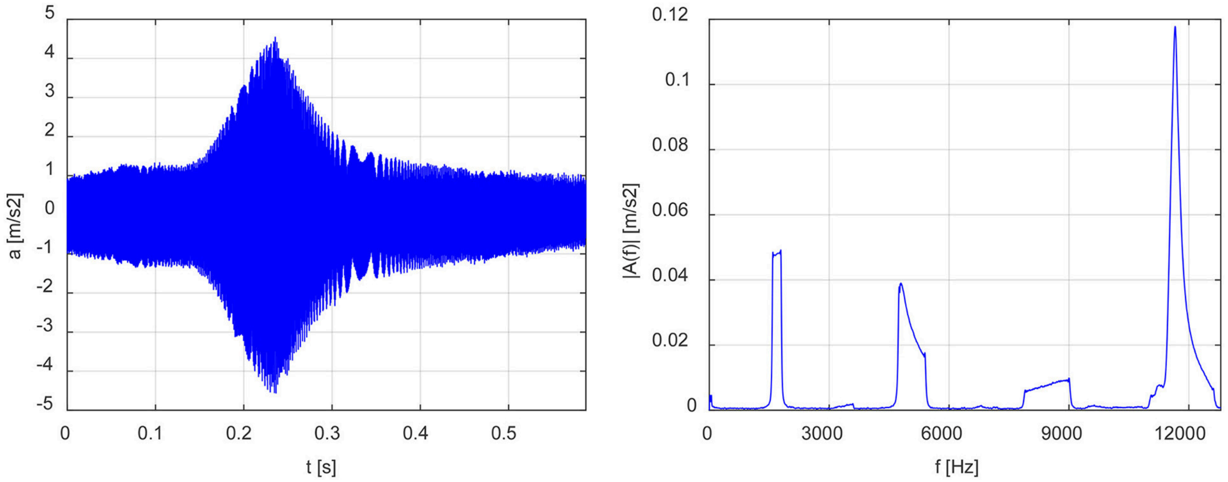

FIGURE 5 | Example of the windowed time history and the corresponding FFT. A linear swept-sine excitation with a start frequency of 1,000 Hz and an end frequency of 3,000 Hz has been applied in 10 s. Frequency limits of about 1,800 and 2,000 Hz have been imposed for the FFT.

TABLE 3 | Attenuation performance of specimens characterized by different both inclusion spacings and cement cover for linear swept-sine excitations along the *x*-axis, backward and forward.

Δf_r Hz	f_{begin} Hz	Specimen	backward $\lvert A\rvert_{\text{N}}$ [m/s^2]	x η_{N} [%]	forward $\lvert A\rvert_{\text{N}}$ [m/s^2]	x η_{N} [%]
400–1,200	749	S0	0.014241	0.0	0.014255	0.0
		8C	0.012441	12.6	0.012751	10.6
		8V	0.010710	24.8	0.009859	30.8
		27C	0.009210	35.3	0.010768	24.5
		27V	0.013628	4.3	0.013976	2.0
		64C	0.010576	25.7	0.010762	24.5
		64V	0.011374	20.1	0.012168	14.6
1,000–3,000	1,699	S0	0.047505	0.0	0.047801	0.0
		8C	0.043266	8.9	0.044827	6.2
		8V	0.042138	11.3	0.036794	23.0
		27C	0.033734	29.0	0.036627	23.4
		27V	0.052640	-10.8	0.051047	-6.8
		64C	0.039625	16.6	0.036999	22.6
		64V	0.037095	21.9	0.043223	9.6
3,300–8,000	4,000	S0	0.089994	0.0	0.076733	0.0
		8C	0.054305	39.7	0.052492	31.6
		8V	0.056054	37.7	0.081951	-6.8
		27C	0.092723	-3.0	0.097101	26.5
		27V	0.002522	97.2	0.001008	98.7
		64C	0.025531	71.6	0.080936	-5.5
		64V	0.049667	44.8	0.096245	-25.4
5,000–12,200	9,000	S0	0.037292	0.0	0.037899	0.0
		8C	0.029785	20.1	0.030578	19.3
		8V	0.022334	40.1	0.030233	20.2
		27C	0.034257	8.1	0.028600	24.5
		27V	0.036171	3.0	0.032474	14.3
		64C	0.018919	49.3	0.025625	32.4
		64V	0.025231	32.3	0.022420	40.8

Figure 6B plots the corresponding efficiency η_{N}. **Figures 6C,D** report the same plots for the tests in direction *z*.

4. DISCUSSION

The experimental program conducted on metaconcrete samples newly casted was planned with the aim of exploring the sonic range of frequency, and of revealing whether the regularity and the symmetry of the pattern of the inclusion may cause reductions or differences in the efficiency of waves attenuation, with respect to the behavior observed in the first experimental validation of metaconcrete, see Briccola et al. (2017).

Because of the different specimen geometry, the experimental setup differed from the one used in Briccola et al. (2017). First, a transient signal in the form of a linear swept-frequency sinusoidal excitation was chosen instead of a discretely dwelled-frequency sinusoidal waveform. This choice was done to exclude the possibility to miss the actual resonant behavior of the inclusions. Second, four windows of frequencies were defined centered at the numerically estimated resonance frequencies, to offer the opportunity to explore in larger detail the region where resonant is expected to occur. This choice was suggested by the observation that a linear sweep in the frequency range of interest may represent a good compromise between the amplitude of excitation needed and time necessary to perform all the tests on the seven specimens and to post-process the signals, cf. Gloth and Sinapius (2004).

The results, averaged over six (three forward and three backward), of the linear swept-sine excitation tests in direction *x* are collected in **Table 2**. The ratio η_{N} can be considered as a measure of the attenuation properties of the metaconcrete within each eigenfrequency band. The experimental values indicated that, with respect to the plain concrete, metaconcrete specimens reduce the average amplitude of the acceleration power-spectra up to 60%. The beneficial behavior was observed in particular for higher eigenfrequencies and more densely packed specimens, while at the lowest eigenfrequency the average reduction of the amplitude lowered to 20–30%.

In general, results indicated that the efficiency of metaconcrete increased with the density of the inclusions, while tests did not show a marked dependence on the cement cover. **Table 2** shows that the first two experimental eigenfrequencies, estimated with a numerical analysis, were very close to the theoretical estimate f_I^T, Equation (1). In general, the third and fourth eigenvalues are not predictable from the composition and microstructure of metaconcrete and there is not any theoretical suggestion of

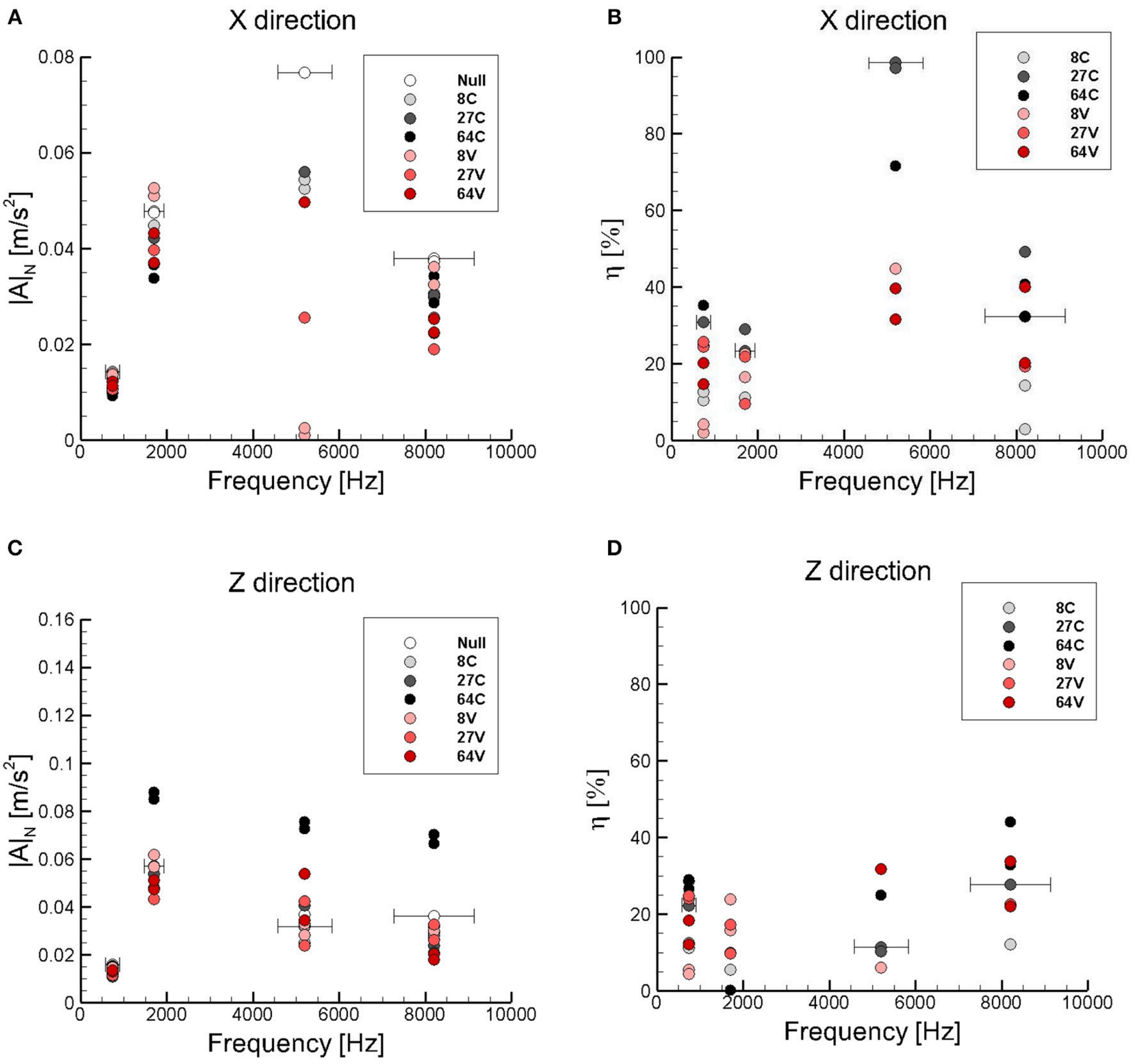

FIGURE 6 | Values of the FFT acceleration amplitude $|A|_N$ and efficiency η_N averaged in the eigenfrequency bands (visualized by the horizontal bars) for the seven specimens. Signal transmitted in *x* and *z* directions. **(A)** Average FFT acceleration amplitude for signal in *x* direction. **(B)** Efficiency for *x* direction. **(C)** Average FFT acceleration amplitude for signal in *z* direction. **(D)** Efficiency for *z* direction.

their values. The two highest eigenvalues were related to a higher attenuation of the transmitted signal. Regrettably, the tackled frequencies were in the high side of the range of interest of this research, although still within the sound spectra.

The tests in *x* direction conducted on the specimen labeled 27 V gave contradictory results and were not considered in the subsequent analyses. The anomalous behavior was probably related to the imperfect casting of the specimen, which exhibited several holes and gaps on the surface. In fact, the abnormal average attenuation observed for this specimen (98%) was probably due to the presence of voids that activated a mechanism of wave attenuation different from the energy trapping typical of metaconcrete. The tests in *y* direction were perfectly corresponding to the test in the *x* direction. Also in this case, specimen 27 V did not behave in the expected manner.

The tests conducted in *z* direction did not provide uniform results. Also in this case, the anomalies could be attributed to the sub-segregation of the components due to the casting procedure. A refined casting technique can be implemented to avoid this problem before performing other tests.

A direct comparison with the results obtained in Briccola et al. (2017) was not possible, since in the present analysis attenuation ratios averaged over frequency intervals, instead of single values, have been considered. The type of attenuation parameter considered is necessarily less marked than the one introduced in the previous study (direct comparison of the output signal magnitude). In the present setup, where the vibration was originated by a speaker, there was no the possibility to measure an input signal that could be used to define the attenuation of the single specimen. Therefore, the choice was to compare the behavior of metaconcrete specimens and the behavior of the plain concrete specimen.

In this terms, the conclusion on the results of the experimental program can be drawn as follows. Tests confirmed that metaconcrete provides attenuation of the acceleration signal within a limited range of frequencies centered at one of the numerically predicted resonant frequencies. The attenuation in lattice-like patterned specimens was not affected by the direction of the signal along the horizontal symmetry axis, while the behavior in vertical direction was rather different, suggesting the possible segregation of the inclusions. No differences were observed in the inversion of the direction of the signal.

As far as the attenuation due to Bragg scattering was concerned, tests were not able to reveal an evidence of the phenomenon and the influence of it on the global attenuation properties. Probably the small size of the specimens, with respect to the size of the inclusions, was not sufficient to establish the quantitative contribution of the phenomenon.

DATA AVAILABILITY

The dataset generated for this study can be requested to the authors.

AUTHOR CONTRIBUTIONS

DB planned the experimental program, conducted part of the tests, and contributed to the writing of the paper. MT conducted the remaining tests and elaborated the results into tables and figures. TN has designed and cast the specimens. AP has supervised the research and completed the paper.

ACKNOWLEDGMENTS

The kind assistance of Marco Cucchi and Massimo Iscandri in the setup of the tests is gratefully acknowledged.

REFERENCES

An, X., Fan, H., and Zhang, C. (2018). Elastic wave and vibration bandgaps in two-dimensional acoustic metamaterials with resonators and disorders. *Wave Motion* 80, 69–81. doi: 10.1016/j.wavemoti.2018.04.002

Bonanomi, L., Theocharis, G., and Daraio, C. (2015). Wave propagation in granular chains with local resonances. *Phys. Rev.* 91:033208. doi: 10.1103/PhysRevE.91.033208

Briccola, D., Ortiz, M., and Pandolfi, A. (2017). Experimental validation of metaconcrete blast mitigation properties. *J. Appl. Mech* 84:6. doi: 10.1115/1.4035259

Cheng, Z., Lin, W., and Shi, Z. (2018). Wave dispersion analysis of multi-story frame building structures using the periodic structure theory. *Soil Dyn. Earthq. Eng.* 106, 215–230. doi: 10.1016/j.soildyn.2017.12.024

Dertimanis, V., Antoniadis, I., and Chatzi, E. (2016). Feasibility analysis on the attenuation of strong ground motions using finite periodic lattices of mass-in-mass barriers. *J. Eng. Mech.* 142:04016060. doi: 10.1061/(ASCE)EM.1943-7889.0001120

El Sherbiny, M. G., and Placidi, L. (2018). Discrete and continuous aspects of some metamaterial elastic structures with band gaps. *Arch. Appl. Mech.* 88, 1725–1742. doi: 10.1007/s00419-018-1399-1

Fabbrocino, F., and Carpentieri, G. (2017). Three-dimensional modeling of the wave dynamics of tensegrity lattices. *Composite Struct.* 173, 9–16. doi: 10.1016/j.compstruct.2017.03.102

Gloth, G., and Sinapius, M. (2004). Analysis of swept-sine runs during modal identification. *Mech. Syst. Signal Proc.* 18, 1421–1441. doi: 10.1016/S0888-3270(03)00087-6

Hu, R., and Oskay, C. (2018). Spatial–temporal nonlocal homogenization model for transient anti-plane shear wave propagation in periodic viscoelastic composites. *Comput. Methods Appl. Mech. Eng.* 342, 1–31. doi: 10.1016/j.cma.2018.07.037

Hu, R., and Oskay, C. (2019). Multiscale nonlocal effective medium model for in-plane elastic wave dispersion and attenuation in periodic composites. *J. Mech. Phys. Solids* 124, 220–243. doi: 10.1016/j.jmps.2018.10.014

Kettenbeil, C., and Ravichandran, G. (2018). Experimental investigation of the dynamic behavior of metaconcrete. *Int. J.Impact Eng.* 111, 199–207. doi: 10.1016/j.ijimpeng.2017.09.017

Khan, M., Li, B., and Tan, K. (2018). Impact load wave transmission in elastic metamaterials. *Int. J. Impact Eng.* 118, 50–59. doi: 10.1016/j.ijimpeng.2018.04.004

Krödel, S., Thomé, N., and Daraio, C. (2015). Wide band-gap seismic metastructures. *Extreme Mech. Lett.* 4, 111–117. doi: 10.1016/j.eml.2015.05.004

Krushynska, A. O., Kouznetsova, V. G., and Geers, M. G. D. (2014). Towards optimal design of locally resonant acoustic metamaterials. *J. Mech. Phys. Solids* 71, 179–196. doi: 10.1016/j.jmps.2014.07.004

Li, Z., Hu, H., and Wang, X. (2018). A new two-dimensional elastic metamaterial system with multiple local resonances. *Int. J. Mech. Sci.* 149, 273–284. doi: 10.1016/j.ijmecsci.2018.09.053

Maleki, M., and Khodakarami, M. (2017). Feasibility analysis of using metasoil scatterers on the attenuation of seismic amplification in a site with triangular hill due to sv-waves. *Soil Dyn. Earthq. Eng.* 100, 169–182. doi: 10.1016/j.soildyn.2017.05.036

Mitchell, S. J., Pandolfi, A., and Ortiz, M. (2014). Metaconcrete: designed aggregates to enhance dynamic performance. *J. Mech. Phys. Solids* 65, 69–81. doi: 10.1016/j.jmps.2014.01.003

Mitchell, S. J., Pandolfi, A., and Ortiz, M. (2015). Investigation of elastic wave transmission in a metaconcrete slab. *Mech. Mater.* 91, 295–303. doi: 10.1016/j.mechmat.2015.08.004

Mitchell, S. J., Pandolfi, A., and Ortiz, M. (2016). Effect of brittle fracture in a metaconcrete slab under shock loading. *J. Eng. Mech.* 142. doi: 10.1061/(ASCE)EM.1943-7889.0001034

Pandolfi, A., and Ortiz, M. (2012). An eigenerosion approach to brittle fracture. *Int. J. Numeric. Methods Eng.* 92, 694–714. doi: 10.1002/nme.4352

Sridhar, A., Kouznetsova, V., and Geers, M. (2016). Homogenization of locally resonant acoustic metamaterials towards an emergent enriched continuum. *Comput. Mech.* 57, 423–435. doi: 10.1007/s00466-015-1254-y

Wang, C., Liu, Z., Gao, L., Xu, D., and Zhuang, Z. (2017). Analytical and numerical modeling on resonant response of particles in polymer matrix under blast wave. *Comput. Mater. Sci.* 140, 70–81. doi: 10.1016/j.commatsci.2017.08.034

Zhong, R., Pai, P. F., Zong, Z., Deng, H., and Ruan, X. (2018). Metamaterial i-girder for vibration absorption of composite cable-stayed bridge. *J. Eng. Mech.* 144:04018045. doi: 10.1061/(ASCE)EM.1943-7889.0001467

Conflict of Interest Statement: The authors declare that the research was conducted in the absence of any commercial or financial relationships that could be construed as a potential conflict of interest.

ORIGINAL RESEARCH
published: 14 March 2019
doi: 10.3389/fmats.2019.00030

Application of a Laser-Based Time Reversal Algorithm for Impact Localization in a Stiffened Aluminum Plate

Marco Miniaci[1,2]*, **Matteo Mazzotti**[3], **Maciej Radzieński**[2], **Pawel Kudela**[2], **Nesrine Kherraz**[4], **Federico Bosia**[4], **Nicola M. Pugno**[5,6,7] **and Wieslaw Ostachowicz**[2]

[1] EMPA, Laboratory of Acoustics and Noise Control, Dübendorf, Switzerland, [2] Institute of Fluid-Flow Machinery, Polish Academy of Science, Gdańsk, Poland, [3] Civil, Architectural & Environmental Engineering (CAEE) Department, Drexel University, Philadelphia, PA, United States, [4] Department of Physics and Nanostructured Interfaces and Surfaces Centre, University of Torino, Torino, Italy, [5] Laboratory of Bio-Inspired and Graphene Nanomechanics, Department of Civil, Environmental and Mechanical Engineering, University of Trento, Trento, Italy, [6] School of Engineering and Materials Science, Queen Mary University of London, London, United Kingdom, [7] Ket Lab, Edoardo Amaldi Foundation, Rome, Italy

Non-destructive testing and structural health monitoring (SHM) techniques using elastic guided waves are often limited by material inhomogeneity or geometrical irregularities of the tested parts. This is a severe restriction in many fields of engineering such as aerospace or aeronautics, where typically one needs to monitor composite structures with varying mechanical properties and complex geometries. This is particularly true in the case of multiscale composite materials, where anisotropy and material gradients may be present. Here, we provide an impact localization algorithm based on time reversal and laser vibrometry to cope with this type of complexity. The proposed approach is shown to be insensitive to local elastic wave velocity or geometrical features. The technique is based on the correlation of the measured impact response and a set of measured test data acquired at various grid points along the specimen surface, allowing high resolution in the determination of the impact point. We present both numerical finite element simulations and experimental measurements to support the proposed procedure, showing successful implementation on an eccentrically stiffened aluminum plate. The technique holds promise for advanced SHM, potentially in real time, of geometrically complex composite structures.

Keywords: impact localization, guided waves, numerical simulations, structural health monitoring, time reversal, laser vibrometer measurements

OPEN ACCESS

Edited by:
Julian J. Rimoli,
College of Engineering, Georgia Institute of Technology, United States

Reviewed by:
Shangchao Lin,
Florida State University, United States
Paolo S. Valvo,
University of Pisa, Italy

***Correspondence:**
Marco Miniaci
marco.miniaci@gmail.com

Specialty section:
This article was submitted to Mechanics of Materials, a section of the journal Frontiers in Materials

Received: *22 October 2018*
Accepted: *12 February 2019*
Published: *14 March 2019*

Citation:
Miniaci M, Mazzotti M, Radzieński M, Kudela P, Kherraz N, Bosia F, Pugno NM and Ostachowicz W (2019) Application of a Laser-Based Time Reversal Algorithm for Impact Localization in a Stiffened Aluminum Plate. Front. Mater. 6:30. doi: 10.3389/fmats.2019.00030

1. INTRODUCTION

Assessment of the integrity of structural components is of great importance for aerospace vehicles and systems, for land and marine transportation, for civil infrastructures, for the oil industry as well as for other biological and mechanical applications (Grandt, 2004). It is well-known that accidental impacts may generate hidden damage in structures, which can develop under cyclic loading, until it endangers the integrity of the whole structure. In some cases, propagation of undetected damage can be the cause of the structural failure. One of the most well-known cases of this occurred when the composite tile on the leading edge of the wing of the Space Shuttle Columbia fractured due to impact with a piece of foam insulation, leading to a catastrophic failure of the whole vehicle on February 1, 2003 (NASA, 2003).

In order to prevent this scenario, the capability to identify impacts and then to monitor potential damage evolution in the neighborhood of the impact is of crucial importance. With this in mind, the use of Structural Health Monitoring (SHM) approaches based on guided elastic waves driven by a network of piezoelectric transducers has attracted the interest of several researchers in recent decades (Ostachowicz et al., 2011).

For isotropic plates, several techniques, known as hyperbolic approaches, have been proposed for impact localization over the years, the majority of which locate the point of impact after detecting the acoustic emission signal generated by the impact event using at least three sensors and applying standard or modified triangulation techniques (De Marchi et al., 2011). When the assumption of isotropy is removed, the standard triangulation technique fails and alternative methods need to be used. Various approaches for anisotropic (Kundu et al., 2012) and inhomogeneous plate-like (Hajzargerbashi et al., 2011) structures have been proposed, including threshold-based procedures (Kundu et al., 2009), peak detection techniques (Tracy and Chang, 1998; Seydel and Chang, 2001) and cross-correlation schemes (White, 1969). However, these methods are predictive on regular geometries whereas the presence of stiffeners, rivets, and other geometrical irregularities, reduce their diagnostic potential.

To overcome these difficulties, other approaches based on direct strategies and inverse methods have recently been proposed. While the first type requires *ad-hoc* designed transducers (Salamone et al., 2010; Senesi et al., 2010; Baravelli et al., 2013; De Marchi et al., 2018), the second makes use of a database of responses generated by impacts (Staszewski et al., 2000; Coverley and Staszewski, 2003; Park J. et al., 2009; Ciampa and Meo, 2012). In this context, Park et. al. recently proposed a new impact localization algorithm based on time reversal (TR) and scanning laser Doppler vibrometer (SLDV) measurements applied to Lamb waves (Park et al., 2012). The use of TR in Lamb wave applications was first explored by Ing and Fink (1988, 1996) and later extensively used both for damage detection in plates (Wang et al., 2004; Park et al., 2007; Gliozzi et al., 2015; Miniaci et al., 2017) and for impact localization (Sohn et al., 2011; Park et al., 2012). Lamb waves are extensively involved in plate-like structures for non-invasive inspection because of their guided nature allowing for large area inspection. However, their dispersion often limits their use because of the complex waveform of acquired signals since pulse distortion occurs due to the variation of modal group velocities. Because of this the received signals are often difficult to interpret (Ostachowicz et al., 2011) and TR becomes an attractive tool to overcome the problem of dispersion in guided elastic waves. This technique only requires minimal prior knowledge of the monitored structures and no specific information relative to the properties of the propagating medium (Ing and Fink, 1988; Park et al., 2007).

In this work, the procedure proposed in Park et al. (2012) is applied to locate simulated impacts in a reinforced aluminum plate. Although in general, the larger the number of transducers used for the collection of the training data, the smaller the variation in the localization performance is, we show that in our case a single piezoelectric transducer is sufficient to achieve adequate training data capable of unambiguously providing the impact location with good accuracy. This is possible thanks to the relatively small irregularity of the location surrounding the transducer and to the possibility of thoroughly cleaning the bonding surface and thus properly gluing the transducer to the specimen.

2. A TIME-REVERSAL BASED PROCEDURE FOR IMPACT LOCATION

2.1. Time-Reversal Basic Principles

The concept of TR applied to Lamb waves is here briefly recalled with the support of **Figure 1**. Elastic guided waves are excited into a plate-like structure by means of a tone burst signal $U_D(t)$ at point A (the subscript D is used to distinguish the signal in the direct propagation phase from the reconstructed one, named D, r, in a time reversal experiment). This elastic wave propagates from A to B in the plate where it is recorded as $U_{acq}(t)$. This signal can be then time inverted $U_{acq}(-t)$ and used as the input signal in B. The final stage is to acquire the corresponding signal $U_{D,r}(-t)$ in A again.

If the source is point-like, TR allows to focus back to the source irrespective of the medium complexity (Cassereau and Fink, 1992; Fink, 1992; Wu et al., 1992). Spatial reciprocity is not broken by velocity dispersion, multiple scattering, mode conversion, anisotropy, refraction or attenuation, as long as the latter is linear with respect to the wave amplitude. This remains true even if the propagation medium is inhomogeneous with variations of density and stiffness which reflect, scatter, and refract the acoustic waves. On the contrary, non-linear elastic effects may break spatial reciprocity (and therefore focusing through TR), as do those effects that lead to wave velocity variations along the direct and inverse propagation paths (Park H.W. et al., 2009). Contrary to the case of bulk waves, TR of Lamb waves is complicated by their dispersion and multi-modal nature (Park H.W. et al., 2009).

2.2. Procedure Description

In what follows the impact localization algorithm originally proposed by Park et al. (2012) is briefly recalled.

First, Lamb guided waves are excited in the specimen under test by means of a surface-mounted piezoelectric (PZT) transducer (red circle in **Figure 2A**) reproducing an impact-like time-history (a square signal, for instance). A training data set of signals $g_i(t)$, with $i = 1, 2, ..., m$ (**Figure 2B**), is then collected recording the out-of-plane velocity at the desired m points with a Scanning Laser Vibrometer, denoted in **Figure 2A** with black dots within the target scanning area bounded by the red dashed line.

Now let us suppose that the structure is subjected to an impact within the scanned area (**Figure 2C**) and that the guided waves response $f(t)$ is recorded by the same piezoelectric used to generate the training dataset (**Figure 2D**). At this

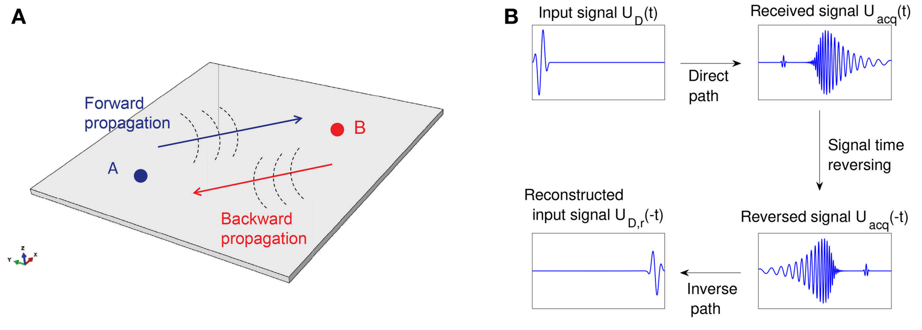

FIGURE 1 | (A) Schematic representation of time reversal (TR) procedure for Lamb waves in a plate-like structure. **(B)** A tone burst excitation $U_D(t)$ is provided at point A, generating elastic guided waves in the plate that are recorded as $U_{acq}(t)$ in B. This acquired signal is then time-inverted as $U_{acq}(-t)$ and used as the input signal in B. The acquired signal at point A is the inverted reconstruction $U_{D,r}(-t)$ of the original signal.

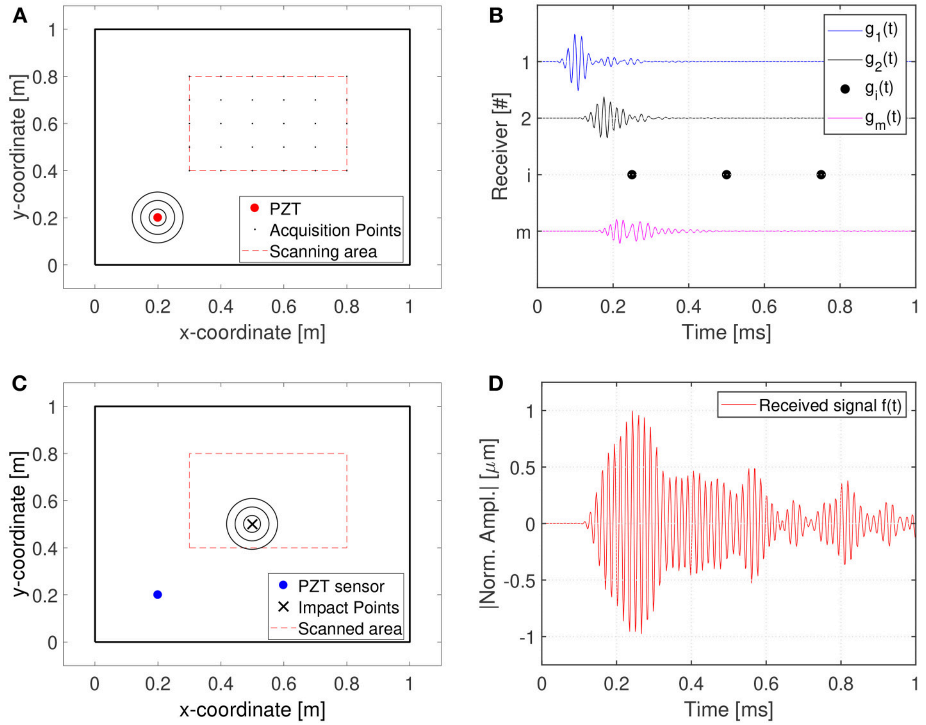

FIGURE 2 | Schematics of the proposed technique for impact localization: **(A)** scanning area; **(B)** training data set acquisition; **(C)** actual impact event; **(D)** actual impact Impulse Response Function (IRF).

point, the correlations between the actual impact response $f(t)$ and the responses of the training data set $g_i(t)$ are computed. Because of the dispersion of Lamb waves, without any numerical manipulation the correlation is very poor, since the compared signals are completely different. However, it can be mathematically shown that if the correlation is written as a function of inverted signal $f(T-t) = \tilde{f}(t)$ (being T the duration of the acquired signal), the $g_i(t)$ with maximum correlation to the actual impact response $f(t)$ can be used to identify the impact location. The correlation correlation between $f(t)$ and $g(t)$ is defined as follows (see Park et al., 2012; Miniaci, 2014 for further details):

$$(f \star g)(\tau) = \int_{-\infty}^{+\infty} f(t) g(\tau + t) \mathrm{d}t \tag{1}$$

where $\star$ denotes the correlation operation. On the other hand, the convolution of two functions is defined as:

$$(f \otimes g)(\tau) = \int_{-\infty}^{+\infty} f(t) g(\tau - t) \mathrm{d}t \tag{2}$$

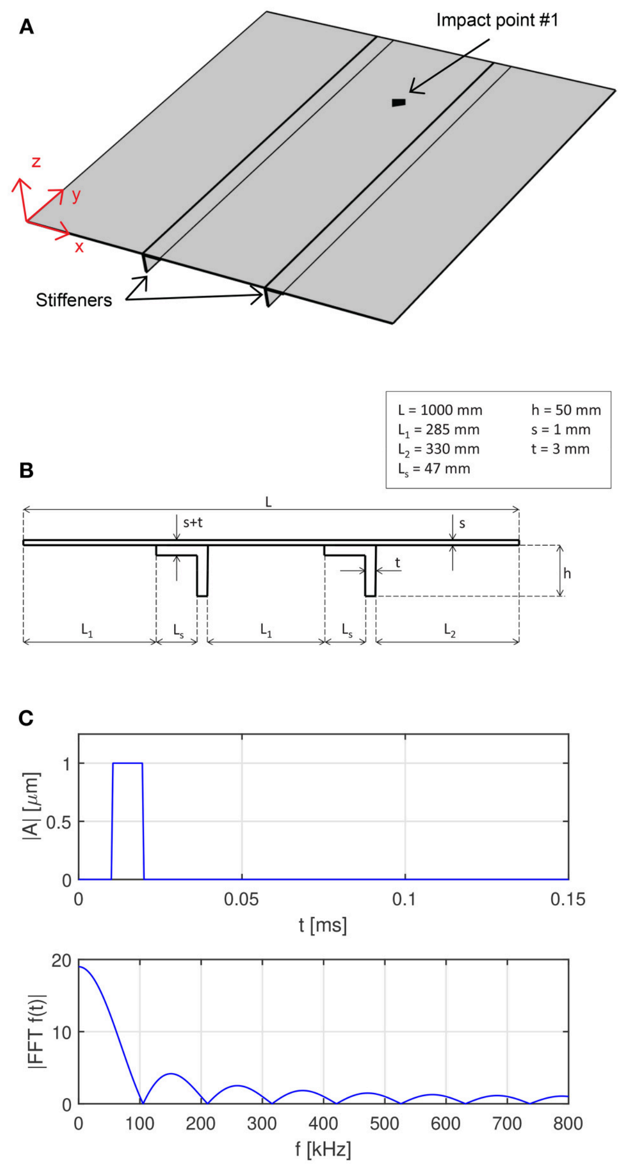

FIGURE 3 | A schematic representation of the tested specimen: **(A)** isometric view and **(B)** cross-section. The drawings are not to scale, for sake of clarity. The light gray rectangle indicate the scanning area. **(C)** Time history (top panel) and its frequency content (bottom panel) of the excitation signal (chosen as a square pulse to simulate an actual impact event).

where ⊗ is the convolution operation. Comparison between Equations (1, 2) reveals that the correlation and convolution are related to each other as follows:

$$f \star g = \tilde{f} \otimes g = \int_{-\infty}^{+\infty} \tilde{f}(t) g(\tau - t) \mathrm{d}t \tag{3}$$

Equation (3) shows that the correlation between two signals is mathematically equivalent to the convolution between one and the time-reversed version of the other one. By applying the Fourier transform, the convolution in the time domain is transformed into a simple multiplication in the frequency domain:

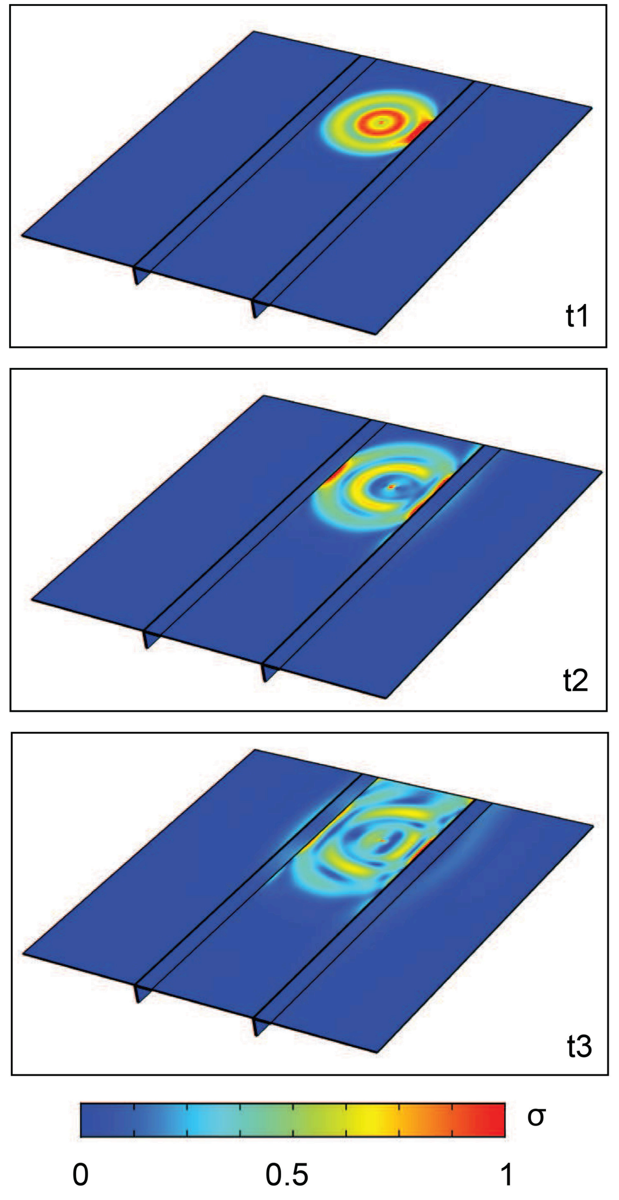

FIGURE 4 | Three snapshots of the guided wave propagation in terms of normalized Von Mises stress at different time steps $t1 = 0.5$ ms, $t2 = 0.75$ ms and $t3 = 1$ ms after the simulated impact is applied. It is possible to observe how the stiffeners confine and guide much of the energy, and thus of the available information to determine the impact. This is due to the much higher rigidity of the stiffeners with respect to the plate.

$$\mathcal{F}\{f \otimes g\} = \mathcal{F}\{f\} \cdot \mathcal{F}\{g\} \tag{4}$$

where $\mathcal{F}$ denotes the Fourier transform operator. The convolution is reconstructed by taking the inverse Fourier transform of Equation (4):

$$f \otimes g = \mathcal{F}^{-1}\{\mathcal{F}\{f\} \cdot \mathcal{F}\{g\}\} \tag{5}$$

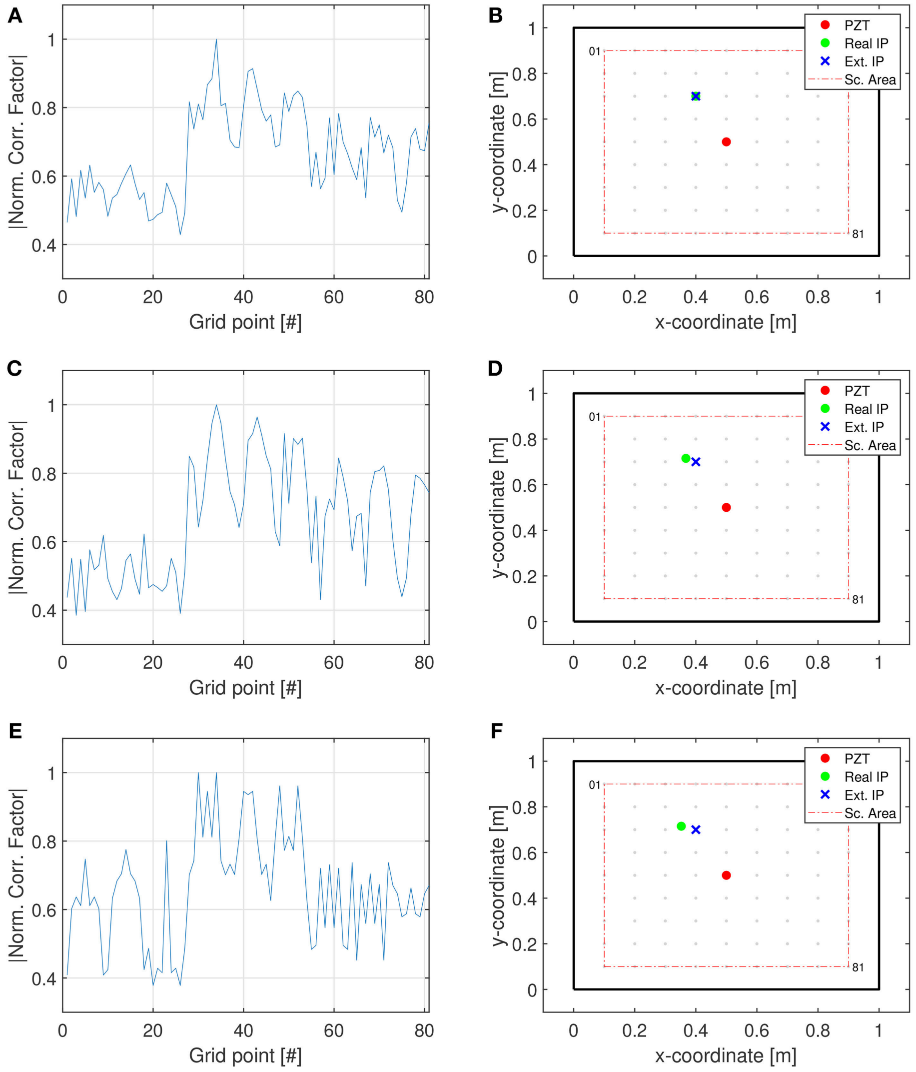

FIGURE 5 | Numerical results. **(A,C,E)** Normalized correlation values between the signal registered at each grid point and the signal of the actual impact points (1-D plots). **(B,D,F)** The estimated points of impact are then derived and highlighted in a 2-D visualization. The gray dots denote the scanning points, the red circle the acquisition point, the green spot the real impact positions and the blue crosses the estimated ones.

Since this new expression involves only Fourier and inverse Fourier transforms and point-wise multiplications, the correlation or convolution can be computed effectively:

$$f \star g = f(-t) \otimes g = \mathcal{F}^{-1}\{\mathcal{F}\{f(-t)\} \cdot \mathcal{F}\{g\}\} \tag{6}$$

The maximum correlation value, obtained using Equation (6) is designated as the most likely impact point (Park et al., 2012).

3. IMPACT LOCALIZATION: NUMERICAL AND EXPERIMENTAL RESULTS

3.1. Description of the Tested Specimen

The reviewed impact localization algorithm is tested on a reinforced aluminum plate, schematically shown in **Figures 3A,B**. The specimen is 1,000 mm in length and 1,000 mm in width. It is composed of a flat aluminum 1-mm thick plate reinforced by two unidirectional eccentric stiffeners with L cross-section. The width of both the web and the flange of the stiffeners is 3 mm. The stiffeners are parallel to the specimen edges and are attached to the plate along their full length. Material properties are the following: Young's modulus $E = 68$ GPa, Poisson's ratio 0.32 and density $\rho = 2,700$ kg/m^3 (Miniaci, 2014).

3.2. Numerical Application

The reliability of the proposed technique is first tested numerically by means of a transient Finite Element (FE) analysis simulating the propagation of guided waves in the aforementioned specimen. The implemented model is shown in

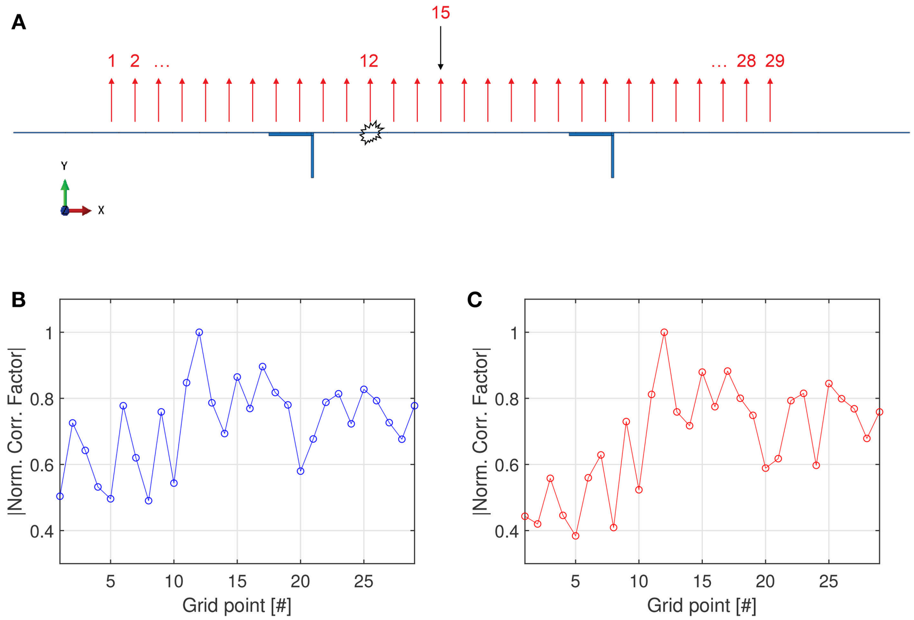

FIGURE 6 | Numerical results. **(A)** Representation of the 2D finite element model under plane strain assumption. The black arrow shows the position where elastic waves have been excited into the specimen (through an imposed out-of-plane displacement of the corresponding mesh node) in phase 1. It also represents the collecting position during phase 2 (i.e., after the actual impact has occurred). The location of the acquisition points composing the training data are indicated with red arrows. **(B,C)** Normalized correlation values between the signal registered at each grid point and the signal of the actual impact points (1-D plots) for the aluminum II and steel cases, respectively. Additional numerical simulations showing the effectiveness of the TR-based technique regardless of the material properties of the specimen.

TABLE 1 | Young's modulus, density and Poisson's ratio of the stiffened plate used for additional numerical simulations in order to prove the effectiveness of the technique regardless the material properties of the sample.

Material	Young's modulus E [GPa]	Density ρ [kg·m^{-3}]	Actual impact point x-coordinate [mm]	Estimated impact point and *x*-coordinate [mm]
Aluminum (II)	70.5	2,750	390	12–387.5
Stainless steel	210	7,850	390	12–387.5

The following case studies are considered: aluminum (with slightly different properties with respect to those initially considered in the manuscript) and stainless steel. The Table also reports the actual impact point x-coordinate [mm] and the estimated ones (along with the grid point number).

Figure 3A. A full 3*D* propagation field is calculated by using linear hexahedral brick elements of C3D8R type for a total number of $2,686,684$ nodes. To ensure accuracy to the time-transient FE simulations, the plate domain is discretized with elements of maximum side length $L_{max} = 1$ mm and the time integration step kept as $t_{int} \leq 1e - 8$ s (De Marchi et al., 2013). To reproduce the experimental conditions, wave reflection, generated by both plate edges and stiffeners, as well as geometrical attenuation, due to wave radiation, are taken into account. Impact is simulated by imposing an out-of-plane displacement in the form of a sharp square pulse (see **Figure 3C**), which reproduces the kind of excitation that may occur in an impact event. In the FE analysis only 81 scanning points covering a square scanning area of 900 × 900 mm are considered.

Figure 4 shows three snapshots of the simulated guided wave propagation in terms of normalized Von Mises stress at different time steps $t1 = 0.5$ ms, $t2 = 0.75$ ms, and $t3 = 1$ ms after the simulated impact is applied. It is possible to observe how the stiffeners confine and guide much of the energy, and thus of the available information to determine the impact. This is due to the much higher rigidity of the stiffeners with respect to the plate.

The following impact cases are considered:

(i) Impact location corresponding to a grid point (results are shown in **Figures 5A,B**);
(ii) Impact location corresponding to a random point within the area delimited by the stiffeners (results are shown in **Figures 5C,D**);
(iii) Impact location almost equidistant from two grid points (results are shown in **Figures 5E,F**);

Corresponding signals are collected and processed as explained in section 2.2. Results are presented in **Figure 5**, confirming the reliability of the method. **Figure 5** reports the normalized correlation values between the signal registered at each grid point and the signal of the actual impact points (1-D plots) as well as

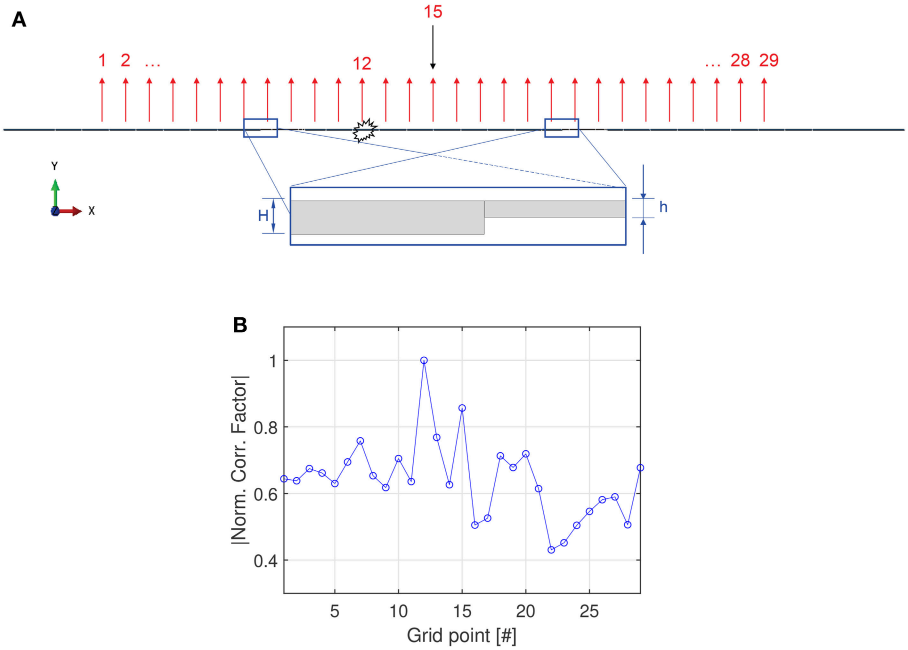

FIGURE 7 | Numerical simulations showing the effectiveness of the TR-based technique regardless of the geometrical properties of the specimen. **(A)** Representation of the 2D finite element model under plane strain assumption. The stiffeners have been replaced by tapers of half the plate thickness h = 0.5; H = 0.5 mm. All the other parameters are left unaltered with respect to **Figure 6**. **(B)** The impact location still is predicted with good accuracy.

the estimated points of impact derived in a 2-D visualization. The gray dots denote the scanning points, the red circle the acquisition point, the green spot the real impact positions and the blue crosses the estimated ones. Specifically, it appears that when the impact point coincides with an acquisition point (**Figure 5B**), the correlation presents a higher value (**Figure 5A**) than for a random point (**Figures 5C,E**) and the impact location can be predicted extremely accurately (**Figure 5B**). Therefore, numerical simulations show that the farther the impact point is from a scanning point, the smaller the correlation value is. The minimum is achieved when an impact occurs at a location equidistant between scanning points (**Figures 5E,F**).

3.3. Additional Numerical Considerations

In what follows, we verify the effectiveness of the TR-based technique regardless of the material and geometrical properties of the specimen. To do this, additional numerical simulations have been carried out (without loss of generality and for the sake of a reduction in computation time, a 2D plane strain model has been implemented see **Figure 6A**). First, two additional numerical simulations, in which the material properties of the specimen have been changed by small and large amounts with respect to those considered initially, have been performed (refer to **Table 1** for the adopted properties), in the case of an impact occurring inside the area delimited by the stiffeners (in #12) and training data collected in #15 (see **Figure 6A**). In order to verify that the TR-based procedure is not dependent on the local elastic wave velocity, exactly the same configuration is maintained for the two study cases, but with different material properties (aluminum II in **Figure 6B** and steel **Figure 6C**, respectively). **Figures 6B,C** report the normalized correlation values between the signal calculated at each grid point and the signal of the actual impact points (1-D plots), clearly proving the independence of the procedure from wave velocity. This is in accordance with a fundamental symmetry principle of TR (Fink et al., 2000), if the geometry and excitation/acquisition conditions are left unaltered (Miniaci et al., 2017).

Secondly, the stiffeners have been replaced by tapers running through half of the thickness of the plate, as shown in **Figure 7**, in order to show the effectiveness of the TR-based technique regardless of the geometrical properties of the specimen. In this case, too, the possibility to correctly locating the impact is fully supported by the numerical simulations.

Finally, we performed additional numerical simulations to check the reliability of the TR-based technique in the case of an impact occurring outside the area delimited by the stiffeners (for instance in #23 with respect to **Figure 8**) and training data collected through a transducer still bonded between the two stiffeners (in #15). Here too, without loss of generality and to reduce computation time, a 2D plane strain model has been implemented, as shown in **Figure 8A**. Black and red arrows have the same meaning as in the previous cases. We found that the accuracy of the technique in detecting impacts outside the area delimited by the stiffeners is strongly correlated to the quantity of energy the geometrical irregularity (i.e., the stiffeners) allow to reach the detection point. Indeed, since the thickness of the stiffeners is three times that of the plate, they confine and guide most of the energy (the amplitude of the wave

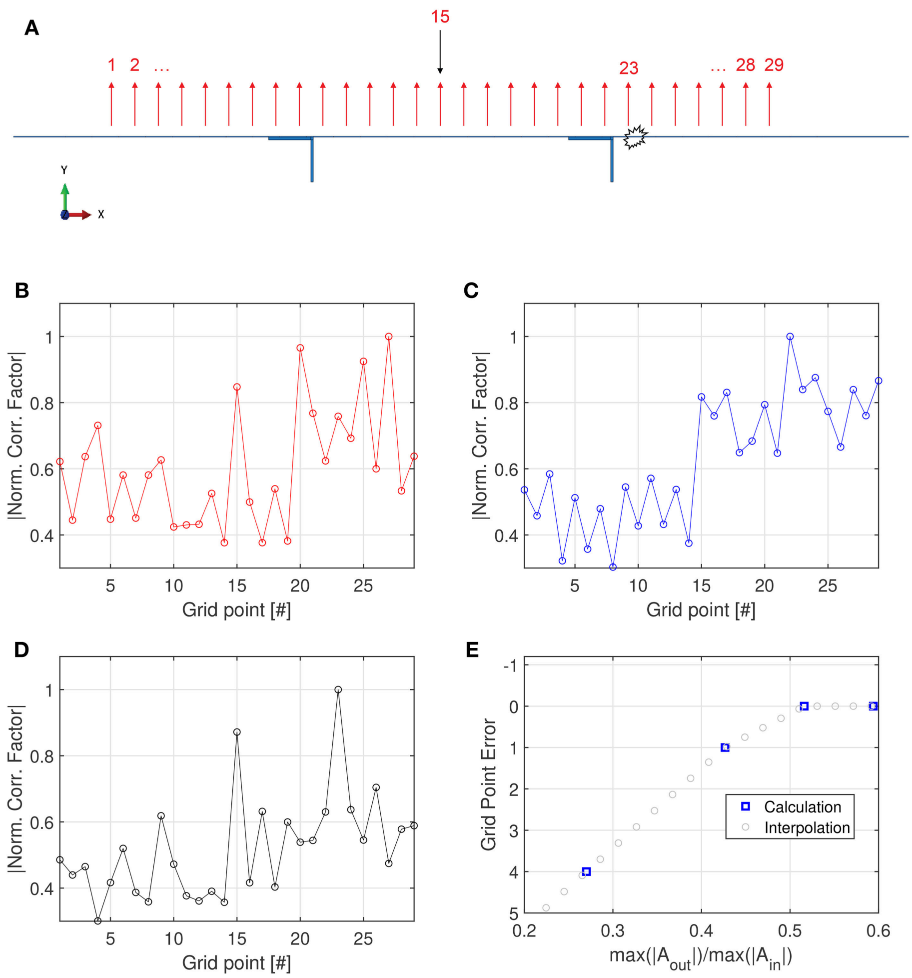

FIGURE 8 | (A) Representation of the 2D finite element model under plane strain assumption in the case of an impact occurring outside the area delimited by the stiffeners (#23) and transducer for the training data collection bonded between the stiffeners (#15). The black arrow shows the position where elastic waves are excited into the specimen in phase 1. It also represents the collecting positions of the training data during phase 2, i.e., after the actual impact has occurred (in #23). The location of the acquisition points composing the training data are indicated with red arrows. **(B–D)** Numerical results show the accuracy of the technique in terms of normalized correlation values between the signal registered at each grid point and the signal of the actual impact point (1-D plots) as the ratio of the maximum of the wave amplitudes registered outside (A_{out}) and inside (A_{in}) the area delimited by the stiffeners increases : **(B)** $A_{out}/A_{in} = 0.283$, **(C)** $A_{out}/A_{in} = 0.415$, and **(D)** $A_{out}/A_{in} = 0.511$. **(E)** Calculated and extrapolated values of the grid point error as a function of the wave amplitude outside and inside the region delimited by the stiffeners.

beyond the stiffeners is more than 3 times smaller than that inside the stiffeners), strongly limiting the information reaching the transducer in #15 (in the case of impact occurring outside the area delimited by the stiffeners and training data collected from a transducer bonded between the stiffeners). Therefore, in this specific case with huge impedance mismatch, another map of training data would be required to correctly identify the impact location (see **Figure 8B**). This condition corresponds to a small ratio between the maximum of the wave amplitudes calculated outside (A_{out}) and inside (A_{in}) the area delimited by the stiffeners (0.283). However, if the rigidity of the stiffeners is decreased, a larger wave amplitude is allowed to pass beyond them and the accuracy of the technique increases, as for instance in the case reported in **Figures 8C,D**, corresponding to the cases of $A_{out}/A_{in} = 0.415$ and $A_{out}/A_{in} = 0.511$, respectively. Thus, it emerges that the method can still be applied insofar as sufficient wave amplitude is guaranteed beyond the geometrical irregularities (quantitatively a zero-grid point error is reached for a ratio of 0.5 see **Figure 8D**).

3.4. Experimental Application

The tested specimen is shown in **Figure 9A**. The red circle represents the position of both the piezoelectric transducers used as actuator for the data training acquisition and of the SLDV acquisition point in impact tests. The testing region (768 × 803 mm), represented as the yellow rectangular box, is composed of a regular grid with 93 × 91 acquisition points. Impacts are simulated in correspondence of the three points shown in **Figure 9A**, that were randomly chosen within the area delimited by the stiffeners, and denoted by black stars.

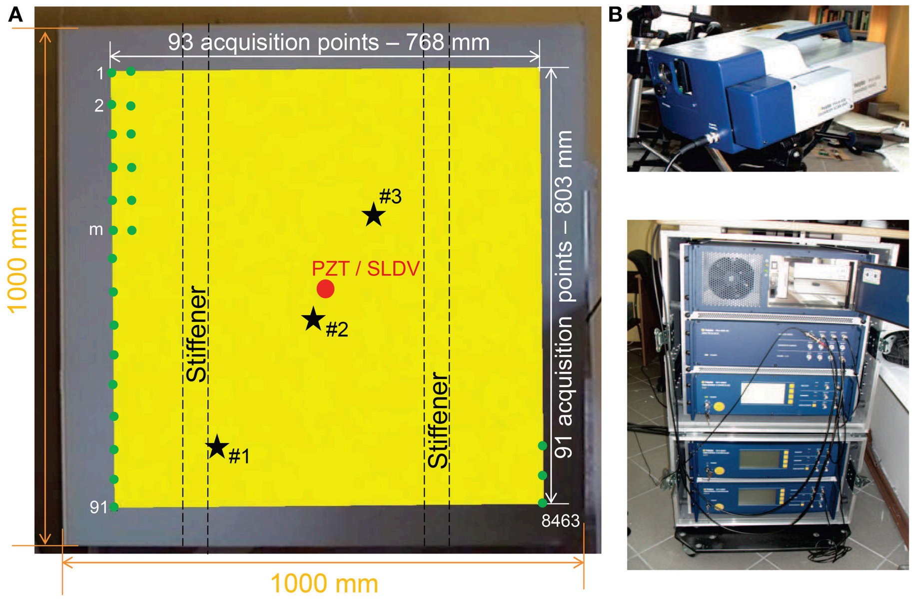

FIGURE 9 | (A) Photograph of the tested specimen. The red circle represents the position of both the PZT transducer used as actuator for the data training acquisition and the SLDV acquisition in impact tests. The yellow rectangle represents the scanned portion of the plate (testing region) during the training acquisition phase and consists of a 93 × 91 grid of acquisition points (green dots) in the horizontal and vertical directions, respectively. The unknown impact points - #1, #2, and #3 - are represented by means of black stars and chosen within the area delimited by the stiffeners. **(B)** SLDV experimental setup.

Elastic guided waves are excited in the specimen using a ceramic piezoelectric disk of diameter 10 mm made of Sonox® by CeramTec® glued to the surface of the investigated sample using commercial super-glue. A scanning measurement head (PSV 400 by Polytec®) connected to a data acquisition system and a steering circuit (**Figure 9B**) is used to perform the out-of-plane measurements of the velocities over the target area. The pulse excitation is fed from a TGA1241 function generator by Thurlby Thandar Instruments and amplified through an EPA-104 amplifier by Piezo Systems® Inc, inducing a 20 V_{pp} signal. In order to improve measurements accuracy, the investigated specimen is covered with self-adesive retro-reflective film by ORALITE®. This allows to improve the laser vibrometer signal level at each measurement point regardless of the incidence angle of the measurement beam on the surface (Ostachowicz et al., 2011).

The training data collection process is realized using the square pulse shown in **Figure 3C** applied to the piezoelectric transducer. For each scanning point, 16, 384 samples are collected over 8 ms by the SLDV at a sampling rate of 256 kHz, and signals are averaged 128 times to improve the signal-to-noise ratio. Intervals of 50 ms are provided between two consecutive pulse excitations to allow signals to decay close to the background noise level before a new data collection. Measurement of all time signals from 8, 463 scanning points takes 8 h.

The results are shown in **Figure 10**, where the normalized correlation values between the signal registered at each grid point and the signal of the actual impact points (**Figures 10A,C,E**) are presented. The estimated point of impact is then derived and highlighted in **Figures 10B,D,F**. The gray dots denote all the scanning points, the red circle the acquisition point whereas the green spot the real impact position and the blue cross the estimated one. It clearly emerges that the algorithm is able to precisely identify the impact point for all the three considered cases. A very good accuracy, within 0.5 cm, is obtained regardless of the impact position (Miniaci, 2014).

4. CONCLUSIONS

This work presents an impact localization algorithm based on TR and laser-vibrometry. The main idea is to locate an impact event by simply comparing the actual impact response with IRFs obtained from a grid of training points. This technique is shown to be very powerful particularly in the case of irregular waveguides or complex structures since it does not require the knowledge of the local wave velocity or the structural geometry. Its main advantages over existing techniques are thus that: (a) it can be applied to complex structures with additional structural features such as ribs, stiffeners, and rivet connections; (b) only simple correlation calculations are required for impact localization, making it attractive for real-time automated monitoring; (c) high spatial resolution in impact localization can be achieved. A significant advantage of the present approach compared to previous realizations of the technique is the use of a single instead of multiple transducers, thus simplifying its experimental realization in applications considerably.

Both numerical and experimental results confirm the capability of the method to identify unknown impact positions without a priori knowledge of the tested specimen. The described

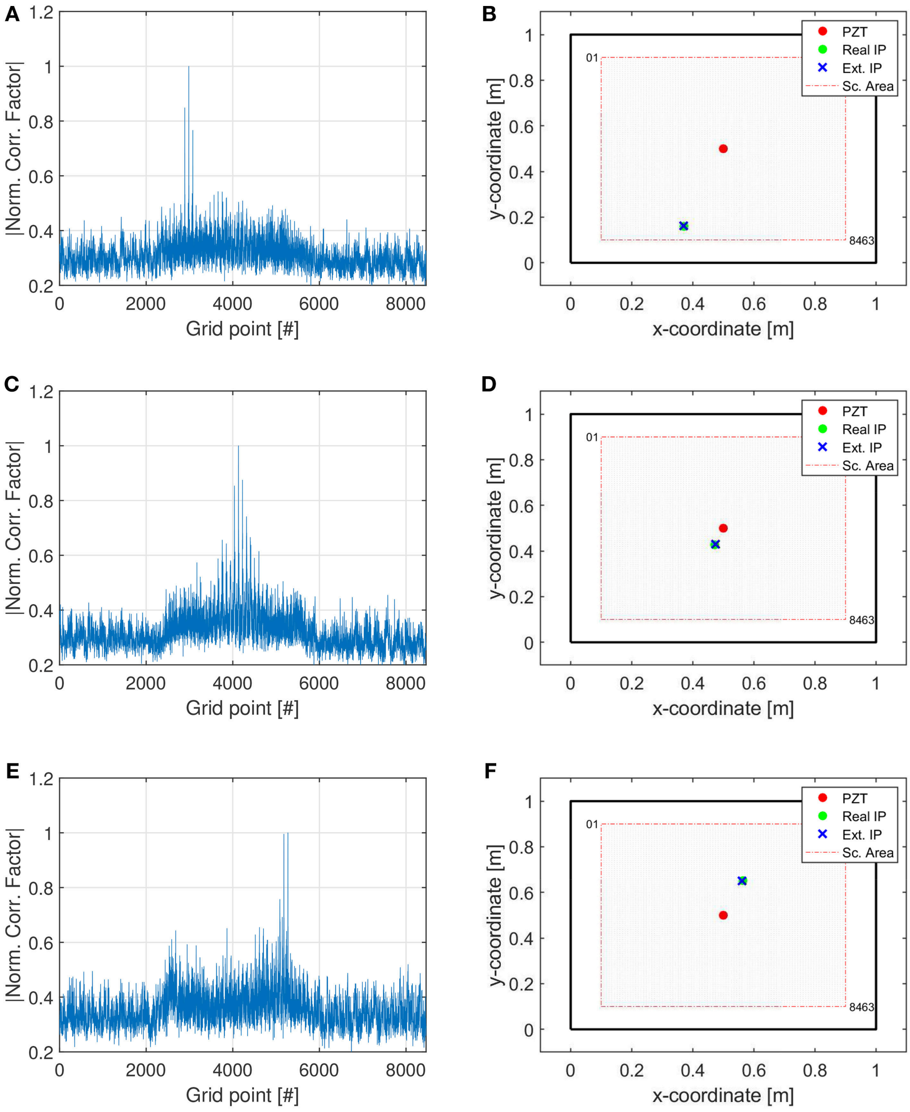

FIGURE 10 | Experimental results. **(A,C,E)** Normalized correlation values between the signal registered at each grid point and the signal of the actual impact points (1-D plots). **(B,D,F)** The estimated points of impact are then derived and highlighted in a 2-D visualization. The gray dots denote the scanning points, the red circle the acquisition point, the green spot the real impact positions and the blue crosses the estimated ones.

procedure is here validated using only a single acquisition point. Tests also show that the localization of trial impacts can be successfully achieved regardless of the impact position (near the sensor, far from the sensor, near a plate edge, near a stiffener).

Although many methods are already available, the present method is particularly well-suited to impact localization in complex structures, such as parts fabricated using multiscale composite materials, thanks to its unique potential to treat in the same manner different kinds of waveguides, both isotropic and anisotropic, homogeneous and inhomogeneous with simple or irregular geometries. In this work, the training data was obtained over a grid of square points. However, a more complex disposition of the SLDV acquisition points minimizing their distance (such as for instance a triangular disposition) may reduce the training data acquisition time.

Future developments may include the optimal grid point disposition for the training data and additional tests in order to examine the robustness of the proposed approach under temperature variations.

DATA AVAILABILITY

The datasets generated for this study are available on request to the corresponding author.

AUTHOR CONTRIBUTIONS

MMin performed most of the experimental and numerical work. MMaz, MR, PK, and WO contributed to experiments. NK to the simulations. FB and NP to discussions and to the writing of the paper.

FUNDING

MMin has received funding from the European Union's Horizon 2020 research and innovation programme under the Marie Skłodowska-Curie grant agreement n. 754364. NK was supported by Progetto d'Ateneo/Fondazione San Paolo Metapp, n. CSTO160004. FB is supported by the FET Proactive Neurofibres grant n. 732344, the COST Action 15125 DENORMS (Designs for Noise Reducing Materials and Structures), and by Progetto d'Ateneo/Fondazione San Paolo Metapp, n. CSTO160004. NP was supported by the European Commission H2020 under the Graphene Flagship Core 2 No. 785219 (WP14 Composites) and the FET Proactive Neurofibres grant n. 732344, as well as by the Italian Ministry of Education, University and Research (MIUR) under the Departments of Excellence grant L.232/2016. Some of the contents of the present work first appeared in MMin's Ph.D. thesis and are referenced in the text by Miniaci (2014).

REFERENCES

Baravelli, E., Senesi, M., Ruzzene, M., and De Marchi, L. (2013). Fabrication and characterization of a wavenumber-spiral frequency-steerable acoustic transducer for source localization in plate structures. *IEEE Trans. Instrument. Meas.* 62, 2197–2204. doi: 10.1109/TIM.2013.2255992

Cassereau, D., and Fink, M. (1992). Time-reversal of ultrasonic fields. III. theory of the closed time-reversal cavity. *IEEE Trans. Ultrason. Ferroelectr. Frequency Control* 39, 579–592. doi: 10.1109/58.156176

Ciampa, F., and Meo, M. (2012). Impact detection in anisotropic materials using a time reversal approach. *Struct. Health Monitor.* 11, 43–49. doi: 10.1177/1475921710395815

Coverley, P. T., and Staszewski, W. J. (2003). Impact damage location in composite structures using optimized sensor triangulation procedure. *Smart Mater. Struct.* 12:795. doi: 10.1088/0964-1726/12/5/017

De Marchi, L., Marzani, A., and Miniaci, M. (2013). A dispersion compensation procedure to extend pulse-echo defects location to irregular waveguides. *NDT E Int.* 54, 115–122. doi: 10.1016/j.ndteint.2012.12.009

De Marchi, L., Marzani, A., Speciale, N., and Viola, E. (2011). A passive monitoring technique based on dispersion compensation to locate impacts in plate-like structures. *Smart Mater. Struct.* 20:035021. doi: 10.1088/0964-1726/20/3/035021

De Marchi, L., Testoni, N., and Marzani, A. (2018). Spiral-shaped piezoelectric sensors for lamb waves direction of arrival (doa) estimation. *Smart Mater. Struct.* 27:045016. doi: 10.1088/1361-665X/aab19e

Fink, M. (1992). Time reversal of ultrasonic fields. I. basic principles. *IEEE Trans. Ultrason. Ferroelectr. Frequency Control* 39, 555–566. doi: 10.1109/58.156174

Fink, M., Cassereau, D., Derode, A., Prada, C., Roux, P., Tanter, M., et al. (2000). Time-reversed acoustics. *Rep. Prog. Phys.* 63:1933. doi: 10.1088/0034-4885/63/12/202

Gliozzi, A. S., Miniaci, M., Bosia, F., Pugno, N. M., and Scalerandi, M. (2015). Metamaterials-based sensor to detect and locate nonlinear elastic sources. *Appl. Phys. Lett.* 107:161902. doi: 10.1063/1.4934493

Grandt, A. (2004). *Fundamentals of Structural Integrity: Damage Tolerant Design and Nondestructive Evaluation*. Hoboken, NJ: John Wiley.

Hajzargerbashi, T., Kundu, T., and Bland, S. (2011). An improved algorithm for detecting point of impact in anisotropic inhomogeneous plates. *Ultrasonics* 51, 317–324. doi: 10.1016/j.ultras.2010.10.005

Ing, R.-K., and Fink, M. (1988). Time-reversed lamb waves. *Ultrason. Ferroelectr. Frequency Control* 45, 1032–1043. doi: 10.1109/58.710586

Ing, R. K., and Fink, M. (1996). "Time recompression of dispersive lamb waves using a time reversal mirror-application to flaw detection in thin plates," in *1996 IEEE Ultrasonics Symposium* (San Antonio, TX), 659–663.

Kundu, T., Das, S., and Jata, K. V. (2009). Detection of the point of impact on a stiffened plate by the acoustic emission technique. *Smart Mater. Struct.* 18:035006. doi: 10.1088/0964-1726/18/3/035006

Kundu, T., Nakatani, H., and Takeda, N. (2012). Acoustic source localization in anisotropic plates. *Ultrasonics* 52, 740–746. doi: 10.1016/j.ultras.2012.01.017

Miniaci, M. (2014). *Behaviour and Applications of Elastic Waves in Structures and Metamaterials*. Ph.D. thesis, Alma Mater Studiorum.

Miniaci, M., Gliozzi, A. S., Morvan, B., Krushynska, A., Bosia, F., Scalerandi, M., et al. (2017). Proof of concept for an ultrasensitive technique to detect and localize sources of elastic nonlinearity using phononic crystals. *Phys. Rev. Lett.* 118:214301. doi: 10.1103/PhysRevLett.118.214301

NASA (2003). *Columbia Accident Investigation Board*. Report.

Ostachowicz, W., Kudela, P., Krawczuk, M., and Zak, A. (2011). *Guided Waves in Structures for SHM: The Time - Domain Spectral Element Method*. Chichester: A John Wiley & Sons, Ltd.; Wiley.

Park, B., Sohn, H., Olson, S. E., DeSimio, M. P., Brown, K. S., and Derriso, M. M. (2012). Impact localization in complex structures using laser-based time reversal. *Struct. Health Monitor.* 11, 577–588. doi: 10.1177/1475921712449508

Park, H. W., Kim, S. B., and Sohn, H. (2009). Understanding a time reversal process in lamb wave propagation. *Wave Motion* 46, 451–467. doi: 10.1016/j.wavemoti.2009.04.004

Park, H. W., Sohn, H., Law, K. H., and Farrar, C. R. (2007). Time reversal active sensing for health monitoring of a composite plate. *J. Sound Vibr.* 302, 50–66. doi: 10.1016/j.jsv.2006.10.044

Park, J., Ha, S., and Chang, F. (2009). Monitoring impact events using a system-identification method. *AIAA* 47:2011. doi: 10.2514/1.34895

Salamone, S., Bartoli, I., Leo, P. D., Scala, F. L. D., Ajovalasit, A., D'Acquisto, L., et al. (2010). High-velocity impact location on aircraft panels using macro-fiber composite piezoelectric rosettes. *J. Intell. Mater. Syst. Struct.* 21, 887–896. doi: 10.1177/1045389X10368450

Senesi, M., Xu, B., and Ruzzene, M. (2010). Experimental characterization of periodic frequency-steerable arrays for structural health monitoring. *Smart Mater. Struct.* 19:055026. doi: 10.1088/0964-1726/19/5/055026

Seydel, R., and Chang, F.-K. (2001). Impact identification of stiffened composite panels: I. system development. *Smart Mater. Struct.* 10:354. doi: 10.1088/0964-1726/10/2/323

Sohn, H., DeSimio, M. P., Olson, S. E. B. K., and Derriso, M. (2011). "Impact localization in an aircraft fuselage using laser based time reversal," in *Proceedings of SPIE - The International Society for Optical Engineering* (San Diego, CA), 7984.

Staszewski, W. J., Worden, K., Wardle, R., and Tomlinson, G. R. (2000). Fail-safe sensor distributions for impact detection in composite materials. *Smart Mater. Struct.* 9:298. doi: 10.1088/0964-1726/9/3/308

Tracy, M., and Chang, F.-K. (1998). Identifying impacts in composite plates with piezoelectric strain sensors, part II: Experiment. *J.*

Intell. Mater. Syst. Struct. 9, 929–937. doi: 10.1177/1045389X9800901109

Wang, C. H., Rose, J. T., and Chang, F.-K. (2004). A synthetic time-reversal imaging method for structural health monitoring. *Smart Mater. Struct.* 13:415. doi: 10.1088/0964-1726/13/2/020

White, P. H. (1969). Cross correlation in structural systems: dispersion and nondispersion waves. *J. Acous. Soc. Am.* 45, 1118–1128. doi: 10.1121/1.1911582

Wu, F., Thomas, J., and Fink, M. (1992). Time reversal of ultrasonic fields. II. experimental results. *IEEE Trans. Ultrason. Ferroelectr. Frequency Control* 39, 567–578. doi: 10.1109/58.156175

Conflict of Interest Statement: The authors declare that the research was conducted in the absence of any commercial or financial relationships that could be construed as a potential conflict of interest.

frontiers
in Materials

ORIGINAL RESEARCH
published: 22 March 2019
doi: 10.3389/fmats.2019.00040

On the Design of Superstable Prestressed Frameworks

Scott D. Kelly[1], *Andrea Micheletti*[2]* *and Alessandro Tiero*[2]

[1] *Department of Mechanical Engineering and Engineering Sciences, University of North Carolina at Charlotte, Charlotte, NC, United States,* [2] *Department of Civil and Computer Science Engineering, University of Rome "Tor Vergata," Rome, Italy*

The strength and stiffness of prestressed lattices, and their mechanical behavior, depend strongly on the underlying graph and the nodal conformation geometry. A special class of structures is that of superstable frameworks, that is, prestressed frameworks which are stable independently of material properties and level of prestress. After reviewing the main related notions and results in rigidity theory, we exploit the characterization of superstability for generic configurations to establish a construction for superstable systems on a given number of nodes generically placed in two or three dimensions.

Keywords: universal rigidity, superstability, generic configuration, Grünbaum polygon, tensegrity frameworks

Edited by:
Chiara Daraio,
California Institute of Technology,
United States

Reviewed by:
Francesco Dal Corso,
University of Trento, Italy
Anastasiia O. Krushynska,
University of Trento, Italy

****Correspondence:***
Andrea Micheletti
micheletti@ing.uniroma2.it

Specialty section:
This article was submitted to
Mechanics of Materials,
a section of the journal
Frontiers in Materials

Received: *12 December 2018*
Accepted: *20 February 2019*
Published: *22 March 2019*

Citation:
Kelly SD, Micheletti A and Tiero A
(2019) On the Design of Superstable
Prestressed Frameworks.
Front. Mater. 6:40.
doi: 10.3389/fmats.2019.00040

1. INTRODUCTION

The mechanical behavior of latticed structures is greatly affected by the properties of the underlying graph and the geometrical conformation of nodal positions. The simplest and most commonly adopted model is that of bar-and-joint framework, i.e., a graph together with a spatial placement of its vertices, or nodes. In **Figure 1** different types of framework are shown (cf. e.g., Gortler et al., 2010; Connelly, 2013). If a set of edge lengths is compatible with a finite motion, then the framework is *flexible* (**Figure 1A**). When a framework is *rigid* at a given configuration, there is no other configuration close to it with same edge lengths (**Figure 1B**). If the edge lengths are compatible with just one configuration in d dimensions, then the framework is *globally rigid* (**Figure 1C**). If that configuration is unique even if embedded in a higher dimensional space, then the framework is *universally rigid* (**Figure 1D**).

A distinction can be made between generic configurations, those for which the nodal coordinates are algebraically independent, and nongeneric ones, which do not satisfy this condition (cf. e.g., Gortler et al., 2010; Connelly, 2013). As we will see in the next section, in case of a generic configuration on n nodes, the minimum number of edges required for universal rigidity is equal to $e = dn - d(d+1)/2 + 1$, that is, $e = 2n - 2$ for $d = 2$ and $e = 3n - 5$ for $d = 3$.

Universal rigidity is strictly connected to superstability, the property of prestressed frameworks for which they are stable independently of the constitutive material properties and level of prestress. (Connelly, 1982; Zhang and Ohsaki, 2007; Micheletti, 2013). In particular, in the generic case, universal rigidity and superstability are equivalent (Connelly, 1982; Gortler and Thurston, 2014).

After reviewing the relevant notions and results in rigidity theory, we provide a specific construction to determine minimal generically universally rigid frameworks, i.e., generically universally rigid frameworks with the minimum number of edges, for an assigned set of nodal positions in two or three dimensions. The frameworks obtained with such a construction can be seen as a generalization of Grünbaum polygons (**Figure 2**) (Grünbaum and Shephard, 1978; Roth and Whiteley, 1981). In case of nongeneric configurations, it is possible to decrease the number of

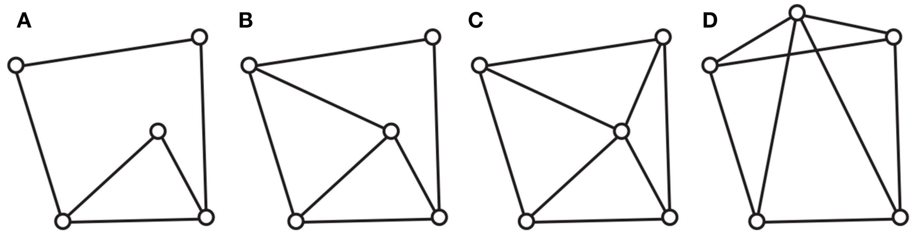

FIGURE 1 | Frameworks in two-dimensions belonging to different rigidity classes: flexible **(A)**, rigid **(B)**, globally rigid **(C)**, and universally rigid **(D)**.

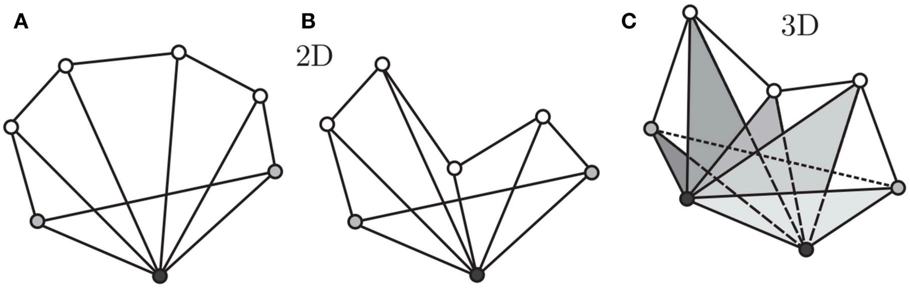

FIGURE 2 | A Grünbaum polygon **(A)**, and its nonconvex generalizations in two **(B)** and three dimensions **(C)**. Center nodes and neighboring nodes (as defined in Section 3.1) are depicted in black and gray, respectively.

edges further (**Figure 3**); however, limited theoretical results are available for nongeneric systems, and we plan to consider this case in a future study. Our main results (Theorems 9 and 10) are presented in Section 3. Basic definitions and supporting results are reviewed in Section 2.

2. BASIC RIGIDITY DEFINITIONS AND RESULTS

Different classes of rigidity can be defined for frameworks, and in each of them the generic and nongeneric cases can be distinguished. Prestressed (or prestressable) systems naturally comes into play when characterizing globally rigid and universally rigid frameworks. In writing the present section, we borrowed some of the notation, terminology, and examples from the cited literature and in particular from Connelly (2013) and Gortler et al. (2010).

2.1. Rigidity Classes

Let E^d be the d-dimensional Euclidean space and V^d the associated vector space. A *graph* $\mathcal{G} = (\mathcal{N}, \mathcal{E})$ is given by a set $\mathcal{N}$ of *n nodes* together with a set $\mathcal{E}$ of *e edges* connecting pairs of‘ nodes. The edge connecting nodes $i, j \in \mathcal{N}$ is denoted by $ij \in \mathcal{E}$. Graphs are finite and undirected, without loops or multiple edges. A *configuration* in E^d for the graph $\mathcal{G}$ is an assignment of a position vector $p_i \in V^d$ to each node $i \in \mathcal{N}$, so that a corresponding point $P_i \in E^d$ is determined by its position with respect to a chosen origin $O \in E^d$. We denote by $p \in V^{nd}$ the vector grouping all nodal position vectors. A *framework* is given by a graph together with a configuration, that is, $\mathcal{F} = (\mathcal{G}, p)$ is a framework with graph $\mathcal{G}$ and configuration p.

Associated to a framework is the set $\mathcal{L}(\mathcal{G}, p)$ of the half-squared edge-lengths,

$$\mathcal{L}(\mathcal{G}, p) = \{\lambda_{ij} \in \mathbb{R}^+, ij \in \mathcal{E} : \lambda_{ij} = \frac{1}{2}|p_i - p_j|^2\}\,.$$

A configuration q is *admissible* for $(\mathcal{G}, p)$ if $\mathcal{L}(G, q) = \mathcal{L}(G, p)$. Two configurations p and q are *congruent*, and we write $p \equiv q$, if $|p_i - p_j| = |q_i - q_j|$ for every choice of i and j in $\mathcal{N}$. Equivalently, two configurations are congruent if they differ by an isometry of E^d, i.e., a composition of translations, rotations and reflections. A framework $(\mathcal{G}, p)$ is *rigid* if there is an $\varepsilon > 0$ such that any other admissible configuration q for which $|p - q| < \varepsilon$ is congruent to p.

The jacobian of $\mathcal{L}(\mathcal{G}, p)$, which is an e-by-dn matrix, is the *rigidity matrix*, R. A framework is *infinitesimally rigid* if the rank of R is equal to $nd - d(d+1)/2$, or equivalently, if the only solutions to the system of equations $R\dot{p} = 0$ are *rigid velocities*, i.e., nodal velocities in a rigid motion (**Figure 4**). For example, the equation corresponding to the edge ij in this system is given by

$$(p_i - p_j) \cdot (\dot{p}_i - \dot{p}_j) = 0$$

which is obtained by setting equal to zero the first derivative of λ_{ij}. The solutions of $R\dot{p} = 0$ which are not rigid velocities are called *mechanisms*.

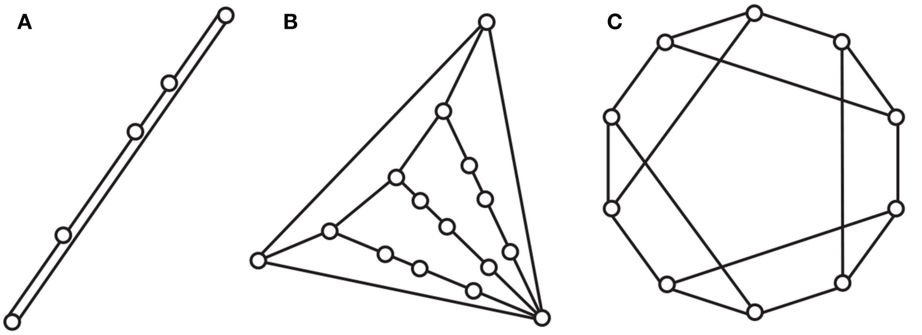

FIGURE 3 | Examples of nongeneric minimal systems. All these frameworks have less than $2n - 2$ edges and are universally rigid in two dimensions. In **(A)** all nodes need to stay aligned; **(B)** a *cable net* is attached to a *triangle*; **(C)** a system which we call *Snelson polygon*.

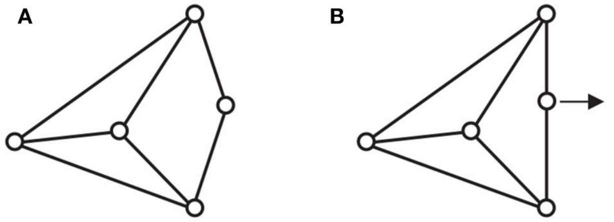

FIGURE 4 | An infinitesimally rigid framework **(A)** and a rigid framework which is not infinitesimally rigid (b). The horizontal nodal velocity vector shown in **(B)**, when all the other nodes are fixed, cause null changes in length but it is not a rigid velocity.

A framework $(\mathcal{G}, p)$ is *globally rigid* if any admissible configuration q is congruent to p (**Figure 5**). A framework is *universally rigid* if it is globally rigid in all dimensions (**Figure 6**). Universal rigidity implies global rigidity, which implies infinitesimal rigidity, which implies rigidity.

2.2. Generic Rigidity

A configuration is *generic* if the coordinates in p are algebraically independent over the integers, i.e., if the nodal coordinates do not satisfy any nontrivial polynomial equation with integer coefficients. Intuitively, if the configuration is nongeneric, then it is special in some way. For example the framework in **Figure 7A** is globally rigid, while the one in **Figure 7B**, where three nodes are aligned on a diagonal, is not. Another example is given in **Figure 4**, with configurations **Figures 4A,B** being respectively generic and nongeneric.

A framework $(\mathcal{G}, p)$ is *generically rigid* if it is rigid and p is generic. Rigidity is a generic property, i.e., it is a property of the graph, not the configuration: if a framework is rigid at a generic configuration then it is rigid at every other generic configuration. Moreover, at generic configurations, rigidity and infinitesimal rigidity are equivalent.

The minimum number of edges necessary for generic rigidity are $2n - 3$ in 2D and $3n - 6$ in 3D. Intuitively, in 2D, we can start with an edge connecting two nodes, then iteratively adding one node connected to the other nodes by two noncollinear edges. In 3D, we can start with a nondegenerate *triangle* (three vertices and three edges), then iteratively adding one *tripod*, i.e., a node connected to the other nodes by three noncoplanar edges. These constructions constitute particular *Henneberg sequences* (Eren et al., 2004b): sequences of operations which preserve minimal generic rigidity.

2.3. Stresses and Tensegrities

The characterization of global rigidity has been given in the literature in terms of *stress*. A stress ω is an assignment of a real number ω_{ij} to each edge ij of the framework. A *selfstress* for $(\mathcal{G}, p)$ is a stress satisfying at every node i the nodal equilibrium equation

$$\sum_j \omega_{ij}(p_j - p_i) = 0\,,$$

where the summation is extended to every node j connected to node i by an edge. The equilibrium equations can be written in matrix form as

$$A\omega = 0\,,$$

with A the dn-by-e *equilibrium matrix*. Selfstresses belong to the nullspace of the equilibrium matrix. One classic result is that $A = R^T$, so that the number of independent selfstresses s and mechanisms m are related to n and e by the following rule

$$dn - d(d+1)/2 - e = m - s\,, \tag{1}$$

where $d(d+1)/2$ is the number of independent rigid motions in E^d. This rule follows from the orthogonality of the fundamental subspaces (nullspace and image of the transposed) of R and A.

A fundamental object is the *stress matrix*, Ω, a n-by-n matrix whose entries are defined as follows:

$$\Omega_{ij} = \begin{cases} 0\,, & i \neq j, ij \notin \mathcal{E} \\ -\omega_{ij}\,, & i \neq j, ij \in \mathcal{E} \\ \sum_h \omega_{ih}\,, & i = j \end{cases}$$

where ω is a selfstress. The stress matrix is equal to the weighted Laplacian of the graph, with weights given by the selfstress values

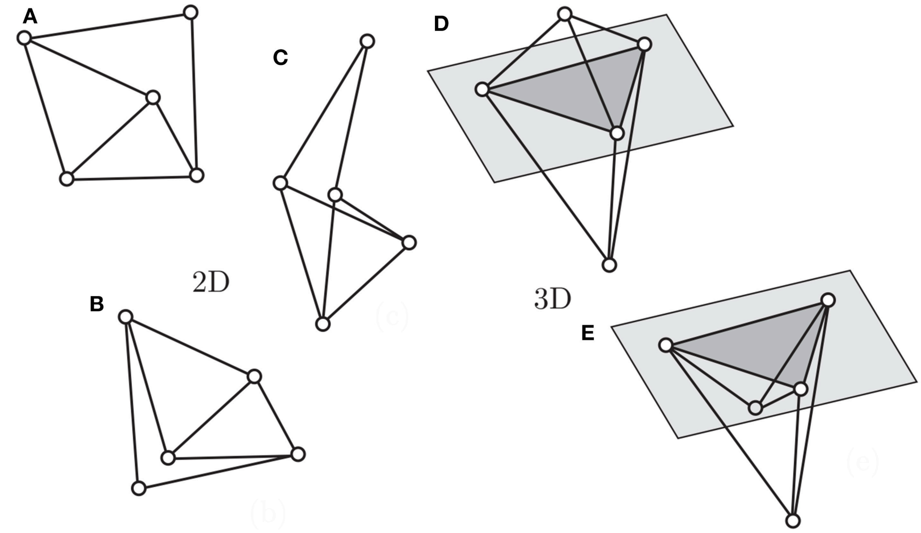

FIGURE 5 | The rigid frameworks **(A)**, in two dimensions, and **(D)**, in three dimensions, are not globally rigid: there exist more than one non-congruent admissible configurations, for example, **(B,C)** for **(A)**, and **(E)** for **(D)**.

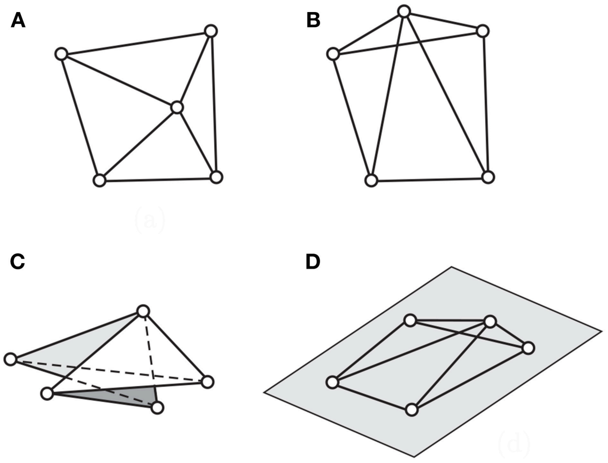

FIGURE 6 | Globally rigid **(A)** and universally rigid **(B)** frameworks. When these are considered in three dimensions, the framework **(A)** can flex out of plane, as in **(C)**, the one in **(B)** can only stay in a plane **(D)**.

on the edges. Notice that the weights can be either positive or negative, so that classic results on positively-weighted Laplacians do not apply.

A useful characterization has been given as follows (Connelly, 1982, 2013). A framework in E^d with the affine span of $p_1, \ldots, p_n$ being all E^d and a nonzero selfstress is *superstable* if the following conditions hold:

1. Ω is positive semidefinite;
2. Ω has rank $n - d - 1$;
3. there are no affine admissible motions.

Theorem 1. *Connelly (1982), see also Connelly (2013) A superstable framework is universally rigid.*

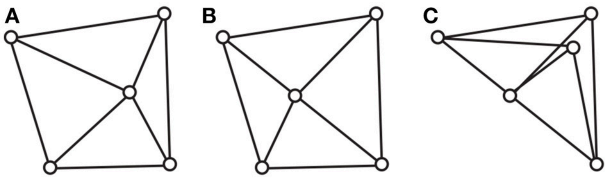

FIGURE 7 | globally rigid framework **(A)**, which loses this property in the nongeneric configuration **(B)**, where three nodes are aligned on a diagonal. For the latter framework the configuration **(C)** is also possible.

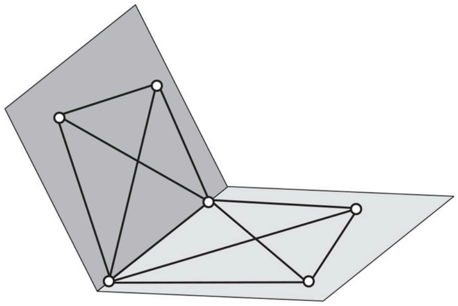

FIGURE 8 | This framework for $d = 3$ satisfies conditions (1) and (2), but not condition (3) of Theorem 1, there is an affine motion changing the angle between the highlighted planes, preserving all bar lengths.

Condition (1) implies that if there is another admissible configuration, then it has the same selfstress; condition (2) then implies that this other configuration is an affine image of the original one, and condition (3) implies that the affine image is actually congruent to the original configuration (cf. **Figure 8**). A particular class of superstable frameworks is that of cablenets, i.e., externally anchored frameworks where each edge has positive stress (**Figure 9A**).

Now we turn to generic configurations. A *simplex* in E^d is a framework on the complete graph on $d + 1$ nodes, e.g., triangles in E^2 or tetrahedra in E^3. Simplices (and all frameworks on complete graphs) are universally rigid by definition, since admissible configurations must be congruent to each other. Every generic globally rigid framework in E^d which is not a simplex (i.e., it has at least $d + 2$ nodes) admits at least one independent selfstress. This follows from the next theorem. A framework is *redundantly rigid* if it is rigid after the removal of an edge. A graph is c-connected if at least c nodes have to be removed from the graph to disconnect it.

Theorem 2. *Hendrickson (1992). If a framework with $n \geq d+2$ is generically globally rigid in E^d then it is redundantly rigid and $(d+1)$-connected.*

For $d = 2$ the theorem holds with an "if and only if" condition (Berg and Jordan, 2003, cf Connelly, 2013). Since generic redundant rigidity implies that there exist at least a selfstress, $s \geq 0$ and that there are no mechanisms, $m = 0$, it follows from (1) that in a generically globally rigid framework the number of edges is equal to or higher than

$$e = dn - d(d+1)/2 + 1\,, \tag{2}$$

e.g., $2n - 2$ in 2D or $3n - 5$ in 3D.

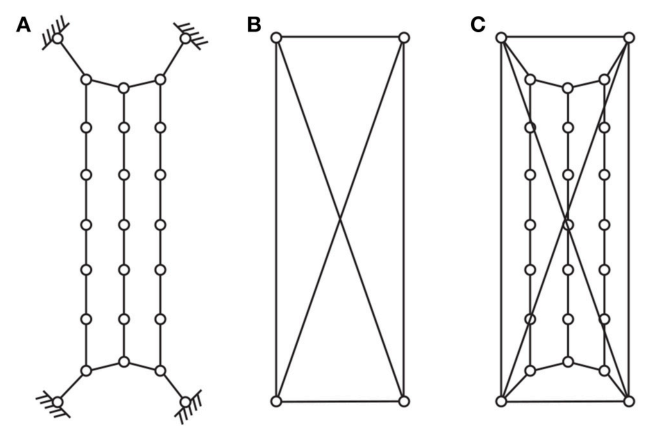

FIGURE 9 | A cablenet **(A)** can be anchored to a universally rigid framework **(B)** to obtain another universally rigid framework **(C)**.

A complete characterization of generic global rigidity has been given in the following theorem.

Theorem 3. *A framework with $n \geq d + 2$ is generically globally rigid in E^d if and only if there is a nonzero selfstress whose stress matrix has rank $n - d - 1$.*

The "if" part is due to Connelly (1982), the "only if" part to Gortler et al. (2010).

The next theorem provide the converse of Theorem 1 in the generic case.

Theorem 4. *Gortler and Thurston (2014). A universally rigid framework $(\mathcal{G}, p)$ with p generic and $n \geq d + 2$ is superstable.*

It is worth noticing that while global rigidity is a generic property, universal rigidity is not: if framework is universally rigid in a certain generic configuration, it can lose this property in a different generic configuration (compare cases (c) and (d) in **Figure 1**).

A less strict condition consists in requiring a configuration to be *general*. A configuration in E^d is general if no $d + 1$ nodes are affinely dependent, e.g., there are no three collinear nodes in $d = 2$, or there are no three collinear nodes and no four coplanar nodes in $d = 3$. In this case we have the following result.

Theorem 5. *Alfakih and Ye (2013). A framework $(\mathcal{G}, p)$ with p general and $n \geq d + 2$ is universally rigid if there is a nonzero selfstress whose stress matrix is positive semi-definite with rank $n - d - 1$.*

It has been shown in Alfakih et al. (2013) that the converse of this theorem holds for $(d + 1)$-lateration graphs, i.e., graphs obtained from a simplex by applying a sequence of $(d + 1)$-valent node additions, i.e., the addition of a node connected by $d + 1$ edges to the other nodes. An analogous result regarding global rigidity has been obtained previously in Anderson et al.

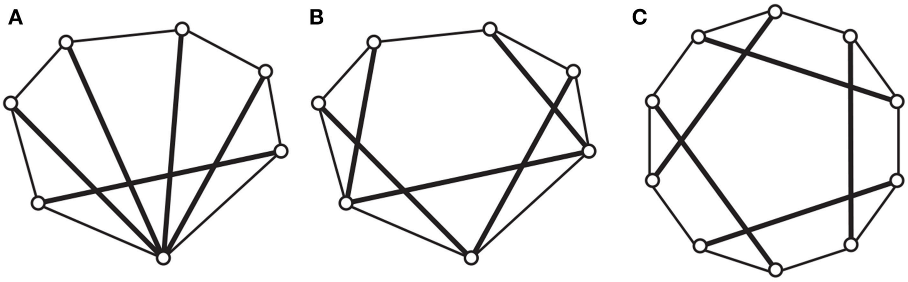

FIGURE 10 | Polygons satisfying Theorem 6: **(A)** a Grünbaum polygon; **(B)** a Cauchy polygon; **(C)** a Snelson polygon. Thin and thick lines corresponds respectively to cables and struts.

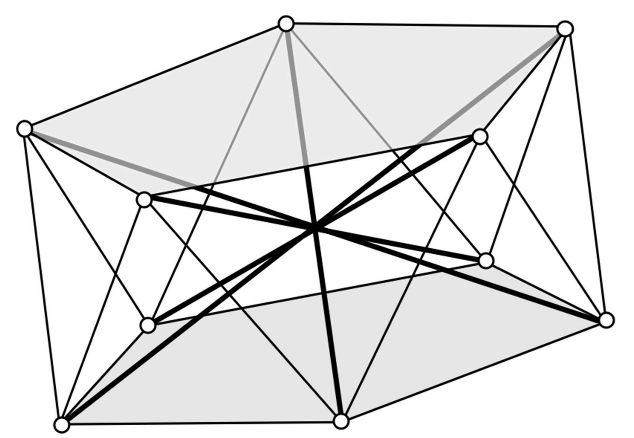

FIGURE 11 | A centrally symmetric framework with the shape of a pentagonal antiprism (with highlighted bases), see Theorem 7.

(2006). The number of edges of frameworks obtained in this way is

$$e = (d + 1)n - (d + 2)(d + 1)/2 ,$$

that is $e = 3n - 6$ for $d = 2$ and $e = 4n - 10$ for $d = 3$.

For n large, these values of e are 50% and 33% higher than the minimum value given by (2), respectively for $d = 2$ and $d = 3$.

By considering frameworks with a stress, the notion of tensegrity framework naturally comes into play. Indeed, many results have been first obtained for tensegrity frameworks, and then applied to the particular case of bar-frameworks.

A tensegrity framework is a framework where each edge can be labeled as a bar, a cable, or a strut: bars cannot change length, cables cannot increase in length, and struts cannot decrease in length. It turns out that a tensegrity framework is globally/universally rigid if the corresponding bar-framework is and the stress is *proper*, that is, cables have positive stress, and struts negative (Connelly, 2013). In other words, there is no difference between a bar-framework with a stress satisfying the theorems above and a tensegrity framework, with same graph and configuration, whose edges are labeled accordingly: cables if the stress is positive, struts if the stress is negative. Bars can be placed anywhere.

We conclude this section by reporting three results about known classes of frameworks. The first one is about convex polygons.

Theorem 6. *(Tensegrity polygons, Connelly, 1982). A tensegrity framework with the shape of a convex polygon, with cables on the outside, struts inside, and a proper a selfstress, is universally rigid (**Figure 10**).*

In the next section we will focus on the polygons like those in **Figures 2A**, **10A**, first described by Grünbaum and Shephard (1978).

The second result is about three-dimensional frameworks.

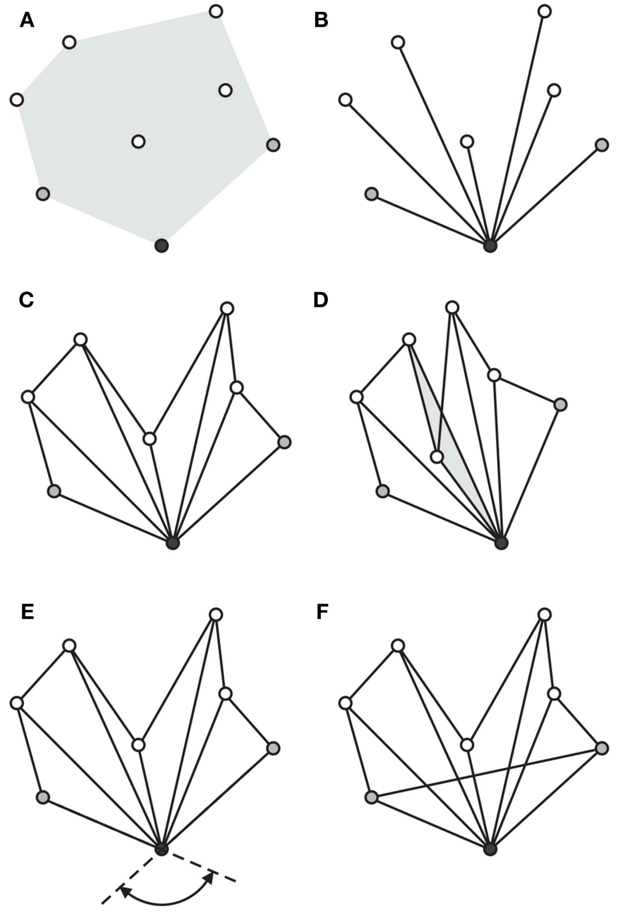

FIGURE 12 | Construction of a nonconvex Grünbaum polygon starting from a set of points in 2D: **(A)** three nodes corresponding to three consecutive vertices on the boundary of the convex hull of the set, the middle node is the *center* (in black), the other two nodes are its *neighbors* (in gray); **(B)** all the nodes are connected to the center by edges; **(C)** edges added to form adjacent triangles, so as to obtain a *fan*; **(D)** one of the admissible configurations of this fan, obtained by reversing the triangle shown (in light gray); **(E)** the completely unfolded configuration of the fan maximize the angle shown; **(F)** universal rigidity is obtained by adding the last edge between the two neighbors of the center.

Theorem 7. *(Central symmetric tensegrity polyhedra, Lovász, 2001; Bezdek and Connelly, 2006). Every tensegrity framework with the shape of a centrally symmetric polyhedron, with cables outside, bars connecting diametrically opposite pairs of vertices, and a proper selfstress, is universally rigid (**Figure 11**).*

The third result is about combining different frameworks together.

Theorem 8. *(Attachments, Ratmanski, 2010). Given two universally rigid frameworks in general position, it is possible to combine them into a universally rigid assembly if they have $d + 1$ nodes in common.*

Analogous results for globally rigid frameworks are presented in Eren et al. (2004a) and Connelly (2011).

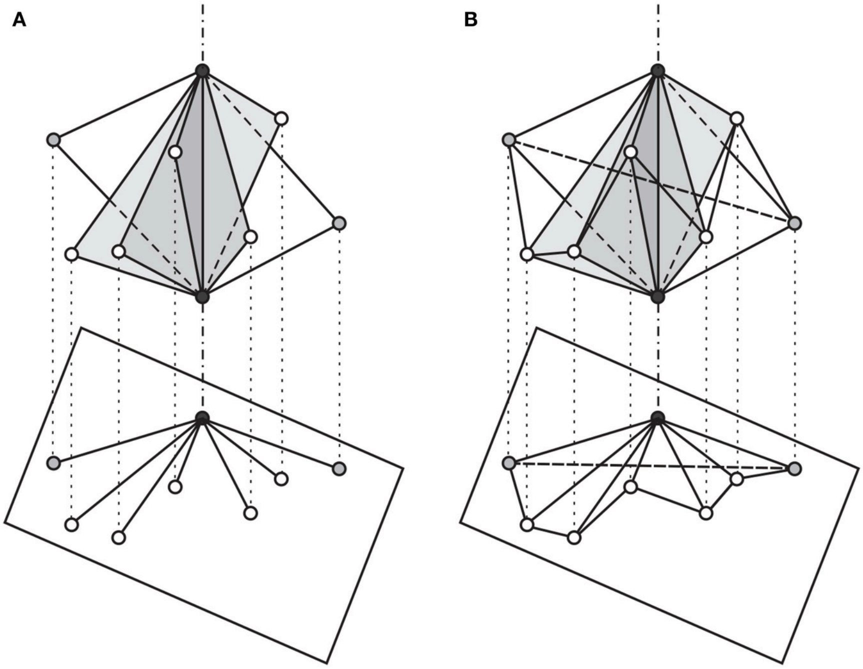

FIGURE 13 | Two phases, **(A)** and **(B)**, of the Construction of a three-dimensional Grünbaum framework, and the corresponding projection onto a nonconvex Grünbaum polygon (see description in Section 3.2).

3. CONSTRUCTION OF MINIMAL GENERIC UNIVERSALLY RIGID FRAMEWORKS

In this section we show that it is always possible to construct frameworks on n given nodes in E^2 or E^3 with the minimum number of edges (2), irrespective of the generic/nongeneric property of the configuration. Such frameworks belong to a new class which generalizes that of Grünbaum polygons (Grünbaum and Shephard, 1978).

3.1. Generalized Grünbaum Polygons

Grünbaum polygons are frameworks obtained by placing nodes and edges at the vertices and the sides of a convex polygon, then by choosing one node, the *center node* (in black in **Figure 2A**), and by connecting all the other nodes to it with an edge, except the two *neighboring nodes* (in gray in **Figure 2A**). The construction is completed by adding one edge connecting the two neighboring nodes.

We provide here a similar construction to assign $(2n-2)$ edges to a given a set of nodes in E^2 in order to obtain a universally rigid framework. We will call the resulting framework a *nonconvex Grünbaum polygon* (**Figure 12**).

First, the convex hull of the nodes is constructed and three consecutive vertices on its boundary coinciding with three nodes are chosen (**Figure 12A**), the middle one becomes the center to which all the other nodes are connected (**Figure 12B**). Then, additional edges are added to form a contiguous sequence of triangles sharing the center as a vertex (**Figure 12C**), plus the last edge connecting the two neighboring nodes (**Figure 12F**).

Theorem 9. *Every nonconvex Grünbaum polygon is universally rigid.*

Proof. Up to the addition of the last edge, the framework can be viewed as forming a kind of *fan* shape which "unfold" from the center node (**Figure 12C**). This incomplete framework admits a number of configurations equal to 2^f, where f is the number of internal edges or *folds* of the fan (**Figure 12D**). The distance between the two neighboring nodes will reach a maximum only when the fan is completely unfolded. It follows that by adding the last edge between the two neighboring nodes, the unfolded configuration is unique.

By embedding this framework in a higher dimensional Euclidean space, the situation does not change. Since each triangle of a fan is universally rigid by itself and it can only rotate about a fold, relative to its neighboring triangles, the triangle inequality ensure that the distance between the two neighboring nodes has a global maximum when the fan is flat, therefore the Grümbaum polygon is universally rigid. □

Notice that this proof is valid for both convex and nonconvex Grünbaum polygons. Notice also that the construction works even if the center is aligned with its neighbors, or if two or more fold are collinear. The result holds even if the configuration is nongeneric, the main requirement being that the center and its neighbors are on the boundary of the convex hull.

3.2. Three-Dimensional Grünbaum Frameworks

In three dimensions we can obtain a perfectly analogous result for assigning $(3n-5)$ edges red to a given set of nodes in E^3. We construct the convex hull of this set. There will be at least four vertices of the hull forming two adjacent triangles, sharing one edge of the convex hull. The shared edge is the *central edge* of the framework, the two nodes on this edge are the *central nodes*, while the other two are the *neighboring nodes*. Now, we can add edges connecting each of the neighboring nodes to the central nodes. We do the same with the remaining nodes, by connecting them to the central nodes. In this way, we obtain a set of triangles in space, all sharing one edge (**Figure 13A**). Then, for each couple of neighboring triangles, we add an edge between the nodes so as to form a tetrahedron. Finally, the last edge of this construction is added between the two neighboring nodes (**Figure 13B**).

An easy way of visualizing this framework is to project it along the direction of the central edge onto a plane, resulting in a fan-like framework, a nonconvex Grünbaum polygon. Similarly to what we have done before, we can consider the incomplete framework obtained by removing the last edge and argue that this admits a number of configuration equal to 2^f, with f defined for the projected framework as in the two-dimensional case. Among all these configurations, the one which is completely "unfolded" gives the maximum distance between the neighboring nodes, still using this term in analogy with the two-dimensional case. Once we add the last edge in this configuration, we obtain a globally rigid structure, which, by the triangle inequality is also universally rigid. We call frameworks obtained in this way *3D Grünbaum framework* and state the following theorem.

Theorem 10. *Every 3D Grünbaum framework is universally rigid.*

Notice that we can view these kind of frameworks, both in 2*D* and in 3*D*, as obtained by anchoring the nodes to a simplex, in the same way as we can anchor a cable-net to a (universally) rigid structure (**Figure 9**).

Notice also that we can find other generalized Grünbaum frameworks. For example, the one shown in **Figure 14** (top right) has two centers, corresponding to two fans with one side in common. It is easy to see that, in order

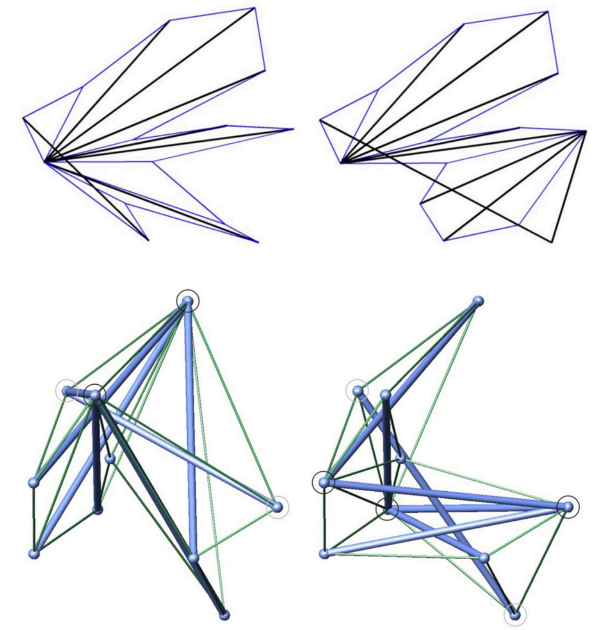

FIGURE 14 | (Top) Two universally rigid frameworks obtained from the same randomly generated nodal positions in E^2. The one on the top right is composed of two fans. Thin and thick edges correspond respectively to positive and negative stresses. **(Bottom)** Two constructions for the same randomly generated nodal positions in E^3. The one on the bottom right is composed by two fans. Black circles locate the central edges, gray circles locate the neighboring nodes. Thin and thick edges correspond respectively to positive and negative stresses.

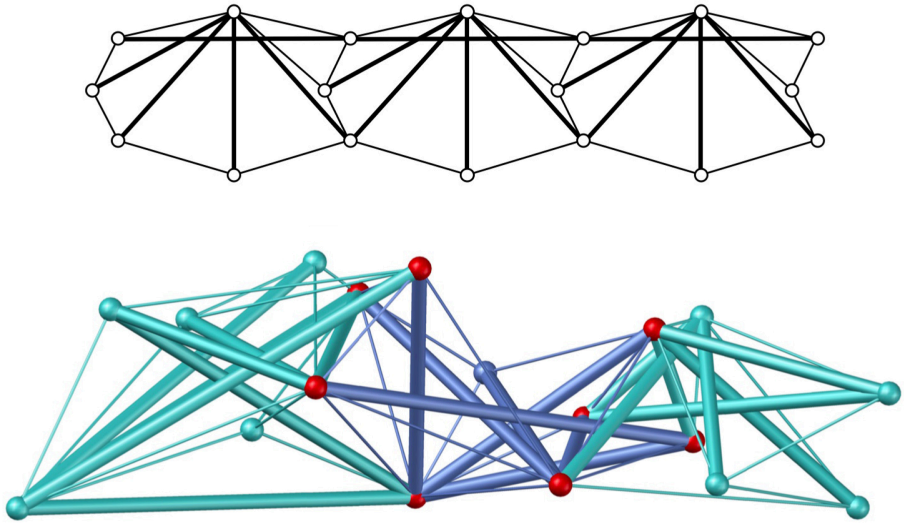

FIGURE 15 | (Top) A modular universally rigid framework in E^2 obtained by repetition of a universally rigid module. **(Bottom)** Construction of a modular universally rigid framework in E^3 for randomly generated nodal positions. The framework is composed by three universally rigid subframeworks (depicted in different color), each sharing four nodes with the adjacent one.

for multiple-fans frameworks to be universally rigid the centers should be on opposite sides of the edge connecting the neighbors. Analogous constructions exist also in three dimensions (**Figure 14**, bottom right).

In **Figure 15** we present two examples of application of Theorems 9, 10 in combination with Theorem 8. These examples shows how to avoid the occurrence of bars of excessive length by considering modular frameworks. In **Figure 15** (top), a universally rigid framework in E^2 is obtained by repetition of a universally rigid module, with adjacent modules having three nodes in common. In **Figure 15** (bottom), a universally rigid framework on randomly generated nodal positions in E^3 is composed by three universally rigid subframeworks, each sharing four nodes with the adjacent one. Space-filling universally rigid assemblies can be obtained in analogous fashion.

4. CONCLUDING REMARKS

After reviewing the main concepts and results in rigidity theory, we have given a construction for generic universally rigid frameworks in two and three dimensions with the minimum number of edges, with a significant improvement over existing methods. All together, these notions provide a set of useful tools that engineers can use to design superstable structural and mechanical systems, with guaranteed strength and stiffness properties. Additional applications include sensor networks, multi-agent systems, and protein conformation analysis. Our constructions relies on the computation of the convex hull of the set of nodes, a relatively quick operation, even if performed dynamically, i.e., if nodes are sequentially added and removed (see Hert and Schirra, 2018). For nongeneric configurations the number of edges can be further reduced, with the limitation that any change of configuration must happen on a lower-dimensional nongeneric manifold. The problem of constructing minimal nongeneric universally rigid frameworks will be the subject of future work.

AUTHOR CONTRIBUTIONS

SK and AM contributed conception and design of the study. All authors contributed to developing the study, wrote sections of the manuscript, revised it, read and approved the submitted version.

FUNDING

AM gratefully acknowledges the financial support from the Italian Ministry of Education, University, and Research (MIUR) under the FFABR grant L.232/2016.

ACKNOWLEDGMENTS

An earlier version of this work appeared in the preprint (Kelly and Micheletti, 2014) uploaded in the arXiv repository.

REFERENCES

Alfakih, A. Y., Taheri, N., and Ye, Y. (2013). On stress matrices of (d + 1)-lateration frameworks in general position. *Math. Programming* 137, 1–17. doi: 10.1007/s10107-011-0480-0

Alfakih, A. Y., and Ye, Y. (2013). On affine motions and bar frameworks in general positions. *Lin. Algeb. Applic.* 438, 31–36. doi: 10.1016/j.laa.2012.08.031

Anderson, B. D. O., Belhumeur, P. N., Eren, T., Goldenberg, D. K., Morse, A. S., Whiteley, W., et al. (2006). Graphical properties of easily localizable sensor networks. *J. Wirel. Netw.* 15, 177–191. doi: 10.1007/s11276-007-0034-9

Berg, A., and Jordan, T. (2003). A proof of connelly's conjecture on 3-connected circuits of the rigidity matroid. *J. Combin. Theory Ser. B.* 88, 77–97. doi: 10.1016/S0095-8956(02)00037-0

Bezdek, K., and Connelly, R. (2006). Stress matrices and m matrices. *Oberwolfach Rep.* 3, 678–680. doi: 10.4171/OWR/2006/12

Connelly, R. (1982). Rigidity and energy. *Invent. Math.* 66, 11–33. doi: 10.1007/BF01404753

Connelly, R. (2011). "Combining globally rigid frameworks," in *Classical and Modern Mathematics in the Wake of Boris Nikolaevich Delone* (Moscow: MAIK Nauka/Interperiodica).

Connelly, R. (2013). "Tensegrities and global rigidity," in *Shaping Space*, ed M. Senechal (New York, NY: Springer), 267–278. doi: 10.1007/978-0-387-92714-5_21

Eren, T., Anderson, B. D. O., Whiteley, W., Morse, A. S., and Belhumeur, P. N. (2004a). "Merging globally rigid formations of mobile autonomous agents," in *AAMAS '04 Third International Joint Conference on Autonomous Agents and Multiagent Systems*, Vol. 3, (Washington, DC; New York, NY: IEEE Computer Society), 1260–1261

Eren, T., Andreson, B. D. O., Morse, A. S., Whiteley, W., and Belhumeur, P. N. (2004b). Operations on rigid formations of autonomous agents. *Commun. Inform. Syst.* 3, 223–258. doi: 10.4310/CIS.2003.v3.n4.a2

Gortler, S. J., Healy, A. D., and Thurston, D. P. (2010). Characterizing generic global rigidity. *Am. J. Math.* 132, 897–939. doi: 10.1353/ajm.0.0132

Gortler, S. J., and Thurston, D. P. (2014). Characterizing the universal rigidity of generic frameworks. *Disc. Comput. Geom.* 51, 1017–1036. doi: 10.1007/s00454-014-9590-9

Grünbaum, B., and Shephard, G. C. (1978). *Lectures on Lost Mathematics.* Lecture notes. Syracuse, NY: Syracuse University.

Hendrickson, B. (1992). Conditions for unique graph realizations. *SIAM J. Comput.* 21, 65–84. doi: 10.1137/0221008

Hert, S., and Schirra, S. (2018). "3D convex hulls," in *CGAL User and Reference Manual, 4.13 Edn* (CGAL Editorial Board).

Kelly, S. D., and Micheletti, A. (2014). A class of minimal generically universally rigid frameworks. arXiv:1412.3436v1.

Lovász, L. (2001). Steinitz representations of polyhedra and the Colin de Verdiére number. *J. Combinat. Theory Ser. B* 82, 223–236. doi: 10.1006/jctb.2000.2027

Micheletti, A. (2013). "Bistable regimes in an elastic tensegrity structure," *Proceedings of the Royal Society A*, Vol. 469.

Ratmanski, K. (2010). Universally rigid framework attachments. *arXiv:1011.4094*, 16.

Roth, B., and Whiteley, W. (1981). Tensegrity frameworks. *Trans. Am. Math. Soc.* 265, 419–446. doi: 10.1090/S0002-9947-1981-0610958-6

Zhang, J. Y., and Ohsaki, M. (2007). Stability conditions for tensegrity structures. *Int. J. Solids Struc.* 44, 3875–3886. doi: 10.1016/j.ijsolstr.2006.10.027

Conflict of Interest Statement: The authors declare that the research was conducted in the absence of any commercial or financial relationships that could be construed as a potential conflict of interest.

frontiers in Materials

ORIGINAL RESEARCH
published: 11 April 2019
doi: 10.3389/fmats.2019.00050

Analysis of Low Frequency Acoustic Stop Bands in Cubic Arrays of Thick Spherical Shells With Holes

*Guillaume Dupont[1], Alexander Movchan[2], Stefan Enoch[3] and Sébastien Guenneau[3]**

[1] Aix Marseille Univ, CNRS, Centrale Marseille, IRPHE, Marseille, France, [2] Department of Mathematical Sciences, The University of Liverpool, Liverpool, United Kingdom, [3] Aix Marseille Univ, CNRS, Centrale Marseille, Institut Fresnel, Marseille, France

We analyse the propagation of airborne pressure waves through a three-dimensional array of rigid coated spheres (shells) in air. When we dig a channel terminated by an air cavity in each rigid shell we observe the appearance of a low frequency stop band. Each shell with a hole acts as a Helmholtz resonator supporting a low frequency localized mode. Isofrequency surfaces and contours reveal the strong anisotropy of the periodic structure at the edge of the stop band. A simple mechanical model of springs and masses allows for asymptotic estimates of the low frequency stop band for elongated channels. Increasing the radius of an air channel shifts up the position, and enlarges, the low frequency stop band. Adding holes in shells also shifts up the frequency of the stop band, and embedded shells lead to additional stop bands. Localization effect induced by a large defect in a periodic macrocell of Helmholtz resonators is finally investigated.

Keywords: finite elements, bloch waves, acoustic metamaterials, Helmholtz resonators, multiscale asymptotic, stop band, localized mode

Edited by:
Chiara Daraio,
California Institute of Technology,
United States

Reviewed by:
Gennady Mishuris,
Aberystwyth University,
United Kingdom
Massimiliano Gei,
Cardiff University, United Kingdom

***Correspondence:**
Sébastien Guenneau
s.guenneau@imperial.ac.uk;
sebastien.guenneau@fresnel.fr

Specialty section:
This article was submitted to
Mechanics of Materials,
a section of the journal
Frontiers in Materials

Received: *20 January 2019*
Accepted: *11 March 2019*
Published: *11 April 2019*

Citation:
Dupont G, Movchan A, Enoch S and Guenneau S (2019) Analysis of Low Frequency Acoustic Stop Bands in Cubic Arrays of Thick Spherical Shells With Holes. Front. Mater. 6:50.
doi: 10.3389/fmats.2019.00050

1. INTRODUCTION: ACOUSTIC METAMATERIALS

In the tracks of photonic crystals, phononic crystals (Dowling, 2008) have provided a fillip for research in acoustic stop band structures (Kushwaha et al., 1993; Kafesaki and Economou, 1999) within which light or sound is prohibited to propagate due to multiple scattering between periodically spaced inclusions. In 2000, Liu et al. provided the first numerical and experimental evidence of frequency dispersive elastic parameters of locally resonant structures for elastic waves in three-dimensional arrays of thin coated spheres (Liu et al., 2000): The effective parameters were shown to turn negative where low frequency stop bands occur. This important work paved the way toward acoustic analogs of electromagnetic meta-materials, such as fluid-solid composites for the control of pressure waves (Auriault and Bonnet, 1985; Auriault, 1994; Liu et al., 2000; Goffaux et al., 2002; Ho et al., 2003; Elford et al., 2004; Hirsekorn et al., 2004; Li and Chan, 2004; Movchan and Guenneau, 2004; Fang et al., 2006; Mei et al., 2006; Guenneau et al., 2007b; Hou et al., 2007; Wang et al., 2008; Chalmers et al., 2009; Norris, 2009; Lemoult et al., 2011; Auriault and Boutin, 2012; Boutin, 2013; Boutin and Becot, 2015). Using asymptotic methods for fields in multi-structures (Kozlov et al., 1999; Movchan et al., 2002), it has been proposed to use arrays of cylinders with a split ring cross section as building blocks for two-dimensional localized resonant acoustic structures displaying negative refraction (Movchan and Guenneau, 2004; Guenneau et al., 2007a), based on analogies with split ring resonators (SRRs), introduced by Pendry in the context of electromagnetic waves almost 20 years ago (Pendry et al., 1999). Magnetic activity of metamaterials occurs near resonances of SRRs, which was essential for instance in the design of the first electromagnetic cloak (Schurig et al., 2006), and similar designs have been proposed for acoustic cloaks (Craster et al., 2013).

In a series of articles, the research group of Auriault developed asymptotic models of locally resonant structures (Auriault and Bonnet, 1985; Auriault, 1994; Auriault and Boutin, 2012), some of which predate the birth of acoustic metamaterials with the seminal work of the research group of Ping Shen (Liu et al., 2000). Low frequency stop bands in arrays of 2D Helmholtz resonators with elongated necks have been studied in (Movchan and Guenneau, 2004; Guenneau et al., 2007a) as mentioned above, with further predictions and measurements of sound transmission in elastic shells in air in Krynkin et al. (2010). However, 3D Helmholtz resonators with elongated neck position inside the cavity and periodically distributed in a fluid have been introduced in (Boutin, 2013; Boutin and Becot, 2015). Therein, Boutin and coauthors have shown that the macroscopic fields (pressure P and velocity $\mathbf{V}$) satisfy the following equation of mass conservation and generalized Darcy Law:

$$\nabla \cdot \mathbf{V} = \frac{i\omega\Phi}{K} P + \frac{Q}{\mid Y \mid}\ ,\ \mathbf{V} = \frac{-\mathbf{T}}{\eta} \nabla P \tag{1}$$

where K is the effective bulk modulus (including thermal effects) of the matrix, ω the resonant frequency, $i^2 = -1$, Φ and $\mathbf{T}$ are the porosity and dynamic permeability tensor (including viscosity effects) when considering the resonators as perfectly rigid spheres, η is the viscosity of the fluid-matrix, $\mid Y \mid$ is the volume of the 3D unit cell Y and Q is the flux emitted by the resonator into the fluid matrix in response to the pressure acting on it. The case of the Helmholtz resonator with a single elongated neck has been not only derived, but also experimentally tested, in Boutin (2013) and Boutin and Becot (2015). And the fluid need not be inviscid.

There is a vast amount of literature on the role of the neck in such Helmholtz resonators (Groeneweg, 1969; Alster, 1972; Orris et al., 1974; Gaunaurd and Uberall, 1982; Lim et al., 1990; Hinders et al., 1995; Selamet and Dickey, 1995; Mead, 1996; Aberg et al., 1997; Selamet et al., 1997; Chen et al., 1998; Baird et al., 1999; Seo et al., 2005; Ivansson, 2006; Duan et al., 2007; Zhao et al., 2007; Zhou et al., 2010; Wang and Mak, 2012; Li et al., 2013). Recently, periodic structures consisting of SRRs have been revisited thanks to refined homogenization techniques, which allow to rigorously link the geometrical parameters to frequency dependent effective parameters (Mercier et al., 2017). Analogs of SRRs have been proposed for in-plane elastic waves (Guenneau et al., 2007b), that allows for bending and rotational vibrations having lower resonant frequencies than compressional vibrations, and thus make good candidates for building blocks of mechanical metamaterials, which might make possible some mechanical cloak, see Kadic et al. (2013) for a review of metamaterials beyond electromagnetics. Milton, Briane and Willis provided a thorough mathematical frame for cloaking for certain types of elastodynamic waves in structural mechanics, in the framework of modified Willis equations (Milton et al., 2006). On the other hand, coupled in-plane pressure and shear waves were numerically shown to be detoured around a finite size obstacle by a specially designed cloak with an anisotropic heterogeneous elasticity tensor without the minor symmetries (Brun et al., 2009) without resorting to Willis media. Nonetheless, SRRs like in Guenneau et al. (2007b) make an interesting candidate to achieve such Cosserat-type metamaterials. Actually, a similar type of resonant elastic structure already led to a negatively refracting medium (Zhu et al., 2014), where the elastic chirality (which is a hallmark of a Cosserat medium) was put forward in conclusive experiments. The need for mechanical metamaterials with elasticity tensor without the minor symmetry motivates the extension of homgenization results of Mercier et al. (2017) to the Navier system. Importantly, the acoustic wave equation is invariant under coordinate changes (Norris, 2008, 2009), so acoustic metamaterials via geometric transform can thus achieve enhanced control of pressure waves via a simpler route. A simple example of a periodic system is a periodic lattice, whose dynamic response is well defined by Green's functions. Dynamic Green's functions in periodic lattices and their asymptotics were analyzed in Movchan and Slepyan (2014) and Vanel et al. (2016). Localization of electromagnetic waves within a two-dimensional grating of spheres embedded in the three-dimensional space and the high-frequency homogenisation approximations were studied in Maling et al. (2017).

A downfall of SRRs is that they do not allow for doubly negative acoustic parameters, so one would need a second type of inclusion within the periodic cell to achieve a goal of a negative refractive index in order to design a super lens like Pendry proposed in his seminal paper (Pendry, 2000). In 2004, Li and Chan proposed a design of negative acoustic metamaterial based on a multiple scattering theory approach (Li and Chan, 2004), which has been revisited recently by applied mathematicians using homogenization theory for bubbly fluids (Ammari et al., 2017a,b) with hybridization of Minnaert resonances (Minnaert, 1933). This is somewhat related to homogenization of high-contrast periodic structures (Figotin and Kuchment, 1998). Potential applications of bubbly media in super lensing and total absorption have been experimentally shown (Lanoy et al., 2015; Leroy et al., 2015). Such soft metamaterials (Brunet et al., 2015) are currently investigated by many groupings in the world, but they might not always be compatible with industrial processes.

Although SRRs might not achieve double negative acoustic parameters, they seem to be quite straightforward to engineer for ultrasonic waves. Fang *et al.* experimentally demonstrated a dynamic effective negative stiffness in a chain of air filled Helmholtz's resonators for ultrasonic waves (Fang et al., 2006). Moreover, it has been also shown using asymptotic techniques that surface water waves propagating within an array of fluid filled SRRs display a negative effective density (Farhat et al., 2009). A focussing effect through a finite array of such resonators was numerically achieved, with a resolution of a third of the wavelength. The negative effective density, reinterpreted as a negative effective gravity, has been further confirmed theoretically and experimentally (Hu et al., 2011, 2017). Fluid filled SRRs have been experimentally tested in a 17 meter long water channel for filtering effects with a dike using grooved vertical cylinders (Dupont et al., 2017). Similar

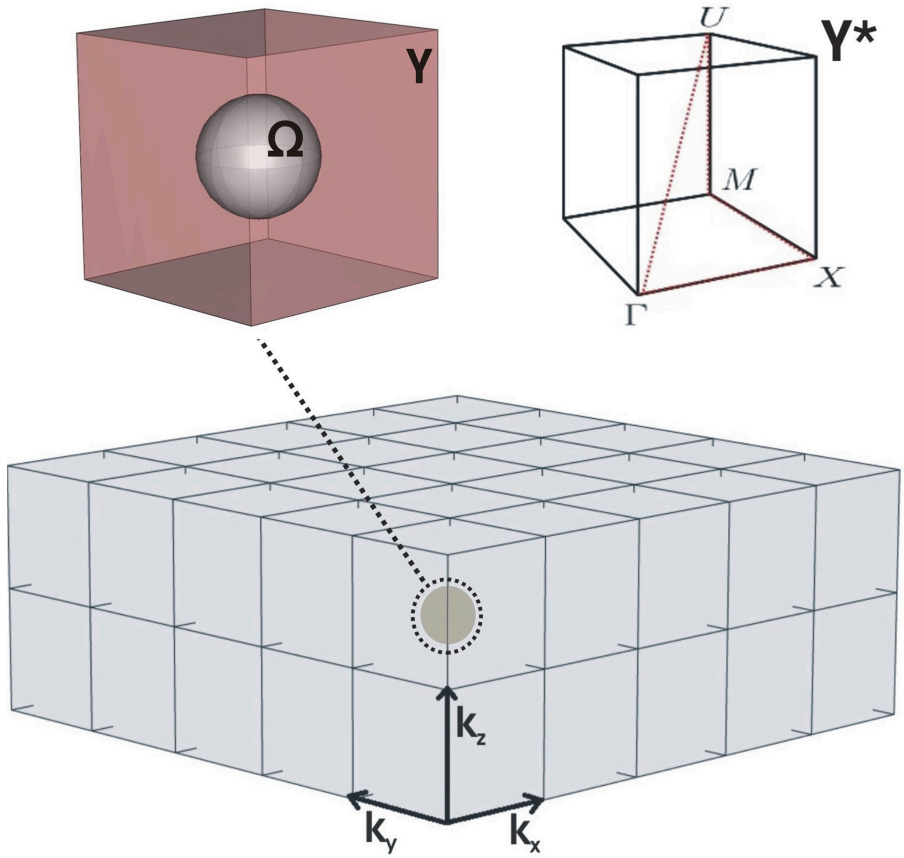

FIGURE 1 | Three-dimensionnal phononic crystal, periodic cell Y with a rigid sphere Ω in physical space and irreducible Brillouin zone ΓXMU of the periodic cell Y^* in reciprocal space with the three components of the Floquet-Bloch vector $k = (k_x, k_y, k_z)$.

filtering effects have been experimentally demonstrated for sound waves interacting with a doubly periodic array of Helmholtz's resonators shaped as soda cans (Lemoult et al., 2011). However, we note that in that case, there is no neck, just a hole, as soda cans are thin shells. In the present paper, we would like to revisit the concepts of SRRs in the case of pressure waves propagating in a three-dimensional array of 3D Helmholtz resonators with elongated necks. In order to simplify the mathematical setup, we shall consider airborne acoustic waves, in which case rigid (Neumann type) boundary conditions can be considered on resonant elements. Compared to problems of linear elasticity, the present study does not deal with dynamic degeneracies at low frequencies, which may occur for certain type of geometries of elastic systems, resulting in a group of very small eigenvalues being separated from the remaining spectrum.

2. MOTIVATION: SPECTRAL PROPERTIES OF A PERIODIC ARRAY OF RIGID SPHERES

Let us start with an illustrative numerical result for a spectral problem for the Helmholtz operator within a periodic cubic array of rigid spheres: the unknown is a pressure wave field, here sound in air (wave speed $c = 340 \ m.s^{-1}$). Neumann boundary conditions are prescribed on the contour of each defect and standard Floquet-Bloch conditions are set on an elementary cell of the periodic structure. The finite element formulation was implemented in the COMSOL Multiphysics Package to compute the eigenvalues and to generate the corresponding eigenfields. We present in **Figure 1** the periodic structure we want to study and in **Figure 2** the corresponding dispersion diagram for eigenfrequencies ω (in unit of rad.s^{-1}) as a function of the Floquet-Bloch parameter k (in unit of m^{-1}): along the horizontal axis we have the values of modulus of $\mathbf{k}$, where k stands for the position vector of a point on the contour ΓXMU within the irreducible Brillouin zone. We note the absence of bandgaps with the presence of rigid spheres. This lack of intervals of forbidden frequencies motivates the present study: how can one create a stop band without further increasing the size of the rigid spheres?

3. SETUP OF THE SPECTRAL PROBLEM: THE CONTINUUM MODEL

Let us first recall the finite element set-up. We consider the Helmholtz equation:

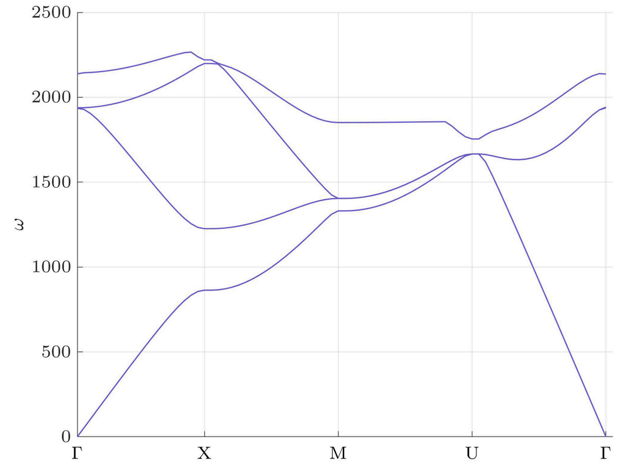

FIGURE 2 | Dispersion diagram for a periodic array (pitch $d = 1$ m) of spherical rigid inclusions ($R = 0.4$ m) representing the frequency ω (rad.s^{-1}) of pressure waves in air, vs. the wavenumber $|\mathbf{k}|$ (m^{-1}), projection of the Bloch vector k along the edges of ΓXMU.

$$\nabla.\left(\frac{1}{\rho(x,y,z)}\nabla p(x,y,z)\right)+\frac{\omega^2}{K(x,y,z)}p(x,y,z)=0 \qquad (2)$$

where ρ (kg.m^{-3}), K (Pa) are the density and bulk modulus of the medium and ω (rad.s^{-1}) is the angular wave frequency of the pressure field p.

Due to the periodicity of the lattice, we look for solutions of (2) in terms of Floquet-Bloch waves (Floquet, 1883; Bloch, 1928; Bensoussan et al., 1978; Brillouin, 1978; Wilcox, 1978; Kittel, 1986). So, for a cubic array of unit cells Y,

$$p(x+1,y+1,z+1)=p(x,y,z)e^{i(k_x+k_y+k_z)} \qquad (3)$$

where k_x, k_y and k_z are components of the Bloch vector $\mathbf{k}$ within the Brillouin zone $Y^* = [0,\pi]^3$ (Joannopoulos et al., 1995; Gazalet et al., 2013).

The implementation in the finite element package is fairly straightforward (Hladky-Hennion et al., 1991; Nicolet et al., 2004). We first multiply equation (2) by a smooth test function v and using integration by parts, we obtain the so-called weak form of the time-harmonic acoustic equation

$$-\int_Y \rho^{-1}\nabla p\cdot\nabla v dxdydz+\int_{\partial Y}\rho^{-1}\frac{\partial p}{\partial n}vds+\omega^2\int_Y K^{-1}pvdxdydz=0 \qquad (4)$$

where $\partial f/\partial n = \nabla f\cdot\mathbf{n}$ with $\mathbf{n}$ the unit outward normal to the boundary ∂Y of Y, and ds the infinitesimal surface element on ∂Y.

We note that the weak formulation holds for heterogeneous fluids as ρ and K can be spatially varying. In particular, this model works for domains such as a homogeneous fluid filled with a periodic array of rigid obstacles. For the finite element implementation, (4) is discretised using test functions taking values on nodes of a tetrahedral mesh of the basic cell (first order tetrahedral elements), see e.g., (Nicolet et al., 2004) for further details. From (4), we note that setting rigid boundary conditions on an inclusion amounts to assuming Neumann (natural) homogeneous data, whereas transmission conditions at the interface between various fluid phases mean that the quantity $\rho^{-1}\partial p/\partial n$ is preserved across the interface. We note that in the case of airborne pressure waves, the contrast in density between air and inclusions made of metal or even polymer is sufficiently large to assume Neumann data, but this simplification does not hold if we replace air by water.

Let us now consider a periodic array of defects $\Omega_1,\ldots,\Omega_N$ embedded in an elementary cell $Y =]0;1[^3$. Let $p(x,y,z)$ satisfy the Helmholtz equation in $Y\setminus\bigcup_{j=1}^{N}\overline{\Omega_j}$. We also assume that p satisfies Neumann boundary conditions on the contours of defects, where $\mathbf{n}$ denotes the unit outward normal to the boundary $\partial\Omega_j$ of a defect Ω_j:

$$\left.\frac{\partial p}{\partial n}\right|_{\partial\Omega_j}=0\,,\quad j=1,\ldots,N \qquad (5)$$

We would like to consider a particular case when the defects $\Omega_1,\ldots,\Omega_N$ are spherical shells with thin air channels connecting an air-filled interior cavity to the exterior surrounding air. These defects can be modeled as multistructures (Kozlov et al., 1999) in the following way,

$$\Omega_{(N)}=\left\{a_{(N)}<\sqrt{x^2+y^2+z^2}<b_{(N)}\right\}\setminus\overline{\bigcup_{j=1}^{N}\Pi_{\varepsilon(N)}^{(j)}} \qquad (6)$$

where $a_{(N)}$ and $b_{(N)}$ are given constants and $\Pi_{\varepsilon(N)}^{(j)}$ is the thin channel.

4. ASYMPTOTIC APPROXIMATION: A DISCRETE SPRING-MASS MODEL

In this section, we derive an asymptotic approximation of the field in thin channels $\Pi_\varepsilon^{(j)}$, see **Figure 3**,

$$\Pi_\varepsilon^{(j)}=\Big\{(x,y,z)\in R^3: 0<x<l_j,\ \sqrt{y(t)^2+z(t)^2}<\varepsilon h_j(t),\ (0\le t\le 2\pi)\Big\} \qquad (7)$$

where l_j is the length of the j^{th} bridge, $\varepsilon h_j(t)$ the radius of its varying cross-section D_ε (parametrized by a positive real t). Here, ε is a small positive non-dimensionnal parameter. To derive the asymptotic expansions, we introduce the scaled variables $\xi=(y/\varepsilon,z/\varepsilon)$.

Without loss of generality, and for the sake of simplicity, we drop the superscript j. In Π_ε, the time-harmonic wave equation takes the rescaled form

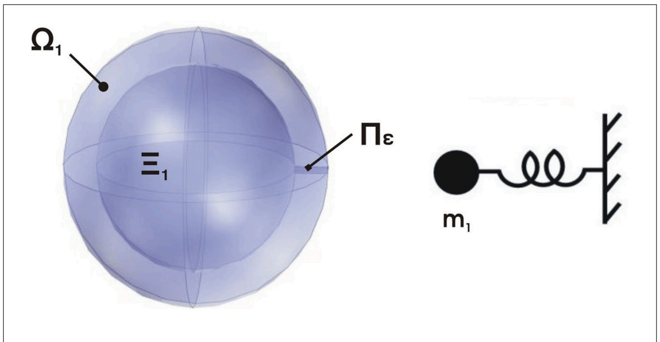

FIGURE 3 | Geometry of the inclusions and the Helmholtz oscillator consisting of one spring connected to a mass at one end and fixed at the other end.

$$\left\{\frac{1}{\rho}\left(\frac{1}{\varepsilon^2}\Delta_\xi+\frac{\partial^2}{\partial x^2}\right)+\frac{\omega^2}{K}\right\}p=0\,, \tag{8}$$

with the Neumann boundary conditions

$$\left.\frac{\partial p}{\partial n}\right|_{\partial D_\xi}=0 \tag{9}$$

The field p is approximated in the form

$$p\sim p^{(0)}(x,y,z)+\varepsilon^2 p^{(1)}(x,y,z) \tag{10}$$

To leading order, we obtain

$$\left\{\begin{array}{lll}\Delta_\xi p^{(0)} &= 0 & \text{on} \quad D_\xi\\ \nabla_\xi p^{(0)} &= 0 & \text{on} \quad \partial_{D_\xi}\end{array}\right. \tag{11}$$

Hence, $p^{(0)}=p^{(0)}(x)$ (it is $\xi-$ independent). Assuming that $p^{(0)}$ is given, we derive that the function $p^{(1)}$ satisfies the following model problem on the scaled cross-section of Π_ε

$$\left\{\begin{array}{llll}\Delta_\xi p^{(1)} &= -\dfrac{1}{\rho}\dfrac{\partial^2 p^{(0)}}{\partial x^2}+\dfrac{\omega^2}{K}p^{(1)} & \text{in} & D_\xi\\ \nabla_\xi p^{(1)}\cdot\mathbf{n}=0 & & \text{on} & \partial_{D_\xi}\end{array}\right. \tag{12}$$

The condition of solvability for the problem has the form:

$$\frac{1}{\rho}\frac{d^2p^{(0)}}{dx^2}+\frac{\omega^2}{K}p^{(0)}=0\,,\quad 0<x<l_j \tag{13}$$

Hence, we have shown that to the leading order we can approximate the field p in the thin channel Π_ε by the function $p^{(0)}$ which satisfies the Helmholtz's equation in one-space dimension. We now assume that the field is periodic over the cell since it is localized. This shows that the average of the eigenfield over the macro-cell vanishes. Indeed, let χ_1 denote the value of the field in the large body Σ of the multi-structure Ω and let χ_2 (which we normalize to 1) denote the value of the field within the complementary area of the macro-cell $Y\setminus\Omega$ excluding the thin channels. Taking $\nu=1$ in (4), we deduce that

$$\omega^2\int_Y \rho p dxdydz=-\int_{\partial Y\cup\partial\Omega}K\frac{\partial p}{\partial n}dS=0 \tag{14}$$

This shows that the average of the field p over Y vanishes, hence by neglecting the small volume of the thin channels, we obtain

$$\chi_1\text{meas}_\Sigma+\chi_2\text{meas}_{Y\setminus\Omega}=O(\varepsilon) \tag{15}$$

where meas_Σ and $\text{meas}_{Y\setminus\Omega}$ denote, respectively the volumes of Σ and $Y\setminus\Omega$.

We now consider two cases. The first one is the study of an array of simple spherical shells with either one or six thin channels, and the other one is the study of an array of double spherical shells with one thin channel in each shell. Since we have q thin channels, we have q separate eigensolutions V_j, $(j=1,...,q)$, corresponding to the vibrations of thin domains $\Pi_\varepsilon^{(j)}$

$$\rho^{-1}V_j''(x)+K^{-1}\omega^2V_j(x)=0\,,\quad 0<x<l_j\,, \tag{16}$$

$$V_j(0)=\chi_2=-\chi_1\frac{\text{meas}(\Xi)}{\text{meas}(\mathrm{Y}\setminus\Omega)}\,. \tag{17}$$

We note that $V_j(0)$ is equal to a non-zero constant and also that $V_j(l_j)=\chi_1$. Next, we need to take into account that some boundary layers occur at the end regions of thin ligaments. These boundary layers are characterized by exponential decay when the boundary conditions for the functions V_0 (the leading term in the asymptotic expansion of the thin bridge solutions) are chosen in a specific way. In our case, integrating (2) over $\Sigma\cup\Pi_\varepsilon^{(1)}\cup\cdots\cup\Pi_\varepsilon^{(q)}$ and applying the divergence (or Gauss) theorem, we obtain to order $O(\varepsilon)$

$$K^{-1}I_jV_j'(l_j)=M_j\omega^2V_j(l_j)\,, \tag{18}$$

where

$$I_j=\int_0^{2\pi}\varepsilon h_j(t)\,dt\,. \tag{19}$$

All the channels are connected to Ξ, hence, $V_1(l_1)=...=V_q(l_q)=V$. We note that the boundary layer condition (18) can be interpreted as Newton's second law.

The solution of the problem $(16)-(18)$ (that one can interpret in terms of a spring-mass model like in **Figure 3**) has the form

$$V_j(x)=-\frac{\chi_2[\cos((\omega/c)l_j)-1]}{\sin((\omega/c)l_j)}\sin\left(\frac{\omega}{c}x\right)+\chi_2\cos\left(\frac{\omega}{c}x\right) \tag{20}$$

where $c=\sqrt{K/\rho}$ and the frequency ω is given as the solution of the following equation:

$$\sum_{j=1}^{n}\left(I_j\cot\left(\frac{\omega l_j}{c}\right)\right)=\frac{m_jc}{K}\omega \tag{21}$$

where we invoked (18). Looking at a first low frequency, we deduce an explicit asymptotic approximation

$$\omega \sim \sqrt{\sum_{j=1}^{n} \left(\frac{I_j}{l_j}\right)} \sqrt{\frac{K}{M}} \left(1 + \frac{\text{meas}(\Xi)}{\text{meas}(\text{Y} \setminus \Omega)}\right) \qquad (22)$$

This estimate actually holds for the frequency ω_2 of the upper edge of the phononic band gap. We note that if we take $V(0) = 0$ instead of $V(0) = \text{meas}(\Xi)/\text{meas}(Y \setminus \Omega)$, we estimate the frequency of the lower-edge of the phononic band gap. We also notice that the boundary layer condition (18) is only valid at order $0(\varepsilon)$, so it needs to be refined if one wants to improve the frequency estimate in (22).

4.1. Eigenfrequency Estimate in the Case of a Single Spherical Shell With one or six Thin Channels

We report in **Figures 4**, **5** finite element computations for a periodic cell of sidelength $d = 1$ m with a simple spherical shell with one thin channel. We then proceed with the same shell with six thin channels. The geometry of the elementary cell and associated spring-mass model are given in **Figure 6** and finite element computations are shown in **Figures 7**, **8**. The interior and exterior radii of the shell are respectively 0.3 and 0.4 m, the thin channels have the same length 0.1m and radii 0.01 m. Therefore, the frequency estimates are (in rad.s^{-1}):

$$\omega_1 \sim 52.1107 \quad , \quad \omega_2 \sim 54.0796 \qquad (23)$$

for one thin channel, which are in good agreement with the finite element values

$$\omega_1^* = 51.4250 \quad , \quad \omega_2^* = 55.2638 \qquad (24)$$

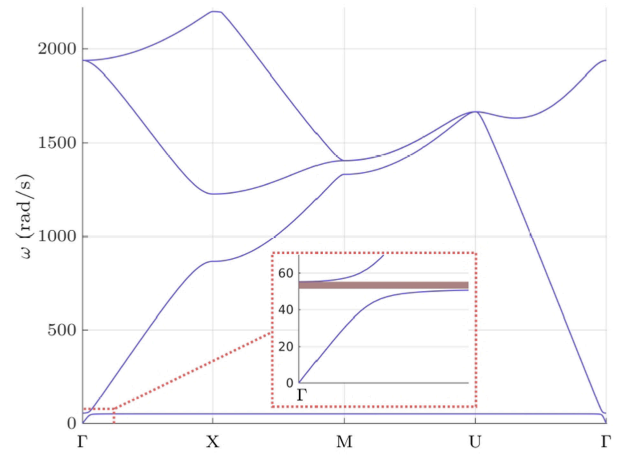

FIGURE 4 | Dispersion diagram for a periodic array (pitch $d = 1$m) of spherical rigid shells (inner radius 0.3 m and outer radius 0.4 m) with one thin channel (length 0.1 m and radius 0.01 m) representing the frequency ω (rad.s^{-1}) of pressure waves in air vs. the wavenumber $k = |\mathbf{k}|$ (m^{-1}), projection of the Bloch vector k along the edges of the irreducible Brillouin zone ΓXMU shown in **Figure 1**. We note the appearance of a frequency stop band for $\omega \in [51.4250, 55.2638]$ rad.s^{-1}.

for one thin channel, and

$$\omega_1 \sim 127.6447 \quad , \quad \omega_2 \sim 132.4676 \qquad (25)$$

for six thin channels, which are in good agreement with the finite element values

$$\omega_1^* = 125.6586 \quad , \quad \omega_2^* = 134.8155 \qquad (26)$$

for six thin channels.

This demonstrates that the discrete model provides accurate estimates for the lower and upper edges of the ultra-low frequency stop band. This is therefore a useful tool which can be used in the design of acoustic metamaterials. Importantly, we note that the spring-mass counterpart of the shell with 6 holes, is like in **Figure 6**, which corresponds to an LC electrical circuit with one capacitance C and six inductances L in series corresponding to the mass and springs, respectively, see e.g., Guenneau et al. (2007a) for an analysis of two-dimensional acoustic metamaterials.

4.2. Dependence of low Frequency Stop Band on Radius of Thin Channel

Before we move to more complex geometries, we would like to investigate the case of Helmholtz resonators with thicker channels, that would prevent viscous effects for pressure waves entering the thin channels in manufactured prototypes. We note that there is an obvious limitation of the asymptotic model. Indeed, the accuracy of the eigenfrequency estimate relies heavily on the smallness of the parameter ϵ, which essentially requires elongated channels (in other terms ligaments or necks). We have checked the lack of robustness of the asymptotic estimates with respect to the elongation of channels, when we changed the radius of the thin channel for a Helmholtz resonator with a single channel like in **Figure 3**. We therefore focus on finite element results which are shown in **Table 1**, and one can see that although the low frequency stop band is preserved for increasing values of the radius, its position is shifted up and it is enlarged. These results are good news for forthcoming experiments.

4.3. Eigenfrequency Estimate in the Case of a Double Spherical Shell With One Thin Channel

Let us now consider the case of and LC circuit with more than one capacitance. The simplest model of interest is that of an LC circuit with two capacitances and two inductors. This corresponds to a mechanical model like in **Figure 10**.

In the numerical example we now have $\varepsilon^2 h_2^2 = 3.14 \times 10^{-4}\text{m}^2$, $\varepsilon^2 h_1^2 = 7.85 \times 10^{-5}\text{m}^2$, $l_2 = 0.1$m, $l_1 = 0.05$m, and the masses (in kilogram)

$$\begin{aligned} m_1 &= \rho V_1 = \frac{4000}{3} \pi r_1^3 \\ m_2 &= \rho V_2 = \frac{4000}{3} \pi \left(r_1^3 + (b_2^3 - a_2^3)\right) + 10^3 \varepsilon^2 h_1^2 l_1 \end{aligned} \qquad (27)$$

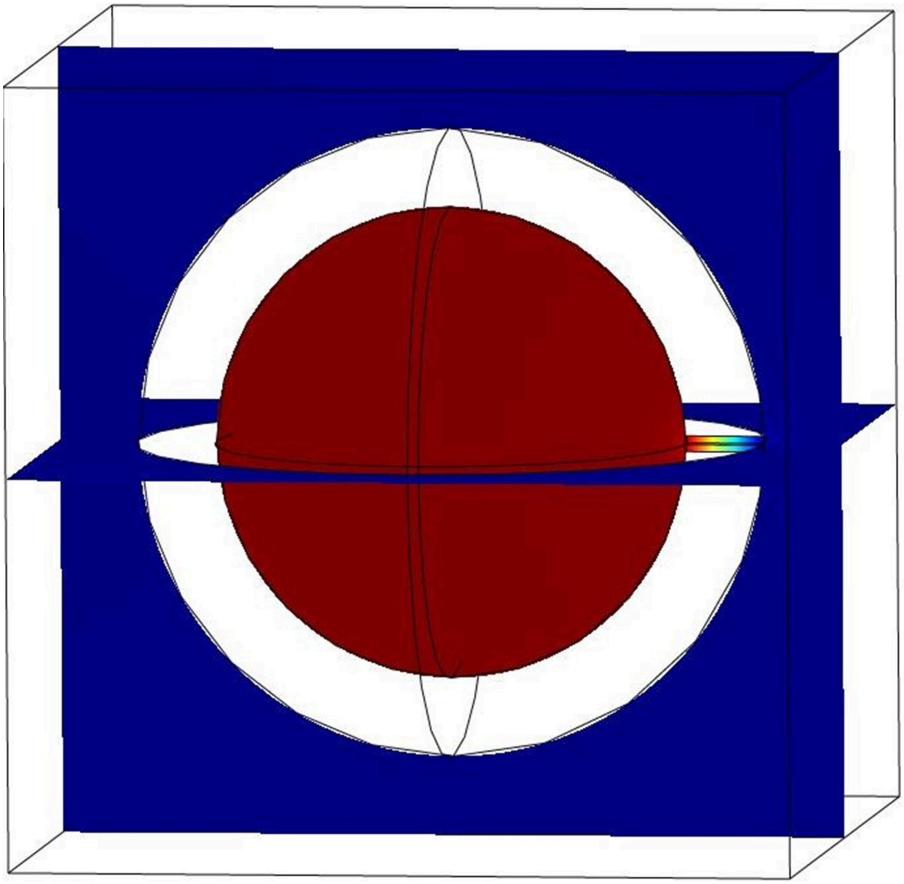

FIGURE 5 | The eigenfunction corresponding to the eigenfrequency $\omega_1^* = 51.4250$ rad.s^{-1} for one thin channel. Blue color corresponds to nearly vanishing amplitude of the eigenmode u, while red color corresponds to it maximum value. The pressure field p is constant inside the inner cavity and outside the shell, but it varies rapidly inside the thin channel: it is a localized eigenmode responsible for the stop band in **Figure 4**, which is well approximated by a spring mass model.

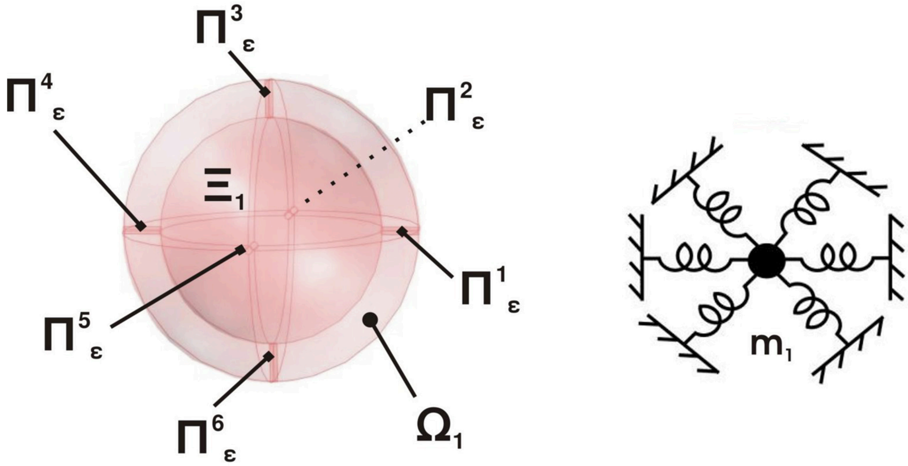

FIGURE 6 | Geometry of the inclusions and the Helmholtz oscillator consisting of six springs connected to a mass at one end and fixed at the other end.

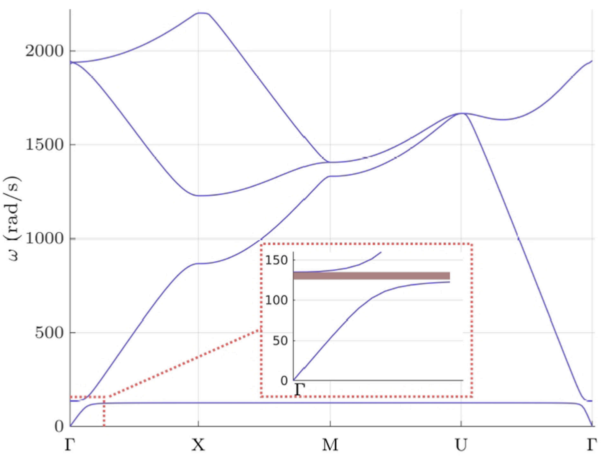

FIGURE 7 | Dispersion diagram for a periodic array (pitch $d = 1$ m) of spherical rigid shells (inner radius $R = 0.3$ m and outer radius $R = 0.4$ m) with six thin channels (length 0.1 m and radius 0.01m) representing the frequency ω (rad.s^{-1}) of pressure waves in air vs. the wavenumber $|\mathbf{k}|$ (m^{-1}), projection of the Bloch vector k along the edges of the irreducible Brillouin zone ΓXMU. We note the appearance of a frequency stop band for $\omega \in [125.6586, 134.8155]$ rad.s^{-1} which is wider and at higher frequencies than the stop band in **Figure 4**: the more identical thin channels, the higher the resonant frequency of the localized mode.

where ρ is the density of air ($\sim$ 1.225kg.m^{-3}), V_1 and V_2 the volumes air occupies in Ξ_1 and Ξ_2, r_1 is the interior radius for the domain Ξ_1 and a_2, b_2 are respectively the interior and exterior radii for the domain Ξ_2. In our case, $r_1 = 0.1$m, $a_2 = 0.15$m and $b_2 = 0.2$m. The formula (22) gives the following values for the first eigenfrequencies (in rad.s^{-1}) of the multistructures $\Pi_{\varepsilon(1)} \bigcup \Xi_{(1)}$ and $\Pi_{\varepsilon(2)} \bigcup \Xi_{(2)}$:

$$\omega_1 \sim 124.2641 \quad , \quad \omega_2 \sim 208.4109 \tag{28}$$

The corresponding angular frequencies (in rad.s^{-1}) associated with the standing waves in the periodic structure were obtained numerically, and from the band diagram in **Figure 11** they are

$$\omega_1^* = 55.2128 \quad , \omega_2^* = 118.9750 \tag{29}$$

Formula (22) leads to frequency estimates in (28) that do not capture the eigenfrequency ω_1^*, that corresponds to the localized eigenmode shown in the left part of **Figure 12**, but we observe a good agreement between frequency estimate ω_1 and ω_2^*, associated with the eigenmode shown in right part of **Figure 12**. The estimate for the eigenfrequency ω_1^* can be found if the domain $\Pi_{\varepsilon(2)} \bigcup \Xi_{(2)}$ is replaced by the domain $\Pi_{\varepsilon(2)} \bigcup \Omega_{(2)} \bigcup \Pi_{\varepsilon(1)} \bigcup \Omega_{(1)}$. In this case, the eigenfrequency ω_1^*

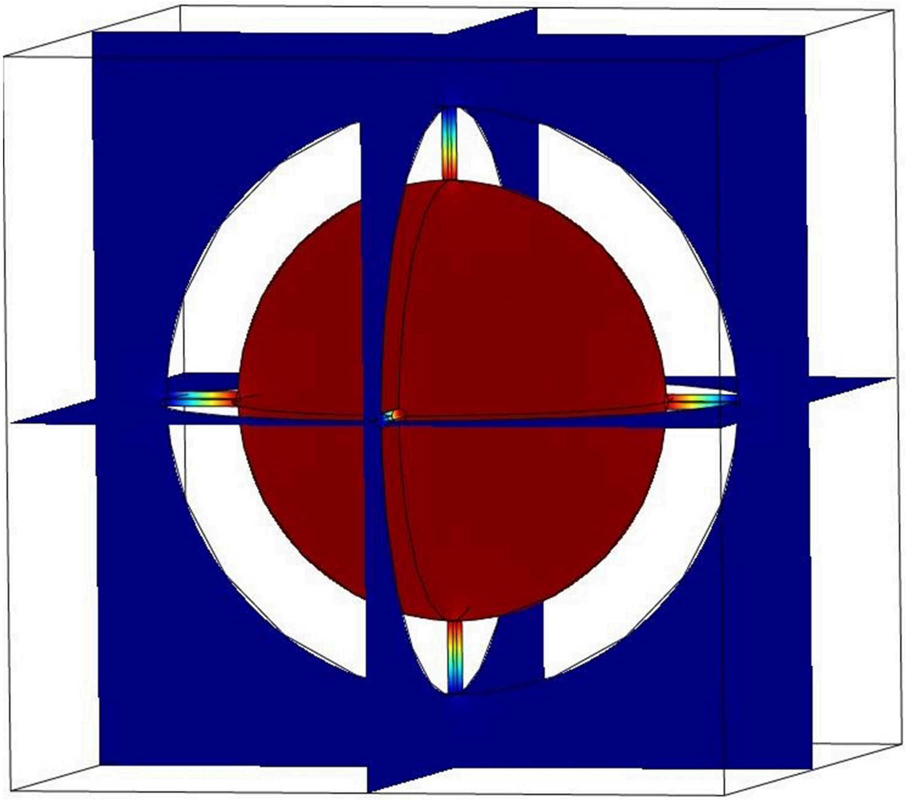

FIGURE 8 | The eigenfunction corresponding to the eigenfrequency $\omega_1^* = 125.6586$ rad.s^{-1} for six thin channels responsible for the stop band in **Figure 7**. This frequency is well approximated by the spring mass discrete model which provides us with the frequency estimate $\omega_1 = 127.6447$ rad.s^{-1}.

TABLE 1 | Values of the extrema of the gap with respect to the radius of the thin channel, for the Helmholtz resonator like in **Figure 3**.

r (m)	0.010	0.012	0.014	0.016	0.018	0.020	0.025	0.030	0.035	0.040	0.045	0.050
ω_{min}	51.4250	62.9523	72.5144	81.8465	90.9279	99.7964	120.9971	141.3007	160.7574	179.3317	197.2263	214.4251
ω_{max}	55.2638	67.6568	77.9375	87.9765	97.7465	107.2948	130.1329	152.0110	173.1273	193.0588	212.4465	231.0001

*See also **Figure 9** for a graphical representation of the Table.*

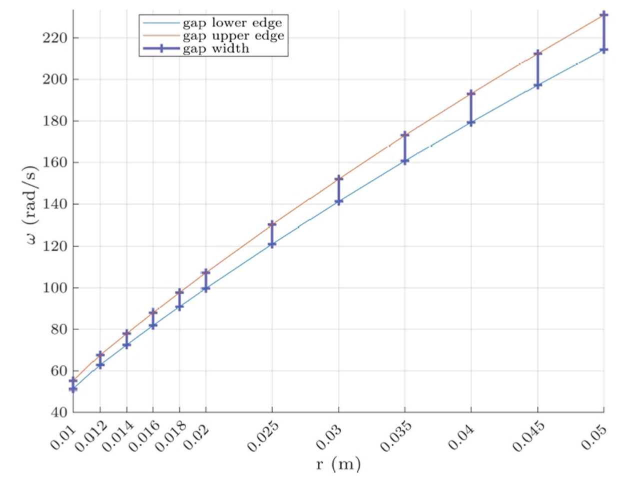

FIGURE 9 | Modification of the gap width and position with respect to the radius of the thin channel of the Helmholtz resonator with a single shell like in **Figure 3**. The eigenfrequency estimates $\omega_1 \sim 52.1107$ and $\omega_2 \sim 54.0796$ compare well with finite element results $\omega_1^* \sim 51.4250$ and $\omega_2^* \sim 55.2638$ for $r = 0.01$m, see **Table 1**. Note the non linear scale for r.

is approximated by the first positive eigenvalue of the problem

$$\rho^{-1} V_1''(x) + K^{-1}\omega^2 V_1(x) = 0\,, \quad 0 < x < l_1 \tag{30}$$

$$V_1(0) = 0\,, \tag{31}$$

$$K^{-1} I_1 V_1'(l_1) - K^{-1} I_2 V_2'(0) = m_1 \omega^2 V_1(l_1)\,, \tag{32}$$

$$\rho^{-1} V_2''(x) + K^{-1}\omega^2 V_2(x) = 0\,, \quad 0 < x < l_2 \tag{33}$$

$$\lambda^{-1} I_2 V_2'(l_2) = m_2 \omega^2 V_2(l_2)\,, \tag{34}$$

$$V_2(0) = V_1(l_1)\,, \tag{35}$$

where $V_1(x)$, $V_2(x)$ are the eigenfunctions defined on $(0, l_1)$ and $(0, l_2)$, respectively, and the masses m_1, m_2 are defined by (in kilogram)

$$m_1 = \frac{4000}{3}\pi r_1^3\,,\; m_2 = \frac{4000}{3}\pi\left(b_2^3 - a_2^3\right) \tag{36}$$

Taking into account that $\omega_0 = O(\varepsilon)$, we deduce that it can be approximated as the first positive solution of the following algebraic equation:

$$m_1 m_2 l_1 l_2 \omega^4 - K\omega^2\left(l_2 I_1 m_1 + I_1 l_2 m_2 + I_2 m_1 l_1\right) + K^2 I_1 I_2 = 0 \tag{37}$$

so that $\omega_0 \sim 82.76057$ rad.s^{-1}, which provides a reasonably accurate approximation of $\omega_1* = 55.2128$ rad.s^{-1}. However, a further refinement of this asymptotic estimate would require adding higher order corrections and thus solving boundary layer type problems as discussed in Kozlov et al. (1999), and this falls beyond the scope of the present paper.

5. ISOFREQUENCY SURFACES, DYNAMIC EFFECTIVE ANISOTROPY AND LOCALIZED MODES

Thus far, we have only analyzed dispersion curves, but it has been known for over 80 years that one needs to be extra careful regarding analysis of say electronic band structures (Bouckaert et al., 1936), as there are examples showing that stop band edges might be reached strictly within the Brillouin zone, and so it is not enough to describe its edges to characterize the band spectrum (Harrison et al., 2007). We would like to investigate dynamic effective anisotropy effects near the edge of the low frequency stop band, and localization effects induced by local resonators such as in Movchan et al. (2006),Bigoni et al. (2013),Craster et al. (2013), and Llewellyn Smith and Davis (2010) for a frequency on the acoustic band.

Here, we provide representation for isofrequencies near the lower edge of the first stop band for the case of a Helmholtz resonator with one thin channel as in **Figure 4**. However, we observed very similar features in all other cases. We first note in **Figure 13** that the distortion of the isofrequency surfaces increases when we move toward the lower edge of the stop band. A small change in the frequency leads to a dramatic change in the isofrequency surface. Besides, the observation of isofrequency (or slowness) contours in **Figure 13** confirms that anisotropy increases near the edge of the stop band as contours become more and more elongated. Researchers in photonics used vanishing group velocity near stop band edges to achieve self-guiding of light in 2D photonic crystals in the past 20 years (Kosaka et al., 1999; Witzens et al., 2002; Chigrin et al., 2003). Such an effect is known in the applied mathematics and waves literature as a dynamic effective anisotropy (Slepyan et al., 1987; Ayzenberg-Stepanenko and Slepyan, 2008; Craster et al., 2009, 2010; Colquitt et al., 2012; Schnitzer, 2017) : for an isotropic medium, the isofrequency surface is spherical, and the corresponding isofrequency contours are circular. On the edge of the stop band, the extreme elongation of isofrequency contours reveals an extreme dynamic

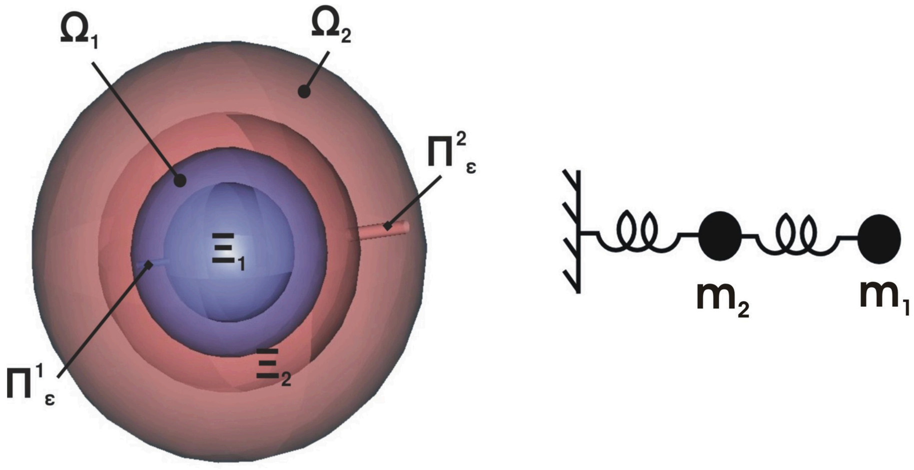

FIGURE 10 | Geometry of the inclusions and the Helmholtz oscillator consisting of two masses connected by a spring, with one of them connected to a fixed domain.

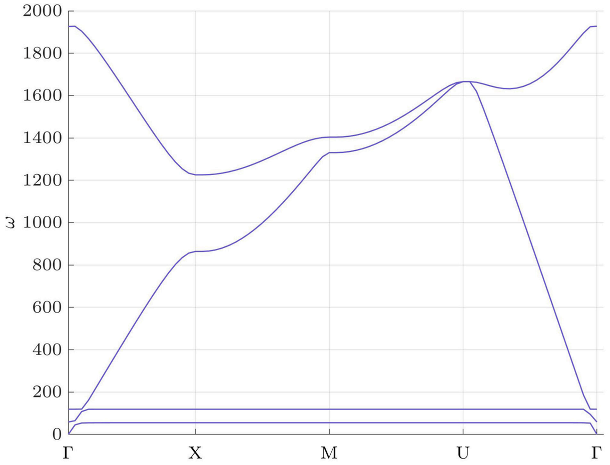

FIGURE 11 | Dispersion diagram for a periodic array (pitch $d = 1$m) of double spherical rigid shells (radius of spheres from inner to outer are 0.1, 0.15, 0.3, and 0.4 m) with one thin channel in each shell (respectively of lengths 0.05 and 0.1 m and radii 0.005 and 0.01 m) representing the frequency ω (rad.s^{-1}) of pressure waves in air vs. the wavenumber $k = |\mathbf{k}|$ (m^{-1}), projection of the Bloch vector k along the edges of the irreducible ΓXMU. We note the appearance of two frequency stop bands for $\omega \in [55.2128, 58.5863]$ rad.s^{-1} and $\omega \in [118.9750, 119.0959]$ rad.s^{-1}.

anisotropy. We note that some dynamic effective anisotropy of 3D dynamic lattices displays similar isofrquency surfaces to ours near stop band edges (Vanel et al., 2016). This could be used to achieve as aforementioned highly directive phenomena, in a way similar to what was demonstrated experimentally for transverse electromagnetic waves (Ceresoli et al., 2015). Another striking effect is that of wave localization, when one creates one or more defects in a periodic structure. Usually, this is achieved in high frequency stop bands, when the wave wavelength is on the same order as the periodicity. Here, the wave localization is achieved either at resonances of resonators, see upper panel in **Figure 14**, or as shown in the lower panel of the same figure, at a frequency $\omega_1^* = 559.2042$ rad.s^{-1} located in a part of the acoustic band sandwiched between the low frequency stop band and another region of vanishing group velocity near the X symmetry point in **Figure 4**, so this has the additional feature of being below the Bragg frequency regime. We note that from **Figure 14**, this localized mode can be approximated as a monopole given by the first derivative of the spherical Bessel function of the first kind $j_n(\omega r/c)$, where r is the radial position. The lowest root corresponding to the lowest frequency of the cavity is the frequency given by the root of the transcendental equation (simply derived by separation of variables in Helmholtz's equation (2) written in spherical coordinates and assuming that $\partial p/\partial n = 0$ on the boundary of the defect) :

$$j_1'(\omega a/c) = 0\,. \tag{38}$$

Bearing in mind that the first root of j_1' is 2.0816 and taking $a = 1.25$m as the radius of a dashed circle within which the defect mode seems to be mostly confined in **Figure 14**, (38) leads to the frequency estimate $\omega_1 = 566.19$ rad.s^{-1}, which is in good agreement with the finite element computation $\omega_1^* = 559.2042$ rad.s^{-1}. This method of the effective sphere is the analogous concept to effective disk in doubly periodic structures with defects (Movchan et al., 2007).

6. CONCLUSION

In this paper, we have seen that it is possible to sculpt the Bloch spectrum of three-dimensional phononic crystals almost *ad libitum* simply by digging some holes and adding cavities in rigid spheres periodically arranged along a cubic lattice. One of the main achievements of our numerical study is the appearance of ultra-low frequency stop bands at frequencies predicted quantitalively by an asymptotic model, that can be viewed as a 3D counterpart of (Movchan and Guenneau, 2004).

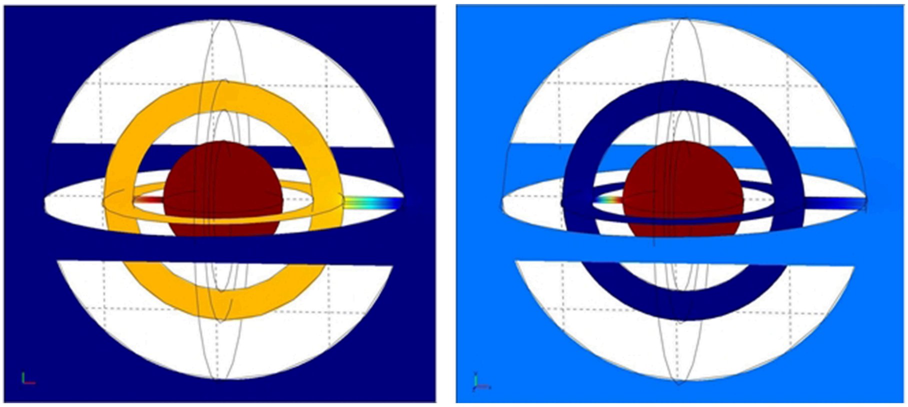

FIGURE 12 | Eigenfunctions for embedded resonators corresponding to the eigenfrequency $\omega_1^* = 55.2128$ rad.s^{-1} (left panel) and corresponding to the eigenfrequency $\omega_2^* = 118.975$ rad.s^{-1} (right panel). In left panel both canals vibrates, while in right panel only the inner canal does. The second eigenfrequency $\omega_2^* = 118.975$ rad.s^{-1} is reasonably well approximated by the first eigenfrequency of the spring mass model which gives and $\omega_1 = 124.2641$ rad.s^{-1} and $\omega_2 = 208.4109$ rad.s^{-1}.

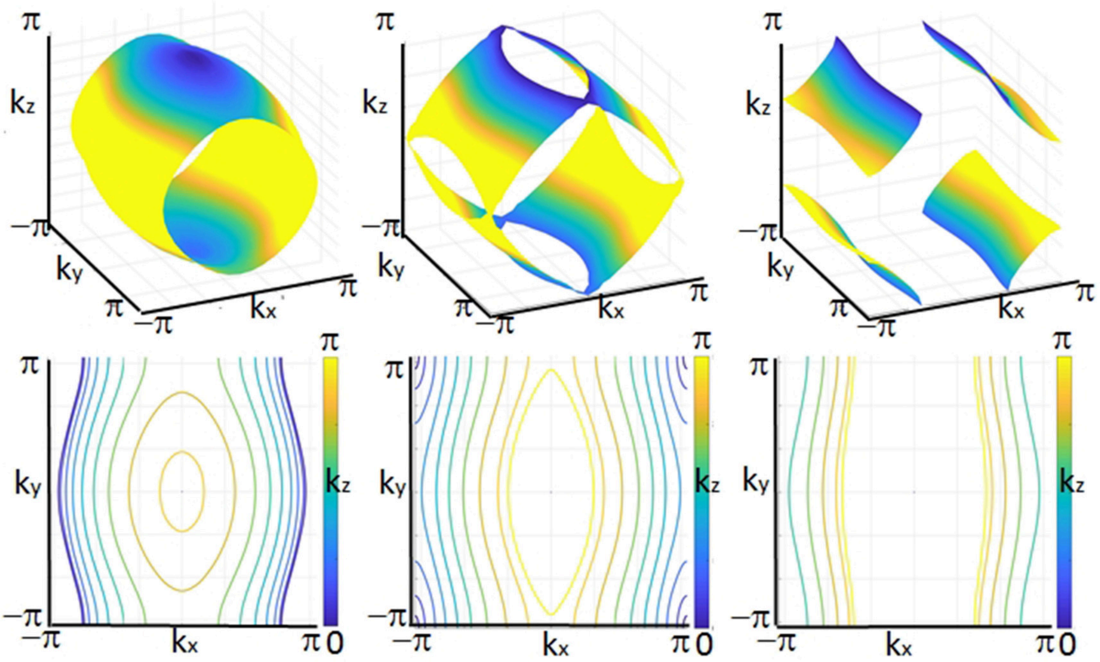

FIGURE 13 | Representative isofrequency surfaces $k_Z(k_X, k_Y)$ in the first Brillouin zone **(upper panel)** and associated isofrequency contours in the plane (k_X, k_Y) for $k_Z \in (0, \pi)$ **(lower panel)** at frequency $\omega = 51.42$ rad.s^{-1} **(left panel)**, $\omega = 51.4215$ rad.s^{-1} **(middle panel)** and $\omega = 51.423$ rad.s^{-1} **(right panel)**; The surfaces and contours flatten when the frequency moves toward the lower edge of the stop band in **Figure 4**. and thus dynamic effective anisotropy increases.

We also conducted some elementary shape optimization (by varying the size, diameter and number of channels in a rigid sphere of constant radius) in order to enhance the control of the location and the number of low frequency stop bands, thanks to our asymptotic estimates. Our asymptotic results could be further used for a homogenization study in the spirit of the 2D analysis conducted in Mercier et al. (2017) to address the effective parameters of our acoustic system. However, the acoustic metamaterial we have analyzed would allow only frequency dependent effective bulk modulus, and in order to achieve a frequency dependent effective density and thus double negative acoustic parameters near resonances, one needs to introduce a second type of resonator in the periodic cell. Therefore, achieving a design of an acoustic superlens through negative refraction requires a more complex design. However, a cubic array of rigid spheres does not support any

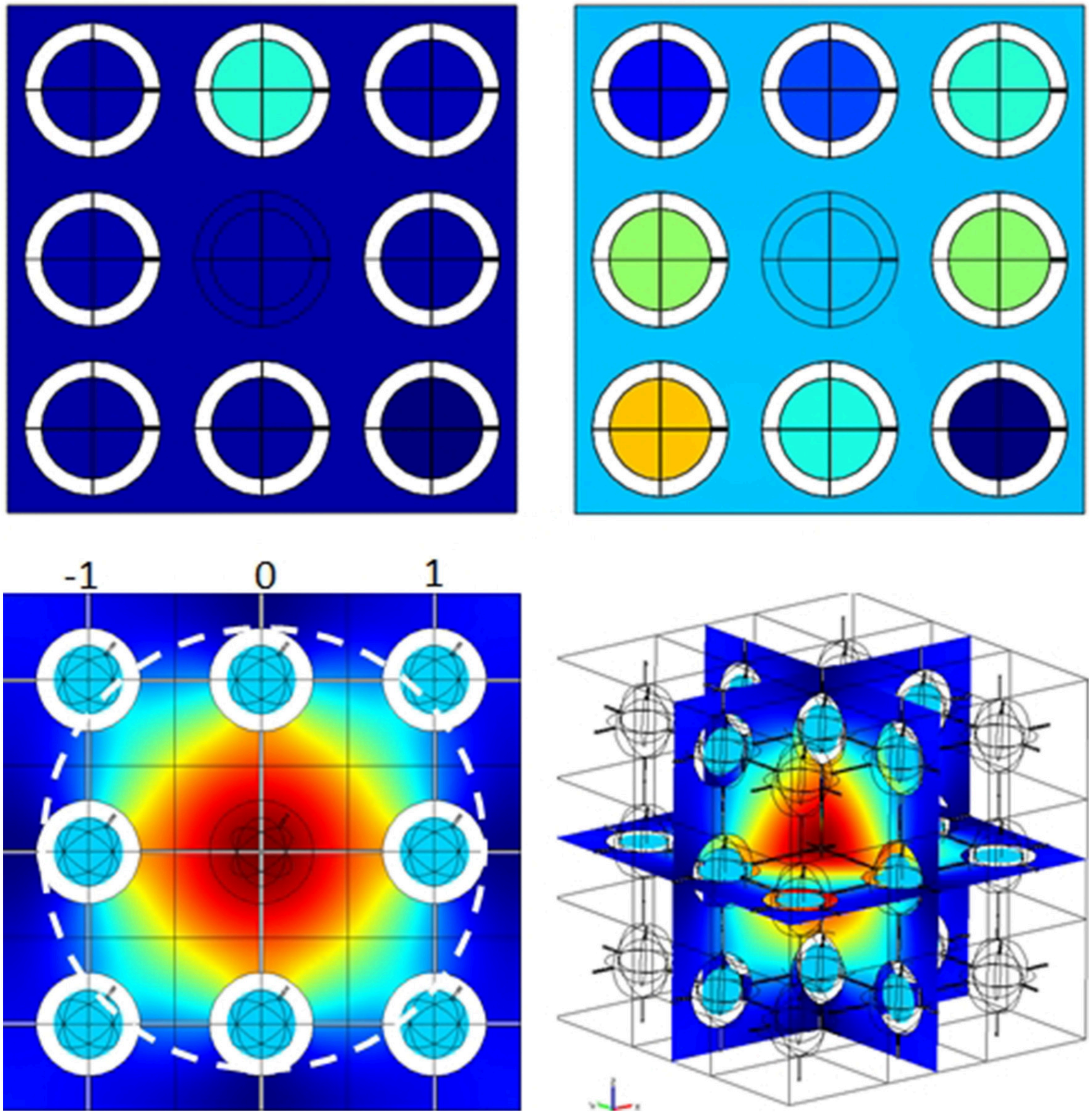

FIGURE 14 | Representative eigenfunctions for a macrocell of 26 resonators as in **Figures 4**, **5** with a defect (air instead of resonator) in the middle. Upper panel: Eigenfunctions corresponding to an eigenfrequency $\omega_0^* = 52.3545$ rad.s^{-1} in the ultra-low frequency stop band of **Figure 4**. Lower panel: Eigenfunction corresponding to an eigenfrequency $\omega_1^* = 559.2042$ rad.s^{-1} above the low frequency stop band of **Figure 4**, which is approximated by the first root of (38) i.e., the fundamental resonance of an effective spherical cavity (marked by dashed circle) of radius $a = 1.25$ m.

complete stop band, even in the densely packed configuration, so the acoustic metamaterial which we studied has markedly different filtering properties compared with phononic crystals with rigid spheres: multistructures make possible tunable ultra-low frequency stop bands (associated with very flat dispersion curves i.e., localized eigenmodes). Finally, we illustrate in **Figure 14** a possible application of the ultra-low frequency stop band in order to localize a mode of a wavelength larger than the pitch of the array of resonators. One can also envisage sculpting a line defect thanks to the removal of a few resonators in a larger macrocell, that would make a low frequency waveguide. We further note that considering shells of same diameter with holes of varying diameters, or spheres with varying diameters and identical or varying holes would make possible graded phononic crystals with a larger low frequency stop band, thanks to the overlap of numerous low frequency stop bands. This could lead to a three dimensional counterpart to the acoustic rainbow put forward in Zhu et al. (2013). Indeed, many embedded spheres would make this possible, since the band diagram **11** suggests N embedded spheres would lead to N low frequency stop bands that might hybridize. Similarly, one could envisage to reflect, detour, or focus, pressure waves using the low frequency stop band within which effective parameters are expected to take negative values as it is now well-established for the two-dimensional counterpart of such kind of acoustic metamaterials. We hope our work will foster experimental efforts toward 3D acoustic metamaterials for airborne and underwater sound filtering effects. At first sight, the implementation of the former seems more straightforward, since the latter would require further theoretical and numerical investigation of conversion of pressure waves propagating in the fluid into pressure and shear waves propagating in the shells. For instance, in the derivation of the asymptotic estimates, the boundary layer analysis will be more involved. Nevertheless, it might be easier to perform underwater experimental characterization of the sonic metamaterial.

AUTHOR CONTRIBUTIONS

GD performed all numerics, AM derived the asymptotic formulae, SG wrote the manuscript and SE participated in the physical interpretation of results. All authors reviewed the manuscript and contributed to the study.

FUNDING

This research has been funded in part by ERC (SG received funding from ERC as a PI of an ERC starting grant 279673 during the period 2011–2016, with GD a postdoc on that grant in 2014-2015) and by EPSRC (AM received funding from EPSRC as a co-PI of research grant EP/L024926/1 during the period 2015-2018 and SG is a named collaborator who is currently hosted in the group of Prof. R. Craster at Imperial College who is the PI on that grant).

ACKNOWLEDGMENTS

AM acknowledges funding of the EPSRC as a co-investigator on program grant EP/L024926/1 on Mathematical fundamentals of Metamaterials for multiscale Physics and Mechanics. SG is thankful for a visiting position in the department of mathematics at Imperial College London and support from EPSRC as a named collaborator on grant EP/L024926/1. Insightful discussions with Prof. R.V. Craster are acknowledged.

REFERENCES

Aberg, M., and Gudmundson, P. (1997). The usage of standard finite element codes for computation of dispersion relations in materials with periodic microstructure. *J. Acoust. Soc. Am.* 102, 2007–2013.

Alster, M. (1972). Improved calculation of resonant frequencies of helmholtz resonators. *J. Sound Vib.* 24, 63–85.

Ammari, H., Fitzpatrick, B., Lee, H., Yu, S., and Zhang, H. (2017b). Double-negative acoustic metamaterials. *arxiv:1709.08177v2.*

Ammari, H., and Zhang, H. (2017a). Effective medium theory for acoustic waves in bubbly fluids near Minnaert resonant frequency. *SIAM J. Math. Anal.* 49, 3252–3276. doi: 10.1137/16M1078574

Auriault, J. L. (1994). Acoustics of heterogeneous media: macroscopic behavior by homogenization. *Curr. Top. Acoust. Res.* 1, 63–90.

Auriault, J. L., and Bonnet, G. (1985). Dynamique des composites élastiques périodiques, *Arch. Mech.* 37, 269–284.

Auriault, J. L., and Boutin, C. (2012). Long wavelength inner-resonance cut-off frequencies in elastic composite materials. *Int. J. Solids Struct.* 49, 3269–3281. doi: 10.1016/j.ijsolstr.2012.07.002

Ayzenberg-Stepanenko, M., and Slepyan, L. I. (2008). Resonant-frequency primitive waveforms and star waves in lattices. *J. Sound Vib.* 313, 812–821. doi: 10.1016/j.jsv.2007.11.047

Baird, A. M., Kerr, F. H., and Townend, D. J. (1999). Wave propagation in a viscoelastic medium containing fluid-filled microspheres. *J. Acoust. Soc. Am.* 105, 1527–1538.

Bensoussan, A., Lions, J., and Panainicolaou, G. (1978). *Asymptotic Analysis for Periodic Structures*. North Holland: Springer Verlag.

Bigoni, D., Guenneau, S., Movchan, A. B., and Brun, M. (2013). Elastic metamaterials with inertial locally resonant structures : application to lensing, high-directivity and localisation. *Phys. Rev. B* 87, 174303. doi: 10.1103/PhysRevB.87.174303

Bloch, F. (1928). Uber die quantenmechanik der elektronen in kristallgittern. *Z. Phys.* 52, 555–600.

Bouckaert, L.P., Smoluchowski, R., Wigner, E. (1936). Theory of brillouin zones and symmetry properties of wave functions in crystals. *Phys. Rev.* 50, 58–67.

Boutin, C. (2013). Acoustics of porous media with inner resonators. *J. Acoust. Soc. Am.* 134, 4717–4729. doi: 10.1121/1.4824965

Boutin, C., and Becot, F. X. (2015). Theory and experiments on poro-acoustics with inner resonators. *Wave Motion* 54, 76–99. doi: 10.1016/j.wavemoti.2014.11.013

Brillouin, L. (1978). *Wave Propagation in Periodic Structures*. New York, NY: Dover Publications.

Brun, M., Guenneau, S., and Movchan, A. B. (2009). Achieving control of in-plane elastic waves. *Appl. Phys. Lett.* 94:061903. doi: 10.1063/1.3068491

Brunet, T., Merlin, A., Mascaro, B., Zimny, K., Leng, J., Poncelet, O., et al. (2015). Soft 3D acoustic metamaterial with negative index. *Nat. Mater.* 14:384. doi: 10.1038/nmat4164

Ceresoli, L., Abdeddaim, R., Antonakakis, T., Maling, B., Chmiaa, M., Sabouroux, P. et al. (2015). Dynamic effective anisotropy: asymptotics, simulations, and microwave experiments with dielectric fibers. *Phys. Rev. B* 92, 174307. doi: 10.1103/PhysRevB.92.174307

Chalmers, L., Elford, D. P., Kusmartsev, F. V., and Swallowe, G. M. (2009). Acoustic band gap formation in two-dimensional locally resonant sonic crystals comprised of helmholtz resonators. *Int. J. Mod. Phys. B* 23, 4234–4243. doi: 10.1142/S0217979209063390

Chen, K. T. Chen, Y. H., Lin, K. Y., and Weng, C. C. (1998). The improvement of the transmission loss of a duct by adding Helmholtz resonators. *Appl. Acoust.* 57, 71–82.

Chigrin, D. N., Enoch, S., Torres, C. M. S., Tayeb, G. (2003). Self-guiding in two-dimensional photonic crystals. *Opt. Express* 11, 1203–1211. doi: 10.1117/12.463861

Colquitt, D. J., Jones, I. S., Movchan, N. V., Movchan, A. B., McPhedran, R. C. (2012). Dynamic anisotropy and localization in elastic lattice systems. *Waves Random Complex Media* 22, 143–159. doi: 10.1080/17455030.2011.633940

Craster, R. V., and Guenneau, S. (eds.). (2013). *Acoustic Metamaterials : Negative Refraction, Imaging, Lensing and Cloaking*. Springer Series in Materials Science Vol. 166.

Craster, R. V., Kaplunov, J., and Postnova, J. (2010). High-frequency asymptotics, homogenisation and localisation for lattices. *Q. J Mech. Appl. Math.* 63, 497–519. doi: 10.1093/qjmam/hbq015

Craster, R. V., Nolde, E., and Rogerson, G. A. (2009). Mechanism for slow waves near cutoff frequencies in periodic waveguides. *Phys. Rev. B* 79, 045129. doi: 10.1103/PhysRevB.79.045129

Dowling, J. P. (2008). *Photonic and Sonic Band Gap Metamaterial Bibliography*. Available online at: https://web.archive.org/web/20070726070938/http://phys.lsu.edu/%7Ejdowling/pbgbib.html

Duan, Y. T., Koch, W., Linton, C. M., and Mciver, M. (2007). Complex resonances and trapped modes in ducted domains. *J. Fluid Mech.* 571, 119–147. doi: 10.1017/S0022112006003259

Dupont, G., Remy, F., Kimmoun, O., Molin, B., Guenneau, S., and Enoch, S. (2017). Type of dike using C-shaped vertical cylinders. *Phys. Rev. B* 96, 180302. doi: 10.1103/PhysRevB.96.180302

Elford, D. P., Chalmers, L., Kusmartsev, F. V., and Swallowe, G. M. (2004). Matryoshka locally resonant sonic crystal. *J. Acoust. Soc. Am.* 130, 649–655. doi: 10.1121/1.3643818

Fang, N., Xi, D., Xu, J., Ambati, M., Srituravanich, W., Sun, C., et al. (2006). Ultrasonic metamaterials with negative modulus. *Nature* 5:452. doi: 10.1038/nmat1644

Farhat, M., Guenneau, S., Enoch, S., and Movchan, A. B. (2009). Negative refraction, surface modes, and superlensing effect via homogenization near resonances for a finite array of split-ring resonators. *Phys. Rev. E* 80, 046309. doi: 10.1103/PhysRevE.80.046309

Figotin, A., and Kuchment, P. (1998). Spectral properties of classical waves in high-contrast periodic media. *SIAM J. Appl. Math.* 58, 683–670.

Floquet, G.(1883). Sur les équations différentielles linéaires a coefficients périodiques, *Ann. l'Ecole Normale Supérieure* 12, 47–88.

Gaunaurd, G. C., and Uberall, H. (1982). Resonance theory of the effective properties of perforated solids. *J. Acoust. Soc. Am.* 71, 282–295.

Gazalet, J., Dupont, S., Kastelik, J. C., Rolland, Q., and Djafari-Rouhani, B. (2013). A tutorial survey on waves propagating in periodic media: electronic, photonic and phononic crystals. Perception of the Bloch theorem in both real and Fourier domains. *Wave Motion* 50, 619–654. doi: 10.1016/j.wavemoti.2012.12.010

Goffaux, C., Sánchez-Dehesa, J., Levy Yeyati, A., Lambin, P. H., Khelif, A., Vasseur, J. O., et al. (2002). Evidence of Fano-like interference phenomena in locally resonant materials. *Phys. Rev. Lett.* 88:225502. doi: 10.1103/PhysRevLett.88.225502

Groeneweg, J. F. (1969). *Current Understanding of Helmholtz Resonator Arrays as Duct Boundary Conditions, in a Conference Held at NASA Headquarters*. Washington, DC: NASA.

Guenneau, S., Movchan, A. B., and Movchan, N. V. (2007b). Localized bending modes in split ring resonators. *Physica B* 394, 141.

Guenneau, S., Movchan, A. B., Petursson, G., and Ramakrishna, S. A. (2007a). Acoustic meta-materials for sound focussing and confinement. *New J. Phys.* 9:399. doi: 10.1088/1367-2630/9/11/399

Harrison, J. M., Kuchment, P., Sobolev, A., Winn, B. (2007). On occurrence of spectral edges for periodic operators inside the Brillouin zone. *J. Phys. A* 40, 7597. doi: 10.1088/1751-8113/40/27/011

Hinders, M. K., Rhodes, B. A., and Fang, T. M. (1995). Particle-loaded composites for acoustic anechoic coatings. *J. Sound Vib.* 185, 219–246.

Hirsekorn, M. (2004). Small-size sonic crystals with strong attenuation bands in the audible frequency range. *Appl. Phys. Lett.* 84, 3364–3366. doi: 10.1063/1.1723688

Hladky-Hennion, A. C., and Decarpigny, J.-N. (1991). Analysis of the scattering of a plane wave by a doubly periodic structure using the finite element method: application to Alberich anechoic coatings. *J. Acoust. Soc. Am.* 90, 3356–3367.

Ho, K. M., Cheng, C., Yang, Z., Zhang, X., and Sheng, P. (2003). Broadband locally resonant sonic shields. *Appl. Phys. Lett.* 83, 5566–5568. doi: 10.1063/1.1637152

Hou, Z. L., Liu, J., Kuang, W., Liu, Y., and Wu, S. (2007). Sonic crystal with open resonant cavities. *Phys. Rev. E* 75, 026608. doi: 10.1103/PhysRevE.75.026608

Hu, X., Chan, C. T., Ho, K.-M., and Zi, J. (2011). Negative effective gravity in water waves by periodic resonator arrays. *Phys. Rev. Lett.* 106:174501. doi: 10.1103/PhysRevLett.106.174501

Hu, X., Zi, J., Chan, C. T., and Ho, K.-M. (2017). Experimental observation of negative effective gravity in water waves. *Sci. Rep.* 3:1916. doi: 10.1038/srep01916

Ivansson, S. (2006). Sound absorption by viscoelastic coatings with periodically distributed cavities. *J. Acoust. Soc. Am.* 119, 3558–3567. doi: 10.1121/1.2190165

Joannopoulos, J., Meade, R., and Winn, J. (1995). *Photonic Crystals: Molding the Flow of Light*. Princeton University Press.

Kadic, M., Buckmann, T., Schittny, R., and Wegener, M. (2013). Metamaterials beyond electromagnetism *Rep. Progr. phys.* 76:126501. doi: 10.1016/j.physb.2006.12.064

Kafesaki, M., and Economou, E. N. (1999). Multiple-scattering theory for three-dimensional periodic acoustic composites. *Phys. Rev. B* 60, 11993.

Kittel, C. (1986). *Introduction to Solid State Physics*. New York, NY: John Wiley and Sons.

Kosaka, H., Kawashima, T., Tomita, A., Notomi, M., Tamamura, T., Sato, T., et al. (1999). Self-collimating phenomena in photonic crystals. *Appl. Phys. Lett.* 74:1212.

Kozlov, V. A., Mazya, V. G., and Movchan, A. B. (1999). *Asymptotic Analysis of Fields in Multi-Structures*. Oxford: Oxford Research Monographs; Oxford University Press.

Krynkin, A., Umnova, O., Yung, A., Chong, B., Aherzadeh, T. S., and Attenborough, K. (2010). Predictions and measurements of sound transmission through a periodic array of elastic shells in air. *J. Acoust. Soc. Am.* 128, 3496–3506. doi: 10.1121/1.3506342

Kushwaha, M.S., Halevi, P., Dobrzynski, L., and Djafari-Rouhani, B. (1993). Acoustic band structure of periodic elastic composites. *Phys. Rev. Lett.* 71, 2022–2025.

Lanoy, M., Pierrat, R., Lemoult, F., Fink, M., Leroy, V., and Tourin, A. (2015). Subwavelength focusing in bubbly media using broadband time reversal. *Phys. Rev. B* 91, 224202. doi: 10.1103/PhysRevB.91.224202

Lemoult, F., Fink, M., and Lerosey, G. (2011). Acoustic Resonators for Far-Field Control of Sound on a Subwavelength Scale *Phys. Rev. Lett.* 107:064301 doi: 10.1103/PhysRevLett.107.064301

Leroy, V., Strybulevych, A., Lanoy, M., Lemoult, F., Tourin, A., and Page, J. H. (2015). Superabsorption of acoustic waves with bubble metascreens. *Phys. Rev. B* 91, 020301. doi: 10.1103/PhysRevB.91.020301

Li, J., and Chan, C. T. (2004). Double negative acoustic metamaterial. *Phys. Rev. E* 70, 055602. doi: 10.1103/PhysRevE.70.055602

Li, J. B., Wang, Y. S., and Zhang, C. H. (2013). Tuning of acoustic bandgaps in phononic crystals with Helmholtz resonators. *J. Vib. Acoust.* 135:031015. doi: 10.1115/1.4023812

Lim, R., and Hackman, R. H. (1990). A parametric analysis of attenuation mechanisms in composites designed for echo reduction. *J. Acoust. Soc. Am.* 87, 1076–1103.

Liu, Z. Y., Zhang, X. X., Mao, Y. W., Zhu, Y. Y., Yang, Z. Y., Chan, C. T., et al. (2000). Locally resonant sonic materials. *Science* 289:1734. doi: 10.1126/science.289.5485.1734

Llewellyn Smith, S. G., and Davis, A. M. J. (2010). The split ring resonator. *Proc. R. Soc. A* 466, 3117–3134. doi: 10.1098/rspa.2010.0047

Maling, B. J., Colquitt, D. J., Craster, R. V. (2017). The homogenisation of Maxwell's equations with applications to photonic crystals and localised waveforms on gratings. *Wave Motion* 69, 35–49. doi: 10.1016/j.wavemoti.2016.11.003

Mead, D. (1996). A general theory of harmonic wave propagation in linear periodic systems with multiple coupling. *J. Sound Vib.* 27, 429–438.

Mei, J., Liu, Z., Wen, W., and Sheng, P. (2006). Effective Mass Density of Fluid-Solid Composite. *Phys. Rev. Lett.* 96:024301. doi: 10.1103/PhysRevLett.96.024301

Mercier, J. F., Marigo, J. J., and Maurel ,A. (2017). Influence of the neck shape for Helmholtz resonators. *J. Acoust. Soc. Am.* 142:3703. doi: 10.1121/1.5017735

Milton, G. W., Briane, M., and Willis, J. R. (2006). On cloaking for elasticity and physical equations with a transformation invariant form. *New J. Phys.* 8:248. doi: 10.1088/1367-2630/8/10/248

Minnaert, M. (1933). On musical air-bubbles and the sounds of running water, The London, Edinburgh, Dublin Philos. *Mag. J. Sci.* 16, 235–248.

Movchan, A. B., and Guenneau, S. (2004). Split-ring resonators and localized modes. *Phys. Rev. B* 70, 125116. doi: 10.1103/PhysRevB.70.125116

Movchan, A. B., Movchan, N. V., Guenneau, S., and McPhedran, R. C. (2007). Asymptotic estimates for localized electromagnetic modes in doubly periodic structures with defects. *Proc. R. Soc. A* 463, 1045–1067. doi: 10.1098/rspa.2006.1800

Movchan, A. B., Movchan, N. V., and Haq, S. (2006). Localised vibration modes and stop bands for continuous and discrete periodic structures. *Mater. Sci. Eng. A* 431, 175–183. doi: 10.1016/j.msea.2006.05.145

Movchan, A. B., Movchan, N. V., and Poulton C. G. (2002). *Asymptotic Models of Fields in Dilute and Densely Packed Composites*. London: Imperial College Press.

Movchan, A. B., and Slepyan, L.I. (2014). Resonant waves in elastic structured media: dynamic homogenisation versus Green's functions. *Int. J. Solids Struct.* 51, 2254–2260. doi: 10.1016/j.ijsolstr.2014.03.015

Nicolet, A., Guenneau, S., Geuzaine, C., and Zolla, F. (2004). Modeling of electromagnetic waves in periodic media with finite elements. *J. Comp. Appl. Math.* 168, 321–329. doi: 10.1016/j.cam.2003.07.002

Norris, A. N. (2008). Acoustic cloaking theory. *Proc. R. Soc. A* 464, 2411–2434. doi: 10.1098/rspa.2008.0076

Norris, A. N. (2009). Acoustic metafluids. *J. Acoust. Soc. Am.* 125, 839–849.

Orris, R. M., and Petyt, M. (1974). A finite element study of harmonic wave propagation in periodic structures. *J. Sound Vib.* 33, 223–236.

Pendry, J. B. (2000) Negative refraction makes a perfect lens, *Phys. Rev. Lett.* 85, 3966–3969. doi: 10.1103/PhysRevLett.85.3966

Pendry, J. B., Holden, A. J., Robbins, D. J., and Stewart, W. J. (1999). Magnetism from conductors and enhanced nonlinear phenomena. *IEEE Trans. Microwave Theory Tech.* 47:2075.

Schnitzer, O. (2017). Waves in slowly varying band-gap media. *SIAM J. Appl. Math.* 77, 1516–1535. doi: 10.1137/16M110784X

Schurig, D., Mock, J. J., Justice, B. J., Cummer, S. A., Pendry, J. B., Starr, A. F. (2006). Metamaterial electromagnetic cloak at microwave frequencies. *Science* 314, 977–980. doi: 10.1126/science.1133628

Selamet, A., and Dickey, N. S. (1995). Theoretical, computational and experimental investigation of Helmholtz resonators with fixed volume: lumped versus distributed analysis. *J. Sound Vib.* 187, 358–367.

Selamet, A., Radavich, P. M., Dickey, N. S., and Novak, J. M. (1997). Circular concentric Helmholtz resonator. *J. Acoust. Soc. Am.* 101, 41–51.

Seo, S. H., and Kim, Y. H. (2005). Silencer design by using array resonators for low-frequency band nose reduction. *J. Acoust. Soc. Am.* 118, 2332–2338. doi: 10.1121/1.2036222

Slepyan, L. I., and Tsareva, V. (1987). Energy flux for zero group velocity of the carrying wave. *Sov. Phys. Dokl.* 32, 522–524.

Vanel, A. L., Craster, R. V., Colquitt, D. J., Makwana, M. (2016). Asymptotics of dynamic lattice Green's functions. *Wave Motion* 67, 15–31. doi: 10.1016/j.wavemoti.2016.05.010

Wang, X., and Mak, C.-M. (2012). Wave propagation in a duct with a periodic Helmholtz. *J. Acoust. Soc. Am.* 131:1172. doi: 10.1121/1.3672692

Wang, Z. G., Lee, S. H., Kim, C. K., Park, C. M., Nahm, K., and Nikitov, S. A. (2008). Acoustic wave propagation in one-dimensional phononic crystals containing helmholtz resonators. *J. Appl. Phys.* 103:064907. doi: 10.1063/1.2894914

Wilcox, C. (1978). Theory of bloch waves. *J. d'Analyse Mathématique* 33, 146–167.

Witzens, J., Loncar, M., Scherer, A. (2002). Self-collimation in planar photonic crystals. *IEEE J. Select. Top. Quant. Electron.* 8, 1246–1257. doi: 10.1109/JSTQE.2002.806693

Zhao, H. G., Liu, Y. Z., Yu, D. L., Wang, G., Wen, J. H., and Wen, X. S. (2007). Absorptive properties of three-dimensional phononic crystal. *J. Sound Vib.* 303, 185–194. doi: 10.1016/j.jsv.2007.01.004

Zhou, X. Z., Wang, Y. S., and Zhang, C. (2010). Three-dimensional sonic band gaps tuned by material parameters. *Appl. Mech. Mater.* 29, 1797–1802. doi: 10.4028/www.scientific.net/AMM.29-32.1797

Zhu, J., Chen, Y., Zhu, X., Garcia-Vidal, F. J., Yin, X., Zhang, W., et al. (2013). Acoustic rainbow trapping. *Sci. Rep.* 3:1728. doi: 10.1038/srep01728

Zhu, R., Liu, X. N., Hu, G. K., Sun, C. T., and Huang, G. L. (2014). Negative refraction of elastic waves at the deep-subwavelength scale in a single-phase metmaterial. *Nat. commun.* 5:5510. doi: 10.1038/ncomms6510

Conflict of Interest Statement: The authors declare that the research was conducted in the absence of any commercial or financial relationships that could be construed as a potential conflict of interest.

frontiers in Materials

ORIGINAL RESEARCH
published: 18 April 2019
doi: 10.3389/fmats.2019.00059

Mechanical Behavior of Anisotropic Composite Materials as Micropolar Continua

Nicholas Fantuzzi[1]*, Patrizia Trovalusci*[2]** *and Snehith Dharasura*[1]

[1] Department of Civil, Chemical, Environmental, and Materials Engineering, University of Bologna, Bologna, Italy, [2] Department of Structural and Geotechnical Engineering, Sapienza University of Rome, Rome, Italy

The macroscopic behavior of materials with anisotropic microstructure described as micropolar continua is investigated in the present work. Micropolar continua are characterized by a higher number of kinematical and dynamical descriptors than classical continua and related stress and strain measures, namely the micro-rotation gradient (curvature) and the relative rotation with their work conjugated counterparts, the micro-couple, and the skew-symmetric part of the stress, respectively. The presence of such enriched strain and stress fields can be detected especially when concentrated forces and/or geometric discontinuities are present. The effectiveness of the micropolar model to represent the mechanical behavior of materials made of particles of prominent size has been widely proved in the literature, in this paper we focus on the capability of this model to grossly capture the behavior of anisotropic solids under concentrated loads for which the relative strain, that is a peculiar strain measure of the micropolar model, can have a salient role. The effect of material anisotropy in the load diffusion has been investigated and highlighted with the aid of numerical parametric analyses, performed for two dimensional bodies with increasing degrees of anisotropy using a finite element approach specifically conceived for micropolar media with quadratic elements implemented within Comsol Multiphysics© framework. The present studied cases show that a significant diffusion and redistribution of the load is due to an increasing in the level of material anisotropy.

Keywords: cosserat continua, anisotropic media, relative rotation, composites/masonry, finite element method

OPEN ACCESS

Edited by:
Chiara Daraio,
California Institute of Technology,
United States

Reviewed by:
Francesco Dal Corso,
University of Trento, Italy
Cesare Davini,
International Centre for Mechanical
Sciences, Italy

****Correspondence:***
Patrizia Trovalusci
patrizia.trovalusci@uniroma1.it

Specialty section:
This article was submitted to
Mechanics of Materials,
a section of the journal
Frontiers in Materials

Received: *08 December 2018*
Accepted: *25 March 2019*
Published: *18 April 2019*

Citation:
Fantuzzi N, Trovalusci P and
Dharasura S (2019) Mechanical
Behavior of Anisotropic Composite
Materials as Micropolar Continua.
Front. Mater. 6:59.
doi: 10.3389/fmats.2019.00059

INTRODUCTION

A material can be defined complex due to the presence of an internal structure and to its complex constitutive behavior. As well-known, in the description of complex materials, such as composites, the discrete, and heterogeneous nature of matter must be taken into account, because interfaces and material internal phases dominate the gross behavior. The presence of material internal structure can be accounted by direct discrete modeling, with generally high computational cost (Suzuki et al., 1991; Baggio and Trovalusci, 2000; Rapaport and Rapaport, 2004; Yang et al., 2010; Godio et al., 2017; Baraldi et al., 2018; Reccia et al., 2018) or by adopting multiscale or coarse-graining techniques for deriving homogenized continua (Budiansky, 1965; Sanchez-Palencia, 1987; Nemat-Nasser et al., 1996; Blanc et al., 2002; Curtin and Miller, 2003; Jain and Ghosh, 2009; Trovalusci and Ostoja-Starzewski, 2011; Nguyen et al., 2012; Sadowski et al., 2014; Altenbach and Sadowski, 2015; Greco et al., 2016. However, the classical Cauchy model (Grade 1) is not reliable in the presence of problems dominated by the microstructure size, both in the non-linear, such as in the case of strain localization phenomena, and linear regimes (de Borst, 1991; Sluys et al., 1993; Masiani and Trovalusci, 1996; Trovalusci and Masiani, 1999, 2003).

In the framework of a multiscale modeling aimed at deriving homogenized continua suitable for representing the material microstructure, avoiding physical inadequacies and theoretical/computational problems—such as: ill-conditioning in the field equations and mesh-dependency in numerical solutions—the "non-local" character of the description is crucial. Non-locality, by definition, implies the presence of internal lengths and spatial dispersion properties in wave propagation (Kunin, 1982), which allow to bypass the above mentioned drawbacks. Besides the so-called explicit/strong non-local theories (Eringen, 1972, 1999; Maugin, 1993), implicit/weak non-local formulations, referred to continua with extra degrees of freedom of various kind (Mindlin, 1964; Capriz, 1989; Eringen, 1999; Gurtin, 2000; Trovalusci, 2014), have been proposed in order to deal with problems in which a characteristic internal length, *l* (material length), is comparable to the macroscopic length, *L* (structural length). This continua, also named multifield continua, reveal the hidden microstructure, which affects the macroscopic mechanical properties, by means of the additional kinematic and work-conjugated dynamic descriptors (Trovalusci and Augusti, 1998; Forest, 2009; Trovalusci et al., 2010; Capecchi et al., 2011; Forest and Trinh, 2011; Trovalusci, 2014; Trovalusci and Pau, 2014). In particular, in the works (Trovalusci and Augusti, 1998; Trovalusci et al., 2010; Trovalusci, 2014) the presence of a microstructure made of different kind of inclusions (fibers, microcracks/pores) and the ability of multifield continua to represent dispersion phenomena with particular reference to microcraked bars under free and forced oscillations has been investigated.

Among this latter kind of non-local models, many papers showed the advantages of micropolar models (e.g., formulated in Nowacki, 1970; Stojanović, 1972; Eringen, 1999, and widely investigated also from the experimental point of view Lakes and Benedict, 1982; Yang and Lakes, 1982; Lakes, 1983, 1986; Bauer et al., 2012; Rueger and Lakes, 2016) for investigating problems with general heterogeneities and/or discontinuities within the context of multiscale/coarse-graining approaches, which allow to preserve memory of the original organization of materials with periodic or random microstructure (Forest and Sab, 1998; Forest et al., 1999; Stefanou et al., 2008; Trovalusci et al., 2015, 2017). Moreover, special attention to the micropolar continua with constrained rotations (Toupin, 1962; Sokolowski, 1972), always referring to multiscale descriptions (Bouyge et al., 2001; Leonetti et al., 2018) has been reserved. In particular, the micropolar modeling has been effectively adopted for solving problems wherein the solid is made of an assembly of rigid particles undergoing displacements and rotations and interacting with each other via forces and couples, as masonry-like materials or fiber-reinforced composites, both in the linear and non-linear frameworks (Masiani and Trovalusci, 1996; Trovalusci and Masiani, 1999; Sansalone et al., 2006; Pau and Trovalusci, 2012; Trovalusci and Pau, 2014).

In the present work, we want to focus on the behavior of anisotropic composite assemblies, that can be polycrystals with grain boundaries or thin interfaces as well as brick/block masonry, and in particular on material parameters with different degrees of anisotropy. To this regard, it is worth noting that the micropolar continuum, differently from the couple-stress continuum, that is a micropolar continuum with constrained rotations (Sokolowski, 1972; Masiani and Trovalusci, 1996 Appendix), and also from second gradient continuum (Bacigalupo and Gambarotta, 2011; Trovalusci and Pau, 2014), presents the peculiar strain measure of the relative rotation between the local rigid rotation (macrorotation) and the microrotation that is related to the skew symmetric part of strain and then, in terms of work expended, to the skew symmetric part of the stress, whose contribution has significant role in anisotropic media (Pau and Trovalusci, 2012; Trovalusci and Pau, 2014). It is worth noting that, the different behavior between micropolar without and with constrained rotations media, for which the relative rotation is null, is also of interest for investigating the loss of ellipticity of problems leading to strain localization phenomena (Bigoni and Gourgiotis, 2016; Gourgiotis and Bigoni, 2016). Such effects are expected to be governed by both material size (de Borst, 1991; Sluys et al., 1993) and also the degree of anisotropy.

In a recent work (Leonetti et al., 2019), by adopting the coarse-graining procedure presented in Masiani and Trovalusci (1996); Trovalusci and Masiani (1999), the behavior of orthotropic brick/block masonry panels under compressive loads at the top, described as equivalent micropolar continua, has been investigated by varying the brick size and the load footprint, showing the capability of the micropolar model to distribute the load depending on the brick size. In the present work, the effect of the degree of anisotropy of the (coarse) continuum micropolar model on the strain/stress diffusion is studied. The same coarse-graining procedure is used which can be shown to be actually dependent both on the brick size, shape and texture of the original (fine) lattice model. The simulations have been carried out for a panel under localized loads, using a standard finite element approach based on a micropolar finite element implementation, with quadratic and linear interpolation functions for the displacement and rotation fields, developed in Fantuzzi et al. (2018) following the approach in Providas and Kattis (2002) and implemented within Comsol Multiphysics© framework (Comsol, 2017). The results are presented in terms of contour plots of displacement, stress and relative rotation, the significant strain measure related to the non-symmetrical part of the strain.

The present work is structured as follows. After the introductory section, the mechanics of anisotropic micropolar continua is illustrated with particular emphasis on anisotropic composite assemblies in section Mechanics of Anisotropic Micropolar Continuum. Section Finite Element Formulation is dedicated to the finite element implementation. Section Numerical Simulations presents the numerical applications and discussions about the novel results presented in this work. Finally some conclusions and remarks are given.

MECHANICS OF ANISOTROPIC MICROPOLAR CONTINUUM

The micropolar continuum is a well-known model equipped by theoretical, numerical, and experimental studies in the literature (Nowacki, 1970; Stojanović, 1972; Lakes and Benedict, 1982; Yang and Lakes, 1982; Lakes, 1983, 1986; Bauer et al., 2012; Rueger and Lakes, 2016). This continuum is made of particles which can undergo independent displacements and rotations and belongs to a class of generalized continua of the so-called implicit non-local type (Eringen, 1999; Trovalusci, 2014). Reducing the description to two-dimensional (2D) media, each material particle in the 2D frame has 3 degrees of freedom: the (macro) displacements components, u_1, u_2 , and rotation, ϕ (micro-rotation). The local linearized kinematic compatibility relations take the form:

$$\begin{aligned} \varepsilon_{11} &= u_{1,1}, \quad \varepsilon_{22} = u_{2,2}, \quad \varepsilon_{12} = u_{1,2} + \phi, \\ \varepsilon_{21} &= u_{2,1} - \phi, \chi_{31} = \phi_{,1}, \quad \chi_{32} = \phi_{,2}, \end{aligned} \tag{1}$$

where ε_{ij} $(i, j = 1, 2)$ indicate the components of the strain tensor, while χ_{31}, χ_{32} indicate the only independent components of the curvature tensor. The term $\theta = (u_{2,1} - u_{1,2})/2$ is the local rigid rotation (macro-rotation) in such a way that:

$$\varepsilon_{12} = u_{1,2} - \theta + \phi, \quad \varepsilon_{21} = u_{2,1} + \theta - \phi \tag{2}$$

Interaction among particles is described by stresses and micro-couples as:

$$t_i = \sigma_{ij} n_j, \; m_3 = \mu_{3j} n_j. \tag{3}$$

where σ_{ij} and μ_{ij} $(i, j = 1, 2)$ are the components of the non-symmetric stress and couple-stress tensors, respectively, n_j being the components of the outward normal to the continuum boundary. Equilibrium equations can be carried out, in the case of body micro-couple neglected, as:

$$\sigma_{ij,j} + b_i = 0, \; \mu_{3j,j} - e_{ij3}\sigma_{ij} = 0, \tag{4}$$

b_i being the components of the body force.

Linearly anisotropic stress-strain relations of the micropolar two-dimensional continuum assume the following matrix form:

$$\begin{bmatrix} \sigma_{11} \\ \sigma_{22} \\ \sigma_{12} \\ \sigma_{21} \\ \mu_{31} \\ \mu_{32} \end{bmatrix} = \begin{bmatrix} A_{1111} & A_{1122} & A_{1112} & A_{1121} & B_{111} & B_{112} \\ A_{2211} & A_{2222} & A_{2212} & A_{2221} & B_{221} & B_{222} \\ A_{1211} & A_{1222} & A_{1212} & A_{1221} & B_{121} & B_{122} \\ A_{2111} & A_{2122} & A_{2112} & A_{2121} & B_{211} & B_{212} \\ B_{111} & B_{122} & B_{112} & B_{121} & D_{11} & D_{12} \\ B_{211} & B_{222} & B_{212} & B_{221} & D_{21} & D_{22} \end{bmatrix} \begin{bmatrix} \varepsilon_{11} \\ \varepsilon_{22} \\ \varepsilon_{12} \\ \varepsilon_{21} \\ \chi_{31} \\ \chi_{32} \end{bmatrix}. \tag{5}$$

By considering hyperelastic materials, the following major symmetries hold: $A_{ijhk} = A_{hkij}$, $B_{ijh} = B_{hij}$, $D_{ij} = D_{ji}$ $(i, j, h, k = 1, 2)$.

FINITE ELEMENT FORMULATION

The two-dimensional problem of micropolar continua is solved through the finite element implementation proposed in Leonetti et al. (2019), where displacement/rotation components are ordered in the vectors $\boldsymbol{u} = \begin{bmatrix} u_1 & u_2 \end{bmatrix}^T$, $\boldsymbol{\phi} = [\phi]$, and the stress and strain components in the vectors $\boldsymbol{\sigma} = \begin{bmatrix} \sigma_{11} & \sigma_{22} & \sigma_{12} & \sigma_{21} \end{bmatrix}^T$, $\boldsymbol{\mu} = \begin{bmatrix} \mu_{31} & \mu_{32} \end{bmatrix}^T$, $\boldsymbol{\varepsilon} = \begin{bmatrix} \varepsilon_{11} & \varepsilon_{22} & \varepsilon_{12} & \varepsilon_{21} \end{bmatrix}^T$, $\boldsymbol{\chi} = \begin{bmatrix} \chi_{31} & \chi_{32} \end{bmatrix}^T$.

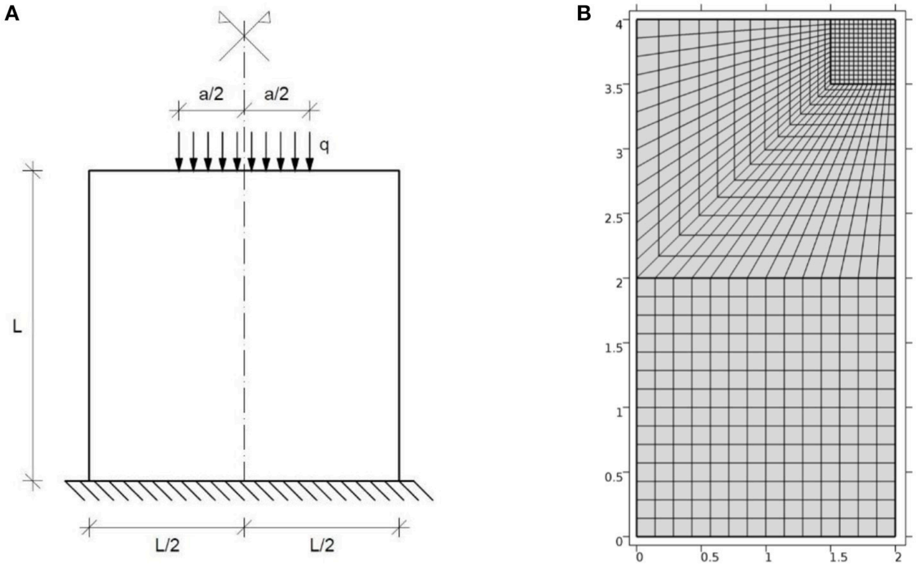

FIGURE 1 | (A) Sketch of the present problem with **(B)** present finite element mesh.

The weak form of the present problem has to be formulated in order to carry out the finite element implementation, and, considering a domain Ω with boundary Γ_N, writes:

$$\int_{\Omega} \delta\boldsymbol{\varepsilon}^T \boldsymbol{\sigma}\, dA + \int_{\Omega} \delta\boldsymbol{\chi}^T \boldsymbol{\mu}\, dA = \int_{\Omega} \delta\boldsymbol{u}^T \mathbf{b}\, dA + \int_{\Gamma_N} \delta\boldsymbol{u}^T \bar{\boldsymbol{t}}\, dl + \int_{\Gamma_N} \delta\boldsymbol{\phi}^T \overline{\boldsymbol{m}}\, dl \quad \forall \delta\boldsymbol{u}, \delta\boldsymbol{\phi}, \tag{6}$$

with δ denoting the variation operator, $\boldsymbol{b}$ the body force vector, $\bar{\boldsymbol{t}}$ and $\bar{\boldsymbol{m}}$ the traction and couple-traction vectors applied on the boundary $\boldsymbol{\Gamma}_N$. Note that, the curvature vector $\boldsymbol{\chi}$ is due to the first-order partial derivatives of the micro-rotation, thus C^0 finite elements are adopted.

Finite element approximation though interpolation functions $\boldsymbol{N}_u$ and $\boldsymbol{N}_\phi$ is given by $\boldsymbol{u} = \boldsymbol{N}_u \tilde{\boldsymbol{u}}, \boldsymbol{\phi} = \boldsymbol{N}_\phi \tilde{\boldsymbol{\phi}}$, where the over tilde vectors indicate the kinematic parameters correspondent to in-plane displacements and rotations at the nodes. Quadratic interpolation functions for the displacements and linear ones for the rotations have been assumed, as it was introduced in Leonetti et al. (2019). Thus, displacements are modeled with nine nodes, whereas micro-rotation are related to the four corner nodes. Interpolation function vectors are given in matrix form as:

$$\boldsymbol{N}_u = \begin{bmatrix} N_1^u & 0 & \cdots & N_9^u & 0 \\ 0 & N_1^u & \cdots & 0 & N_9^u \end{bmatrix}, \quad \boldsymbol{N}_\phi = \begin{bmatrix} N_1^\phi & \cdots & N_4^\phi \end{bmatrix}, \tag{7}$$

Thus, the micropolar strains given by Equation (1) can be written as:

$$\boldsymbol{\varepsilon} = \boldsymbol{L}\boldsymbol{u} + \boldsymbol{M}\boldsymbol{\phi}, \ \boldsymbol{\chi} = \nabla\boldsymbol{\phi}, \tag{8}$$

where the matrix operators $\boldsymbol{L}$ and $\boldsymbol{M}$ are defined as:

$$\boldsymbol{L} = \begin{bmatrix} \frac{\partial}{\partial x_1} & 0 & \frac{\partial}{\partial x_2} & 0 \\ 0 & \frac{\partial}{\partial x_2} & 0 & \frac{\partial}{\partial x_1} \end{bmatrix}^T, \quad \boldsymbol{M} = \begin{bmatrix} 0 & 0 & 1 & -1 \end{bmatrix}^T. \tag{9}$$

Then Equation (8) becomes:

$$\begin{aligned} \boldsymbol{\varepsilon} &= \boldsymbol{L}\boldsymbol{N}_u \tilde{\boldsymbol{u}} + \boldsymbol{M}\boldsymbol{N}_\phi \tilde{\boldsymbol{\phi}} = \begin{bmatrix} \boldsymbol{L}\boldsymbol{N}_u & \boldsymbol{M}\boldsymbol{N}_\phi \end{bmatrix} \begin{Bmatrix} \tilde{\boldsymbol{u}} \\ \tilde{\boldsymbol{\phi}} \end{Bmatrix} = \boldsymbol{B}_\varepsilon \boldsymbol{d}, \ \boldsymbol{\chi} = \nabla\left(\boldsymbol{N}_\phi \tilde{\boldsymbol{\phi}}\right) \\ &= \begin{bmatrix} \boldsymbol{0} & \nabla\boldsymbol{N}_\phi \end{bmatrix} \begin{Bmatrix} \tilde{\boldsymbol{u}} \\ \tilde{\boldsymbol{\phi}} \end{Bmatrix} = \boldsymbol{B}_\chi \boldsymbol{d}, \end{aligned} \tag{10}$$

Where $\boldsymbol{d}$ indicates the unknown vector of nodal displacements. The matrices $\boldsymbol{B}_\varepsilon$ and $\boldsymbol{B}_\chi$ collect the derivatives of the interpolation functions matrices $\boldsymbol{N}_u$ and $\boldsymbol{N}_\phi$. Therefore, the constitutive relations (5) become:

$$\boldsymbol{\sigma} = \boldsymbol{D}_{\varepsilon\varepsilon}\boldsymbol{B}_\varepsilon \boldsymbol{d} + \boldsymbol{D}_{\varepsilon\chi}\boldsymbol{B}_\chi \boldsymbol{d}, \ \boldsymbol{\mu} = \boldsymbol{D}_{\varepsilon\chi}^T \boldsymbol{B}_\varepsilon \boldsymbol{d} + \boldsymbol{D}_{\chi\chi}\boldsymbol{B}_\chi \boldsymbol{d}, \tag{11}$$

where:

$$\begin{aligned} \boldsymbol{D}_{\varepsilon\varepsilon} &= \begin{bmatrix} A_{1111} & A_{1122} & A_{1112} & A_{1121} \\ A_{2211} & A_{2222} & A_{2212} & A_{2221} \\ A_{1211} & A_{1222} & A_{1212} & A_{1221} \\ A_{2111} & A_{2122} & A_{2112} & A_{2121} \end{bmatrix}, \\ \boldsymbol{D}_{\varepsilon\chi} &= \begin{bmatrix} B_{111} & B_{112} \\ B_{221} & B_{222} \\ B_{121} & B_{122} \\ B_{211} & B_{212} \end{bmatrix}, \ \boldsymbol{D}_{\chi\chi} = \begin{bmatrix} D_{11} & D_{12} \\ D_{21} & D_{22} \end{bmatrix}. \end{aligned} \tag{12}$$

Note that coupling between classical and micro-polar effects are considered by matrix $\boldsymbol{D}_{\varepsilon\chi}$. Finally, the algebraic finite element problem (without body forces) reads:

$$\begin{aligned} \delta\boldsymbol{d}^T & \underbrace{\int_{\Omega} \left(\boldsymbol{B}_\varepsilon^T \boldsymbol{D}_{\varepsilon\varepsilon}\boldsymbol{B}_\varepsilon + \boldsymbol{B}_\varepsilon^T \boldsymbol{D}_{\varepsilon\chi}\boldsymbol{B}_\chi + \boldsymbol{B}_\chi^T \boldsymbol{D}_{\varepsilon\chi}^T \boldsymbol{B}_\varepsilon + \boldsymbol{B}_\chi^T \boldsymbol{D}_{\chi\chi}\boldsymbol{B}_\chi\right) dA}_{\boldsymbol{K}} \ \boldsymbol{d} \\ &= \delta\boldsymbol{d}^T \underbrace{\int_{\boldsymbol{\Gamma_N}} \begin{bmatrix} \boldsymbol{N}_u^T \bar{\boldsymbol{t}} \\ \boldsymbol{N}_\phi^T \bar{\boldsymbol{m}} \end{bmatrix} dl}_{\boldsymbol{F}} \ \forall \delta\boldsymbol{d}, \end{aligned} \tag{13}$$

TABLE 1 | Constant mechanical properties used in all computations.

A_{1111}	$3.75 \cdot 10^4$MPa
A_{2222}	$1.5 \cdot 10^4$MPa
A_{1212}	$0.75 \cdot 10^4$MPa
A_{2121}	$3 \cdot 10^4$MPa
D_{11}	$1.125 \cdot$ MN
D_{22}	$0.375 \cdot$ MN

TABLE 2 | Mechanical properties used in *Configuration 1*.

	Material#1	Material#2	Material#3	Material#4
A_{1121}	10^4MPa	$1.5 \cdot 10^4$MPa	$2 \cdot 10^4$MPa	$2.5 \cdot 10^4$MPa
A_{2212}	$0.25 \cdot 10^4$MPa	$0.375 \cdot 10^4$MPa	$0.5 \cdot 10^4$MPa	$0.625 \cdot 10^4$MPa

TABLE 3 | Mechanical properties used in *Configuration 2*.

	Material#1	Material#2	Material#3	Material#4
A_{1122}	0 MPa	$0.5 \cdot 10^4$MPa	10^4MPa	$1.5 \cdot 10^4$MPa
D_{12}	0 MN	0.5 MN	1 MN	1.5 MN

TABLE 4 | Mechanical properties used in *Configuration 3*.

	Material#1	Material#2	Material#3	Material#4
A_{1112}	$0.25 \cdot 10^4$MPa	$0.30 \cdot 10^4$MPa	$0.35 \cdot 10^4$MPa	$0.40 \cdot 10^4$MPa
A_{2221}	10^4MPa	$1.2 \cdot 10^4$MPa	$1.4 \cdot 10^4$MPa	$1.6 \cdot 10^4$MPa

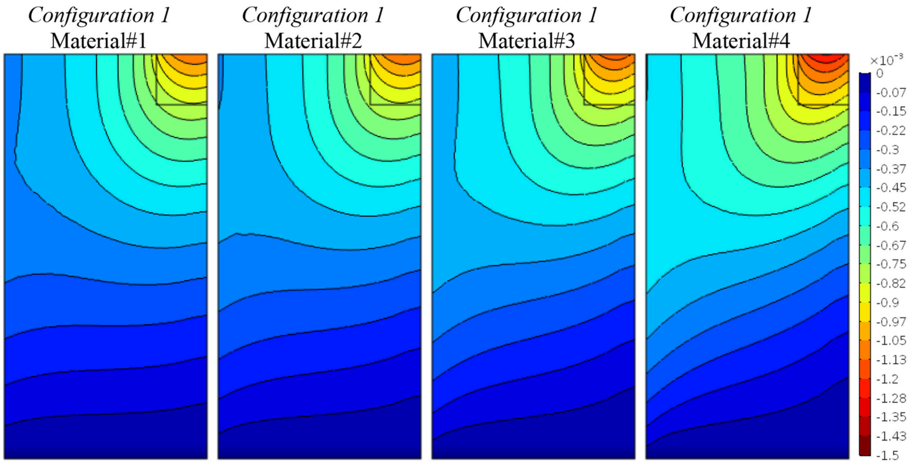

FIGURE 2 | Configuration 1, vertical displacement component, u_2, contour plots for four material cases (Material#1/Material#4 minimum/maximum anisotropy degree).

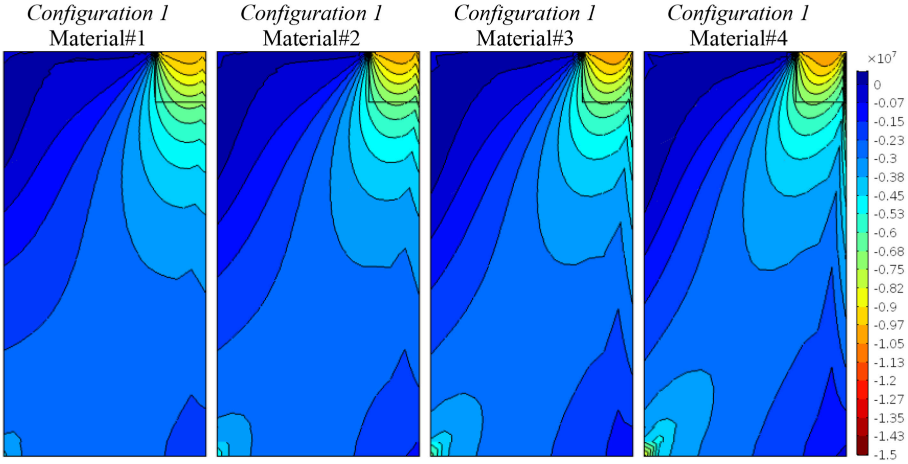

FIGURE 3 | Configuration 1, vertical stress component, σ_{22}, contour plots for four material cases (Material#1/Material#4 minimum/maximum anisotropy degree).

where $\boldsymbol{K}$ and $\boldsymbol{F}$ indicate the stiffness matrix and the nodal force vector of the adopted finite element for describing 2D linearly elastic anisotropic micropolar bodies. A classical Gauss-Legendre integration is considered for computing the integral terms appearing in Equation (13).

The present model has been implemented within the framework of Comsol Multiphysics® software (Comsol, 2017).

NUMERICAL SIMULATIONS

The present study aims at investigating the mechanical behavior of two-dimensional anisotropic micropolar media under localized loads by varying the degree of anisotropy, through the change in the material properties identified using the coarse-graining procedure described in Masiani and Trovalusci (1996), Trovalusci and Masiani (1999), considering at the (fine) micro-level anisotropic brick/block assemblies of different textures and related aspect and ratios, and at the macroscopic (coarse) level an energy equivalent micropolar continua.

It has been widely shown that homogenized micropolar models prove to be suitable of retaining memory of the behavior of the actual composite microstructure in the presence of high gradients of deformation, that occur even in the elastic range when load or geometrical singularities are present (Masiani and Trovalusci, 1996; Trovalusci and Masiani, 1999; Sansalone et al., 2006). In particular, due to the presence of the relative strain measure, it has been shown that micropolar continua perform better than classic and other generalized continua when non-symmetric shear effects have to be accounted for, as in the case of strongly orthotropic media (Pau and Trovalusci, 2012; Trovalusci and Pau, 2014).

The role of scale effects in orthotropic media under the action of a load applied on portions of variable size of the boundary of the body and the consequences in terms of strain

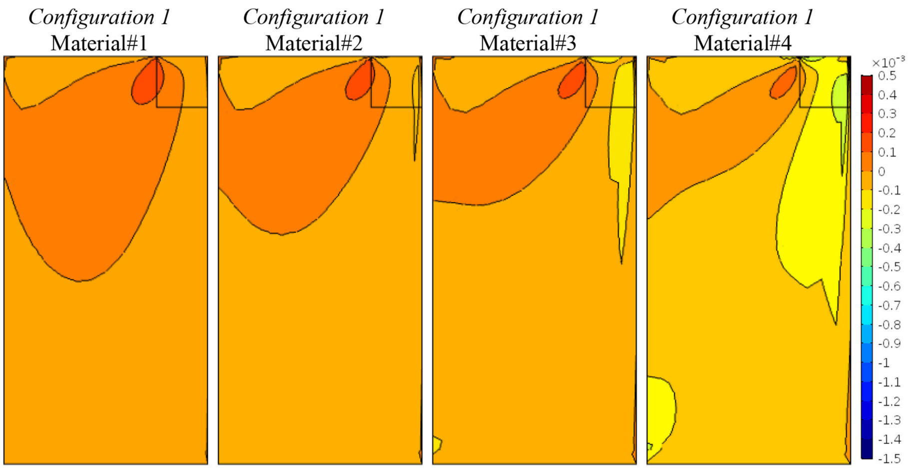

FIGURE 4 | Configuration 1, relative rotations, $\theta - \phi$, contour plots for four material cases (Material#1/Material#4 minimum/maximum anisotropy degree).

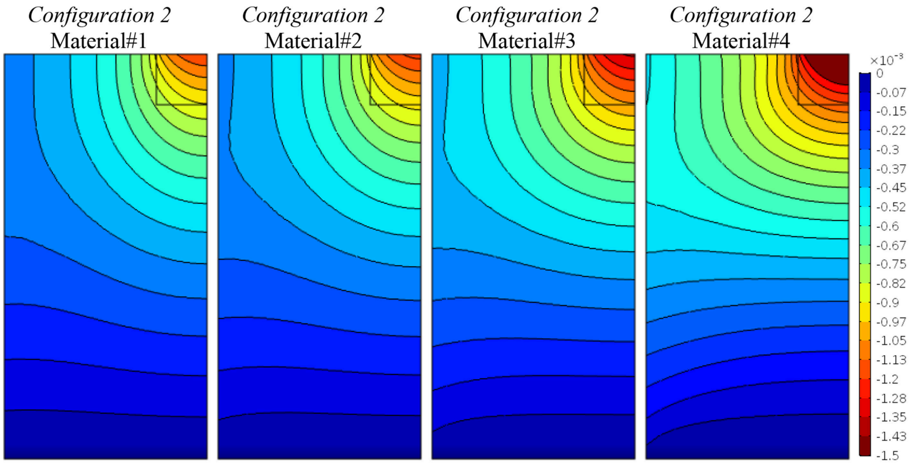

FIGURE 5 | Configuration 2, vertical displacement component, u_2, contour plots for four material cases (Material#1/Material#4 minimum/maximum anisotropy degree).

and stress diffusion have been highlighted by the parametric analyses performed in the recent work (Leonetti et al., 2019). The present work, does not accounts for size effects but focuses on the response of anisotropic micropolar media, under localized loads, in the presence of an increasing degree of anisotropy. The strain/stress diffusion has been numerically investigated according to the constitutive relations considered, that couple the effect of normal and shear stress/strain, as well as couple stress and curvature in orthogonal direction. This study highlights aspects that, in the Authors' knowledge, have not been previously investigated in materials with anisotropies. These aspects can be also interesting in the perspective of dealing with significant problems of loss of ellipticity followed by strain localization phenomena, with folding and/or fracture for instance, that affect both classical and constrained micropolar materials (Sluys et al., 1993; Nguyen et al., 2012; Bigoni and Gourgiotis, 2016; Gourgiotis and Bigoni, 2016).

The problem numerically investigated is a square domain of width $L = 4\,\mathrm{m}$, only fixed at the bottom edge and subjected to a top load acting on length size $a/L = 0.25$ (**Figure 1A**) and pressure $q = 10\,\mathrm{MPa}$. Due to the symmetry of the problem only half of the domain has been analyzed and the correspondent finite element mesh is depicted in **Figure 1B**. Parametric analyses have been performed by increasing the coefficients representing material anisotropy according to the following three different configurations that have been selected in order to investigate separately the role of different cases of anisotropy.

Table 1 reports the independent material coefficients that are considered constant in the simulations. The other coefficients increase according to a constant parameter allowing to represent four different degrees of anisotropy from a minimum (defined as Material #1) to a maximum (Material #4) value.

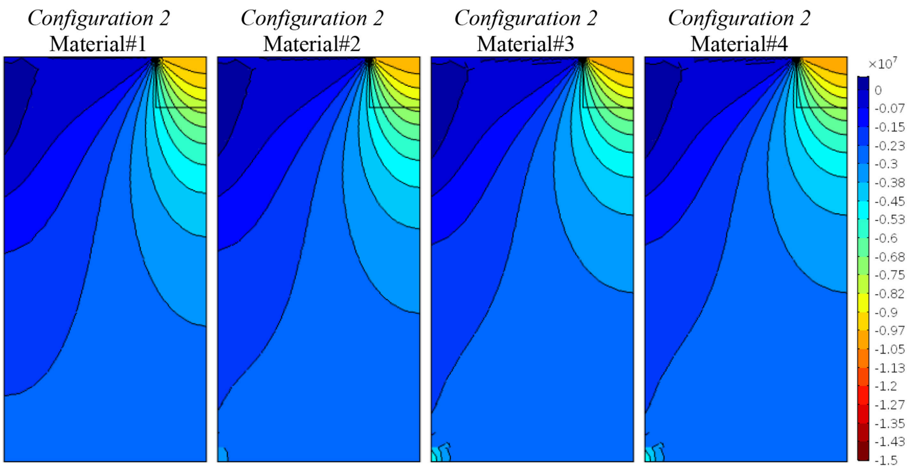

FIGURE 6 | Configuration 2, vertical stress component, σ_{22}, contour plots for four material cases (Material#1/Material#4 minimum/maximum anisotropy degree).

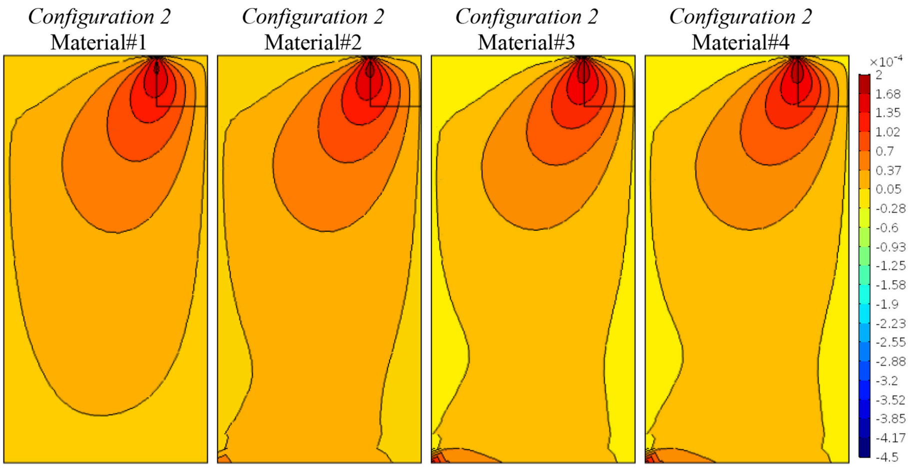

FIGURE 7 | Configuration 2, relative rotations, $\theta - \phi$, contour plots for four material cases (Material#1/Material#4 minimum/maximum anisotropy degree).

Configuration 1:

$$\begin{bmatrix} \sigma_{11} \\ \sigma_{22} \\ \sigma_{12} \\ \sigma_{21} \\ \mu_{31} \\ \mu_{32} \end{bmatrix} = \begin{bmatrix} A_{1111} & & & \boldsymbol{A}_{1121} & & \\ & A_{2222} & \boldsymbol{A}_{2212} & & & \\ & \boldsymbol{A}_{1222} & A_{1212} & & & \\ \boldsymbol{A}_{2111} & & & A_{2121} & & \\ & & & & D_{11} & \\ & & & & & D_{22} \end{bmatrix} \begin{bmatrix} \varepsilon_{11} \\ \varepsilon_{22} \\ \varepsilon_{12} \\ \varepsilon_{21} \\ \chi_{31} \\ \chi_{32} \end{bmatrix}, \quad (14)$$

accounts for the increment of the constitutive elastic coefficients (reported in bold in Equation (14)) coupling the normal stresses σ_{11}, σ_{22} with the non-symmetric shear strains ε_{21}, ε_{12}, respectively, and the non-symmetric shear stresses σ_{12}, σ_{21} with the normal strains ε_{22}, ε_{11}, respectively: $A_{1121} = A_{2111}$ and $A_{2212} = A_{1222}$. The implemented values are listed in **Table 2** and their values for the four materials configurations considered (ranging from Material#1, with the lower degree of anisotropy, up to Matrerial#4 with the higher degree of anisotrpoy) are obtained by considering the increase through a parameter corresponding to $(A_{1212} - A_{2212})/4$ and $(A_{2121} - A_{1121})/4$, respectively. This choice is arbitrary, but it allows us to define an increasing degree of material anisotropy obtaining plausible results, as the elastic constants on the main diagonal are generally predominant with respect to the out-of-diagonal terms, suitable to highlight the effects of interest.

Configuration 2:

$$\begin{bmatrix} \sigma_{11} \\ \sigma_{22} \\ \sigma_{12} \\ \sigma_{21} \\ \mu_{31} \\ \mu_{32} \end{bmatrix} = \begin{bmatrix} A_{1111} & \boldsymbol{A}_{1122} & & & & \\ \boldsymbol{A}_{2211} & A_{2222} & & & & \\ & & A_{1212} & & & \\ & & & A_{2121} & & \\ & & & & D_{11} & \boldsymbol{D}_{12} \\ & & & & \boldsymbol{D}_{21} & D_{22} \end{bmatrix} \begin{bmatrix} \varepsilon_{11} \\ \varepsilon_{22} \\ \varepsilon_{12} \\ \varepsilon_{21} \\ \chi_{31} \\ \chi_{32} \end{bmatrix}, \quad (15)$$

considers a micropolar orthotropic material, where the variable elastic coefficients (reported in bold in Equation (15)) are:

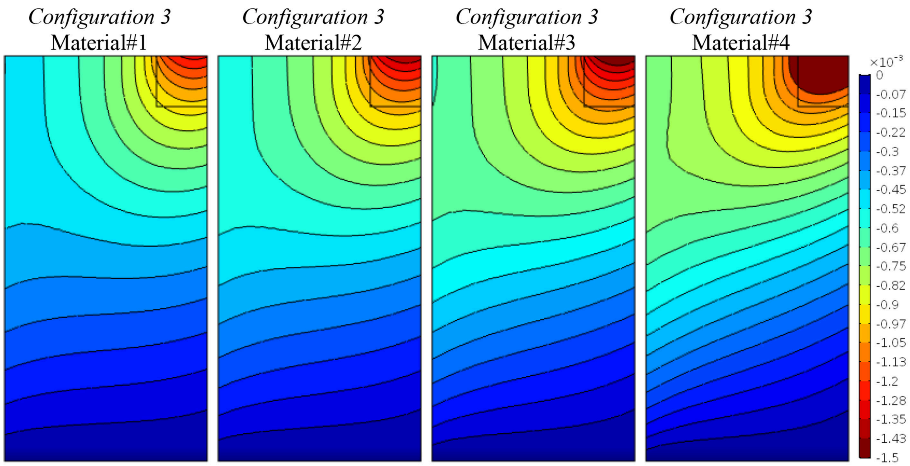

FIGURE 8 | Configuration 3, vertical displacement component, u_2, contour plots for four material cases (Material#1/Material#4 minimum/maximum anisotropy degree).

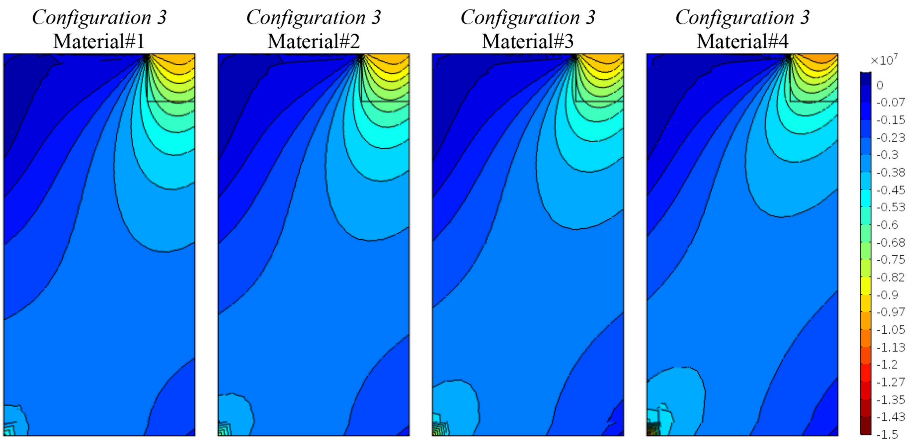

FIGURE 9 | Configuration 3, vertical stress component, σ_{22}, contour plots for four material cases (Material#1/Material#4 minimum/maximum anisotropy degree).

$A_{1122} = A_{2211}$ and $D_{12} = D_{21}$, respectively concerns the classical "Poisson effect" and a corresponding micropolar out-of-diagonal effect in the model. The values provided are listed in **Table 3**. Also in this case the increase from Material#1 (with no Poisson's effect) to Material#4 (with the higher Poisson's effect) has been put constant.

Configuration 3:

$$\begin{bmatrix} \sigma_{11} \\ \sigma_{22} \\ \sigma_{12} \\ \sigma_{21} \\ \mu_{31} \\ \mu_{32} \end{bmatrix} = \begin{bmatrix} A_{1111} & & \mathbf{A_{1112}} & & & \\ & A_{2222} & & \mathbf{A_{2221}} & & \\ \mathbf{A_{1211}} & & A_{1212} & & & \\ & \mathbf{A_{2122}} & & A_{2121} & & \\ & & & & D_{11} & \\ & & & & & D_{22} \end{bmatrix} \begin{bmatrix} \varepsilon_{11} \\ \varepsilon_{22} \\ \varepsilon_{12} \\ \varepsilon_{21} \\ \chi_{31} \\ \chi_{32} \end{bmatrix}, \quad (16)$$

takes into account the increment of the material coefficients (reported in bold in Equation (16)) that couple the normal stresses σ_{11}, σ_{22} with the correspondent non-symmetric shear strains ε_{12}, ε_{21}, respectively, and the non-symmetric shear stresses σ_{12}, σ_{21} with the normal strains ε_{11}, ε_{22}, respectively: $A_{1112} = A_{1211}$ and $A_{2221} = A_{2122}$. The implemented values are listed in **Table 4**, and their values for the four materials configurations considered are obtained by considering the increase of a parameter corresponding to $(A_{1212} - A_{1112})/10$ and $(A_{2121} - A_{2221})/10$, respectively. This arbitrary choice was due on the observed strongly coupling (normal/transversal) effects on the micropolar response. As for *Configuaration 1,* it allows us to define an increasing degree of material anisotropy obtaining results suitable to highlight the relevant effects.

Figures 2–4 represent the contour lines of the vertical component of displacement, u_2, the vertical stress component, σ_{22}, and relative rotation, $\theta - \phi$, for *Configuration 1*, in which the coupling material properties between normal stresses and the correspondent shear strains, and vice-versa, increase (Equation (14)) as above described. In terms of displacements (**Figure 1**) it can be observed that, due to the normal stress/shear strain/ coupling, the more the anisotropic degree, and the related

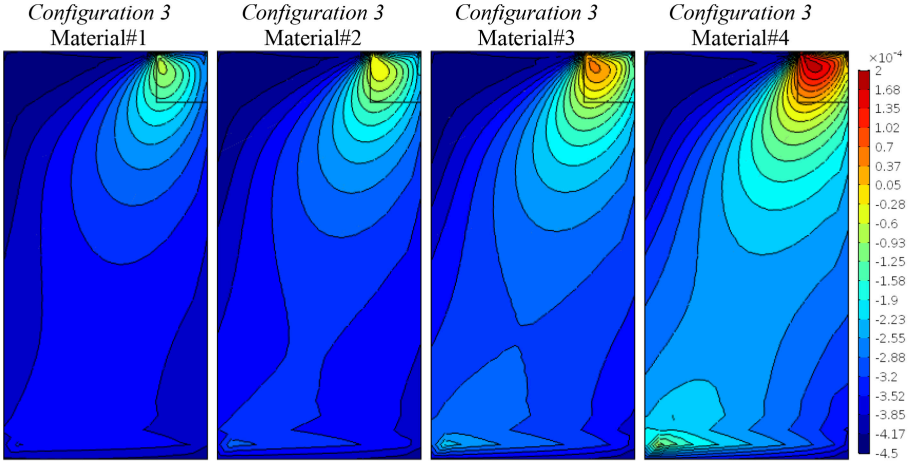

FIGURE 10 | Configuration 3, relative rotations, $\theta - \phi$, contour plots for four material cases (Material#1/Material#4 minimum/maximum anisotropy degree).

coupling, increases, from Material#1 to Material#4, the more the load distributes affecting the panel in its bottom part. Correspondingly, in terms of vertical stresses (**Figure 3**) the coupling due to anisotropy increases the stress diffusion. This effect is highlighted also by the relative rotation plot (**Figure 4**), wherein the micropolar effect of $\theta - \phi$ increases in Material#4 case due to the presence of a strongly anisotropy/coupling between normal and shear components.

Figures 5–7 show the results obtained for *Configuration 2*, characterized by the orthotropic material symmetry, which considers the classical and, in a sense, micropolar "Poisson's effect" through the terms A_{1122}, D_{12}. The first material case (Material#1) corresponds to the one with null Poisson's effect ($A_{1122} = D_{12} = 0$), whereas the others have increasing coefficients through a constant value as shown in **Table 3**. In **Figure 5** the contour lines of the vertical component of displacement field, u_2, diffuse depending on the degree of anisotropy. Analogously, for the vertical stress component, σ_{22}, in **Figure 6** we can observe the same phenomenon. In both cases the curves are more distributed in the case of higher degrees of orthotropy. **Figure 7** shows that the relative rotation, $\theta - \phi$, map does not change, as this component is not affected by the elastic coefficients involved. For pointing out the correspondences between classical and micropolar elastic moduli the reader may refer to the work [Trovalusci and Masiani (1999), section 4].

Finally, **Figures 8–10** are related to *Configuration 3,* which couples normal and shear stress/strain components as described in Equation (16). The present condition influences more the solution as it can be seen in **Figure 8**, where the vertical displacement component, u_2, changes homogeneously showing a wider diffusion related to the increasing of the degree of anisotropy. The same can be said for the vertical stress in **Figure 9**, where the reaction stresses at the bottom increases as the coupling effect increases. The most interesting representation is due to the relative rotation (**Figure 10**) where a strong boundary effect is shown. The field becomes distorted at the top (where the vertical load is applied) and at the bottom (even though an homogenous boundary condition has been applied) as the coupling mechanical properties are increased. The contour plot distortion at the bottom is due to the strong discontinuity between a clamped horizontal boundary condition and a free one on the left vertical edge.

FINAL REMARKS

This work proposes a numerical finite element solution of an anisotropic micropolar panel subjected to a concentrated pressure on a small portion of the top boundary, and the effect on the mechanical behavior of this body has been investigated for particular cases of material anisotropy. The stress diffusion under concentrated load in masonry assemblies has been widely investigated also from the experimental point of view (Bigoni and Noselli, 2010). In earlier works it has been shown that while the micropolar model is able to distribute the load depending on the element size, the classical continuum lacking in material internal lengths does not entail such effect. Moreover, the micropolar model, differently from the couple stress (micropolar with microtation constrained to be equal to the local rigid rotation) and second gradient model, presents the peculiar strain measure of relative rotation suitable to take into account the non-symmetries in strain and stress that are predominant in strongly anisotropic assemblies (Pau and Trovalusci, 2012; Trovalusci, 2014; Trovalusci and Pau, 2014).

In the present work, attention has been given to the effect of different degrees of material anisotropy, not only orthotropy, for micropolar bodies subjected to localized loads, particularly focusing on the strain measure of the relative rotation. It has been highlighted that the anisotropic elastic coefficients of the micropolar continuum, which couple normal stresses with non-symmetric shear strains and vice-versa, have the effect of distributing the load according to the degree of anisotropy of the reference material. The coefficients that relate normal stress to normal strain components in the orthogonal directions, as well as the coefficients relating the couple-stress to the curvature components in the orthogonal direction, governing the classical and, in a sense, micropolar Poisson's effect, instead, does not significantly affect the response of the micropolar continuum. All the analyzed cases showed that an increasing level of anisotropy corresponds to a significant distribution of the load in terms of stresses within the continuum.

It can be concluded that when dialing with materials made of particles assembled according to strong anisotropies it is advisable to resort to micropolar theories. As further development, we expect to investigate the ability of unconstrained anisotropic micropolar models to detect strain localization phenomena.

AUTHOR CONTRIBUTIONS

NF and PT wrote and revise the paper. SD carried out all numerical simulations.

ACKNOWLEDGMENTS

The authors acknowledge Dr. Lorenzo Leonetti, University of Calabria, for providing the Comsol® framework and for implementing the model at Section Finite Element Formulation for the present investigation.

FUNDING

This research was supported by the Italian Ministry of University and Research, P.R.I.N. 2015, Project 2015JW9NJT Advanced mechanical modeling of new materials and structures for the solution of 2020 Horizon challenges, Sapienza Research Unit (Grant B86J16002300001), and by Sapienza University, Grant 2016 (B82F16005920005).

REFERENCES

Altenbach, H., and Sadowski, T. (2015). *Failure and Damage Analysis of Advanced Materials*. Wien: Springer-Verlag.

Bacigalupo, A., and Gambarotta, L. (2011). Non-local computational homogenization of periodic masonry. *Int. J. Multiscale. Comput. Eng*. 9, 565–578. doi: 10.1615/IntJMultCompEng.2011002017

Baggio, C., and Trovalusci, P (2000). Collapse behaviour of three-dimensional brick-block systems using non linear programming. *Struct. Eng. Mech*. 10, 181–195. doi: 10.12989/sem.2000.10.2.181

Baraldi, D., Reccia, E., and Cecchi, A. (2018). In plane loaded masonry walls: DEM and FEM/DEM models. a critical review. *Meccanica* 53, 1613–1628. doi: 10.1007/s11012-017-0704-3

Bauer, S., Dettmer, W. G., Perić, D., and Schäfer, M. (2012). Micropolar hyperelasticity: constitutive model, consistent linearization and simulation of 3D scale effects. *Comput. Mech*. 50, 383–396. doi: 10.1007/s00466-012-0679-9

Bigoni, D., Gourgiotis, P. A. (2016). Folding and faulting of an elastic continuum. *Proc. Royal Soc. A*. 472:20160018.

Bigoni, D., and Noselli, G. (2010). Localize stress percolation through dry masonry walls. Part I – Experiments. *Eur. J. Mech A/Solids*. 29, 291–298. doi: 10.1016/j.euromechsol.2009.10.009

Blanc, C., Le Bris, C., and Lions, P. L. (2002). From molecular models to continuum mechanics. *Arch. Rat. Mech. Anal*. 164, 341–381. doi: 10.1007/s00205-002-0218-5

Bouyge, F., Jasiuk, I., and Ostoja-Starzewski, M. (2001). Micromechanically based couple-stress model of an elastic two-phase composite. *Int. J. Solids Struct*. 38, 1721–1735. doi: 10.1016/S0020-7683(00)00132-3

Budiansky, B. (1965). On the elastic moduli of some heterogeneous materials. *J. Mech. Phys. Solids* 13, 223–227.

Capecchi, D., Ruta, G., and Trovalusci, P. (2011). Voigt and Poincaré's mechanistic–energetic approaches to linear elasticity and suggestions for multiscale modelling. *Arch. Appl. Mech*. 81, 1573–1584. doi: 10.1007/s00419-010-0502-z

Capriz, G. (1989). *Continua with Microstructure*. Berlin: Springer-Verlag. doi: 10.1007/978-1-4612-3584-2

Comsol, A. B. (2017). *Comsol Multiphysics Physics Builder Manual*. Stockholm: Comsol.

Curtin, W. A., and Miller, R. E. (2003). Atomistic/continuum coupling in computational materials science. *Model. Simul. Mater. Sci. Eng*. 11, R33–R68. doi: 10.1088/0965-0393/11/3/201

de Borst, R. (1991). Simulation of strain localization: a reappraisal of the Cosserat continuum. *Eng. Comput*. 8, 317–332. doi: 10.1108/eb023842

Eringen, A. C. (1972). Linear theory of nonlocal elasticity and dispersion of plane waves. Int. *J. Eng. Sci*. 10, 425–435. doi: 10.1016/0020-7225(72)90050-X

Eringen, A. C. (1999). *Microcontinuum Field Theories*. New York, NY: Springer-Verlag. doi: 10.1007/978-1-4612-0555-5

Fantuzzi, N., Leonetti, L., Trovalusci, P., and Tornabene, F. (2018). Some novel numerical applications of Cosserat continua. *Int. J. Comput. Meth*. 15:1850054. doi: 10.1142/S0219876218500548

Forest, S. (2009). Micromorphic approach for gradient elasticity, viscoplasticity, and damage. *J. Eng. Mech*. 135, 117–131. doi: 10.1061/(ASCE)0733-9399(2009)135:3(117)

Forest, S., Dendievel, R., and Canova, G. R. (1999). Estimating the overall properties of heterogeneous Cosserat materials. *Model. Simul. Mater. Sci. Eng*. 7, 829–840. doi: 10.1088/0965-0393/7/5/314

Forest, S., and Sab, K. (1998). Cosserat overall modeling of heterogeneous materials. *Mech. Res. Commun*. 25, 449–454. doi: 10.1016/S0093-6413(98)00059-7

Forest, S., and Trinh, D. K. (2011). Generalised continua and the mechanics of heterogeneous material. *Zeitschrift für Angewandte Mathematik und Mechanik* 91, 90–109. doi: 10.1002/zamm.201000109

Godio, M., Stefanou, I., Sab, K., Sulem, J., and Sakji, S. (2017). A limit analysis approach based on Cosserat continuum for the evaluation of the in-plane strength of discrete media: application to masonry. *Eur. J. Mech. A Solids*. 66, 168–192. doi: 10.1016/j.euromechsol.2017.06.011

Gourgiotis, P. A., Bigoni, D. (2016). Stress channelling in extreme couple-stress materials Part I: Strong ellipticity, wave propagation, ellipticity, and discontinuity relations. *J. Mech. Phys. Solids*. 88, 150–168. doi: 10.1016/j.jmps.2015.09.006

Greco, F., Leonetti, L., Luciano, R., and Nevone Blasi, P. (2016). Effects of microfracture and contact induced instabilities on the macroscopic response of finitely deformed elastic composites. *Compos. Part B. Eng*. 107, 233–253. doi: 10.1016/j.compositesb.2016.09.042

Gurtin, M. E. (2000). *Configurational Forces as Basis Concept of Continuum Physics*. Berlin: Springer-Verlag.

Jain, J. R., and Ghosh, S. (2009). Damage evolution in composites with a homogenization-based continuum damage mechanics model. *Int. J. Damage Mech*. 18, 533–568. doi: 10.1177/1056789508091563

Kunin, I. A. (1982). *Elastic Media with Microstructure, I-II*. Berlin: Springer-Verlag.

Lakes, R. S. (1983). Size effect and micromechanics of a porous solid. *J. Mat. Sci*. 18, 2572–2580.

Lakes, R. S. (1986). Experimental microelasticity of two porous solids. *Int. J. Solids. Struct*. 22, 55–63. doi: 10.1016/0020-7683(86)90103-4

Lakes, R. S., and Benedict, R. L. (1982). Noncentrosymmetry in micropolar elasticity. *Int. J. Eng. Sci*. 20, 1161–1167. doi: 10.1016/0020-7225(82)90096-9

Leonetti, L., Fantuzzi, N., Trovalusci, P., and Tornabene, F. (2019). Scale effects in orthotropic composite assemblies as micropolar continua: a comparison between weak and strong-form finite element solutions. *Materials* 12:758. doi: 10.3390/ma12050758

Leonetti, L., Greco, F., Trovalusci, P., Luciano, R., and Masiani, R. (2018). A multiscale damage analysis of periodic composites using a couple-stress/Cauchy multidomain model: application to masonry structures. *Compos. Part B. Eng*. 141, 50–59. doi: 10.1016/j.compositesb.2017.12.025

Masiani, R., and Trovalusci, P. (1996). Cosserat and cauchy materials as continuum models of brick masonry. *Meccanica* 31, 421–432. doi: 10.1007/BF00429930

Maugin, G. (1993). *Material Inhomogeneities in Elasticity*. London: Chapman and Hall. doi: 10.1007/978-1-4899-4481-8

Mindlin, R. D. (1964). Micro-structure in linear elasticity. *Arch. Ration Mech. Anal*. 16, 51–78. doi: 10.1007/BF00248490

Nemat-Nasser, S., Hori, M., and Datta, S. K. (1996). Micromechanics: overall properties of heterogeneous materials. *J. Appl. Mech*. 63:561. doi: 10.1115/1.2788912

Nguyen, V. P., Lloberas-Valls, O., Stroeven, M., and Sluys, LJ. (2012). Computational homogenization for multiscale crack modelling, Implementational and computational aspects. *Int. J. Numer. Meth. Engng*. 89, 192–226. doi: 10.1002/nme.3237

Nowacki, W. (1970). *Theory of Micropolar Elasticity*. Udine: Springer-Verlag. doi: 10.1007/978-3-7091-2720-9

Pau, A., and Trovalusci, P. (2012). Block masonry as equivalent micropolar continua: the role of relative rotations. *Acta Mech*. 223, 1455–1471. doi: 10.1007/s00707-012-0662-8

Providas, E., and Kattis, M. A. (2002). Finite element method in plane Cosserat elasticity. *Comput. Struct*. 80, 2059–2069. doi: 10.1016/S0045-7949(02)00262-6

Rapaport, D. C., and Rapaport, D. C. R. (2004). *The Art of Molecular Dynamics Simulation*. Cambridge, UK: Cambridge University Press.

Reccia, E., Leonetti, L., Trovalusci, P., and Cecchi, A (2018). A multiscale/multidomain model for the failure analysis of masonry walls: a validation with a combined FEM/DEM approach. *Int. J. Mult. Comp. Eng*. 16, 325–343. doi: 10.1615/IntJMultCompEng.2018026988

Rueger, Z., and Lakes, R. S. (2016). Cosserat elasticity of negative Poisson's ratio foam: experiment. *Smart Mater. Struct*. 25:054004. doi: 10.1088/0964-1726/25/5/054004

Sadowski, T., Trovalusci, P., Schrefler, B., de Borst, R. (2014). Multi-scale and multi-physics modelling for complex materials. *Meccanica* 49, 2549–2550. doi: 10.1007/s11012-014-0040-9

Sanchez-Palencia, E, and Zaoui, A. (1987). *Homogenization Techniques For Composite Media*. Lecture Notes In Physics. Springer.

Sansalone, V., Trovalusci, P., and Cleri, F. (2006). Multiscale modelling of materials by a multifield approach: microscopic stress and strain distribution in fiber-matrix composites. *Acta Mater*. 54, 3485–3492. doi: 10.1016/j.actamat.2006.03.041

Sluys, L. J., de Borst, R., and Mühlhaus, H. B. (1993). Wave propagation, localization and dispersion in a gradient-dependent medium. *Int. J. Solid. Struct*. 30, 1153–1171. doi: 10.1016/0020-7683(93)90010-5

Sokolowski, M (1972). *Theory of Couple-stresses in Bodies with Constrained Rotations*, Udine: Springer-Verlag.

Stefanou, I., Sulem, J., and Vardoulakis, I. (2008). Three-dimensional cosserat homogenization of masonry structures: elasticity. *Acta Geotech*. 3, 71–83. doi: 10.1007/s11440-007-0051-y

Stojanović, B. (1972). *Recent Developments in the Continua of Polar Elasticity*. Udine: Springer-Verlag.

Suzuki, T., Takeuchi, S., and Yoshinaga, H. (1991). *Dislocation Dynamics and Plasticity*. Berlin: Springer-Verlag.

Toupin, R. A. (1962). Elastic materials with couple-stresses. *Arch Ration. Mech. Anal*. 11, 385–414. doi: 10.1007/BF00253945

Trovalusci, P. (2014). "Molecular approaches for multifield continua: origins and current developments," in *Multiscale Modeling of Complex Materials: Phenomenological, Theoretical and Computational Aspects,* eds T. Sadowski, P. Trovalusci. (Berlin: Springer Int Centre for Mechanical Sciences), 211–278.

Trovalusci, P., and Augusti, G. (1998). A continuum model with microstructure for materials with flaws and inclusions. *J. Phys. IV*. 8, 383–390.

Trovalusci, P., De Bellis, M. L., and Masiani, R. (2017). A multiscale description of particle composites: From lattice microstructures to micropolar continua. *Comp. Part B Eng*. 128, 164–173. doi: 10.1016/j.compositesb.2017.06.015

Trovalusci, P., and Masiani, R. (1999). Material symmetries of micropolar continua equivalent to lattices. *Int. J. Solid Struct*. 36, 2091–2108. doi: 10.1016/S0020-7683(98)00073-0

Trovalusci, P., and Masiani, R. (2003). Non-linear micropolar and classical continua for anisotropic discontinuous materials. *Int. J. Solid. Struct*. 40, 1281–1297. doi: 10.1016/S0020-7683(02)00584-X

Trovalusci, P., and Ostoja-Starzewski, M. (2011). Multiscale mechanical modelling of complex materials and engineering applications 2. *Int. J. Mult. Comp. Eng*. 9, 7–9. doi: 10.1615/IntJMultCompEng.2011002870

Trovalusci, P., Ostoja-Starzewski, M., De Bellis, M. L., and Murrali, A. (2015). Scale-dependent homogenization of random composites as micropolar continua. *Eur. J. Mech A Solids*. 49, 396–407. doi: 10.1016/j.euromechsol.2014.08.010

Trovalusci, P., and Pau, A. (2014). Derivation of microstructured continua from lattice systems via principle of virtual works: the case of masonry-like materials as micropolar, second gradient and classical continua. *Acta Mech*. 225, 157–177. doi: 10.1007/s00707-013-0936-9

Trovalusci, P., Varano, V., and Rega, G. (2010). A generalized continuum formulation for composite materials and wave propagation in a microcracked bar. *J. Appl. Mech*. 77:061002. doi: 10.1115/1.4001639

Yang, D., Sheng, Y., Ye, J., and Tan, Y. (2010). Discrete element modeling of the microbond test of fiber reinforced composite. *Comput Mater Sci*. 49, 253–259. doi: 10.1016/j.commatsci.2010.05.003

Yang, J. F. C., and Lakes, R. S. (1982). Experimental study of micropolar and couple stress elasticity in compact bone in bending. *J. Biomechanics*. 15, 91–98.

Conflict of Interest Statement: The authors declare that the research was conducted in the absence of any commercial or financial relationships that could be construed as a potential conflict of interest.

frontiers in Materials

ORIGINAL RESEARCH
published: 24 April 2019
doi: 10.3389/fmats.2019.00086

Dome-Shape Auxetic Cellular Metamaterials: Manufacturing, Modeling, and Testing

Nathanael Easey[1], Dmytro Chuprynyuk[1], W. M. Syazwan Wan Musa[1], Angus Bangs[1], Yousef Dobah[1,2], Anton Shterenlikht[1] and Fabrizio Scarpa[1]*

[1] Faculty of Engineering, University of Bristol, Bristol, United Kingdom, [2] Department of Mechanical Engineering, University of Jeddah, Jeddah, Saudi Arabia

We present in this work the manufacturing, modeling, and testing of dome-shaped cellular structures with auxetic (negative Poisson's ratio) behavior. The auxetic configurations allow the creation of structures with synclastic (i.e., dome-shaped) curvatures, and this feature is used to evaluate the performance of cellular metamaterials under quasi-static indentation conditions. We consider here different cellular geometries (re-entrant, arrow-head, tri-chiral, hexagonal) and the implications of their manufacturing using 3D printing techniques with PLA material. The dome-shaped configurations are modeled using full-scale non-linear quasi-static and explicit dynamic FE models that represent both the geometry and approximate constitutive models of the PLA filament material derived from tensile tests on dogbone specimens. The cellular metamaterials samples are subjected to indentation tests, with maps of strains obtained through DIC measurements. The correlation between experimental and numerical simulations is good, and shows the peculiar indentation behavior of these cellular structures. We also perform a comparative analysis by simulation of the force/displacement, strain and fracture history during quasi-static loading, and discuss the performance of the different cellular topologies for these dome-shape metamaterial designs.

Keywords: auxetic domes, snap-through, buckling, re-entrant, arrow-head, tri-chiral, non-linear FE, digital image correlation

OPEN ACCESS

Edited by:
Fernando Fraternali,
University of Salerno, Italy

Reviewed by:
Anastasiia O. Krushynska,
University of Groningen, Netherlands
Luciano Teresi,
Roma Tre University, Italy

***Correspondence:**
Fabrizio Scarpa
F.Scarpa@bristol.ac.uk

Specialty section:
This article was submitted to Mechanics of Materials, a section of the journal Frontiers in Materials

***Received:** 06 October 2018*
***Accepted:** 08 April 2019*
***Published:** 24 April 2019*

Citation:
Easey N, Chuprynyuk D, Musa WMSW, Bangs A, Dobah Y, Shterenlikht A and Scarpa F (2019) Dome-Shape Auxetic Cellular Metamaterials: Manufacturing, Modeling, and Testing. Front. Mater. 6:86. doi: 10.3389/fmats.2019.00086

1. INTRODUCTION

A mechanical metamaterial is a multiscale system of materials with engineered mechanical properties that can vary dramatically from those of the base material. Mechanical materials can therefore exhibit some global unusual deformation mechanisms. Lattice structures are a popular example of mechanical metamaterials because of their high strength to density ratio, compared to traditional structural materials (Ashby, 2006). Another important aspect of lattice structures is their tailorable mechanical response, both at global and hierarchical scale (Sun and Pugno, 2013).

A subset of mechanical metamaterials is represented by auxetics. While conventional cellular foams and rubber-like materials have a Poisson's ratio varying from $\nu \approx 0.5$ (incompressible) to $\nu = 0$ (e.g., cork) with decreasing density, auxetics possess instead a negative Poisson's ratio. Negative ν means that the elongation in one direction is accompanied by an elongation in the transverse direction. On the opposite, the auxetic material will shrink under compression. Auxetic structures can be deployed to provide a required indentation resistance (Evans and Alderson, 2000), high compressive and shear stiffness (Sanami et al., 2014), and high energy absorption (Mohsenizadeh et al., 2015). In biomedical applications of auxetics have been sought in bone implants (Warmuth et al., 2017; Kolken et al., 2018). Auxetics can be also developed by applying patterns of cuts and holes (Grima et al., 2005). Perforated auxetic composite plates have been used in a hybrid flexible cushioning support for multiple sclerosis patients (Mohanraj et al., 2016).

The mechanical properties of lattices can be changed dramatically (Ashby, 2006) by varying the connectivity of the struts and the angles between the same struts at joints, therefore creating auxeticity in essentially bending-dominated lattices (Grima et al., 2010; Bouakba et al., 2012; Saxena et al., 2016). Auxetic structures exhibit synclastic behavior when bent, i.e., they deform into dome shapes (Alderson and Alderson, 2007), rather than saddle ones, which are typical of structures with positive ν. This makes auxetics useful in applications such as pressure vessels (Adachi, 1968) and anti-blast protections (Sahu and Gupta, 2015). Auxetic domes designs could therefore be suitable for protective equipment applications. A lower cell density in an auxetic lattice also leads to lower stiffness and higher bending and rotation motion of the struts (Scarpa et al., 2000; Carneiro et al., 2016), and this increases the effective negative effective Poisson's ratio ν_a (Carneiro et al., 2016). The energy absorption of chiral auxetic topologies is greater than that of the re-entrant dome as the strut thickness increased and the ν_a reduced (Scarpa et al., 2000). This suggests that there is a smaller dependence on cell geometry configurations like the tri-chiral lattice.

The energy absorption of a foam increases with density, because the indenter/impactor force is distributed over a larger number of cells (Lakes and Elms, 1993; Fleck and Qiu, 2007). The increase of the cell density in a structure like an auxetic dome should therefore lead to a greater amount of strut deformation, and thus to higher energy absorption.

In the arrow-head topology ν_a grows from a negative value to zero with increasing strain (Yang et al., 2018). The arrow-head and re-entrant topology has higher energy dissipation than the hexagonal lattice due to the negative in-plane ν_a. The re-entrant topology has the highest energy absorption (Yang et al., 2018). Both re-entrant and arrow-head topologies are significantly anisotropic (Zied et al., 2015).

Plasticity and non-linear geometry have a significant effect on FE modeling of deformation of auxetic structures (Zhang et al., 2018). Structures ranging from a unit cell to full scale geometrical models have been modeled successfully with beam elements and 3D solid elements (Blachut and Galletly, 1988).

Although auxetic foams have received a lot of attention (Lakes and Elms, 1993; Zied et al., 2015; Yang et al., 2018), little research has been done on auxetic dome-shaped structures. The work presented in this paper focuses on the buckling and post-buckling behavior of novel auxetic lattice domes, such as those shown in **Figure 1**.

2. DOMES AND THE EFFECT OF THE POISSON'S RATIO

In 1946 Reissner showed that the term $(1-\nu^2)^{1/2}$, where ν is the Poisson's ratio of the material, appears in the linear differential equations for normal displacements, w, in thin shallow spherical shells (Reissner, 1946). Reissner considered a spherical shell segment being shallow if the ratio of its height to the base diameter did not exceed 1/8. Ashwell extended Reissner's theory to large deflections w and showed that a spherical shell segment loaded by an inward point load, F, does not exhibit instability (Ashwell, 1960). Ashwell also demonstrated that the linear theory predicts a linear relationship between F and w, while his non-linear theoretical model predicts a non-linear $F(w)$ response, but still with no loss of elastic stability. A snap-through instability (buckling) is predicted when distributed load (external pressure), p, is applied to a spherical shell, with the same term $(1-\nu^2)^{1/2}$ appearing in the expression for the critical pressure, p_c (Budiansky, 1960), see Equation (1), where E is the Young's modulus, and R and t are the shell radius of curvature and thickness respectively.

$$p_c = \frac{2E}{\sqrt{3(1-\nu^2)}}\left(\frac{t}{R}\right)^2 \tag{1}$$

Leckie showed that a snap through instability does indeed occur under the application of an inward radial force thorough a rigid "boss" of a finite diameter, if plastic deformation is allowed (Leckie, 1969). However, as a plastic deformation is incompressible, no dependence of the critical load on ν was found. This aspect is reinforced also by the particular case we consider in the following example. The loading case is somewhat intermediate between an inward radial force and external pressure on a simply supported spherical shell segment (hereafter–a dome) compressed between a pair of rigid plates. A preliminary non-linear elastic FE study using full 3D solid theory and an isotropic elastic homogeneous material shows that, although a snap-through behavior is clearly present, no sensitivity to ν is also apparent (see **Figure 2**). In this figure w has been scaled by the dome thickness t; F^* is the applied load scaled as shown in Equation (2). The parameters h and b correspond to the dome height and the base radius, respectively.

$$F^* = \frac{F}{ERt}\frac{h}{b} \tag{2}$$

In this particular example the following dimensions have been considered: $R = 50$ mm, $b = 40$ mm, $h = 20$ mm, $t = 2$ mm. The Young's modulus $E = 2,774$ MPa represents a polymeric material (typical PLA used in 3D printing). The elements considered in this simulations were 2nd order tetra elements C3D10 (Dassault Systèmes, 2014). The models feature 4 elements through the thickness. The Abaqus eigenvalue (Dassault Systèmes, 2014) results for the "boss" loading of a simply supported

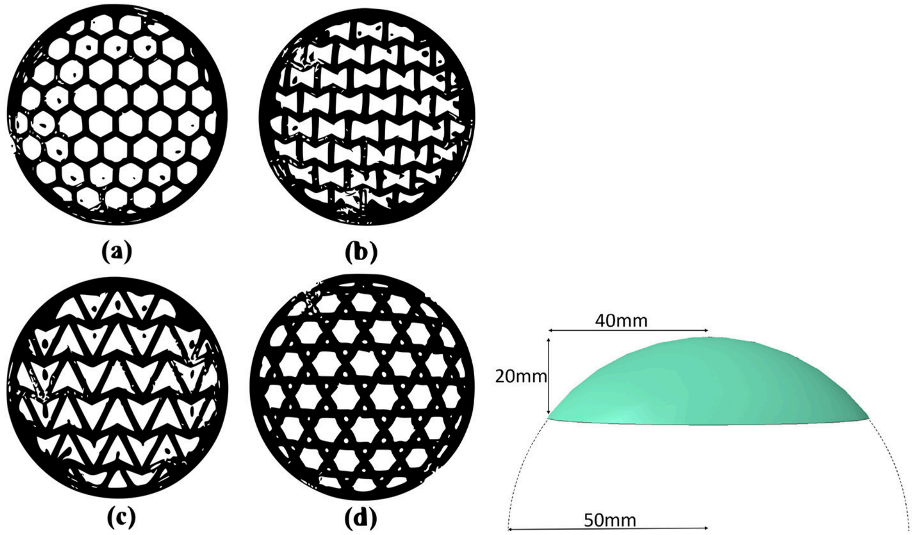

FIGURE 1 | The four cellular topologies considered here **(Left)**: (a) hexagonal, (b) re-entrant, (c) arrow, and (d) tri-chiral. An arrow-head dome PLA specimen **(Left)** and the spherical dome dimensions **(Right)**. The sphere radius is 50 mm. The dome height is 20 mm and the dome base radius is 40 mm.

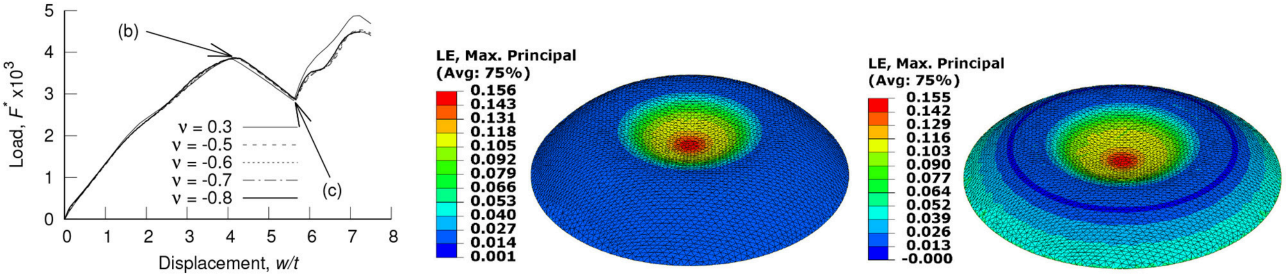

FIGURE 2 | FE snap-through response in the plate compression of a solid dome, showing: **(Left)** a snap through response, and the maximum principal logarithmic strain, ϵ_1, at **(Middle)** buckling and **(Right)** after snap-through.

dome are shown in **Figure 3**. Note that the predicted critical loads are 3 order of magnitude higher than from plate compression. However, the shape of the curve is the one given by Equation (1).

Figures 2, **3** suggest that the issue of the stability of domes with different Poisson's ratio values is complex, and cannot be simply resolved by using existing analytical solutions. In this work we tackle this particular problem with a program of experimental and numerical experiments on lattice domes, which possess different lattice geometries that mimic varying Poisson's ratios.

3. EXPERIMENTS

3.1. PLA Mechanical Properties

The domes were manufactured from PLA using a Raise3D N1 system with fused filament fabrication (FFF) to extrude the filament into layers, with a single nozzle. The CAD model was converted to the stereolithography (STL) format, compatible with the 3D printer "slicing" software IdeaMaker. IdeaMaker eventually translates the model into a G-code file that contains commands of tool path and amount of extruded material for the printer to execute and produce the domes. The "slicing" process involves applying internal support structures to the model to prevent the dome from collapsing, as the struts can overhang at angles greater than 35° (Baumann et al., 2016). A photo of the 3D printer used for this work is provided as **Supplementary Material**.

The domes were manufactured with the following topologies: hexagonal, tri-chiral, re-entrant, and arrow-head. A 0.2 mm turquoise colored filament was used with 100% infill ratio, extruder temperature of 235°, 0.2 mm layer height, and 65° print bed temperature. The strut thickness and width were 2 mm.

FFF 3D printing is known to induce mechanical anisotropy in finished components due to its method of material deposition. To reduce the printed material anisotropy, the "slicing" software changes printer's tool path by 90° at every layer by default. Thus, it had to be edited manually to enforce specific direction at all the layers. To measure this anisotropy, dog-bone specimens of 6 configurations were made, see **Figure 4**.

The tensile tests were carried out at a rate of 2 mm/min using a clip gauge, according to ASTM D638-14 (2014) valid for 3D printed polymers. The clip gauge, with a resolution of 0.5%, was

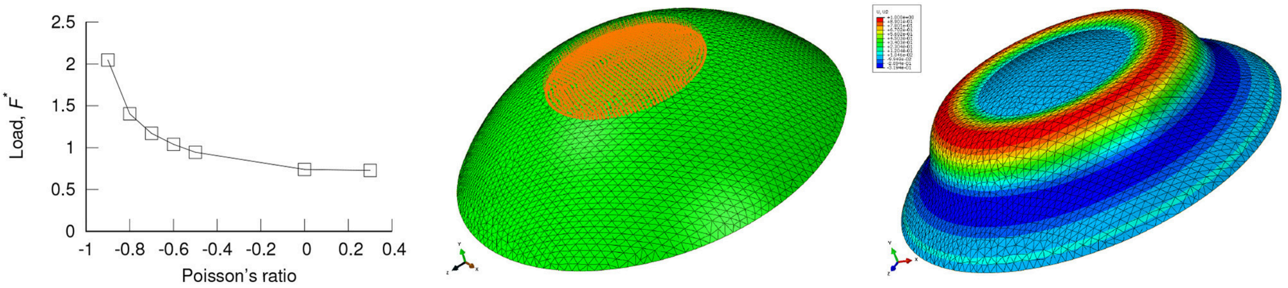

FIGURE 3 | Eigenvalue analysis for "boss" loading of a solid dome, showing: **(Left)** the buckling load, (middle) the prescribed displacement of the "boss" area and **(Right)** the 1st buckling mode.

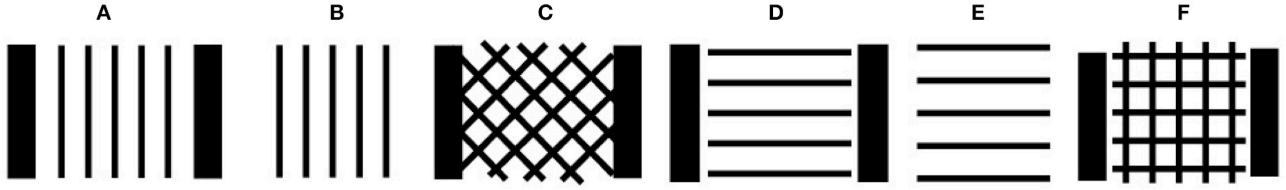

FIGURE 4 | Six layouts for printing dog-bone specimens: **(A)** 90° with support walls, **(B)** 90° without support walls, **(C)** ±45° with support walls, **(D)** 0° with support walls, **(E)** 0° without support walls, and **(F)** 0°/90° with support walls.

chosen over the strain gauges because it allows quicker placement on the samples and less time for the experimental set up (Motra et al., 2014). The load cell uncertainty was also 0.5% The cross section area (for stress calculations) was measured with Vernier calipers with 0.02 mm resolution.

The measured PLA Young's modulus was $E = 2742 \pm 129$ MPa, which agrees with the published data ($E = 2852 \pm 88$ MPa; Innofil3D, 2017). The mean yield stress is 15 MPa and the mean flow curve is provided as a **Supplementary Material**.

3.2. Compression Testing of Domes

The compression tests have been carried out with a Shimadzu Universal testing equipped with a 10 kN load cell. A very low displacement rate (3 mm/min) was used to avoid strain rate effects, as the PLA properties are severely affected by the strain rate (Richeton et al., 2006). The tests were performed at room temperature, well below the PLA glass transition temperature of 59°C (Narladkar et al., 2008).

The use of Digital Image Correlation (DIC) required that the top and/or the bottom surfaces of the dome were visible. A rig was designed to allow cameras to view the dome through transparent acrylic plates, while being out of the way, **Figure 5**. A steel plate was used at the base. Three 8 mm diameter steel threaded rods were used to attach 10 mm thick acrylic plates. The base diameter was 250 mm.

Given the relatively low stiffness of the acrylic, it was important to measure the compliance of the rig, to subtract from the measured dome displacement. Equation (3) expresses the rig compliance as displacement δ, in mm, vs. applied force F, in N.

$$\delta = 0.02849F^{0.545} \tag{3}$$

The DIC and load/displacement data were captured at 10 Hz.

3.3. Digital Image Correlation (DIC)

A LaVision portable 3D StrainMaster DIC system was used, with two illumination sources and two M-Lite 5 Megapixel cameras, 20mm lenses and polarizing filters (LaVision, 2017). The kit was mounted on a leveled stand and placed within the experimental rig, see **Figure 5**.

A zero mean normalized sum of squared difference correlation function (ZNSSD) has been shown to be the most effective for 3D DIC, because it compensates for errors associated with intensity change along the deformation (Pan et al., 2010). For an image subset with dimensions $2M + 1 \times 2M + 1$ pixels, the ZNSSD correlation function is given in Equation (4).

$$C = \sum \left(\frac{f(x_i, y_j) - f_m}{\sqrt{\sum (f(x_i, y_j) - f_m)^2}} - \frac{g(x'_i, y'_j) - g_m}{\sqrt{\sum (g(x'_i, y'_j) - g_m)^2}} \right)^2 \tag{4}$$

where all summation is for i and j from $-M$ to M, $f_m = \frac{1}{(2M+1)^2} \sum f(x_i, y_j)$ and $g_m = \frac{1}{(2M+1)^2} \sum g(x'_i, y'_j)$; and f and g are pixel intensities in the reference and the target subsets respectively (Pan et al., 2010).

The DIC method is inherently subjective. Numerous parameters affect the quality of DIC results, such as the lighting, the camera exposure (Zhu et al., 2018), the focal length (Reu et al., 2015), the surface pattern (Lecompte et al., 2006; Sutton et al., 2009; Reu et al., 2015), as well as the accuracy of the calibration.

A subset size of 13 × 13 pixels was used, as it allows approximately three dominant features within a single subset.

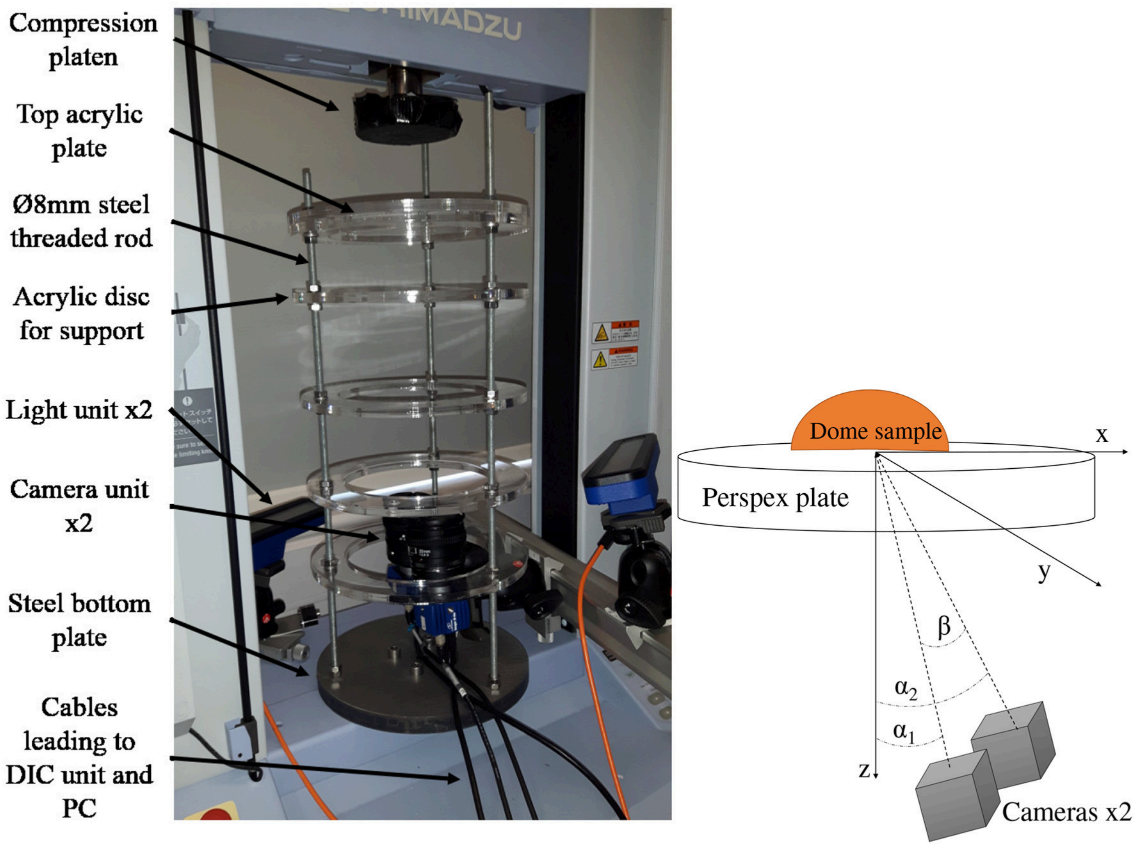

FIGURE 5 | The loading rig for the DIC application **(Left)** and a schematic of the positioning of the cameras **(Right)**.

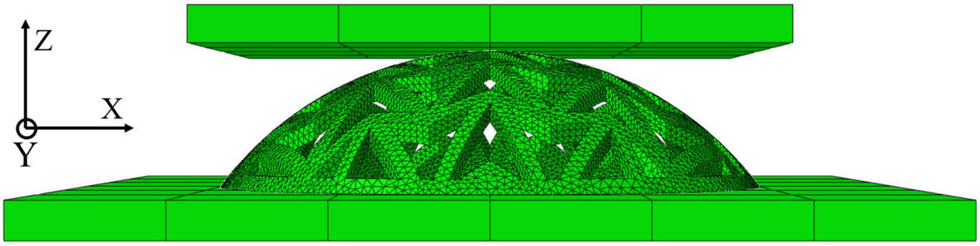

FIGURE 6 | Schematic of the FE dome compression test.

This was found to be the optimum value in this work and consistent with best practice in literature (McGinnis et al., 2005). To increase the spatial resolution, the step between the subsets was 3 pixels, giving a 10 pixel overlap. A moving average smoothing kernel of 9 × 9 pixels was used for the strain data. The main purpose of smoothing in this work is to reduce the noise produced at the strut edges. The kernel size was chosen to reduce areas of outlying high strains without noticeably reducing the accuracy of the displacements.

The refraction effects due to imaging through the acrylic plates were measured by varying the angle between the camera optical axis and the normal to the plate. The maximum difference was 0.6%, i.e., the effects of refraction could be considered negligible.

The DIC displacement agrees to within 1% with the Shimadzu displacement, which was validated to within 0.02 mm using Vernier calipers, 0.03% of the dome height. This comparison is provided as a **Supplementary Material**.

4. FE MODELING OF THE EXPERIMENTS

The Abaqus FE package was used (Dassault Systèmes, 2014) to model the compression of the auxetic cellular domes. Both implicit and explicit solvers were used, depending on the analysis.

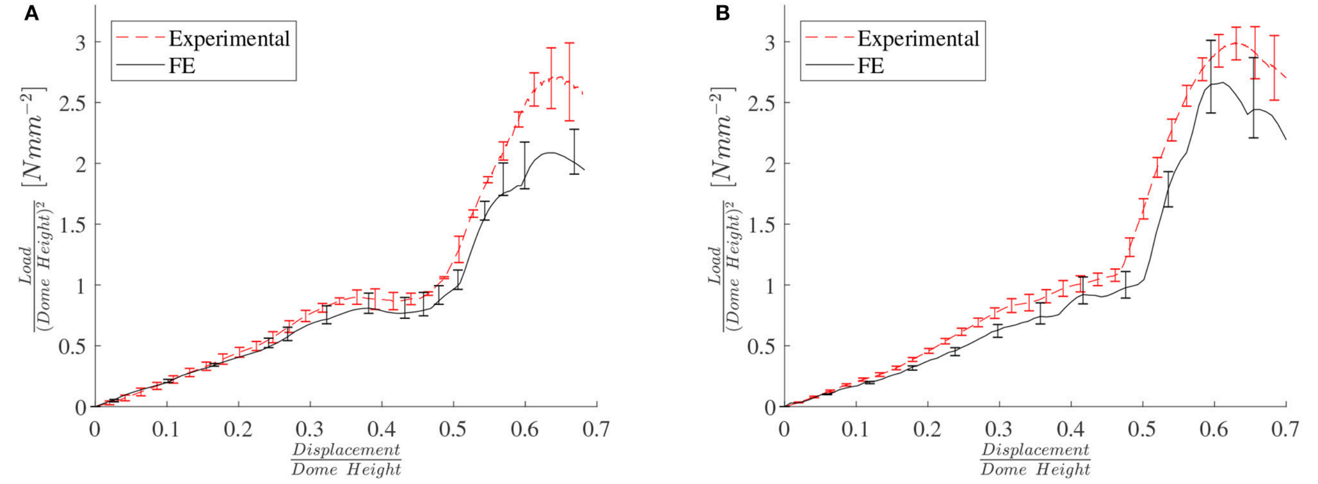

FIGURE 7 | FE vs. experimental load/displacement results for **(A)** arrow-head and **(B)** re-entrant topologies.

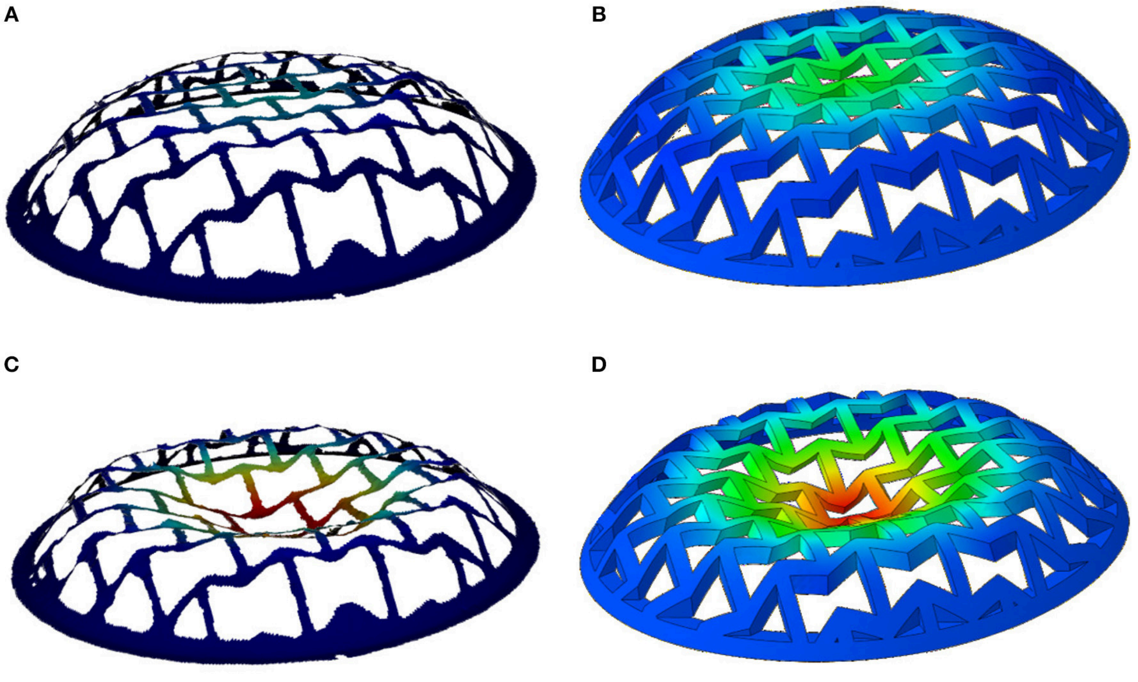

FIGURE 8 | DIC vs. FE vertical displacements (DIC on the left and FE on the right), showing **(A,B)** at the onset of buckling, and **(C,D)** when the dome center touches the bottom plate.

Continuum 3D 10-node quadratic tetrahedral elements (Abaqus type C3D10) were used and isotropic homogeneous material properties were assumed, with isotropic hardening. An analysis of the material's Poisson's ratio concluded that it has a negligible effect on the buckling load or post-buckling behavior. Therefore, the reference value of $\nu = 0.3$ was used in all simulations (Farah et al., 2016). While a mesh sensitivity analysis (provided as a **Supplementary Material**) shows that a global mesh size of 1.5 mm was acceptable for post-buckling analysis.

The static analysis was performed using Newton-Raphson and Riks methods. The Riks method is typically used to model the snap through buckling in solid domes. However, since lattice domes (and auxetic domes in particular) exhibit a much weaker snap through effect, the Newton-Raphson method with displacement control was found in this work to be sufficiently stable. Element deletion was used for modeling fracture propagation with the explicit dynamic solver (Abaqus/Explicit). Fracture simulations used the Johnson-Cook

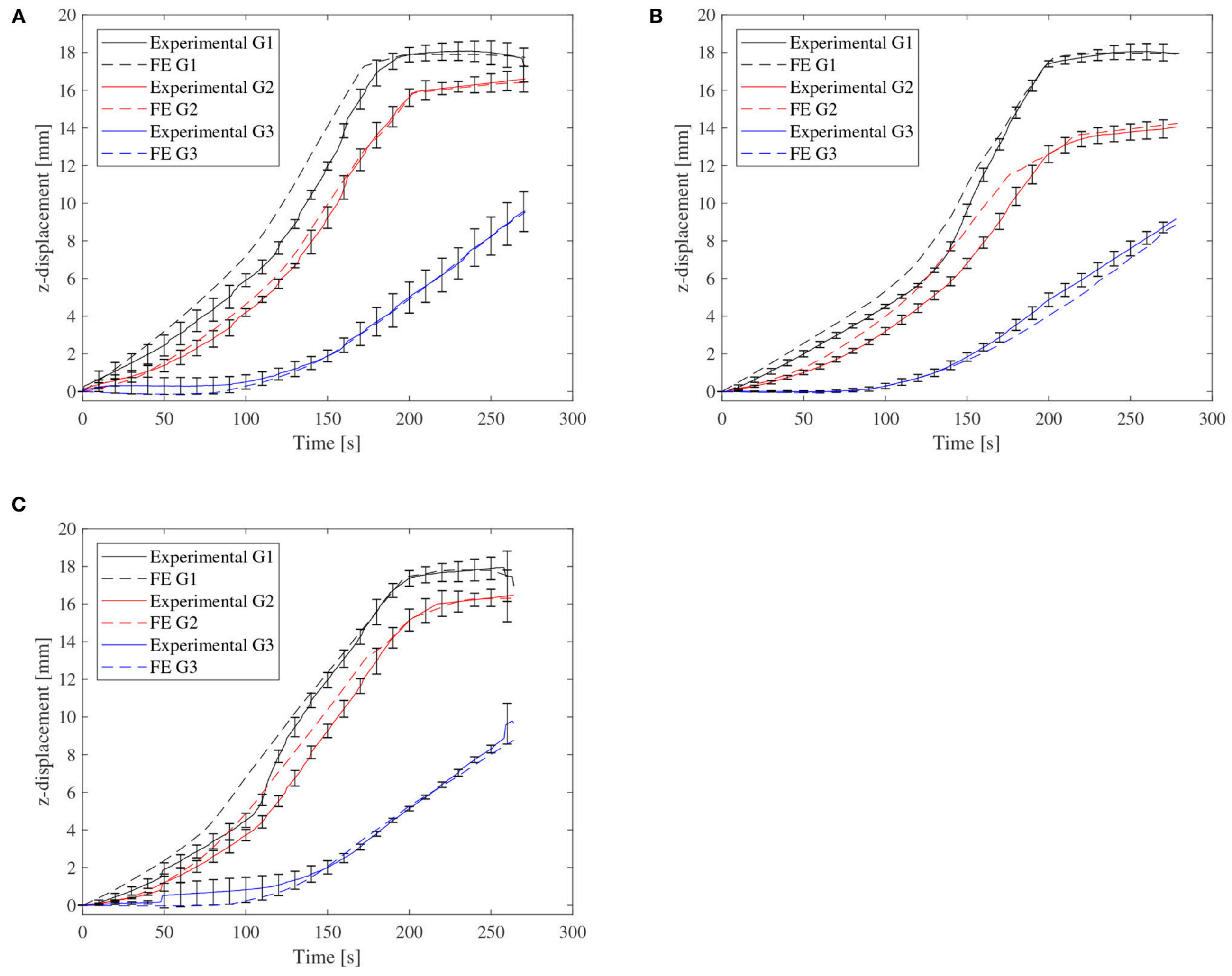

FIGURE 9 | DIC vs. FE displacement at 3 points on the domes, showing: **(A)** arrow-head, **(B)** re-entrant, and **(C)** tri-chiral topologies.

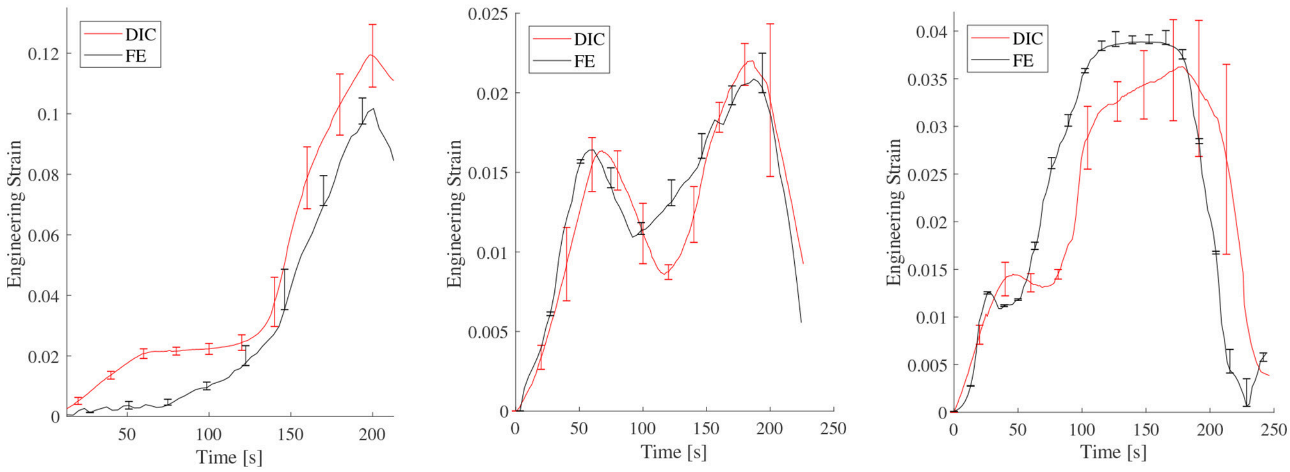

FIGURE 10 | DIC vs FE engineering strain on struts belonging to the central cell, for **(Left)** re-entrant topology (axial strut), **(Middle)** re-entrant topology (diagonal strut), and **(Right)** tri-chiral topology (single strut).

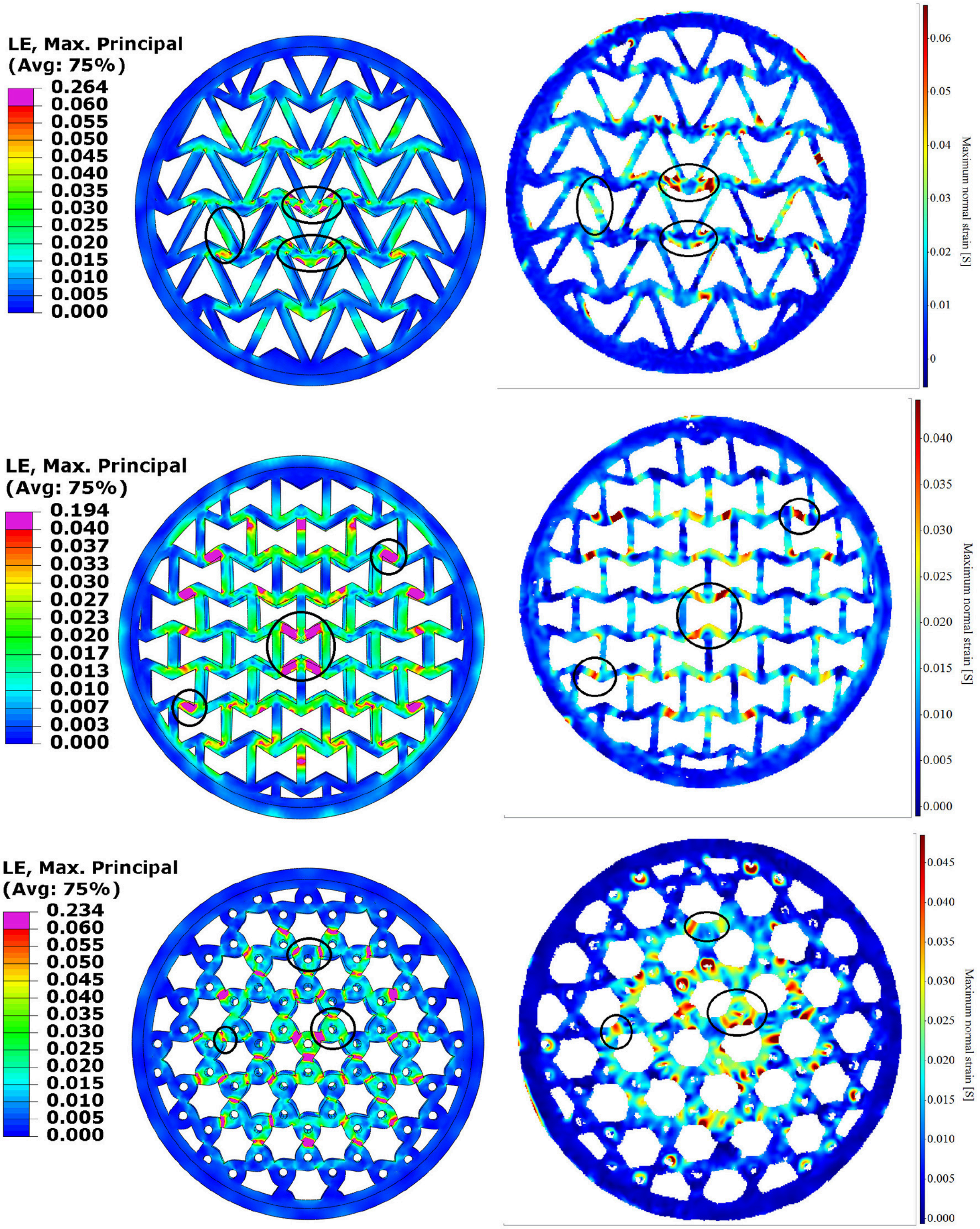

FIGURE 11 | FE **(Left)** vs. DIC **(Right)** ϵ_1 at buckling for 3 topologies: arrow-head in the top row, re-entrant in the middle row and tri-chiral in the bottom row. The most interesting features have been circled.

(JC) hardening and the JC failure criterion (Johnson and Cook, 1985) due to their simplicity and ready availability in the Abaqus explicit dynamic solver (tuning JC is described in **Supplementary Material**).

Schematics of the FE compression test is shown in **Figure 6**, where the bottom plate was fixed and the top plate was moved vertically down under displacement control. Both plates were modeled as rigid bodies and the interaction between them

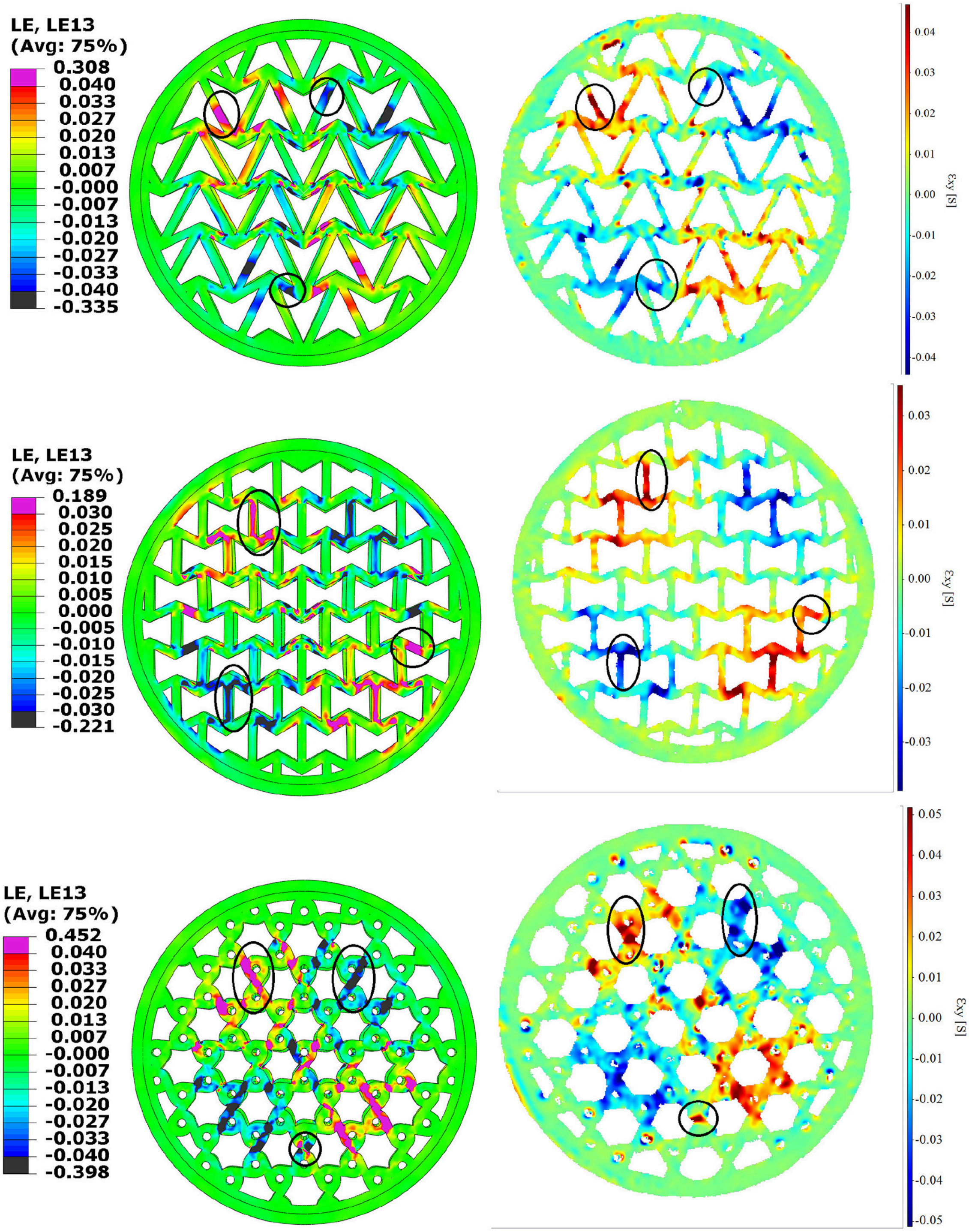

FIGURE 12 | FE **(Left)** vs. DIC **(Right)** ϵ_{23} at buckling for 3 topologies: arrow-head in the top row, re-entrant in the middle row and tri-chiral in the bottom row.

and the dome was defined as friction contact. the friction coefficient, μ, of the interaction was found to have a significant affect on buckling in the FE simulations, with higher friction increasing the buckling load and the post-buckling stiffness. It was found that $\mu = 0.4$ gives the best agreement between the FE results and the DIC data regarding the change in dome base diameter.

Once the FE model was calibrated, several parametric studies were performed (presented as a **Supplementary Material**) showcasing their affect on the dome performance.

TABLE 1 | Mean values and uncertainty of the Poisson's ratio, for 2D lattices, and of anisotropy for the domes.

	2D lattices		Domes	
Topology	***ν***	**Uncertainty [%]**	***a***	**Uncertainty [%]**
Re-entrant	–0.425	3.1	–0.499	12.8
Arrow-head	–0.315	9.8	–0.285	6.5
Tri-chiral	–0.72	11.1	–0.987	3.1
Hexagonal	0.8–1 (Ashby, 1983)	N/A	–0.95	6.7

5. RESULTS

Figure 7 shows a very good agreement between the FE and the experimental results for the arrow-head and re-entrant domes. The experimental data error bars represent here the standard deviation from 5 experiments. For the FE, the error bars represent the mean and the upper and the lower bounds of the flow curve. Note that the re-entrant topology exhibits virtually no snap through behavior, and even the arrow-head topology shows a much lower snap though compared to the one exhibited by a solid dome (**Figure 2**).

The 3D printing using PLA produces struts of uneven thickness. Our measurements showed that the mean strut thickness was 2.14 mm with a standard deviation of 0.07 mm. The FE strut also thickness varied due to the limitations of converting a CAD model into a FE mesh. The mean thickness of the struts in the Finite Element models was in reality equal to 2.12 mm, with a standard deviation of 0.14 mm. This small systematic error might explain the higher experimental loads observed in **Figure 7**.

The Finite Element results have been computed by considering both large geometric deformations and the non-linear mechanical properties of the PLA material. A question may arise about the importance in the mechanical response of the architecture of the domes vs. the core material behavior. To this end we have performed simulations related to arrow, re-entrant and trichiral configurations under large geometric deformations, but with linear elastic material only (see **Figure S5** right). The equivalent Young's modulus of the PLA has also been varied to assess any material scaling effect on the response. The results clearly show that up to a scaled displacement of 0.4–0.5 the response of the dome is negligibly dependent of the mechanical properties (both linear and non-linear—**Figure 7**). The first post-buckling occurrence in the response is scarcely dependent upon the linearity or non-linearity of the core materials properties, and appear at the same scaled displacement value. These are clear indications that the force/displacement behavior of these cellular domes under indentation is essentially governed by the architecture of the lattice.

Figure 8 shows a very good qualitative agreement of the displacement contour plots between DIC and FE, and an excellent quantitative agreement is seen in **Figure 9**, which shows vertical (z) displacement at the center of the dome (G1), and points located 2 struts away from the top (G2), and 4 struts away from the top (G3). The DIC error bars are standard deviations from 5 experiments.

Figure 10 shows a very good match between the DIC and FE engineering strains in the struts of the central cell, up to the end of the simulation/experiment, (**Figure 7**). The time variable in the graphs corresponds to the displacement steps of the indentor surface. One can also notice a dramatic change in the strain histories between the 3 different auxetic topologies.

Figure 11 compares FE vs. DIC ϵ_1 and **Figure 12** compares FE vs. DIC ϵ_{13}, or ϵ_{xz}, where z is the vertical direction. Note that the LaVision's "normal" in **Figure 11** means principal (LaVision, 2017). All contour plots show the onset of buckling, and the matching color bars are used for FE and DIC for ease of comparison. Regions of particular interest are circled in these figures.

Two-dimensional (flat) lattice specimens were also printed and tested under tension to measure the lateral contraction and determine an equivalent Poisson's ratio, ν for the lattice structures (**Table 1**). Analytical models of 2D tri-chiral lattices report $\nu = -1$ (Prall and Lakes, 1997), whereas our 2D tests give $\nu = -0.72$. However, Prall and Lakes (1997) assumed zero specimen thickness; for higher thicknesses or lower slenderness ratios of the struts the shear deformation of the cross section becomes important (Scarpa et al., 2000).

The coefficient a for the domes is defined as the ratio between the diameter extension along x to the diameter contraction in y under a compression along z. Thus, a is an indicator of anisotropy, as well as of the Poisson's ratio of the dome lattices. The hexagonal lattice has $a \approx -1$, because it is an isotropic topology, which expands equally in x and y under compression. Note that the 3 auxetic lattices show similar trends for ν and a.

Fracture was observed experimentally during the testing of the re-entrant, hexagonal, and tri-chiral domes. An example is shown in **Figure 13B**, which is a DIC shear strain map. The region circled in red, on the outer rim of the dome, was where the ductile fracture first appeared. Soon after, the fracture propagated fast toward the center of the dome along the path indicated by the black dashed line. These later fractures were all brittle.

Explicit dynamic FE simulations of fracture were then carried out using the JC failure criterion, on the 3 topologies (**Figure 13**). In all cases the fracture initiation was predicted at the outer rim. Fracture propagation was simulated using the element removal technique. The solid and the arrow-head domes showed a significant plastic strain prior to fracture, whereas, the tri-chiral dome fractured with little plasticity. This could be attributed to the rotation of the tri-chiral cells, which represents another deformation mechanism to absorb energy, aside from the bending/stretching/shear of the struts.

The SEM images of the PLA fracture surfaces are provided as **Supplementary Material**. The amount of plastic deformation in the 3D printed PLA depends on the print direction. Voids and coalescence are signs of ductile fracture in 3D printed polymers (Torrado Perez et al., 2014; Gao and Qiang, 2017). Brittle fracture is seen as the presence of "river lines," which are a sign of two surfaces being rapidly torn apart, like those on a cleavage fracture in crystalline materials. There is evidence of both ductile and brittle fractures in the SEM images.

Figure 14 compares compression response of domes with 4 lattice topologies (3 auxetic and hexagonal). The tri-chiral

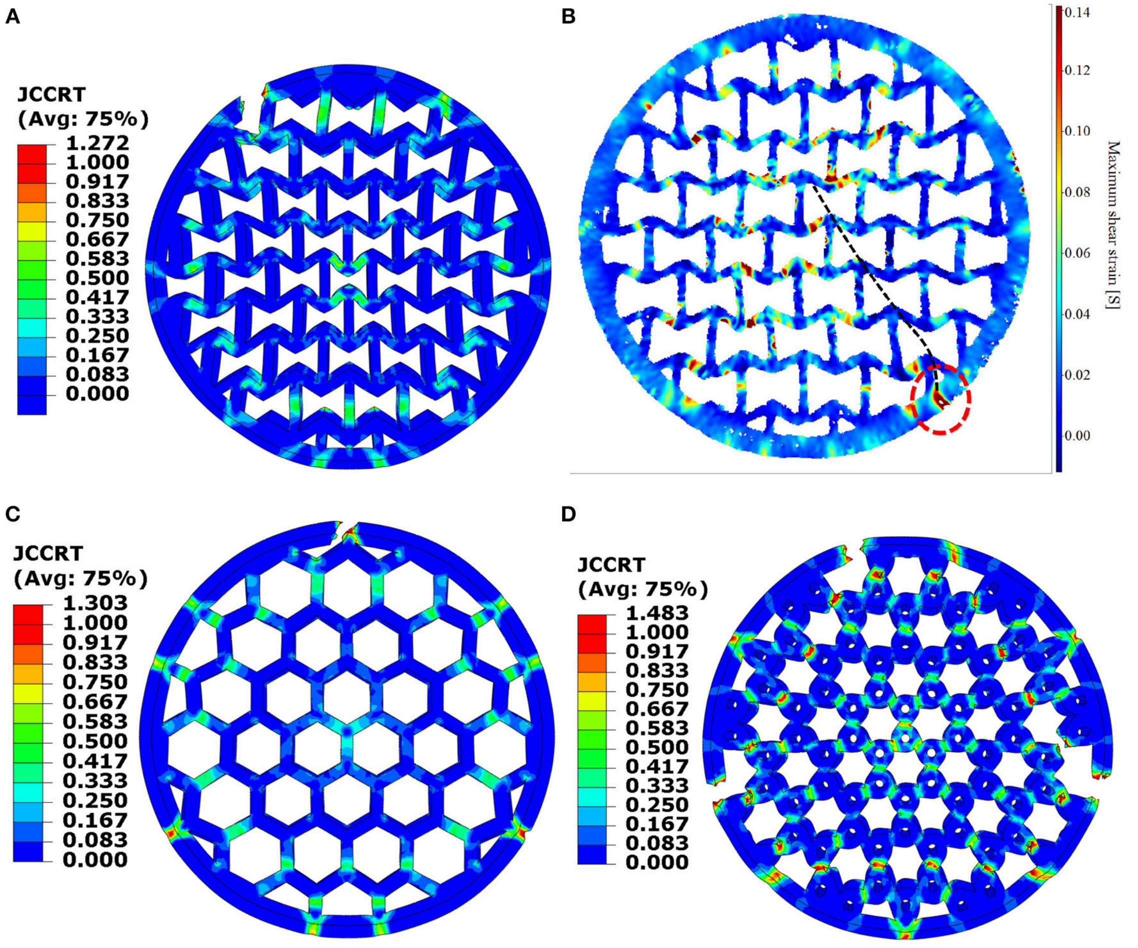

FIGURE 13 | FE vs. DIC fracture initiation, showing: **(A)** FE re-entrant, **(B)** DIC re-entrant, **(C)** hexagonal, and **(D)** tri-chiral topologies. FE data is the value for the JC fracture criterion. DIC data is the maximum shear strain.

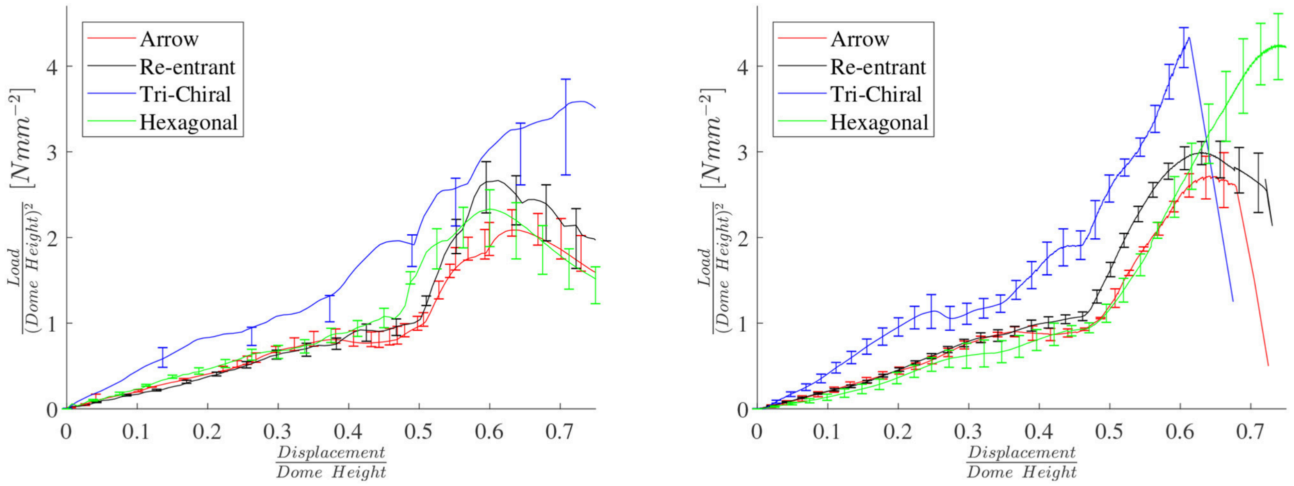

FIGURE 14 | FE **(Left)** and experimental **(Right)** load/displacement curves from buckling tests for 4 dome topologies.

topology shows a load which is monotonically increasing (within the data uncertainty), with little indication of buckling. The other 3 topologies show similar response, even though the hexagonal lattice is not auxetic.

6. CONCLUSIONS

An accurate and optimized DIC method was produced and used to successfully validate the FE models of auxetic cellular domes. Very good agreement was achieved between DIC and FE for the onset of buckling and post-buckling response, including strain, displacement, and loads. Experimental results are highly dependent on the errors and inaccuracies in 3D printing.

Auxetic cellular domes offer less indentation resistance under compressive loading than solid domes. They also show reduced snap-through in comparison with conventional lattices and solid domes. Tri-chiral topologies show higher resistance to compression than conventional lattices, which in turn show marginally higher resistance than the re-entrant topologies. The smallest snap-through effect is observed with the re-entrant topology. The cell density and dome curvature (contact size) were shown to affect the compressive resistance and the severity of snap-through.

We are currently working on assessing the dynamic response of auxetic lattices, using a similar experimental and modeling setup. These results will be presented in a follow-up publication.

AUTHOR CONTRIBUTIONS

NE and DC made the test rig and conducted all experimental work. WM and AB run the elasto-plastic FE simulations. YD created the dome CAD models. AS did the eigenvalue analysis and directed the work. FS directed the work. YD, AS, and FS wrote the paper.

ACKNOWLEDGMENTS

This work was supported by EPSRC UK grant EP/R013047/1. We acknowledge the use of the computational facilities of the Advanced Computing Research Centre, University of Bristol, https://www.acrc.bris.ac.uk.

SUPPLEMENTARY MATERIAL

The Supplementary Material for this article can be found online at: https://www.frontiersin.org/articles/10.3389/fmats.2019.00086/full#supplementary-material

REFERENCES

Adachi, J. (1968). *Stresses and Buckling in Thin Domes Under Internal Pressure*. Technical report, Army Materials and Mechanics Research Center, Watertown, MA.

Alderson, A., and Alderson, K. L. (2007). Auxetic materials. *Proc. Inst. Mech. Eng. G J. Aerospace Eng.* 221, 565–575. doi: 10.1243/09544100JAERO185

Ashby, M. (2006). The properties of foams and lattices. *Philos. Trans. R. Soc. Lond. A Math. Phys. Eng. Sci.* 364, 15–30. doi: 10.1098/rsta.2005.1678

Ashby, M. F. (1983). The mechanical properties of cellular solids. *Metallurg. Trans. A* 14, 1755–1769. doi: 10.1007/BF02645546

Ashwell, D. G. (1960). "On the large deflection of a spherical shell with an iward point load," in *The Theory of Thin Elastic Shells, Proc. IUTAM Symposium*, ed W. T. Koiter (Delft), 43–63.

ASTM D638-14 (2014). *Standard Test Method for the Tensile Properties of Plastics*. Technical report, ASTM international.

Baumann, F., Bugdayci, H., Grunert, J., Keller, F., and Roller, D. (2016). Influence of slicing tools on quality of 3d printed parts. *Comput. Aided Design Appl.* 13, 14–31. doi: 10.1080/16864360.2015.1059184

Blachut, J., and Galletly, G. D. (1988). Clamped torispherical shells under external pressure - some new results. *J. Strain Anal. Eng. Design* 23, 9–24. doi: 10.1243/03093247V231009

Bouakba, M., Bezazi, A., and Scarpa, F. (2012). Fe analysis of the in-plane mechanical properties of a novel voronoi-type lattice with positive and negative poisson's ratio configurations. *Int. J. Solids Struct.* 49, 2450–2459. doi: 10.1016/j.ijsolstr.2012.05.007

Budiansky, B. (1960). "Buckling of clamped shallow spherical shells," in *The Theory of Thin Elastic Shells, Proc. IUTAM Symposium*, ed W. T. Koiter (Delft), 64–94.

Carneiro, V. H., Puga, H., and Meireles, J. (2016). Analysis of the geometrical dependence of auxetic behavior in reentrant structures by finite elements. *Acta Mech. Sin.* 32, 295–300. doi: 10.1007/s10409-015-0534-2

Dassault Systèmes (2014). *Abaqus CAE*.

Evans, K. E., and Alderson, A. (2000). Auxetic materials: functional materials and structures from lateral thinking! *Adv. Mater.* 12, 617–628. doi: 10.1002/(SICI)1521-4095(200005)12:9<617::AID-ADMA617>3.0.CO;2-3

Farah, S., Anderson, D. G., and Langer, R. (2016). Physical and mechanical properties of PLA, and their functions in widespread applications—A comprehensive review. *Adv. Drug Deliv. Rev.* 107, 367–392. doi: 10.1016/j.addr.2016.06.012

Fleck, N. A., and Qiu, X. (2007). The damage tolerance of elastic–brittle, two-dimensional isotropic lattices. *J. Mech. Phys. Solids* 55, 562–588. doi: 10.1016/j.jmps.2006.08.004

Gao, H., and Qiang, T. (2017). Fracture surface morphology and impact strength of cellulose/PLA composites. *Materials* 10, 1–11. doi: 10.3390/ma10060624

Grima, J., Alderson, A., and Evans, K. (2005). Auxetic behaviour from rotating rigid units. *Phys. Status Solidi B* 242, 561–575. doi: 10.1002/pssb.200460376

Grima, J. N., Oliveri, L., Attard, D., Ellul, B., Gatt, R., Cicala, G., et al. (2010). Hexagonal honeycombs with zero poisson's ratios and enhanced stiffness. *Adv. Eng. Mater.* 12, 855–862. doi: 10.1002/adem.201000140

Innofil3D (2017). *Technical Data Sheet PLA 1.75 mm, V3.0*. Available online at: http://www.polymaker.com/wp-content/uploads/2015/06/PolyMax-PLA_TDS-v1.pdf

Johnson, G. R., and Cook, W. H. (1985). Fracture characteristics of three metals subjected to various strains, strain rates, temperatures and pressures. *Eng. Fract. Mech.* 21, 31–48. doi: 10.1016/0013-7944(85)90052-9

Kolken, H. M. A., Janbaz, S., Leeflang, S. M. A., Lietaert, K., Weinans, H. H., and Zadpoor, A. A. (2018). Rationally designed meta-implants: a combination of auxetic and conventional meta-biomaterials. *Mater. Horiz.* 5, 28–35. doi: 10.1039/C7MH00699C

Lakes, R., and Elms, K. (1993). Indentability of conventional and negative poisson's ratio foams. *J. Compos. Mater.* 27, 1193–1202. doi: 10.1177/002199839302701203

LaVision (2017). Digital Image Correlation (DIC) system hardware and software user manual. *StrainMaster 1.0*.

Leckie, F. A. (1969). "Plastic instability of a spherical shell," in *Theory of Thin Shells, Proc. 2nd IUTAM Symposium*, ed F. I.Niordson (Copenhagen), 358–373.

Lecompte, D., Smits, A., Bossuyt, S., Sol, H., Vantomme, J., Hemelrijck, D. V., et al. (2006). Quality assessment of speckle patterns for digital image correlation. *Opt. Lasers Eng.* 44, 1132–1145. doi: 10.1016/j.optlaseng.2005.10.004

McGinnis, M. J., Pessiki, S., and Turker, H. (2005). Application of three-dimensional digital image correlation to the core-drilling method. *Exp. Mech.* 45, 359–367. doi: 10.1007/BF02428166

Mohanraj, H., Ribeiro, S. L. M. F., Panzera, T. H., Scarpa, F., Farrow, I. R., Jones, R., et al. (2016). Hybrid auxetic foam and perforated plate composites for human body support. *Phys. Status Solidi B* 253, 1378–1386. doi: 10.1002/pssb.201600106

Mohsenizadeh, S., Alipour, R., Nejad, A. F., Rad, M. S., and Ahmad, Z. (2015). Experimental investigation on energy absorption of auxetic foam-filled thin-walled square tubes under quasi-static loading. *Proc. Manufact.* 2, 331–336. doi: 10.1016/j.promfg.2015.07.058

Motra, H., Hildebrand, J., and Dimmig-Osburg, A. (2014). Assessment of strain measurement techniques to characterise mechanical properties of structural steel. *Eng. Sci. Technol. Int. J.* 17, 260–269. doi: 10.1016/j.jestch.2014.07.006

Narladkar, A., Balnois, E., Vignaud, G., and Grohens, Y. (2008). Difference in glass transition behavior between semi crystalline and amorphous poly(lactic acid) thin films. *Macromol. Symp.* 273, 146–152. doi: 10.1002/masy.200851321

Pan, B., Xie, H., and Wang, Z. (2010). Equivalence of digital image correlation criteria for pattern matching. *Appl. Opt.* 49, 5501–5509. doi: 10.1364/AO.49.005501

Prall, D., and Lakes, R. (1997). Properties of a chiral honeycomb with a poisson's ratio of -1. *Int. J. Mech. Sci.* 39, 305–314. doi: 10.1016/S0020-7403(96)00025-2

Reissner, E. (1946). Stresses and small displacements of shallow spherical shells. II. *J. Math. Phys.* 25, 279–300. doi: 10.1002/sapm1946251279

Reu, P. L., Sweatt, W., Miller, T., and Fleming, D. (2015). Camera system resolution and its influence on digital image correlation. *Exp. Mech.* 55, 9–25. doi: 10.1007/s11340-014-9886-y

Richeton, J., Ahzi, S., Vecchio, K., Jiang, F., and Adharapurapu, R. (2006). Influence of temperature and strain rate on the mechanical behavior of three amorphous polymers: characterization and modeling of the compressive yield stress. *Int. J. Solids Struct.* 43, 2318–2335. doi: 10.1016/j.ijsolstr.2005.06.040

Sahu, R., and Gupta, P. (2015). Blast diffusion by different shapes of domes. *Defence Sci. J.* 65, 77–82. doi: 10.14429/dsj.65.6908

Sanami, M., Ravirala, N., Alderson, K., and Alderson, A. (2014). Auxetic materials for sports applications. *Proc. Eng.* 72, 453–458. doi: 10.1016/j.proeng.2014.06.079

Saxena, K. K., Das, R., and Calius, E. P. (2016). Three decades of auxetics research-materials with negative Poisson's ratio: a review. *Adv. Eng. Mater.* 18, 1847–1870. doi: 10.1002/adem.201600053

Scarpa, F., Panayiotou, P., and Tomlinson, G. (2000). Numerical and experimental uniaxial loading on in-plane auxetic honeycombs. *J. Strain Anal. Eng. Design* 35, 383–388. doi: 10.1243/0309324001514152

Sun, Y. T., and Pugno, N. (2013). In plane stiffness of multifunctional hierarchical honeycombs with negative poisson's ratio sub-structures. *Compos. Struct.* 106, 681–689. doi: 10.1016/j.compstruct.2013.05.008

Sutton, M. A., Orteu, J.-J., and Schreier, H. (2009). *Image Correlation for Shape, Motion and Deformation Measurements: Basic Concepts,Theory and Applications, 1st Edn*. Springer Publishing Company, Incorporated.

Torrado Perez, A. R., Roberson, D. A., and Wicker, R. B. (2014). Fracture surface analysis of 3D-printed tensile specimens of novel ABS-based materials. *J. Fail. Anal. Prev.* 14, 343–353. doi: 10.1007/s11668-014-9803-9

Warmuth, F., Osmanlic, F., Adler, L., Lodes, M. A., and Korner, C. (2017). Fabrication and characterisation of a fully auxetic 3d lattice structure via selective electron beam melting. *Smart Mater. Struct.* 26, 1–8. doi: 10.1088/1361-665X/26/2/025013

Yang, C., Vora, H. D., and Chang, Y. (2018). Behavior of auxetic structures under compression and impact forces. *Smart Mater. Struct.* 27, 1–12. doi: 10.1088/1361-665X/aaa3cf

Zhang, J., Dong, G. L., and Wang, R. Z. (2018). Tensile behavior of an auxetic structure: Analytical modeling and finite element analysis. *Int. J. Med. Sci.* 136, 143–154. doi: 10.1016/j.ijmecsci.2017.12.029

Zhu, H., Liu, X., Chen, L., Ma, Q., and Ma, S. (2018). Influence of imaging configurations on the accuracy of digital image correlation measurement. *Meas. Sci. Technol.* 29:035205. doi: 10.1088/1361-6501/aa9e6a

Zied, K., Osman, M., and Elmahdy, T. (2015). Enhancement of the in-plane stiffness of the hexagonal re-entrant auxetic honeycomb cores. *Phys. Status Solidi B* 252, 2685–2692. doi: 10.1002/pssb.201552164

Conflict of Interest Statement: The authors declare that the research was conducted in the absence of any commercial or financial relationships that could be construed as a potential conflict of interest.

ORIGINAL RESEARCH
published: 04 July 2019
doi: 10.3389/fmats.2019.00117

The Effects of Defects and Damage in the Mechanical Behavior of Ti6Al4V Lattices

Russell Goodall[1]*, Everth Hernandez-Nava[1], Sarah N. M. Jenkins[1], Lorna Sinclair[1], Emily Tyrwhitt-Jones[1], Mohammad A. Khodadadi[1], Donald H. Ip[2] and Hassan Ghadbeigi[2]

[1] Department of Materials Science and Engineering, The University of Sheffield, Sheffield, United Kingdom, [2] Department of Mechanical Engineering, The University of Sheffield, Sheffield, United Kingdom

With recent advances in manufacturing methods for metals with defined, complex shapes, the investigation of metallic lattice materials (metals containing significant porosity with a regular arrangement of the solid, frequently in the form of thin structural members or struts) has become more common. These materials show many interesting properties, and may have the capacity to be more highly engineered and optimized for a given application than the random structures of other microcellular metals, such as metallic foams and sponges, permit. However, the novel structure brings new structure-properties correlations to bear on the mechanical behavior of the materials. This paper examines one type of lattice, made from titanium alloy (Ti6Al4V) and fabricated by Electron Beam Melting (EBM), a material which typically shows only limited plasticity on deformation. The overall mechanical response is governed by the cooperative deformation of a very large number of individual struts that make up the lattice, and thus there is great potential for significant impact from damage arising due to defects in individual struts in the assembly. We explore the effect of simulated processing defects (missing struts) on the lattice properties, and how deformation and failure is distributed across the lattice after the onset of failure. To gain knowledge of how lattices deform, samples of various geometries, designed to probe compression, indentation-compression and tension (in the form of bending) are produced and tested under Digital Image Correlation (DIC) mapping. The understanding gained here will be of great use in designing new metallic lattice structures with greater damage tolerance and resistance to failure.

Keywords: Ti6Al4V, lattices, additive manufacture, mechanical properties, digital image correlation

Edited by:
Seunghwa Ryu,
Korea Advanced Institute of Science & Technology, South Korea

Reviewed by:
Francesco Dal Corso,
University of Trento, Italy
Domenico De Tommasi,
Politecnico di Bari, Italy

Correspondence:
Russell Goodall
r.goodall@sheffield.ac.uk

Specialty section:
This article was submitted to Mechanics of Materials, a section of the journal Frontiers in Materials

Received: *01 November 2018*
Accepted: *08 May 2019*
Published: *04 July 2019*

Citation:
Goodall R, Hernandez-Nava E, Jenkins SNM, Sinclair L, Tyrwhitt-Jones E, Khodadadi MA, Ip DH and Ghadbeigi H (2019) The Effects of Defects and Damage in the Mechanical Behavior of Ti6Al4V Lattices. Front. Mater. 6:117. doi: 10.3389/fmats.2019.00117

INTRODUCTION

Advances in novel manufacturing methods, such as Additive Manufacturing (AM) techniques (Murr et al., 2012; Frazier, 2014), have led to the ability to create porous metal structures with great control over the form the material takes. Porous metals can be desirable to achieve specific behaviors, such as the ability to be crushed, to permit fluid transport or to allow an extra level of tailorability (that of the structure) to obtain the desired properties of the material (Goodall, 2013). AM, with the ability to leave spaces or retain regions of unmelted powder that can be removed from the structure after processing, is well-adapted to the needs of porous metal production, especially those based on regular structures (although stochastic structures may also be produced (Hernandez-Nava et al., 2015); while production of such lattices is possible without AM (e.g., by using sheet metal manufacturing techniques, for example; Kooistra and Wadley, 2007; Queheillalt and Wadley, 2009), or only using AM to assist with creating investment and molds used in processing (Chiras et al., 2002), it is much facilitated by the direct use of the technique. Nevertheless, it has to be recognized that AM methods impose certain constraints over the physical structure of the material processed, both at the level of the part geometry, and also on the microstructure and the defect population (Tammas-Williams et al., 2015).

There is scope for much exploration of different possible porous forms. While not without limits, the range of structures with the potential to be made by metal AM is much wider than the examples already reported. Complex lattices with highly engineered designs have been produced (for example Amendola et al., 2015, 2016; Dumas et al., 2017), and relatively well-characterized forms such as the diamond structure (where the position of the struts replicates the tetrahedral orientations of the atomic bonds in the structure of the diamond form of carbon) are the more common. This type of structure has also been adapted to make more complex designs, such as density-graded lattices (Grunsven et al., 2014), and similar lattices can be designed to be elastically isotropic (Xu et al., 2016). Lattices have the potential to be highly engineered, creating materials with combinations of mechanical properties and density that are not found in other materials, as indicated by several theoretical studies of lattice geometries [see e.g., (Fleck et al., 2010; Berger et al., 2017)] and the review in Schaedler and Carter (2016). As well as forming parts which can be exploited for their good weight-specific properties, AM manufactured lattices could serve in specialized applications, such as biomedical implants (Wally et al., 2015; Elahinia et al., 2016).

Analysis of mechanical performance of as-manufactured AM parts is however vital; in particular, it is important to know more about how the behavior of lattices is influenced by microstructure and defects. These are dependent on the processing conditions of the AM methods used, but also potentially the interaction of these with the lattice geometry being made. For example, it is known that such lattices contain porosity as a defect [see for example (Hernandez-Nava et al., 2016)]. Here the effect of severe defects of this type is probed by testing diamond and simple cubic lattices (where the struts are oriented along the edges of a cube) made with the deliberate removal of struts from the build file. The diamond structure lattice is then further tested in a range of loading conditions, combined with Digital Image Correlation (DIC) (Pan et al., 2009) to examine deformation fields and the failure modes, and how they correlate with the structure of the lattices and mechanical properties of the material within them.

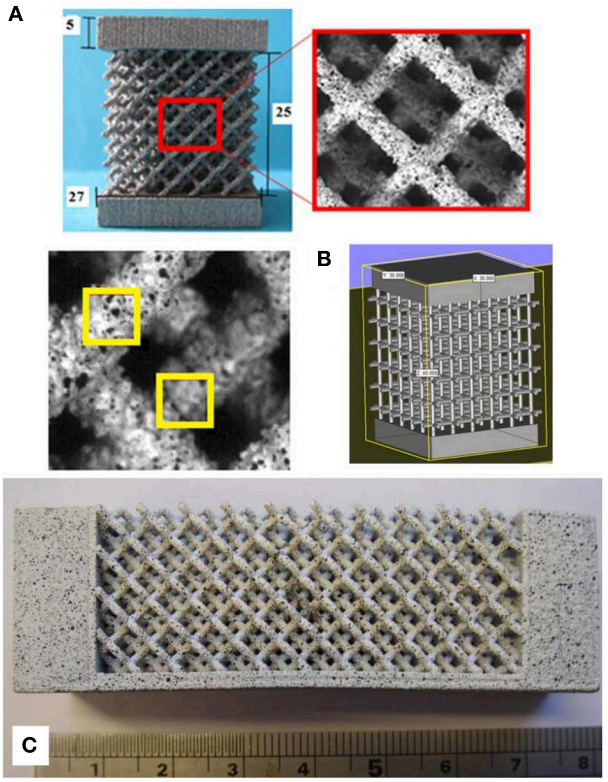

FIGURE 1 | (A) an undefected diamond lattice compression sample with integrated solid block on the upper and lower faces and a magnified view of the speckle pattern used for DIC and subsets used to analyze the images compared with the diameter of struts, **(B)** an example of the input file used in the EBM process, this time showing a simple cubic structure lattice, and **(C)** a bend sample consisting of diamond lattice structure and dense metal, designed so the neutral axis lies on the interface.

METHODS

Lattice Design

Lattices created were based on either a "diamond" lattice (an arrangement where the struts are positioned as the interatomic bonds in the unit cell of diamond), or a "simple cubic" arrangement (where struts lie along the edges of a cube, and cubes are arranged adjacently to each other) of struts (see **Figure 1**). In each case the struts were designed to be cylinders with 1 mm diameter, and each sample was a cube composed of 6 unit cells in each direction (5 in the case of the simple cubic structure), making them well above the limit found for consistent properties in metallic lattices (Morrish et al., 2017). Each side length of the lattice sample was 25 mm, and solid blocks of material with a dimension of 27 × 27 × 5 mm were also incorporated into these lattices (at the top and bottom edges) to make a sandwich structures; this was done in order to improve the contact at the test machine anvil surface and the samples. The blocks were manufactured simultaneously with the lattice in the form of the same part. One set of samples was made without the blocks for assessment in compression with DIC observation, to ensure the failure mode was not affected by the blocks.

These basic lattice designs were taken and in some cases defects were deliberately introduced. These took the form of struts within the lattice deleted manually from the CAD file, representing the effect of a serious defect essentially removing the load supporting capacity of the strut. Such samples were produced with various percentages of the struts removed at random (by a random number generation method and manual deletion of corresponding struts); 1, 5, and 10% for the diamond structure and 1, 3, 5, and 7% for the simple cubic. A single unit cell of the diamond structure contains 16 struts, so the samples contained 3,456 struts. Samples with 1, 5, and 10% levels of defects therefore have 35, 173, and 346 struts removed (rounding up to the nearest whole number of struts), respectively. A simple cubic unit cell has only three struts, and so the actual number removed was in this case lower to achieve comparable percentage reductions. At even the lowest levels, this is likely to represent a much higher defect concentration that would occur in realistic processing of such lattices by additive manufacturing methods like EBM (it should be noted that in all the samples processed in this work, no observations of fully missing or broken struts on building were made), but the high level will ensure that measureable effects are generated within a tractable number of test samples, and allow the overall trends to be identified.

Two different sets of defected samples were created for each defect concentration, where in each case the defects were placed in random locations as determined by the random number generation process, with first the structure for 1% missing struts being made, and then further struts being removed from this structure to create 5% and subsequently 10%. Three identical samples of each structure at each defect level were made. The simple cubic lattices were further produced in a series of different strut thicknesses (an effective way to change the density), with nominal strut diameters of 0.8, 1.0, 1.2, and 1.5 mm. When produced these gave lattices with average porosity of 94.4, 92.6, 89.0, and 83.8%, respectively. The stress-strain curves produced on mechanical testing were analyzed to identify the Young's modulus and the 0.2% offset yield strength as characteristics of the elastic and plastic response.

The next part of the investigation was concerned with the distribution of deformation in lattices during mechanical deformation under different loading arragements, particularly once permanent deformation and damage had occurred, and the failure modes shown. Samples consisting of lattice cubes of the diamond structure were made to the same dimensions as those used for the defect investigation (see **Figure 1**). Additional test samples where the upper dense plate extended only half way across the specimen were also manufactured to introduce an unequal compressive load and an indentation-compression deformation situation, as shown in **Figures 6A1,2**. The whole section of the top plate is loaded in the former while in the latter the section where the plate was not present is not directly loaded. It was also desired to explore lattice behavior under tension. In order to implement a tensile stress field to the lattice structure, bespoke bending specimens were designed and produced. Bending beams (**Figures 1B**, **7**, **8**) were designed in such a way to ensure the lattice structure is in the tensile stress mode, attached to a solid dense layer that would experience the compressive stresses due to bending and provides the required support for the loading mechanism. This was done by using the modulus data determined for the lattice under compression (without defects) and the data of the known modulus of the dense material, then calculating the thicknesses of the two layers (when combined in a bi-material beam) that would result in the neutral axis being positioned at the interface between them when they were loaded in bending. Thus, the dense material would be entirely in compression, and the lattice entirely in tension, albeit with a non-uniform distribution of magnitude.

Lattice Manufacture

Lattice samples were built from Ti6Al4V powder using the standard build settings on an Arcam AB® A2 machine (commercially available EBM equipment). The Ti6Al4V preheat for 50 μm layers was followed by the standard Arcam Ti6Al4V 50 μm layer net theme, comprised of three contour passes followed by a hatch.

Lattice Characterization

Samples were mechanically tested in compression. A Zwick Roell Z050 test rig supporting a 50 kN load cell was used to run compression tests under a displacement-controlled regime, ensuring an initial strain rate of 10^{-3} s^{-1}. The displacement of the end plates was measured with a Zwick Roell VideoXtens video extensometer with a data capture rate of 25 frames per second. The plates were prepared in order to reduce the AM building surface roughness and generate smooth, flat surfaces to contact the loading rig.

The full field planar strain distribution was also measured for the samples of diamond lattices in the form of compression cubes, cubes which were loaded on only half of their thickness (indentation-compression) and bend samples (**Figure 1**) during testing using a 2D-DIC to measure the local strain field. The consecutive images recorded using the DIC system were also used to observe the damage mechanisms and identify the local strain values at the observed damage initiation sites. Speckle patterns were painted onto the surface of the samples in order to provide random features for the DIC analysis. The Least Square search algorithm provided by LaVision was used to analyse images using 32 pixels subsets with a step size of 19 pixels. **Figure 1A** shows the selected subset size in relation to the strut dimensions.

RESULTS AND DISCUSSION

Effect of Missing Strut Defects

The samples designed and produced to address the magnitude of the effect of severe defects which might arise during building (building errors, surface roughness related defects, or the concentration of significant levels of porosity) were tested, and the variation in Young's modulus and yield strength with defect concentration for the diamond structure is shown in **Figure 2**. As well as establishing the potential role of defects in lattice mechanics, this understanding is important for the design of components with lattices, to understand how such defects as might arise statistically during processing will affect performance.

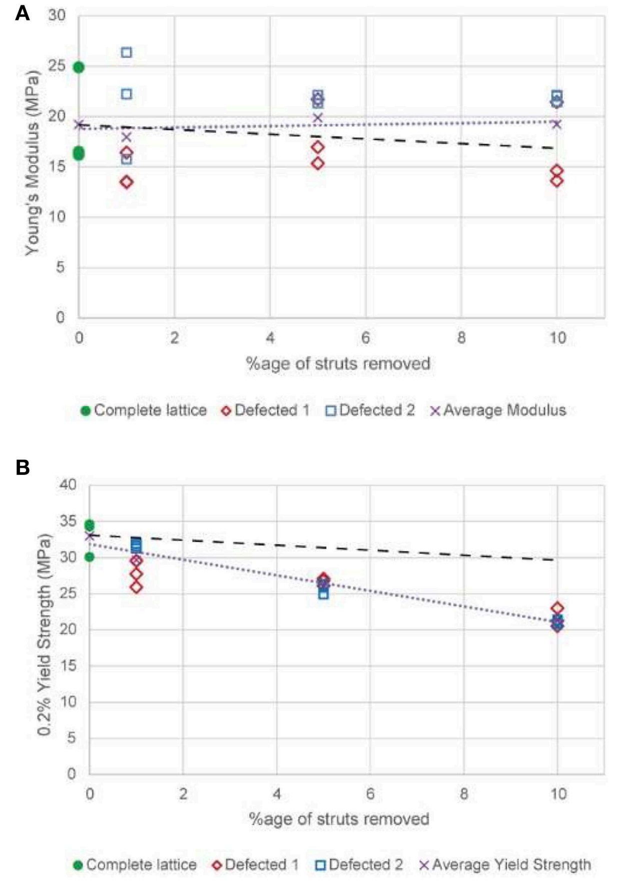

FIGURE 2 | The variation in **(A)** Young's modulus and **(B)** 0.2% offset yield strength for diamond structure lattices made with various proportions of missing struts. Defected 1 and Defected 2 represent the two different structures produced by randomly removing struts from the CAD model. The fine dotted trend lines shown represents the best least square fit to the average of all samples at a particular concentration of missing struts. The larger dotted lines represent the predictions of a simple model for the impact of the missing struts, as discussed in the text.

From **Figure 2A** it can be seen that the effect of the removal of struts, even up to a relatively high level, does not apparently have a consistent effect on the Young's modulus. The trend line for these data is almost horizontal, and there is significant scatter in the data. This indicates that there are factors other than the overall number of missing struts that have a significant effect on the Young's modulus, at least up to the maximum (and relatively elevated compared to the likely occurrence in processing) level of defects explored. The identity of one of these factors is suggested by the observation that the two different random structures formed have a significant, and roughly consistent, difference between their modulus values at all levels of defects. This indicates that for elastic behavior the location of struts removed may be especially significant, with the removal of struts from key areas (which could exist due to irregular strut shape at the microscale and non-uniform load distribution arising from the previously-removed struts) affecting the behavior much more than from others (e.g. those at the surface). This in turn would imply that within the structure some struts could be more heavily loaded than others, and that the diamond lattice (at least in the as-manufactured form, if not in the geometrically perfect version of the original CAD model design) is not optimally mechanically efficient.

In order to make an assessment of the impact of the defects which would be expected theoretically, we begin by treating the lattice as an array of separate volume elements, each with effective mechanical properties. For a perfect lattice, each of these elements has the same response to load, which has an identical stress-strain response to that of the whole lattice. Where a defect is present we assume that the resistance to load is zero, reflecting the binary nature of the defects introduced in this work (i.e., struts are either present or are entirely removed).

The volume elements can be combined in numbers equivalent to the unit cells used, to allow the correct ratio of defects to be introduced. Cells in columns along the loading direction can be combined using a Reuss (equal stress) model, which, under the simple assumption that the defected cell supports no load, gives a zero modulus for the column. Columns can be combined with a Voight (equal strain) model, giving simply that the Young's modulus of the defected material should be equal to $(1\text{-}f)E$, where f is the fraction of defects and E is the Young's modulus of the perfect lattice.

This allows the penalty of different defect concentrations to be estimated, and a line of slope $-E$ is plotted on **Figure 2A**, starting at the mean value of the complete lattice modulus, to show this effect. This line shows that there would be expected to be a negative trend, which is not clearly seen in the data, however, over the range examined, the magnitude of this trend is actually rather small, and is within both the experimental error range and the range of results produced from the different, random structures. Therefore, the results obtained are consistent with a penalty to the elastic properties of defects of the range predicted.

On the other hand, the plastic deformation results show a clear trend for decreasing strength when an increasing number of struts is removed (see **Figure 2B**), and the scatter between the different structures, and within repeat tests on the same structure, is much less. This in turn suggests that removing struts has a much greater effect on plastic behavior. The same, simplistic argument can be applied as was used to understand the elastic properties. This indicates that, under an equal stress model, the penalty for defects should be the same, i.e. that the yield stress of defected material should be $(1\text{-}f)\sigma_y$, where f is the fraction of defects and σ_y is the yield strength of the lattice in the undefected condition. A line of this slope is also plotted on **Figure 2B**.

In the case of strength, it is clearly seen that the penalty for defects in the material is higher than predicted, with the slope being closer to $-3\sigma_y$ than $-\sigma_y$. The reason for this departure is that the mechanics of deformation are more complex than for the simple model in the case of permanent deformation. It is known (e.g., Gibson and Ashby, 1997) that missing cell walls or struts in porous materials can also affect the mode of deformation, with the tendency for defects to contribute to the nucleation and propagation of deformation bands in ordered structures (Silva and Gibson, 1997). Finite element analysis could be one way of further analyzing this effect, though this is likely to be affected by underlying anisotropy of material response, such as that which could arise in titanium alloys where the microstructure has a preferential orientation, and may require specific definitions of the properties of different struts (Rashed et al., 2016). Such modeling may also be rendered more complex by the uneven surface shown by real additively manufactured lattices, which has been suggested previously to be responsible for real lattices not achieving the same level of strength as predicted by FE simulations (Ozdemir et al., 2017), though there has been recent work toward developing advanced FE approaches to incorporate these kinds of structural variations (Lozanovski et al., 2019).

Lattice samples based on a simple cubic lattice, with defects incorporated have also been produced, and, unlike the diamond lattices, have been created at various densities. Testing of these samples gave the results in **Figure 3**, showing the variation in the offset yield strength with inclusion of artificial defects. Data points plotted are the averages for different defect structures and repeats. As the lattices evidently show very different strength with density variations, the data are normalized here to the offset yield strength of the artificial defect-free lattice of the corresponding density. These data show several things in relation to the defect tolerance of lattices. Firstly, taking the cubic samples of different density collectively, the trend in behavior seems the same in each, indicating that it is the nature of the structure, rather than the amount of porosity or metal, which influences the behavior with regard to defects of this type. This is logical, as in each case a complete strut is removed; if defects of uniform size were used it might be expected that the higher density material would be affected to a lesser extent, by having more remaining metal to support load. The second observation is a striking difference between the trend for the diamond lattice structure and that for cubic. Diamond lattices show a continual, relatively gradual decline in strength with increasing concentration of defects. Cubic lattices on the other hand display an initial sharp fall in strength to less than half the initial value, which is followed by continued gradual decline, with a slope similar to the decline in strength in diamond lattices. Note that the lines in **Figure 3** correspond to a linear fit of all points for the diamond lattice data, but just the points for samples with introduced defects for cubic data.

The large decrease in compressive strength seen with cubic samples containing a low percentage of defects, contrary to the behavior of the diamond lattices, must relate to the geometrical differences between these structures. In a cubic lattice tested in compression along the axis of one of the cube edges, removal of struts may remove struts in the column orientation (i.e., lying along to loading direction), which would previously have been supporting significant load (indeed, for a sample of 5 × 5 × 5 unit cells, removal of 1% of the struts makes it slightly more likely that a strut aligned with the compression direction is removed than that one is not). The effect of this will be to change the mode of failure; rather than depending on the buckling of

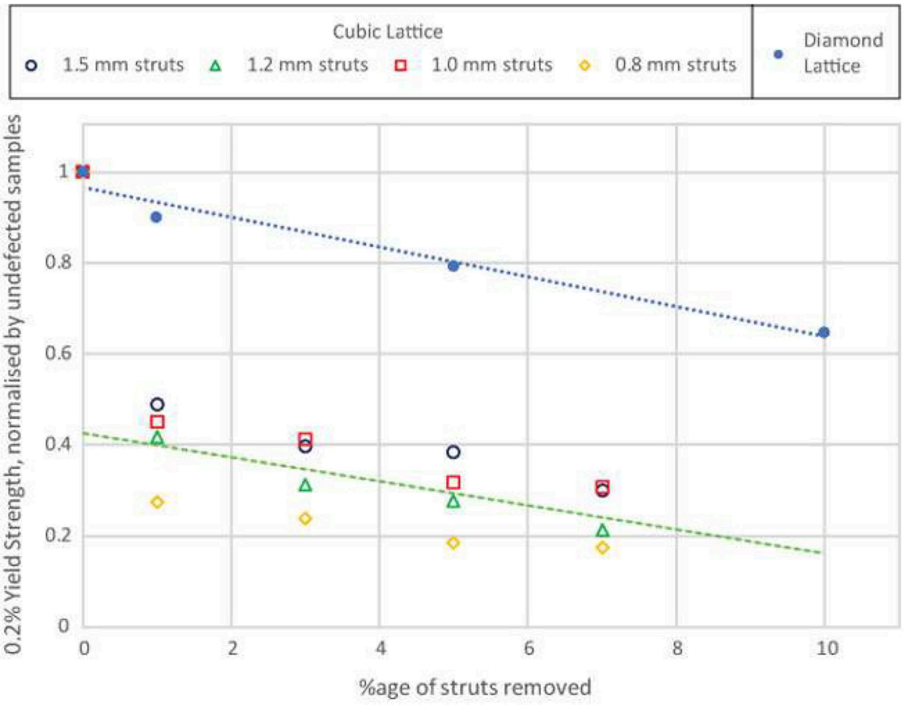

FIGURE 3 | The variation in 0.2% offset yield strength for cubic structure lattices, normalized by defect-free structures, made with various proportions of missing struts, for different densities. Data points are the averages of results from different structures and repeats with the same defect fraction. The trend line shown represents the best fit to the average of all samples at a particular concentration of missing struts.

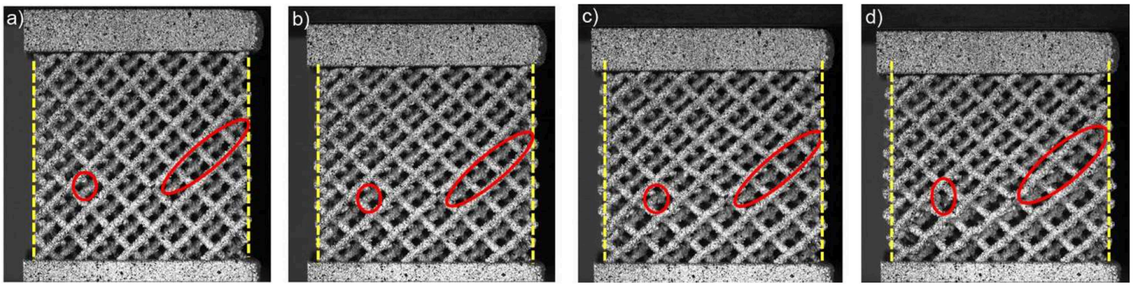

FIGURE 4 | Deformation and damage development in compression **(a)** undeformed structure, **(b)** initial buckling mode that shows barrelling effect (vertical lines added to aid observation, **(c)** damage initiation at the highlighted nodal position, **(d)** final fracture at the nodes. The video from which these stills were taken is available online.

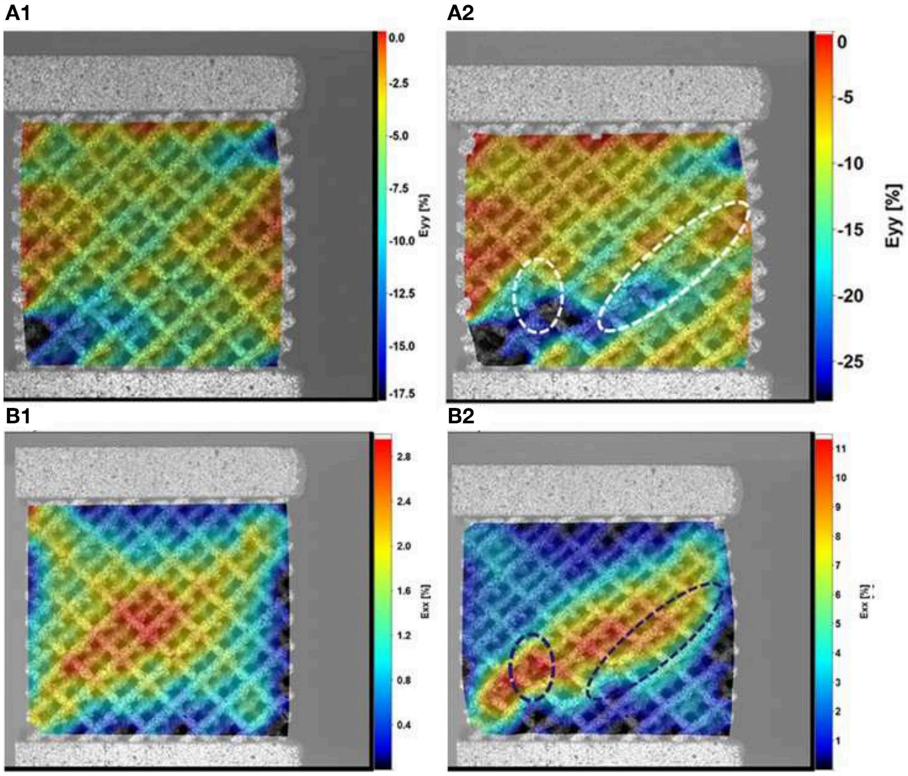

FIGURE 5 | Local strain distribution in *y* **(A1,A2)** and *x* **(B1,B2)** directions, relative to the test, for samples under compression, **(A1,B1)** at the maximum compressive force and **(A2,B2)** at the point of final fracture. The load was applied in the same direction as the build, *y* direction in the figure (vertical).

columns, the mode of the initial permanent deformation will change to the failure of cantilever beams. This change of failure mechanism between artificial defect-free and the lowest level of defects tested could explain the large fall in strength seen. For a diamond lattice, because of the multiple connectivity at nodes along the direction of load transmission, the removal of random struts is less likely to cause such a significant change in the operating failure mechanism. This greater defect dependence of the cubic lattice compared to diamond also agrees with earlier findings (Hernandez-Nava et al., 2016) that the cubic lattice is stronger for a given density, i.e., that it is more mechanically efficient.

The strength of lattice materials of different types therefore seems to be highly dependent on defects. While a theoretical description of the exact influence of defects on mechanisms of deformation is complex, worthy of further study, in this investigation we proceeded to explore the phenomena of the deformation mechanics of lattices in more detail.

Damage Mechanisms and Strain Distribution

In order to explore the mechanisms of deformation and damage in the lattices, a set of samples, including both compression and

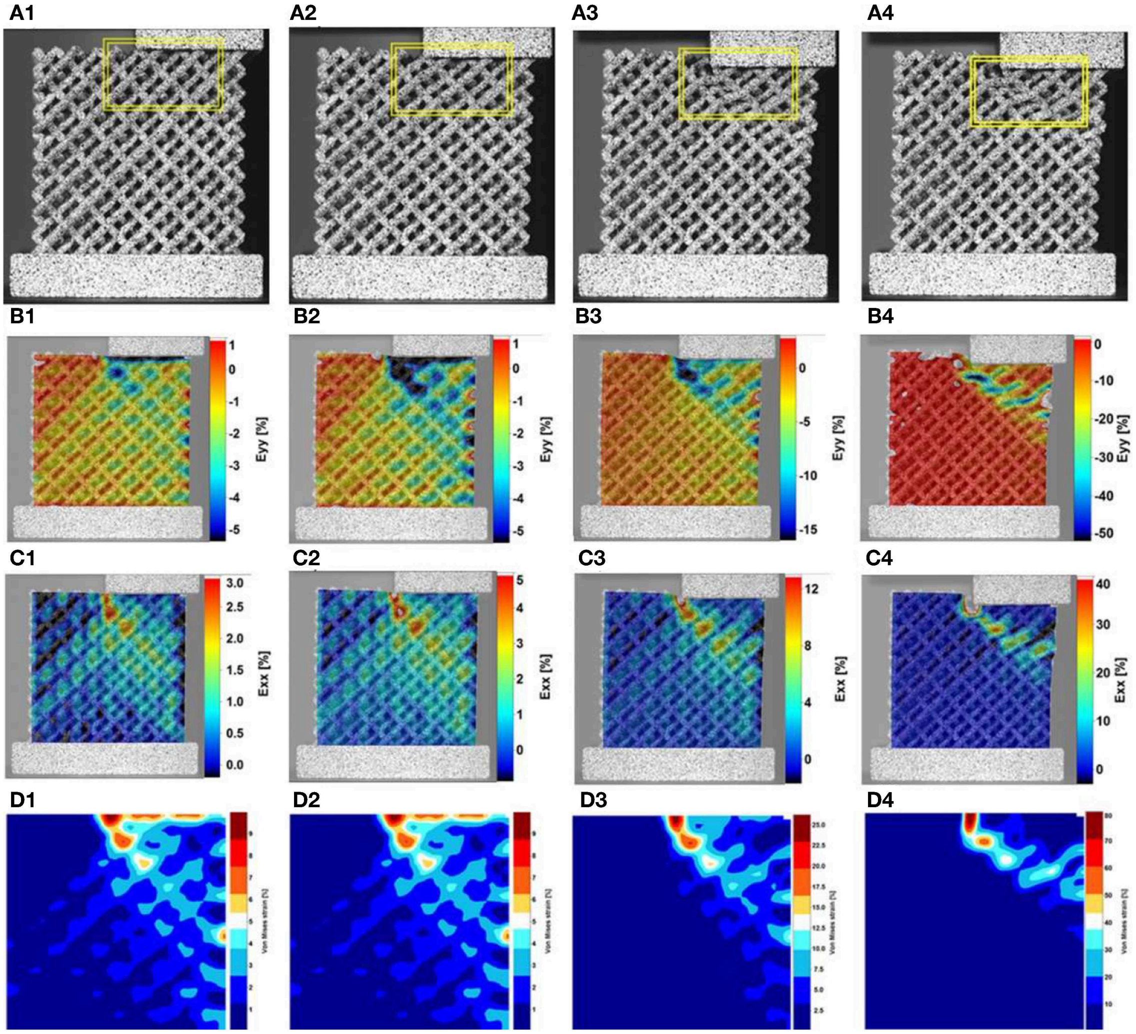

FIGURE 6 | (A1–A4) deformation and damage development in unequal compression samples. Strain distribution in directions *y* **(B1–B4)**, and *x* **(C1–C4)**, relative to the test, and **(D1–D4)** von-Mises strain distribution at various stages of deformation. The load was applied in the same direction as the build, *y* direction in the figure (vertical).

bending geometry, was made for mechanical testing combined with DIC analysis to measure the developing strain field. The bending samples were tested at the same displacement rate as the compression samples to satisfy the consistency requirements.

Deformation and damage development in samples subjected to compressive loading is shown in **Figure 4** (also available as a video online). It has been found that the solid block (which is connected to the struts at the surface nodes) restricts the deformation of the samples at the interface nodal positions. This forces the material to experience a barrelling deformation up to the maximum applied load, where damage initiates. The implemented restriction prevents failure from initiating at the upper or lower contact points, and ensures failure occurs within the body of the structure. Otherwise, the mode of failure and the failure path appear to be comparable to samples tested without the solid block. Damage starts by crack initiation at the nodal position, highlighted in red in **Figure 4**; however, no sign of catastrophic failure was observed at the struts. Similar deformation patterns were observed in the samples subjected to unequal compression experiments (where the loading is a combination of compression and indentation) wherein the compressive stress was followed by local shear deformation within the structure (**Figure 5**). Several deformation mechanisms, including tensile, compression and shear, were activated in the latter experimental setup, as the samples passed beyond the uniform compressive state. Although tensile and compressive deformation fields were observed in different parts of the samples, the failure occurred at the nodal positions located inside the localized shear zone.

The strain distributions in **Figure 6** show that the applied forces were transferred to the structure with the maximum equivalent strains measured at nodal positions in contact

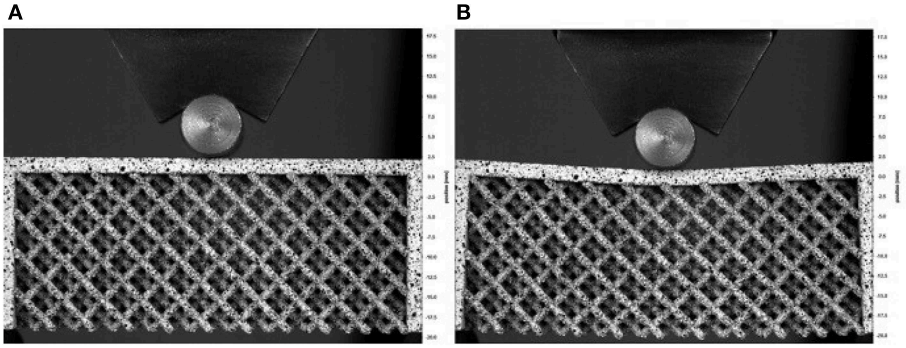

FIGURE 7 | Bending test sample **(A)** at early stages of the experiment and **(B)** just before the final failure.

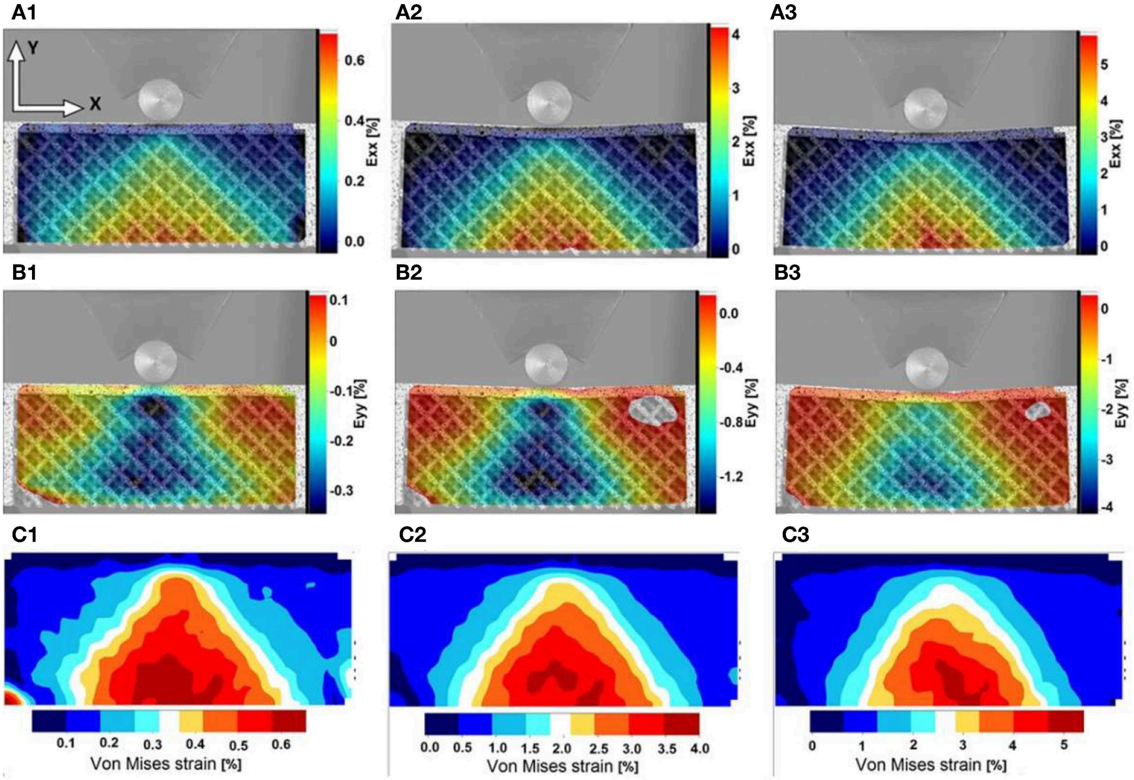

FIGURE 8 | Distribution of **(A1–A3)** axial strain E_{xx}, **(B1–B3)** axial E_{yy} and **(C1–C3)** von-Mises equivalent strain during the bending experiment showing the maximum local strain of about 5% at the onset of crack initiation and propagation within the structure.

with solid blocks (**Figure 6C1**). This is followed by further deformation localization in the regions directly below the upper block. **Figures 6A3,4** indicate that struts are bending toward the end of the experiment, leading to higher strain values in x and y directions (in plane directions in the test) at the nodes. According to the strain distributions, failure occurs at about 45° with respect to the loading direction. This shows that the sample does not undergo failure under compressive stress directly (i.e., the failure does not initiate directly under the loaded plate), rather it is a mixed-mode failure, initiated at the interface between the half plate and the struts (the loaded and unloaded regions). This is in accordance with what would be expected, with failure initiating where stress concentration occurs.

Figure 7 shows the test setup for the bending experiments before and after failure. This setup is critically important, as the lattice structure is subjected to a tensile stress field (which is difficult to engineer in samples of lattices that can be tested without risk of interface failure) and damage is observed to start from the lower set of cells where maximum tensile stress is expected. A very limited amount of plastic deformation was

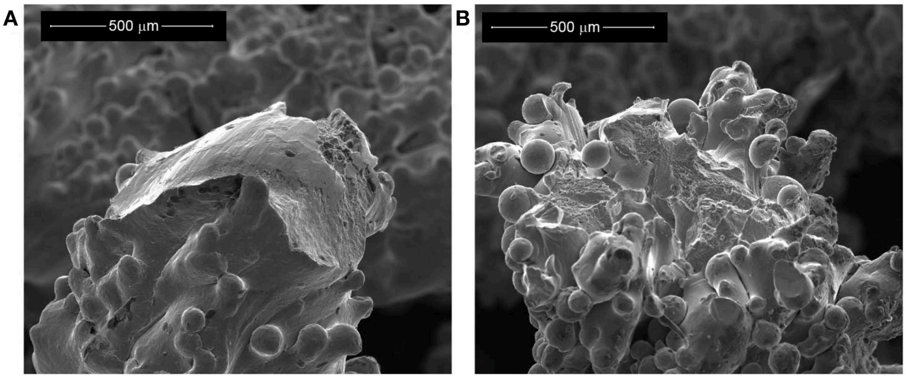

FIGURE 9 | Scanning Electron Microscope images of the post-test failure surfaces in samples deformed by compression **(A)**, and in tension **(B)**, the latter using the bending beam sample approach.

observed at the solid layer in contact with the loading roller. It should be noted that in this case the samples are imaged in the plane of the build, with the test direction being in plane.

Strain distribution within the lattice structure during the bending experiment is shown in **Figure 8** for three different times during the loading cycle which correspond to the start of the test, middle of the test and just before the failure of the sample. According to the results, the in-plane longitudinal strain (E_{xx}, **Figures 8A1–3**), representative of uni-axial stress at the tensile side of the sample, increases from the start of loading and reaches a maximum value of 5% (measured by DIC) just before fracture. The results show the strain is localized directly below the contact point with the roller where the maximum tensile stress occurs. Additionally, the distribution of the E_{yy} strain component indicates that the lattice structure is absorbing the applied deformation as the strain concentration point is shifted toward the center of the structure, away from the stress free boundaries. This may indicate that the internal layers of the structure are taking more compressive deformation compared to the free surfaces at the boundaries.

The distribution of equivalent von-Mises strain for the bending samples is shown in **Figures 8C1–3**. The equivalent strain is throughout localized at the outer layer of the structure and reaches a critical value of 5% just before failure. This value is almost identical to the E_{xx} strain; tensile deformation is considered to be the dominant mode of deformation. Therefore, the investigated lattice structures show very different mechanical behavior dependent on the nature of the applied external load, with higher resistance to failure in compression, where a total deformation of about 10% is reached, compared with tension, where the total deformation is about 5%. These measured values could be used to develop a strain-based failure criterion for more complex loading scenarios, as well as in predicting the damage tolerance of structures made from such lattices.

The presence of the different modes of deformation observed is confirmed, and their effects demonstrated, by examination of the fracture surfaces in the samples (**Figure 9**). Looking across many broken struts, failure is most frequently observed to occur at the nodes where struts interconnect, where, if the struts are imagined as bending beams [a common description in theoretical models of the deformation of porous materials (Gibson and Ashby, 1997)], the maximum equivalent strains would be expected.

The failure point is typically where a strut meets a node (the root of the strut), and not through the node itself, as this is the site of stress concentration, in a similar way to any macrostructure. Observation of the broken surfaces (such as those in **Figure 9**) shows limited local plastic deformation under both tensile and compressive loading, with cracking sometimes observed in regions of the strut away from the failure point, though this is difficult to identify consistently and with high confidence, due to the surface roughness. This effect means that struts fail before buckling, which would be theoretically predicted to be the failure mode for many lattice structures (Fan et al., 2009). The high degree of surface roughness is evident (as typically observed in EBM struts in the absence of post-processing treatment (Lhuissier et al., 2016). A significant contribution to this roughness comes from a large number of spherical features of around 50 μm in size, almost certainly particles of the original powder, which were not fully molten and have been incorporated into the strut surface.

The higher surface to volume ratio in lattice materials (i.e., more material in a lattice is within a small number of beam passes of the surface of the struts) may be expected to have an influence on the behavior. This could happen due to the surface roughness, which results in a significant amount of material that is not directly load-bearing. Furthermore, in **Figure 9** several regions can be seen where there are canyon-like surface features (similar to the type II surface defects as defined in Lhuissier et al. (2016), most likely formed as material becomes molten with incomplete melting of the solid below, leading to differences in volume and difficulty in the material producing a fully solid continuous strut (Hernandez-Nava et al., 2016). The form of such features could easily develop into cracks, either during cooling due to thermal stresses, or on loading. A high concentration of available crack-like defects could contribute to reduced failure strains in material with limited ductility, as observed here.

A further effect of the surface can be described as a skin effect. The surface region is usually formed by a contour pass that tracks the outline in the layer, while interior spaces are melted in a hatching pattern. This difference in heat input and melt pool shape, combined with additional nucleation points on unmelted powder particles, produces a finer grain structure and weaker texture at the surface, dominating where sections are < 2 mm thick (Antonysamy et al., 2013); true of the entire structure of the lattices examined here. This layer may be more prone to the propagation of cracks and would act to constrain and reduce the ductility of the interior material, in an effect similar to surface hardening. The observation from testing is, as is commonly seen in mechanical tests of EBM titanium lattices, that the ductility of the individual struts is low, and both of the effects described above (surface roughness leading to cracking and the skin effect) would promote the kinds of low-ductility failures seen.

CONCLUSIONS

This work investigates the impact of defects, in the form of engineered missing struts, on the mechanical properties of Additively Manufactured (EBM) titanium lattices with the diamond and cubic structures under compressive and tensile loading conditions.

The presence of high levels of missing strut defects, up to 10%, is not found to reduce the elastic modulus of the diamond lattices in a consistent manner; the effect appears sensitive to the precise location of such defects. On the other hand, there is a systematic decrease in strength as defect populations are increased. As shown by the comparison with cubic lattices, this decrease appears not to be influenced by the lattice density (at least when the defects comprise whole struts) but the connectivity of the lattice along the loading direction and the potential for removal of key struts to change the failure mechanism can have a large impact. This further suggests that the diamond lattice structure, which shows greater defect tolerance than the simple cubic lattice, is less mechanically efficient.

It is seen that locally failure occurs at the stress concentration at the interface between strut and node under all conditions explored, and that the failure is brittle, possibly resulting from localized tensile loading due to localized bending. The position of the failures correlating with the observed regions of highest strains indicates that a strain-based failure criterion could be applied with good accuracy for these materials. For the diamond lattice explored, the critical total deformation is about 5% for tensile conditions and about 10% for compression.

AUTHOR CONTRIBUTIONS

The experiments were conceived by RG and HG. EH-N carried out the manufacture of the specimens. SJ, LS, ET-J, MK, and DI performed the experiments and analyzed the results. The results were interpreted and the paper written by RG, EH-N, and HG.

ACKNOWLEDGMENTS

EH-N is supported by, and access to the Additive Manufacturing facilities is provided through, the EPSRC Hub Manufacture using Advance Powder Process (MAPP) (EP/P006566/1). RG would like to acknowledge a Fellowship supported by the Royal Academy of Engineering under the RAEng/Leverhulme Trust Senior Research Fellowships Scheme.

REFERENCES

Amendola, A., Hernández-Nava, E., Goodall, R., Todd, I., Skelton, R. E., and Fraternali, F. (2015). On the additive manufacturing, post-tensioning and testing of bi-material tensegrity structures. *Comp. Struct.* 131, 66–71. doi: 10.1016/j.compstruct.2015.04.038

Amendola, A., Smith, C. J., Goodall, R., Auricchio, F., Feo, L., Benzoni, G., et al. (2016). Experimental response of additively manufactured metallic pentamode materials confined between stiffening plates. *Comp. Struct.* 142, 254–262. doi: 10.1016/j.compstruct.2016.01.091

Antonysamy, A. A., Meyer, J., and Prangnell, P. B. (2013). Effect of build geometry on the β-grain structure and texture in additive manufacture of Ti-6Al-4V by selective electron beam melting. *Mater. Character.* 84, 153–168. doi: 10.1016/j.matchar.2013.07.012

Berger, J. B., Wadley, H. N. G., and McMeeking, R. M. (2017). Mechanical metamaterials at the theoretical limit of isotropic elastic stiffness. *Nature* 543, 533–537. doi: 10.1038/nature21075

Chiras, S., Mumm, D. R., Evans, A. G., Wicks, N., Hutchinson, J. W., Dharmasena, K., et al. (2002). The structural performance of near-optimized truss core panels. *Int. J. Solids Struct.* 39, 4093–4115. doi: 10.1016/S0020-7683(02)00241-X

Dumas, M., Terriault, P., and Brailovski, V. (2017). Modelling and characterization of a porosity graded lattice structure for additively manufactured biomaterials. *Mater. Des.* 121, 383–392. doi: 10.1016/j.matdes.2017.02.021

Elahinia, M., Moghaddam, N. S., Andani, M. T., Amerinatanzi, A., Bimber, B. A., and Hamilton, R. F. (2016). Fabrication of NiTi through additive manufacturing: a review. *Prog. Mat. Sci. U.S.A.* 83, 630–663. doi: 10.1016/j.pmatsci.2016.08.001

Fan, H., Jin, F., and Fang, D. (2009). Uniaxial local buckling strength of periodic lattice composites. *Mater. Des.* 30, 4136–4145. doi: 10.1016/j.matdes.2009.04.034

Fleck, N. A., Deshpande, V. S., and Ashby, M. F. (2010). Micro-architectured materials: past, present and future. *Proc. Roy. Soc. A* 466, 2495–2516. doi: 10.1098/rspa.2010.0215

Frazier, W. E. (2014). Metal additive manufacturing: a review. *J. Mater. Eng. Perform.* 23, 1917–1928. doi: 10.1007/s11665-014-0958-z

Gibson, L. J., and Ashby, M. F. (1997). *Cellular Solids.* Cambridge: Cambridge University Press.

Goodall, R. (2013). "Porous metals: foams and sponges," in *Advances in Powder Metallurgy,* eds. I. Chang and Y. Zhao (Oxford: Woodhead Publishing Limited), 273–307.

Grunsven, W.,v., Hernandez-Nava, E., Reilly, G. C., and Goodall, R. (2014). Fabrication and mechanical characterisation of titanium lattices with graded porosity. *Metals (Basel).* 4, 401–409. doi: 10.3390/met4030401

Hernandez-Nava, E., Smith, C. J., Derguti, F., Tammas-Williams, S., Leonard, F., Withers, P. J., et al. (2015). The effect of density and feature size on mechanical properties of isostructural metallic foams produced by additive manufacturing. *Acta Mater.* 85, 387–395. doi: 10.1016/j.actamat.2014.10.058

Hernandez-Nava, E., Smith, C. J., Derguti, F., Tammas-Williams, S., Leonard, F., Withers, P. J., et al. (2016). The effect of defects on the mechanical response of Ti-6Al-4V cubic lattice structures fabricated by electron beam melting. *Acta Mater.* 108, 279–292. doi: 10.1016/j.actamat.2016.02.029

Kooistra, G. W., and Wadley, H. N. G. (2007). Lattice truss structures from expanded metal sheet. *Mater. Des.* 28, 507–514. doi: 10.1016/j.matdes.2005.08.013

Lhuissier, P., Formanoir, C.,d., Martin, G., Dendievel, R., and Godet, S. (2016). Geometrical control of lattice structures produced by EBM through chemical etching: investigations at the scale of individual struts. *Mater. Des.* 110, 485–493. doi: 10.1016/j.matdes.2016.08.029

Lozanovski, B., Leary, M., Tran, P., Shidid, D., Qian, M., Choong, P., et al. (2019). Computational modelling of strut defects in SLM manufactured lattice structures. *Mater. Des.* 171:107671. doi: 10.1016/j.matdes.2019.107671

Morrish, S. J. N., Todd, I., and Goodall, R. (2017). Size effects in compression in electron beam melted Ti6Al4V diamond structure lattices. *Mater. Lett.* 190, 138–142. doi: 10.1016/j.matlet.2016.12.130

Murr, L., Gaytan, S., Ramirez, D., Martinez, E., Hernandez, J., Amato, K., et al. (2012). Metal fabrication by additive manufacturing using laser and electron beam melting technologies. *J. Mater. Sci. Technol.* 28, 1–14. doi: 10.1016/S1005-0302(12)60016-4

Ozdemir, Z., Tyas, A., Goodall, R., and Askes, H. (2017). Energy absorption in lattice structures in dynamics: nonlinear FE simulations. *Int. J. Impact Eng.* 102, 1–15. doi: 10.1016/j.ijimpeng.2016.11.016

Pan, B., Qian, K., Xie, H., and Asundi, A. (2009). Two-dimensional digital image correlation for in-plane displacement and strain measurement: a review. *Measure. Sci. Technol.* 20:062001. doi: 10.1088/0957-0233/20/6/062001

Queheillalt, D. T., and Wadley, H. N. (2009). Titanium alloy lattice truss structures. *Mater. Des.* 30, 1966–1975. doi: 10.1016/j.matdes.2008.09.015

Rashed, M. G., Ashraf, M., Mines, R. A. W., and Hazell, P. J. (2016). Metallic microlattice materials: a current state of the art on manufacturing, mechanical properties and applications. *Mater. Des.* 95, 518–533. doi: 10.1016/j.matdes.2016.01.146

Schaedler, T. A., and Carter, W. B. (2016). Architected cellular materials. *Annu. Rev. Mater. Res.* 46, 187–210. doi: 10.1146/annurev-matsci-070115-031624

Silva, M. J., and Gibson, L. J. (1997). The effects of non-periodic microstructure and defects on the compressive strength of two-dimensional cellular solids. *Int. J. Mech. Sci.* 39, 549–563. doi: 10.1016/S0020-7403(96)00065-3

Tammas-Williams, S., Zhao, H., Léonard, F., Derguti, F., Todd, I., and Prangnell, P. B. (2015). XCT analysis of the influence of melt strategies on defect population in Ti−6Al−4V components manufactured by selective electron beam melting. *Mater. Character.* 102, 47–61. doi: 10.1016/j.matchar.2015.02.008

Wally, Z. J., Grunsven, W. v., Claeyssens, F., Goodall, R., and Reilly, G. C. (2015). Porous titanium for dental implant applications. *Metals* 5, 1902–1920. doi: 10.3390/met5041902

Xu, S., Shen, J., Zhou, S., Huang, X., and Xie, Y. M. (2016). Design of lattice structures with controlled anisotropy. *Mater. Des.* 93, 443–447. doi: 10.1016/j.matdes.2016.01.007

Conflict of Interest Statement: The authors declare that the research was conducted in the absence of any commercial or financial relationships that could be construed as a potential conflict of interest.

Advantages of publishing in Frontiers

OPEN ACCESS
Articles are free to read
for greatest visibility
and readership

FAST PUBLICATION
Around 90 days
from submission
to decision

HIGH QUALITY PEER-REVIEW
Rigorous, collaborative,
and constructive
peer-review

TRANSPARENT PEER-REVIEW
Editors and reviewers
acknowledged by name
on published articles

Frontiers
Avenue du Tribunal-Fédéral 34
1005 Lausanne | Switzerland

Visit us: www.frontiersin.org
Contact us: info@frontiersin.org | +41 21 510 17 00

REPRODUCIBILITY OF RESEARCH
Support open data
and methods to enhance
research reproducibility

DIGITAL PUBLISHING
Articles designed
for optimal readership
across devices

FOLLOW US
@frontiersin

IMPACT METRICS
Advanced article metrics
track visibility across
digital media

EXTENSIVE PROMOTION
Marketing
and promotion
of impactful research

LOOP RESEARCH NETWORK
Our network
increases your
article's readership